Rubem P. Mondaini *Editor*

Trends in Biomathematics: Chaos and Control in Epidemics, Ecosystems, and Cells

Selected Works from the 20th BIOMAT Consortium Lectures, Rio de Janeiro, Brazil, 2020

Springer

Trends in Biomathematics: Chaos and Control in Epidemics, Ecosystems, and Cells

Rubem P. Mondaini
Editor

Trends in Biomathematics: Chaos and Control in Epidemics, Ecosystems, and Cells

Selected Works from the 20th BIOMAT Consortium Lectures, Rio de Janeiro, Brazil, 2020

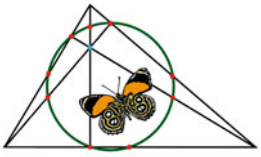

Springer

Editor
Rubem P. Mondaini
President, BIOMAT Consortium
International Institute for Interdisciplinary
Sciences
Rio de Janeiro, Brazil

Federal University of Rio de Janeiro
Rio de Janeiro, Brazil

ISBN 978-3-030-73240-0 ISBN 978-3-030-73241-7 (eBook)
https://doi.org/10.1007/978-3-030-73241-7

Mathematics Subject Classification: 92Bxx, 92-08, 92-10, 92Dxx, 92D30, 92D40, 92D99

This Springer imprint is published by the registered company Springer Nature Switzerland AG
The registered company address is: Gewerbestrasse 11, 6330 Cham, Switzerland

Preface

This book is, as a rule, a collection of selected papers for publication after a final peer-reviewed evaluation of the papers presented at the scientific sessions of the BIOMAT 2020 International Symposium. The organization of this 20th International Symposium of the BIOMAT series has been planned soon after the BIOMAT 2019, to be also the celebration of the organization of 20 international BIOMAT conferences every year since the year 2001, with the foundation of the BIOMAT Consortium (http://www.biomat.org). We did not expect the emergence of a sad, awful situation of pandemics as everybody. However, we now dare to say that we are proud to confirm that the members of the International BIOMAT Consortium community have offered clear proof of the resilience of their dedication to scientific research and their love and curiosity of the structure of natural phenomena despite all difficulties for creative work and effective scientific discussions. No retreat! No surrender! – this was written on the flag of our scientific and academic ambitions.

The BIOMAT 2020 International Symposium has been organized as an e-conference for the first time. With the help of all our colleagues/authors of accepted works for presentation on sessions of a BIOMAT conference, the BIOMAT Consortium has succeeded once more at assembling professional researchers and research students from several countries and continents. On the BIOMAT 2020, we had participants from 18 countries on 20 scientific sessions from Monday morning to Friday night, 02nd to 06th November 2020, on a scientific program of 33 contributed talks and 13 keynote speaker talks. We got an expert collaboration from RNP – the Brazilian Academic Network – and we take this opportunity to express our sincere thanks to Dr. Beatriz Zoss and Dr. Luiz Coelho from RNP for their professional expertise and all their patience to give us tips of procedure on something that had been “terra incognita” for us before the organization of the BIOMAT 2020, at least for the president of the BIOMAT Consortium!

We have also managed to cope with the difficulties of working on an e-conference, with participants living in different time zones, and we selected the Greenwich MeanTime (GMT) as a reference. The presentations have been scheduled from 10:00 a.m. to 04:45 p.m. (GMT+0) to maximize the attendance of participants in countries of four continents. We have been motivated all the time,

among all hindrances, by the aim of organizing an emblematic e-conference, with the additional duty of celebrating 20 years of a successful international series. We have done our best to succeed, but despite the success, we sincerely hope not to have to do it again.

We would like to acknowledge the gentle and efficient help of Dr. Simão C. de Albuquerque Neto from the Federal University of Rio de Janeiro for his attentive collaboration on the coordination of the e-platform during all the sessions of the BIOMAT 2020. Dr. Albuquerque Neto is also a joint author of so many contributions to the field of amino acid statistical distributions on protein domain families in which we have worked in the past years.

Since the first BIOMAT conference, in Rio de Janeiro, in 2001, and especially on this online version of the BIOMAT 2020, I have been indebted to my wife Carmem Lucia for her collaboration, patience, and belief in the difficult mission of her husband. Her continuous contribution to the staff at the BIOMAT Consortium has been invaluable during all these years.

Rio de Janeiro, Brazil
06 Nov 2020

Rubem P. Mondaini

Editorial Board of the BIOMAT Consortium

Contents

Mathematical Modeling of Macroalgae-Borne Pathogen Transmission in Corals

Susmita Halder, Samares Pal, and Joydeb Bhattacharyya

1 Introduction

Coral diseases have been identified as the most important contributors to the global degradation of coral reef ecosystems. Among all of the coral diseases, BBD (Black Band Disease) is considered as one of the most important contributors to the decline of coral reefs. Molecular examinations by Richardson [1] uncover that cyanobacteria and a complex consortium of different microorganisms are the primary causative agents of BBD. This microbial community is responsible for creating a chemical environment that digests off and dissolves the coral tissue away from the skeleton [2]. Rutzler et al. [3] point out that healthy corals can become infected with BBD by direct contact. However, field observations by Antonelli [4] recommended that apart from direct contact, injured corals may become infected with BBD when placed at a distance apart. As observed by Aeby and Santavy [5], the transmission of BBD on injured corals is vector-mediated, capable of spreading by the contaminated environment.

Several macroalgae species contain multiple hydrophobic compounds that directly damage coral tissues by transferring hydrophobic allelochemicals present on algal surfaces [6, 7]. Field observations by Andras et al. [8], Rasher et al. [9] demonstrate that corals when in contact with toxic-macroalgae species experience

We thank the anonymous reviewer for his careful reading of the manuscript entitled "Mathematical Modeling of Macroalgae-Borne Pathogen Transmission in Corals" and his many insightful comments and suggestions.

S. Halder · S. Pal (✉)
Department of Mathematics, University of Kalyani, Nadia, West Bengal, India

J. Bhattacharyya
Department of Mathematics, Karimpur Pannadevi College, Nadia, West Bengal, India

R. P. Mondaini (ed.), *Trends in Biomathematics: Chaos and Control in Epidemics, Ecosystems, and Cells*, https://doi.org/10.1007/978-3-030-73241-7_1

reduced fecundity and even higher mortality. Also, the release of allelochemicals by toxic macroalgae helps the microbes to transmit pathogens associated with corals. As the physical contact between corals and macroalgae increases owing to the proliferation of benthic macroalgae in coral reefs, the susceptibility of coral disease increases. This leads to an unhealthy and weaker coral class in coral reefs overgrown by fast-growing macroalgae. The abundance of macroalgae in coral reefs changes the community structure toward macroalgae-dominated coral reef ecosystem. The combinations of the outbreak of BBD and the proliferation of macroalgae are detrimental to coral reef ecosystems. Our model originates from the models used in [10, 11] and is a direct extension of the model studied in [11] by subdividing coral population into susceptible and infected classes and by assuming that macroalgae recruit externally from the surrounding seascape. The tissues of corals in the wake of being infected by BBD are stripped from the coral surface, and macroalgae rapidly colonize the exposed skeleton, preventing any subsequent recuperation of corals from the infection [12]. This prompts us to consider a model where the disease spreads among coral population according to a Susceptible→Infected (SI) type compartmental epidemiological model [13]. The main emphasis of this chapter will be put in analyzing the dynamic behavior of the system and finding out the long-term consequences of BBD and reduction in herbivory on coral resilience and persistence.

2 The Basic Model

Firstly, we model three benthic groups: corals, turf algae, and toxic macroalgae, competing for space on the seabed by considering a fraction of seabed available for their growth. The coral population affected by BBD is subdivided into two classes, viz. susceptible and infected. In formulating the model, we assume that macroalgae are always present in coral reef ecosystem irrespective of the abundance of corals in seabed. Let $M(t)$, $C_S(t)$, $C_I(t)$, and T be the fractions of seabed covered by macroalgae, disease-free corals, and turf algae, respectively, so that $M(t) + C_S(t) + C_I(t) + T(t) = c_0$ (constant) at any instant t. The concentration of free-living pathogen (FLP) in the environment at time t is given by $W(t)$. Susceptible corals become infectious by the contaminated environment. Infectious corals contaminate the environment by shedding pathogen that is capable of growth and survival in the environment. For simplicity, we have ignored the possibility of any empty space in the seabed. Figure 1 depicts a schematization of our eco-epidemiological model.

We make the following assumptions in formulating the mathematical model:

(H_1) Corals are overgrown by macroalgae, at a rate α.
(H_2) Macroalgae spread vegetatively over algal turfs at a rate a.
(H_3) Colonization rate of newly immigrated macroalgae on algal turf is b.
(H_4) Corals recruit to and overgrow algal turfs at a rate r.
(H_5) Macroalgae and corals have natural mortality rates d_m and d_c, respectively.

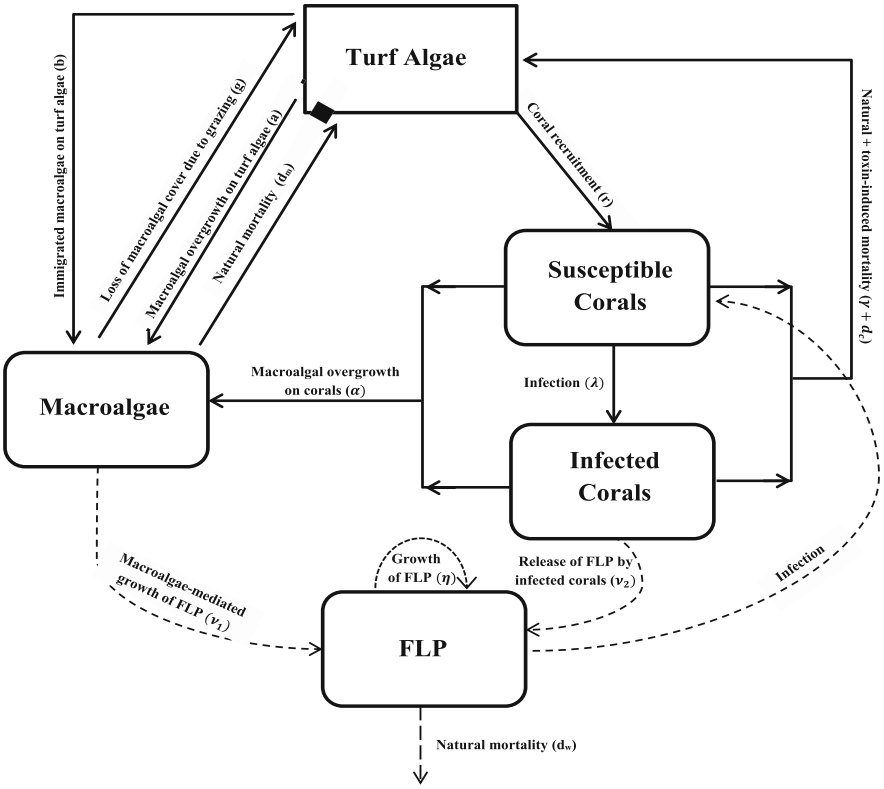

Fig. 1 Schematic representation of the eco-epidemiological model

(H_6) The death rate of corals from macroalgal toxicity is γ.

(H_7) The disease-induced death rate of infected corals is δ.

(H_8) The grazing rate of herbivorous fish on macroalgae is $\frac{g(1-\beta)}{c_0-(C_S+C_I)}$ per unit area of algal cover, where g is the maximal grazing rate of herbivorous fish in the absence of harvesting and β represents the harvest-mediated reduction in grazing of herbivorous fish ($0 \leq \beta < 1$).

(H_9) The rate of transmission of infection from the pathogens in the environment to susceptible corals is λ.

(H_{10}) The rate of release of pathogens into the environment under the influence of toxic macroalgae and infected corals are ν_1 and ν_2, respectively.

(H_{11}) The growth rate of pathogens in the environment is η.

(H_{12}) $\frac{1}{d_w}$ represents the average time that an infectious pathogen exists in the environment.

(H_{13}) $\frac{1}{k}$ represents the carrying capacity of FLP.

The equations representing reef dynamics in the presence of grazing are given by

$$\begin{aligned}
\frac{dM}{dt} &= M\left\{\alpha(C_S + C_I) - \frac{g(1-\beta)}{M+T} - d_m\right\} + (aM+b)T \\
\frac{dC_S}{dt} &= C_S\{rT - (\alpha+\gamma)M - \lambda W - d_c\} \\
\frac{dC_I}{dt} &= \lambda C_S W - C_I\{(\alpha+\gamma)M + d_c + \delta\} \\
\frac{dT}{dt} &= \frac{gM(1-\beta)}{M+T} + d_m M + (d_c + \gamma M)(C_S + C_I) + \delta C_I - T(aM + b + rC_S) \\
\frac{dW}{dt} &= \nu_1 M + \nu_2 C_I + W\{\eta(1 - kW) - d_w\},
\end{aligned} \tag{1}$$

where $0 < M(0) < 1, 0 \le C_S(0) < 1, 0 \le C_I(0) < 1, 0 < T(0) < 1$, and $W(0) > 0$.

Without any loss of generality, we assume that $c_0 = 1$. Then from (1), we obtain

$$\begin{aligned}
\frac{dM}{dt} &= M\left\{\alpha(C_S+C_I) - \frac{g(1-\beta)}{1-C_S-C_I} - d_m\right\} + (aM+b)(1-M-C_S-C_I) \equiv F^1 \\
\frac{dC_S}{dt} &= C_S\{r(1-M-C_S-C_I) - (\alpha+\gamma)M - \lambda W - d_c\} \equiv F^2 \\
\frac{dC_I}{dt} &= \lambda C_S W - C_I\{(\alpha+\gamma)M + d_c + \delta\} \equiv F^3 \\
\frac{dW}{dt} &= \nu_1 M + \nu_2 C_I + W\{\eta(1-kW) - d_w\} \equiv F^4,
\end{aligned} \tag{2}$$

where $0 < M(0) < 1, 0 \le C_S(0) < 1, 0 \le C_I(0) < 1$, and $W(0) > 0$.

We observe that right-hand sides of the equations in the system (2) are smooth functions of the variables M, C_S, C_I, W and the parameters. As long as these quantities are non-negative, local existence and uniqueness properties hold in $R^4_+ = \{(M, C_S, C_I, W) : M > 0, C_S, C_I \ge 0, W > 0\}$.

Lemma 2.1 *For all $\epsilon > 0$, there exists $t_\epsilon > 0$ such that all the solutions of* (2) *enter into the set*

$$\left\{(M, C_S, C_I, W) \in \mathbf{R}^4 : M(t) + C_S(t) + C_I(t) + W(t) < 1 + \tfrac{1}{k}\left(1 + \sqrt{\tfrac{k(\nu_1+\nu_2)}{\eta} + 1}\right) + \epsilon\right\} \text{ whenever } t \ge t_\epsilon.$$

Proof We have $\frac{d}{dt}(W(t)) \le \nu_1 + \nu_2 + \eta W(t)\{1 - kW(t)\}$.

Let $U(t)$ be the solution of $\frac{d}{dt}U(t) = \nu_1 + \nu_2 + \eta U(t)\{1 - kU(t)\}$, satisfying $U(0) = W(0)$.

Then, $U(t) = \frac{1}{k} + m\left(\frac{ce^{2mk\eta t} - 1}{ce^{2mk\eta t} + 1}\right)$, where $m = \sqrt{\frac{\nu_1+\nu_2}{k\eta} + \frac{1}{k^2}}$ and $c = \frac{m + U(0) - \frac{1}{k}}{m - U(0) + \frac{1}{k}}$.

This implies $U(t) \to m + \frac{1}{k}$, as $t \to \infty$.

Applying the standard theorem of differential inequality, it follows that $\lim_{t\to\infty} \sup W(t) \leq m + \frac{1}{k}$.

Also, $0 < M(t) + C_S(t) + C_I(t) \leq 1$ for all $t \geq 0$ implies $M(t) + C_S(t) + C_I(t) + W(t) \leq 1 + m + \frac{1}{k}$ as $t \to \infty$.

3 Equilibria and Their Stability

In this section, we determine biologically feasible equilibrium solutions of the model and investigate the dependence of their stability on several key parameters.

The system (2) possesses the following equilibria:

(i) Coral-free equilibrium $E_0 = (M_0, 0, 0, W_0)$ always exists, where $M_0 = \frac{a-b+g(1-\beta)-d_m+\sqrt{\{a-b+g(1-\beta)-d_m\}^2+4ab}}{2a}$ and $W_0 = \frac{\eta-d_w+\sqrt{(\eta-d_w)^2+4k\eta\nu_1 M_0}}{2k\eta}$.

(ii) Interior equilibrium $E^* = (M^*, C_S^*, C_I^*, W^*)$, where M^* is a positive root of the equation

$r(1 - M - f_2(M) - f_3(M)) - (\alpha + \gamma)M - \lambda f_1(M) - d_c = 0$, $C_S^* = f_3(M^*)$, $C_I^* = f_2(M^*)$ and $W^* = f_1(M^*)$, where

$f_1(M) = \frac{-B\pm\sqrt{B^2-4AC}}{2A}$, $f_2(M) = \frac{f_1(M)\{d_w-\eta(1-kf_1(M))\}-\nu_1 M}{\nu_2}$, $f_3(M) = \frac{f_2(M)}{\lambda f_1(M)}\{(\alpha+\gamma)M + d_c + \delta\}$,

$A = \frac{\lambda^2}{r^2}(aM + b)(aM - \alpha M + b)$,

$B = \frac{M\lambda}{r}\left\{\alpha\left(1 - 2M - \frac{2(\alpha+\gamma)M}{r} - \frac{2d_c}{r} - d_m\right)\right\} + \frac{\lambda(aM+b)}{r}\left\{\frac{2(\alpha+\gamma)M}{r} + \frac{2d_c}{r} + M\right\}$ and

$C = \left[M\left\{\alpha\left(1 - M - \frac{(\alpha+\gamma)M}{r} - \frac{d_c}{r}\right) - d_m\right\} + (aM + b)\left(\frac{(\alpha+\gamma)M}{r} + \frac{d_c}{r}\right)\right] \cdot \left(M - \frac{(\alpha+\gamma)M}{r} - \frac{d_c}{r}\right) - g(1-\beta)M.$

At E_0, the eigenvalues of the Jacobian matrix of the system (2) are $-\sqrt{\{a - b + g(1-\beta) + d_m\}^2 + 4ab}$, $r - d_c - M_0(r + \alpha + \gamma) - \lambda W_0$, $-\{(\alpha+\gamma)M_0 + d_c + \delta\}$ and $-\sqrt{(\eta - d_w)^2 + 4k\eta\nu_1 M_0}$.

Therefore, all the eigenvalues of the Jacobian matrix at E_0 are negative if $\lambda > \frac{r-d_c-M_0(r+\alpha+\gamma)}{W_0}$. This gives the following lemma:

Lemma 3.1 *The system* (2) *is locally asymptotically stable at* E_0 *if* $\lambda > \frac{r-d_c-M_0(r+\alpha+\gamma)}{W_0}$.

Therefore, with high BBD-transmission rate, the system stabilizes at macroalgae-dominated steady state with complete elimination of corals.

Lemma 3.2 *If* $\alpha > g(1-\beta) + a + \frac{b}{M_0}$, *the system* (2) *undergoes a transcritical bifurcation at* E_0 *when* λ *crosses* $\lambda_* = \frac{r-d_c-M_0(r+\alpha+\gamma)}{W_0}$.

Proof At $\lambda = \lambda_*$, the Jacobian matrix J_0 at E_0 becomes

$$\begin{pmatrix} -\sqrt{(b-a+g(1-\beta)+d_m)^2+4ab} & 0 & 0 & v_1 \\ \{\alpha-g(1-\beta)-a\}M_0-b & 0 & \lambda W_0 & 0 \\ \{\alpha-g(1-\beta)-a\}M_0-b & 0 & -\{(\alpha+\gamma)M_0+d_c+\delta\} & v_2 \\ 0 & 0 & 0 & -\sqrt{(\eta-d_w)^2+4k\eta v_1 M_0}. \end{pmatrix}^T$$

Therefore, the zero eigenvalue of the Jacobian matrix is simple.

Let V and W be the eigenvectors corresponding to the zero eigenvalues for J_0 and J_0^T, respectively.

Then, we obtain $V = \begin{pmatrix} v_1 & v_2 & v_3 & v_4 \end{pmatrix}^T$ and $W_1 = \begin{pmatrix} 0 & 1 & 0 & 0 \end{pmatrix}^T$, where $v_1 = \frac{[\{\alpha-g(1-\beta)-a\}M_0-b]\{(\alpha+\gamma)M_0+d_c+\delta+\lambda W_0\}}{\lambda W_0}$, $v_2 = \frac{(\alpha+\gamma)M_0+d_c+\delta}{\lambda W_0}$, $v_3 = 1$ and

$v_4 = \frac{v_1[\{\alpha-g(1-\beta)-a\}M_0-b]\{(\alpha+\gamma)M_0+d_c+\delta+\lambda W_0\}+\lambda v_2 W_0}{\lambda W_0\sqrt{(\eta-d_w)^2+4k\eta v_1 M_0}}$.

Let us express the system (2) in the form $\dot{X} = f(X;\lambda)$, where $X = \begin{pmatrix} M & C_S & C_I & W \end{pmatrix}^T$ and $f(X;\lambda) = \begin{pmatrix} F^1 & F^2 & F^3 & F^4 \end{pmatrix}^T$.

Then, we have $W^T f_\lambda(E_0;\lambda_*) = 0$, and so no saddle-node bifurcation occurs at E_0 when λ crosses λ_*.

Also, $Df_\lambda(E_0;\lambda_*)V = \begin{pmatrix} 0 & -\frac{(\alpha+\gamma)M_0+d_c+\delta}{\lambda} & \frac{(\alpha+\gamma)M_0+d_c+\delta}{\lambda} & 0 \end{pmatrix}^T$ and so

$W^T[Df_\gamma(E_0;\lambda_*)V] = -\frac{(\alpha+\gamma)M_0+d_c+\delta}{\lambda} < 0.$

Also, we have

$$D^2 f(E_0;\lambda_*)(V,V) = \begin{pmatrix} -2av_1^2+2v_1\{\alpha-a-g(1-\beta)\}(v_2+1)-4gM_0(1-\beta)(v_2^2+v_2+1) \\ -2(r+\alpha+\gamma)v_1v_2-2rv_2-2\lambda v_2v_4-2rv_2^2 \\ -2(\alpha+\gamma)v_1+2\lambda v_2v_4 \\ -2kv_4^2. \end{pmatrix}$$

This gives $W^T[D^2 f(E_0;\lambda_*)(V,V)] = -2v_2[(r+\alpha+\gamma)v_1+r(1+v_2)+\lambda v_4]$.

If $\alpha > g(1-\beta)+a+\frac{b}{M_0}$ holds, then $W^T[D^2 f(E_0;\lambda_*)(V,V)] < 0$, and so, by Sotomayor's theorem [14], it follows that the system (2) undergoes a transcritical bifurcation at E_0 when λ crosses λ_* (cf. Fig. 2a).

The system is persistent if the boundary equilibrium E_0 repels interior trajectories [15]. The condition given in the following lemma rules out the possibility of extinction of any organism in the system.

Lemma 3.3 *All the organisms in the system will persist if* $\lambda < \lambda_*$.

The characteristic equation of the Jacobian J^* of the system (2) evaluated at E^* is $\mu^4 + A\mu^3 + B\mu^2 + C\mu + D = 0$, where

$A = aM^* + \frac{b}{M^*}(1-C_S^*-C_I^*) + \left(r+\frac{\eta}{C_I^*}\right)C_S^*,$

$B = B_1 + \left\{(\alpha-a)M^* - b - \frac{gM^*}{(1-C_S^*-C_I^*)^2}\right\}B_2,\ C = C_1 - \left\{(\alpha-a)M^* - b - \frac{gM^*}{(1-C_S^*-C_I^*)^2}\right\}C_2,$

$B_1 = \left[\left(aM^* + \frac{b(1-C_S^*-C_I^*)}{M^*}\right)\left(r+\frac{\eta}{C_I^*}\right) + (r+\lambda)(\lambda C_I^*+\eta) + \frac{r\eta C_S^*}{C_I^*}\right]C_S^*,$

$B_2 = (r+\alpha)C_S^* + \alpha C_I^*,\ C_1 = \left\{(r+\lambda)(\lambda C_I^*+\eta) + \frac{r\eta C_S^*}{C_I^*}\right\}\left(aM^* + \frac{b(1-C_S^*-C_I^*)}{M^*}\right)C_S^*,$

$C_2 = \left\{(2\alpha+r)\lambda C_I^* + \left(1-\frac{C_S^*}{C_I^*}\right)(r+\alpha)\eta\right\}C_S^*,$

$D = P_1 + \left\{(\alpha-a)M^* - b - \frac{gM^*}{(1-C_S^*-C_I^*)^2}\right\}P_2,$

$P_1 = \left[\left(aM^* + \frac{b(1-C_S^*-C_I^*)}{M^*}\right)\left(aM^* + r + \frac{\eta}{C_I^*} + \frac{b(1-C_S^*-C_I^*)}{M^*}\right) + \frac{r\eta C_S^*}{C_I^*} + (r+\lambda)(\lambda C_I^*+\eta)\right]\left(r+\frac{\eta}{C_I^*}\right)C_S^*,$

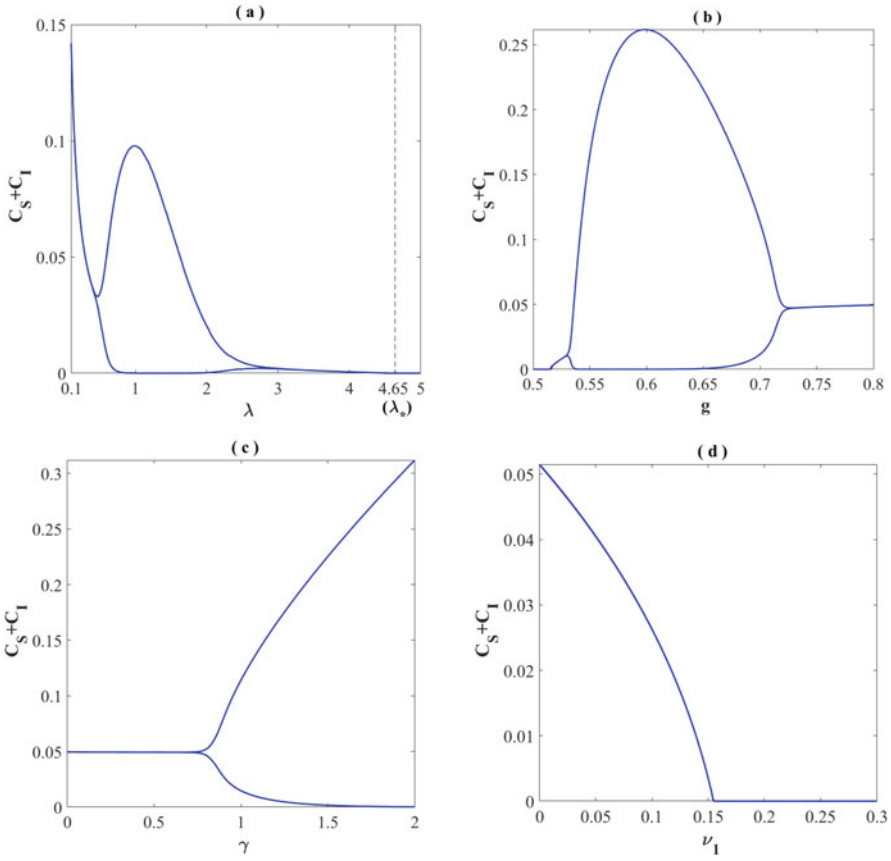

Fig. 2 Bifurcation diagrams of (**a**) λ, (**b**) g, (**c**) γ, and (**d**) ν_1 versus the equilibrium value of coral cover

and $P_2 = \left(aM^* + rC_S^* + \frac{b(1-C_S^*-C_I^*)}{M^*}\right)\{(r+\alpha)C_S^* + \alpha C_I^*\} + (r+2\alpha)(\eta + \lambda C_I^*)C_S^*$.

Also, we have $A, C_1 > 0$ and $B_i, P_i > 0 (i = 1, 2)$.

Therefore, the system (2) is locally asymptotically stable at E^* if $AB > C$ and $ABC > C^2 + A^2D$.

Also, we have $A, C_1 > 0$ and $B_i, P_i > 0 (i = 1, 2)$.

Now, we will study the Hopf bifurcation of the system (2) at E^*, taking g as the bifurcation parameter.

Solving $ABC - C^2 - A^2D = 0$, the critical value of bifurcation parameter g can be obtained, say $g = g^*$.

At $g = g^*$, the characteristic equation is

$$\left(\mu^2 + \frac{C}{A}\right)\left(\mu^2 + \mu A + \frac{AD}{C}\right) = 0.$$

For $g = g^*$, let $\mu_i (i = 1, \ldots, 4)$ be the roots of the characteristic equation with the pair of purely imaginary roots as $\mu_1 = i\omega_0$ and $\mu_2 = \bar{\mu_1}$, where $\omega_0 = \sqrt{\frac{C(g^*)}{A(g^*)}}$.

Now, if μ_3 and μ_4 are not real, then $Re\mu_3 = \frac{\mu_3+\mu_4}{2} = -\frac{1}{2}A(g^*) < 0$. If μ_3 and μ_4 are real roots, then $\mu_3 + \mu_4 < 0$ and $\mu_3\mu_4 = \frac{A(g^*)D(g^*)}{C(g^*)} = \frac{D(g^*)}{\omega_0^2} > 0$ implies $\mu_3, \mu_4 < 0$.

Therefore, only a pair of eigenvalues of the characteristic equation $F(\mu) = 0$ at $g = g*$ are purely imaginary.

Let $\psi(g) = A(g)B(g)C(g) - (C(g)^2 + A(g)^2D(g))$. Since ψ is continuously differentiable function of g, then there exists an open interval $(g^* - \epsilon, g^* + \epsilon)$ such that $\mu_i(g) = p_i(g) + iq_i(g)$, for all $g \in (g^* - \epsilon, g^* + \epsilon)$.

To verify the condition of Hopf bifurcation at $g = g^*$, we put $p+iq$ in $F(\mu) = 0$, and then separating the real and imaginary parts, we obtain

$$p^4 + p^3A + p^2(B - 6q^2) + p(C - 3q^2A) + q^4 + D = 0$$

and

$$q^2(4p + A) = 4p^3 + 3p^2A + 2pB + C.$$

Differentiating $F(\mu) = 0$ with respect to g and then putting $g = g^*$, we get

$$\left(\frac{dp_i}{dg}\right)\Big|(g = g^*) = \left(\frac{KL_1 - LK_1}{JK_1 - J_1K}\right)(g = g^*) \neq 0, \tag{3}$$

$If K(g^*)L_1(g^*) \neq K_1(g^*)L(g^*)$ and $J(g^*)K_1(g^*) \neq J_1(g^*)K(g^*)$ which is the transversality condition of Hopf bifurcation, where $J = 4p^3 + 3Ap^2 + (2B - 12q^2)p + C - 3Aq^2$, $K = -12p^2 - 6pqA + 4q^3$, $L = p^3A' + p^2B' + pC' - 3pq^2A' + D'$, $J_1 = 12p^2 + 6Ap + 2B - 4q^2$, $K_1 = -2Aq - 8pq$, $L_1 = 3p^2A' + 2pB' + C' - q^2A'$.

Therefore, the above system undergoes a Hopf bifurcation if

(i) $A(g^*), B(g^*), C(g^*), D(g^*) > 0$.
(ii) $A(g^*)B(g^*) > C(g^*)$.
(iii) $A(g^*)B(g^*)C(g^*) > C(g^*)^2 + A(g^*)^2D(g^*)$.
(iv) $K(g^*)L_1(g^*) \neq K_1(g^*)L(g^*)$, $J(g^*)K_1(g^*) \neq J_1(g^*)K(g^*)$.

We investigate numerically the effect of the various parameters on the qualitative behavior of the system using parameter values given in Table 1 throughout, unless otherwise stated.

To identify the impact of infection rate (λ) on coral cover, in Fig. 2a, we plot the solutions of the nullcline equations in the $(C_S+C_I)-\lambda$ plane, yielding a bifurcation diagram. It is observed that at a low infection rate, there is a high coral cover. As the infection rate increases, the system undergoes a Hopf bifurcation leading to an oscillatory dynamics of the system. From Fig. 2a, it is seen that the periodic orbits emerging from a Hopf bifurcation start to grow with an increase in the values of λ

Table 1 Parameter values used in the numerical analysis

Parameters	Description of parameters	Value	Reference
α	Macroalgal overgrowth rate on corals	0.1	[16]
β	Harvest-mediated grazing loss	0.1	[17]
γ	Toxin-induced death rate of infected corals	0.1	[17, 18]
δ	Disease-induced death rate of infected corals	0.1	–
r	Recruitment rate of susceptible corals on turf algae	0.55	[16]
a	Macroalgal vegetative growth rate on algal turfs	0.77	[16]
b	Immigration rate of macroalgae on algal turf	0.005	[16]
d_m	Natural mortality rate of macroalgae	0.1	[11]
d_c	Natural mortality rate of corals	0.24	[16]
g	Maximal macroalgae-grazing rate of herbivores	0.8	[16]
λ	Rate of infection	0.3	[18]
ν_1	Rate of release of FLP by macroalgae	0.01	[18]
ν_2	Pathogen-shedding rate by infectious corals	0.3	[18]
$\frac{1}{d_m}$	Average time FLPs exist in environment	100	[18]
$\frac{1}{k}$	Carrying capacity of FLP	3	–
η	Intrinsic growth rate of FLP	0.001	–

before reaching to a peak value. After that, the periodic orbits start shrinking with the increase in the value of λ, and eventually the system becomes stable with a low coral cover (when $\lambda < \lambda_*$). For $\lambda > \lambda_*$, the coral becomes extinct from the system.

From Fig. 2b, we see that for a low grazing rate (g), the corals will no longer be able to survive in the system. With an increase in the grazing rate, initially, the system turns to an oscillatory state from a low macroalgae-dominated coexistence state followed by a coral-dominated stable coexistence state.

Figure 2c shows the effect of macroalgal toxicity (γ) on corals. It is observed that the system becomes stable at the coexistence steady state when the macroalgal toxicity is low. With an increase in the value of γ, the system undergoes a Hopf bifurcation at some critical value of γ. Figure 2c refers to a bifurcation diagram showing the growth of periodic orbits emerging from a Hopf bifurcation of the system as γ is increased.

To identify the role of macroalgae on the growth of FLP, in Fig. 2d, we plot a bifurcation diagram with ν_1 as a bifurcation parameter. It is observed that the coral cover gradually decreases with the increase in the value of ν_1, and eventually, the corals cease to exist in the system when the value of ν_1 crosses some critical threshold.

Figure 3a represents a bifurcation diagram of α versus equilibrium value of coral cover. It is observed that any increase in the macroalgal growth rate decreases the coral cover. When the macroalgal growth rate becomes sufficiently high, corals can no longer survive and the system becomes macroalgae-dominated and coral-free.

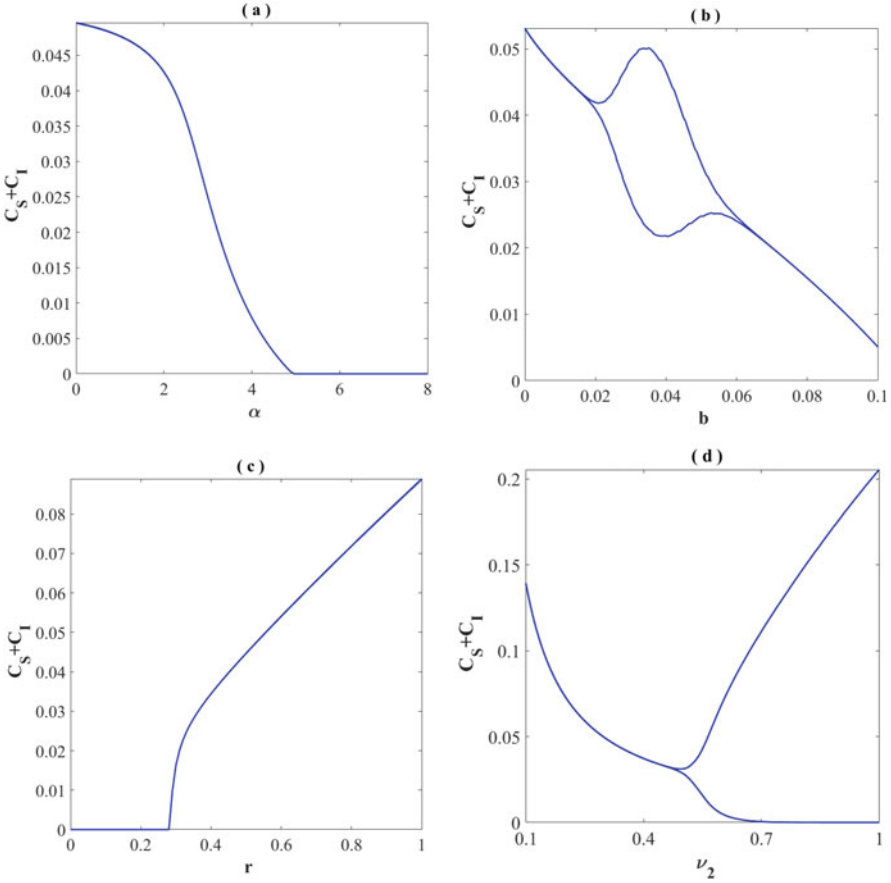

Fig. 3 Bifurcation diagrams of (**a**) α, (**b**) b, (**c**) r, and (**d**) ν_2 versus the equilibrium value of coral cover

To identify the impact of macroalgal immigration rate (b) on coral cover, in Fig. 3b, we plot the solutions of the nullcline equations, yielding a bifurcation diagram. It is observed that the coral cover becomes high with minimal colonization of macroalgae on algal turf. With an increase of the macroalgal colonization rate, the coral cover starts getting depleted followed by an oscillatory coexistence state and an eventual complete elimination of the corals.

Figure 3c represents the effect on the coral cover for different growth rates of corals (r). It is observed that, under macroalgal toxicity, the diseased corals cannot be able to survive in the system if their growth rates are sufficiently low. It is also observed that the faster-growing corals have a greater chance of survival in the system amid macroalgal toxicity and coral disease.

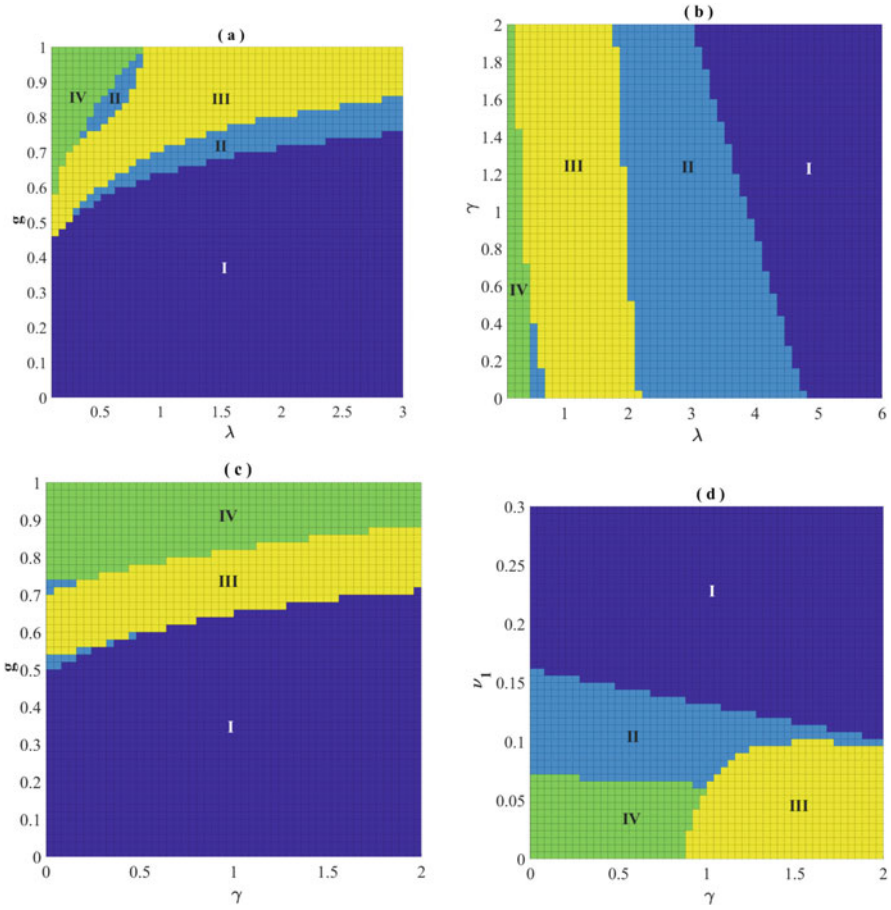

Fig. 4 Two-parameter bifurcation plots with (**a**) λ, g as active parameters, (**b**) λ, γ as active parameters, (**c**) γ, g as active parameters, and (**d**) γ, ν_1 as active parameters (region-I indicates coral-depleted state; region-II indicates macroalgae-dominated coexistence state; region-III indicates oscillatory coexistence state; region-IV indicates coral-dominated coexistence state)

From Fig. 3d, we see that low shedding rate of FLP by infected corals stabilizes the system at the coexistence state, while higher pathogen-shedding rate by infected corals changes the dynamics of the system to an oscillatory coexistence state.

To identify the combined effect of λ and g on coral cover, in Fig. 4a, we plot a two-parameter bifurcation diagram with λ and g as active parameters. It is observed that the lower grazing rate is detrimental to the survival of corals even with low disease transmission rate. A coral-dominated coexistence state (cf. Fig. 4a, region-IV) exists only when the grazing rate is sufficiently high together with low disease transmission rate. It is also observed that even with high grazing rate, the system

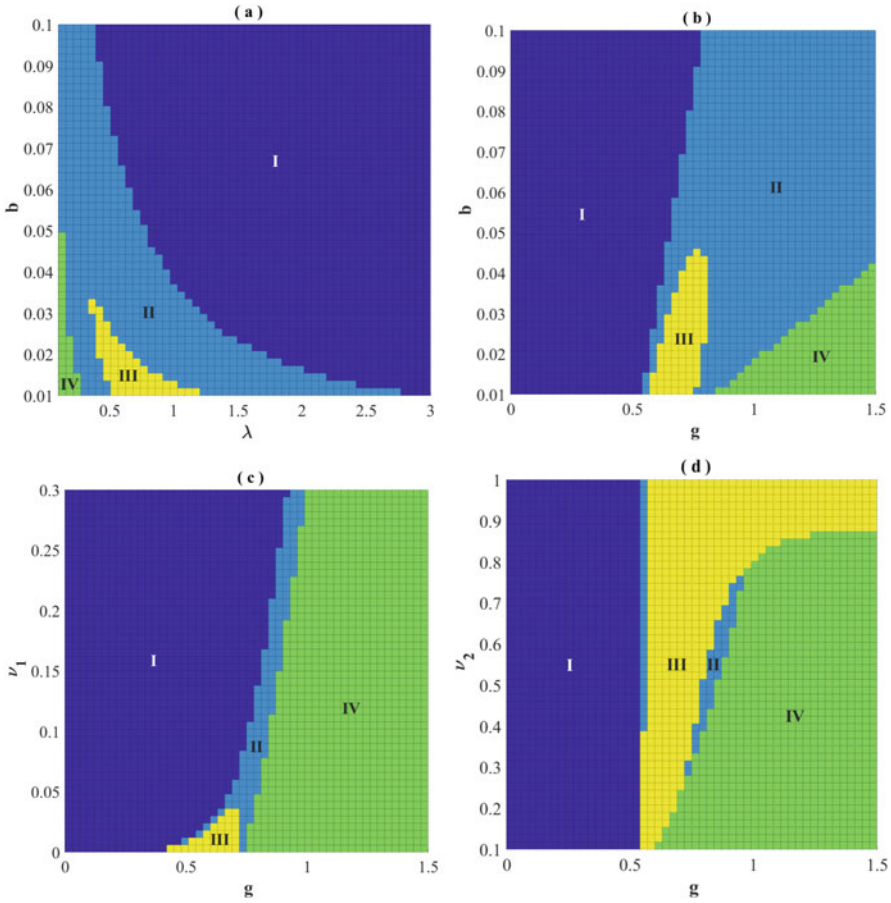

Fig. 5 Two-parameter bifurcation plots with (**a**) λ, b as active parameters, (**b**) g, b as active parameters, (**c**) g, ν_1 as active parameters, and (**d**) g, ν_2 as active parameters (region-I indicates coral-depleted state; region-II indicates macroalgae-dominated coexistence state; region-III indicates oscillatory coexistence state; region-IV indicates coral-dominated coexistence state)

becomes oscillatory (cf. Fig. 4a, region-III) when the disease transmission rate is high.

The impact of macroalgal colonization rate on turf algae (b) together with disease transmission rate on the coral cover is represented in Fig. 5a. It is observed that the coral-dominated stable state exists only at a low infection rate and low macroalgal immigration rate. It is also observed that as the algal immigration rate increases, the basin of attraction of the stable coexistence state shrinks.

To identify the combined effect of λ and γ on coral cover, in Fig. 4b, we plot a two-parameter bifurcation diagram with λ and γ as active parameters, keeping all other parameters as in Table 1. It is observed that with a low disease transmission rate, the system becomes stable at the coral-dominated coexistence state (cf. Fig. 4b, region-IV) even at a high macroalgal toxicity level. With an increase in the disease transmission rate, the system becomes oscillatory (cf. Fig. 4b, Region-III). Further, increase in the transmission rate stabilizes the system at a macroalgae-dominated coexistence state (cf. Fig. 4b, region-II) followed by the complete elimination of the corals (cf. Fig. 4b, region-I). When the system is stable at macroalgae-dominated coexistence state, increase in macroalgal toxicity rate eliminates corals from the system.

The combined effect of the parameters γ and g on the coral cover is given in Fig. 4c. It is seen that with sufficiently high grazing rate, the system will be coral-dominated irrespective of macroalgal toxicity level. From Fig. 4d, it is seen that a coral-dominated stable state is only possible when the macroalgal toxicity is low and when macroalgae-mediated pathogen growth is at a low level.

The combined effect of grazing and macroalgal immigration rate is represented by Fig. 5b. It is seen that grazing plays an active role in the existence of the coexistence state of the system, while the rate of macroalgal immigration plays a dominant role for the switching of coral-dominated coexistence state to macroalgae-dominated coexistence state. It is seen that the coral-dominated coexistence state exists only when the grazing rate is sufficiently high and the macroalgal immigration rate is low. Figure 5c and d show the combined effect of grazing and pathogen-shedding rates by macroalgae and infected corals, respectively. While either figure shows that lower grazing rate is detrimental for corals, with high grazing rate the system becomes coral-dominated even with high macroalgae-mediated pathogen growth (cf. Fig. 5c). On the other hand, with high grazing rate the coral-dominated state is only possible when the pathogen-shedding rate by infected corals is low (cf. Fig. 5d).

4 Discussion

We have considered an eco-epidemiological model to study the dynamics of coral reef benthic system in which macroalgae and corals are competing to occupy turf algae in the presence of microbial infection on corals. In our model, the immigration of algae from other areas of the seabed is taken into account. Underwood et al. [19] observed that for some coral reefs, it may be appropriate to exclude the immigration of coral larvae. We model a coral reef ecosystem in which coral larvae do not immigrate. Firstly, we analyze the system in the absence of time delays. We first perform equilibrium and stability analysis on our 4D non-linear ODE model and find that the model is capable of exhibiting a transcritical bifurcation associated with the elimination of corals and a Hopf bifurcation arises when the rate of disease transmission becomes high. The effect of grazing on hysteresis supports the observations from previous modeling analyses by Blackwood et al. [11], Mumby

et al. [10], and Fung et al. [20, 21]. It is noteworthy that in our model, grazing played an important role in the existence of the coral-dominated stable state. It is observed that at a high microbial infection rate, the system initially becomes oscillatory by undergoing a Hopf bifurcation at the coexistence state followed by a coral-depleted stable state. In this case, the extinction of coral population is due to natural fluctuations that become very likely when the oscillation drives the coral population to small size. Further, analytical and numerical simulations demonstrate the following conclusions:

(i) The corals get eliminated from the system when the macroalgal grazing rate by herbivores is low. Increase of grazing intensity by herbivores increases the resilience of the coral-dominated regime, justifying the observations of Blackwood et al. [11] and Mumby et al. [10]. The system exhibits a Hopf bifurcation when the grazing intensity is increased from a low threshold level, resulting in a change of transition from a macroalgae-dominated stable state to an oscillatory coexistence state.
(ii) The system becomes macroalgae-dominated when the macroalgal immigration on algal turfs becomes high. In this case, a higher rate of herbivory stabilizes the system at the coral-dominated state, while a higher rate of disease transmission stabilizes the system at the coral-free stable state.
(iii) A coral-dominated stable state exists when both the macroalgae-mediated FLP growth and disease transmission rate are low.
(iv) Even with a high macroalgal toxicity level on corals, higher grazing rate by herbivores helps in retaining a coral-dominated steady state.

From analytical and numerical observations, we observe that higher grazing rate of herbivores increases the resilience of the coral-macroalgae coexistence regime. Further, the colonization rate of macroalgae on algal turf is detrimental to the coral reef ecosystem affected by the coral disease.

Acknowledgments SH was supported by the fellowship from the Council of Scientific and Industrial Research (CSIR), Govt. of India. JB was supported by the grants from West Bengal State Council of Science and Technology (WBSCST), Govt. of West Bengal, India (Grant No. ST/P/S&T/16G-06/2018). SP acknowledges the financial grants from WBSCST, Govt. of West Bengal, India (Grant No. ST/P/S&T/16G-22/2018).

References

1. L.L. Richardson, Black band disease. *In: Rosenberg E, Loya Y (eds) Coral health and disease*, Springer, Heidelberg, (2004), 325–336.
2. S.H. Sokolow, P. Foley, J.E. Foley, A. Hastings and L.L. Richardson, *Disease dynamics in marine metapopulations: modelling infectious diseases on coral reefs*, Journal of Applied Ecology, **46**, (2009), 621–631.
3. K. Rützler and D.L. Santavy, *The Black Band Disease of Atlantic Reef Corals: I. Description of the Cyanophyte Pathogen*, P.S.Z.N.I. Mar. Ecol., **4(4)**, (1983), 301319.

4. P.L. Antonelli, *Nonlinear allometric growth. I. Perfectly cooperative systems*, Mathematical Modelling, **4(4)**, (1983), 367–372.
5. G.S. Aeby and D.L. Santavy, *Factor affecting susceptibility of the coral Montastrea faveolata to black-band disease*, Mar. Ecol. Prog. Ser., **318**, (2006), 103–110.
6. R.M. Bonaldo, M.E. Hay, *Seaweed-Coral Interactions: Variance in Seaweed Allelopathy, Coral Susceptibility, and Potential Effects on Coral Resilience*, PLOS ONE, **9(1)**, (2014), e85786.
7. C.L. Birrell, L.J. McCook, B.L. Willis, L. Harrington, *Chemical effects of macroalgae on larval settlement of the broadcast spawning coral Acropora millepora*, Marine Ecology Progress Series, **362**, (2008), 129–137.
8. T.D. Andras, T.S. Alexander, A. Gahlena, R.M. Parry, F.M. Fernandez, J. Kubanek, M.D. Wang, M.E. Hay, *Seaweed allelopathy against coral: surface distribution of seaweed secondary metabolites by imaging mass spectrometry*, Journal of Chemical Ecology, **38**, (2012), 1203–1214.
9. D.B. Rasher, E.P. Stout, S. Engel, J. Kubanek, M.E. Hay, *Macroalgal terpenes function as allelopathic agents against reef corals*, Proceedings of the National Academy of Sciences, **108(43)**, (2011), 17726–17731.
10. P.J. Mumby, A. Hastings, H.J. Edwards, *Thresholds and the resilience of Caribbean coral reefs*, Nature, **450**, (2007), 98–101.
11. J.C. Blackwood, A. Hastings, P.J. Mumby, *The effect of fishing on hysteresis in Caribbean coral reefs*, Theoretical Ecology, **5**, (2012), 105–114.
12. S.H. Yee, D.L. Santavy and M.G. Barron, *Assessing the effects of disease and bleaching on Florida Keys corals by fitting population models to data*, Ecological Modelling, **222**, (2011), 1323–1332.
13. A.M. Bate and F.M. Hilker, *Complex Dynamics in an Eco-epidemiological Model*, Bull. Math. Biol., **75**, (2013), 2059–2078.
14. Perko, L., 2001, Differential Equations and Dynamical Systems. Third Edition, Springer, New York.
15. Cantrell, R.S., Cosner, C., Ruan, S.: Intraspecific interference and consumer-resource dynamics. Discrete and Continuous Dynamical Systems (Series B). 4(3), 527–546(2004).
16. T. Elmhirst, S.R. Connolly and T.P. Hughes, *Connectivity, regime shifts and the resilience of coral reefs*, Coral Reefs, **28**, (2009), 949–957.
17. J. Bhattacharyya, S. Pal, *Hysteresis in coral reefs under macroalgal toxicity and overfishing*, Journal of Biological Physics, **41**, (2015), 151–172.
18. J. Bhattacharyya, S. Pal, *Macroalgal allelopathy in the emergence of coral diseases*, Discrete & Continuous Dynamical Systems-B, **22**(3), (2017), 741–762.
19. J.N. Underwood, L.D. Smith, M.J.H. Oppen and J.P. Gilmour, *Ecologically relevant dispersal of corals on isolated reefs: implications for managing resilience*, Ecological Applications, **19(1)**, (2009), 18–29.
20. T. Fung, R.M. Seymour and C.R. Johnson, *Alternative stable states and phase shifts in coral reefs under anthropogenic stress*, Ecology, **92**, (2011), 967–982.
21. T. Fung, R.M. Seymour and C.R. Johnson, *Warning signals of regime shifts as intrinsic properties of endogenous dynamics*, The American Naturalist, **182**, (2013), 208–222.

Oscillatory Behavior of a Delayed Ratio-Dependent Predator–Prey System with Michaelis–Menten Functional Response

Sándor Kovács, Szilvia György, and Noémi Gyúró

1 Introduction

Based on the results in [11], the authors of [13] have considered the ratio-dependent predator–prey system with the Michaelis–Menten functional response

$$\left.\begin{aligned} \dot{x} &= rxg(x,K) - \sum_{i=1}^{n} y_i p_i\left(\frac{y_i}{x}\right), \\ \dot{y}_i &= y_i p_i\left(\frac{y_i}{x}\right) - d_i y_i, \quad (i \in \{1,\dots,n\}) \end{aligned}\right\}, \tag{1}$$

where the dot means differentiation with respect to time t; $x(t) \geq 0$ denotes the quantity of the prey at time t and $y_i(t) \geq 0$ are the numbers or densities of the ith predator ($i \in \{1,\dots,n\}$) at time t. It was assumed that the per capita growth rate of prey in the absence of predators is $rg(x,K)$ where $r > 0$ denotes the maximal growth rate of prey and $K > 0$ is the carrying capacity of environment with respect to the prey; furthermore, the death rate $d_i > 0$ of the ith predator is constant, and the per capita birth rate of the same predator is $p_i\left(\frac{y_i}{x}\right)$, where the functions g and p_i have the following forms:

$$g(x,K) :\equiv 1 - \frac{x}{K} \qquad \text{and} \qquad p_i\left(\frac{y_i}{x}, a_i\right) :\equiv \frac{m_i x}{a_i y_i + x},$$

S. Kovács (✉)
Department of Numerical Analysis, Eötvös Loránd University, Budapest, Hungary
e-mail: alex@ludens.elte.hu

S. György · N. Gyúró
Eötvös Loránd University, Budapest, Hungary

R. P. Mondaini (ed.), *Trends in Biomathematics: Chaos and Control in Epidemics, Ecosystems, and Cells*, https://doi.org/10.1007/978-3-030-73241-7_2

and a_i is the ith half-saturation constant, namely, in the case where p_i is a bounded function for fixed

$$a_i > 0, \qquad m_i := \sup_{x, y_i > 0} p_i(x, y_i a_i)$$

is the maximal birth rate of the ith predator ($i \in \{1, \ldots, n\}$). For the survival of the predator, it is clearly necessary that the maximal birth rate be larger than the death rate: $m_i > d_i$ ($i \in \{1, \ldots, n\}$). This will be assumed in the sequel.

In order to have more realism, the authors of paper [13] took into account that the predator's growth rate at present depends on past quantities and, therefore, a continuous density function ρ was introduced whose role is to weight moments of the past (cf. [8]). Thus, they replaced the quantity x by

$$q(t) := \int_{-\infty}^{t} x(\tau)\rho(t - \tau)\,\mathrm{d}\tau \qquad (t \in [0, \infty)), \tag{2}$$

where the density function ρ satisfies the requirements

$$\rho(s) \geq 0 \quad (s \in [0, \infty)), \qquad \int_0^\infty \rho(s)\,\mathrm{d}s = 1.$$

Note that it is necessary to assume that the function ρ is smooth: $\rho \in \mathfrak{C}^1$. Thus, the system governing the dynamics of the predator–prey community is taken up in the form

$$\left.\begin{aligned} \dot{x} &= rxg(x, K) - \sum_{i=1}^{n} y_i p_i \left(\frac{y_i}{x}\right), \\ \dot{y}_i &= y_i p_i \left(\frac{y_i}{q}\right) - d_i y_i \quad (i \in \{1, \ldots, n\}). \end{aligned}\right\} \tag{3}$$

In [13], the authors could give in the case of one prey and two predators, i.e., when $n = 2$, parameter values for which the above system loses its stability, and they conjectured that there may be periodic solution occurrence.

This chapter is organized as follows. In the next section, assuming that the density function ρ is a solution of homogeneous linear differential equations with constant coefficients, i.e., it has the form

$$\rho_m(s) := \frac{h^{m+1} s^m e^{-hs}}{m!} \qquad (s \in [0, +\infty)) \tag{4}$$

where $m \in \mathbb{N}_0$, we perform linear stability analysis of the interior equilibrium in the case of $m \in \{0, 1\}$. In the section that follows, the conjecture in [13] is proved. We show that if the parameter is varied and crosses a critical value, periodic

solutions arise via Hopf bifurcation. Finally, a numerical simulation for supporting the theoretical analysis is also given.

2 The System with Delay

In case of $m = 0$, the weight function is exponentially decaying ("*exponential fading memory*") and has the form

$$\rho_0(s) = he^{-hs} \qquad (s \in [0, +\infty)), \tag{5}$$

and in case of $m = 1$, it takes the form

$$\rho_1(s) = h^2 se^{-hs} \qquad (s \in [0, +\infty)), \tag{6}$$

where for both cases we have $h > 0$ (cf. Fig. 1). Fargue has shown in [3] that if the density ρ has the form (4), then system (3) is equivalent to a system of ordinary differential equations of higher dimension. The exponential fading memory was used by several authors (cf. e.g., [1, 2, 4, 6, 15, 17, 18]). The authors of [5, 7, 9] used the memory with hump in order to make their model more realistic.

2.1 Exponential Fading Memory

Assuming that the influence of the past is fading away exponentially, i.e., for arbitrary $h > 0$ (5) and

$$h \int_{-\infty}^{t} \rho_0(-h(t-\tau))\,\mathrm{d}\tau = \int_0^{\infty} \exp(-hs)\,\mathrm{d}s = 1$$

holds, we have for the quantity q in (2)

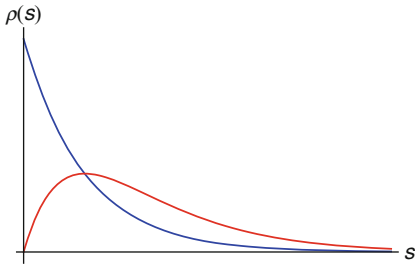

Fig. 1 The density functions: blue exponential fading memory and red memory with a hump

$$\dot{q}(t) = h(x(t) - q(t)) \qquad (t \in [0, +\infty)).$$

The smaller the h the longer is the time interval in the past in which the values of x are taken into account, i.e., $1/h$ is the "measure of the influence of the past." Hence, system (3) is equivalent in its qualitative dynamical behavior to the following system of ordinary differential equations:

$$\left.\begin{aligned} \dot{x} &= rxg(q, K) - \sum_{i=1}^{n} y_i p_i \left(\frac{y_i}{x}\right), \\ \dot{y}_i &= y_i p_i \left(\frac{y_i}{q}\right) - d_i y_i \quad (i \in \{1, \ldots, n\}), \\ \dot{q} &= h(x - q). \end{aligned}\right\} \tag{7}$$

We note that the equivalence above takes place over the time interval $[0, \infty)$; furthermore, if $(x, y_1, \ldots, y_n) : [0, \infty) \to \mathbb{R}^{n+1}$ is the solution of (3) corresponding to the continuous and bounded initial function $\widetilde{x} : (-\infty, 0] \to \mathbb{R}$ and the initial values $y_i^0 := y_i(0)$ $(i \in \{1, \ldots, n\})$ (i.e., $x(t) := \widetilde{x}(t)$ $(t < 0)$), then

$$(x, y_1, \ldots, y_n, q) : [0, \infty) \to \mathbb{R}^{n+2}$$

is the solution of (3) satisfying the initial values

$$x(0) = \widetilde{x}(0), \quad y_i(0) = y_i^0 \qquad (i \in \{1, \ldots, n\})$$

and

$$q(0) = q^0 := h \int_{-\infty}^{0} \widetilde{x}(\tau) \exp(h\tau)\, \mathrm{d}\tau$$

and vice versa. (Clearly, if the initial values $x(0)$, y_i^0, and q^0 related to system (3) are prescribed, then the function $\widetilde{x}$ is not uniquely determined.)

2.2 *Memory with a Hump*

Assume now that the weight function is given by (6) and for $t \in [0, +\infty)$ introduces notations

$$\begin{aligned} q(t) &:= h^2 \int_{-\infty}^{t} (t-\tau)x(\tau)\exp(-h(t-\tau))\,\mathrm{d}\tau, \\ r(t) &:= h \int_{-\infty}^{t} x(\tau)\exp(-h(t-\tau))\,\mathrm{d}\tau. \end{aligned} \tag{8}$$

Then, we have

$$\dot{q} = h(r-q), \qquad \text{resp.} \qquad \dot{r} = h(x-r),$$

and furthermore, it is easy to see that system (3) is equivalent on $[0,+\infty)$ in the sense described following (7) to the system

$$\left.\begin{aligned} \dot{x} &= rxg(x,K) - \sum_{i=1}^{n} y_i p_i\left(\frac{y_i}{x}\right), \\ \dot{y}_i &= y_i p_i\left(\frac{y_i}{q}\right) - d_i y_i \quad (i \in \{1,\dots,n\}), \\ \dot{q} &= h(r-q), \\ \dot{r} &= h(x-r). \end{aligned}\right\} \tag{9}$$

3 The Case of One Prey and Two Predators

As it was done in [13], we also assume that the community consists of one prey and two predators, i.e., $n=2$ holds. This means that that system (7) takes the form

$$\left.\begin{aligned} \dot{x} &= rx\left(1-\frac{x}{K}\right) - m_1\frac{xy_1}{a_1y_1+x} - m_2\frac{xy_2}{a_2y_2+x}, \\ \dot{y}_1 &= m_1\frac{xy_1}{a_1y_1+x} - d_1y_1, \\ \dot{y}_2 &= m_2\frac{xy_2}{a_2y_2+x} - d_2y_2. \end{aligned}\right\} \tag{10}$$

In [11], it was showed that system (10) is dissipative, i.e., all of its solutions are bounded and the positive octant of the phase space $\mathbb{R}^3$ is an invariant region; furthermore, if we extend it for

$$\mathbb{R}^3_+ := \left\{(x,y_1,y_2) \in \mathbb{R}^3 : \ x \geq 0,\ y_1 \geq 0,\ y_2 \geq 0\right\}$$

by $\dot{x} = 0$, $\dot{y}_i = 0$ if $x^2 + y_i^2 = 0$ for any i ($i \in \{1; 2\}$), then the extended system has four equilibria on the boundary of the positive octant of the phase space, namely

$$E^0(0, 0, 0), \qquad E^1(K, 0, 0), \qquad E_i^2(\widehat{x}_i, \widehat{y}_1, \widehat{y}_2) \quad (i \in \{1; 2\}),$$

where for $i, j \in \{1; 2\}$: $j \neq i$ we have

$$\hat{x}_i := K\left(1 - \frac{1}{r}\frac{m_i - d_i}{a_i}\right), \qquad \hat{y}_i := \frac{m_i - d_i}{d_i a_i}\hat{x}, \quad \hat{y}_j = 0,$$

and it has one interior equilibrium $E^*(x^*, y_1^*, y_2^*)$ where for $i \in \{1; 2\}$ we have

$$x^* := K\left(1 - \frac{1}{r}\sum_{i=1}^{2}\frac{m_i - d_i}{a_i}\right) \qquad \text{and} \qquad y_i^* := \frac{m_i - d_i}{d_i a_i}x^*.$$

Note that equilibria E^0 and E^1 always exist. The equilibria E_i^2 ($i \in \{1; 2\}$) and E^* may or may not exist. In particular, E_i^2 exists ($i \in \{1; 2\}$) if

$$\frac{m_i - d_i}{a_i} < r \qquad \text{and} \qquad m_i > d_i$$

hold. The interior equilibrium E^* that represents the coexistence of all species exists if maximal growth rates $m_i - d_i$ of the predators are positive and the sum of the ratios of the growth rates and half-saturation constants of the predators is less than the intrinsic growth rate of the prey, i.e.,

$$m_i > d_i \qquad \text{and} \qquad \sum_{i=1}^{2}\frac{m_i - d_i}{a_i} < r \tag{11}$$

hold.

Introducing delays with density functions (5) and (6), system (10) goes into

$$\left.\begin{aligned}
\dot{x} &= rx\left(1 - \frac{x}{K}\right) - m_1\frac{xy_1}{a_1y_1 + x} - m_2\frac{xy_2}{a_2y_2 + x},\\
\dot{y}_1 &= m_1\frac{qy_1}{a_1y_1 + q} - d_1y_1,\\
\dot{y}_2 &= m_2\frac{qy_2}{a_2y_2 + q} - d_2y_2,\\
\dot{q} &= h(x - q)
\end{aligned}\right\} \tag{12}$$

and into

$$\left.\begin{aligned}
\dot{x} &= rx\left(1-\frac{x}{K}\right)-m_1\frac{xy_1}{a_1y_1+x}-m_2\frac{xy_2}{a_2y_2+x},\\
\dot{y}_1 &= m_1\frac{qy_1}{a_1y_1+q}-d_1y_1,\\
\dot{y}_2 &= m_2\frac{qy_2}{a_2y_2+q}-d_2y_2,\\
\dot{q} &= h(r-q),\\
\dot{r} &= h(x-r).
\end{aligned}\right\} \tag{13}$$

From the biological point of view, we are only interested in the case when the interior equilibrium exists because the other equilibria are unstable when no delay is concerned (cf. [11]). If condition (11) holds, then interior equilibria of (10), resp. (12) and of (13) are

$$E^* := (x^*, y_1^*, y_2^*),$$

resp.

$$E_{d0}^* := (x^*, y_1^*, y_2^*, x^*) \qquad \text{and} \qquad E_{d1}^* := (x^*, y_1^*, y_2^*, x^*, x^*).$$

In order to determine the stability of equilibria E^*, resp. E_{d0}^* and E_{d1}^* of systems (10), resp. (12) and (13) one has to compute the Jacobians

$$J(x, y_1, y_2) := \begin{bmatrix}
j_{11} & -\dfrac{m_1x^2}{(a_1y_1+x)^2} & -\dfrac{m_2x^2}{(a_2y_2+x)^2}\\
\dfrac{a_1m_1y_1^2}{(a_1y_1+x)^2} & \dfrac{m_1x^2}{(a_1y_1+x)^2}-d_1 & 0\\
\dfrac{a_2m_2y_2^2}{(a_2y_2+x)^2} & 0 & \dfrac{m_2x^2}{(a_2y_2+x)^2}-d_2
\end{bmatrix}$$

resp.

$$J(x, y_1, y_2, q) := \begin{bmatrix}
j_{11} & -\dfrac{m_1x^2}{(a_1y_1+x)^2} & -\dfrac{m_2x^2}{(a_2y_2+x)^2} & 0\\
0 & \frac{m_1q^2}{(a_1y_1+q)^2}-d_1 & 0 & \dfrac{a_1m_1y_1^2}{(a_1y_1+q)^2}\\
0 & 0 & \dfrac{m_2q^2}{(a_2y_2+q)^2}-d_2 & \dfrac{a_2m_2y_2^2}{(a_2y_2+q)^2}\\
h & 0 & 0 & -h
\end{bmatrix}$$

and

$$J(x, y_1, y_2, q, p) := \begin{bmatrix} j_{11} & -\frac{m_1 x^2}{(a_1 y_1 + x)^2} & -\frac{m_2 x^2}{(a_2 y_2 + x)^2} & 0 & 0 \\ 0 & \frac{m_1 q^2}{(a_1 y_1 + q)^2} - d_1 & 0 & \frac{a_1 m_1 y_1^2}{(a_1 y_1 + q)^2} & 0 \\ 0 & 0 & \frac{m_2 q^2}{(a_2 y_2 + q)^2} - d_2 & \frac{a_2 m_2 y_2^2}{(a_2 y_2 + q)^2} & 0 \\ 0 & 0 & 0 & -h & h \\ h & 0 & 0 & 0 & -h \end{bmatrix}$$

at these equilibria, where

$$j_{11} := r - \frac{2rx}{K} - \frac{a_1 m_1 y_1^2}{(a_1 y_1 + x)^2} - \frac{a_2 m_2 y_2^2}{(a_2 y_2 + x)^2}.$$

If we take parameter values (cf. [13])

$$m_1 := 16, \quad m_2 := 18, \quad d_1 := 8, \quad d_2 := 12, \quad a_1 := 4, \quad a_2 := 2, \quad K := 0.1, \tag{14}$$

then the dependence of E^*, resp. E^*_{d0} and E^*_{d1}, on the parameter r (in fact on the maximal growth rates from the prey) is as follows:

$$E^* := \left(0.1\left(1 - \frac{5}{r}\right), \frac{1}{40}\left(1 - \frac{5}{r}\right), \left(1 - \frac{5}{r}\right)\right),$$

resp.

$$E^*_{d0} := \left(0.1\left(1 - \frac{5}{r}\right), \frac{1}{40}\left(1 - \frac{5}{r}\right), \frac{1}{40}\left(1 - \frac{5}{r}\right), 0.1\left(1 - \frac{5}{r}\right)\right)$$

and

$$E^*_{d1} := \left(0.1\left(1 - \frac{5}{r}\right), \frac{1}{40}\left(1 - \frac{5}{r}\right), \frac{1}{40}\left(1 - \frac{5}{r}\right), 0.1\left(1 - \frac{5}{r}\right), 0.1\left(1 - \frac{5}{r}\right)\right).$$

Under this restriction, we have

$$J := J(E^*) := \begin{bmatrix} 8 - r & -4 & -8 \\ 1 & -4 & 0 \\ 1 & 0 & -4 \end{bmatrix}$$

resp.

$$J_0 := J(E^*_{d0}) := \begin{bmatrix} 8-r & -4 & -8 & 0 \\ 0 & -4 & 0 & 1 \\ 0 & 0 & -4 & 1 \\ h & 0 & 0 & -h \end{bmatrix}$$

and

$$J_1 := J(E^*_{d1}) := \begin{bmatrix} 8-r & -4 & -8 & 0 & 0 \\ 0 & -4 & 0 & 1 & 0 \\ 0 & 0 & -4 & 1 & 0 \\ 0 & 0 & 0 & -h & h \\ h & 0 & 0 & 0 & -h \end{bmatrix}.$$

We calculate the characteristic polynomials of J, resp. J_0 and J_1, using Faddeev–Leverrier method (cf. [10]) and with the help of block matrices. The characteristic polynomial of the Jacobian J has the form

$$\chi_J(z) := z^3 + a_2 z^2 + a_1 z + a_0 \qquad (z \in \mathbb{K}),$$

where

$$a_2 = -\mathrm{Tr}(J) = r,$$

$$a_1 = \frac{1}{2}\left\{(\mathrm{Tr}(J))^2 - \mathrm{Tr}(J^2)\right\} = 8r - 36,$$

$$a_0 = -\det(J) = 16r - 80.$$

The equilibrium E^* is feasible if and only if $r > 5$ holds. In this case, χ_J is a stable polynomial since it fulfills the Routh–Hurwitz condition (cf. [8]): its coefficients have the same sign and

$$a_1 a_2 - a_0 = (8r - 36)r - 16r + 80 = 8r^2 - 52r + 80 = 4(r-4)(r-5/2) > 0.$$

As a consequence, E^* is asymptotically stable if it exists. The characteristic polynomial χ_{J_0} is calculated as follows. From the definition, we have

$$\chi_{J_0}(z) = \det(zI_4 - J) = (-1)^4 \det(J - zI_4)$$

$$= \det \left[\begin{array}{cc|cc} 8-r-z & -4 & -8 & 0 \\ 0 & -4-z & 0 & 1 \\ \hline 0 & 0 & -4-z & 1 \\ h & 0 & 0 & -h-z \end{array}\right]$$

$$= -\frac{1}{8} \det \left[\begin{array}{cc|cc} r+z-8 & 4 & 8 & 0 \\ 0 & -32-8z & 0 & 8 \\ \hline 0 & 0 & -4-z & 1 \\ h & 0 & 0 & -h-z \end{array}\right] = -\frac{1}{8} \det \left[\begin{array}{c|c} A & B \\ \hline C & D \end{array}\right].$$

Since A and B commute, we get (cf. [16])

$$\det(zI_4 - J_0) = -\frac{1}{8} \det[DA - CB]$$

$$= -\frac{1}{8} \det \left[\begin{bmatrix} -4-z & 1 \\ 0 & -h-z \end{bmatrix} \begin{bmatrix} r+z-8 & 4 \\ 0 & -32-8z \end{bmatrix} - 8h \begin{bmatrix} 0 & 0 \\ 1 & 0 \end{bmatrix}\right]$$

$$= -\frac{1}{8} \det \left[\begin{bmatrix} (4+z)(r-8+z) & 4(4+z)-4-z \\ 0 & (h+z)(4+z) \end{bmatrix} - 8h \begin{bmatrix} 0 & 0 \\ 1 & 0 \end{bmatrix}\right]$$

$$= -\frac{1}{8} \det \begin{bmatrix} -(4+z)(r-8+z) & -4(4+z)-8(4+z) \\ -8h & 8(h+z)(4+z) \end{bmatrix}$$

$$= (4+z)(r-8+z)(h+z)(4+z) - 12h(4+z)$$

$$= (4+z)\left\{z^3 + (h+r-4)z^2 + ((h+4)r - 4(h+8))z + 4h(r-5)\right\}.$$

The characteristic polynomial χ_{J_1} can be computed as follows.

$$\chi_{J_1}(z) := \det(zI_5 - J_1) = (-1)^5 \det(J_1 - zI_5)$$

$$= -\det \begin{bmatrix} 8-r-z & -4 & -8 & 0 & 0 \\ 0 & -4-z & 0 & 1 & 0 \\ 0 & 0 & -4-z & 1 & 0 \\ 0 & 0 & 0 & -h-z & h \\ h & 0 & 0 & 0 & -h-z \end{bmatrix}$$

$$= -(h+z)^2(4+z)^2(8-r-z).$$

It is easy to see that J_1 is stable only if $r > 8$, whereas the stability of J_0 depends on the third-order polynomial

$$z^3 + \alpha(h)z^2 + \beta(h)z + \gamma(h) \qquad (z \in \mathbb{K}), \tag{15}$$

where

$$\alpha(h) := h + r - 4, \qquad \beta(h) := (h+4)r - 4(h+8), \qquad \gamma(h) := 4h(r-5).$$

In order to have Hopf bifurcation in case of J_0, one has to show that a pair of complex conjugate eigenvalues of J_0 crosses the imaginary axis with non-zero velocity, while the rest of the eigenvalues continue to have negative or positive real parts. This is fulfilled if (cf. [8, 14])

- the so-called eigenvalue crossing condition holds, i.e., the characteristic polynomial χ_{J_0} has a pair of pure imaginary roots $\mu(h) \pm \imath\nu(h)$ and no other roots with zero real parts, for which at a critical value h_* of the bifurcation parameter h

$$\mu(h_*) = 0, \qquad \nu(h_*) \neq 0; \qquad (\sigma(J_0)\backslash\{\pm\imath\nu(h_*)\}) \cap \imath\mathbb{R} = \emptyset,$$

  hold;
- the **transversality condition** holds, i.e., $\mu'(h_*) \neq 0$ is fulfilled.

Clearly, for every $h > 0$, we have $\gamma(h) > 0$ because $r > 5$ holds.

Next, we use a lemma for which a proof is given in Appendix of [12].

Lemma 3.1 *Let $I \subset \mathbb{R}$ an open interval $\alpha, \beta, \gamma : I \to \mathbb{R}$ smooth functions. Then, the polynomial*

$$P(z) := z^3 + \alpha z^2 + \beta z + \gamma \qquad (z \in \mathbb{K})$$

fulfills at some $h = h^* \in I$ the eigenvalue crossing condition and the transversality condition if

$$\alpha(h^*) \neq 0, \qquad \beta(h^*) > 0, \qquad \gamma(h^*) = \alpha(h^*)\beta(h^*) \tag{16}$$

and

$$\frac{\mathrm{d}}{\mathrm{d}h}\{\alpha(h)\beta(h) - \gamma(h)\}|_{h=h^*} \neq 0 \tag{17}$$

hold.

Thus, the eigenvalue crossing condition holds for the polynomial in (15) if and only if

$$\beta(h) := (h+4)r - 4(h+8) > 0, \qquad \alpha(h) := h + r - 4 \neq 0$$

and

$$\alpha(h)\beta(h) - \gamma(h) := (h + r - 4)\{(h + 4)r - 4(h + 8)\} - 4h(r - 5) \neq 0.$$

The authors in [13] have chosen for $r := 7$ the value $h^* := 1$ that is seemingly not critical. No wonder that they could not observe and prove periodic oscillation. Solving equation $\alpha(h)\beta(h) = \gamma(h)$, we have

$$h_H := h_* = \frac{1 + \sqrt{17}}{2}.$$

Because

$$\alpha(h_*) = \frac{\sqrt{17} + 7}{2} \neq 0 \qquad \text{and} \qquad \beta(h_*) = \frac{3\sqrt{17} - 5}{2} > 0,$$

the eigenvalue crossing condition holds at this value of the parameter h. Thus, we are able to prove the occurrence of limit cycles from the interior equilibrium E^*_{d0} of the system (12).

Theorem 3.1 *Suppose that conditions in* (14) *hold and* $r = 7$*, then at the critical value* h_H *of the bifurcation parameter* h *the equilibrium* E^*_{d0} *of the system* (12) *undergoes a Hopf bifurcation:* E^*_{d0} *loses its stability and a branch of periodic solutions emerges from* E^*_{d0} *near* $h = h_H$*.*

Proof We need to check whether the transversality condition (17) holds. Indeed, at the critical value $h = h_H$, we have

$$\frac{\mathrm{d}}{\mathrm{d}h}(\alpha\beta - \gamma)(h_H) = -[8 - 3(3 + h) - 7(4 + h) + 4(8 + h)]_{h=h_H} = 3\sqrt{17} \neq 0,$$

which proves our statement. □

Figure 2 shows the time evolution of system (12) if Hopf bifurcation occurs.

4 Stability of the Bifurcating Periodic Solution

In this section, we shall present a very brief summary of the projection method (cf. [14]) in order to decide whether the bifurcation is super- or subcritical. Under supercritical bifurcation, we mean the case when the equilibrium E^*_{d0} has lost its stability with occurrence of periodic solutions that are orbitally asymptotically stable (i.e., for values of the bifurcation parameter h less than h_H), while in the subcritical case, the periodic solutions are unstable and exist for hs when the equilibrium E^*_{d0} is still asymptotically stable (i.e., for values of h greater than h_H).

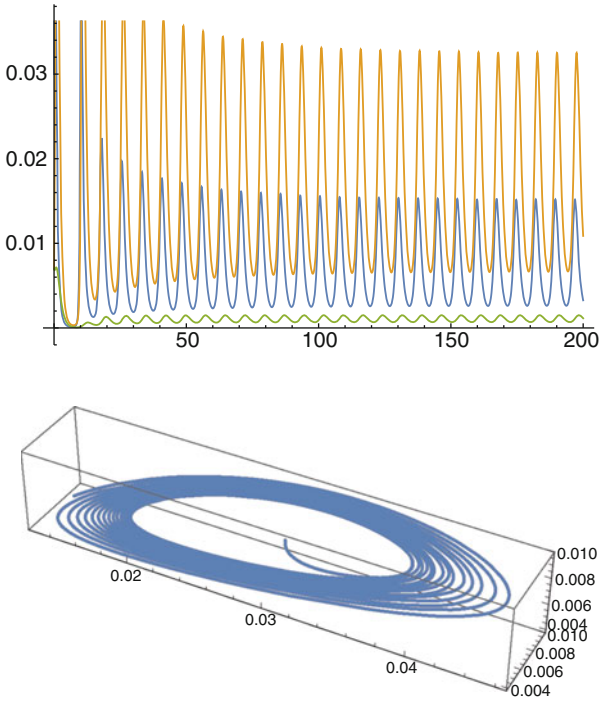

Fig. 2 The periodic solution of system (12) near $h = h_H$

Clearly, system (12) has the form

$$(\dot{u}, \dot{v}, \dot{w}, \dot{z}) = \mathbf{F}(u, v, w, z, h), \tag{18}$$

where

$$F_1(u, v, w, z, h) := ru\left(1 - \frac{u}{K}\right) - m_1\frac{uv}{a_1v + u} - m_2\frac{uw}{a_2w + u},$$

$$F_2(u, v, w, z, h) := m_1\frac{zv}{a_1v + z} - d_1v,$$

$$F_3(u, v, w, z, h) := m_2\frac{zw}{a_2w + z} - d_2w,$$

$$F_4(u, v, w, z, h) := h(u - z)$$

and h is the bifurcation parameter. Define the bilinear, resp. trilinear functions

$$\mathfrak{B} = (B_1, B_2, B_3, B_4) : \mathbb{K}^4 \times \mathbb{K}^4 \to \mathbb{K}^4,$$

resp.

$$\mathfrak{C} = (C_1, C_2, C_3, C_4) : \mathbb{K}^4 \times \mathbb{K}^4 \times \mathbb{K}^4 \to \mathbb{K}^4$$

by

$$B_i(\mathbf{x}, \mathbf{y}) := \sum_{j,k=1}^{4} \left. \frac{\partial^2 F_i(\boldsymbol{\xi}, h_H)}{\partial \xi_j \partial \xi_k} \right|_{\boldsymbol{\xi} = E^*_{d0}} x_j y_k, \qquad (i \in \{1, 2, 3, 4\}),$$

resp. by

$$C_i(\mathbf{x}, \mathbf{y}, \mathbf{z}) := \sum_{j,k,l=1}^{4} \left. \frac{\partial^3 F_i(\boldsymbol{\xi}, h_H)}{\partial \xi_j \partial \xi_k \partial \xi_l} \right|_{\boldsymbol{\xi} = E^*_{d0}} x_j y_k z_l \qquad (i \in \{1, 2, 3, 4\}).$$

The Jacobian J_0 at the critical parameter value $h = h_H$ will be denoted by $\mathfrak{A}$:

$$\mathfrak{A} := \left. \frac{\partial \mathbf{F}(\boldsymbol{\xi}, h_H)}{\partial (u, v, w, z)} \right|_{\boldsymbol{\xi} = E^*_{d0}}.$$

Clearly, $\imath\omega$ and $-\imath\omega$ are eigenvalues of $\mathfrak{A}$ with left and right eigenvectors $\mathbf{p}, \mathbf{q} \in \mathbb{K}^4$, i.e., satisfying

$$\mathfrak{A}\mathbf{q} = \imath\omega\mathbf{q}, \qquad \mathfrak{A}^T\mathbf{p} = -\imath\omega\mathbf{p} \tag{19}$$

and normalized by setting

$$\langle \mathbf{p}, \mathbf{q} \rangle = 1 \tag{20}$$

where $\langle \cdot, \cdot \rangle$ is the standard scalar product in $\mathbb{C}^4$, antilinear in the first argument.

To examine the supercriticality, resp. subcriticality, of the bifurcating solution, one has to compute the sign of the first Poincaré–Lyapunov coefficient

$$l_1 = \frac{1}{2\omega} \cdot \Re \left(\langle \mathbf{p}, \mathcal{H}_{21} \rangle \right), \tag{21}$$

where

$$\mathcal{H}_{21} := \mathfrak{C}(\mathbf{q}, \mathbf{q}, \overline{\mathbf{q}}) + 2\mathfrak{B}(\mathbf{q}, \mathbf{h}_{11}) + \mathfrak{B}(\overline{\mathbf{q}}, \mathbf{h}_{20}),$$

resp.

$$\mathbf{h}_{11} := \mathfrak{A}^{-1}\mathfrak{B}(\mathbf{q}, \overline{\mathbf{q}}) \qquad \text{and} \qquad \mathbf{h}_{20} := (2\imath\omega I_3 - \mathfrak{A})^{-1}\,\mathfrak{B}(\mathbf{q}, \mathbf{q}).$$

In case of $l_1 < 0$ (resp. $l_1 > 0$), we have supercritical (resp. subcritical) bifurcation.

Acknowledgments The authors were supported in part by the European Union, co-financed by the European Social Fund (EFOP-3.6.3-VEKOP-16-2017-00001).

References

1. M. Cavani; M. Farkas: *Bifurcations in a predator-prey model with memory and diffusion. I: Andronov-Hopf bifurcation* Acta Math. Hungar. **16**(3), 213–229 (1994).
2. J. M. Cushing: *Integrodifferential Equations and Delay Models in Population Dynamics*, Lecture Notes in Biomathematics, 20, Berlin: Springer Verlag, 1977.
3. D. Fargue: *Réductibilité des systèmes héréditaires à des systèmes dynamiques (régis par des équations différentielles ou aux dérivés partielles)* (French) C. R. Acad. Sci. Paris Sér. **277**, B471–B473 (1973).
4. M. Farkas: *Stable oscillations in a predator-prey model with time lag*, J. Math. Anal. Appl. **102**, 175–188 (1984).
5. A. Farkas; M. Farkas: *Stable oscillations in a more realistic predator-prey model with time lag* Asymptotic methods in mathematical physics (Russian) **304**, 250–256 (1988).
6. A. Farkas; M. Farkas, G. Szabó: *Multiparameter bifurcation diagrams in predator-prey models with time lag* J. Math. Biol. **26**, 93–103 (1988).
7. M. Farkas; M. Kotsis: *Modelling predator-prey and wage-employment dynamics* Dynamic economic models and optimal control (Vienna, 1991), 513–526, North-Holland, Amsterdam, 1992.
8. Farkas, M.: *Periodic Motions*, Berlin, Heidelberg and New York: Springer-Verlag, 1994.
9. J. D. Ferreira; C. A. T. Salazar; P. C. C. Tabares: *Weak Allee effect in a predator-prey model involving memory with a hump* Nonlin. Anal. **14**(1), 536–548 (2013).
10. R. R. Gantmacher: *The theory of matrices. Vol. 1.*, AMS Chelsea Publishing, Providence, RI, 1998.
11. K. Kiss, S. Kovács: *Qualitative behavior of n-dimensional ratio-dependent predator-prey systems*. Appl. Math. Comput. **199**(2), 535–546 (2008).
12. S. Kovács; S. György; N. Gyúró: *On an Invasive Species Model with Harvesting*, in: Trends in Biomathematics: Modeling Cells, Flows, Epidemics, and the Environment (ed. R. Mondaini), pp. 299–334 (Springer 2020)
13. K. Kiss, J. Tóth: *n-dimensional ratio-dependent predator-prey systems with memory*, Differential Equations and Dynamical Systems, **17**(1-2), 17–35 (2009).
14. Y. A. Kuznetsov: *Elements of applied bifurcation theory, Third edition*. Applied Mathematical Sciences, Berlin, Heidelberg, New York and Tokyo: Springer-Verlag, 2004.
15. N. MacDonald: *Time delay in predator-prey models, II. Bifurcation theory* Math. Biosci. **33**, 227–234 (1977).
16. J. R. Silvester: *Determinants of Block Matrices*, The Mathematical Gazette, **84**(501), 460–467 (2000).
17. G. Szabó: *A remark on M. Farkas: "Stable oscillations in a predator-prey model with time lag"* J. Math. Anal. Appl. **102**(1) (evszam), 205–206 (1987).
18. G. Stépán: *Great delay in a predator-prey model* Nonlin. Anal. **10**, 913–929 (1986).

Dynamical Analysis of Phytoplankton–Zooplankton Interaction Model by Using Deterministic and Stochastic Approach

Anal Chatterjee and Samares Pal

1 Introduction

Plankton are the backbone of marine ecosystem, which live mostly in watery environments such as seas, water column of oceans, and fresh water. They are strongly dependent on ambient nutrient's concentrations. In the marine ecosystem, phytoplankton are known as self-feeding components and play a major role in controlling the global carbon cycle that has direct impact on climate regulation. The dynamical swift growth and drastic decrease of plankton represent a phenomenon known as bloom.

Harmful algal blooms (HABs) are increasing in frequency worldwide [1, 2] and have a negative impact on aquaculture, coastal tourism, and human health [3]. Many theories are available to explain the bloom phenomenon. Some of the researchers use "top-down" mechanism [4–7] to explain the bloom, that is, according to them the occurrence of phytoplankton bloom depends on their grazing pressure, whereas others use "bottom-up" mechanism [8–11], that is, the occurrence of bloom depends on the availability of the nutrient. On the other hand, some of the scientists consider the simultaneous effect of both "top-down" and "bottom-up" mechanisms to explain the bloom phenomenon [12, 13].

The change in population density of one species has the ability to affect the growth of several other species by producing allelopathic toxins or stimulators. This is also a responsible factor for seasonal change in population density of various phytoplankton species. The toxins liberated by the phytoplankton may be regarded as an anti-grazing strategy[14].

A. Chatterjee (✉)
Department of Mathematics, Barrackpore Rastraguru Surendranath College, Kolkata, India

S. Pal
Department of Mathematics, University of Kalyani, Kalyani, India

R. P. Mondaini (ed.), *Trends in Biomathematics: Chaos and Control in Epidemics, Ecosystems, and Cells*, https://doi.org/10.1007/978-3-030-73241-7_3

The anti-grazing strategy is important for the existence of the phytoplankton species. It also plays a vital role in many zooplankton species largely determined by the ways in which the species of phytoplankton can resist mutual extinction due to competition or persistence despite grazing pressure from zooplankton[15]. Phytoplankton are small relative to their predatory enemies in the pelagic, and they will not survive an encounter with a grazer without any anti-grazing strategy. Therefore, various anti-grazing strategies such as cell morphology, presence of gelatinous substances, or aggregation to form patches, and filamentous structures are observed for phytoplankton [16–18]. A stochastic model may describe more realistically a natural system and therefore is considered in order to provide a clearer understanding of the situation. Recently, general deterministic and stochastic N-P-Z models with toxin-producing phytoplankton have been examined in [19–23].

Based on such observations, in this chapter, we extended the model proposed in [13] by taking into account the competition between phytoplankton and zooplankton in the presence of phytoplankton patches on the zooplankton community and observed its effect on the dynamical system. In this chapter, to capture the effect of phytoplankton patches on the zooplankton community, we propose a functional response that is not a monotonically increasing function of the prey density, but rather it is only monotonically increasing up to a certain threshold density and then becomes monotonically decreasing. We also assumed that these patches have a negative impact on the growth of zooplankton.

In the second model, we present the stochastic system. Numerical examples will be provided to illustrate the complexity of the interaction.

2 The Mathematical Model

The study of the defense mechanism through the formation of patches becomes more important if such patches have the ability to release toxin chemicals, like in the case of dinoflagellates.

Let $N(t)$ be the concentration of the nutrient at time t. Let $P(t)$ and $Z(t)$ be the concentrations of toxin-producing phytoplankton (TPP) and zooplankton population, respectively, at time t. Let N^0 be the constant input of nutrient concentration and D be the dilution rate [24]. The constant D^{-1} has the physical dimension of a time and represents the average time that nutrient and waste products spend in the system [25]. Let α_1 and α_2 be the nutrient uptake rate for the phytoplankton population and the conversion rate of nutrient for the growth of phytoplankton population, respectively ($\alpha_2 \leq \alpha_1$). Here, c is the predation rate and e is the conversion rate of zooplankton population ($c \leq e$). Let μ_1 be the mortality rate of the phytoplankton population and μ_2 be the mortality rate of the zooplankton population. Let μ_3 ($\mu_3 \leq \mu_1$) be the nutrient recycle rate after the death of

phytoplankton population and μ_4 ($\mu_4 \leq \mu_2$) be the nutrient recycle rate after the death of zooplankton population. We choose the Holling type II functional form to describe the grazing phenomena with K_1 and K_2 as half-saturation constants. The most important parameter is ρ that may be defined as the measure of the toxicity, which is directly proportional to the fraction of phytoplankton-forming patches and inversely proportional to the number of phytoplankton-forming patches. Suppose a fraction $K(0 \leq K \leq 1)$ of the phytoplankton population aggregates to form n patches. For the predation term, the standard mass action incidence can easily be taken, over the fraction $1 - K$ of the free phytoplankton. We propose here a more complicated mechanism for the release of poison. Note that the population in each patch will be $\frac{1}{n}KP$. Let us introduce a new parameter $\rho \equiv (\frac{K}{n})^{\frac{2}{3}}$. If the $3D$ patch in the ocean can be assumed to be roughly spherical, its radius will be proportional to $[\frac{KP}{n}]^{\frac{1}{3}}$, so that its surface is proportional to $[\frac{KP}{n}]^{\frac{2}{3}} = \rho P^{\frac{2}{3}}$ as suggested in [26]. We assume that the phytoplankton can detect the presence of zooplankton and release the poison in self-defense, and this will leak into the surrounding water through the surface of the patch that is proportional to $\rho P^{\frac{2}{3}}$. With the above biological assumptions, our model system is

$$\left.\begin{aligned}
\frac{dN}{dt} &= D(N^0 - N) - \frac{\alpha_1 PN}{K_1 + N} + \mu_3 P + \mu_4 Z \equiv G_1(N, P, Z) \\
\frac{dP}{dt} &= \frac{\alpha_2 PN}{K_1 + N} - \frac{c(1-K)PZ}{K_2 + P} - \mu_1 P \equiv G_2(N, P, Z) \\
\frac{dZ}{dt} &= \frac{e(1-K)PZ}{K_2 + P} - \mu_2 Z - e\rho P^{2/3} Z \equiv G_3(N, P, Z)
\end{aligned}\right\}. \tag{1}$$

The system (1) has to be analyzed with the following initial conditions,

$$N(0) > 0,\ P(0) > 0,\ Z(0) > 0. \tag{2}$$

Explicitly, the Jacobian matrix at $\overline{E} = (\overline{N}, \overline{P}, \overline{Z})$ can be defined as

$$\overline{V} = \begin{bmatrix}
-D - \frac{\alpha_1 K_1 \overline{P}}{(K_1+\overline{N})^2} & -\frac{\alpha_1 \overline{N}}{K_1+\overline{N}} + \mu_3 & \mu_4 \\
\frac{K_1 \alpha_2 \overline{P}}{(K_1+\overline{N})^2} & \frac{\alpha_2 \overline{N}}{K_1+\overline{N}} - \frac{K_2 c(1-K)\overline{Z}}{(K_2+\overline{P})^2} - \mu_1 & -\frac{c(1-K)\overline{P}}{K_2+\overline{P}} \\
0 & \frac{K_2 e(1-K)\overline{Z}}{(K_2+\overline{P})^2} - \frac{2e\rho\overline{Z}}{3\overline{P}^{\frac{1}{3}}} & \frac{e(1-K)\overline{P}}{K_2+\overline{P}} - \mu_2 - e\rho\overline{P}^{\frac{2}{3}}
\end{bmatrix}. \tag{3}$$

3 Some Preliminary Results

3.1 Positive Invariance

The system (1) is not homogeneous due to the presence of constant supply of nutrients N^0. Therefore, $(0, 0, 0)$ cannot be a solution of equilibrium points. It is easy to verify that $G_1(X) > 0$ when $N = 0$, $P > 0$, and $Z > 0$ by choosing $X(0) \in \mathbf{R}^3_+$. Hence, the trajectories becomes part of positive octant on the plane $N = 0$. The staying coordinate planes will be the solution of the respective equilibrium equation. According to existence and uniqueness theorem, the trajectories cannot approach to unfeasible domain from positive octant, which indicates that solution remains in positive octant. This ensures that the system is well defined.

3.2 Equilibria

The system (1) possesses the following equilibria: plankton-free equilibrium $E_0 = (N^0, 0, 0)$, zooplankton-free equilibrium $E_1(N_1, P_1, 0)$, and coexistence equilibrium $E^* = (N^*, P^*, Z^*)$.

3.2.1 Plankton-Free Equilibrium

E_0 is always feasible. The eigenvalues evaluate from (3) at E_0 are $-D < 0$, $-\mu_2 < 0$, and $\mu_1(R_0 - 1)$. Thus, it is clearly indicated that E_0 is asymptotically stable if

$$R_0 = \frac{\alpha_2 N^0}{(\mu_1 + D_1)(K_1 + N^0)} < 1 \tag{4}$$

holds.

3.2.2 Plankton-Free Equilibrium

The population levels at E_1 are $N_1 == \frac{\mu_1 K_1}{\alpha_2 - \mu_1}$ and $P_1 = \frac{D\alpha_2[N^0(\alpha_2-\mu_1)-K_1\mu_1]}{(\alpha_2-\mu_1)(\alpha_1\mu_1-\mu_3\alpha_2)}$. Feasibility at E_1 exists if $\max\left\{\mu_1, \frac{(N^0+K_1)\mu_1}{N^0}\right\} < \alpha_2 < \frac{\alpha_1\mu_1}{\mu_3}$. Factorizing Jacobian (3) at E_1 gives one explicit eigenvalue $\frac{e(1-K)P_1}{K_2+P_1} - \mu_2 - e\rho P_1^{\frac{2}{3}}$ and the quadratic equation $\lambda^2 + \lambda\left(D + \frac{\alpha_1 K_1 P_1}{(K_1+N_1)^2}\right) + \frac{K_1\alpha_2 P_1}{(K_1+N_1)^2}\left(\frac{\alpha_1 N_1}{K_1+N_1} - \mu_3\right) = 0$. Clearly, two roots are negative real parts at E_1. Therefore, stability of E_1 is ensured by

$$\frac{(1-K)P_1}{K_2+P_1} > \frac{\mu_2}{e} + \rho P_1^{\frac{2}{3}}. \tag{5}$$

3.2.3 Coexistence Equilibrium

The coexistence equilibrium at $E^*=(N^*, P^*, Z^*)$ is $Z^*=\frac{[(\alpha_2-\mu_1)N^*-K_1\mu_1](K_2+P^*)}{c(K_1+N^*)(1-K)}$, while P^* is ensured by solving $e^3\rho^3P^{*5}+3K_2e^3\rho^3P^{*4}+[3K^2e^3\rho^3-\{e(1-K)-\mu_2\}^3]P^{*3}+[K_2^3e^3\rho^3+3\{e(1-K)-\mu_2\}^2\mu_2K_2]P^{*2}-3\{e(1-K)-\mu_2\}\mu_2^2K_2^2P^*+\mu_2^3K_2^3=0$. Now putting the value of P^* and Z^* in first equation of the system (1), we get the value of N^*. It is impossible to find the explicit form of N^*, P^*, and Z^* with only system parameters. Therefore, we need to investigate feasibility and stability criteria of coexistence at E^* numerically.

At E^*, the Jacobian matrix of the system (1) can be written as

$$V^* = \begin{bmatrix} m_{11} & m_{12} & m_{13} \\ m_{21} & m_{22} & m_{23} \\ 0 & m_{32} & 0 \end{bmatrix},$$

where $m_{11} = -D - \frac{K_1\alpha_1P^*}{(K_1+N^*)^2} < 0$, $m_{12} = -\frac{\alpha_1N^*}{K_1+N^*} + \mu_3 < 0$, $m_{13} = \mu_4 > 0$; $m_{21} = \frac{K_1\alpha_2P^*}{(K_1+N^*)^2} > 0$, $m_{22} = \frac{c(1-K)P^*Z^*}{(K_2+P^*)^2} > 0$, $m_{23} = -\frac{\gamma_1P^*}{K_2+P^*} < 0$, $m_{32} = \frac{K_2e(1-K)Z^*}{(K_2+P^*)^2} - \frac{2e\rho Z^*}{3P^{*\frac{1}{3}}} \in \mathbf{R}$.

The characteristic equation is

$$y^3 + Q_1y^2 + Q_2y + Q_3 = 0, \tag{6}$$

where $Q_1 = -(m_{11} + m_{22})$, $Q_2 = m_{11}m_{22} - m_{12}m_{21} - m_{23}m_{32}$; $Q_3 = m_{11}m_{23}m_{32} - m_{13}m_{32}m_{21}$. By the Routh–Hurwitz criterion, all roots of the above equation have negative real parts if and only if $Q_i > 0$, and $Q_1Q_2 - Q_3 > 0, i = 1, 2, 3$. Now $Q_1 > 0$ is implied by $D + \frac{K_1\alpha_1P^*}{(K_1+N^*)^2} + \frac{K_2\gamma_1Z^*}{(K_2+P^*)^2} > \frac{\gamma_1Z^*}{K_2+P^*}$.

Here, we consider two cases depending on the sign of m_{32}.

Case 1: When $m_{32>0}$, then $Q_2 > 0$ if $m_{11}m_{21}+m_{23}m_{32} < m_{11}m_{22}$ since $m_{11}m_{22} < 0$, $m_{12}m_{21} < 0$, and $m_{23}m_{32} < 0$.

Also, $Q_3 = (m_{11}m_{23} - m_{13}m_{21})m_{32} > 0$ if $m_{11}m_{23} > m_{13}m_{21}$ since $m_{11}m_{23} > 0$ and $m_{13}m_{21} > 0$.

Case 2: When $m_{32<0}$, then $Q_2 > 0$ if $-m_{12}m_{21} > m_{23}m_{32} - m_{11}m_{22}$ since $m_{11}m_{22} < 0$, $m_{12}m_{21} < 0$, and $m_{23}m_{32} > 0$.

Also, $Q_3 = (m_{11}m_{23} - m_{13}m_{21})m_{32} > 0$ if $m_{11}m_{23} < m_{13}m_{21}$ since $m_{11}m_{23} > 0$ and $m_{13}m_{21} > 0$.

In addition, according to Routh–Hurwitz criterion, $Q_1Q_2 - Q_3 > 0$ must be satisfied if $Q_1Q_2 > Q_3$, which indicates that the system becomes locally asymptotically stable at E^* depending upon system parameters.

Remark 1 The system could have a Hopf bifurcation at the coexistence equilibrium if the following two conditions are satisfied,

$$Q_1(N_c^0)Q_2(N_c^0) - Q_3(N_c^0) = 0,\ Q_1'(N_c^0)Q_2(N_c^0) + Q_1(N_c^0)Q_2'(N_c^0) - Q_3'(N_c^0) \neq 0. \tag{7}$$

3.3 Hopf Bifurcation at Coexistence

Let us consider a value $N^0 = N_c^0$ such that $Q_1(N_c^0)Q_2(N_c^0) - Q_3(N_c^0) = 0$. Then at $N^0 = N_c^0$, the characteristic equation (6) becomes $(\rho + Q_1)(\rho^2 + Q_2) = 0$. Clearly, the equation has three roots that are $\pm\sqrt{Q_2}i$ and $-Q_1$, i.e., two roots are a pair of purely complex roots and third root is negative. To examine the transversality condition, let us consider any point N^0 of ϵ-neighborhood of N_c^0 where $\rho_{1,2} = a(N^0) \pm ib(N^0)$. Putting this in (6) and separating the real and imaginary parts, we get the following results:

$$a^3 - 3ab^2 + p_1(a^2 - b^2) + p_2a + p_3 = 0 \tag{8}$$

$$(3a^2b - b^3) + 2p_1ab + p_2 = 0. \tag{9}$$

Since $b(N^0) \neq 0$, then from (9), we have $b^2 = 3a^2 + 2Q_1a + Q_2$.

Putting the value of b^2 in (6), we have

$$8a^3 + 8Q_1a^2 + 2a(Q_1^2 + Q_2) + Q_1Q_2 - 3 = 0. \tag{10}$$

Now differentiating w.r.t N^0 at $N^0 = N_c^0$, we get the following results $\left[\frac{da}{dN^0}\right]_{N^0=N_c^0} = -\left[\frac{1}{2(Q_1^2+Q_2)}\frac{d}{dN^0}(Q_1Q_2 - Q_3)\right]_{N^0=N_c^0} \neq 0$ provided $\left[\frac{d}{dN^0}(Q_1Q_2 - Q_3)\right]_{N^0=N_c^0} \neq 0$, i.e., the second condition of (7).

Theorem 1 *The direction of Hopf bifurcation is determined by the value μ_{22}. If $\mu_{22} > 0$ (< 0), then the Hopf bifurcation is supercritical (subcritical) and the bifurcating periodic solutions exist for $N^0 > N_c^0$.*

The stability and the period of the bifurcating periodic solutions are, respectively, determined by the parameters β_2 and τ_2 defined in the proof. The solutions are orbitally stable (unstable) if $\beta_2 < 0$ (> 0) and the period increases (decreases) if $\tau_2 > 0$ (< 0).

Proof The computational details are very elaborated; therefore, we just outline the sketch of the proof by using normal form theory [27]. Here, Remark 1 indicates the conditions of Hopf bifurcation.

Let us indicate by a bar the system parameters; the eigenvector corresponding to the eigenvalue $\sigma = \mathbf{i}\eta_2$ is

$$\omega\left[\frac{(\mathbf{i}\eta_2)^2 - m_{22}(\mathbf{i}\eta_2) - m_{32}m_{23}}{m_{21}m_{32}}, \frac{\mathbf{i}\eta_2}{V_{32}}, 1\right]^T, \quad \omega \in \mathbf{R}.$$

The eigenvector corresponding to the eigenvalue e_1 is

$$\omega\left[\frac{e_1^2 - m_{22}e_1 - m_{32}m_{23}}{m_{21}m_{32}}, \frac{e_1}{m_{32}}, 1\right]^T, \quad \omega \in \mathbf{R}.$$

Let us interpret the following quantities:

$$b_{11} = -\frac{\eta_2^2 + m_{32}m_{23}}{m_{21}m_{32}}, \quad b_{12} = \frac{\eta_2 m_{22}}{m_{21}m_{32}}, b_{13} = \frac{e_1^2 - m_{22}e_1 - m_{32}m_{23}}{m_{21}m_{32}}, \quad b_{21} = 0,$$
$$b_{22} = -\frac{\eta_2}{m_{32}}, \quad b_{23} = \frac{e_1}{m_{32}}, \quad b_{31} = 1,\ b_{32} = 0,\ b_{33} = 1.$$

Applying the transformation

$$N = N^* + b_{11}x_1 + b_{12}y_1 + b_{13}z_1,$$
$$P = P^* + b_{21}x_1 + b_{22}y_1 + b_{23}z_1,$$
$$Z = Z^* + b_{31}x_1 + b_{32}y_1 + b_{33}z_1,$$

system (1) is then reduced to

$$\frac{dx_1}{dt} = \frac{W_3Q_2 - W_1b_{22} + W_2b_{12}}{Q_2 - Q_1} := H^1,$$
$$\frac{dy_1}{dt} = \frac{(Q_2 - Q_1 + Q_3)W_1 + Q_4W_2 + (b_{13}Q_1 - b_{11}Q_2)W_3}{b_{12}(Q_2 - Q_1)} := H^2,$$
$$\frac{dz_1}{dt} = \frac{W_1b_{22} - W_2b_{12} - W_3Q_1}{Q_2 - Q_1} := H^3, \quad (11)$$

where as a shorthand we have introduced the following quantities:

$$Q_1 = b_{11}b_{22} - b_{21}b_{12}, \quad Q_2 = b_{13}b_{22} - b_{23}b_{12}, \quad Q_3 = b_{11}b_{22} - b_{13}b_{22},$$
$$Q_4 = b_{13}b_{12} - b_{11}b_{12}, \quad W_1 = \bar{D}(\bar{N^0} - N^* - b_{11}x_1 - b_{12}y_1 - b_{13}z_1)$$

$$-\frac{\bar{\alpha_1}(N^*+b_{11}x_1+b_{12}y_1+b_{13}z_1)(P^*+b_{21}x_1+b_{22}y_1+b_{23}z_1)}{\bar{K_1}+N^*+b_{11}x_1+b_{12}y_1+b_{13}z_1}$$
$$+\bar{\mu_3}(P^*+b_{21}x_1+b_{22}y_1+b_{23}z_1)+\bar{\mu_4}(Z^*+b_{31}x_1+b_{32}y_1+b_{33}z_1)$$

$$W_2=\frac{\bar{\alpha_2}(N^*+b_{11}x_1+b_{12}y_1+b_{13}z_1)(P^*+b_{21}x_1+b_{22}y_1+b_{23}z_1)}{\bar{K_1}+N^*+b_{11}x_1+b_{12}y_1+b_{13}z_1}$$
$$-\frac{\bar{c}(1-\bar{K})(P^*+b_{21}x_1+b_{22}y_1+b_{23}z_1)(Z^*+b_{31}x_1+b_{32}y_1+b_{33}z_1)}{\bar{K_2}+P^*+b_{21}x_1+b_{22}y_1+b_{23}z_1}$$
$$-\bar{\mu_1}(P^*+b_{21}x_1+b_{22}y_1+b_{23}z_1),$$
$$W_3=\frac{\bar{e}(1-\bar{K})(P^*+b_{21}x_1+b_{22}y_1+b_{23}z_1)(Z^*+b_{31}x_1+b_{32}y_1+b_{33}z_1)}{\bar{K_2}+P^*+b_{21}x_1+b_{22}y_1+b_{23}z_1}-$$
$$\bar{e}\bar{\rho}(P^*+b_{21}x_1+b_{22}y_1+b_{23}z_1)^{\frac{2}{3}}(Z^*+b_{31}x_1+b_{32}y_1+b_{33}z_1).$$

The origin is the equilibrium point of the new system (11). At it, several entries vanish after simplifying the Jacobian of (11):

$$\frac{\partial H^1}{\partial x_1}=\frac{\partial H^2}{\partial y_1}=\frac{\partial H^1}{\partial z_1}=\frac{\partial H^3}{\partial x_1}=\frac{\partial H^3}{\partial y_1}=\frac{\partial H^2}{\partial z_1}=0.$$

Further, the following auxiliary quantities can be explicitly calculated in terms of the system parameters, but we omit the explicit formulae in view of their excessive length.

$$D_{11}=\frac{\partial H^3}{\partial z_1},\quad g_{11}=\frac{1}{4}\left[\frac{\partial^2 H^1}{\partial x_1^2}+\frac{\partial^2 H^2}{\partial y_1^2}+\mathbf{i}\left(\frac{\partial^2 H^2}{\partial x_1^2}+\frac{\partial^2 H^1}{\partial y_1^2}\right)\right],$$
$$g_{02}=\frac{1}{4}\left[\frac{\partial^2 H^1}{\partial x_1^2}-\frac{\partial^2 H^2}{\partial y_1^2}-2\frac{\partial^2 H^2}{\partial x_1\partial y_1}+\mathbf{i}\left(\frac{\partial^2 H^2}{\partial x_1^2}-\frac{\partial^2 H^1}{\partial y_1^2}\right)+2\frac{\partial^2 H^1}{\partial x_1\partial y_1}\right],$$
$$g_{20}=\frac{1}{4}\left[\frac{\partial^2 H^1}{\partial x_1^2}-\frac{\partial^2 H^2}{\partial y_1^2}+2\frac{\partial^2 H^2}{\partial x_1\partial y_1}+\mathbf{i}\left(\frac{\partial^2 H^2}{\partial x_1^2}-\frac{\partial^2 H^1}{\partial y_1^2}\right)-2\frac{\partial^2 H^1}{\partial x_1\partial y_1}\right],$$

$$G_{21}=\frac{1}{8}\left[\frac{\partial^3 H^1}{\partial x_1^3}+\frac{\partial^3 H^1}{\partial x_1\partial y_1^2}+\frac{\partial^3 H^2}{\partial^2 x_1\partial y_1}+\frac{\partial^3 H^2}{\partial y_1^3}\right]$$
$$+\frac{\mathbf{i}}{8}\left[\frac{\partial^3 H^2}{\partial x_1^3}+\frac{\partial^3 H^2}{\partial x_1\partial y_1^2}-\frac{\partial^3 H^1}{\partial^2 x_1\partial y_1}-\frac{\partial^3 H^1}{\partial y_1^3}\right],$$

$$G_{110} = \frac{1}{2}\left[\frac{\partial^2 H^1}{\partial x_1 \partial z_1} + \frac{\partial^2 H^1}{\partial y_1 \partial z_1} + \mathbf{i}\left(\frac{\partial^2 H^2}{\partial x_1 \partial z_1} - \frac{\partial^2 H^2}{\partial y_1 \partial z_1}\right)\right],$$

$$G_{101} = \frac{1}{2}\left[\frac{\partial^2 H^1}{\partial x_1 \partial z_1} - \frac{\partial^2 H^1}{\partial y_1 \partial z_1} + \mathbf{i}\left(\frac{\partial^2 H^2}{\partial x_1 \partial z_1} + \frac{\partial^2 H^2}{\partial y_1 \partial z_1}\right)\right],$$

$$h_{11} = \frac{1}{4}\left[\frac{\partial^2 H^3}{\partial x_1^2} + \frac{\partial^2 H^3}{\partial y_1^2}\right], \quad h_{20} = \frac{1}{4}\left[\frac{\partial^2 H^3}{\partial x_1^2} - \frac{\partial^2 H^3}{\partial y_1^2} - 2\mathbf{i}\frac{\partial^2 H^3}{\partial x_1 \partial y_1}\right],$$

$$\omega_{11} = -\frac{h_{11}}{D_{11}}, \quad \omega_{20} = -\frac{h_{20}}{D_{11} - 2\mathbf{i}\omega_0}, \quad g_{21} = G_{21} + 2G_{110}\omega_{11} + G_{101}\omega_{20}.$$

The values of μ_{22} and τ_2, obtained from [27, 28], can now be calculated from the above quantities,

$$c_1(0) = \frac{\mathbf{i}}{2\omega_0}[g_{20}g_{11} - 2|g_{11}|^2 - \frac{1}{3}|g_{02}|^2] + \frac{g_{21}}{2},$$

$$\mu_{22} = -\frac{\mathrm{Re}[c_1(0)]}{u'(0)}, \quad \tau_2 = -\frac{\mathrm{Im}[c_1(0)] + \mu_{22}\omega'(0)}{\omega(0)}, \quad \beta_2 = 2\mathrm{Re}[c_1(0)].$$

Stating finally [27], if the root of the characteristic equation increases for increasing values of the bifurcation parameter N^0, namely $u'(0) > 0$, the periodic solution emanating from the equilibrium for $\mu_{22} > 0$ is supercritical, while it is subcritical for $\mu_{22} < 0$.

4 The Stochastic Model

In this section, we study the stochastic stability of the coexistence equilibrium and the impact of environmental fluctuation by introducing environmental parameters in model system. Also, we assume that all parameters are constants irrespective of time.

An existing deterministic system can be developed by two ways. Firstly, to develop the stochastic system, we can replace some of the environmental parameters by some random parameters in the deterministic model. Secondly, without altering any particular parameter in deterministic dynamic equations, we can add a randomly fluctuating driving force [29].

Here, we apply the second approach. The Gaussian white noise type stochastic perturbation of the state variables around their steady values E^* is very effective to model rapidly fluctuating phenomena that are proportional to the distances N,

P, Z of each population from their equilibrium values N^*, P^*, Z^* [30]. Based on the above assumption, we develop the deterministic system (1) by the following stochastic model:

$$\begin{aligned} dN &= G_1(N, P, Z)dt + \sigma_1(N - N^*)d\xi_t^1, \\ dP &= G_2(N, P, Z)dt + \sigma_2(P - P^*)d\xi_t^2, \\ dZ &= G_3(N, P, Z)dt + \sigma_3(Z - Z^*)d\xi_t^3, \end{aligned} \tag{12}$$

where real constant parameters σ_1, σ_2, and σ_3 be the intensities of environmental fluctuations, and $\xi_t^i = \xi_i(t)$, $i = 1, 2, 3$, are the standard Wiener processes independent of each other [31].

The system (12) can be written as an Itō stochastic differential system of the type

$$dX_t = G(t, X_t)dt + g(t, X_t)d\xi_t, \quad X_{t0} = X_0, \tag{13}$$

where the solution $X_t = (N, P, Z)^T$, for $t > 0$, is known as Itō process. Here, G is the drift coefficient or it can be written as slowly varying continuous component. The diagonal matrix $g = \text{diag}[\sigma_1(N - N^*), \sigma_2(P - P^*), \sigma_3(Z - Z^*)]$ is defined as diffusion coefficient. It can be expressed as the rapidly varying continuous random component, and $\xi_t = (\xi_t^1, \xi_t^2, \xi_t^3)^T$ be a three-dimensional stochastic process having scalar Wiener process components with increments $\Delta\xi_t^j = \xi_j(t + \Delta t) - \xi_j(t)$ that are independent Gaussian random variables $\mathbf{N}(0, \Delta t)$. The system (12) is known as multiplicative noise as the diffusion matrix g depends upon the solution of X_t.

4.1 Stochastic Stability of the Coexistence Equilibrium

The stochastic differential system (12) can be centered at its coexistence equilibrium E^* by introducing the perturbation vector $U(t) = (u_1(t), u_2(t), u_3(t))^T$, with $u_1 = N - N^*$, $u_2 = P - P^*$, $u_3 = Z - Z^*$. To derive the asymptotic stability in the mean square sense by the Lyapunov functions method, working on the complete nonlinear equations (12) could be attempted, following [32]. But for simplicity, we deal with the stochastic differential equations obtained by linearizing (12) about the coexistence equilibrium E^*. The linearized version of (13) around E^* is given by

$$dU(t) = F_L(U(t))dt + g(U(t))d\xi(t), \tag{14}$$

where now $g(U(t)) = \text{diag}[\sigma_1 u_1, \sigma_2 u_2, \sigma_3 u_3]$ and

$$F_L(U(t)) = \begin{bmatrix} m_{11}u_1 + m_{12}u_2 + m_{13}u_3 \\ m_{21}u_1 + m_{22}u_2 + m_{23}u_3 \\ m_{31}u_1 + m_{32}u_2 + m_{33}u_3 \end{bmatrix} = MU,$$

and the coexistence equilibrium corresponds now to the origin $(u_1, u_2, u_3) = (0, 0, 0)$. Let $\Omega = \left[(t \geq t_0) \times R^3, t_0 \in R^+\right]$, and let $\Theta(t, X) \in C^{(1,2)}(\Omega)$ be a differentiable function of time t and twice differentiable function of X. Let further

$$L_\Theta(t, u) = \frac{\partial \Theta(t, u(t))}{\partial t} + f^T(u(t)) \frac{\partial \Theta(t, u)}{\partial u} + \frac{1}{2} \mathrm{tr}\left[g^T(u(t)) \frac{\partial^2 \Theta(t, u)}{\partial u^2} g(u(t))\right], \quad (15)$$

where

$$\frac{\partial \Theta}{\partial u} = \left(\frac{\partial \Theta}{\partial u_1}, \frac{\partial \Theta}{\partial u_2}, \frac{\partial \Theta}{\partial u_3}\right)^T, \quad \frac{\partial^2 \Theta(t, u)}{\partial u^2} = \left(\frac{\partial^2 \Theta}{\partial u_j \partial u_i}\right)_{i,j=1,2,3}.$$

With these positions, we now recall the following result [33].

Theorem 2 *Assume that the functions* $\Theta(U, t) \in C_3(\Omega)$ *and* L_Θ *satisfy the inequalities*

$$r_1 |U|^\alpha \leq \Theta(U, t) \leq r_2 |U|^\alpha, \quad (16)$$

$$L_\Theta(U, t) \leq -r_3 |U|^\alpha, \quad r_i > 0, \quad i = 1, 2, 3, \quad \alpha > 0. \quad (17)$$

Then, the trivial solution of (14) is exponentially α*-stable for all time* $t \geq 0$.

Remark 2 For $\alpha = 2$ in (16) and (17), the trivial solution of (14) is exponentially mean square stable; furthermore, the trivial solution of (14) is globally asymptotically stable in probability [33].

Theorem 3 *Assume* $m_{ij} < 0$, $i, j = 1, 2, 3$, *and that for some positive real values of* ω_k, $k = 1, 2$, *the following inequality holds*

$$\left[2(1 + \omega_2)m_{22} + 2m_{32}\omega_2 - (1 + \omega_2)\sigma_2^2\right][2m_{13}\omega_1 + 2m_{23}\omega_2 \quad (18)$$
$$-(\omega_1 + \omega_2)\sigma_3^2\Big] > \left[m_{12}\omega_1 + m_{22}\omega_2 + m_{23}(1 + \omega_2) + m_{32}(\omega_1 + \omega_2)\right]^2.$$

Then, if $\sigma_1^2 < -2m_{11}$, *it follows that*

$$\sigma_2^2 < -\frac{2m_{22}(1 + \omega_2) + 2m_{32}\omega_2}{1 + \omega_2}, \quad \sigma_3^2 < -\frac{2m_{13}\omega_1 + 2m_{23}\omega_2}{\omega_1 + \omega_2}, \quad (19)$$

where

$$\omega_1{}^* = \frac{m_{21}}{m_{13} + m_{11} - m_{12} - m_{32}}, \quad \omega_2{}^* = \frac{m_{11} + m_{13}}{m_{12} - (m_{13} + m_{11}) + m_{32}}, \quad (20)$$

and the zero solution of system (12) is asymptotically mean square stable.

Proof We consider the Lyapunov function

$$\Theta(u(t)) = \frac{1}{2}\left[\omega_1(u_1+u_3)^2 + {u_2}^2 + \omega_2(u_2+u_3)^2\right],$$

where ω_k are the real positive constants to be chosen later.

It is easy to check that inequalities (16) are true for $\alpha = 2$. Furthermore,

$$\begin{aligned} L_\Theta(u(t)) = {} & [m_{22}(1+\omega_2) + m_{32}\omega_2]\,u_2^2 + [m_{13}\omega_1 + m_{23}\omega_2]\,u_3^2 \\ & + u_1u_2\,[m_{12}\omega_1 + m_{21}(1+\omega_2) + m_{32}\omega_1] + u_2u_3\,[m_{12}\omega_1 + m_{22}\omega_2 + m_{23}(1+\omega_2) \\ & + m_{32}(\omega_1+\omega_2)] + u_3u_1\,[m_{13}\omega_1 + m_{11}\omega_1 + m_{21}\omega_2] \\ & + m_{11}\omega_1u_1^2 + \frac{1}{2}\mathrm{tr}\left[g^T(u(t))\frac{\partial^2\Theta}{\partial u^2}g(u(t))\right]. \end{aligned}$$

Now observe that

$$\frac{\partial^2\Theta}{\partial u^2} = \begin{vmatrix} \omega_1 & 0 & \omega_1 \\ 0 & 1+\omega_2 & \omega_2 \\ \omega_1 & \omega_2 & \omega_1+\omega_2 \end{vmatrix},$$

so that we can evaluate the trace term as follows,

$$\mathrm{tr}\left[g^T(u(t))\frac{\partial^2\Theta}{\partial u^2}g(u(t))\right] = \omega_1{\sigma_1}^2{u_1}^2 + (1+\omega_2){\sigma_2}^2{u_2}^2 + (\omega_1+\omega_2){\sigma_3}^2{u_3}^2.$$

Using then (20), the Lyapunov function becomes $L_\Theta(u(t)) = -u^T Qu$, with the real symmetric matrix

$$Q = \begin{vmatrix} -m_{11}\omega_1 - \frac{1}{2}\omega_1\sigma_1^2 & 0 & 0 \\ 0 & -(1+\omega_2)m_{22} - \omega_2m_{32} - \frac{1}{2}(1+\omega_2)\sigma_2^2 & Q_{23} \\ 0 & Q_{23} & Q_{33} \end{vmatrix},$$

where

$$Q_{23} = -\frac{m_{12}\omega_1 + m_{22}\omega_2 + m_{23}(1+\omega_2) + m_{32}(\omega_1+\omega_2)}{2}$$

and $Q_{33} = -m_{13}\omega_1 - m_{23}\omega_2 - \frac{1}{2}(\omega_1+\omega_2)\sigma_3^2$. Easily, the inequality $L_\Theta(u(t)) \le -u^T Qu$ holds. On the other hand, (18) and (19) imply that Q is positive-definite, and therefore, all its eigenvalues $\lambda_i(Q),\ i = 1, 2, 3$, are the positive real numbers. Let $\lambda_m = \min\{\lambda_i(Q),\ i = 1, 2, 3\} > 0$. From the previous inequality for $L_\Theta(u(t))$, we thus get

$$L_{\Theta}(u(t)) \leq -\lambda_m |u(t)|^2,$$

thus completing the proof.

Remark 3 Theorem 3 provides the necessary conditions for the stochastic stability of the coexistence equilibrium E^* under environmental fluctuations [34]. Thus, the internal parameters of the model together with the intensities of the environmental fluctuations help in maintaining the stability of the stochastic system.

5 Numerical Simulations

In this section, the dynamic characteristics of plankton species are being emphasized with the help of numerical simulations. We start with a reference parameter set (cf. Table 1 [13, 26]) in which the criterion for existence at E^* is satisfied. We observe that the equilibrium of coexistence is locally asymptotically stable under the given set of parametric values (cf. Fig. 1a). Now by varying the different parametric values, we study the dynamic behavior of system (1).

5.1 Effects of N^0

If the value of constant nutrient input $N^0 = 4.2$ is increased, the system exhibits oscillations around E^*. But for low value of $N^0 = 2.2$, the system switches to

Table 1 A set of parametric values

Parameter	Definition	Default value
N^0	Constant input of nutrient	4
D	Dilution rate of nutrient	1.65
ρ	The degree of toxicity	0.018
α_1	Nutrient uptake rate for the phytoplankton	1.2
α_2	Conversion rate of nutrient for the growth of phytoplankton	1
μ_1	Mortality rate of phytoplankton	0.6
μ_2	Mortality rate of zooplankton	0.2
μ_3	Nutrient recycle rate due to the death of phytoplankton	0.06
μ_4	Nutrient recycle rate due to the death of zooplankton	0.06
c	Predation rate of zooplankton	1
e	Conversion rate of zooplankton	0.8
K_1	Half-saturation constant for phytoplankton	0.6
K_2	Half-saturation constant for zooplankton	2
K	The fraction of phytoplankton aggregates	0.55

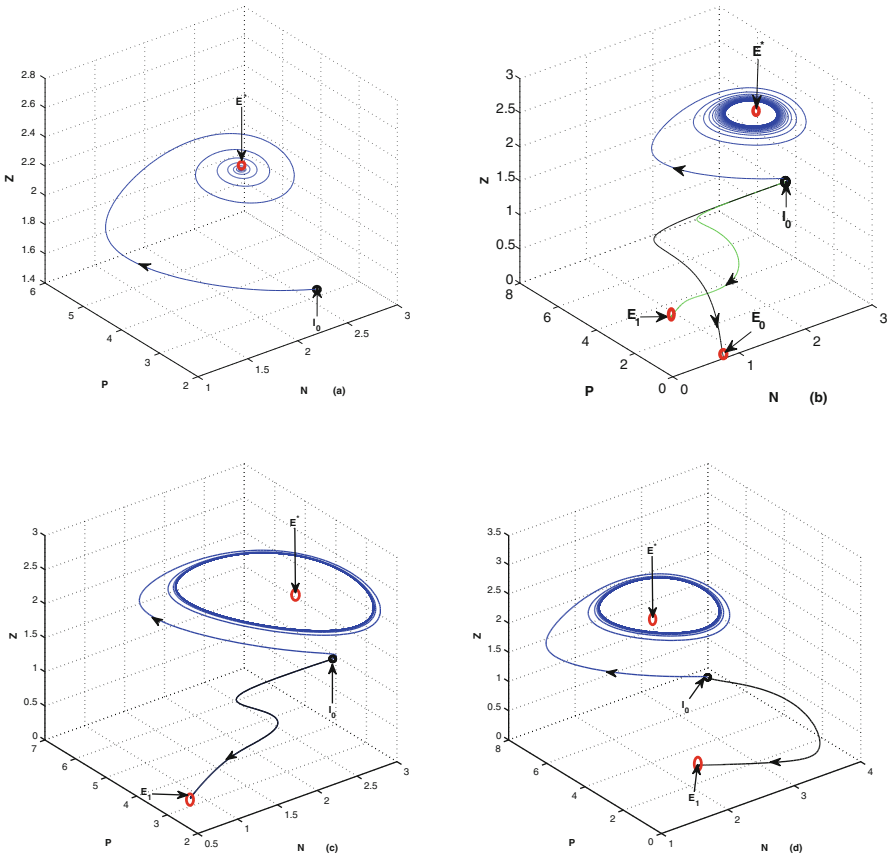

Fig. 1 **(a)** The equilibrium point E^* is stable for the parametric values as given in Table 1. **(b)** The figure depicts oscillatory behavior around the positive interior equilibrium point E^* of system (1) for $N^0 = 4.2$ (blue line), zooplankton-free equilibrium E_1 for $N^0 = 2.2$ (green line), and plankton-free equilibrium E_0 for $N^0 = 0.8$ (black line). **(c)** The figure depicts oscillatory behavior around the positive interior equilibrium point E^* of system (1) for $D = 1.85$ (blue line) and zooplankton-free equilibrium E_1 for $D = 0.7$ (black line). **(d)** The figure depicts oscillatory behavior around the positive interior equilibrium point E^* of system (1) for $\mu_1 = 0.56$ (blue line) and zooplankton-free equilibrium E_1 for $\mu_1 = 0.8$ (black line)

zooplankton-free equilibrium E_1. Further decreasing the value of N^0 from 2.2 to 0.8, the system shifts to plankton-free equilibrium E_0 (cf. Fig. 1b).

5.2 *Effects of D*

The system (1) can switch to oscillatory behavior around E^* for high value of dilution rate of nutrient, $D = 1.85$. Also, our observation indicates that for low

value of $D = 0.8$, the trajectory approaches zooplankton-free equilibrium E_1 (cf. Fig. 1c).

5.3 Effects of μ_1

Decreasing the value of μ_1 from 0.6 to 0.56, the stable equilibrium switches to oscillatory behavior around E^*. On the other hand, the system shifts to zooplankton-free equilibrium E_1 due to high value of $\mu_1 = 0.8$ (cf. Fig. 1d).

5.4 Effects of μ_2

The system (1) exhibits oscillations around E^* for low value of $\mu_2 = 0.195$. Further, it is noted that at high value of $\mu_2 = 0.25$, the stable equilibrium switches to zooplankton-free equilibrium E_1 (cf. Fig. 2a).

5.5 Effects of K

Taking $K = 0.53$, the system exhibits oscillatory behavior around the positive interior equilibrium E^*. But it is observed that the stable equilibrium shifts to zooplankton-free equilibrium E_1 due to high value of $K = 0.65$ (cf. Fig. 2b).

5.6 Effects of ρ

Taking amount of toxicity $\rho = 0.014$, the stable equilibrium switches to oscillatory behavior around the positive interior equilibrium E^*. But increasing the value of ρ from 0.018 to 0.3, the system switches to zooplankton-free equilibrium E_1 (cf. Fig. 2c).

5.7 Hopf Bifurcation

Figure 3a–c depicts the different steady-state behaviors of nutrient, phytoplankton, and zooplankton in the system (1) for the parameter N^0. Here, we see a Hopf bifurcation point at $N_c^0 = 4.18$ (denoted by a red star (H)) with first Lyapunov coefficient being $-1.101668e^{-002}$, which indicates that a stable limit cycle bifurcates from the equilibrium and loses its stability. Here, $N^0 = 2.40$ (BP) denotes the branch point

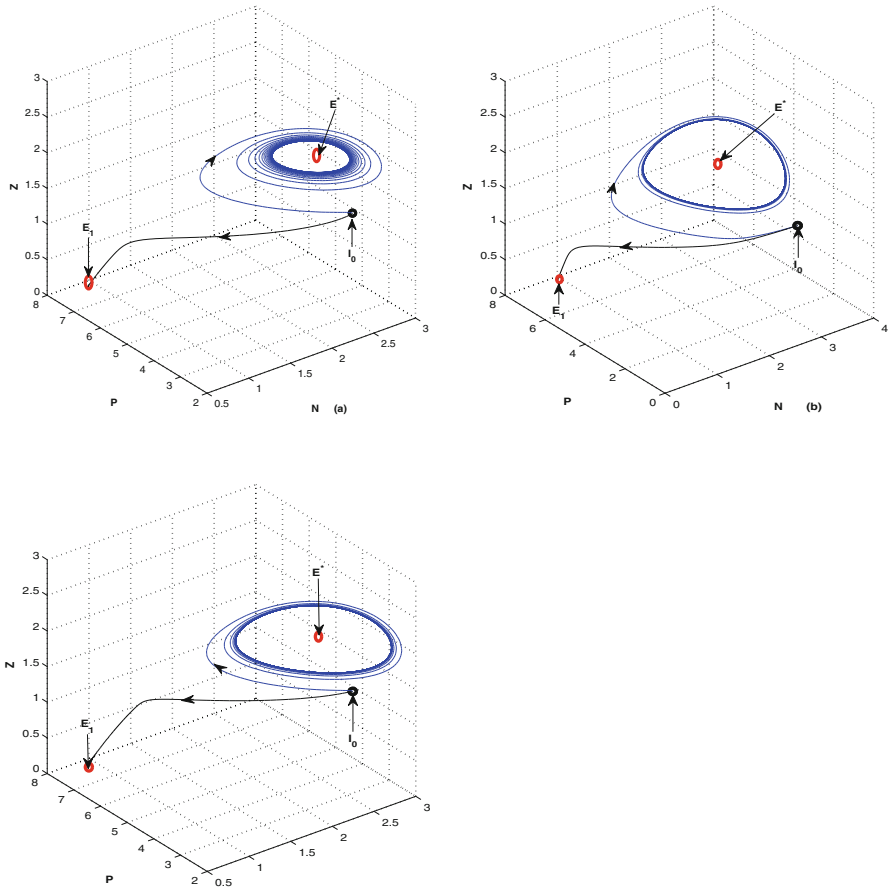

Fig. 2 **(a)** The figure depicts oscillatory behavior around the positive interior equilibrium point E^* of system (1) for $\mu_2 = 0.195$ (blue line) and zooplankton-free equilibrium E_1 for $\mu_2 = 0.25$ (black line). **(b)** The figure depicts oscillatory behavior around the positive interior equilibrium point E^* of system (1) for $K = 0.53$ (blue line) and zooplankton-free equilibrium E_1 for $K = 0.65$ (black line). **(c)** The figure depicts oscillatory behavior around the positive interior equilibrium point E^* of system (1) for $\rho = 0.014$ (blue line) and the zooplankton-free equilibrium E_1 for $\rho = 0.03$ (black line)

of the system (1) where zooplankton go to extinction. We have plotted a bifurcation diagram with N^0 as the bifurcation parameter with other three species (cf. Fig. 3d).

Figure 4a–c depicts the different steady-state behaviors of nutrient, phytoplankton, and zooplankton in the system (1) for the parameter D. Here, we observe a Hopf bifurcation point at $D = 1.75$ (denoted by a red star (H)) with first Lyapunov coefficient being $-1.057982e^{-002}$. Here, $D = 0.798$ (BP) indicates the branch point of the system (1). We have displayed a bifurcation diagram when D is treated as the free parameter (cf. Fig. 4d).

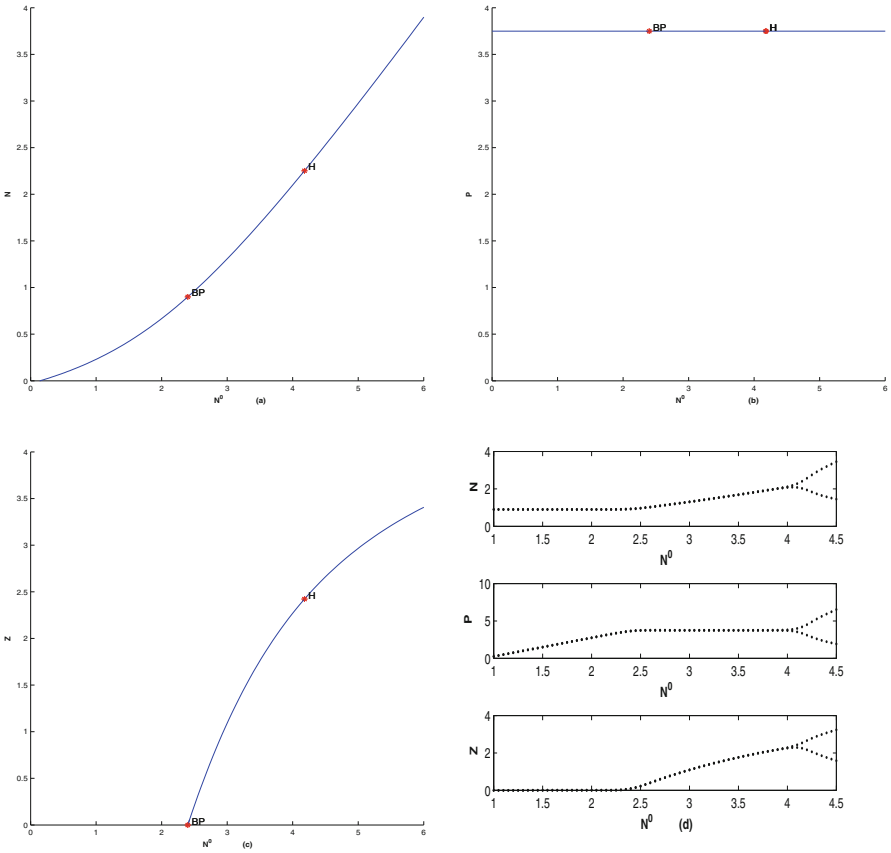

Fig. 3 **(a)** The figure depicts different steady-state behaviors of nutrient for the effect of N^0. (**b**) The figure depicts different steady-state behaviors of phytoplankton for the effect of N^0. (**c**) The figure depicts different steady-state behaviors of zooplankton for the effect of N^0. **(d)** The bifurcation diagram for N^0

From Fig. 5a–c, it follows different stability behaviors for free parameter μ_2. At $\mu_2 = 0.196$, the Hopf point indicates the supercritical bifurcation with first Lyapunov coefficient $-1.136241e^{-002}$. It is clearly indicated that zooplankton become extinct at $\mu_2 = 0.229760$ (BP). Here, LP denotes the limit point. Further, we have plotted a bifurcation diagram with constant nutrient input μ_2 as the bifurcation parameter with other three species (cf. Fig. 5d). For a clear understanding of a dynamic change due to change in μ_1, ρ, and K, we have plotted three bifurcation diagrams separately (cf. Fig. 6a–c). We have simulated a family of stable limit cycles bifurcating from Hopf point when ρ is the free parameter (cf. Fig. 6d). Finally, we have plotted two-parameter bifurcation diagrams for $N^0 - D$, $N^0 - \mu_1$, $N^0 - K$, and $N^0 - \rho$, respectively (Fig. 7a–d), to show the stable zone at E^*. All the numerical results are summarized in Table 2.

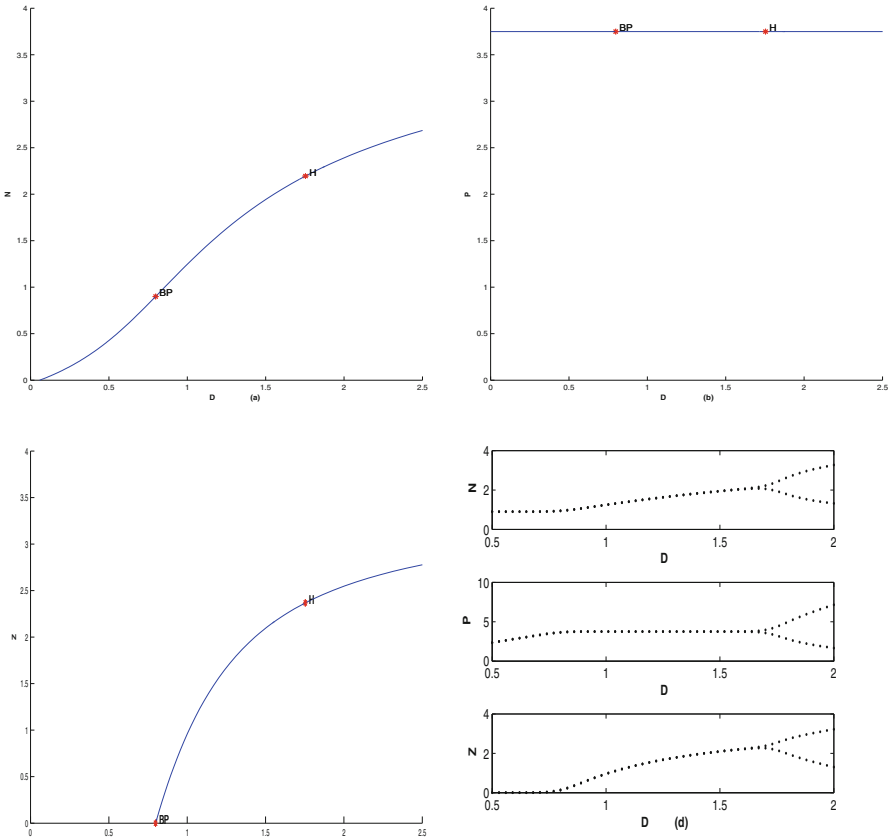

Fig. 4 **(a)** The figure depicts different steady-state behaviors of nutrient for the effect of D. (**b**) The figure depicts different steady-state behaviors of phytoplankton for the effect of D. (**c**) The figure depicts different steady-state behaviors of zooplankton for the effect of D. **(d)** The bifurcation diagram for D

5.8 Environmental Fluctuations

Next, we examine the dynamical behavior of the system in the presence of environmental disturbances. To study the stochastic differential equation numerically using MATLAB software, we apply the Euler–Maruyama method. Firstly, we satisfy the condition for asymptotic stability at coexistence equilibrium in the mean square sense that depends on system parameters of model system (12) and σ_1, σ_2, and σ_3. Taking $\sigma_1 = 0.1$, $\sigma_2 = 0.1$, and $\sigma_3 = 0.14$, the values of intensities of the environmental perturbations with reference set of parametric values as in Table 1 for which all the three species coexist and the system is stochastically stable (cf. Fig. 8a). But when we increase the values of intensities of the environmental

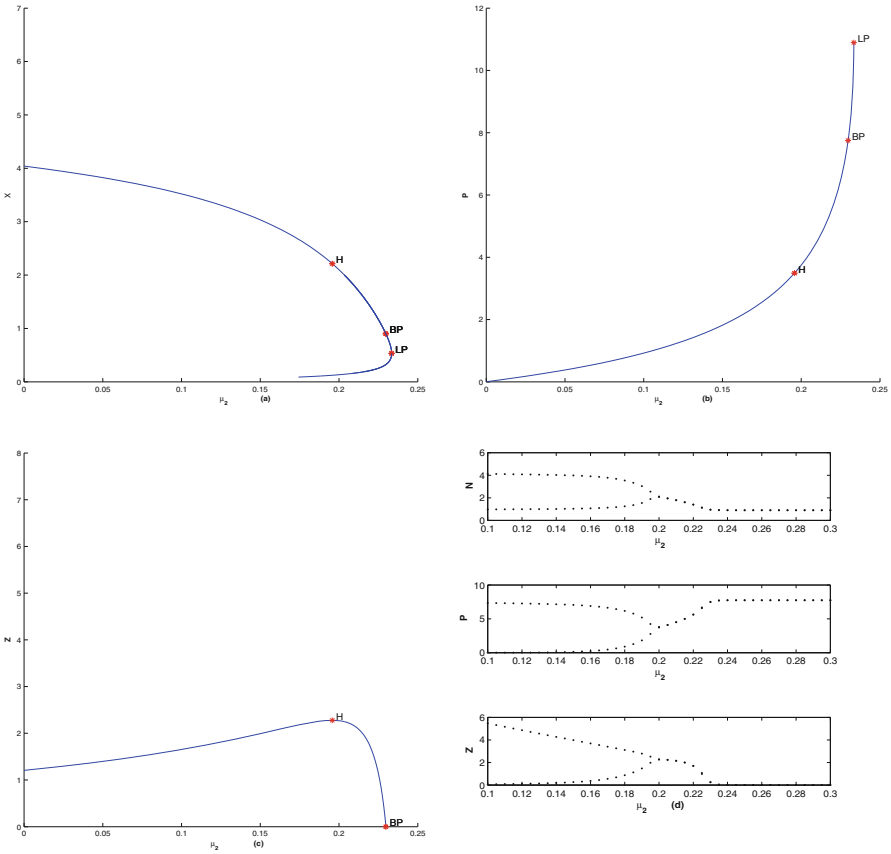

Fig. 5 **(a)** The figure depicts different steady-state behaviors of nutrient for the effect of μ_2. (**b**) The figure depicts different steady-state behaviors of phytoplankton for the effect of μ_2. (**c**) The figure depicts different steady-state behaviors of zooplankton for the effect of μ_2. **(d)** The bifurcation diagram for μ_2

perturbations, $\sigma_1 = 0.3$, $\sigma_2 = 0.2$, and $\sigma_3 = 0.15$, the coexistence equilibrium becomes unstable (cf. Fig. 8b).

6 Discussion

We have considered a nutrient–phytoplankton–zooplankton interaction model in which toxin-producing phytoplankton (TPP) aggregate to defend itself from the zooplankton predation. Their main features are the use of general nutrient uptake functions and instantaneous nutrient recycling. We further investigate the impact of model parameters by either varying one of them or combining some of them.

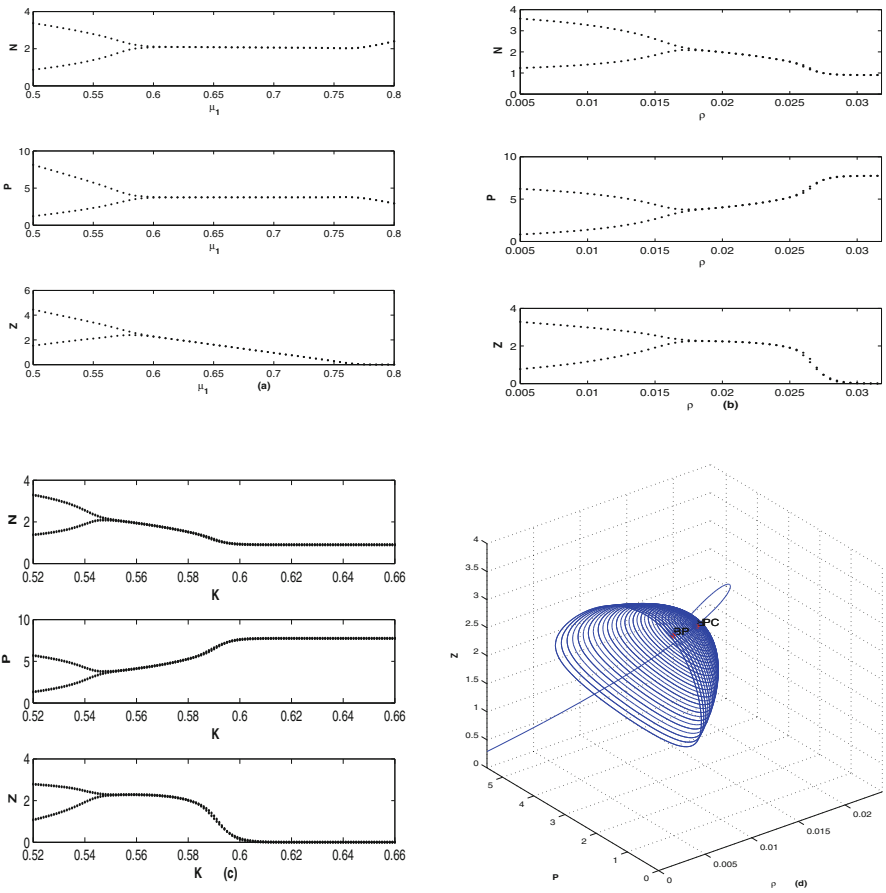

Fig. 6 **(a)** The bifurcation diagram for μ_1. **(b)** The bifurcation diagram for ρ. **(c)** The bifurcation diagram for K. **(d)** The family of limit cycles bifurcating from the Hopf point H for ρ

Firstly, the model is studied analytically, and the threshold values for the feasibility and stability of the three possible steady states namely plankton-free, zooplankton-free, and coexistence equilibria are determined. If the system parameter values satisfy suitable conditions, these equilibrium states are related to each other by transcritical bifurcations. Next analytical results are performed for a Hopf bifurcation at the coexistence equilibrium that is supported by numerical simulations. By changing the various parameters, persistent oscillations occur. The bifurcation diagrams of Figs. 3 and 4 indicate that increasing values of the nutrient input as well as of its dilution rate lead to sustained population oscillations. The same outcome occurs if instead we decrease the mortality rate of plankton population rate, the degree of toxicity, and the fraction of phytoplankton aggregates. These results indicate that to avoid recurrence bloom and to prevent zooplankton

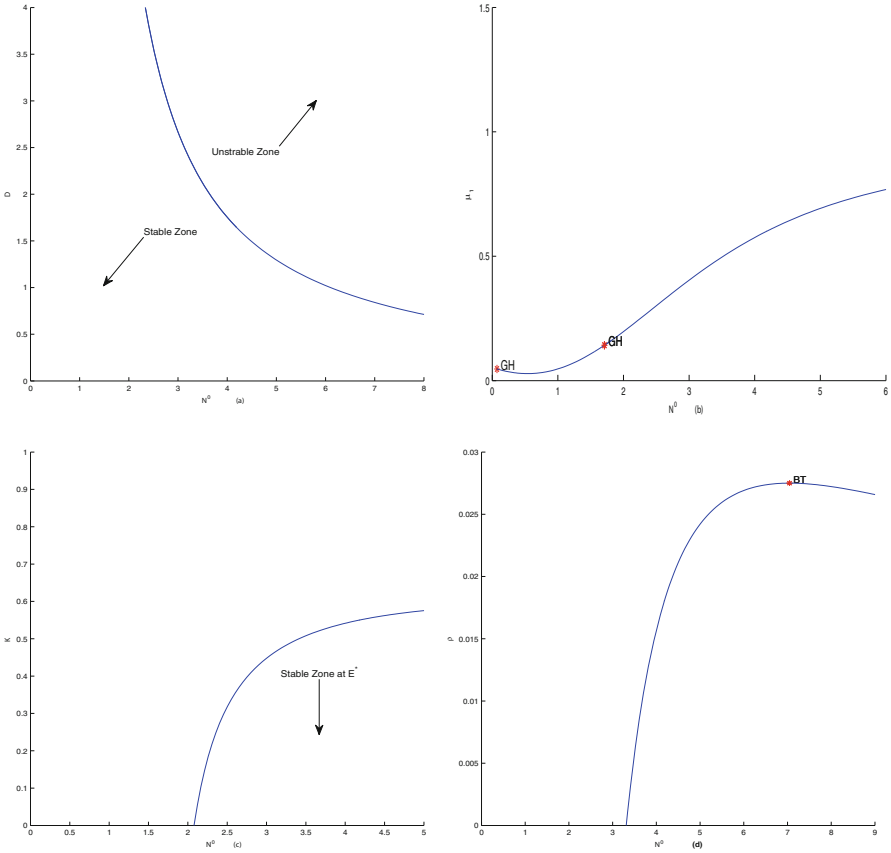

Fig. 7 **(a)** The two-parameter bifurcation diagram for $N_0 - D$. **(b)** The two-parameter bifurcation diagram for $N_0 - \mu_1$. **(c)** The two-parameter bifurcation diagram for $N_0 - K$. **(d)** The two-parameter bifurcation diagram for $N_0 - \rho$

from extinction, a suitable range is necessary for the constant nutrient input, dilution rate of nutrient, mortality rate of both plankton population, and degree of toxicity. Next, we assume environmental noise in the model. It is observed that low values of noise intensities lead to stochastic asymptotic stability of the system. But slightly higher values of noise intensities may lead to oscillations with high amplitudes. It is clearly indicated that our model system persists to be stochastically stable if it satisfies suitable conditions that involve both the maximum size of the environmental random fluctuations and the model parameters.

Table 2 Natures of equilibrium points

Parameters	Values	Eigenvalues	Equilibrium points
N^0	4.179998	$(-1.8582, \pm 0.107212i)$	Hopf (H)
	2.399359	$(-2.59529, -0.254198, 0)$	Branch point (BP)
D	1.753770	$(-1.97839, \pm 0.105751i)$	Hopf (H)
	0.798046	$(-1.57999, -0.417547, 0)$	Branch point (BP)
μ_2	0.195716	$(-1.84882, \pm 0.108783i)$	Hopf (H)
	0.229760	$(-3.768, -0.361995, 0)$	Branch point (BP)
	0.533205	$(-7.40619, -0.461418, 0)$	Limit point (LP)
μ_1	0.575143	$(-1.88529, \pm 0.111077i)$	Hopf (H)
	0.772012	$(-1.89088, -0.148792, 0)$	Branch point (BP)
ρ	0.015674	$(-1.84885, \pm 0.111284i)$	Hopf (H)
	0.027499	$(-3.768, -0.361995, 0)$	Branch point (BP)
K	0.541502	$(-1.84877, \pm 0.110211i)$	Hopf (H)
	0.596800	$(-3.768, -0.361995, 0)$	Branch point (BP)
$N^0 - \mu_1$	(1.710668, 0.142322)	$(-3.20526, \pm 0.145281i)$	Generalized Hopf (GH)
	(0.072670, 0.046703)	$(-8.19909, \pm 0.0300249ii)$	Generalized Hopf (GH)
$N^0 - \rho$	(7.0466980.027502)	$(-1.96543, 0, 0)$	Bogdanov–Takens (BT)

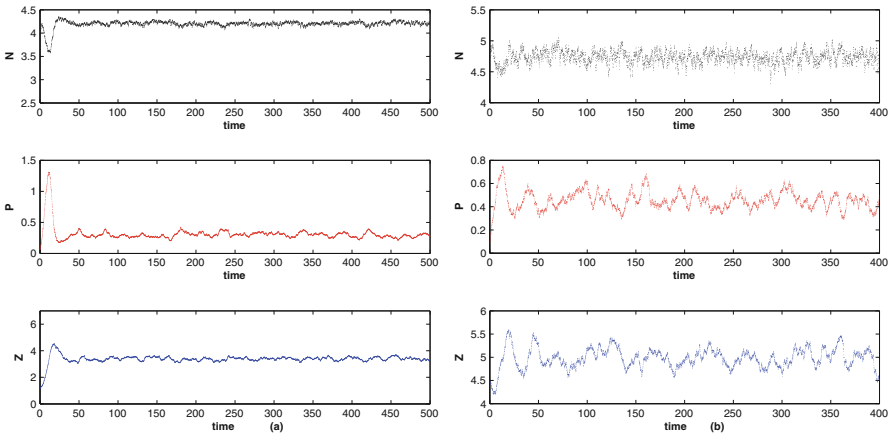

Fig. 8 **(a)** The figure depicts the solution of system is stochastically stable for $\sigma_1 = 0.1$, $\sigma_2 = 0.1$, and $\sigma_3 = 0.14$. **(b)** The figure depicts the solution of system is stochastically unstable for $\sigma_1 = 0.3$, $\sigma_2 = 0.2$, and $\sigma_3 = 0.15$

References

1. T.J. Smayda, Primary production and the global epidemic of phytoplankton blooms in the sea: A linkage?, in Novel Phytoplankton Blooms: Causes and Impact of Recurrent Brown Tides and Other Unusual Blooms, E.M. Cosper et al., eds., Springer Verlag, Berlin, 449–483 (1989).
2. G.M. Hallegraeff, A review of harmful algal blooms and their apparent global increase. *Phycologia* **32**, 79–99 (1993).

3. D.M. Anderson, Y. Kaoru and A.W. White, Estimated Annual Economic Impacts from Harmful Algal Blooms (HABs) in the United States Sea, Woods Hole Sea Grant, Woods Hole, MA, 2000.
4. J.W. Pitchford and J. Brindley, Iron limitation, grazing pressure and oceanic high nutrient-low chlorophyll (HNLC) regions. *J. Plank. Res.* **21**, 525–547 (1999).
5. D.R. Clother and J. Brindley, Excitability of an age-structured plankton ecosystem. *J. Math. Biol.* **39**, 377–420 (1999).
6. A.M. Edwards and J. Brindley, Zooplankton mortality and the dynamical behaviour of plankton population models. *Bull. Math. Biol.* **61**, 303–339 (1999).
7. J.E. Truscott and J. Brindley, Ocean plankton populations as excitable media. *Bull. Math. Biol.* **56**, 981–998 (1994).
8. T.U. Chan, B.J. Robson and D.P. Hamilton, Modelling phytoplankton succession and biomass in seasonal West Australian estuary. *Verh. Int. Ver. Limnol.* **28(2)**, 1086–1088 (2003).
9. B.J. Robson and D.P. Hamilton, Three-dimensional modelling of a Microcystis bloom event in the Swan River estuary. *Ecol. Model.* **174/1-2**, 203–222 (2004).
10. R. Segal, A.M. Waite and D.P. Hamilton, Transition from planktonic to benthic algal dominance along a salinity gradient. *Hydrobiologia* **556**, 119–135 (2006).
11. A. Huppert, B. Blasius and L. Stone, A model of phytoplankton blooms. *Amer. Natur.* **159**, 156–171 (2002).
12. S. Pal, S. Chatterjee and J. Chattopadhyay, Role of toxin and nutrient for the occurrence and termination of plankton bloom. Results drawn from field observations and a mathematical model, *Biosyst.* **90(1)**, 87–100 (2007).
13. A. Chatterjee, S. Pal and S. Chatterjee, Bottom up and top down effect on toxin producing phytoplankton and its consequence on the formation of plankton bloom, *Appl. Math. Comput.*, **218(7)**, 3387–398 (2011).
14. M.F. Watanabe, H.D. Park and M. Watanabe, Composition of Microcystis species and heptapeptide toxins. *Verh. Int. Verein. Limnol.* **25**, 2226–2229 (1994).
15. S.M. Mayeli, S. Nandini and S.S.S. Sarma, The efficacy of Scenedesmus morphology as a defense mechanism against grazing by selected species of rotifers and cladocerans. *Aqua. Ecol.* **38**, 515–524 (2004).
16. D.O. Hessen and E. Van Donk, Morphological changes in Scenedesmus induced by substances released from Daphnia. *Arch. Hydrobiol.* **127**, 129–140 (1993).
17. W. Lampert, Laboratory studies on zooplankton-cyanobacteria interactions. *N.Z. J. Mar. Freshwater Res.* **21**, 483–490 (1987).
18. M. Lynch, Aphanizomenon blooms: Alternate control and cultivation by Daphnia pulex. *Am. Soc. Limnol. Oceanogr. Spec. Symp.* **3**, 299–304 (1980).
19. S.R.J. Jang and E.J. Allen, Deterministic and stochastic nutrient-phytoplankton-zooplankton models with periodic toxin producing phytoplankton. *Appl. Math. Comput.* **271**, 52–67 (2015).
20. A. Chatterjee, S. Pal and E. Venturino, A plankton-nutrient model with Holling type III response function. *Trends in Biomathematics: Modeling, Optimization and Computational Problems*, Springer International Publishing AG, pp. 167–188 (2018).
21. T.M. M De Silva and S.R.J. Jang, Stochastic modeling of phytoplankton-zooplankton interactions with toxin producing phytoplankton. *J. Biol. Syst.* **26(1)**, 87–106 (2018).
22. B.I. Camara, R. Yamapi and H. Mokrani, Environmental stochastic effects on phytoplankton-zooplankton dynamics, *Nonlinear Dyn.* **96**, 2013–2029 (2019).
23. Z. Chen, S. Zhang and C. Wei, Dynamics of a stochastic phytoplankton-toxin phytoplankton-zooplankton model. *ADV DIFFER EQU-NY* **2019:347**, (2019).
24. A.G. Fredrickson and G. Stephanopoulos, Microbial competition, *Science*, **213(4511)**, 972–979 (1981).
25. H.L. Smith, Competitive coexistence in an oscillating chemostat, *SIAM J. Appl. Math.* **40(3)**, 498–522 (1981).
26. J. Chattopadhyay, S. Chatterjee, E. Venturino, Patchy agglomeration as a transition from monospecies to recurrent plankton blooms, *J. Theor. Biol.* **253**, 289–295 (2008).

27. B.D. Hassard, N.D. Kazarinoff and Y.H. Wan, Theory and application of Hopf bifurcation, Cambridge University Press, Cambridge (1981).
28. A. Sen, D. Mukherjee, B.C. Giri and P. Das, Stability of limit cycle in a prey-predator system with pollutant. *Appl. Math. Sci*, **5(21)**, 1025–1036 (2011).
29. P.K. Tapaswi and A. Mukhopadhyay, Effects of environmental fluctuation on plankton allelopathy, *J. Math. Biol.* 39, 39–58 (1999).
30. E. Beretta, V.B. Kolmanowskii and L. Shaikhet, Stability of epidemic model with time delays influenced by stochastic perturbations, *Math. Comp. Simul.* **45 (3-4)**, 269–277 (1998).
31. I.I. Gikhman and A.V. Skorokhod, The Theory of Stochastic Process-I, Springer, Berlin, (1979).
32. L. Shaikhet, Lyapunov Functionals and Stability of Stochastic Functional Differential Equations. Springer, Dordrecht, Heidelberg, New York, London, 2013.
33. V.N. Afanas'ev, V.B. Kolmanowskii and V.R. Nosov, Mathematical Theory of Control Systems Design, Kluwer Academic, Dordrecht, (1996).
34. M. Bandyopadhyay and J. Chattopadhyay, Ratio-dependent predator-prey model: Effect of environmental fluctuation and stability, *Nonlinearity* **18**, 913–936 (2005).

Predicting the COVID-19 Spread Using Compartmental Model and Extreme Value Theory with Application to Egypt and Iraq

Mahmoud A. Ibrahim, Amenah Al-Najafi, and Attila Dénes

1 Introduction

Coronavirus disease 2019 (COVID-19) is an infectious disease caused by the severe acute respiratory syndrome coronavirus 2 (SARS-CoV-2) that is a respiratory pathogen. The disease spreads mainly through respiratory droplets that are produced when an infected person coughs, sneezes, sings, speaks, or breathes. The most common symptoms of COVID-19 are fever, dry cough, fatigue, shortness of breath, sore throat, muscle pain, loss of smell, loss of appetite, headache, and conjunctivitis [1, 2]. Most infected persons (about 80%) develop mild to moderate illness and recover without hospitalization. About 20% become seriously ill and require oxygen, and 5% become critically ill and require intensive care. The background of the disease in Iraq and Egypt can be found in [3].

A variety of mathematical models have been developed to understand the epidemiological features of COVID-19 and the transmission dynamics for many countries, including France [4], Germany [5], Hungary [9], the UK [6], and the USA [7, 8]. Ibrahim and Al-Najafi [3] studied the spread of COVID-19 epidemic in Iraq and Egypt by using compartmental, logistic regression, and Gaussian models, providing a forecast of the spread of COVID-19 in Iraq. Furthermore, we predicted the possible start of the second wave of the COVID-19 epidemic in Egypt using generalized SEIR with time-periodic transmission rate. Here, we

M. A. Ibrahim (✉)
Bolyai Institute, University of Szeged, Szeged, Hungary

Department of Mathematics, Faculty of Science, Mansoura University, Mansoura, Egypt
e-mail: mibrahim@math.u-szeged.hu

A. Al-Najafi · A. Dénes
Bolyai Institute, University of Szeged, Szeged, Hungary
e-mail: amenah@math.u-szeged.hu; densea@math.u-szeged.hu

R. P. Mondaini (ed.), *Trends in Biomathematics: Chaos and Control in Epidemics, Ecosystems, and Cells*, https://doi.org/10.1007/978-3-030-73241-7_4

establish a compartmental mathematical model for the spread of COVID-19, taking into account presymptomatic, mildly, and symptomatically infected individuals. We estimate the parameters that provide the best fit to the incidence data from both countries.

Extreme value theory (EVT) is widely applied in many disciplines, including public health. We refer to some of these studies, Lim et al. [10], in which EVT was used to model the extremes in dengue case counts using provincial-level data in Thailand from 1993 to 2018. Lim et al. [11] analyzed the dengue incidence data in Singapore by using time-varying extreme mixture (tvEM) methods to account for the time dependence of dengue case numbers over extreme and non-extreme time periods. In [12], the annual maxima of pneumonia and influenza deaths were plotted against the return level over the period 1979–2011. Chen et al. [13] used EVT to forecast the probability of outbreaks of highly pathogenic influenza. In more recent research, the EVT has been used to project the future of COVID-19 confirmed cases in Italy, Australia, Iran, South Africa, the USA, and Chile [14]. Here, we estimate the return level and the return period of the COVID-19 epidemic to predict the future of the disease in Egypt and Iraq. We provide several scenarios for the possible peak and its timing using Gaussian2 fit model.

This chapter is organized as follows. Section 2 describes the various methods applied in our work, while the results provided by these methods are given in Sect. 3. This chapter is concluded by a discussion in Sect. 4.

2 Methods

2.1 Compartmental Model for COVID-19 Transmission

The population is divided into seven compartments: susceptible (denoted by $S(t)$), exposed ($E(t)$), presymptomatic infected ($P(t)$), symptomatically infected ($I_s(t)$), mildly infected ($I_m(t)$), treated ($I_T(t)$), and recovered individuals ($R(t)$). The total size of the population at any time t is given by $N(t) = S(t) + E(t) + P(t) + I_m(t) + I_s(t) + I_T(t) + R(t)$.

The transmission dynamics is shown in the flow diagram in Fig. 1, and our model takes the form

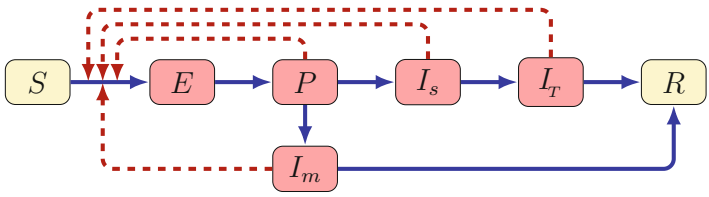

Fig. 1 Follow diagram of the COVID-19 transmission

$$
\begin{aligned}
S'(t) &= -\beta \frac{\kappa_p P(t) + \kappa_m I_m(t) + I_s(t) + \kappa_T I_T(t)}{N(t)} S(t), \\
E'(t) &= \beta \frac{\kappa_p P(t) + \kappa_m I_m(t) + I_s(t) + \kappa_T I_T(t)}{N(t)} S(t) - \nu_e E(t), \\
P'(t) &= \nu_e E(t) - \nu_p P(t), \\
I'm(t) &= \theta \nu_p P(t) - \gamma_m I_m(t), \\
I's(t) &= (1-\theta)\nu_p P(t) - \gamma_s I_s(t), \\
I_T'(t) &= \gamma_s I_s(t) - \gamma_T I_T(t) - \delta_T I_T(t), \\
R'(t) &= \gamma_m I_m(t) + \gamma_T I_T(t).
\end{aligned}
\tag{1}
$$

The description of the model parameters is listed in Table 1. Susceptibles are those who can be infected through COVID-19. Once having contracted the disease, an individual moves up to the exposed class; these individuals do not yet have symptoms and can not transfer the virus to susceptible individuals. Exposed individuals progress to presymptomatic class, and these individuals do not yet have symptoms but can transfer the virus. Following the incubation period, presymptomatic individuals move to one of the symptomatically infected class and the mildly infected class, based on whether or not that individual shows symptoms or not. Mildly infected individuals progress to the symptomatically compartment or the recovered class. Symptomatically infected individuals move to the treated compartment, which includes those who reported hospitalized. After the infectious period, the treated persons move to the recovered class. To keep our model simpler, we do not add separate compartments for the quarantined individuals. In particular, β represents the transmission rate from symptomatically infected to susceptible, while $\beta\kappa_p$, $\beta\kappa_m$, and $\beta\kappa_T$ are the transmission rates from presymptomatic, mildly infected, and treated to susceptible, respectively. The length of the latent period for humans is $1/\nu$, while $1/\gamma_m$, $1/\gamma_T$ denote the lengths of the infected period for mildly and symptomatically infected people, respectively. The parameter θ is the fraction of mildly infected among all the infected people.

Table 1 Description of the model (1) parameters

Parameters	Descriptions
β	Transmission rate from infectious classes to susceptible
$\kappa_p, \kappa_m, \kappa_T$	The relative transmissibility of P, I_m and I_T, respectively
θ	Proportion of asymptomatic infections
γ_s	Progression rate from I_s to I_T
γ_m, γ_T	Recovery rates
δ_T	Disease-induced death rate
ν_e, ν_p	Incubation rates

2.1.1 Derivation of the Basic Reproduction Number

By using the next generation method introduced in [19], we derive a formula for the basic reproduction number of (1). Then by considering the infectious states E, P, I_m, I_s, and I_T in (1) and substituting the values in the disease-free equilibrium $(N, 0, 0, 0, 0, 0, 0)$, we calculate the matrices F and V for the new infection terms and the remaining transfer terms. These two matrices are, respectively, given by

$$F = \begin{bmatrix} 0 & \beta\kappa_p & \beta\kappa_m & \beta & \beta\kappa_T \\ 0 & 0 & 0 & 0 & 0 \\ 0 & 0 & 0 & 0 & 0 \\ 0 & 0 & 0 & 0 & 0 \\ 0 & 0 & 0 & 0 & 0 \end{bmatrix} \quad \text{and} \quad V = \begin{bmatrix} \nu_e & 0 & 0 & 0 & 0 \\ -\nu_e & \nu_p & 0 & 0 & 0 \\ 0 & -\theta\nu_p & \gamma_m & 0 & 0 \\ 0 & -(1-\theta)\nu_p & 0 & \gamma_s & 0 \\ 0 & 0 & 0 & -\gamma_s & \gamma_T + \delta_T \end{bmatrix}.$$

According to [19], the basic reproduction number is the largest absolute eigenvalue of FV^{-1}, and thus, it is given by

$$\mathcal{R}_0 = \rho(FV^{-1}) = \frac{\beta\kappa_p}{\nu_p} + \frac{\theta\beta\kappa_m}{\gamma_m} + \frac{(1-\theta)\beta\nu_e}{\nu_p\gamma_s} + \frac{(1-\theta)\beta\nu_e\kappa_T}{\nu_p(\gamma_T + \delta_T)}. \tag{2}$$

Besides calculating the basic reproduction number $\mathcal{R}_0$ of the model (1), effective reproduction rate $\mathcal{R}_{eff} = \mathcal{R}_0 \frac{S(t)}{N}$ can also be estimated by this formula, measuring the average number of secondary cases per infectious case in a population. In addition, the time-dependent reproduction number can be calculated from incidence data (see e.g., [20] for details).

2.2 Return Level Estimation

The application of EVT offers different techniques to study the behavior of a sample with very high or very low levels. One of the important techniques of extreme value theory is the idea of the return level. The return level is strongly related to the return period: it is the quantile that will be reached or exceeded once in every year. In this chapter, we will use it to investigate the upper-tail distribution properties of the infection of the COVID-19 epidemic. In this subsection, we follow the methods and definitions given in [15].

Let X be a random variable with cumulative distribution function F, and the distribution function of this random variable is called excess distribution function over the threshold u denoted by F_u, defined as

$$F_u(x) = P(X - u \leq x \mid X > u) = \frac{F(u+x) - F(u)}{1 - F(u)}, \qquad x \geq 0,$$

where $1 - F(u)$ is the exceedance probability, and the mean excess function of X $e(u) = E(X - u \mid X > u)$ denotes the mean residual life function. The method is based on exceedances over a specified threshold. Assuming that the appropriate distribution is chosen and then the parameters are estimated, it is useful to calculate the return level. For a given threshold u, assume that the generalized Pareto (GP) distribution with scale σ and shape ξ parameters is a suitable model for exceedances. For sufficiently large u, the distribution function of $(X - u)$, conditional on $X > u$, is therefore approximately

$$H(x) = 1 - \left(1 + \frac{\xi x}{\tilde{\sigma}}\right)^{-\frac{1}{\xi}}, \qquad \xi > 0, \tag{3}$$

where $\tilde{\sigma} = \sigma + \xi(u - \mu)$. Let $\zeta_u = P\{X > u\}$, and let x_m be the value that is exceeded once in every m periods on average, and the level x_m will be obtained from

$$x_m = \begin{cases} u + \dfrac{\sigma}{\xi}[(m\zeta_u)^{\xi} - 1] & \xi \neq 0 \\ u + \sigma \log(m\zeta_u) & \xi = 0 \end{cases} \tag{4}$$

provided m is sufficiently large to ensure that $x_m > u$.

To predict the second wave of the COVID-19 epidemic, we apply a Gaussian2 fit model. Let $I(x)$ denote the Gaussian2 function, and it is given by

$$I(x) = \sum_{j=1}^{2} I_j \exp\left(-\left(\frac{x - \mu_j}{\sigma_j}\right)^2\right), \tag{5}$$

where I_j is the amplitude, μ_j is the time of the peak, and σ_j is related to the peak width.

3 Results

3.1 Parameter Estimation for Iraq and Egypt

The data were collected from the Worldometer website [16, 17]. We focus on the data from 22 February to 31 October, 2020 in Iraq and from 15 February to 31 October, 2020 in Egypt.

To estimate the model (1) parameters giving the best fit, we applied Latin hypercube sampling, a method used in statistics to measure simultaneous variation of multiple parameters (see e.g., [18] for details).

Figure 2 shows the model (1) fitted to the daily number of confirmed cases in (a) from Egypt, 15 February 2020 to 31 October 2020, and in (b) from Iraq, 22 February 2020 to 31 October 2020. Our model gives a reasonable good fit for both countries, showing the peak in Egypt and predicting the peak in Iraq. The fitting parameter results are listed in Table 2.

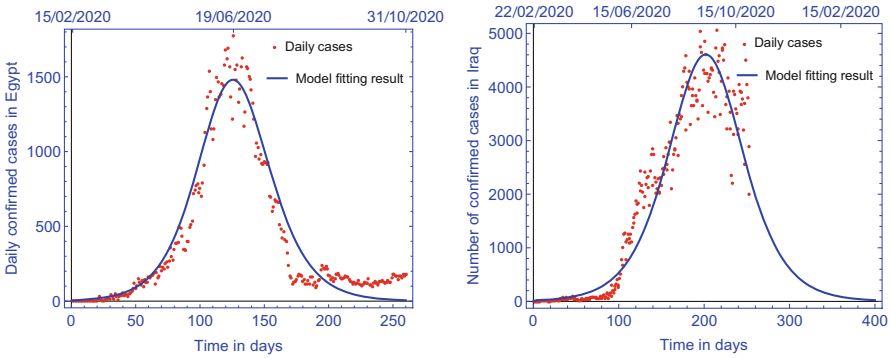

(a) Egypt (b) Iraq

Fig. 2 The model (1) fitted to the daily confirmed cases in (**a**) Egypt and (**b**) Iraq with parameters given in Table 2

Table 2 Parameters and fitted values of model (1) in the case of Iraq and Egypt

Parameters	Value for Iraq $\mathcal{R}_0 = 1.122$	Value for Egypt $\mathcal{R}_0 = 1.129$	Source
β	0.572	0.817	Fitted
κ_p	0.284	0.277	Fitted
κ_m	0.275	0.235	Fitted
κ_T	0.211	0.368	Fitted
θ	0.728	0.805	Fitted
γ_s	0.5	0.255	Fitted
γ_m	0.23	0.203	Fitted
γ_T	0.098	0.336	Fitted
δ_r	0.164	0.191	Fitted
ν_e	0.259	0.155	Fitted
ν_p	0.483	0.93	Fitted

3.2 *Reproduction Numbers*

In order to quantify the effort needed to eradicate infectious diseases, the basic reproduction rate $\mathcal{R}_0$ is an important threshold parameter and is defined as the expected number of secondary infections generated by one infected person in a population where all individuals are susceptible to infection. The basic reproduction number is estimated from the incidence data using exponential growth (EG) method (see e.g., [20] for details), and we found that $\mathcal{R}_0 = 1.047$ for Egypt and $\mathcal{R}_0 = 1.078$ for Iraq. The reproduction number in both countries is greater than one and the disease persists.

Formula (2) gives us the basic reproduction number in any time point by substituting the parameter values into it. To assess the dependence of the basic reproduction number on the parameters that can be subject to control the spread of the virus, the contour plot of the basic reproduction number in terms of the transmission rate (β) and progression rate from symptomatically infected to hospitalized individuals (γ_s) for the two countries is shown in Fig. 3.

Figure 4 shows the effective reproduction number along with the number of symptomatically infected in Egypt and Iraq, 2020–2021, showing that the number of infected individuals begins to decline when the effective reproduction number goes below 1. The highest value of the effective reproduction number is calculated to be about $\mathcal{R}_{eff} \approx 1.129$ in Egypt and $\mathcal{R}_{eff} \approx 1.122$ in Iraq.

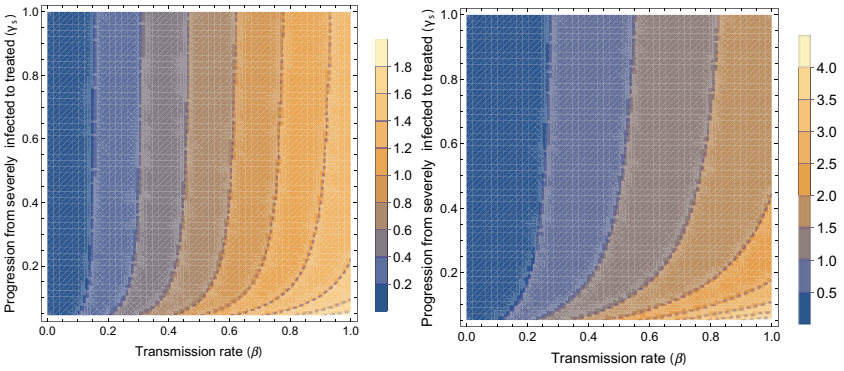

(a) Egypt (b) Iraq

Fig. 3 The contour plot of the basic reproduction number for Iraq and Egypt as a function of transmission rate (β) and progression rate (γ_s) from I_s to I_T

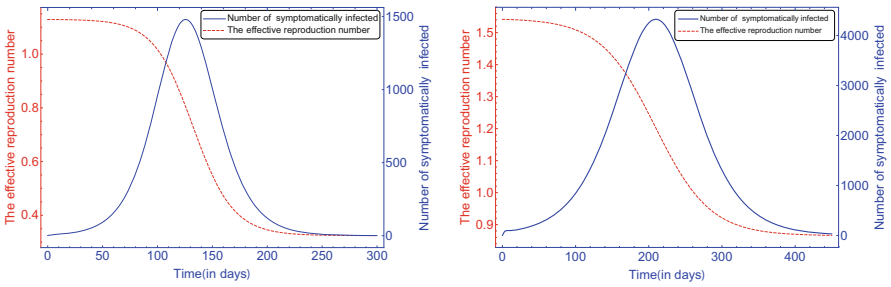

Fig. 4 The effective reproduction number and the number of symptomatically infected in (**a**) Egypt and (**b**) Iraq, 2020–2021

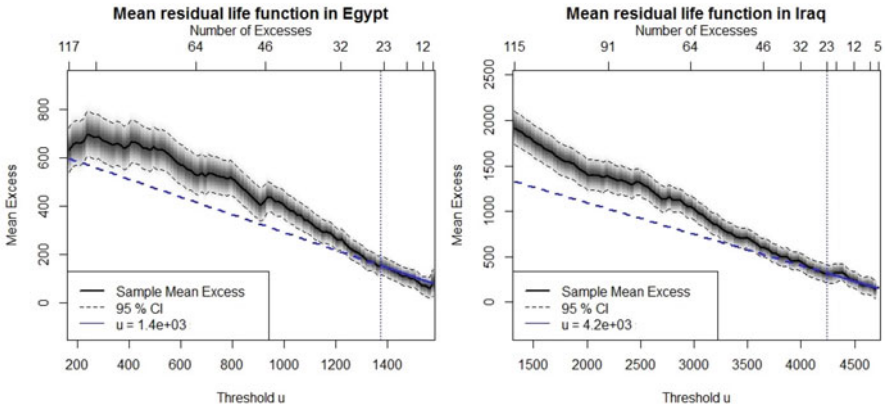

Fig. 5 Mean excess plot with threshold in Iraq and Egypt, 2020

3.3 Prediction of the Second Wave of the COVID-19 Epidemic

The application of the return level required choosing an optimal threshold assuming that data exceeding a specified threshold follows a Pareto distribution to determine an accurate return level estimate. It is very important to choose a plausible threshold value because choosing a threshold value that is too small leads to an imprecise estimate and choosing a threshold value that is too high leads to a biased estimate. The results of the empirical mean excess function show the appropriate threshold value for our data and also the peak value for infections, with the peak value in Iraq being 4200 and in Egypt 1400.

Figure 5 shows the peak values selected for infections, which are 4200 and 1400 in Iraq and Egypt, respectively.

The return level for the peaks corresponding to the selected threshold for 2020 and 2021 is shown in Fig. 6. Over the 2021 period, it indicates that 4434, 4468,

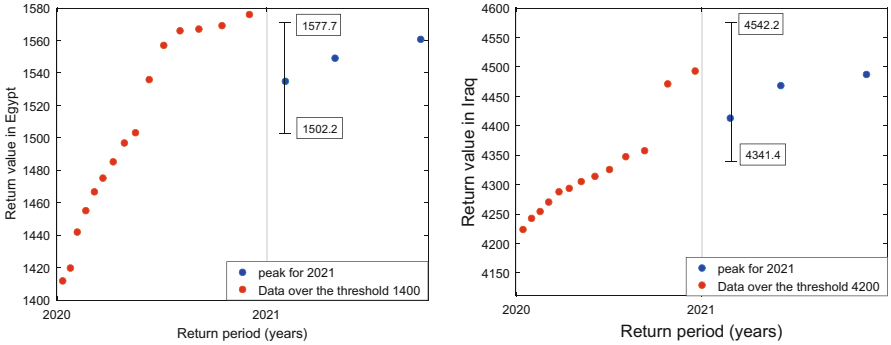

Fig. 6 Return periods and return levels for Egypt and Iraq, 2020–2021

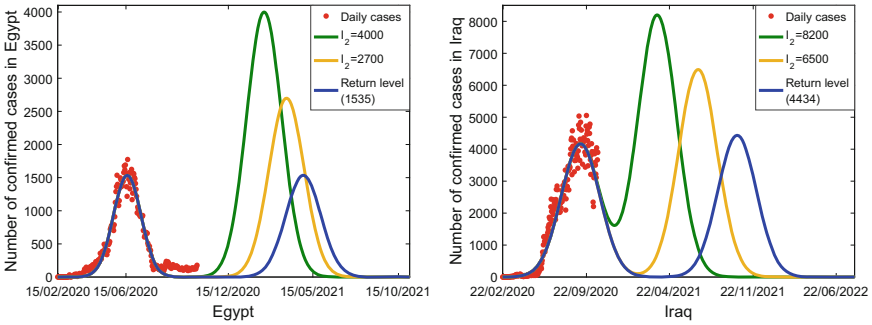

Fig. 7 Two different scenarios with return level to the daily confirmed cases in Egypt and Iraq, 2020–2021

and 4498 infection cases per day are expected to be exceeded in next year in Iraq with confidence intervals (4341.4, 4564.2), (4321, 4704.2), and (4302, 4858.5), respectively, while 1534 (1502.2, 1577.7), 1549 (1511.2, 1598), and 1560 (1523.6, 1661.7) infection cases per day are expected to be exceeded once in the next year in Egypt. The upper and lower confidence intervals for peaks 4468 and 4498 in Iraq and 1549 and 1560 in Egypt indicate low precision and high uncertainty, while the confidence intervals to the peaks 4434 and 1534 for Iraq and Egypt, respectively, revealed narrower and less uncertainty. To predict the spread of COVID-19 in Iraq and Egypt, we apply the Gaussian2 model (5) to estimate the value and time of the expected peak for two different scenarios and estimate the time of the peak that we obtained from return level. Figure 7 shows the daily cases with three expected maximum peak values at its timing in Iraq and Egypt. Table 3 shows the parameters that were used to obtain each scenario and return level estimation. The return level peak timing is estimated to occur on 12 October 2021 with $R^2 = 0.9574$ for Iraq, while on 18 April 2021 in Egypt with $R^2 = 0.9578$. The second wave peak timing is estimated to occur between 21 March and 4 July, 2021 in Iraq, while in Egypt it is estimated to occur between 17 February and 29 March, 2021.

Table 3 Estimated parameter results for two scenarios and return level of the Gaussian model to Iraq and Egypt

	Gaussian2 model		
Parameters	Scenario one	Scenario two	Return level
Iraq			
Estimated peak day cases	8200	6500	4434
Estimated peak date	21/3/2021	04/07/2021	12/10/2021
Goodness of fit (R^2)	0.9675	0.9544	0.9574
Root-mean-square error (RMSE)	364.8	364.9	365
Egypt			
Estimated peak day cases	4000	2700	1535
Estimated peak date	17/02/2021	29/03/2021	28/04/2021
Goodness of fit (R^2)	0.9498	0.9779	0.9578
Root-mean-square error (RMSE)	111.3	111.4	111.7

4 Discussion

We have studied the spread of COVID-19 epidemic in Egypt and Iraq by using compartmental (generalized SEIR) model considering presymptomatic, mildly, and severely infected individuals. We estimated the parameters that best fit the incidence data. Our model provides a reasonable good fit to the incidence data in both countries.

The reproduction number was estimated based on the cumulative confirmed cases by using the exponential growth (EG) method and was found to be 1.078 and 1.047 for Iraq and Egypt, respectively. Using our compartmental model, we obtained a formula for the basic reproduction number that allowed us to calculate the value of $\mathcal{R}_0$. Using the estimated parameter set resulting from fitting our model to the incidence data in both countries, we found that $\mathcal{R}_0 = 1.122$ and $\mathcal{R}_0 = 1.129$ for Iraq and Egypt, respectively. The basic reproduction number is greater than one, indicating that the virus still persists in both countries. The highest value of the effective reproduction number is estimated to be about 1.129 in Egypt and 1.122 for Iraq (see Fig. 4). The contour plots of the basic reproduction number (see Fig. 3) suggest that to control the spread of the COVID-19 outbreak, both countries should work to decrease the transmission rate enough by making more restrictions and precaution measures in the cities that have large numbers of infected people.

The return level for the peaks indicates that infection cases per day are expected to be exceeded once in next year and corresponds to a number of 4434 and 1535 infection cases with narrower and less uncertain confidence intervals in Iraq and Egypt, respectively. The Gaussian2 fit model was used to obtain statistical predictions for the spread of COVID-19 pandemic in Iraq and Egypt, and we fitted the Gaussian2 model to the daily confirmed cases to estimate the value and timing of the expected peak for two different scenarios and to determine the timing of the

peak that we obtained from the return level for both countries. The results of the return level in Iraq illustrate that the predicted daily cases are estimated to be 4434, while the peak values of scenario one and scenario two are expected to be 8200 and 6500 on March 21, 2021 and July 4, 2021, respectively. In Egypt, the predicted daily cases are estimated to be 1535, while the peaks of scenario one and scenario two are expected to be 4000 and 2700 on 17 February and 29 March, 2021, respectively.

References

1. World Health Organization (WHO). Coronavirus. https://www.who.int/health-topics/coronavirus#tab=tab_1
2. Centers for Disease Control and Prevention (CDC). Symptoms of Coronavirus. https://www.cdc.gov/coronavirus/2019-ncov/symptoms-testing/symptoms.html
3. M.A. Ibrahim, A. Al-Najafi, Modeling, Control, and Prediction of the Spread of COVID-19 Using Compartmental, Logistic, and Gauss Models: A Case Study in Iraq and Egypt. *Processes.* **8**(11), 1400 (2020).
4. Di, L. Domenico, G. Pullano, C. E. Sabbatini, P. Y. Bolle, and V. Colizza, Impact of lockdown on COVID-19 epidemic in Île-de-France and possible exit strategies. *BMC Med.* **18**, 240 (2020).
5. M.V. Barbarossa, J. Fuhrmann, J. Heidecke, H.V. Varma, N. Castelletti, J.H. Meinke, S. Krieg, T. Lippert, A first study on the impact of current and future control measures on the spread of COVID-19 in Germany. *medRxiv.* (2020).
6. N.M. Ferguson, D. Laydon, G. Nedjati-Gilani, N. Imai, K. Ainslie, M. Baguelin, S. Bhatia, A. Boonyasiri, Z. Cucunubá, G. Cuomo-Dannenburg, et al. Report 9—Impact of non-pharmaceutical interventions (NPIs) to reduce COVID-19 mortality and healthcare demand, *Imperial College London: London, UK.* (2020). Available online: https://www.imperial.ac.uk/mrc-global-infectious-disease-analysis/covid-19/report-9-impact-of-npis-on-covid-19 (accessed on 31 October 2020).
7. S.M. Moghadas, A. Shoukat, M.C. Fitzpatrick, C.R. Wells, P. Sah, A. Pandey, J.D. Sachs, Z. Wang, L.A. Meyers, B.H. Singer, et al. Projecting hospital utilization during the COVID-19 outbreaks in the United States. *Proc. Natl. Acad. Sci. USA.* **117**, 9122–9126 (2020).
8. J.S. Weitz, COVID-19 epidemic risk assessment for Georgia. *Github: San Francisco, CA, USA.* (2020). Available online: https://github.com/jsweitz/covid-19-ga-summer-2020 (accessed on 31 October 2020).
9. G. Rst, F.A. Bartha, N. Bogya, P. Boldog, A. Dnes, T. Ferenci, K.J. Horvth, A. Juhsz, C. Nagy, T. Tekeli, Z. Vizi, B. Oroszi, Early phase of the COVID-19 outbreak in Hungary and post-lockdown scenarios. *Viruses.* **12**, 708 (2020).
10. J.T. Lim, B.S.L. Dickens, A.R. Cook, Modelling the epidemic extremities of dengue transmissions in Thailand. *Epidemics.* **33**, 100402 (2020).
11. J.T. Lim, Y. T. Han, B. Sue Lee Dickens, L.C. Ng, A.R. Cook, Time varying methods to infer extremes in dengue transmission dynamics. *PLOS Computational Biology.* **16**(10), e1008279 (2020).
12. M. Thomas, M. Lemaitre, M.L. Wilson, C. Viboud, Y. Yordanov, H. Wackernagel, F. Carrat, Applications of extreme value theory in public health. *PloS one.* **11**(7), e0159312 (2016).
13. J. Chen, X. Lei, L. Zhang, B. Peng, Using extreme value theory approaches to forecast the probability of outbreak of highly pathogenic influenza in Zhejiang, China. *PloS one.* **10**(2), e0118521 (2015).
14. M. Aadhityaa, K.S. Kasiviswanathan, I. Ilampooranan, B. Soundharajan, M. Balamurugan, J. He, A global scale estimate of novel coronavirus (COVID-19) cases using extreme value distributions. *medRxiv* (2020).

15. S. Coles, J. Bawa, L. Trenner and P. Dorazio, An introduction to statistical modeling of extreme values. *London: Springer.* **208**, 208 (2001).
16. Worldometer. Available online: https://www.worldometers.info/coronavirus/country/iraq/ (accessed on 31 October 2020).
17. Worldometer. Available online: https://www.worldometers.info/coronavirus/country/egypt/ (accessed on 31 October 2020).
18. M.D. McKay, R.J. Beckman, W.J. Conover, Comparison of three methods for selecting values of input variables in the analysis of output from a computer code. *Technometrics.* **21**, 239–245 (1979).
19. O. Diekmann, J.A.P. Heesterbeek, M.G. Roberts, The construction of next-generation matrices for compartmental epidemic models. *J. R. Soc. Interface.* **7**, 873–885 (2010).
20. T. Obadia, R. Haneef, P. Boëlle, The R_0 package: a toolbox to estimate reproduction numbers for epidemic outbreaks. *BMC Med Inform Decis Mak.* **12**, 147 (2012).

Geometry of Fitness Surfaces and Dynamics of Replicator Systems

A. S. Bratus, A. S. Novozhilov, and T. Yakushkina

1 Introduction: Extremum Principles in Evolution

For almost a century, Fisher's fundamental theorem of natural selection is being discussed and reinterpreted [1–7]. The original study [8] proposed a concept describing the mean fitness behavior through universal law, similar to the second law of thermodynamics in physics. However, it was not defined for any particular replicator system or strictly mathematically formalized. Various representations of the fitness landscape and genetic variance lead to different perceptions of evolutionary dynamics [9–12].

In biological research, a widespread visualization of the fitness landscape is a statistic hypersurface with hills, canyons, and valleys [13, 14]. Evolving population in this metaphor is "moving" across this terrain, experiencing decreases on the way, and reaching toward its peak. From a mathematical perspective, Fisher's postulate means that there exists a Lyapunov function that monotonically increases along the system's adaptive trajectories. Nevertheless, such a function can be found analytically only for a very limited set of problems. One of the examples is a class of replicator equations that have a globally asymptotically stable equilibrium [15].

The idea of having universal laws in biology that can be described by explicit mathematical expressions attracted the attention of many scientists [16–20]. In par-

A. S. Bratus
Department of Mathematical Modeling and System Analysis, Russian University of Transport, Moscow, Russia
e-mail: alexander.bratus@yandex.ru

A. S. Novozhilov
Department of Mathematics, North Dakota State University, Fargo, ND, USA

T. Yakushkina (✉)
School of Business Informatics, National Research University Higher School of Economics, Moscow, Russia

R. P. Mondaini (ed.), *Trends in Biomathematics: Chaos and Control in Epidemics, Ecosystems, and Cells*, https://doi.org/10.1007/978-3-030-73241-7_5

ticular, it inspired many studies of maximization processes in evolution [21–23]. In this chapter, we consider general replicator and Lotka–Volterra systems, analyzing their extremal properties from the standpoint of fitness landscape geometry.

2 Fitness Landscapes of Replicator Systems

Let the vector $\mathbf{u}(t) = (u_1(t), \ldots, u_n(t))$ denote the distribution of species in the population changing over time t. A conventional way to define a replicator system is by the following differential equations [24, 26]:

$$\dot{u}_i = u_i \left((\mathbf{Au})_i - f(\mathbf{u}) \right), \; i = 1, \ldots n, \tag{1}$$

$$(\mathbf{Au})_i = \sum_{j=1}^{n} a_{ij} u_j(t), \quad f(\mathbf{u}) = (\mathbf{Au}, \mathbf{u}),$$

$$\mathbf{u}(t) \in S_n = \left\{ \mathbf{x} \in \mathbb{R}^n : x_i \geq 0, \; \sum_{i=1}^{n} x_i = 1 \right\}.$$

Here and throughout this chapter, $\dot{u}$ denotes a derivative with respect to time t. In the system (1), selection is described by the matrix of fitness coefficients $\mathbf{A} = \{a_{ij}\}_{n \times n}$. The expression $(\mathbf{Au})_i$ stands for the average reproductive success of i-th species and equals to the corresponding element of the vector $\mathbf{Au}$. The term $f = (\mathbf{Au}, \mathbf{u}) = \sum_{i,j=1}^{n} a_{ij} u_i u_j$ is the mean fitness, which assures that $\mathbf{u}(t)$ belongs to the simplex S_n for any time moment t.

To describe a steady state of the system (1), one can write the system of algebraic equations:

$$\mathbf{A}\bar{\mathbf{u}} = f(\bar{\mathbf{u}})\mathbf{1}, \quad \mathbf{1} = (1, \ldots, 1)^T, \bar{\mathbf{u}} \in S_n. \tag{2}$$

Here, $f(\bar{\mathbf{u}})$ is the mean fitness at the equilibrium state $\bar{\mathbf{u}}$.

Adopting the approach proposed in our previous study [27], we examine the geometry of the fitness landscape. We introduce the notation, using the parameters of Eq. (1):

$$\Sigma = \left\{ z = f(\mathbf{u}) : f(\mathbf{u}(t)) = \sum_{i,j=1}^{n} a_{ij} u_i(t) u_j(t), \; \mathbf{u} \in S_n \right\}. \tag{3}$$

The hypersurface Σ is called *fitness landscape*. For each trajectory $\gamma_t \in S_n$ of the system (1), there exists a curve $\Gamma_t \in \Sigma$.

Properties of Σ depend on the type of $\mathbf{A}$. Consider a decomposition of $\mathbf{A}$ into a sum of a symmetric matrix $\mathbf{B}$ and a skew-symmetric matrix $\mathbf{C}$:

$$\mathbf{A} = \mathbf{B} + \mathbf{C}, \quad \mathbf{B} = \frac{1}{2}\left(\mathbf{A} + \mathbf{A}^T\right), \ \mathbf{C} = \frac{1}{2}\left(\mathbf{A} - \mathbf{A}^T\right). \tag{4}$$

Denote the rows of $\mathbf{B}$ and $\mathbf{C}$ as b_i and c_i, respectively. If $\mathbf{A}$ is symmetric itself, then $\mathbf{C} = 0$. Otherwise, since $(\mathbf{Cu}, \mathbf{u}) = 0$, the mean fitness of the system is described solely by $\mathbf{B}$:

$$f(\mathbf{u}) = (\mathbf{Au}, \mathbf{u}) \equiv (\mathbf{Bu}, \mathbf{u}).$$

To estimate the rate of the mean fitness variation, we derive

$$\dot{f}(\mathbf{u}(t)) = \sum_{i=1}^{n} (b_i, \mathbf{u}(t))^2 u_i(t) - f^2(\mathbf{u}(t)) + \sum_{i=1}^{n} (b_i, \mathbf{u}(t))\,(c_i, \mathbf{u}(t))\,u_i(t). \tag{5}$$

For symmetric $\mathbf{A}$, the expression (5) gives

$$\dot{f}(\mathbf{u}) = \sum_{i=1}^{n} (\mathbf{Au})_i^2 u_i - \left(\sum_{i=1}^{n} (\mathbf{Au})_i u_i\right)^2 \geq 0. \tag{6}$$

The latter is the variance of the random variable $(\mathbf{Au})_i$ distributed with the probability $\mathbf{u}$. This statement is known in the literature [28, 29] as Kimura's maximum principle. However, in a general case of Eq. (5), a cubic form is not sign-definite. Hence, the sign of $\dot{f}$ can be negative, and the mean fitness of the population can undergo local decreases. In modern biology, these intervals of fitness reduction are commonly thought to be insignificant. It means that the general dynamics of the mean fitness allows it to reach its maximum value eventually. For quasi-species systems, this hypothesis is proven to be true [30]. The mean fitness in the Eigen model cannot have local minima in any internal point of a simplex, except for the steady states.

To study the fitness landscape behavior in a general case, we need more sophisticated techniques. From a mathematical point of view, the mean fitness function is a quadratic form defined by a symmetric matrix $\mathbf{B}$:

$$f(\mathbf{u}(t)) = (\mathbf{Bu}, \mathbf{u}).$$

Hence, there is an orthogonal transformation $\mathbf{U}$:

$$\mathbf{U}^T\mathbf{BU} = \Lambda = diag(\lambda_1, \ldots, \lambda_n).$$

In the latter expression, the parameters λ_i denote real eigenvalues of the matrix $\mathbf{B}$. Thus, the orthogonal transformation $\mathbf{u} = \mathbf{Uw}$ reduces the quadratic form to the canonical one:

$$f(\mathbf{w}) = \sum_{i=1}^{k} \lambda_i^+ w_i^2 + \sum_{j=k+1}^{n} \lambda_j^- w_j^2. \tag{7}$$

In this formula, we use λ_i^+ and λ_j^- as positive and negative real eigenvalues of $\mathbf{B}$ correspondingly. Note that we assume $|\mathbf{B}| \neq 0$.

Consider the extended classification for quadratic forms on fitness landscapes [27]. The eigenvalues of the matrix $\mathbf{B}$ define the three possible types: *elliptic* if all the eigenvalues are of the same sign, *hyperbolic* if some eigenvalues have opposite signs, and *parabolic* if there are zero eigenvalues.

The study on adaptive fitness landscapes [15] showed that isolated equilibrium point $\bar{\mathbf{u}} \in int S_n$ of the system (1) coincides with the extremum of the fitness landscape if and only if there exists a non-degenerate matrix $\mathbf{M} = \{m_{ij}\}, i, j = 1, \ldots, n$:

$$\mathbf{C} = \mathbf{MB}, \tag{8}$$

and

$$\mathbf{M} \cdot \mathbf{1} = 0, \quad \mathbf{1} = (1, \ldots, 1)^T. \tag{9}$$

If matrix $\mathbf{A}$ is symmetric, then $\mathbf{C} = 0$ and $\mathbf{M} = 0$.

Another non-trivial example is a class of the so-called circulant matrices, for which the conditions (8), (9) take place:

$$\mathbf{A} = \begin{pmatrix} a_1 & a_2 & \ldots & a_{n-1} & a_n \\ a_n & a_1 & \ldots & a_{n-2} & a_{n-1} \\ . & . & . & . & . \\ a_2 & a_3 & \ldots & a_n & a_1 \end{pmatrix}. \tag{10}$$

2.1 Game-Theoretical Approach and Evolutionary Stable Strategies

Consider the existence problem for a local maximum of the fitness landscape Σ. It is closely related to the concept of evolutionary stable strategies (ESS), which is widely used in evolutionary game theory [24, 25]. From this standpoint, the matrix $\mathbf{A}$ can be interpreted as a payoff matrix in a normal-form game with n strategies [24]. Each element a_{ij} describes the profitability of using strategy i against j in the current environment. Thus, these interactions impact the distribution of strategies in the population. We suppose that only pure strategies can be chosen, and the offspring replicates the strategy of the parent. In this sense, the expected profit of particular species with a strategy i is defined through all the possible interactions:

$$f_i(\mathbf{u}) = \sum_{i=1}^{n} a_{ij} u_j = (\mathbf{Au})_i,\ \mathbf{u} \in S_n,$$

which is a fitness value for this species. The expected profit value is the same as the mean fitness of such population:

$$\sum_{i=1}^{n} (\mathbf{Au})_i u_i = f(\mathbf{u}) = (\mathbf{Au}, \mathbf{u})\,.$$

The difference between individual and population profits gives the same expression as in Eq. (1):

$$\frac{\dot{u}_i}{u_i} = (\mathbf{Au})_i - f. \tag{11}$$

Given the approach described above, we can apply the techniques from game theory to the system (1), especially the concept of Nash equilibrium for ESS [25]. Consider the following definition [24]:

Definition 2.1 A steady state $\bar{\mathbf{u}} \in int\, S_n$ is an ESS, if

$$(\bar{\mathbf{u}}, \mathbf{Au}) > (\mathbf{u}, \mathbf{Au}) \tag{12}$$

for all $\mathbf{u} \neq \bar{\mathbf{u}}$ in some neighborhood of $\bar{\mathbf{u}}$ in S_n.

We focus on the connection between the steady states $\bar{\mathbf{u}}$ satisfying the condition (12) and the extremal properties of the fitness landscape Σ.

Lemma 2.1 *If a steady state* $\bar{\mathbf{u}} \in int\, S_n$ *is an ESS, then there is a strict local maximum of the hypersurface* Σ.

Indeed, let $\bar{\mathbf{u}}$ be an ESS. Consider $\mathbf{u} = \bar{\mathbf{u}} + \varepsilon \mathbf{w}$. Since $\mathbf{u} \in S_n$, then $(\mathbf{w}, \mathbf{1}) = 0$. From (12), we get

$$\varepsilon\,(\mathbf{w}, \bar{\mathbf{u}}) + \varepsilon^2\,(\mathbf{w}, \mathbf{Aw}) < 0. \tag{13}$$

Taking into account that $\bar{\mathbf{u}}$ is a steady state, i.e., $\mathbf{A}\bar{\mathbf{u}} = f(\bar{\mathbf{u}})\mathbf{1}$, we derive the inequality:

$$(\mathbf{w}, \mathbf{Aw}) < 0, \mathbf{w} \neq 0,$$

since $\varepsilon\,(\mathbf{w}, \bar{\mathbf{u}})$ goes to zero. □

Note that the converse is not necessarily true: it holds only if conditions (8) and (9) are applicable.

Theorem 2.1 *Let* $\bar{\mathbf{u}} \in int\, S_n$ *be a unique solution to the system (1). Furthermore, assume that it coincides with the local maximum of the hypersurface* Σ. *If this equilibrium is asymptotically stable, then it is an ESS and gives the global maximum for* Σ *over* S_n. *Otherwise, if* $\bar{\mathbf{u}}$ *is unstable, then the global maximum of* Σ *is reached at the boundary of the simplex* $bd\, S_n$.

Assume that an asymptotically stable equilibrium $\bar{\mathbf{u}}$ coincides with a local maximum point of Σ over S_n. Consider the following Lyapunov function:

$$V(\mathbf{u}) = \sum_{i=1}^{n} \left[(u_i - \bar{u}_i) - \bar{u}_i \ln \frac{u_i}{\bar{u}_i} \right] > 0, \mathbf{u} \neq \bar{\mathbf{u}}, V(\bar{\mathbf{u}}) = 0. \tag{14}$$

Hence,

$$\dot{V}(\mathbf{u}) = \sum_{i=1}^{n} \dot{u}_i \left(u_i - \frac{\bar{u}_i}{u_i} \right) = \sum_{i=1}^{n} [(\mathbf{Au})_i - (\mathbf{Au}, \mathbf{u})] (u_i - \bar{u}_i) =$$

$$(\mathbf{Au}, \mathbf{u} - \bar{\mathbf{u}}) < 0, \mathbf{u} \neq \bar{\mathbf{u}}.$$

For some neighborhood $U_\delta(\bar{\mathbf{u}})$ of the steady state:

$$(\bar{\mathbf{u}}, \mathbf{Au}) < (\mathbf{Au}, \mathbf{u}).$$

Since

$$(\mathbf{Au}, \bar{\mathbf{u}}) \leq \max_{\mathbf{u} \in S_n} (\mathbf{Au}, \mathbf{u}),\ \mathbf{u} \in U_\delta(\bar{\mathbf{u}}),$$

then under the conditions (8) and (9), we obtain

$$\mathbf{C} = \mathbf{MB},\ \mathbf{M1} = 0,\ \mathbf{B}\bar{\mathbf{u}} = f(\bar{\mathbf{u}})\mathbf{1}.$$

Finally, we get

$$(\bar{\mathbf{u}}, \mathbf{Au}) = (\bar{\mathbf{u}}, (\mathbf{B} + \mathbf{C})\mathbf{u}) = (\bar{\mathbf{u}}, \mathbf{Bu}) + (\bar{\mathbf{u}}, \mathbf{Cu}) =$$

$$(\mathbf{B}\bar{\mathbf{u}}, \mathbf{u}) - (\mathbf{C}\bar{\mathbf{u}}, u) = f(\bar{\mathbf{u}})(\mathbf{1}, \mathbf{u}) - (\mathbf{MB}\bar{\mathbf{u}}, \mathbf{u}) = f(\bar{\mathbf{u}}),$$

so that

$$f(\bar{\mathbf{u}}) < \max_{\mathbf{u} \in S_n} (\mathbf{Au}, \mathbf{u}). \tag{15}$$

That is, the maximal value of the fitness landscape is not reached at the equilibrium point $\bar{\mathbf{u}} \in int\, S_n$. From Lemma 2.1, it follows this value cannot be

reached at any internal point of the local maximum; therefore, it is reached at the boundary bdS_n. □

Corollary 2.1 *If a steady state* $\bar{\mathbf{u}} \in intS_n$ *of the circulant system is asymptotically stable, then it is also an ESS and a maximum point for the fitness landscape* Σ *over the simplex* S_n. *If* $\bar{\mathbf{u}}$ *is unstable, then global maximum is reached at the boundary* bdS_n.

2.2 Lotka–Volterra System

Consider the general case of the Lotka–Volterra equations in $\mathbb{R}^n_+$:

$$\dot{u}_i = u_i\left(r_i - (\mathbf{Au})_i\right), i = 1, \ldots, n, \tag{16}$$
$$(\mathbf{Au})_i = \sum_{i=1}^{n} a_{ij}u_j, \mathbf{r} = (r_1, \ldots, r_n).$$

It is natural to raise a question, which function is the analogue to the mean fitness of the replicator system in this case. One of the suggestions for this function found in the literature [31] has the form:

$$F(\mathbf{u}) = \sum_{i=1}^{n} r_i u_i - \frac{1}{2}(\mathbf{Au}, \mathbf{u}). \tag{17}$$

Deriving the variation from the expression (17), we get

$$\dot{F}(\mathbf{u}) = \sum_{i=1}^{n} u_i\left(r_i - (\mathbf{Bu})_i\right)^2 + \sum_{i=1}^{n}(\mathbf{Cu})_i\left((\mathbf{Bu})_i - r_i\right)u_i. \tag{18}$$

Here, we applied the formula for the matrix $\mathbf{A}$ factorization (4). The equality (18) is similar to the one (5). In particular, if the matrix $\mathbf{A}$ is symmetric, then $\dot{F}(\mathbf{u}) \geq 0$, which was the case for the general replicator equations.

Theorem 2.2 *Let* $\bar{\mathbf{u}} \in int\mathbb{R}^n_+$ *be a unique stable steady state of the system (16). Furthermore, assume that* $\mathbf{C}$ *in a matrix* $\mathbf{A}$ *decomposition (4) has the form*

$$\mathbf{C} = \mathbf{MB},\ |\mathbf{M}| \neq 0,\ \mathbf{M}\cdot\mathbf{r} = 0. \tag{19}$$

Then, $\bar{\mathbf{u}}$ *is a global maximum point for the hypersurface* $z = F(\mathbf{u}), z \in \mathbb{R}^n$.

Assume that we have an internal steady state $\bar{\mathbf{u}} \in int\mathbb{R}^n_+$. By definition,

$$\mathbf{A}\bar{\mathbf{u}} = \mathbf{r},\ |\mathbf{A}| = 0.$$

Since $\bar{\mathbf{u}}$ is stable, then $\mathbf{B}$ in Eq. (4) is positive-definite. The condition (19) is necessary and sufficient to guarantee the equality $\mathbf{B}\bar{\mathbf{u}} = \mathbf{r}$. This proof follows a similar logic as the one for general replicator systems [15].

A necessary condition for the function $z = F(\mathbf{u})$ having extremum at $\bar{\mathbf{u}}$ holds true, since

$$\left.\frac{\partial F(\mathbf{u})}{\partial u_k}\right|_{\mathbf{u}=\bar{\mathbf{u}}} = r_k - (\mathbf{B}\bar{\mathbf{u}})_k = 0, \tag{20}$$

where $k = 1, \ldots, n$. A sufficient condition for the maximum at $\bar{\mathbf{u}}$ is the matrix $\{z_{kj}\}_{k,j=1}^{n}$ being negative-definite:

$$z_{kj} = \frac{\partial^2 F(\bar{\mathbf{u}})}{\partial u_k \partial u_j} = -b_{kj}, k, j = 1, \ldots, n. \tag{21}$$

Since $\mathbf{B}$ is positive-definite, the latter condition takes place. Therefore, the hypersurface $z = F(\mathbf{u})$ is a convex function in $\mathbb{R}^n_+$. Moreover, the steady state $\bar{\mathbf{u}}$ is the global maximum point for this surface.

Corollary 2.2 *If a unique steady state $\bar{\mathbf{u}} \in int\mathbb{R}^n_+$ is unstable, then the maximum value of the hypersurface $z = F(\mathbf{u})$ is reached at the boundary $bd\mathbf{R}^n_+$.*

Acknowledgments This work is supported by the Russian Science Foundation under grant 19-11-00008.

T.Y. was supported in part by an appointment to the National Library of Medicine (NLM) National Center for Biotechnology Information (NCBI) Research Participation Program. This program is administered by the Oak Ridge Institute for Science and Education through an interagency agreement between the U.S. Department of Energy (DOE) and the National Library of Medicine (NLM). ORISE is managed by ORAU under DOE contract number DE-SC0014664. All opinions expressed in this paper are the author's and do not necessarily reflect the policies and views of NLM, DOE, or ORAU/ORISE.

References

1. W. J. Ewens, *Theor. Popul. Bio.* **36**, 2 (1989).
2. S. Lessard, *Theor. Popul. Bio.* **52**, 2 (1997).
3. P. Ao, *Phys. Life Rev. I*, **2**, 2 (2005).
4. A. Plutynski, *Stud. Hist. Philos. Sci. C* **37**, 1 (2006).
5. S.A. Frank, In: Oxford University Press. Ed. E. Svensson, R. Calsbeek, (2012).
6. W. J. Ewens and S. Lessard, *Theor. Popul. Bio.* **104**, (2015).
7. W. F. Basener and J. C. Sanford, *J. Math. Biol.* **76**, 7 (2018).
8. R. A. Fisher, Ed. J. H. Bennett, Oxford University Press, (1999).
9. J.F. Crow, *Evol.* **56**, 7 (2002).
10. A. Grafen, *J. Royal Stat. Soc.* **52**, 3 (2003).
11. U. Dieckmann, M. Doebeli, J. A. J. Metz, and D. Tautz, Cambridge University Press, (2004).
12. W. J. Ewens, Springer Science & Business Media, (2012).
13. F. J. Poelwijk, D. J. Kiviet, D.M. Weinreich, and S. J. Tans, *Nat.* **445**, 7126 (2007).

14. J. Birch, *Biol. Rev.* **91**, 3(2016).
15. A. S. Bratus, Y. S. Semenov, and A. S. Novozhilov, *Math. Model. Nat. Pheno.* **13**, 3 (2018).
16. I. Stewart, *Philos. Trans. Royal Soc.* **361**, 1807, (2003).
17. S. Wright, *Proc. Sixth Int. Congr. Gen.*, **1**, (1932).
18. M. Kimura, M., Cambridge University Press, (1983).
19. R. Brger, Chichester: Wiley,(2000).
20. S.H. Rice, Sinauer Associates, (2004).
21. G. A. Parker and J. M. Smith, *Nat.* **348**, 6296 (1990).
22. A. Grafen, *J. Theor. Bio.* **238**, 3 (2006).
23. A. Grafen, *J. Genet.* **87**, 4 (2008).
24. J. Maynard Smith, Cambridge University Press, (1982).
25. J. Hofbauer, and K. Sigmund, Cambridge University Press (1988).
26. P. Schuster, and K. Sigmund, *J. Theor. Bio.* **100**, 3 (1983).
27. S. Drozhzhin, T. Yakushkina, and A. Bratus, arXiv preprint (2019).
28. M. Kimura, *Her.* **12**,2 (1958).
29. A. W. F. Edwards, *Adv. Appl. Probab.* **6**, 1 (1974).
30. M. Eigen, *Natur.* **58**, 10 (1971).
31. I. Svirezhev, and D.O. Logofet, *Nauka*, (1978).

In-Host Dynamics of the Human Papillomavirus (HPV) in the Presence of Immune Response

Z. Chazuka, G. M. Moremedi, and E. Rapoo

1 Introduction

High-risk human papillomavirus types (16, 18, 31, 45) are one of the major contributory causes of cervical cancer in women worldwide with about 80% of women infected by HPV mainly due to sexual activities within their lifetime [6, 8]. Most HPV cases in women are normally cleared by the immune system within a year provided that there is quick detection. Due to either late detection or no detection, some HPV infections will lie dormant or latently until there is natural clearance or they develop into persistent HPV infections [7]. When fully functional, the human body is well organised with great defences against infection and reinfection. It has the skin as the immediate defence mechanism since it has a tough layer of cells called (*keratinocytes*) that are constantly producing keratin. The skin is equipped with glands that secrete substances such as fatty acids and enzymes that break down bacteria. It is important to always keep the skin intact so as to avoid possible attacks by viruses. However, during sexual intercourse, viruses such as HPV take advantage of abrasion of the epidermal lining of the genital or oral mucosa [13] to enter into the body as a result of abrasion of the epithelium. The body is also equipped with an innate and adaptive immune response system ready to identify and eradicate infection on a day-to-day basis provided they are prompted into action. However, infections such as HPV make it very hard for the immune response to be prompted into action due to their immune-evasive behaviour.

Work Supported and Funded by the UNISA Masters and Doctoral Research Bursary 2020.
This work is supported by the School of Natural Sciences, Chinhoyi University of Technology Zimbabwe.

Z. Chazuka (✉) · G. M. Moremedi · E. Rapoo
Department of Mathematical Sciences, University of South Africa, Johannesburg, South Africa

R. P. Mondaini (ed.), *Trends in Biomathematics: Chaos and Control in Epidemics, Ecosystems, and Cells*, https://doi.org/10.1007/978-3-030-73241-7_6

Mathematical modelling of the in-host dynamics of infections such as HPV makes it easy to understand the interactions necessary for a virus to spread within cells. In relation to the mathematical modelling of HPV, there are a few in-host models as compared to between-host models presented in literature. Smith et al. [10] presented an in-host mathematical model that looked at the link between low-risk HPV and high-risk HPV types [10]. The model also looked at the impact of vaccination, competition between HPV low-risk and high-risk types within cells and the probable co-infection dynamics. Simulations from the model indicated that if there is no vaccination, then both low-risk and high-risk viral types coexist [10]. However, Smith? et al. [10] did not explore the effects of immune response in the presence of vaccination, which then left out an important aspect in the dynamics of HPV within the body. Spencer Hunt in his thesis presents a mathematical model for HPV in the presence of immune response without vaccination [1]. In this particular work, Hunt creates three models, that is, a basic HPV model with immune response, the extended model with immune response and the memory model that incorporates immune response and delay. In the basic HPV, Hunt establishes that using the reproduction number for the model, one can be able to establish eradication or persistence of infection. In the memory model, Hunt considered the possibility of developing memory cells after an infection or the absence thereof and the effect of such on the reproduction number $\mathcal{R}_0$. The results indicated that in the presence of memory cells as long as the effective reproduction number $\mathcal{R}_e < 1$, HPV infection will eventually be cleared. In the immune response delay model, Hunt presents a model that tries to address the effects of a delay in immune response on the onset of infection. The model includes a time delay from the start of the infection up until the immune response is able to detect HPV; however, there is a flaw in that model in that the detection of the HPV virus by the immune response is purely a random process [7], and probably a stochastic model was appropriate. The results from the model established that there was a certain critical threshold that when reached meant that the immune response would be activated and viral clearance would drive the system to the disease-free equilibrium.

Another interesting research to note is that of Murall et al. [5]. In this particular work, they went on to create an in-host model for HPV that specifically looked at the dynamics of high-risk types in the presence of immune response and vaccination. Results from this study concluded that the removal of the ability of the HPV virus to delay effector cell attack consequently caused $\mathcal{R}_0 > 1$ for cell types with higher oncogene expression. The results also indicated that vaccine imposed immunity could create higher oncogene expression, which in turn has serious consequences on the host [5]. The model also found out that a high antibody response is an effective way of reducing the number of infected cells through reduction of healthy cells by the free HPV virions produced which supported vaccination of women.

This motivates the creation of a model that encompasses the thoughts presented in the papers above and includes latent HPV infections. In the next section, we present the model formulation, section 3 presents the analysis of the model, section 4 presents the disease-free equilibrium and reproduction number, section 5 presents

the sensitivity analysis of the reproduction number, section 6 presents the numerical simulations and finally discussion and conclusion are in section 7.

2 Model Formulation

Our HPV model considers basal layer cells of the epithelium within the genital mucosa that are constantly at risk of HPV infection during sexual intercourse. This particular mathematical model is made up of susceptible target cells denoted by $T_s(t)$, which represent healthy cells that are at risk of getting infected upon abrasion of the epithelium. These cells are assumed to die naturally at a rate μ. When HPV enters or infects a healthy target cell $T_s(t)$, it merges its DNA with that of the cell such that the cell is altered and no longer operates like a normal cell. Infection of the healthy target cells is assumed to be done at a rate given by

$$\frac{\beta V}{\gamma + T_s}, \tag{1}$$

where β is the transmission rate of the HPV virus, $V(t)$ is the free HPV virus, $T_s(t)$ is the total number of uninfected epithelial cells given that are susceptible to infection and γ is the concentration of the epithelial cells where infection is half-maximal [5, 13]. The model incorporates latently infected cells, and these are target cells within the basal layer that lie dormant or do not show any cytological changes for a certain period before either clearing HPV infection or becoming infectious target cells. We denote these type of cells within the model by $L(t)$. Inclusion of latently infected cells takes into account the undetectable HPV infection that in the long run can develop into persistent HPV if not cleared by the immune system. We assume that natural death of latently infected cells occurs at a rate μ, while clearance of latent HPV infection as a result of immune response occurs at a rate θ. Latently infected cells will also heal and return to the susceptible class at a rate ϕ. Infectious target cells for the model are denoted by $I_1(t)$. The model assumes that after a certain period, the latently infected cells can subsequently mature into infectious target cells at a rate ψ and therefore progress to the $I_1(t)$ class. Natural death of the $I_1(t)$ cells occurs at a rate μ. Throughout the model, clearance of HPV infection as a result of immune response is assumed to occur at a rate θ within all cell classes. Due to oncogene expression at a rate of $0 \leq \epsilon \leq 1$, $I_1(t)$, cells are converted into transit amplifying cells $I_2(t)$ that prompt immune response due to unusual cell activity [5, 13]. These cells are assumed to self-proliferate at a rate $r\epsilon$, where r is the transit-amplifying cells recruitment rate [5, 13] and $r\epsilon \leq \mu$ and $0 \leq r \leq 1$. $I_2(t)$ cells die naturally at a rate μ and due to bursting release free virion(s). Free virus production within the model is assumed to occur at a rate of $N_2\mu(I_1 + I_2)$, where N_2 is the burst size that is due to virus particles produced by the $I_1(t)$ and $I_2(t)$ cells in a lifetime. Free virion(s) are assumed to die naturally at a rate δ. Immune response in the form of cytotoxic target cells (CTLs) is assumed

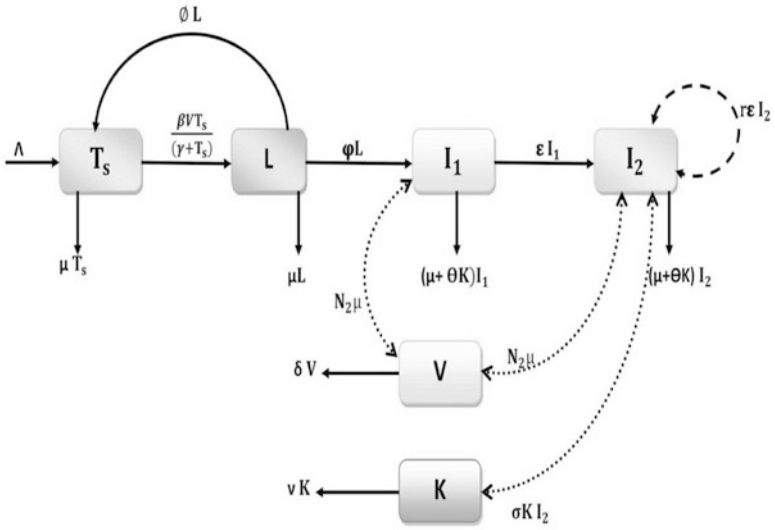

Fig. 1 In-host dynamics of HPV in the presence of immune response

to be initiated through a rapid and abnormal cell growth of $I_2(t)$ cells indicating a peculiar change within the system. The model assumes that the proliferation rate of immune response cells is given by σ [5, 13] and that immune response cells die naturally at a rate ν. This leads us to the flow diagram for the basic HPV model with the immune response of Fig. 1; this model's flow diagram leads us to the following model equations:

$$\begin{aligned}
T_s' &= \Lambda + \phi L - \left(\frac{\beta V}{(\gamma + T_s)} + \mu\right) T_s, \\
L' &= \frac{\beta V T_s}{(\gamma + T_s)} - (\mu + \psi + \phi) L, \\
I_1' &= \psi L - (\epsilon + \mu + \theta K) I_1, \\
I_2' &= \epsilon I_1 + r\epsilon I_2 - (\mu + \theta K) I_2, \\
V' &= N_2 \mu (I_1 + I_2) - \delta V, \\
K' &= \sigma I_2 K - \nu K.
\end{aligned} \tag{2}$$

3 Preliminary Analysis of the HPV Model

3.1 Positivity and Boundedness of Solutions

Model system (2) describes the dynamics of high-risk HPV in human cells within the genital mucosa, and hence we prove that all the variables $T_s(t), L(t), I_1(t), I_2(t), V(t)$ and $K(t)$ are non-negative for all time $t > 0$. This leads us to the following important theorem that we state and prove.

Theorem 3.1 *Let the initial conditions of* (2) *satisfy* $T_{s0} > 0, L_0 > 0, I_{10} > 0, I_{20} > 0, V_0 > 0$ *and* $K_0 > 0$. *Provided the unique solutions for system* (2) *exist on an interval* $[0, t_0]$ *for some* $t_0 > 0$*; then,* $T_s(t), L(t), I_1(t), I_2(t), V(t)$ *and* $K(t)$ *will be bounded and remain positive* $\forall t \in [0, t_0]$.

Proof We adopt the method by [14], and hence we initially prove that $T_s(t)$ is positive for $t \geq 0$; otherwise, there exists a positive t_0 such that $T_s(t) > 0$ for $t \in [0, t_0)$, and hence $T_s(t_0) = 0$. Using the equation,

$$T_s' = \Lambda + \phi L - \left(\frac{\beta V}{(\gamma + T_s)} + \mu\right) T_s. \tag{3}$$

Using the above equation, we note that $T_s(t)$ is strictly positive $\forall t \in [0, t_0)$. We establish that $T's(t_0) = \Lambda + \phi L \geq 0$, which implies that $T_s(t) < 0$, which is therefore a contradiction to the fact that $T_s(t) > 0$ for $t \in [0, t_0)$. Based on this, we have the following:

$$\begin{aligned}
L'|_{L=0} &= \frac{\beta V T_s}{(\gamma + T_s)} \geq 0,\\
I_1'|_{I_1=0} &= \psi L \geq 0,\\
I_2'|_{I_2=0} &= \epsilon I_1 \geq 0,\\
V'|_{V=0} &= N_2\mu(I_1 + I_2) \geq 0,\\
K'|_{K=0} &= 0.
\end{aligned} \tag{4}$$

It can clearly be seen that $T_s(t) \geq 0, L(t) \geq 0, I_1(t) \geq 0, I_2(t) \geq 0, V(t) \geq 0, K(t) \geq 0, \quad \forall\ t \in [0, t_0)$ meaning that any solution within $T_s(t), L(t), I_1(t), I_2(t), V(t)$ and $K(t)$ of model (2) is positive for all $t \geq 0$.

We prove that the system is dissipative, that is, all solutions of models system (2) are uniformly bounded in a proper subset of $\Omega \subset \mathbb{R}^6_+$, as indicated by the lemma.

Lemma 3.1 *Let* $T_s(t) > 0, L(t) >= 0, I_1(t) >= 0, I_2(t) >= 0, V(t) >= 0$ *and* $K(t) >= 0$. *Then, there exist* $T_s(t) > 0,\ L(t) >= 0,\ I_1(t) >= 0,\ I_2(t) >=$

$0,\ V(t) >= 0$ *and* $K(t) >= 0$ *such that for* $T_s(t),\ L(t),\ I_1(t),\ I_2(t),\ V(t),\ K(t),$ $\limsup_{t\to\infty}(T_s(t)) \le T_{sM},\ \limsup_{t\to\infty}(L(t)) \le L_M,\ \limsup_{t\to\infty}(I_1(t)) \le I_{1M},\ \limsup_{t\to\infty}(I_2(t)) \le I_{2M},\ \limsup_{t\to\infty}(V(t)) \le V_M,\ \limsup_{t\to\infty}(K(t)) \le K_M,\ \forall t \in [0, t_0]$.

The presence of HPV viral infection decreases the number of healthy T_s cells, and hence initially at $t = 0$ we expect that the number of healthy target cells to be close to the total cell population. Therefore, if the system is disease-free, it means that all other equations of system (2) reduce to zero except for

$$T_s' = \Lambda + \phi L - \left(\frac{\beta V}{(\gamma + T_s)} + \mu\right) T_s, \tag{5}$$

which reduces to

$$T_s' \le \Lambda - \mu T_s, \tag{6}$$

when evaluated at a disease-free equilibrium. So, based on that fact, we can find an expression for $T_s'(t)$ as follows:

$$T_s' + \mu T_s = \Lambda, \tag{7}$$

which can easily be solved using the integrating method approach to obtain

$$T_s(t) = \frac{\Lambda}{\mu} + Ae^{-\mu t}, \tag{8}$$

where A is a constant; hence, by inputting the initial conditions $T_s(0) = T_0$, we obtain the following result:

$$T_s(t) = \frac{\Lambda}{\mu} + \left(T_0 - \frac{\Lambda}{\mu}\right) e^{-\mu t}. \tag{9}$$

Taking limits on the above expression gives

$$\limsup_{t\to\infty} T_s(t) = \limsup_{t\to\infty} \left[\frac{\Lambda}{\mu} + (T_0 - \frac{\Lambda}{\mu})e^{-\mu t}\right] = \frac{\Lambda}{\mu}, \tag{10}$$

and therefore the population of cells will grow towards $\dfrac{\Lambda}{\mu}$. In order to also show that all other cells of system (2) are also bounded, we recall that all constants for the system are positive, and hence it follows that

$$T's(t) + L(t) + I'1(t) + I'2(t) = \Lambda - \mu(T_s + L + I_1 + I_2) + r\epsilon I_2, \tag{11}$$

and this can be rewritten as

$$T's(t) + L'(t) + I'1(t) + I'2(t) \leq \Lambda - min\{\mu\}(T_s + L + I_1 + I_2), \tag{12}$$

and hence using the integrating factor approach yields

$$\int e^{min\{\mu\}t} d(T_s + L + I_1 + I_2) \leq \int \Lambda e^{min\{\mu\}t} dt, \tag{13}$$

which is equal to

$$(T_s + L + I_1 + I_2) \leq \frac{\Lambda}{min\{\mu\}} + c_0 e^{-min\{\mu\}t}, \tag{14}$$

where c_0 is a constant of integration. Taking lim sup on both sides of the above equation yields

$$\limsup_{t\to\infty}(T_s + L + I_1 + I_2) \leq \limsup_{t\to\infty} \frac{\Lambda}{min\{\mu\}} + c_0 e^{-min\{\mu\}t} = \frac{\Lambda}{min\{\mu\}}. \tag{15}$$

Let $T_{sM}(t) = L_M(t) = I_{1M}(t) = I_{2M}(t) = \dfrac{\Lambda}{min\{\mu\}}$ such that $(T_s + L + I_1 + I_2)$ is bounded and so is $T_s(t), L(t), I_1(t), I_2(t)$, since

$$\{T_s(t), L(t), I_1(t), I_2(t)\} \leq (T_s + L + I_1 + I_2)(t). \tag{16}$$

So, $T_s(t) \leq T_{sM},\ L(t) \leq L_M,\ I_1(t) \leq I_{1M},\ I_2(t) \leq I_{2M},\ \forall t \in [0, t_0]$. Now, considering the virus population, we recall that

$$\frac{dV}{dt} = N_2\mu(I_1 + I_2) - \delta V, \tag{17}$$

where $(I_1 + I_2) \leq \dfrac{\Lambda}{\mu}$, and hence it follows that

$$\frac{dV}{dt} \leq N_2\Lambda - \delta V, \tag{18}$$

which by solving, using the integrating factor approach, yields

$$V(t) \leq \frac{N_2\Lambda}{\delta} + A_0 e^{-\delta t}, \tag{19}$$

where A_0 is a constant. By applying the initial conditions, we obtain

$$V(t) \leq \frac{N_2\Lambda}{\delta} + (V_0 - \frac{N_2\Lambda}{\delta})e^{-\delta t}. \tag{20}$$

Now, taking lim sup limits on both sides of the above equation yields

$$\limsup_{t\to\infty} V(t) \leq \limsup_{t\to\infty} \frac{N_2\Lambda}{\delta} + \left(V_0 - \frac{N_2\Lambda}{\delta}\right) e^{-\delta t} = \frac{N_2\Lambda}{\delta}, \tag{21}$$

and hence we choose $V_M = \dfrac{N_2\Lambda}{\delta}$ such that $V(t) \leq V_M$, and since I_1 and I_2 are bounded, it suffices that $V(t)$ is also bounded for all $t \in [0, t_0]$. All feasible solutions to model system (2) are therefore positively bounded by

$$\Omega = \{T_s(t), L(t), I_1(t), I_2(t), V(t), K(t \in \mathbb{R}^6 + \mid T_s \leq \frac{\Lambda}{\mu}\}. \tag{22}$$

The region is considered of biological interest and is positively invariant and attracting. □

4 The Disease-Free Equilibrium and the Reproduction Number $\mathcal{R}_0$

In order to find the disease-free equilibrium point, we consider all infectious compartments $\{L, I_1, I_2, V\}$ to be equal to zero such that model system (2) yields a disease-free equilibrium given by

$$\mathcal{E}_0 = \left(\frac{\Lambda}{\mu}, 0, 0, 0, 0, 0\right). \tag{23}$$

We find R_0 using the next generation matrix approach by Van den Driessche and Watmough [12]. We proceed to construct the $\mathcal{F}$ and $\mathcal{V}$ matrices for model system (2) as follows:

$$\mathcal{F} = \begin{pmatrix} 0\,0\,0 & \dfrac{\Lambda\beta}{(\Lambda+\gamma\mu)} \\ 0\,0\,0 & 0 \\ 0\,0\,0 & 0 \\ 0\,0\,0 & 0 \end{pmatrix}, \mathcal{V} = \begin{pmatrix} (\mu+\psi+\phi) & 0 & 0 & 0 \\ -\psi & (\epsilon+\mu) & 0 & 0 \\ 0 & -\epsilon & \mu - r\epsilon & 0 \\ 0 & -N_2\mu & -N_2\mu & \delta \end{pmatrix}, \tag{24}$$

such that the spectral radius $\rho(FV^{-1})$ is given by

$$\mathcal{R}_0 = \frac{\beta\Lambda\psi N_2\mu(\mu+\epsilon-r\epsilon)}{\delta(\gamma\mu+\Lambda)(\psi+\phi+\mu)(\mu-r\epsilon)(\epsilon+\mu)}, \tag{25}$$

where $\mu - r\epsilon > 0, 0 < r < 1,\ \ 0 < \epsilon < 1$, the assumption being that as oncogene expression increases, $(\mu - r\epsilon)$ decreases and when oncogene expression decreases,

$(\mu - r\epsilon)$ approaches μ, and hence the reproduction number is positive as required. We establish the stability of the disease-free equilibrium by stating the following theorem.

Theorem 4.1 *The disease-free equilibrium for model (2) is locally asymptotically stable provided that $\mathcal{R}_0 < 1$ and unstable when $\mathcal{R}_0 > 1$.*

Proof The Jacobian for model (2) calculated at the disease-free equilibrium gives

$$J(\mathcal{E}_0) = \begin{pmatrix} -\mu & \phi & 0 & 0 & -\dfrac{\Lambda\beta}{(\Lambda+\gamma\mu)} & 0 \\ 0 & -(\mu+\psi+\phi) & 0 & 0 & \dfrac{\Lambda\beta}{(\Lambda+\gamma\mu)} & 0 \\ 0 & \psi & -(\epsilon+\mu) & 0 & 0 & 0 \\ 0 & 0 & \epsilon & -(\mu-r\epsilon) & 0 & 0 \\ 0 & 0 & N_2\mu & N_2\mu & -\delta & 0 \\ 0 & 0 & 0 & 0 & 0 & -\nu \end{pmatrix}. \tag{26}$$

The first two eigenvalues of the above Jacobian matrix are $\lambda_1 = -\mu$ and $\lambda_2 = -\nu$, while the remaining eigenvalues are found by solving the quartic polynomial:

$$P(\lambda) = \lambda^4 + a_1\lambda^3 + a_2\lambda^2 + a_3\lambda + a_4, \tag{27}$$

where

$$\begin{aligned} a_1 &= 3\mu + \psi + \phi + \epsilon(1-r) + \delta > 0 \\ a_2 &= \delta(3\mu + \epsilon(1-r) + \psi + \phi) + (\mu + \psi + \phi)(2\mu + \epsilon(1-r)) \\ &+(\epsilon + \mu)(\mu - r\epsilon) > 0 \\ a_3 &= \delta(\mu + \psi + \phi)(2\mu + \epsilon(1-r)) + (\epsilon + \mu)(\mu - r\epsilon)(\delta + \mu + \psi + \phi) > 0 \\ a_4 &= \delta(\mu + \epsilon)(\mu + \psi + \phi)(\mu - r\epsilon)\,[1 - \mathcal{R}_0] > 0. \end{aligned} \tag{28}$$

In order to establish whether the eigenvalues of the polynomial above have negative real parts, we state the following lemma.

Lemma 4.1 *The eigenvalues of the fourth degree polynomial $P(\lambda) = \lambda^4 + a_1\lambda^3 + a_2\lambda^2 + a_3\lambda + a_4$ have negative real parts provided that $a_1 > 0$, $a_2 > 0$, $a_3 > 0$ and $a_3(a_1a_2 - a_3) - a_1^2a_4 > 0$, where a_0, a_1, a_2, a_3 and a_4 are given above.*

Proof In order to show that the Routh–Hurwitz condition is satisfied, let

$$\alpha = (3\mu + \psi + \phi + \epsilon(1-r) + \delta),\ \alpha_1 = (\mu + \psi + \phi),\ \alpha_2 = (2\mu + \epsilon(1-r))$$

and $\alpha_3 = (\epsilon + \mu)(\mu - r\epsilon)$; hence,

$$\begin{aligned} a_3(a_1a_2 - a_3) = \delta^3\alpha\alpha_1\alpha_2 + \delta^2\alpha_3(\alpha_1 + \alpha^2 + \alpha\alpha_1 + \alpha) + \delta\alpha_3\alpha_2(\alpha_2\alpha_1 + \alpha_3\alpha_2) \\ + \delta\alpha_1\alpha(\alpha\alpha_3 + \alpha_1\alpha_2^2) + \alpha_1\alpha_2\alpha_3(\alpha_3 + \alpha\alpha_1) \end{aligned} \tag{29}$$

and

$$a_1^2 a_4 = (1 - \mathcal{R}_0)\left[\delta^3\alpha_3\alpha_1 + 2\delta^2\alpha\alpha_1\alpha_3 + \delta\alpha^3\alpha_1\alpha^2\right] \tag{30}$$

such that

$$\begin{aligned} a_3(a_1a_2 - a_3) - a_1^2 a_4 &= \delta^3\alpha_2(\alpha_3 + \alpha\alpha_1) + \delta^2\alpha_3(\alpha_1 + \alpha\alpha_2) \\ &+ \delta\alpha_2\alpha_3(\alpha_2\alpha_1 + \alpha_3 + \alpha\alpha_1) + \delta\alpha_1^2\alpha\alpha_2^2 \\ &+ \alpha_1\alpha_2\alpha_3(\alpha_3 + \alpha\alpha_1) + \mathcal{R}_0\alpha_1\alpha_3\left[\delta\alpha^2 + \delta^3 + 2\delta^2\alpha\right] > 0, \end{aligned} \tag{31}$$

and hence the Routh–Hurwitz condition is satisfied implying that the quartic polynomial has roots with negative real parts. Thus, the disease-free equilibrium is locally asymptotically stable when $\mathcal{R}_0 < 1$ and unstable otherwise. This completes the proof. □

4.1 Global Stability Analysis of the Disease-Free Equilibrium

The disease-free equilibrium is locally stable provided that $\mathcal{R}_0 < 1$ around $\mathcal{E}_0$. In order to prove global stability of model system (2), we state the following theorem.

Theorem 4.2 *The disease-free equilibrium for system* (2) *is globally stable provided that* $\mathcal{R}_0 < 1$ *around* $\mathcal{E}_0$.

Proof We prove global stability of an in-host model through following the work by Shuai and van den Driessche [9]. We recall that for our particular model

$$\mathcal{R}_0 = \frac{\beta\Lambda\psi N_2\mu(\mu + \epsilon - r\epsilon)}{\delta(\gamma\mu + \Lambda)(\psi + \mu + \phi)(\mu - r\epsilon)(\epsilon + \mu)}. \tag{32}$$

The Perron–Frobenius theorem states that every non-negative matrix can be obtained as a limit of positive matrices. Therefore, there exists an eigenvector with non-negative parts, and the corresponding eigenvalue is non-negative and will be greater than or equal, in its absolute value, to all other eigenvalues of the matrix [3]. So, let $\mathcal{X} = (L, I_1, I_2, V)^T$, and based on the work by Shuai and van den Driessche [9], we construct a Lyapunov function of the form

$$\mathcal{L} = u^T\mathcal{V}^{-1}\mathcal{X},$$

and we let

$$\mathcal{X}' = (\mathcal{F} - \mathcal{V})\mathcal{X} - f(x, T_s).$$

The matrix $\mathcal{V}^{-1}\mathcal{F}$ is reducible, and hence the left eigenvector is given by $u^T = (0, 0, 0, 1)$, since the only non-zero column for the reducible matrix is column four. Therefore, the Lyapunov function $\mathcal{L}$ is given as

$$\mathcal{L} = \frac{N_2\mu\psi(\mu+\epsilon-r\epsilon)}{\delta(\psi+\phi+\mu)(\mu-r\epsilon)(\epsilon+\mu)}L + \frac{N_2\mu(\mu+\epsilon-r\epsilon)}{\delta(\mu-r\epsilon)(\epsilon+\mu)}I_1 + \frac{N_2\mu}{\delta(\mu-r\epsilon)}I_2 + \frac{1}{\delta}V$$

$$= \frac{\mathcal{R}_0(\gamma+T_{s0})}{\beta T_{s0}}\left(L + \frac{(\mu+\psi+\phi)}{\psi}I_1 + \frac{(\mu+\psi+\phi)(\epsilon+\mu)}{\psi(\mu+\epsilon-r\epsilon)}I_2 + \frac{(\mu+\psi+\phi)(\epsilon+\mu)(\mu-r\epsilon)}{N_2\mu\psi(\mu+\epsilon-r\epsilon)}V\right).$$

It follows from the above calculation that

$$\mathcal{L}' = u^T\mathcal{V}^{-1}(\mathcal{F}-\mathcal{V})\mathcal{X} - u^T\mathcal{V}^{-1}f(x,y), \tag{33}$$

where

$$(\mathcal{F}-\mathcal{V})\mathcal{X} = \begin{pmatrix} -(\mu+\psi+\phi) & 0 & 0 & \frac{\beta T_{s0}}{(\gamma+T_{s0})} \\ \psi & -(\epsilon+\mu) & 0 & 0 \\ 0 & \epsilon & -(\mu-r\epsilon) & 0 \\ 0 & N_2\mu & N_2\mu & -\delta \end{pmatrix} \begin{pmatrix} L \\ I_1 \\ I_2 \\ V \end{pmatrix}, \tag{34}$$

and

$$f(x,y) = (\mathcal{F}-\mathcal{V})\mathcal{X} - F(x,y) + V(x,y).$$

Hence, using the vectors and matrices found above in the calculation of $\mathcal{R}_0$, we obtain

$$f(x,T_s) = \begin{pmatrix} \frac{\beta V T_{s0}}{(\gamma+T_{s0})} - \frac{\beta V T_s}{(\gamma+T_s)} \\ \theta K I_1 \\ \theta K I_2 \\ 0 \end{pmatrix}, \tag{35}$$

and hence

$$u^T\mathcal{V}^{-1}f(x,T_s) = \frac{\mathcal{R}_0(\gamma+T_{s0})}{T_{s0}}\left(\frac{T_{s0}}{\gamma+T_{s0}} - \frac{T_s}{\gamma+T_s}\right)V + \theta K(I_1+I_2), \tag{36}$$

and

$$u^T\mathcal{V}^{-1}(\mathcal{F}-\mathcal{V})\mathcal{X} = (\mathcal{R}_0-1)\,V + \theta K(I_1+I_2); \tag{37}$$

finally,

$$\mathcal{L}' = u^T \mathcal{V}^{-1}(\mathcal{F} - \mathcal{V})\mathcal{X} - u^T \mathcal{V}^{-1} f(x, y)$$

$$= (\mathcal{R}_0 - 1)\, V - \frac{\mathcal{R}_0(\gamma + T_{s0})}{T_{s0}} \left(\frac{T_{s0}}{\gamma + T_{s0}} - \frac{T_s}{\gamma + T_s} \right) V + \theta K (I_1 + I_2) \leq 0, \tag{38}$$

provided $\mathcal{R}_0 <\leq 1$. It can easily be seen that $\mathcal{L}' = 0$ is satisfied when $V = I_1 = I_2 = K = 0$ and $T_{s0} = T_s$ and also that $L = 0$. Therefore, it can be established that the only largest compact invariant set in $(T_s, L, I_1, I_2, V, K) \in \mathbb{R}^6_+ : \mathcal{L}' = 0$ is the singleton $\{\mathcal{E}_0\}$. We state without proof LaSalle's invariant principle as follows.

Theorem 4.3 *(LaSalle's invariance principle [2]) Assuming that $\mathcal{L}$ is a Lyapunov function for (2) on $\mathcal{G}$. We define $S = \{x \in \mathcal{G} \cap \Omega : \dot{\mathcal{L}} = 0\}$. Let $\mathcal{M}$ be the largest invariant set in S; then, every bounded trajectory for $t \geq 0$ of (2) that remains in $\mathcal{G}$ approaches the set $\mathcal{M}$ as $t \to +\infty$.*

Using the above principle, it suffices to state that the singleton $\{\mathcal{E}_0\}$ is globally asymptotically stable in Ω when $\mathcal{R}_0 < 1$, which completes the proof. □

4.2 The Endemic Equilibrium

Model system (2) has two endemic equilibrium points $\mathcal{E}_1^e$ and $\mathcal{E}_2^*$. In this particular work, we study the dynamics of the CTL-inactivated endemic equilibrium point, which is given by

$$\mathcal{E}_1^e = \{T_s^e, L^e, I_1^e, I_2^e, V^e, K^e\},$$

where

$$T_s^e = \frac{\Lambda}{\mu} - \frac{\Lambda(\mathcal{R}_0 - 1)(\gamma\mu + \Lambda)}{\mu[\mathcal{R}_0\gamma\mu + \Lambda(\mathcal{R}_0 - 1)]} > 0,\ L^e = \frac{\Lambda(\mathcal{R}_0 - 1)(\gamma\mu + \Lambda)}{(\mu + \psi)[\mathcal{R}_0\gamma\mu + \Lambda(\mathcal{R}_0 - 1)]},$$

$$I_1^e = \frac{\Lambda\psi(\mathcal{R}_0 - 1)(\gamma\mu + \Lambda)}{(\mu + \psi)(\epsilon + \mu)[\mathcal{R}_0\gamma\mu + \Lambda(\mathcal{R}_0 - 1)]},$$

$$I_2^e = \frac{\Lambda\psi\epsilon(\mathcal{R}_0 - 1)(\gamma\mu + \Lambda)}{(\mu + \psi)(\mu - r\epsilon)(\epsilon + \mu)[\mathcal{R}_0\gamma\mu + \Lambda(\mathcal{R}_0 - 1)]},$$

$$V^e = \frac{\mathcal{R}_0(\mathcal{R}_0 - 1)(\mu + \psi + \phi)(\Lambda + \gamma\mu)^2}{(\mu + \psi)[\mathcal{R}_0\gamma\mu + \Lambda(\mathcal{R}_0 - 1)]},\ K^e = 0. \tag{39}$$

4.3 The CTL-Activated Reproduction Number $\mathcal{R}_K$

There exists a CTL-activated immune response reproduction number that represents the life span of a CTL cell. Based on model (2) for $(\sigma I_2 - \nu \leq 0)$, the CTL immune response reproduction number is given by

$$\mathcal{R}_K = \frac{\Lambda\sigma\psi\epsilon(\mathcal{R}_0 - 1)(\gamma\mu + \Lambda)}{\nu(\mu + \psi)(\mu - r\epsilon)(\epsilon + \mu)[\mathcal{R}_0\gamma\mu + \Lambda(\mathcal{R}_0 - 1)]}. \tag{40}$$

We state without proof the following lemma.

Lemma 4.2 *Conditions governing the CTL-inactivated/activated equilibrium are*

(1) *if* $\mathcal{R}_0 > 1$ *and* $\mathcal{R}_K \leq 1$, *then the CTL-inactivated endemic equilibrium* $\mathcal{E}_1^e$ *is globally asymptotically stable.*
(2) *if* $\mathcal{R}_0 > 1$ *and* $\mathcal{R}_K \geq 1$, *then the CTL-inactivated endemic equilibrium* $\mathcal{E}_1^e$ *is unstable, while the CTL-activated equilibrium endemic is globally asymptotically stable.*

The CTL inactivated endemic equilibrium $\mathcal{E}_1^e$ presents a situation where there is HPV infection among cells yet the innate immune response is not responsive or is suppressed [14]. We present numerical simulations that present the dynamics of HPV in the absence of immune response.

5 Sensitivity Analysis of $\mathcal{R}_0$.

In order to establish which control methods are effective in the reduction of the spread of HPV in-host, we carry out a sensitivity analysis. This analysis helps us to identify those particular parameters that have an impact on $\mathcal{R}_0$. The best measure of sensitivity is the calculation of the elasticity index which is given by

$$\Gamma_p^{\mathcal{R}_0} = \frac{\partial\mathcal{R}_0}{\partial p} \times \frac{p}{\mathcal{R}_0}, \tag{41}$$

where p is the parameter of interest. Using the parameters in Table 1 below, the following normalised sensitivity indices were calculated and tabulated.

Using the parameters from Table 1, we obtain the sensitivity indices.
The results of Table 2 indicate that β, N_2 and δ are the highly sensitive parameters of the model. The results indicate that an increase in the transmission rate by 10% will also result in an increase in $\mathcal{R}_0$ by 10%, an increase in the burst size N_2 indicates an increase in $\mathcal{R}_0$ by 10% and an increase in the natural viral death δ by 10% will result in a decrease in $\mathcal{R}_0$ by 10%. These key parameters are mainly involved in viral transmission and replication, and hence the less the viral particles are as a result of

Table 1 Table of parameters

Parameter	**Value**	**Description**	Source
Λ	36000 cells per ml per day	$CD4^+$ epithelial cell recruitment rate	[4]
β	0.0067 virion(s) per day	HPV infection rate	[13]
δ	0.05 cells per day	Virion death rate	Est.
μ	0.048 per day	Cells death rate	[5]
N_2	1000 virion(s) per cell	HPV burst size.	[13]
θ	0.01 per day	HPV clearance rate	[10]
γ	10^6	Epithelial cell concentration for infection half-maximal	[5]
ψ	0.03	Mature rate of latently infected cells	[1]
σ	0.001 cells per ml	CTL expansion rate	Est.
ν	0.5 cells per ml	CTL death rate	Est.
ϵ	varied between $0-1$	Oncogene expression	[5]
r	0.01	Transit-amplifying cells recruitment rate	[5]
ϕ	0.002	Natural clearance of HPV as a result of healing of cells	[10]

Table 2 Table of sensitivity indices for $\mathcal{R}_0$

Parameter	Sensitivity	Parameter	Sensitivity
β	100%	ϕ	−88.5%
N_2	100%	μ	−66.13%
δ	−100%	ϵ	1.9%
Λ	57.14	r	1.45%
ψ	95.58%	γ	−54.14%

reduction in transmission, burst size and increase in viral death of natural death, the less the spread of HPV among cells. It can also be seen that a decrease in the epithelial cell concentration by 5.7% implies an increase in $\mathcal{R}_0$ by 5.7%, while an increase in ψ the progression rate of latently infected cells to the infected cells class I_1 by 9.5% implies an increase in $\mathcal{R}_0$ by 9.5%; this is a due to the fact that I_1 cells are key in the spread of HPV. Oncogene expression $\epsilon = 0.1$ has little effect on $\mathcal{R}_0$ while increasing its value also increases $\mathcal{R}_0$, and finally the transit amplifying rate has the least significant effect on $\mathcal{R}_0$. These two parameters are highly dependent on each other; by this, we mean that the proliferation of I_1 into I_2 is dependent on the oncogene expression rate, so the higher the rate is, the more significant effect on $\mathcal{R}_0$.

6 Numerical Simulations

We present numerical simulations that show the infection dynamics of HPV in the presence of immune response. The simulations show the stability of the disease-free point therefore supporting our theoretical claims above. We use parameters sourced from literature given in Table 1 above and obtain the simulations below. According to the simulations presented below in Fig. 2, the disease-free equilibrium is given by $\mathcal{E}_0 = (7.5 \times 10^5, 0, 0, 0, 0, 0)$ and is found to be globally asymptotically stable as indicated. Figure 2 indicates that over time, the infected classes will converge to zero, while the healthy cells class T_s converges to (7.5×10^5) showing that the disease-free equilibrium is stable when $\mathcal{R}_0 < 1$.

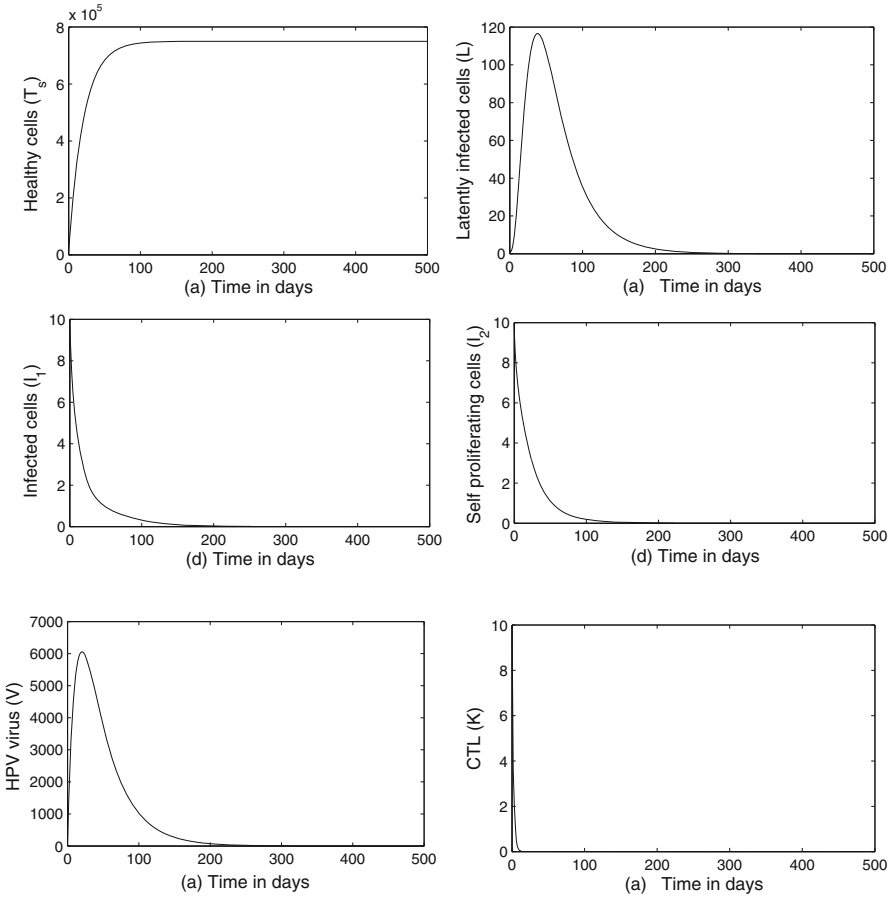

Fig. 2 In-host dynamics of HPV in the presence of immune response for classes $T_s(t), L(t), I_1(t), I_2(t)$, $\mathcal{R}_0 = 0.1591 < 1$ and with $\epsilon = 0.01$ and all other parameters taken from Table 1

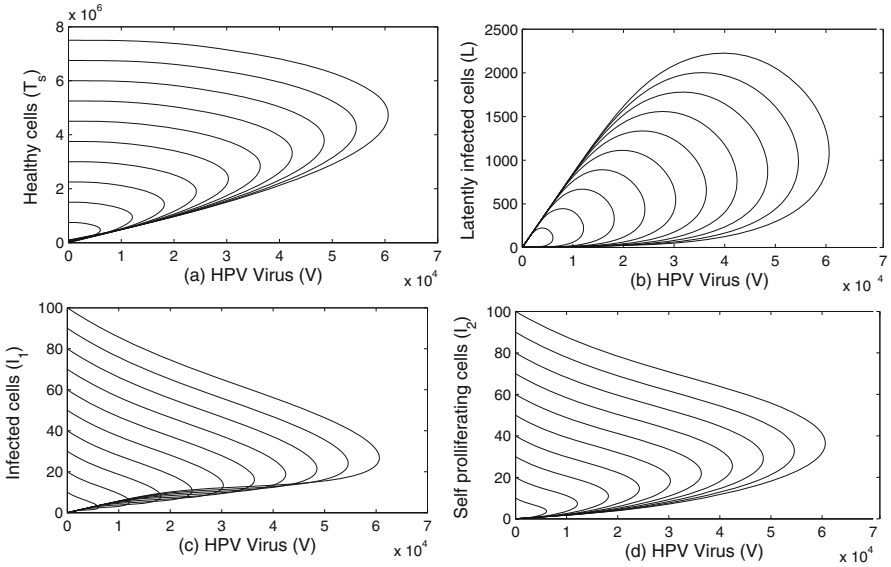

Fig. 3 Phase diagrams for the in-host dynamics of HPV in the presence of immune response for classes $V(t)$, $K(t)$, $\mathcal{R}_0 = 0.1591 < 1$ and with $\epsilon = 0.01$ and all other parameters as of Table 1

The phase portraits for the disease free equilibrium are given in (Fig. 3) above. The phase plots above support the stability of the disease free equilibrium as it can be seen that Fig. 3a indicates that when the HPV virus is introduced as a result of the abrasion of the epithelial cells, the healthy cells T_s gradually decrease relative to the virus population. This continues until the virus reaches a viral load peak, and then we suddenly observe a gradual decrease in the virus till it reaches zero. The above trend can be as a result of the fact that though $\mathcal{R}_0 < 1$, the immune system has the ability to suppress the viral load at some point within the infection. The remaining phase plots, Figs. 3b–d, also support the existence of a globally asymptotically stable disease free equilibrium given $\mathcal{R}_0 < 1$.

The dynamics of the first endemic equilibrium point $\mathcal{E}_1^e$ also known as the CTL free equilibrium are given by the simulations in Fig. 4 below. The simulations in Fig. 4a–f show the behaviour of HPV in the absence of CTL action as a probable result of immune evasion. The figures also indicate that in the absence of immune response, infected cells increase, while the healthy cells decrease to a minimal value. Figure 4b–e also specifically shows some form of delay in the increase of infected cells and virus cells in the early days between 0 and 150 days. The simulations indicate that classes $T_s(t)$, $L(t)$, $I_1(t)$, $I_2(t)$, $V(t)$ and $K(t)$ converge to the CTL-free endemic equilibrium given by $\mathcal{E}_1^e = (3.2 \times 10^4, 4.418 \times 10^5, 2.419 \times 10^4, 2.183 \times 10^5, 2.932 \times 10^8, 0)$, with $\mathcal{R}_0 = 13.8090 > 1$ and $\mathcal{R}_K = 0.0563 < 1$. The corresponding phase portraits for the endemic point $\mathcal{E}_1^e$ are given in Fig. 5. These phase portraits for the case $\mathcal{R}_0 = 13.809 > 1$ and $\mathcal{R}_K = 0.0563$ clearly

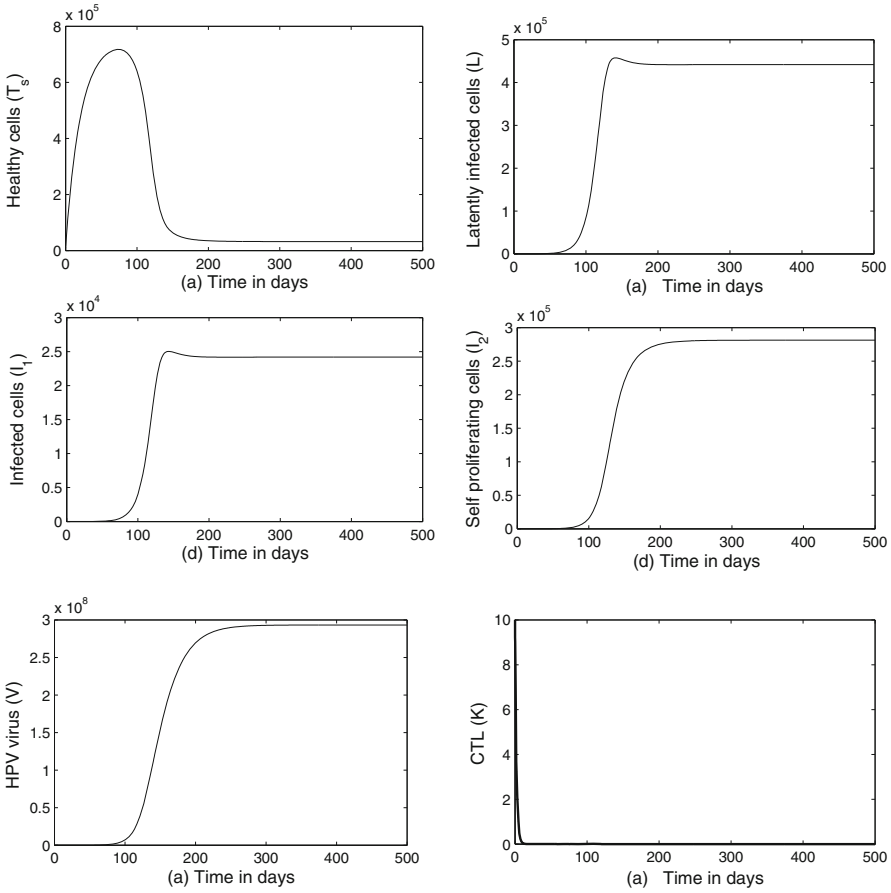

Fig. 4 In-host dynamics of HPV in the absence of immune response for classes $T_s(t), L(t), I_1(t), I_2(t)$, $\mathcal{R}_0 = 13.809 > 1, \mathcal{R}_K = 0.0563$ and with parameters $\epsilon = 0.5$ and $\sigma = 10^{-6}$ and all other parameters taken from Table 1

indicate that upon the introduction of the HPV virus, healthy cells will gradually reduce as the viral load increases, while latently infected cells, infected cells and self proliferating cells will gradually increase. It can also be noted that we will eventually have a situation where self-proliferating cells (I_2) will exceed the number of infected cells (I_1), which promotes the spread of the virus within the cells as long as there is no immune response. Clearly, the phase portraits indicate that the endemic equilibrium point $\mathcal{E}_1^e$ is globally asymptotically stable when $\mathcal{R}_0 > 1, \mathcal{R}_K < 1$.

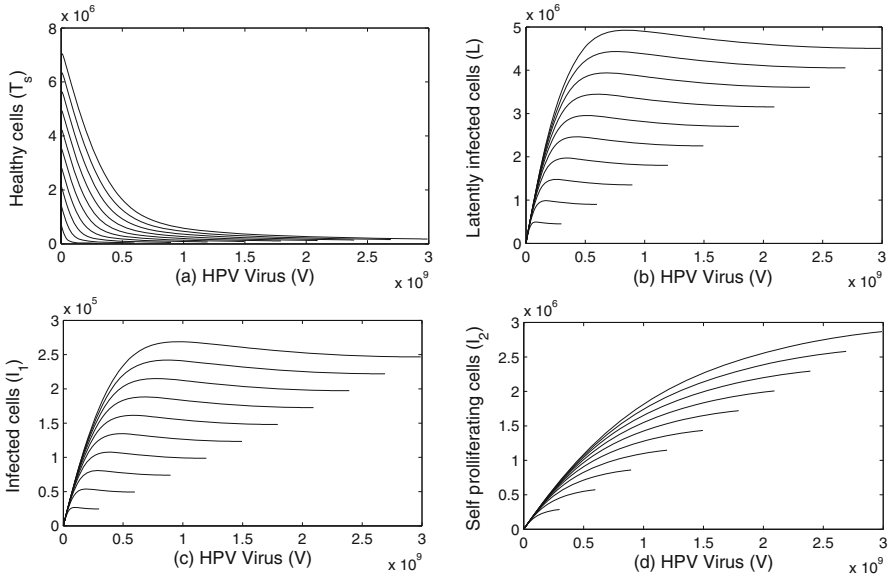

Fig. 5 In-host dynamics of HPV in the absence of immune response for classes $V(t)$, $K(t)$, $\mathcal{R}_0 = 13.809 > 1$, $\mathcal{R}_K = 0.0563$ and with $\epsilon = 0.5$ and $\sigma = 10^{-6}$ and all other parameters as of Table 1

7 Discussion and Conclusion

This chapter looked at the overall dynamics of HPV in the presence of cell proliferation and immune response. An in-host model based on the work by Samantha et al. [13] and Carmen et al. [5] was created with latency incorporated. Latent HPV infections play a significant role in the dynamics of HPV in host. If such infections are not cleared by the immune system, they can develop into persistent infections. The local and global stability of the disease-free equilibrium were analysed, and it was established that the disease-free equilibrium was stable provided that $\mathcal{R}_0 < 1$. The model created had two equilibrium points of which in this chapter we only looked at the stability of the CTL inactive equilibrium $\mathcal{E}_1^e$. Based on extensive research on the viral dynamics of HPV by authors such as Stanley et al. [11] and Sasagawa et al. [8], this particular equilibrium point presents the immune evading behaviour of the HPV virus. The stability of this particular equilibrium point was analysed, and it was established from simulations that in the absence of immune response, self-proliferating cells I_2 will exceed the number of infected cells I_1 thereby spreading infection within cells as long as immune response is absent. A rise in infected cells also implies a rise in latently infected cells and consequently a rise in the HPV virus as a result of viral burst. The biological understanding of the dynamics of HPV as explained by Stanley et al. [11] and Sasagawa et al. [8] supports our mathematical findings. HPV evades the immune system through a number of ways; among these is choosing to infect

the keratinocytes and therefore evading abnormal cell death. Abnormal cell death normally prompts the immune system into action and will also prompt the triggering of inflammatory responses that in turn will prompt the adaptive immune response. HPV will also evade the immune system through the production of oncoproteins E6 and E7 that cause the uncontrolled self-replication of cells through suppression of the $p53$ protein. The modelling of HPV is highly complex, but we believe that the simple model created closely resembles the dynamics of the virus in the absence of immune response. Future work looks at an analysis of the second endemic equilibrium point and its implications on the dynamics of the infection. We will also extend the model to look at the impact of immune suppression as a result of infections such as HIV.

Acknowledgments The authors would like to thank Dr. S.I. Oke (University of Pretoria, South Africa) for proof reading the work and for the valuable comments. This research was supported by the UNISA Master's and Doctoral Bursary.

References

1. HUNT, S. D. *Modelling the Spread of the Human Papillomavirus on the Cervix*. PhD thesis, 2015.
2. LA SALLE, J. P. An invariance principle in the theory of stability.
3. MEYER, C. D. *Matrix analysis and applied linear algebra*, vol. 71. Siam, 2000.
4. MURALL, C. L. *The ecology within: health implications of within-host ecology*. PhD thesis, 2013.
5. MURALL, C. L., BAUCH, C. T., AND DAY, T. Could the human papillomavirus vaccines drive virulence evolution? *Proc. R. Soc. B 282*, 1798 (2015), 20141069.
6. WORLD HEALTH ORGANIZATION. Human Papillomavirus Vaccines: WHO position paper, May 2017 - recommendations. *Vaccine 35*, 43 (2017), 5753.
7. RYSER, M. D., MYERS, E. R., AND DURRETT, R. HPV clearance and the neglected role of stochasticity. *PLoS computational biology 11*, 3 (2015), e1004113.
8. SASAGAWA, T., TAKAGI, H., AND MAKINODA, S. Immune responses against human papillomavirus (HPV) infection and evasion of host defense in cervical cancer. *Journal of Infection and Chemotherapy 18*, 6 (2012), 807–815.
9. SHUAI, Z., AND VAN DEN DRIESSCHE, P. Global stability of infectious disease models using Lyapunov functions. *SIAM Journal on Applied Mathematics 73*, 4 (2013), 1513–1532.
10. SMITH?, R. J., LI, J., MAO, J., AND SAHAI, B. Using within-host mathematical modelling to predict the long-term outcome of human papillomavirus vaccines.
11. STANLEY, M. Immune responses to human papillomavirus. *Vaccine 24* (2006), S16–S22.
12. VAN DEN DRIESSCHE, P., AND WATMOUGH, J. Reproduction numbers and sub-threshold endemic equilibria for compartmental models of disease transmission. *Mathematical biosciences 180*, 1-2 (2002), 29–48.
13. VERMA, M., ERWIN, S., ABEDI, V., HONTECILLAS, R., HOOPS, S., LEBER, A., BASSAGANYA-RIERA, J., AND CIUPE, S. M. Modeling the mechanisms by which HIV-associated immunosuppression influences hpv persistence at the oral mucosa. *PloS one 12*, 1 (2017), e0168133.
14. WESTER, T. Analysis and simulation of a mathematical model of Ebola virus dynamics in vivo. *Society for Industrial and Applied Mathematics 8* (2015), 236–256.

Global Properties and Optimal Control Strategies of a Generalized Ebola Virus Disease Model

Zineb El Rhoubari, Hajar Besbassi, Khalid Hattaf, and Noura Yousfi

1 Introduction

Ebola is the name of a river near the city of Yambuku in the Congo. The virus was identified firstly in this locality in 1976 and bears today the name of this river. Since then, the West Africa countries have experienced sporadic outbreaks with a mortality rate up to 90% [1]. In the 2014–2016 Ebola outbreak, the World Health Organization (WHO) reported more than 11000 deaths and declared a public health emergency of international concern [2, 3]. The virus is introduced and spread in the human population by an unprotected contact with bodily fluids of infected ill or dead humans, non-human primates, and bats.

The fruit bats are recognizing as the natural reservoir of the Ebola virus (EV) [4]. Other studies have shown that bats bear Ebola virus without being ill. For instance, Swanpoel et al. [5] experienced that the virus replicates in bats without being affected. Also, a seropositive bat for Ebola lives healthy over 13 months post-sampling [6]. On the other hand, many mathematical studies have modeled the Ebola transmission in the bat population. In [7], the authors studied the dynamics of a generalized epizootic model in order to understand the long-term transmission of the EVD in the bat population. Furthermore, they studied the global stability of the two equilibria (disease-free and endemic) theoretically and numerically. Buceta and Kaylynn studied in [8] an SIR compartmental model including the bats mobility and

Z. E. Rhoubari (✉) · H. Besbassi · N. Yousfi
Laboratory of Analysis, Modeling and Simulation (LAMS), Faculty of Science Ben M'sik, Hassan II University, Casablanca, Morocco

K. Hattaf
Laboratory of Analysis, Modeling and Simulation (LAMS), Faculty of Science Ben M'sik, Hassan II University, Casablanca, Morocco

Centre Régional des Métiers de l'Education et de la Formation (CRMEF), Casablanca, Morocco

R. P. Mondaini (ed.), *Trends in Biomathematics: Chaos and Control in Epidemics, Ecosystems, and Cells*, https://doi.org/10.1007/978-3-030-73241-7_7

the spatiotemporal climate variability. They are used to understand the migration patterns of bats and to predict the hot spots of Ebola outbreaks in space and time.

The frequent emergence of the disease and the high mortality rate make EVD a major global public health problem. Hence, the disease has caught the attention of many mathematical and biological researchers. Weitz and Dushoff [9] estimated in 2014 that 10% to 30% of EVD cases in the human population are caused by post-death transmission. Motivated by these statistics, Rhoubari et al. [10] proposed a new generalized model of EVD that takes into account the transmission of Ebola from dead humans to the living. The transmission process was modeled by general incidence functions that cover many types of incidence rates existing in the literature. The global stability of equilibria was investigated theoretically and numerically. Moreover, a threshold parameter was given in order to determine whether the disease is extinct or not.

Over the past years, several mathematical models have been built to help public health authorities deciding on vaccination strategies. Classically, the SIR model is used where the population is assumed to be divided into three components: susceptible, S, infected I, and recovered, R. In [11], Laarabi et al. developed an SIR model with saturated incidence rate and saturated treatment function. They are used to minimize the susceptible and infected individuals and to maximize the number of recovered. In the work of Lashari [12], the author has proposed an optimal control problem for an SIR epidemic model and has considered two control strategies: treatment and vaccination. Their impact was discussed through the basic reproduction number. In another study [13], Zaman et al. have formulated a control problem relatively to an SIR model and have shown the impact of vaccinating a percentage of the susceptible population. Those three models do not consider a specific disease neither the methods of transmission. Therefore, they are not applicable to EVD.

Concerning the EVD optimal control problems, most of the existing studies in the literature neglect the post-death transmission. In [14], Rachah and Torres have applied optimal control for an SIR EVD model to show the impact of vaccination on the propagation of the disease in the 2014 outbreak in West Africa. In a next work [15], they have added the exposed component. Using the SEIR model, they have proposed three strategies: control Ebola infection by vaccination of susceptible, minimize exposed and infected, and finally reduce infection by vaccination and education. In a recent work [16], the authors have improved the SEIR model with additional hospitalization, quarantine, and vaccination components. They studied the impact of control in the case of hospitalization (with and without quarantine) and vaccination. Their purpose was to predict the possible future outcome in terms of resource utilization for disease control and the effectiveness of vaccination on sick populations.

In this work, we perform sensitivity analysis of the basic reproduction number with respect to some epidemiological parameters. We find that it is most sensitive to the mortality rate due to EVD. These suggest us to formulate an optimal control problem to minimize the number of infectious by vaccination and/or treatment. In fact, the vaccine stimulates the body's immune system to be resistant against the

infection or the disease. Vaccination is the most effective method for controlling and eradicating infectious diseases and helps to avert between 2 and 3 million deaths each year [17, 18]. For Ebola, the WHO prequalified in 12 November 2019 an Ebola vaccine for the first time. This step will help to accelerate its licensing, access, and rollout in nations most in danger of Ebola outbreaks. This was the quickest vaccine prequalification process directed by WHO [19].

On the other hand, there is no licensed drug to treat the EVD. The standard treatment settles for a supportive therapy providing hydration, oxygen, and medication to support blood pressure and to manage the possible symptoms such as fever and diarrhea.

For all the aforementioned biological considerations, we are focused in this work to determine the suitable Ebola vaccination and/or treatment program with the help of optimal control theory subject to the model given in [10]. To do this, the next section focuses on the sensitivity analysis. Section 3 deals with the formulation of our generalized model and its global properties. Section 4 is devoted to the optimal controls. The study is supported by numerical simulations in Sect. 5. A discussion and conclusions of our results are presented in the last section.

2 Sensitivity Analysis

We have proved in [10] that the global stability of the proposed model is determined by the basic reproduction number R_0 of the form

$$R_0 = \frac{bf\left(\frac{A}{\mu}, 0\right) + (\mu + d)g\left(\frac{A}{\mu}, 0\right)}{(\mu + d + r)b},$$

for any incidence functions f and g satisfying some required assumptions. In particular, for $f(S, I) = \dfrac{\beta_1 S}{1 + \alpha_1 I}$ and $g(S, D) = \dfrac{\beta_2 S}{1 + \alpha_2 D}$, this number is

$$R_0 = \frac{A\beta_1}{\mu(\mu + d + r)} + \frac{(\mu + d)A\beta_2}{b\mu(\mu + d + r)}. \tag{1}$$

In order to show the more crucial parameters for the EVD transmission, we propose to calculate the sensitivity indices of the number R_0 (1) with respect to the parameters given in Table 1. The results are presented in Table 2.

Definition 2.1 The normalized forward sensitivity index of a variable x, which depends differentiably on a parameter p, is $S_p^x = \dfrac{\partial x}{\partial p} \times \dfrac{p}{x}$.

By analyzing the sensitivity indices in Table 2, we deduce that the most sensitive parameter is the death rate due to EVD d. In order to target this sensitive rate, we propose to introduce controls by vaccination and/or treatment.

Table 1 Values for parameters used for sensitivity analysis

Parameter	Definition	Value	Reference
A	The recruitment rate	50	[10]
μ	The natural death rate	0.5	[10]
β_1	The infection rate by infectious individuals	0.005	[10]
β_2	The infection rate by deceased individuals	0.02	[10]
d	The death rate due to the EVD	0.05	[10]
r	The recovery rate	0.05	[10]
b	The burial rate	0.8	[10]

Table 2 Sensitivity indices of R_0 to parameters for the model

Parameter	Sensitivity index
A	1
μ	−1.1860
β_1	0.2711
β_2	0.7455
d	−1.7361
r	−0.0847
b	−0.7455

3 The Model Formulation and Equilibria

In order to find the optimal control rates according to time $u_1(t)$ and $u_2(t)$, we consider the following nonlinear system:

$$\begin{cases} \frac{dS}{dt} = A - \mu S - f(S, I)I - g(S, D)D - u_1 S, \\ \frac{dI}{dt} = f(S, I)I + g(S, D)D - (\mu + d + r + u_2)I, \\ \frac{dR}{dt} = (r + u_2)I - \mu R + u_1 S, \\ \frac{dD}{dt} = (\mu + d)I - bD, \end{cases} \tag{2}$$

where $S(t)$, $I(t)$, $R(t)$, and $D(t)$ are the numbers of susceptible, infectious, recovered, and died individuals at time t. The susceptible population increases at the recruitment rate A and decreases at the natural rate μ. It also decreases and converts into the infectious compartment by effective contact with infectious individuals at rate $f(S, I)I$ or with infectious corpses in traditional burial preparations at rate $g(S, D)D$. The infectious population dies naturally at rate μ or due to the Ebola virus disease at rate d and recovers from the disease at rate r. The number of died individuals decreases directly after burials at rate b. The control functions u_1 and u_2 represent the use of Ebola vaccine for susceptibles and the treatment of the infectious humans, respectively.

As in [10, 20], we assume that the general incidence functions f and g are continuously differentiable in $\mathbb{R}^2_+$ and satisfy the following properties:

(H_1) $f(0, I) = 0$, $\frac{\partial f}{\partial S}(S, I) > 0$, $\frac{\partial f}{\partial I}(S, I) \leq 0$ for all $S, I \geq 0$;

(H_2) $g(0, D) = 0$, $\frac{\partial g}{\partial S}(S, D) > 0$, $\frac{\partial g}{\partial D}(S, D) \leq 0$ for all $S, D \geq 0$.

Epidemiologically, the above hypotheses are reasonable and consistent with the reality. In fact, the first assumption (H_1) on the function $f(S, I)$ means that the incidence rate by direct contact with infectious individuals is equal to zero if there are no susceptible individuals. This incidence rate is increasing when the number of infectious individuals is constant and the number of susceptible individuals increases. Also, it is decreasing when the number of susceptible individuals is constant and the number of infectious individuals increases. Similarly, the second assumption (H_2) on the function $g(S, D)$ means that the incidence rate by died individuals is equal to zero if there are no susceptible individuals. Besides, this incidence rate is increasing when the number of died individuals is constant and the number of susceptible individuals increases. Also, it is decreasing when the number of susceptible individuals is constant and the number of died individuals increases. Therefore, the more susceptible individuals, the more infectious events will occur. However, the higher the number of infectious or died individuals, the less infectious events will be. Furthermore, the biological meaning of (H_1) for other diseases is given in [21, 22].

By simple computation, system (2) always has one disease-free equilibrium $E_f(\frac{A}{\mu+u_1}, 0, 0, 0)$. Then, we define the basic reproduction number of (2) as follows:

$$R_0(u_1, u_2) = \frac{bf\left(\frac{A}{\mu+u_1}, 0\right) + (\mu + d)g\left(\frac{A}{\mu+u_1}, 0\right)}{b(\mu + d + r + u_2)}. \tag{3}$$

Hence, $\frac{\partial R_0}{\partial u_1} = \frac{-A}{b(\mu+u)^2(\mu+d+r+u_2)}\left(b\frac{\partial f}{\partial S} + (\mu + d)\frac{\partial g}{\partial S}\right)$.

Using (H_1) and (H_2), we get $\frac{\partial R_0}{\partial u_1} < 0$.

Also, we have

$$\frac{\partial R_0}{\partial u_2} = \frac{-1}{b(\mu + d + r + u_2)^2}\left(bf\left(\frac{A}{\mu + u_1}, 0\right) + (\mu + d)g\left(\frac{A}{\mu + u_1}, 0\right)\right) < 0.$$

This means that R_0 is a decreasing function of u_1 and u_2 and shows the impact of vaccination and treatment in reducing R_0.

The other equilibrium of (2) satisfies the following equations:

$$A - \mu S - f(S, I)I - g(S, D)D - u_1 S = 0, \tag{4}$$

$$f(S, I)I + g(S, D)D - (\mu + d + r + u_2)I = 0, \tag{5}$$

$$(r+u_2)I-\mu R+u_1S=0, \tag{6}$$

$$(\mu+d)I-bD=0. \tag{7}$$

By (4) to (7), we have

$$bf\left(S,\frac{A-(\mu+u_1)S}{\mu+d+r+u_2}\right)+(\mu+d)g\left(S,\frac{(\mu+d)(A-(\mu+u_1)S)}{b(\mu+d+r+u_2)}\right)=b(\mu+d+r+u_2). \tag{8}$$

Since, $I=\frac{A-(\mu+u_1)S}{\mu+d+r+u_2}\geq 0$, which implies $S\leq \dfrac{A}{\mu+u_1}$, we deduce that there is no equilibrium when $S>\dfrac{A}{\mu+u_1}$.

Define a function ψ on the interval $[0,\frac{A}{\mu+u_1}]$ by

$$\psi(S)=bf\left(S,\frac{A-(\mu+u_1)S}{\mu+d+r+u_2}\right)+(\mu+d)g\left(S,\frac{(\mu+d)(A-(\mu+u_1)S)}{b(\mu+d+r+u_2)}\right)-b(\mu+d+r+u_2).$$

We have $\psi(0)=-b(\mu+d+r+u_2)<0$, $\psi(\dfrac{A}{\mu+u_1})=b(\mu+d+r+u_2)(R_0-1)$ and

$$\psi'(S)=b\left(\frac{\partial f}{\partial S}-\frac{\mu+u_1}{\mu+d+r+u_2}\frac{\partial f}{\partial I}\right)+(\mu+d)\left(\frac{\partial g}{\partial S}-\frac{(\mu+d)(\mu+u_1)}{b(\mu+d+r+u_2)}\frac{\partial g}{\partial D}\right)>0.$$

Thus, for $R_0>1$, there exists a unique endemic equilibrium $E^*(S_*, I_*, R_*, D_*)$ with $S_*\in(0,\dfrac{A}{\mu+u_1})$, $I_*>0$, $R_*>0$, and $D_*>0$.

Therefore, we get the following theorem.

Theorem 3.1 *Let R_0 be defined by* (3)

(i) *System* (2) *always has a disease-free equilibrium* $E_f(\frac{A}{\mu+u_1},0,0,0)$.
(ii) *If* $R_0>1$, *system* (2) *has a unique endemic equilibrium of the form* $E^*(S_*, I_*, R_*, D_*)$ *with* $S_*\in(0,\frac{A}{\mu+u_1})$, $I_*>0$, $R_*>0$, *and* $D_*>0$.

4 The Optimal Control

Our objective in this section is to seek the optimal level of vaccination and treatment in order to minimize the number of infectious individuals. To this end, we consider the following objectif functional:

$$J(u)=\int_0^{t_f}\left(I(t)+\frac{1}{2}\tau_1u_1^2(t)+\frac{1}{2}\tau_2u_2^2(t)\right)dt, \tag{9}$$

where the functions u_1 and u_2 represent the vaccination and the treatment control, respectively. τ_i is a positive weight parameter associated with the control u_i with $i \in \{1, 2\}$ and t_f is the period of control. The goal is to find a pair of an optimal control (u_1^*, u_2^*) such that

$$J(u_1^*, u_2^*) = min\{J(u_1, u_2)|(u_1, u_2) \in \mathcal{U}\},$$

where $\mathcal{U}$ is the control set defined by

$$\mathcal{U} = \left\{(u_1, u_2) : u_i \text{ is measurable}, 0 \leq u_i(t) \leq u_{i\max} \leq 1,\ i = 1, 2,\ \forall t \in [0, t_f]\right\}.$$

4.1 Existence of an Optimal Control

The first result is about the existence of an optimal control. It is given by the following theorem.

Theorem 4.1 *There exists an optimal control $u^* = (u_1^*, u_2^*)$ such that*

$$J(u^*) = min\{J(u)|u = (u_1, u_2) \in U\}.$$

Proof The control and the state variables are positive values. In this minimizing problem, the necessary convexity of the objective functional in $u(t)$ is satisfied. The control set U is also convex and closed by definition. The optimal system is bounded which determines the compactness needed for the existence of the optimal control. In addition, the integrand of J, $I(t) + \frac{1}{2}\tau_1 u_1^2(t) + \frac{1}{2}\tau_2 u_2^2(t)$, is convex on the control $u(t)$. Also, we can easily see that, there exist a constant $\rho > 1$ and positive numbers w_1 and w_2 such that $J(u(t)) \geqslant w_2 + w_1(|u|^2)^{\frac{\rho}{2}}$. ■

4.2 Optimality System

Now, we use Pontryagin's minimum principle [23] in order to find an optimal solution. This principle converts (9) and (2) into a problem of minimizing pointwise a Hamiltonian H, with respect to u, such that

$$\begin{aligned} H = {} & I(t) + \frac{1}{2}\tau_1 u_1^2(t) + \frac{1}{2}\tau_2 u_2^2(t) \\ & + \lambda_1(t)\Big(A - \mu S - f(S, I)I - g(S, D)D - u_1 S\Big) \\ & + \lambda_2(t)\Big(f(S, I)I + g(S, D)D - (\mu + d + r + u_2)I\Big) \end{aligned}$$

$$+\lambda_3(t)\Big((r+u_2)I+u_1S-\mu R\Big)$$

$$+\lambda_4(t)\Big((\mu+d)I-bD\Big),$$

where λ_1, λ_2, λ_3, and λ_4 are adjoint variables.
Next, we determine the adjoint variables λ_1, λ_2, λ_3, and λ_4 suitably by applying the necessary conditions to the Hamiltonian H.

Theorem 4.2 *Let $S^*(t)$, $I^*(t)$, $R^*(t)$, and $D^*(t)$ be optimal state solutions with associated optimal control variable $u^*(t)$ for the control problem (2) and (9). The adjoint variables λ_1, λ_2, λ_3, and λ_4 exist and satisfy*

$$\begin{aligned}
\frac{d\lambda_1}{dt} &= -\lambda_1(t)\Big(-\mu-\frac{\partial f}{\partial S}I^*-\frac{\partial g}{\partial S}D^*-u_1^*(t)\Big)-\lambda_2(t)\Big(\frac{\partial f}{\partial S}I^*+\frac{\partial g}{\partial S}D^*\Big)\\
&\quad -\lambda_3(t)u_1^*(t);\\
\frac{d\lambda_2}{dt} &= -1+\big(\lambda_1(t)-\lambda_2(t)\big)\Big(\frac{\partial f}{\partial S}I^*+f(S^*,I^*)\Big)+\lambda_2(t)\big(\mu+d+r+u_2\big)\\
&\quad -\lambda_3(t)(r+u_2)-\lambda_4(t)\big(\mu+d\big);\\
\frac{d\lambda_3}{dt} &= \mu\lambda_3(t);\\
\frac{d\lambda_4}{dt} &= \big(\lambda_1(t)-\lambda_2(t)\big)\Big(\frac{\partial g}{\partial D}D^*+g(S^*,D^*)\Big)+\lambda_4(t)b,
\end{aligned}$$

with $\lambda_1(t_f)=\lambda_2(t_f)=\lambda_3(t_f)=\lambda_4(t_f)=0$.

Furthermore, the optimal control is given by

$$u_1^*=min\Big(u_{1max},max\Big(\frac{(\lambda_1(t)-\lambda_3(t))S^*(t)}{\tau_1},0\Big)\Big),$$

$$u_2^*=min\Big(u_{2max},max\Big(\frac{(\lambda_2(t)-\lambda_3(t))I^*(t)}{\tau_2},0\Big)\Big).$$

Proof Using Pontryagin's minimum principle, we find

$$\begin{aligned}
\frac{d\lambda_1}{dt} &= -\frac{\partial H}{\partial S},\quad \lambda_1(t_f)=0;\\
\frac{d\lambda_2}{dt} &= -\frac{\partial H}{\partial I},\quad \lambda_2(t_f)=0;\\
\frac{d\lambda_3}{dt} &= -\frac{\partial H}{\partial R},\quad \lambda_3(t_f)=0;
\end{aligned}$$

$$\frac{d\lambda_4}{dt} = -\frac{\partial H}{\partial D}, \quad \lambda_4(t_f) = 0.$$

The optimal control u^* is obtained by solving the equations

$$\frac{\partial H}{\partial u_1} = 0 \text{ and } \frac{\partial H}{\partial u_2} = 0$$

on the interior of the control set and using the property of the control space U. ■

5 Numerical Simulations

In this section, we carry out some numerical simulations in order to illustrate the theoretical results. The incidence functions are chosen as $f(S, I) = \dfrac{\beta_1 S}{1+\alpha_1 I}$ and $g(S, D) = \dfrac{\beta_2 S}{1+\alpha_2 D}$. Hence, system (2) becomes

$$\begin{cases} \frac{dS}{dt} = A - (\mu + u_1)S - \dfrac{\beta_1 SI}{1+\alpha_1 I} - \dfrac{\beta_2 SD}{1+\alpha_2 D}, \\ \frac{dI}{dt} = \dfrac{\beta_1 SI}{1+\alpha_1 I} + \dfrac{\beta_2 SD}{1+\alpha_2 D} - (\mu + d + r + u_2)I, \\ \frac{dR}{dt} = (r + u_2)I - \mu R + u_1 S, \\ \frac{dD}{dt} = (\mu + d)I - bD, \end{cases} \tag{10}$$

where β_1 and β_2 are the infection rates caused by infectious and died human individuals, respectively. The nonnegative constants α_1 and α_2 measure the saturation effect. The other parameters have the same biological meanings as in system (2).

To solve the optimality system, we use an implicit finite difference method. The interval $[t_0, t_f]$ is discretized at the points $t_i = ih + t_0$ (i=0,1,....n), where h is the time step and $t_n = t_f$. Furthermore, the state and adjoint variables $S(t), I(t), R(t), D(t), \lambda_1(t), \lambda_2(t), \lambda_3(t), \lambda_4(t)$ and the control $u(t)$ are defined in terms of nodal points $S_i, I_i, R_i, D_i, \lambda_1^i, \lambda_2^i, \lambda_3^i, \lambda_4^i$ and u^i, respectively. Then, we adapt the technique developed by Gumel et al. [24] to our model as follows:

$$\begin{cases} \frac{S_{i+1}-S_i}{h} = A - (\mu + u_1^i)S_{i+1} - \dfrac{\beta_1 S_{i+1} I_i}{1+\alpha_1 I_i} - \dfrac{\beta_2 S_{i+1} D_i}{1+\alpha_2 D_i}, \\ \frac{I_{i+1}-I_i}{h} = \dfrac{\beta_1 S_{i+1} I_i}{1+\alpha_1 I_i} + \dfrac{\beta_2 S_{i+1} D_i}{1+\alpha_2 D_i} - (\mu + d + r + u_2^i)I_{i+1}, \\ \frac{R_{i+1}-R_i}{h} = (r + u_2^i)I_{i+1} - \mu R_{i+1} + u_1^i S_{i+1}, \\ \frac{D_{i+1}-D_i}{h} = (\mu + d)I_{i+1} - bD_{i+1}. \end{cases} \tag{11}$$

Similarly, we approximate the time derivative of the adjoint variables by their first-order backward difference as follows:

$$\begin{aligned}
\frac{\lambda_1^{n-i}-\lambda_1^{n-i-1}}{h} &= -\lambda_1^{n-i}\left(-\mu-\frac{\beta_1 I_{i+1}}{1+\alpha_1 I_{i+1}}+\frac{\beta_2 D_{i+1}}{1+\alpha_2 D_{i+1}}+u_1^i\right)\\
&\quad -\lambda_2^{n-i}\left(\frac{\beta_1 I_{i+1}}{1+\alpha_1 I_{i+1}}+\frac{\beta_2 D_{i+1}}{1+\alpha_2 D_{i+1}}\right)-\lambda_3^{n-i}u_1^i,\\
\frac{\lambda_2^{n-i}-\lambda_2^{n-i-1}}{h} &= -1+\left(\lambda_1^{n-i}-\lambda_2^{n-i}\right)\left(\frac{\beta_1 S_{i+1}}{1+\alpha_1 I_{i+1}}-\frac{\alpha_1\beta_1 S_{i+1}I_{i+1}}{(1+\alpha_1 I_{i+1})^2}+u_1^i\right)\\
&\quad -\lambda_2^{n-i}\left(\mu+d+r+u_2^i\right)-\lambda_3^{n-i}(r+u_2^i)-\lambda_4^{n-i}(\mu+d),\\
\frac{\lambda_3^{n-i}-\lambda_3^{n-i-1}}{h} &= \mu\lambda_3^{n-i},\\
\frac{\lambda_4^{n-i}-\lambda_4^{n-i-1}}{h} &= \left(\lambda_1^{n-i}-\lambda_2^{n-i}\right)\left(\frac{\beta_2 S_{i+1}}{1+\alpha_2 D_{i+1}}-\frac{\alpha_2\beta_2 S_{i+1}D_{i+1}}{(1+\alpha_2 D_{i+1})}\right)+b\lambda_4^{n-i}.
\end{aligned}$$

The algorithm describing the approximation method for obtaining the optimal control is the following.

Algorithm

Step 1: $S(0)=S_0$, $I(0)=I_0$, $R(0)=R_0$, $D(0)=D_0$, $\lambda_1(t_f)=0$, $\lambda_2(t_f)=0$, $\lambda_3(t_f)=0$, $\lambda_4(t_f)=0$, $u_1(0)=0$, $u_2(0)=0$.

Step 2: for i=0,. . . , n-1, do:

$$S_{i+1}=\frac{(S_i+hA)}{1+h\left(\mu+u_1^i+\frac{\beta_1 I_i}{1+\alpha_1 I_i}+\frac{\beta_2 D_i}{1+\alpha_2 D_i}\right)};$$

$$I_{i+1}=\frac{I_i+h\left(\frac{\beta_1 S_{i+1}I_i}{1+\alpha_1 I_i}+\frac{\beta_2 S_{i+1}D_i}{1+\alpha_2 D_i}\right)}{1+h(\mu+d+r+u_2^i)};$$

$$R_{i+1}=\frac{R_i+h\left((r+u_2^i)I_{i+1}+u_1^i S_{i+1}\right)}{1+h\mu};$$

$$D_{i+1}=\frac{D_i+h(\mu+d)I_{i+1}}{1+hb};$$

$$\begin{aligned}
\lambda_1^{n-i-1} &= \lambda_1^{n-i}-h\left(\lambda_1^{n-i}\left(\mu+u_1^i+\frac{\beta_1 I_{i+1}}{1+\alpha_1 I_{i+1}}+\frac{\beta_2 D_{i+1}}{1+\alpha_2 D_{i+1}}\right)\right.\\
&\quad \left.-\lambda_2^{n-i}\left(\frac{\beta_1 I_{i+1}}{1+\alpha_1 I_{i+1}}+\frac{\beta_2 D_{i+1}}{1+\alpha_2 D_{i+1}}\right)-\lambda_3^{n-i}u_1^i\right);
\end{aligned}$$

$$\lambda_2^{n-i-1} = \lambda_2^{n-i} - h\Big(-1 + (\lambda_1^{n-i} - \lambda_2^{n-i})\big(\frac{\beta_1 S_{i+1}}{1+\alpha_1 I_{i+1}} - \frac{\alpha_1\beta_1 S_{i+1} I_{i+1}}{(1+\alpha_1 I_{i+1})^2}\big)$$
$$+ (\mu + d + r + u_2^i)\lambda_2^{n-i} - \lambda_3^{n-i}(r + u_2^i) - \lambda_4^{n-i}(\mu + d)\Big);$$

$$\lambda_3^{n-i-1} = \lambda_3^{n-i} - h\mu\lambda_3^{n-i};$$

$$\lambda_4^{n-i-1} = \lambda_4^{n-i} - h\Big(\lambda_4^{n-i} b + (\lambda_1^{n-i} - \lambda_2^{n-i})\big(\frac{\beta_2 S_{i+1}}{1+\alpha_2 D_{i+1}} - \frac{\beta_2\alpha_2 S_{i+1} D_{i+1}}{(1+\alpha_2 D_{i+1})^2}\big)\Big).$$

$$H_{i+1} = \frac{(\lambda_1^{n-i-1} - \lambda_3^{n-i-1})S_{i+1}}{\tau_1};$$

$$G_{i+1} = \frac{(\lambda_2^{n-i-1} - \lambda_3^{n-i-1})I_{i+1}}{\tau_2};$$

$$u_1^{i+1} = min\Big(1, max\big(H_{i+1}, 0\big)\Big);$$

$$u_2^{i+1} = min\Big(1, max\big(G_{i+1}, 0\big)\Big);$$

end for

Step 3: for i=0,. . . .,n-1, write

$$S^*(t_i) = S_i, I^*(t_i) = I_i, R^*(t_i) = R_i, D^*(t_i) = D_i, u_1^*(t_i) = u_1^i, u_2^*(t_i) = u_2^i$$

end for

The parameters used for the simulation are the same as in [10] and are $A = 50$, $\mu = 0.5$, $\beta_1 = 0.005$, $\beta_2 = 0.001$, $\alpha_1 = 0.01$, $\alpha_2 = 0.01$, $d = 0.05$, $r = 0.06$, and $b = 0.8$. The initial values are $S_0 = 30$, $I_0 = 10$, $R_0 = 5$, $D_0 = 2$, $u_1^0 = 0$, and $u_2^0 = 0$.

Strategy 1: Use of vaccination only

With the vaccination strategy, we set the treatment control to 0 ($u_2 = 0$). Figure 1 shows that the number of infectious individuals converges to 36.4337 in the presence of the vaccination strategy. This means a decrease of 20.68% of infectious individuals in the absence of any control. The profile of the vaccination control u_1 is represented in Fig. 2.

Strategy 2: Use of treatment and vaccination

Here, both strategies are used to optimize the objectif function J. Figure 3 shows that the number of infectious tends to 26.0276, with −43.34% of infectious individuals in the absence of any control. The optimal vaccination and treatment controls are represented in Fig. 4.

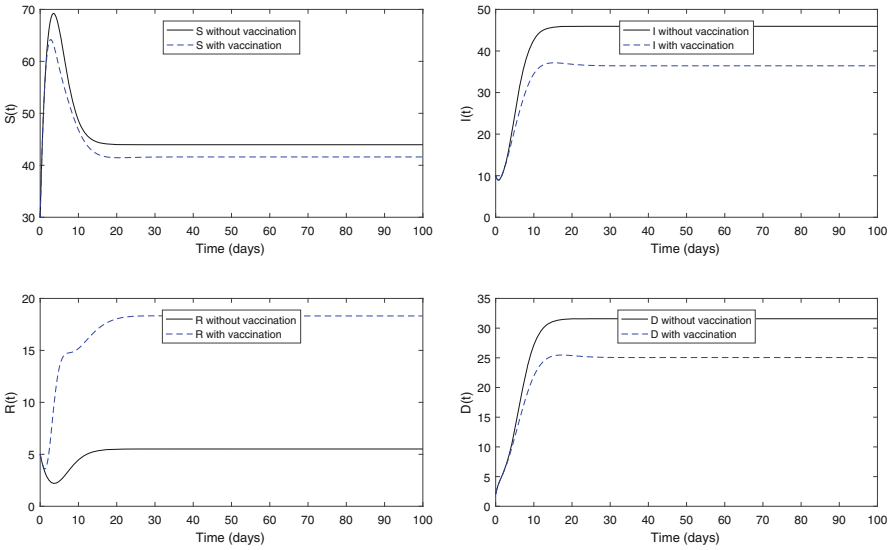

Fig. 1 Susceptible, infectious, recovered, and died individuals with and without vaccination control

Fig. 2 The optimal vaccination control $u_1(t)$

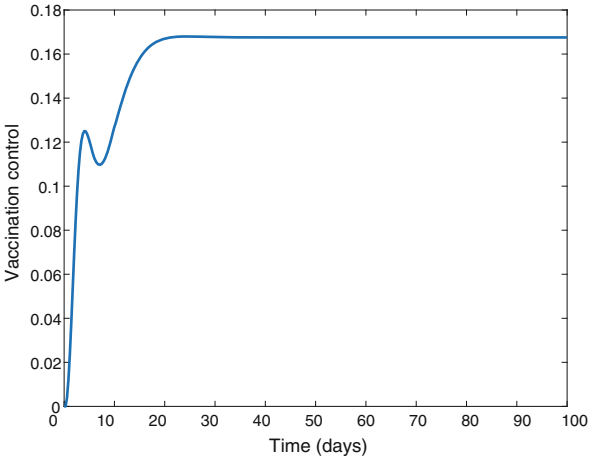

Strategy 3: Use of treatment only

Here, we use only the treatment strategy and set the vaccination control to 0. Figure 5 shows that the number of infectious individuals has decreased by 32.43% by the use of the treatment strategy. The profile of the optimal treatment control is shown in Fig. 6.

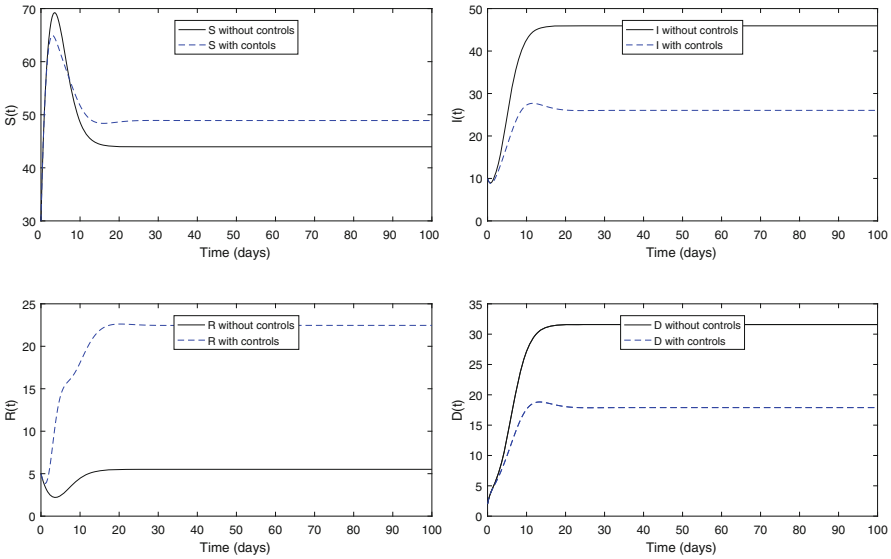

Fig. 3 Susceptible, infectious, recovered, and died individuals with and without both vaccination and treatment controls

Fig. 4 The optimal controls $u_1(t)$ and $u_2(t)$

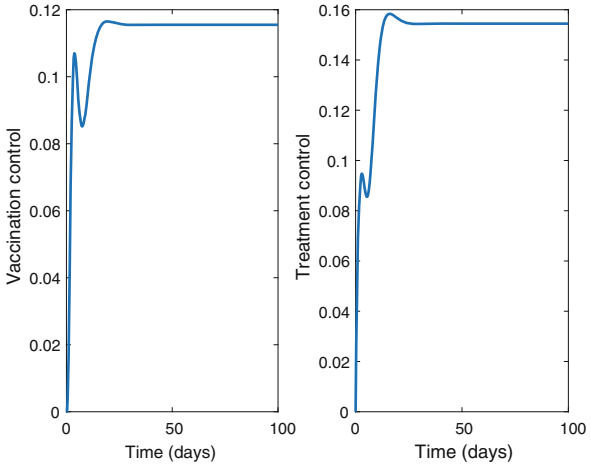

6 Conclusion

In this chapter, we propose optimal control strategies of an EVD model with post-death transmission. Firstly, we determine the most sensitive parameter to the basic reproduction number R_0, which is the death rate due to EVD. Based on this analysis, we proposed three strategies to control the EVD by vaccination and/or treatment. The mechanism of EVD transmission was modeled by two general incidence

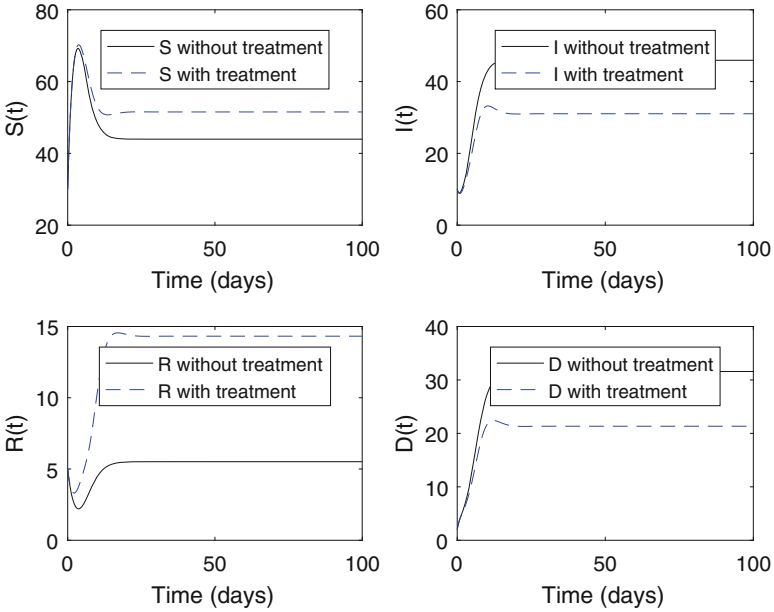

Fig. 5 Susceptible, infectious, recovered, and died individuals with and without the treatment control

Fig. 6 The optimal control $u_2(t)$

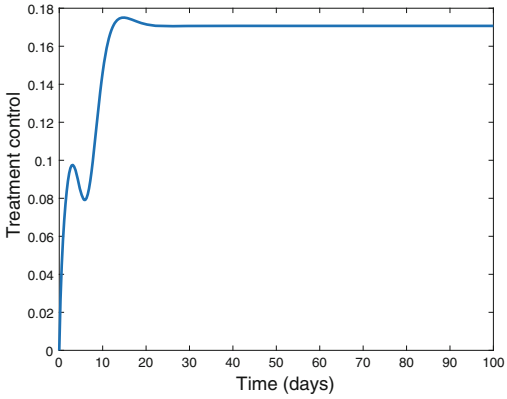

functions that describe the two main modes of Ebola transmission: from living and from dead individuals. These functions cover many incidence rates existing in the literature such as the saturated incidence, the classical bilinear incidence, the Beddington–DeAngelis functional response, the Hattaf–Yousfi functional response, and the Crowley–Martin functional response.

Theoretically, we discuss the existence of equilibria and calculate the basic reproduction number R_0. Also, we construct a suitable objectif function in order to

minimize the number of infectious. By the help of Pontryagin's minimum principle, we establish the necessary conditions for the optimal control problem.

On the other hand, we solved numerically the optimal control problem. For this, we formulate an algorithm based on the backward and forward finite-difference schemes. We used to assess the impact of using only the treatment control or the vaccination control and using both of them. A comparison between controls and the absence of any control has been shown. By an analysis of the numerical results, we found that combining the two controls has a very desirable effect for minimizing the number of infectious.

References

1. WHO, Frequently Asked Questions on Ebola virus disease, Available from: https://www.who.int/emergencies/diseases/ebola/frequently-asked-questions.
2. WHO, Essential medicines and health products, Available from: https://www.who.int/medicines/news/2019/Merck_EVD_vax-intro-roadmap.pdf?ua=1.
3. WHO, Ebola outbreak in West Africa declared a public health emergency of international concern, Available from: http://www.euro.who.int/en/health-topics/emergencies/pages/news/\news/2014/08/ebola-outbreak-in-west-africa-declared-a-public-health-emergency-of-international-concern.
4. E. Leroy, B. Kumulungui, X. Pourrut, P. Rouquet, A. Hassanin, P.Yaba, et al., Fruit bats as reservoirs of Ebola virus, Nature 438 (2005) 575–576.
5. R. Swanepoel, P. A. Leman, F. J. Burt, N. A. Zachariades, L. E. Braack, T. G. Ksiazek, et al., Experimental inoculation of plants and animals with Ebola virus, Emerging infectious diseases 2 (4) (1996) 321–325.
6. D. T. Hayman, P. Emmerich, et al., Long-term survival of an urban fruit bat seropositive for Ebola and Lagos bat viruses, PloS one 5 (8) (2010) e11978.
7. Z. E. Rhoubari, H. Besbassi, K. Hattaf and N. Yousfi, Mathematical Modeling of Ebola Virus Disease in Bat Population, Discrete Dynamics in Nature and Society 2018 (2018).
8. J. Buceta, K. Johnson, Modeling the Ebola zoonotic dynamics: Interplay between enviroclimatic factors and bat ecology, PLoS One 12 (6) (2017) e0179559.
9. J. S. Weitz and J. Dushoff, Modeling post-death transmission of Ebola: challenges for inference and opportunities for control, Scientific reports 5 (2015) 8751.
10. Z. E. Rhoubari, H. Besbassi, K. Hattaf and N. Yousfi, Dynamics of a Generalized Model for Ebola Virus Disease, Trends in Biomathematics: Mathematical Modeling for Health, Harvesting, and Population Dynamics, Springer, Cham, (2019) 35–46.
11. H. Laarabi, M. Rachik, O. E. Kahlaoui et al, Optimal vaccination strategies of an SIR epidemic model with a saturated treatment, Universal Journal of Applied Mathematics 1 (3) (2013) 185–191.
12. A.A Lashari, Optimal control of an SIR epidemic model with a saturated treatment, Applied Mathematics and Information Sciences 1 (10) (2016) p. 185.
13. G. Zaman, Y. H Kang and I. H Jung, Stability analysis and optimal vaccination of an SIR epidemic model, BioSystems 93 (3) (2008) 240–249.
14. A. Rachah and D. FM. Torres, Mathematical modelling, simulation, and optimal control of the 2014 Ebola outbreak in West Africa, Discrete Dynamics in Nature and Society 2015 (2015).
15. A. Rachah and D. FM. Torres, Dynamics and optimal control of Ebola transmission, Mathematics in Computer Science 10 (3) (2016) 331–342.
16. M. D. Ahmad, M. Usman, A. Khan et al, Optimal control analysis of Ebola disease with control strategies of quarantine and vaccination, Infectious diseases of poverty 5 (1) (2016) p. 72.

17. WHO, Immunization, Available at: https://www.who.int/topics/immunization/en/
18. WHO, Vaccines, Available from: https://www.who.int/topics/vaccines/en/
19. WHO, WHO prequalifies Ebola vaccine, paving the way for its use in high-risk countries, 12 November 2019. Available at: https://www.who.int/news-room/detail/12-11-2019-who-prequalifies-ebola-vaccine-paving-the-way-for-its-use-in-high-risk-countries.
20. K. Hattaf, A. A. Lashari, Y. Louartassi and N. Yousfi, A delayed SIR epidemic model with general incidence rate, Electronic Journal of Qualitative Theory of Differential Equations 3 (2013) 1–9.
21. X.-Y. Wang, K. Hattaf, H.-F. Huo, H. Xiang, Stability analysis of a delayed social epidemics model with general contact rate and its optimal control, Journal of Industrial and Management Optimization 12 (4) (2016) 1267–1285.
22. K. Hattaf, N. Yousfi, A numerical method for a delayed viral infection model with general incidence rate, J. King Saud Univ. Sci. 28 (4) (2016) 368–374.
23. Pontryagin, L. S. V. G. Boltyanskii, R. RV. Gamkrelidze and EF. Mishchenko, The mathematical theory of optimal processes, Wiley New York (1962).
24. A. Gumel, P. N. Shivakumar and B. M. Sahai, A mathematical model for the dynamics of HIV-1 during the typical course of infection, Nonlinear Analysis, Theory, Methods and Applications 47 (3) (2001) 1773–1783.

On Whole-Graph Embedding Techniques

L. Maddalena, I. Manipur, M. Manzo, and M. R. Guarracino

1 Introduction

Recently, network embedding, also known as network representation learning [27], has attracted the attention of a wide audience, as witnessed by recent surveys devoted to the subject [6, 27]. Indeed, network analytical techniques have provided significant insights in diverse application areas, such as social sciences, bioinformatics, connectomics, health informatics, and transportation [2, 21, 28, 31, 34, 37, 49].

Different taxonomies have been given for graph embedding methods. They can be distinguished based on the types of sources of the involved information, i.e., graphs that are homogeneous or heterogeneous [6, 27] include auxiliary information or are constructed from non-relational data [6]. They can also be subdivided according to different embedding approaches, such as matrix factorization, deep learning, edge reconstruction, graph kernels, or generative model [6]. Another possible taxonomy is based on the type of the output produced, i.e., the embedding of nodes, edges, subgraphs, or whole graphs [6, 27]. Indeed, networks can be studied at an individual level, where features such as nodes or graph sub-structures are employed for network characterization, node classification, edge prediction, and feature extraction [6, 20]. In other cases, the whole-graph embedding approach,

L. Maddalena (✉) · I. Manipur
National Research Council, Institute for High-Performance Computing and Networking (ICAR), Naples, Italy
e-mail: lucia.maddalena@cnr.it

M. Manzo
ITS, University of Naples "L'Orientale", Naples, Italy

M. R. Guarracino
University of Cassino and Southern Lazio, Cassino, Italy

R. P. Mondaini (ed.), *Trends in Biomathematics: Chaos and Control in Epidemics, Ecosystems, and Cells*, https://doi.org/10.1007/978-3-030-73241-7_8

where entire graphs are embedded in a vector space, is used for graph similarity learning in case of graph classification and clustering [25, 30].

Here, we focus on whole-graph embedding and aim to compare the performance of some representative methods for the task of graph classification. To this end, we consider a set of network datasets that we made publicly available.

This chapter is organized as follows. In Sect. 2, we provide an overview of various approaches for whole-graph embedding, focusing on selected examples. Then, in Sect. 3, we describe how network can be modeled with empirical probability distributions and how to compute their mutual distances. In Sect. 4, we evaluate the classification performance of these approaches on undirected real and synthetic network datasets and compare them to the distribution-based measures used in [17], described in Sect. 3. Moreover, we inspect the network properties that affect the performance of these methods, which could help drive the choice of embedding methods for future applications. Section 5 summarizes our conclusions.

2 Approaches to Whole-Graph Embedding

Given a set of m graphs $\mathcal{G} = \{\mathcal{G}_1, \mathcal{G}_2 \ldots . \mathcal{G}_m\}$, each graph $\mathcal{G}_i = \{\mathcal{V}_i, \mathcal{E}_i, l_i\}_{i=1}^m$, where $\mathcal{V}$ and $\mathcal{E}$ are sets of vertices and edges and l_i the corresponding class label of $\mathcal{G}_i$. Whole-graph embedding approaches aim to learn embeddings individually for each graph $\mathcal{G}_i$ or a single embedding jointly for the set of graphs $\mathcal{G}$, to predict each graph label l_i. Here, an embedding is intended as a mapping of a whole graph (rather than of a node or a subgraph) into a low-dimensional space $\mathbb{R}^d$, $d \ll |\mathcal{V}|$, where the embedding vector is expected to preserve the network features as much as possible [27]. This problem setting can be found in many real-life challenges that involve collections of networks representing instances of the system under study [18]. These include functional brain networks of a cohort of patients (connectomes) [19], chemical compound graphs [40], multilayer networks [8], or other applications that involve dynamic interactions between components that can be described as sequences of static graphs characterizing the dynamic evolution of the system.

Whole-graph embedding methods can be subdivided [27] into graph kernel methods and deep learning methods. Besides these two approaches, in the following, we also consider a matrix factorization approach. It should be observed that, besides approaches directly devoted to whole-graph embedding, the problem can also be tackled using embedding of nodes or sub-structures, combining their results via averaging or max pooling [11, 48]. However, as observed in [33], these lead to suboptimal results.

2.1 Graph Kernels

Kernel methods refer to machine learning algorithms that learn by comparing pairs of data points using particular similarity measures, the kernels [25]. In the case of graphs, graph kernels are based on the comparison of graph sub-structures via kernels [4]. In the graph kernel approach, the inner product of vector representations of graph sub-structures is used for pairwise graph comparisons [6]. These graph sub-structures include graphlets, shortest paths, random walks, and subtree patterns [4, 32, 39, 44, 47]. A survey of graph kernels by Kriege et al. [25] evaluated the performance of many of these methods on benchmark datasets and provided guidelines for their use based on graph properties.

One of the very first graph kernels is the shortest-path (SP) kernel [4]. The basic idea of the SP kernel is to compare the attributes and lengths of the shortest paths between all pairs of vertices in two graphs. First, the original graphs $\mathcal{G}_1$ and $\mathcal{G}_2$ are transformed into shortest-path graphs S_1 and S_2, which contain the same set of nodes as the input graphs and such that there exists an edge between all nodes in S_i, which are connected by a walk in $\mathcal{G}_i$. The SP graph kernel on $S_1 = (V_1, E_1)$ and $S_2 = (V_2, E_2)$ is then defined as

$$k_{SP}(S_1, S_2) = \sum_{e_1 \in E_1} \sum_{e_2 \in E_2} k^{(1)}_{walk}(e_1, e_2),$$

where $k^{(1)}_{walk}$ is a positive definite kernel on edge walks of length 1.

Graph kernels based on random walks (RWs) count the number of label sequences along walks that two graphs have in common. In [44], they are defined using the notion of direct product graph $\mathcal{G}_1 \times \mathcal{G}_2$, i.e., the graph over all possible pairs of vertices from the two graphs such that two vertices in the direct product graph are neighbors if and only if the corresponding vertices are neighbors in both graphs. The RW graph kernel is defined as

$$k_{RW}(\mathcal{G}_1, \mathcal{G}_2) = \sum_{k=0}^{\infty} \mu_k q_\times^T W_\times^k p_\times,$$

where μ_k are coefficients such that the sum converges, $W_\times$ is the weight matrix of the direct product graph $\mathcal{G}_1 \times \mathcal{G}_2$, $p_\times$ and $q_\times$ are initial and stopping probability distributions, and $q_\times^T W_\times^k p_\times$ is the expected similarity between simultaneous length k random walks on $\mathcal{G}_1$ and $\mathcal{G}_2$.

The above kernels follow the concept of convolution kernels, as they decompose the compared graphs and add up the pairwise similarities between their parts. In [24], Kriege et al. study optimal assignment kernels, which assign parts of one object to the parts of the other, such that the total similarity between the assigned parts is maximum. They investigate which base kernels lead to optimal assignment kernels that are valid, i.e., that are symmetric and positive semi-definite, and characterize

a class of so-called *strong kernels*, showing that they are equivalent to kernels obtained from a hierarchical partition of the domain of the kernel. Based on these kernels, they derive the Weisfeiler–Lehman optimal assignment (WL-OA) graph kernel. The Weisfeiler–Lehman subtree kernel counts the vertex colours two graphs have in common in the first h refinement steps. The base kernel for WL-OA corresponds to the number of matching colours in the refinement sequence and is defined for vertices as

$$k(u, v) = \sum_{i=0}^{h} k_\delta(\tau_i(u), \tau_i(v)),$$

where $\tau_i(u)$ indicates the color of vertex u at refinement step i.

2.2 Neural Network- and Deep Learning-Based Embeddings

Several works aim at generalizing neural networks to graphs for the purpose of graph embedding [5, 13, 33, 38]. One of the best known is Graph2vec [33], a neural embedding framework to learn, in an unsupervised way, data-driven representations of entire graphs as fixed-length feature vectors. Inspired by neural document embedding models, the authors extend the model to learn graph embeddings. A graph is viewed as a document and the rooted subgraph of degree d of any graph node (i.e., the subgraph including all nodes reachable in d hops from the node) is viewed as one of the words that compose the document, forming the vocabulary. Given a set of labeled graphs in input, the algorithm extracts all rooted subgraphs and assigns them a unique label. Then, it trains a doc2vec skip-gram model, a feed-forward neural network to learn distributed representations of word sequences, using negative sampling. In the case of unlabeled graphs, nodes are labeled with their degree.

Popular deep learning models used in graph embedding include convolutional neural networks (CNNs) [11, 23, 27, 29, 35, 48, 50] and autoencoders [6, 7, 18, 41, 45]. We focus on autoencoders, unsupervised neural networks able to compress the representation of input data. Here, an encoder maps input data to a smaller dimensional representation space, while a decoder maps the representation space to a reconstruction space. The autoencoder optimizes the encoding and decoding parameters so as to minimize the reconstruction error.

Gutiérrez-Gómez and Delvenne [18] propose the denoising autoencoders method, in the following named DAE, to learn graph embeddings for a collection of networks defined on the same set of nodes. For this purpose, they train a DAE [43] to uncover dissimilar relationships between graphs. This autoencoder is trained to reconstruct a clean version of a noisy input, thus providing a generalizable mapping of the encoding and decoding mappings, independent of the training data. The graphs, represented by powers of their adjacency matrix, are embedded into a

smaller dimensional feature space and mapped to a Euclidean distance matrix that reflects the structural similarity between input samples.

2.3 Matrix Factorization

Matrix factorization-based graph embedding represents graph properties in the form of a matrix and factorizes this matrix to obtain the embedding [6]. In most cases, the input is a graph and the output is a set of node embeddings. The matrices used to represent the graph properties include the node adjacency matrix, Laplacian matrix, and node transition probability matrix [15].

An example of matrix factorization approach to whole-graph embedding is given by "Joint Embedding" (JE) [46], which considers the whole set of graphs $\mathcal{G}$ to extract features for all its graphs. It simultaneously identifies a set of rank one symmetric matrices and projects the graph adjacency matrices A_i into the linear subspace spanned by these matrices. The coefficients obtained by projecting A_i are denoted by $\hat{\lambda}_i \in \mathbb{R}^d$, which is called the loading for graph i. To estimate rank one symmetric matrices and loadings for graphs, the algorithm minimizes the sum of squared Frobenius distances between adjacency matrices and their projections

$$(\hat{\lambda}_1, \ldots, \hat{\lambda}_m, \hat{h}_1, \ldots, \hat{h}_d) = \underset{\lambda_i, ||h_k||=1}{\operatorname{argmin}} \sum_{i=1}^{m} \left|\left| A_i - \sum_{k=1}^{d} \lambda_i[k] h_k h_k^T \right|\right|^2,$$

where d is the dimension of the embedding and $\lambda_i[k]$ indicates the kth element of λ_i.

3 Graph Classification with Distribution-Based Measures

Networks can be represented by probability distributions of their local and global topological properties [16, 17]. Using these representations, the set of distribution distances of a given graph from all the others in the dataset can also be considered as whole-graph embeddings, which can be used for graph classification, as done in [16, 17].

In order to compare this classification approach with the other node embedding methods, we consider two different graph distributions: the node distance distribution (NDD) and the transition matrix (TM) [9, 16]. The NDD $\mathcal{N}_i^r$ of node i in graph $\mathcal{G}_r$ has as its generic element $\mathcal{N}_i^r(h)$ the fraction of nodes in $\mathcal{G}_r$ having distance h from node i. It provides information on global properties of the graph. The TM $\mathcal{T}^r(s)$ of order s for graph $\mathcal{G}_r$ has as its generic element $\mathcal{T}_{i,j}^r(s)$ the probability for node i of reaching node j by a random walker in s steps. The TMs $\mathcal{T}^r(1)$ and $\mathcal{T}^r(2)$ contain local information about the connectivity of the graph $\mathcal{G}_r$.

Given two graphs $\mathcal{G}_p$ and $\mathcal{G}_q$, for each of the described network probability distributions $\mathcal{P}_i^{1,r} = \mathcal{N}_i^r$, $\mathcal{P}_i^{2,r} = \mathcal{T}_i^r(1)$, and $\mathcal{P}_i^{3,r} = \mathcal{T}_i^r(2)$ for node i in graph $\mathcal{G}_r$, $r = p, q$, we consider the network distance

$$\mathcal{M}_l^k(\mathcal{G}^p, \mathcal{G}^q) = \frac{1}{|V|} \sum_{i=1}^{|V|} d(\mathcal{P}_i^{k,p}, \mathcal{P}_i^{k,q}), \quad k = 1, 2, 3, \tag{1}$$

obtained by averaging over all the $|V|$ nodes the Jensen–Shannon distance $d(\mathcal{P}_i^{k,p}, \mathcal{P}_i^{k,q})$ of the probability distributions of their nodes. Moreover, we also consider two further network distances, given as averages of the measures in Eq. (1) [16]

$$\mathcal{D}_l^k(\mathcal{G}^p, \mathcal{G}^q) = \frac{1}{k} \sum_{i=1}^{k} \mathcal{M}_l^k(\mathcal{G}^p, \mathcal{G}^q), \quad k = 2, 3. \tag{2}$$

Using any of the five distribution-based measures of Eqs. (1) and (2), each network in the dataset is represented by the vector containing the distances from all other elements (i.e., the corresponding row of the distance matrix).

4 Experimental Results

4.1 Data

The four datasets used in our experiments consist of two synthetic datasets of undirected and unweighted graphs and two real-world datasets with undirected and weighted graphs. The characteristics of all the datasets are summarized in Table 1. Here, for each dataset, we report the number of graphs and classes, the number of nodes (the same for all graphs), the availability of vertex labels, the average number of edges, the average graph density, if graphs are weighted or not, the minimum and maximum of all the diameters, the average degree, the average assortativity coefficient based on degree, and the average global clustering coefficient [12].

4.1.1 Synthetic Graphs

The LFR dataset, available from https://github.com/leoguti85/GraphEmbs, was generated in the study performed by [18], using the Lancichinetti–Fortunato–Radicchi (LFR) method [26]. The dataset consists of two classes of graphs, all having 81 nodes, generated using two different mixing parameters (μ): 600 graphs with $\mu = 0.1$ and 1000 graphs with $\mu = 0.5$. The parameter $\mu \in [0, 1]$ is the expected proportion of edges having a vertex in one community and the other vertex in a

Table 1 Summary of characteristics of the datasets

	LFR	MREG	Kidney	Brain fMRI
Number of graphs	1600	300	299	124
Number of classes	2	3	3	2
Number of nodes	81	100	1034	263
Average number of edges	844.45	1151.71	3226	19748.88
Average graph/edge density	0.26	0.23	0.01	0.57
Edge weights	×	×	✓	✓
Minimum diameter	3	2	126	0.03
Maximum diameter	7	3	455.36	0.07
Average degree	20.85	23.03	6.24	150.18
Average assortativity coefficient	−0.01	−0.02	−0.13	0.14
Average clustering coefficient	0.34	0.23	0.21	0.66

different community, thus controlling the strength of the community arrangements (well-defined communities for small values and meaningless community structure for high values). LFR networks for each class are shown in Fig. 1-a, where it can be observed that the 6 communities in the left network (obtained with a low μ value and having clustering coefficient equal to 0.55) can be much better perceived than the 5 communities in the right network (obtained with a high μ value and a clustering coefficient equal to 0.21).

The MREG dataset was generated using the multiple random eigen graphs (MREG) model, defined in [46] as

$$(\lambda_i, A_i)_{i=1}^{m} = MREG(F, h_1 \ldots., h_d).$$

Here, $A_1, \ldots, A_m$ are the random adjacency matrices of m graphs, generated with the d-dimensional MREG model. $\{\lambda_i\}_{i=1}^{m}$ are random variables and F denotes their distribution on χ, where $\chi \subseteq \mathbb{R}^d$ such that $x^T y \in [0, 1]$, for all $x, y \in \chi$. $\{h_k\}_{k=1}^{d}$ are vectors that satisfy $\sum_{k=1}^{d} \lambda_i[k] h_k h_k^T \in [0, 1]^{n \times n}$ for all $\lambda \in \chi$. Vectors $\{h_k\}_{k=1}^{d}$ are shared across graphs and represent the joint latent positions of the vertices, while each λ_i represents the parameter of the ith graph relative to the latent positions. A detailed description of the MREG model is given by Wang et al. [46]. Using this model with d=2, a total of 300 graphs with 100 nodes each were generated, with 3 classes and 100 graphs in each class. Here, λ=[24.5, 4.75] for class 1, λ=[20.75, 2.25] for class 2, and λ=[24.5, 2.25] for class 3. Moreover, $h_1, h_2 \in \mathbb{R}^n$, with $n =$ 100 (the number of nodes), where all the entries of h_1 are set to 0.1, while the first half entries of h_2 are set to -0.1 and the remaining to 0.1. These parameters were chosen closely based on the experiment performed by Wang et al. for graph classification, although in our case, we generated three classes of graphs instead of the binary classification problem considered by the authors in [46].

4.1.2 Real Graphs

Functional magnetic resonance imaging (fMRI) time series data [1] from The Center for Biomedical Research Excellence (COBRE) dataset (http://fcon1000.projects.nitrc.org/indi/retro/cobre.html) were converted to fMRI networks in [3]. The processed dataset (https://github.com/jesusdaniel/graphclass) consists of 124 graphs with two classes of 54 Schizophrenia subjects and 70 healthy controls. All graphs contain 263 nodes corresponding to different regions of the brain (see Fig. 1-d). The edges were weighted with the Fisher-transformed correlation between the fMRI time series of the nodes after ranking, in the pre-processing step performed in [3]. For this study, we retained only the positively correlated edge weights.

Kidney metabolic networks were constructed in [16], by integrating gene expression data (Projects TCGA-KIRC and TCGA-KIRP) obtained from the Genomic Data Commons portal (https://portal.gdc.cancer.gov) and the kidney tissue-specific metabolic model [42] from the Metabolic Atlas repository (https://metabolicatlas.org/). In [17], these networks were simplified by retaining only the top eigen central nodes and their adjacent nodes, resulting in networks with 1034 nodes (see Fig. 1-c). The Kidney dataset contains 299 samples divided into three classes: 159 clear cell

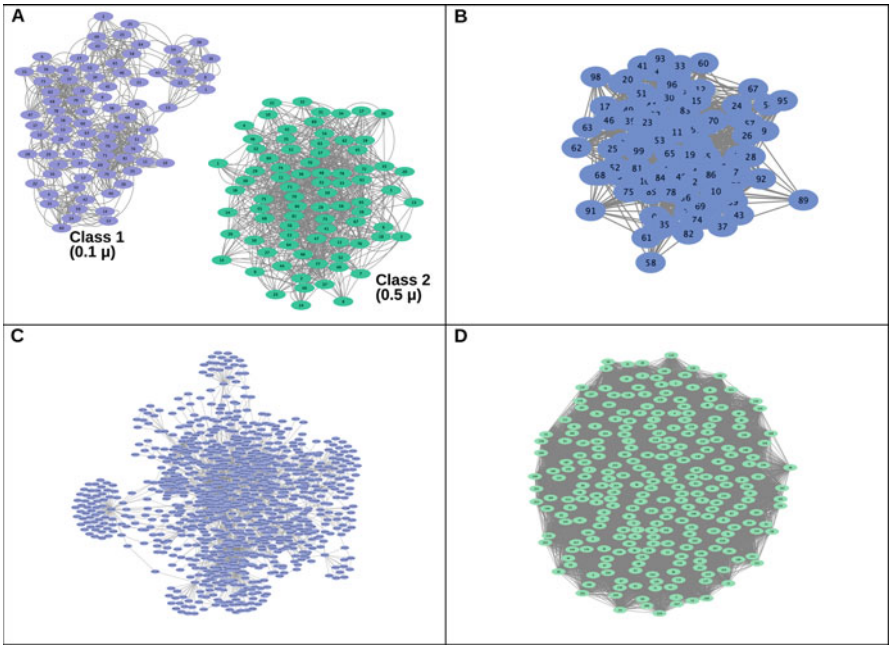

Fig. 1 Network datasets: (**a**) LFR: 2 classes of networks with 0.1μ and 0.5μ each consisting of 81 nodes; (**b**) MREG network with 100 nodes; (**c**) Kidney metabolic network with 1034 nodes (representing metabolites); and (**d**) Brain fMRI network with 263 nodes (representing brain regions). Cytoscape v3.7.1. was used for representing the networks

renal cell carcinoma, 90 papillary renal cell carcinoma, and 50 solid tissue normal samples.

4.2 Empirical Comparison of Methods

We evaluated the performance of the joint embedding (JE) method [46] as a representative of the matrix factorization method, while for autoencoders, we chose the denoising autoencoder (DAE) [18]. We specifically selected the above methods of MF and AE as they are aimed at embedding graphs that have the same sets of nodes. The Python implementations of JE and DAE are available from https://github.com/jesusdaniel/JEG and https://github.com/leoguti85/GraphEmbs, respectively. In order to assess graph kernels, we used WL-OA [24], shortest path (SP) [4], and random walk (RW) [44] kernels. The Matlab implementation of WL-OA, SP, and RW was obtained from [4, 14], and [44], respectively. Finally, the $\mathcal{M}^1$, $\mathcal{M}^2$, $\mathcal{M}^3$, $\mathcal{D}^2$, and $\mathcal{D}^3$ distribution-based measures were calculated using the R package available at https://github.com/cds-group/GraphDistances.

The parameters of the embedding methods reported in Table 2 were chosen so as to maximize the method's accuracy, while the remaining parameters were kept as defined in the respective implementations.

Table 2 Summary of parameters evaluated. Values of the parameters resulting in the best average classification accuracy for all the datasets are reported. In the case of WL-OA, the parameter "Kernel" indicates if OA is added (2) or not (1) to the base WL kernel; the kernel constructs the label tree for the set of graphs up to the specified depth D. For the RW graph kernel, lambda is a scaling parameter required by the routine

		LFR	MREG	Kidney	Brain fMRI
	Parameters				
Autoencoder					
DAE	Embedding dim. (d)	800	1600	1600	1600
	Adjacency power (A^r)	3	2	2	2
Matrix Factorization					
JE	Embedding dim. (d)	2	2	50	2
Graph kernels					
WL-OA	Kernel	1	1	2	1
	Depth (D)	5	5	10	10
SP	–	–	–	–	–
RW	Lambda	10^{-3}	10^{-3}	10^{-2}	10^{-5}
Distribution-based measures					
$\mathcal{M}^1$, $\mathcal{M}^2$, $\mathcal{M}^3$, $\mathcal{D}^2$, $\mathcal{D}^3$	–	–	–	–	–

The output from the evaluated methods was min–max normalized and classified with the support vector machine (SVM) classifier using the LIBSVM implementation [10] available in scikit-learn [36]. For multi-class classification, the one-vs.-rest strategy was used. The 10-fold cross-validation was repeated 10 times, and the average of the accuracy (Acc), precision (Prec), recall (Rec), and f-measure (F1) scores over all the runs was measured to evaluate the classification. These scores are defined in terms of the number of true positives (TPs), true negatives (TNs), false positives (FPs), and false negatives (FNs) as follows:

$$\text{Acc} = \frac{\text{TP} + \text{TN}}{\text{TP} + \text{TN} + \text{FP} + \text{FN}}, \quad \text{Prec} = \frac{\text{TP}}{\text{TP} + \text{FP}},$$

$$\text{Rec} = \frac{\text{TP}}{\text{TP} + \text{FN}}, \quad \text{F1} = \frac{2 * \text{Prec} \cdot \text{Rec}}{\text{Prec} + \text{Rec}}.$$

4.3 Performance Evaluation

Figures 2 and 3 show the distribution of the classification scores obtained by running 10 iterations of the 10-fold cross-validation on the synthetic and real datasets with the various methods, while detailed numerical results are reported in Tables 3 and 4.

All the methods perform well on the LFR dataset, achieving 100% accuracy in most of the cases. Hence, any of the whole-graph embedding methods would be effective on datasets that contain network classes differing from each other by well-defined community properties.

High accuracy for the MREG dataset is achieved only with the JE embedding method, with the rest of the methods performing poorly (<69% accuracy). The dataset, having been constructed using the 2D MREG model, might be an advantage for the JE method, as it is precisely this property that it exploits. Additionally, these networks are highly connected and unweighted and, hence, not ideal for embedding measures relying on path properties.

On the Kidney dataset, the distribution-based measures perform well overall, with the $\mathcal{M}^3$ measure giving the best result. These are closely followed by the DAE and JE methods, and the results for which may be further improved by fine-tuning their parameters. Instead, graph kernel-based methods perform poorly on this dataset.

The distribution-based measures $\mathcal{M}^2$, $\mathcal{M}^3$, $\mathcal{D}^2$, and $\mathcal{D}^3$ achieve the best performance on the Brain fMRI dataset, which results particularly hard for all the other compared methods, consisting of very dense graphs with high average degree but extremely low diameter.

We further analyzed the performance of the DAE, JE, $\mathcal{M}^1$, $\mathcal{M}^2$, and $\mathcal{M}^3$ methods in terms of the total time taken for the computation of the embedding or distances. We focus only on these methods as they performed reasonably well in at

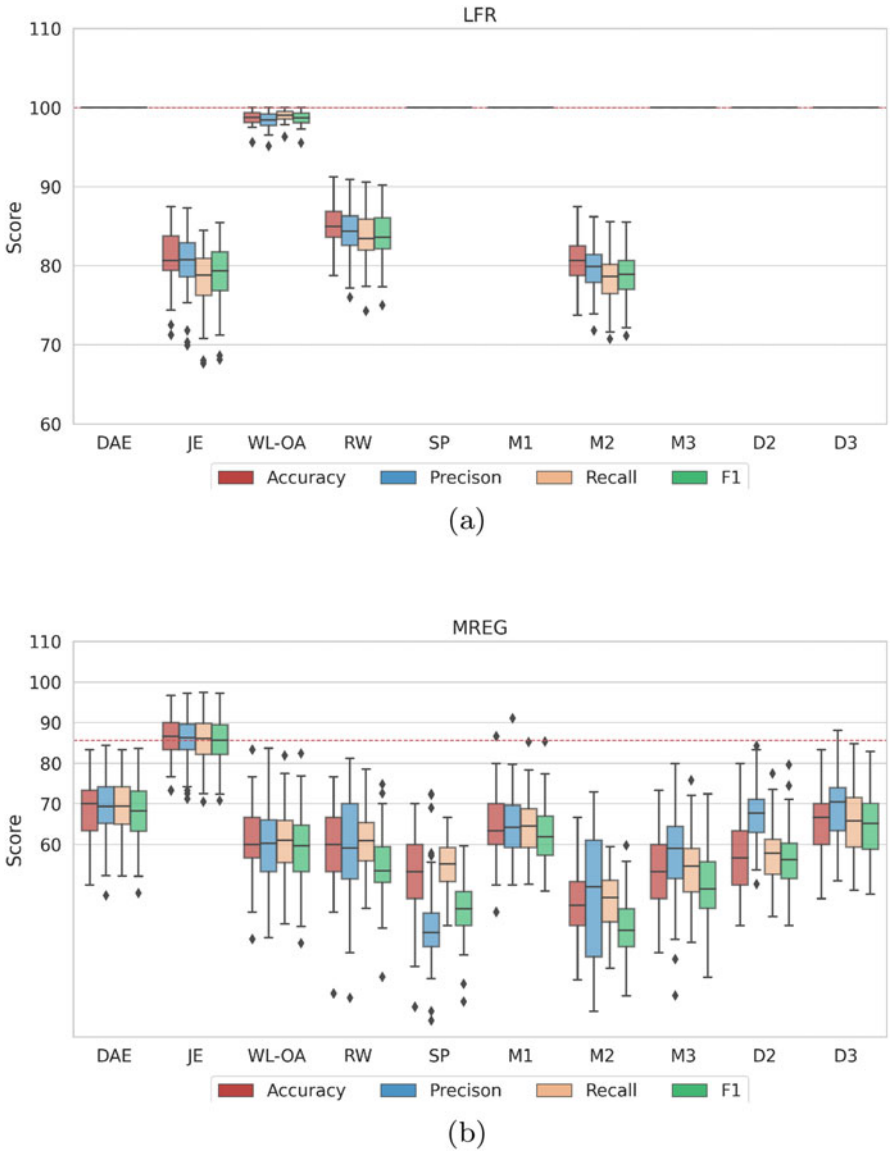

Fig. 2 Distribution of the different classification scores of all the compared methods on the two synthetic datasets: (**a**) LFR and (**b**) MREG. The red dashed line indicates the best average accuracy obtained among all the methods (see Table 3)

least two datasets. We used 50 and 100 graphs each from the LFR and Brain fMRI dataset, which contain 81 and 243 nodes, respectively. All the experiments were performed on a 16 core, 128 GB RAM, and a 64-bit platform cluster node. Figure 4 shows the computational time for all the considered methods.

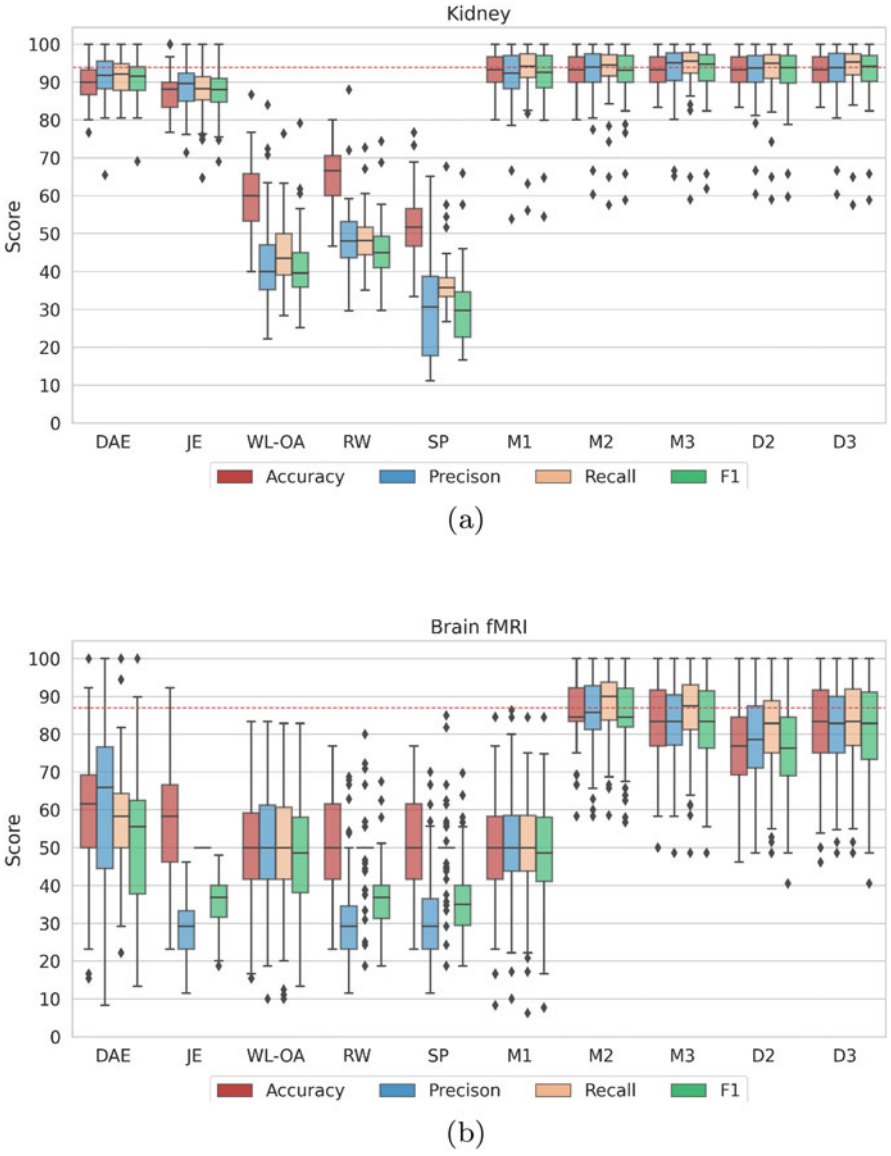

Fig. 3 Distribution of the different classification scores of all the compared methods on the two real datasets: (**a**) Kidney and (**b**) Brain fMRI. The red dashed line indicates the best average accuracy obtained among all the methods (see Table 4)

Table 3 Average classification performance of the compared methods on the synthetic datasets

	LFR				MREG			
	Acc	Prec	Rec	F1	Acc	Prec	Rec	F1
Autoencoder								
DAE	**100.00**	100.00	100.00	100.00	68.53	69.33	69.06	67.93
Matrix factorization								
JE	81.23	80.75	78.49	79.19	**85.63**	86.03	85.87	85.22
Graph Kernels								
WL-OA	98.85	98.52	99.08	98.78	61.07	59.88	60.79	59.35
SP	**100.00**	100.00	100.00	100.00	52.30	39.83	54.73	43.94
RW	85.27	84.44	83.97	84.11	59.43	59.28	60.34	54.74
Distribution-based measures								
$\mathcal{M}^1$	**100.00**	100.00	100.00	100.00	63.57	64.63	64.32	62.42
$\mathcal{M}^2$	80.76	79.89	78.43	78.90	46.33	48.10	46.48	39.74
$\mathcal{M}^3$	**100.00**	100.00	100.00	100.00	53.57	57.79	53.78	49.66
$\mathcal{D}^2$	**100.00**	100.00	100.00	100.00	57.07	67.22	57.29	56.35
$\mathcal{D}^3$	**100.00**	100.00	100.00	100.00	65.03	68.93	65.38	64.33

Table 4 Average classification performance of the compared methods on the real datasets

	Kidney				Brain fMRI			
	Acc	Prec	Rec	F1	Acc	Prec	Rec	F1
Autoencoder								
DAE	90.33	91.13	91.28	90.69	59.24	59.83	57.70	51.68
Matrix factorization								
JE	87.69	88.51	87.98	87.39	56.46	28.23	50.00	35.50
Graph Kernels								
WL-OA	59.71	41.89	44.97	40.78	49.49	50.95	50.72	47.65
SP	51.68	30.81	36.52	29.91	51.24	31.03	49.36	36.27
RW	65.98	48.15	48.62	45.11	51.35	30.40	49.08	35.86
Distribution-based measures								
$\mathcal{M}^1$	92.52	91.80	93.16	92.02	50.18	50.80	49.91	47.90
$\mathcal{M}^2$	93.39	92.83	93.35	92.61	**86.97**	86.35	88.54	86.04
$\mathcal{M}^3$	**93.95**	93.60	94.15	93.51	83.56	82.95	85.20	82.55
$\mathcal{D}^2$	93.22	92.75	93.25	92.58	78.62	78.81	80.57	77.54
$\mathcal{D}^3$	93.75	93.16	94.17	93.27	81.11	81.04	83.21	80.18

In the case of the LFR dataset, we see that DAE is the fastest method, even when the number of graphs is doubled. However, it has a 4 times increase in execution times when rising the number of nodes from 81 to 243 (on the Brain fMRI dataset). In these cases, the JE method runs faster than all the other methods.

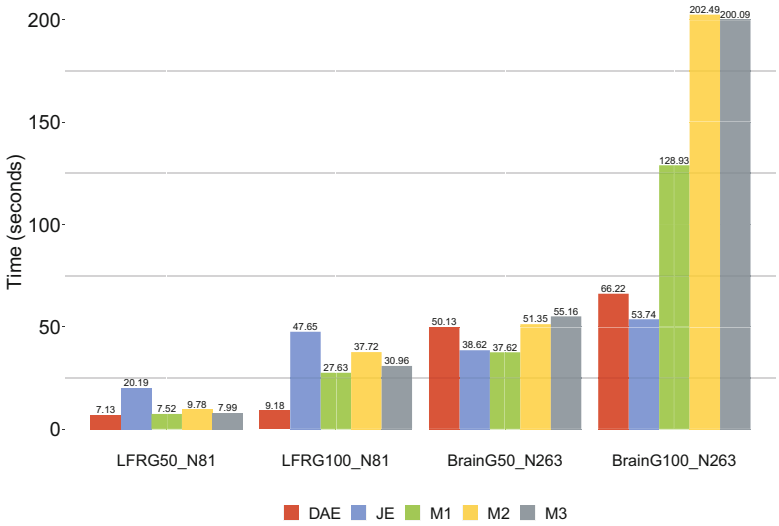

Fig. 4 Computational time. Time (seconds) for computation of embeddings and distances, where G and N are the total number of graphs and nodes, respectively. For example, LFRG50_N81 stands for LFR dataset with 50 graphs, each having 81 nodes

5 Conclusions

In this chapter, we review classes of embedding techniques which jointly embed whole graphs for the task of classification and compare the performance of a selected subset of methods. Although this is not an exhaustive comparison of all whole-graph embedding approaches, we provide results on a collection of undirected synthetic and real-world network datasets that have properties which differ from those commonly used for the evaluation of graph classification [22]. The results show that, in case of unweighted networks that differ based on their community properties, all approaches except JE, RW, and $\mathcal{M}^2$ achieve very high accuracy. On real-world weighted networks with node correspondence, the distribution-based measures are better at discriminating classes than the graph embedding methods compared in this study. Although they have a higher computational time than the other techniques, they should be considered for use, as evidenced by their classification performance.

The datasets and links to the software adopted for our experiments are made publicly available for further comparisons via a GitHub repository at https://github.com/cds-group/GraphDatasets.

Acknowledgments The work of Mario R. Guarracino was conducted within the framework of the Basic Research Program at the National Research University Higher School of Economics (HSE). The work was carried out also within the activities of the authors as members of the ICAR-CNR INdAM Research Unit. Mario Manzo thanks Prof. Alfredo Petrosino for the guidance and supervision during the years of working together.

References

1. CJ Aine, H Jeremy Bockholt, Juan R Bustillo, José M Cañive, Arvind Caprihan, Charles Gasparovic, Faith M Hanlon, Jon M Houck, Rex E Jung, John Lauriello, et al. Multimodal neuroimaging in schizophrenia: description and dissemination. *Neuroinformatics*, 15(4):343–364, 2017.
2. Laura Antonelli, Mario Rosario Guarracino, Lucia Maddalena, and Mara Sangiovanni. Integrating imaging and omics data: A review. *Biomedical Signal Processing and Control*, 52:264–280, 2019.
3. JD Arroyo-Relión, D Kessler, E Levina, and SF Taylor. Network classification with applications to brain connectomics [internet]. *Annals of Applied Statistics. Available*: http://arxiv.org/abs/1701.08140, 2019.
4. Karsten M Borgwardt and Hans-Peter Kriegel. Shortest-path kernels on graphs. In *Fifth IEEE international conference on data mining (ICDM'05)*, pages 8–pp. IEEE, 2005.
5. Joan Bruna, Wojciech Zaremba, Arthur Szlam, and Yann LeCun. Spectral networks and locally connected networks on graphs. In Yoshua Bengio and Yann LeCun, editors, *2nd International Conference on Learning Representations, ICLR 2014, Banff, AB, Canada, April 14–16, 2014, Conference Track Proceedings*, 2014.
6. Hongyun Cai, Vincent W Zheng, and Kevin Chen-Chuan Chang. A comprehensive survey of graph embedding: Problems, techniques, and applications. *IEEE Transactions on Knowledge and Data Engineering*, 30(9):1616–1637, 2018.
7. Shaosheng Cao, Wei Lu, and Qiongkai Xu. Deep neural networks for learning graph representations. In *AAAI*, 2016.
8. A. Cardillo, J. Gmez-Gardees, M. Zanin, and other. Emergence of network features from multiplexity. *Sci Rep*, 3(1344), 2013.
9. L. Carpi, T.A. Schieber, P.M. Pardalos, G. Marfany, C. Masoller, A. Díaz-Guilera, and M.G. Ravetti. Assessing diversity in multiplex networks. *Scientific Reports*, 9(4511), 2019.
10. Chih-Chung Chang and Chih-Jen Lin. Libsvm: A library for support vector machines. *ACM transactions on intelligent systems and technology (TIST)*, 2(3):1–27, 2011.
11. Fengwen Chen, Shirui Pan, Jing Jiang, Huan Huo, and Guodong Long. DAGCN: dual attention graph convolutional networks. In *International Joint Conference on Neural Networks, IJCNN 2019 Budapest, Hungary, July 14–19, 2019*, pages 1–8. IEEE, 2019.
12. Gabor Csardi and Tamas Nepusz. The igraph software package for complex network research. *InterJournal*, Complex Systems:1695, 2006.
13. Michaël Defferrard, Xavier Bresson, and Pierre Vandergheynst. Convolutional neural networks on graphs with fast localized spectral filtering. In Daniel D. Lee, Masashi Sugiyama, Ulrike von Luxburg, Isabelle Guyon, and Roman Garnett, editors, *Advances in Neural Information Processing Systems 29: Annual Conference on Neural Information Processing Systems 2016, December 5–10, 2016, Barcelona, Spain*, pages 3837–3845, 2016.
14. Pierre-Louis Giscard. Weisfeiler-Lehman optimal assignment kernel, 2020.
15. Palash Goyal and Emilio Ferrara. Graph embedding techniques, applications, and performance: A survey. *Knowledge-Based Systems*, 151:78–94, 2018.
16. Ilaria Granata, Mario R Guarracino, Valery A Kalyagin, Lucia Maddalena, Ichcha Manipur, and Panos M Pardalos. Supervised classification of metabolic networks. In *2018 IEEE International Conference on Bioinformatics and Biomedicine (BIBM)*, pages 2688–2693. IEEE, 2018.
17. Ilaria Granata, Mario R Guarracino, Valery A Kalyagin, Lucia Maddalena, Ichcha Manipur, and Panos M Pardalos. Model simplification for supervised classification of metabolic networks. *Annals of Mathematics and Artificial Intelligence*, 88(1):91–104, 2020.
18. Leonardo Gutiérrez-Gómez and Jean-Charles Delvenne. Unsupervised network embeddings with node identity awareness. *Applied Network Science*, 4(1):82, 2019.

19. Patric Hagmann, Leila Cammoun, Xavier Gigandet, Reto Meuli, Christopher J Honey, Van J Wedeen, and Olaf Sporns. Mapping the structural core of human cerebral cortex. *PLOS Biology*, 6(7):1–15, 07 2008.
20. William L Hamilton, Rex Ying, and Jure Leskovec. Representation learning on graphs: Methods and applications. *arXiv preprint arXiv:1709.05584*, 2017.
21. Zifeng Kang, Hanwen Xu, Jianming Hu, and Xin Pei. Learning dynamic graph embedding for traffic flow forecasting: A graph self-attentive method. In *2019 IEEE Intelligent Transportation Systems Conference (ITSC)*, pages 2570–2576. IEEE, 2019.
22. Kristian Kersting, Nils M. Kriege, Christopher Morris, Petra Mutzel, and Marion Neumann. Benchmark data sets for graph kernels, 2016.
23. Thomas N. Kipf and Max Welling. Semi-supervised classification with graph convolutional networks. In *5th International Conference on Learning Representations, ICLR 2017, Toulon, France, April 24–26, 2017, Conference Track Proceedings*. OpenReview.net, 2017.
24. Nils M Kriege, Pierre-Louis Giscard, and Richard Wilson. On valid optimal assignment kernels and applications to graph classification. In *Advances in Neural Information Processing Systems*, pages 1623–1631, 2016.
25. Nils M Kriege, Fredrik D Johansson, and Christopher Morris. A survey on graph kernels. *Applied Network Science*, 5(1):1–42, 2020.
26. Andrea Lancichinetti, Santo Fortunato, and Filippo Radicchi. Benchmark graphs for testing community detection algorithms. *Physical review E*, 78(4):046110, 2008.
27. Bentian Li and Dechang Pi. Network representation learning: a systematic literature review. *Neural Computing and Applications*, pages 1–33, 2020.
28. Peng Liu, Lemei Zhang, and Jon Atle Gulla. Real-time social recommendation based on graph embedding and temporal context. *International Journal of Human-Computer Studies*, 121:58–72, 2019.
29. Z. Luo, L. Liu, J. Yin, Y. Li, and Z. Wu. Deep learning of graphs with ngram convolutional neural networks. *IEEE Transactions on Knowledge and Data Engineering*, 29(10):2125–2139, 2017.
30. Guixiang Ma, Nesreen K Ahmed, Theodore L Willke, and Philip S Yu. Deep graph similarity learning: A survey. *arXiv preprint arXiv:1912.11615*, 2019.
31. Ichcha Manipur, Ilaria Granata, Lucia Maddalena, and Mario Rosario Guarracino. Clustering analysis of tumor metabolic networks. *BMC Bioinformatics*, 21(349), 2020.
32. Mario Manzo. Kgearsrg: Kernel graph embedding on attributed relational sift-based regions graph. *Machine Learning and Knowledge Extraction*, 1(3):962–973, 2019.
33. Annamalai Narayanan, Mahinthan Chandramohan, Rajasekar Venkatesan, Lihui Chen, Yang Liu, and Shantanu Jaiswal. graph2vec: Learning distributed representations of graphs. *arXiv preprint arXiv:1707.05005*, 2017.
34. Walter Nelson, Marinka Zitnik, Bo Wang, Jure Leskovec, Anna Goldenberg, and Roded Sharan. To embed or not: network embedding as a paradigm in computational biology. *Frontiers in genetics*, 10:381, 2019.
35. Mathias Niepert, Mohamed Ahmed, and Konstantin Kutzkov. Learning convolutional neural networks for graphs. In *International conference on machine learning*, pages 2014–2023, 2016.
36. Fabian Pedregosa, Gaël Varoquaux, Alexandre Gramfort, Vincent Michel, Bertrand Thirion, Olivier Grisel, Mathieu Blondel, Peter Prettenhofer, Ron Weiss, Vincent Dubourg, et al. Scikit-learn: Machine learning in python. *the Journal of machine Learning research*, 12:2825–2830, 2011.
37. Gideon Rosenthal, František Váša, Alessandra Griffa, Patric Hagmann, Enrico Amico, Joaquín Goñi, Galia Avidan, and Olaf Sporns. Mapping higher-order relations between brain structure and function with embedded vector representations of connectomes. *Nature communications*, 9(1):1–12, 2018.
38. Franco Scarselli, Marco Gori, Ah Chung Tsoi, Markus Hagenbuchner, and Gabriele Monfardini. The graph neural network model. *IEEE Transactions on Neural Networks*, 20(1):61–80, 2008.

39. Nino Shervashidze, Pascal Schweitzer, Erik Jan Van Leeuwen, Kurt Mehlhorn, and Karsten M Borgwardt. Weisfeiler-lehman graph kernels. *Journal of Machine Learning Research*, 12(9), 2011.
40. A. Srinivasan, R. D. King, S. H. Muggleton, and M. J. E. Sternberg. The predictive toxicology evaluation challenge. In *Proceedings of the 15th International Joint Conference on Artificial Intelligence - Volume 1*, IJCAI'97, page 4–9, San Francisco, CA, USA, 1997. Morgan Kaufmann Publishers Inc.
41. Fei Tian, Bin Gao, Qing Cui, Enhong Chen, and Tie-Yan Liu. Learning deep representations for graph clustering. In *Proceedings of the Twenty-Eighth AAAI Conference on Artificial Intelligence*, AAAI14, page 12931299. AAAI Press, 2014.
42. Mathias Uhlén, Linn Fagerberg, Björn M Hallström, Cecilia Lindskog, Per Oksvold, Adil Mardinoglu, Åsa Sivertsson, Caroline Kampf, Evelina Sjöstedt, Anna Asplund, et al. Tissue-based map of the human proteome. *Science*, 347(6220), 2015.
43. Pascal Vincent, Hugo Larochelle, Yoshua Bengio, and Pierre-Antoine Manzagol. Extracting and composing robust features with denoising autoencoders. In *Proceedings of the 25th International Conference on Machine Learning*, ICML 08, page 10961103, New York, NY, USA, 2008. Association for Computing Machinery.
44. S Vichy N Vishwanathan, Nicol N Schraudolph, Risi Kondor, and Karsten M Borgwardt. Graph kernels. *The Journal of Machine Learning Research*, 11:1201–1242, 2010.
45. Daixin Wang, Peng Cui, and Wenwu Zhu. Structural deep network embedding. In *Proceedings of the 22nd ACM SIGKDD International Conference on Knowledge Discovery and Data Mining*, KDD 16, page 12251234, New York, NY, USA, 2016. Association for Computing Machinery.
46. Shangsi Wang, Jesús Arroyo, Joshua T Vogelstein, and Carey E Priebe. Joint embedding of graphs. *IEEE Transactions on Pattern Analysis and Machine Intelligence*, 2019.
47. Pinar Yanardag and SVN Vishwanathan. Deep graph kernels. In *Proceedings of the 21th ACM SIGKDD International Conference on Knowledge Discovery and Data Mining*, pages 1365–1374, 2015.
48. Zhitao Ying, Jiaxuan You, Christopher Morris, Xiang Ren, William L. Hamilton, and Jure Leskovec. Hierarchical graph representation learning with differentiable pooling. In Samy Bengio, Hanna M. Wallach, Hugo Larochelle, Kristen Grauman, Nicolò Cesa-Bianchi, and Roman Garnett, editors, *Advances in Neural Information Processing Systems 31: Annual Conference on Neural Information Processing Systems 2018, NeurIPS 2018, 3–8 December 2018, Montréal, Canada*, pages 4805–4815, 2018.
49. Xiang Yue, Zhen Wang, Jingong Huang, Srinivasan Parthasarathy, Soheil Moosavinasab, Yungui Huang, Simon M Lin, Wen Zhang, Ping Zhang, and Huan Sun. Graph embedding on biomedical networks: methods, applications and evaluations. *Bioinformatics*, 36(4):1241–1251, 2020.
50. Muhan Zhang, Zhicheng Cui, Marion Neumann, and Yixin Chen. An end-to-end deep learning architecture for graph classification. In Sheila A. McIlraith and Kilian Q. Weinberger, editors, *Proceedings of the Thirty-Second AAAI Conference on Artificial Intelligence, (AAAI-18), the 30th innovative Applications of Artificial Intelligence (IAAI-18), and the 8th AAAI Symposium on Educational Advances in Artificial Intelligence (EAAI-18), New Orleans, Louisiana, USA, February 2–7, 2018*, pages 4438–4445. AAAI Press, 2018.

Semigroup Approaches of Cell Proliferation Models

Y. E. Alaoui and L. Alaoui

1 Introduction

Cell biology is getting heavily dependent on mathematics, and various related biological processes have been formulated using mathematical models that are described by various types of equations. Even if models do not translate all factors related to the complexity of the processes, they can help in providing solutions to the problems at hand. However, in order to understand the mathematical dynamics behind the processes, to extract useful information from the models, and also to come up with better models that could reflect the real behavior associated with the problems at hand, such models alone are not sufficient. For these objectives, mathematical analysis tools are indeed needed to better drive interactions between mathematics and biology. For a solid research, novel mathematical ideas are needed. This is due to the numerous challenges that range, among others, from parameter estimation, effects of their associated changes, hypotheses validation to prevention and control.

Strong analytical mathematical methods that can be applied not only to one particular case but also to a wide range of models are therefore needed to get well-founded interpretation results for the real phenomena. To this end, the theory developed for translation semigroups that are solutions of equations of the type

$$u(t) = \phi(u_t) \tag{1}$$

Y. E. Alaoui (✉)
Faculty of Sciences, University Mohamed V – Agdal, Rabat, Morocco

L. Alaoui
International University of Rabat, Rabat, Morocco

R. P. Mondaini (ed.), *Trends in Biomathematics: Chaos and Control in Epidemics, Ecosystems, and Cells*, https://doi.org/10.1007/978-3-030-73241-7_9

in addition to the theory developed for perturbed semigroups that are solutions of some abstract integral equations of the form

$$u(t) = T_0(t) + \int_0^t T_0^{\odot *}(t-s)\phi(u(s))ds \tag{2}$$

has been very useful in the mathematical analysis of various population dynamics models [1–9] that are the model using either integral equations or partial differential equations or delay differential equations. It provides various tools to derive properties for such models ranging from the existence and positivity of the solutions, the compactness and irreducibility of the solution semigroups to the asymptotic behavior and stability properties.

Mathematical modeling of the cell cycle has received great interest during the last three decades. The need for such modeling is expressed by the need to use mathematical and computational methods to come up with solutions to the complex problems related to the dynamics of epidemics or tumors. Various models have been proposed by many researchers to model the cell growth and proliferation in order to understand such dynamics.

In this chapter, we consider cell models that use either integral equations or partial differential equations to describe the process of cellular proliferation within the cell cycle. Our aim is to provide a general framework for the mathematical study of such models. The framework is based on the use of the theory developed for the class of semigroup of operators that are associated with core operators ϕ and are solutions of equations of the type (1) or (2). The framework allows us to conclude various properties for the solutions of the considered models by simply using assumptions on their associated core operators that are determined using suitable transformations if it is not straightforward.

To be more precise, we consider an integral equation model and two partial differential equation (PDE) models. Each model describes the evolution of cell densities by using relevant factors related to the birth, mortality, reproduction, or immigration factors.

The first model investigated is an integral model [10] that is described by the following equation:

$$n(t,y) = 2\int_0^\infty \int_0^\infty h(y,\xi(\tau,\sigma))\gamma(\tau,\sigma)n(t-\tau,\sigma)d\sigma d\tau, \quad t \geq 0, \text{ a.e. } y \in (0,\infty), \tag{3}$$

where $n(t, y)$ denotes the size density of birth rate with respect to time t and size x. In addition, $h(y, x)$ is the conditional probability that a daughter cell has a size y with the condition that the mother cell size is x and $\gamma(\tau, \sigma)$ is the conditional density such that $\int_{t_1}^{t_2} \gamma(\tau, \sigma)$ is the probability that the duration of cell cycle with initial size σ to lie within $[t_1, t_2]$. The function $\zeta(\tau, \sigma)$ is the final size such that τ is the duration of the cell cycle and σ is the initial size of the cell.

The second model proposed and the first PDE model [11] we are considering describe the interactions between a group of cells characterized by their levels of

differentiation and mutation by taking into consideration the proliferation process and are given as follows:

$$\begin{aligned}
&\frac{\partial}{\partial t}n_{j,i}(a,t)+\frac{\partial}{\partial a}n_{j,i}(a,t)=-(\mu_{j,i}(a)+\beta_{j,i}(a))n_{j,i}(a,t)\\
&n_{j,i}(0,t)=2\sum_{k=j}^{l}\left(p_{j,k,i}\int_0^\infty \beta_{k,i}(a)n_{k,i}(a,t)da\right.\\
&\qquad\left.+q_{j,k,i-1}\int_0^\infty \beta_{k,i-1}(a)n_{k,i-1}(a,t)da\right), \qquad t\geq 0\\
&n_{j,i}(a,0)=\phi_{j,i}(a), \qquad j=1,2,\cdots,l,\ i=0,1,\cdots,m-1,\ N=lm,
\end{aligned} \tag{4}$$

where $n_{j,i}(a,t)$ is the density of the cells that are of age a at time t characterized by their telomeric state j and mutation state i. The parameters $\beta_{j,i}(a)$ and $\mu_{j,i}(a)$ are, respectively, the proliferation and death rate of the cell in the telomeric and mutation class (j,i). $p_{j,k,i}$ is the probability that one of the two cells from a mother cell in the (k,i) class, will be a cell in the (j,i) class, where k and j stand for the telomeric states and i stands for the mutation state. $q_{j,k,i-1}$ is the probability that a cell in the $(k,i-1)$ class will give rise to a mutate cell in the (j,i) class, where k and j stand for the telomeric states and i stands for the mutation state.

The second PDE model we consider treats the case of a cell population that is composed not only of proliferating cells but also of quiescent cells[12]. The model reads as follows:

$$\begin{aligned}
&\frac{\partial}{\partial t}p(t,a)+\frac{\partial}{\partial a}p(t,a)=-\beta(a)p(t,a)-\sigma(a)p(t,a)+\tau(a)q(t,a)\\
&\frac{\partial}{\partial t}q(t,a)+\frac{\partial}{\partial a}q(t,a)=\sigma(a)p(t,a)-\tau(a)q(t,a)\\
&p(t,0)=2b\int_0^\infty \beta(a)p(t,a)da\\
&q(t,0)=2(1-b)\int_0^\infty \beta(a)p(t,a)da,
\end{aligned} \tag{5}$$

where $p(t,a)$ and $q(t,a)$, respectively, denote the densities of cells in the proliferating and the quiescent state. The parameter β is the splitting rate, and σ and τ are, respectively, the transition rates from the proliferate (quiescent) state to the quiescent (proliferate) state.

Within the proposed framework, the analysis of the models we give will be done by first relating each model to translation semigroups. This is done by determining the associated core operators ϕ yielding translation semigroups that are either direct solution semigroups or equivalent to the solution semigroups of the models. This fact allows us in a first step to apply the nice theory developed for such semigroups in [1–9] to conclude various properties related to the solution semigroups of the

models ranging from existence, positivity, and irreducibility to compactness and spectral properties. Such properties are of course obtained by simply making assumptions only on the model parameters defining their core operators. With all such properties, we will be able in a second step to easily deduce the so-called asynchronous exponential growth (AEG) property for the models.

The property AEG is satisfied for a semigroup $\{T(t)\}_{t\geq 0}$ when the assumption

$$(\mathcal{H}_{AEG}) \left(\begin{array}{l} \|e^{-\lambda_0 t} T(t) - P\| \leq M e^{-\delta t}, \text{ for } t > 0, \text{ where } P \text{ is a projection} \\ \text{of rank one} \end{array} \right)$$

is satisfied. The parameter λ_0 is the so-called intrinsic growth constant or the Malthusian parameter. For the cell models, the AEG property means that $\|e^{-\lambda_0 t} n(t, a) - P n_0\|$ exponentially decreases toward 0 when $t \to \infty$. In other words, the cell population exhibits an asymptotic stabilization after multiplication by a Malthusian exponential factor in time around a one-dimensional projection only dependent on the initial cell structure.

Indeed, we prove that the solutions of these models stabilize around a characteristic distribution of the structure. This function does not depend on the initial distribution of the structure. The way we proceed to conclude such AEG is explicitly explained in [2].

2 Cell Cycle Model with Unequal Division and Random Transition

In [10], Arino et al. proposed the integral model (3) based on the assumption of unequal division between daughter cells during cytokinesis that is slightly a modification of the models proposed by [14] and studied in [15, 16]. The author in [10] assumed that the length of the cell cycle is characterized by a conditional density, contrary to [14–16] where the length of the cell cycle is only determined by the initial size.

Let $X = L^1((-\tilde{\theta}, 0), Y)$, where $Y = L^1(0, A)$. The constant $\tilde{\theta}$ is the maximal time a cell can spend during the proliferation, and A is the maximal size of the cell. In this section, we assume

$$(\mathcal{H}_h) \quad \Big(h \in L^\infty((0,A)^2),\ h \geq 0 \Big),$$

$$(\mathcal{H}_\gamma) \quad \Big(\gamma \in L^\infty((0,\tilde{\theta}) \times (0,A)),\ \gamma \geq 0 \Big),$$

$$(\mathcal{H}_\xi) \quad \Big(\xi \text{ is a.e. continuous on } [0,\tilde{\theta}] \times [0,A] \text{ and is with values in } (0,A) \Big)$$

$$(\mathcal{H}_\xi^*) \quad \begin{pmatrix} \text{For } 0 < a < b < A \text{ the support of the function} \\ (\sigma,\tau,x) \mapsto h(x,\xi(\tau,\sigma))\gamma(\tau,\sigma) \text{ on } [(0,A)-(a,b)] \times (0,\tilde{\theta}) \times (a,b) \\ \text{is with Lebesgue measure } \neq 0 \end{pmatrix}.$$

and $$(\mathcal{H}_\alpha) \quad \begin{pmatrix} \text{There exists a nonnegative function } \alpha(\sigma) \text{ such that } \alpha(\sigma) > 0 \\ \text{on the left neighborhood at } \sigma = A \text{ such that the function} \\ h(x,\zeta(\tau,\sigma))\gamma(\tau,\sigma) \geq \alpha(\sigma) \text{ for a.e. } (\sigma,\tau,x) \end{pmatrix}.$$

The core operator $\phi : X \to Y$ is given by

$$\phi(f)(y) = 2\int_0^{\tilde{\theta}} \int_0^A h(y,\xi(\tau,\sigma))\gamma(\tau,\sigma) f(-\tau,\sigma) d\sigma d\tau. \tag{6}$$

Since the operator ϕ is a positive bounded linear operator from X to Y. It is shown in [1] that the operator ϕ defines a bounded positive linear operator from X into Y since the assumptions $(Hh), (H\gamma) and (H\xi)$ hold. Then, we can associate the operator defined in (6) a translation semigroup $\{T_\phi(t)\}_{t\geq 0}$ such that $\{T_\phi(t)\}_{t\geq 0}$ such that

$$T_\phi(t) f = n(t,.), \quad t \geq 0,$$

the semigroup solution of (3) with infinitesimal generator A_ϕ defined by

$$A_\phi f = f'$$
$$D(A_\phi) = \{f \in X,\ f \text{ is absolutely continuous, } f' \in X \text{ and } f(0) = \phi f\}.$$

We associate with the core operator ϕ the operator $\tilde{\phi}_\lambda$ as follows:

$$\tilde{\phi}_\lambda \varphi(y) = \phi(e^{\lambda \cdot} \otimes \varphi) = \int_0^A k_\lambda(y,\sigma)\varphi(\sigma) d\sigma, \quad \varphi \in Y,\ y \in (0,A), \tag{7}$$

where

$$k_\lambda(y,\sigma) = 2\int_0^{\tilde{\theta}} e^{-\lambda\tau} h(y,\zeta(\tau,\sigma))\gamma(\tau,\sigma) d\sigma.$$

This latter is bounded on $(0,A) \times (0,A)$, so the operator $\tilde{\phi}_\lambda$ is weakly compact on Y; in addition, F possesses the Dunford–Pettis property, and we can conclude that

ϕ is of compact type [17]. The irreducibility result comes from the result in [18] and assumption $(\mathcal{H}_\zeta^*)$.

Also, by a straightforward computation, we can show that the semigroup $\{T_\phi(t)\}_{t\geq 0}$ is eventually norm continuous [1]. Then, we can get the AEG property as follows.

Proposition 2.1 *Since $(\mathcal{H}_h)$, $(\mathcal{H}_\gamma)$, $(\mathcal{H}_\zeta)$, and $(\mathcal{H}_\zeta^*)$ are satisfied, there exists a unique solution n of (3) with $n_0 = f$ for $f \in X$, $f \not\equiv 0$. This solution is associated with the semigroup translation such that $n_t = T_\phi(t)f$ for all $t \geq 0$ with the core operator given by (6). There exists an eigenfunction $\mu \in Y$ associated with $\tilde{\phi}_{\lambda_0}$, where λ_0 is the solution of $r(\tilde{\phi}_\lambda) = 1$ such that $(\mathcal{H}_{AEG})$ holds.*

Using the ideas in [9], we can rewrite the model given by (3) using suns and stars framework as an abstract integral equation of the type

$$n_t = T_0(t)f + j^{-1}\int_0^t T_0^{\odot *}(t-s)\phi(n_s)\mathbf{1}_{(-\tilde{\theta},0)}ds. \tag{8}$$

To do it, let us consider the core operator given by (6) defined from $X = L^1((-\tilde{\theta},0)\times(0,A))$ into $Y = L^1(0,A)$. The semigroup $T_0 : X \to X$ is given by

$$T_0(t)f(s,y) = \begin{cases} f(t+s,y) & \text{if } t+s<0 \\ 0 & \text{if } t+s\geq 0 \end{cases}$$

with generator $(A_0 f)(s,y) = \frac{\partial}{\partial s}f(s,y)$ on the domain

$$D(A_0) = \{f \in X,\ f \text{ is absolutely continuous, } f' \in X \text{ and } f(0) = 0\}.$$

The semigroup T_0^* is again translation to the left on $X^* := L^\infty\Big((0,\tilde{\theta})\times(-A,0)\Big)$. This semigroup is not strongly continuous. However, it is strongly continuous on the subspace $X^\odot := C_0\Big((0,\tilde{\theta})\times(-A,0)\Big)$.

The semigroup $T_0^{\odot *} : X^{\odot *} := NBV\Big((-\tilde{\theta},0)\times(0,A)\Big) \to X^{\odot *}$ is also given by the left translation as T_0 with generator $(A_0^{\odot *}f^{\odot *})(s,y) = \frac{\partial}{\partial s}f^{\odot *}(s,y)$ on the domain

$$D(A_0^{\odot *}) = \{f^{\odot *} \in X^{\odot *} : \exists g \in X^{\odot *}/f^{\odot *}(s,y) = \int_s^0 g(t,y)dt, \forall s \in (-\tilde{\theta},0)\}.$$

In addition, the space X is embedded into $X^{\odot *}$ via the transformation j defined by

$$jf(s) := \int_s^0 f(\tau,.)d\tau, \quad \tau \in (-\tilde{\theta},0).$$

Then, via this construction by duality, we can transform our problem (3) into the abstract integral of the type (8). We obtain the following result with slightly modification on the assumptions given above.

Proposition 2.2 *Since* $(\mathcal{H}_h)$, $(\mathcal{H}_\gamma)$, $(\mathcal{H}_\zeta)$, *and* $(\mathcal{H}_\alpha)$ *are satisfied, there exists a unique solution* $n(t)$ *of* (8) *with* $n_0 = f \in X$ *on* $[0, \infty)$. *The family of operators* $T(t) : f \mapsto n_t$ *for* $t \geq$ *defines a* C_0 *semigroup of bounded operators on* X. *Furthermore,* $\{T(t)\}_{t\geq 0}$ *is eventually compact, the operator* $\tilde{\phi}_\lambda$ *is nonsupporting, and* $(\mathcal{H}_{AEG})$ *holds.*

Proof Using well-known results on contraction mapping, we can assure the existence and uniqueness of the solution associated with (8). Further results on compactness can be deduced using the generation expansion such that we set

$$n = n_0 + \mathcal{F}n, \qquad \text{where } n_0 = T_0(t)f;$$

then, we obtain $n = n_0 + \sum_{i=1}^{\infty} \mathcal{F}^i n$, where the first iteration $\mathcal{F}n_0$ is compact by using argument of Arzèla Ascoli. Therefore, our perturbed semigroup is eventually compact since it is a sum of finite sum of compact operators. The nonsupporting property follows from the assumption $(\mathcal{H}_\alpha)$. We can conclude that there exists a unique real root of $r(\tilde{\phi}_\lambda) = 1$ that is simple and dominant eigenvalue of the generator of the perturbed semigroup. We can conclude that the $(\mathcal{H}_{AEG})$ is satisfied. □

3 Cell Cycle Model with Mutation Accumulation and Telomere Hierarchies

In this section, we investigate the model (4) of telomere loss where the model admits a hierarchy at the level of the telomere where the more (least) differentiated cells have the shortest (longest) telomeres. During each round of division, it is hypothesized that one or more mutations can occur. These mutations are inherited by the daughter cells from their mother cell. After a number of mutations, the cell becomes cancerous. The model (4) admits a hierarchy at the level of mutations accumulated. Then, we can divide it into classes, each class corresponds to a telomeric and a mutation state.

Several papers explore models of telomere loss with and without overlapping generations. Arino et al.[19] investigate a linear model with the only source of loss due to the division. The population exhibits a polynomial growth of the telomere classes and asymptotic stabilization of the highest class.

Furthermore, as an extension of the work [19], the authors in [20] added a logistic loss term for each class. The result is the extinction of all the telomere classes that know a polynomial growth.

In this section, we assume

$$(\mathcal{H}_{\beta,\mu})\begin{pmatrix}\beta_{j,i}\in L^1(0,h)\cap L^\infty(0,h),\ \text{there exists some constant } \bar{\beta} \text{ such that}\\ 0<\beta_{j,i}(a)\leq\bar{\beta} \text{ for } 1\leq j\leq l, 0\leq i\leq m-1 \text{ a.e in } (0,h),\\ \mu_{j,i}\in L^1(0,h)\cap L^\infty(0,h) \text{ there exists some constant } \bar{\mu} \text{ such that}\\ 0\leq\mu_{j,i}(a)\leq\bar{\mu} \text{ for } 1\leq j\leq l, 0\leq i\leq m-1 \text{ a.e in } (0,h),\end{pmatrix}$$

and

$$p_{j,k,i}=\begin{cases}0 & \text{for } j>k\ \forall 2\leq j\leq n,\ 0\leq i\leq m-1\\ \dfrac{1}{2} & \text{for } j=k\ \forall 1\leq j\leq n,\ 0\leq i\leq m-1\end{cases}$$

$$q_{j,k,i}=0 \text{ for } j>k,\ \forall 2\leq j\leq n, 0\leq i\leq m-1$$

$$\sum_{k=j}^{n}p_{j,k,i}+\sum_{k=j}^{n}q_{j,k,i}=\frac{1}{2}\ \forall 1\leq j\leq n,\ 0\leq i\leq m-1,$$

where $p_{j,k,i}>0$ and $q_{j,k,i-1}>0$. When $i=0$, one has $q_{j,k,i-1}=0$.

If we write the vector of cell population, $n(a,t):=(N_i(a,t))_{0\leq i\leq m-1}$ with $N_i(a,t):=(n_{j,i}(a,t))_{1\leq j\leq l}$. In addition, we consider the matrix describing the loss due to death or division $M(a):=\mathrm{Diag}(M_i)_{0\leq i\leq m-1}$ with $M_i(a):=\mathrm{Diag}(\mu_{j,i}(a)+\beta_{j,i}(a))_{1\leq j\leq l}$.

$$B(a)=\left(b_{r,s}\right)_{0\leq r,s\leq m-1}=\begin{cases}P_r & \text{if } r=s\\ Q_r & \text{if } r=s+1\\ 0 & \text{otherwise,}\end{cases}$$

where

$$P_i(a)=\left(\tilde{p}_{t,z}\right)_{1\leq t,z\leq l}=\begin{cases}\tilde{p}_{t,t}(a):=\beta_{t,i}(a) & \text{if } t=z\\ \tilde{p}_{t,z+1}:=2\beta_{z+1,i}(a)p_{t,z+1,i} & \text{if } t<z\\ 0 & \text{otherwise}\end{cases}$$

$$Q_i(a)=(\tilde{q}_{t,z})_{1\leq t,z\leq l}=\begin{cases}\tilde{q}_{t,t}:=2\beta_{t,i-1}(a)q_{t,t,i-1} & \text{if } t=z\\ \tilde{q}_{t,z+1}:=2\beta_{z+1,i-1}(a)q_{t,z+1,i-1} & \text{if } t=z\\ 0 & \text{otherwise.}\end{cases}$$

Then, we can rewrite the model (4) as

$$\begin{aligned} \frac{\partial}{\partial t}n(a,t) + \frac{\partial}{\partial a}n(a,t) &= -M(a)n(a,t) \\ n(0,t) &= \int_0^h B(a)n(a,t)da, \end{aligned} \tag{9}$$

we use the transformation $m(a,t) = Z(a)n(a,t)$, and then we obtain the following system:

$$\begin{aligned} \frac{\partial}{\partial t}m(a,t) + \frac{\partial}{\partial a}m(a,t) &= 0 \\ m(0,t) &= \int_0^h B(s)Z^{-1}(s)m(s,t)ds = \phi(m(.,t)), \end{aligned} \tag{10}$$

where the matrix transformation Z is the solution of the first-order differential equation

$$Z'(a) = -Z(a)M(a) \tag{11}$$

with $Z(0) = I$.

Proposition 3.1 *Since $(\mathcal{H}_{\beta,\mu})$ holds, there exists a unique positive solution $n(a,t)$ of (4) for all initial data $\vec{f} \in X := L^1((0,h),\mathbb{R}^N)$ with $h > 0$. This solution satisfies*

$$n(a,t) = G(t)\vec{f}(a) = \begin{cases} Z^{-1}(a)Z(t-a)f(t-a) & \text{if } t-a < 0 \\ Z^{-1}(a)\displaystyle\int_0^h B(s)n(s,t-a)ds & \text{if } t-a \geq 0 \end{cases}$$

for $\vec{f} = \left(f_{1,0}, \cdots, f_{n,m-1}\right)^{tr}$ such that $n(a,0) = \vec{f}$ with $(\chi f)(a) := Z(a)f(s)$, $a \in (0,h)$ such that $Z^{-1}(a =)Diag(Z_i^{-1}(a))_{1\leq i\leq m-1}$ where

$$Z_i^{-1}(a) := \left(\bar{z}_{j,k,i} := \begin{cases} e^{-\int_0^h diag(\mu_{j,i}(\tau)+\beta_{j,i}(\tau))d\tau} & \text{if } k = j \\ 0 & \text{if } k \neq j \end{cases}\right).$$

The solution semigroup $\{G(t)\}_{t\geq 0}$ is given by

$$G(t)\vec{f} = \chi^{-1}T_\phi(t)\chi\vec{f}, \qquad \forall f \in X,$$

where $\{T_\phi(t)\}_{t\geq 0}$ is the semigroup solution of (10) and

$$\phi\vec{f} = \int_0^h B(a)Z^{-1}(a)\vec{f}(a)da.$$

The generator of $\{G(t)\}_{t\geq 0}$ *satisfies*

$$D(A) = \{\vec{f} \in X : f_{j,i} \text{ is absolutely continuous on } (0,h),\ \vec{f}(0) = \int_0^h B(a)\vec{f}(a)da\}$$

$$A\vec{f} = -\vec{f}'(a) - M(a)\vec{f}(a),\ \ \vec{f} \in D(A).$$

Furthermore, the semigroup $\{G(t)\}_{t\geq 0}$ *satisfies* $(\mathcal{H}_{AEG})$.

Proof Since the operator ϕ is a bounded nonnegative operator, we obtain that the translation semigroup $\{T_\phi(t)\}$ exists on X. The associated operator $\tilde{\phi}_\lambda$ is irreducible since $\tilde{z}_{k,k,i}$, β and $p_{j,k,i} > 0$ for $k > j$. The semigroup of translation is eventually compact since it is composed of convolution in X and bounded linear operator. Then, we obtain that the AEG property is satisfied for both semigroups by the equivalence property. □

In order to perform the suns–stars calculus, we consider the case where $\phi = 0$ in (10), and the associated semigroup solution is given by

$$(T_0(t)\vec{g})(a) = \begin{cases} \vec{g}(a-t) & \text{if } a - t > 0 \\ 0 & \text{if } a - t \leq 0. \end{cases} \tag{12}$$

Its infinitesimal generator is

$$D(A_0) = \{\vec{g} \in X : g \text{ is absolutely continuous, } \vec{g}(0) = 0\}$$
$$A_0\vec{f} = -\vec{f}'.$$

The injection j from $L^1((0,h),\mathbb{R}^N)$ into $\mathrm{NBV}((0,h),\mathbb{R}^N)$ is given by

$$(j\vec{g})(a) := \int_0^a \vec{g}(s)ds, \quad a \in (0,h).$$

Then, by integration of the transformed system (10), we obtain

$$\begin{aligned} &\frac{d}{dt}m(t) = A_0^{\odot *} jm(t) + \phi(m(t))\mathcal{H} \\ &m(0) = \vec{f}, \end{aligned} \tag{13}$$

where the operator $A_0^{\odot *}$ is defined as follows:

$$D(A_0^{\odot *}) = \{\varphi \in X^{\odot *}, \varphi(a) = \int_0^a \psi(s)ds\ \forall a \in [0,\tilde{a}] \text{ and } \psi \in X^{\odot *}\}$$
$$A_0^{\odot *}\varphi = -\varphi',$$

and $\mathcal{H}$ is the standard basis of $\mathbb{R}^N$ such that

$$\mathcal{H}_i(a) = \begin{cases} e_i & \text{for } a \in (0, \tilde{a}) \\ 0 & \text{for } a = 0. \end{cases}$$

So, we can rewrite our problem as

$$m(t) = T_0(t)\vec{g} + j^{-1}\left(\int_0^t T_0^{\odot *}(t-s)\phi(m(s))\mathcal{H}ds\right). \tag{14}$$

We obtain the following result [21]:

Proposition 3.2 *The semigroup $(G(t))_{t\geq 0}$ solution of (4) yields $(\mathcal{H}_{AEG})$. There exists a projection $\tilde{Q}$ of rank one, and there exists $\delta > 0$ such that*

$$\|e^{-\lambda_0 t}G(t) - \tilde{Q}\| \leq Me^{-\delta t}, \quad t \geq 0,$$

and $\tilde{Q}$ is such that $\tilde{Q}\vec{f} := \chi^{-1}Q(\chi\vec{f})$, i.e.,

$$\tilde{Q}\vec{f} = C(\chi\vec{f})(e^{\lambda_0 \cdot}Z^{-1}(\cdot) \otimes \zeta_{\lambda_0}), \quad \vec{f} \in X,$$

where

$$Q\vec{f} = C(\vec{f})(e^{\lambda_0 \cdot} \otimes \zeta_{\lambda_0}), \tag{15}$$

and

$$C(\vec{f}) = \frac{\langle \zeta_{\lambda_0}^*, \phi(\theta \mapsto \int_0^\theta e^{-\lambda_0(\theta-s)}\vec{f}(s)ds)\rangle}{\langle \zeta_{\lambda_0}^*, \phi(\theta \mapsto \theta e^{-\lambda_0\theta} \otimes \zeta_{\lambda_0})\rangle}, \quad \vec{f} \in X, \tag{16}$$

where ζ_{λ_0} and $\zeta_{\lambda_0}^*$ are two positive eigenvectors, respectively, of $\tilde{\phi}_{\lambda_0}$ and $\tilde{\phi}_{\lambda_0}^*$ associated with the eigenvalue $r(\tilde{\phi}_{\lambda_0}) = 1$.

4 Cell Cycle Model with Quiescence

In the following, we study the model given by (5) where the cells are in either proliferating or quiescent class. This model is an extension of the model given in [13]. In this section, we consider the space of initial functions

$$X = L^1((0, \tilde{a}), \mathbb{R}^2), \ \tilde{a} > 0$$

and assume

$$(\mathcal{H}_{\beta,\tau,\sigma})\ \big(\beta,\tau,\sigma:(0,\tilde{a})\to\mathbb{R}^{+},\quad \beta,\tau,\sigma\in L^{\infty}(0,\tilde{a}),\beta\not\equiv 0.\big)$$

As the same spirit in Sect. 3, the core operator $\phi: X\to\mathbb{R}^2$ is given by

$$\phi\vec{f}=\int_0^{\tilde{a}} B(s)Z^{-1}(s)\vec{f}(s)ds,$$

where

$$B(a)=\begin{pmatrix}2b\beta(a) & 0\\ 2(1-b)\beta(a) & 0\end{pmatrix},$$

and Z is the solution of (11) with

$$M(a)=\begin{pmatrix}\beta(a)+\sigma(a) & -\tau(a)\\ -\sigma(a) & \tau(a)\end{pmatrix};$$

we obtain then the following result [2] for both frameworks.

Proposition 4.1 *Since $(\mathcal{H}_{\beta,\tau,\sigma})$ holds, the solution semigroup $(G(t))_{t\geq 0}$ exists on X and it is given by*

$$G(t)\vec{f}=\chi^{-1}T_{\phi}(t)\chi\vec{f},\ \textit{for all}\ \vec{f}\in X.$$

Its generator A satisfies

$$D(A)=\{\vec{f}\in W^{1,1}((0,\infty),\mathbb{R}),\ \vec{f}(0)=\int_0^{\infty}B(s)\vec{f}(s)ds\}$$

$$A\begin{pmatrix}p\\ q\end{pmatrix}(s)=\begin{pmatrix}-p'(s)\\ -q'(s)\end{pmatrix}+\begin{pmatrix}-(\beta(s)+\sigma(s))p(s)+\tau(s)q(s)\\ \sigma(s)p(s)-\tau(s)q(s)\end{pmatrix}.$$

Its spectrum yields

$$\begin{aligned}\sigma(A)=\sigma_p(A)&=\{\lambda\in\mathbb{C},\ 1\in\sigma(\bar{\phi}_{\lambda})\}\\ &=\{\lambda\in\mathbb{C},\int_0^{\tilde{a}}e^{-\lambda a}2\beta(a)\left[bz_{1,1}(a)+(1-b)z_{1,2}(a)\right]da=1\}.\end{aligned}$$

In addition, $(G(t))_{t\geq 0}$ is eventually compact and satisfies $(\mathcal{H}_{AEG})$, where $s(A)=\omega(A)$ is a simple pole and a dominant eigenvalue of A and is the unique real solution λ_0 of the equation

$$\int_0^{\tilde{a}}e^{-\lambda a}2\beta(a)\left[bz_{1,1}(a)+(1-b)z_{1,2}(a)\right]da=1.$$

References

1. Y. El Alaoui, L. Alaoui, *Asymptotic Behavior in a cell proliferation Model with Unequal division and Random Transition using translation semigroup,* Indian Journal of Sciences and Technology, Vol. 10, 2017, no. 28.
2. L. Alaoui, Y. El Alaoui, *AEG property of a cell cycle model with quiescence in the light of translation semigroups,* International Journal of Mathematical Analysis, Vol. 9, 2015, no. 51, 2513–2528
3. L. Alaoui, *Nonlinear homogeneous retarded differential equations and population dynamics via translation semigroups,* Semigroup Forum Vol. 63 (2001) 330356
4. L. Alaoui, *Age-dependent population dynamics and translation semigroups,* Semigroup Forum Vol. 57 (1998) 186–207
5. L. Alaoui, *"A cell cycle model and translation semigroups,"* Semigroup Forum Vol. 54, 1997
6. L. Alaoui, *Generators of translation semigroups and asymptotic behavior of the Sharpe-Lotka model,* Diff. Int. Eq., 9 (1996), 343–362
7. L. Alaoui, *Population dynamics and translation semigroups,* dissertation, Univ. of Tbingen, 1995
8. L. Alaoui and O. Arino, *Compactness and spectral properties for positive translation semigroups associated with models of population dynamics,* Diff. Int. Eq., 6 (March 1993), 459–480
9. O. Diekmann, P. Getto and M. Gyllenberg, *Stability and bifurcation analysis of volterra functional equations in the light of suns and stars,* SIAM J . MATH. ANAL. Vol. 39 (2007), No. 4, pp. 10231069
10. O. Arino, M. Kimmel, and M. Zerner, *Analysis of a cell population model with unequal division and random transition*, Lecture Notes in Pure and Appl. Math. 131 (1991), 3–12
11. G. Kapitanov,*A Mathematical Model of Cancer Stem Cell Lineage Population Dynamics with Mutation Accumulation and Telomere Length Hierarchies*, Math. Model. of Nat. Phenom., 7 (01), 136–165, 2012
12. J. Dyson, R. Villella-Bressan, and G. F. Webb, *Asynchronous exponential growth in an age structured population of proliferating and quiescent cells*, Math. Biosci., 177/178 (2002), 73–83. https://doi.org/10.1016/s0025-5564(01)00097-9
13. O. Arino, E. Sanchez, G. F. Webb, *Necessary and sufficient conditions for asynchronous exponential growth in age structured cell populations with quiescence*, J. Math. Anal. and Appl., 215 (1997), 499–513. https://doi.org/10.1006/jmaa.1997.5654
14. M. Kimmel, Z. Darzynkiewicz, O. Arinon and F. Traganos, *Analysis of a Cell Cycle Model Based on Unequal Division of Metabolic Constituents to Daughter Cells During Cytokinesis*, J. Theoret. Biol. 110: 637–664.
15. O. Arino, M. Kimmel, *Asymptotic analysis of a cell cycle model based on unequal division*, SIAM J. Appl. Math., Vol. 47, No. 1, February 1987
16. O. Arino, M. Kimmel, *Asymptotic behavior of a nonlinear functional integral equation of cell kinetics with unequal division*, J. Math. Biol. 27: 341–54, 1989
17. Schaefer, H.H.,*Banach lattices and positive operators*, Springer-Verlag (1974)
18. Zerner, *M.,Quelques propriétés spectrales des opérateurs positifs*, J. Funct. Anal. (1987), 381417
19. O. Arino, E. Sanchez and G.F. Webb. *Polynomial Growth Dynamics of Telomere Loss in a Heterogeneous Cell Population*. In: Dynamic Control Discrete Impulsive System 3 (1997), p.p. 263–282.
20. J. Dyson, R. Villella-Bressan, G. F. Webb, *Asymptotic behaviour of solutions to abstract logistic equations,* Mathematical Biosciences 206 (2007) 216232.
21. Y. El Alaoui, L. Alaoui, *Qualitative Analysis of a PDE Model of Telomere Loss in Proliferating Cell Population in the Light of Suns and Stars,* In "Trends in Biomathematics: Mathematical Modeling for Health, Harvesting, and Population Dynamics - Selected works presented at the BIOMAT Consortium Lectures, Morocco 2018 (Ed., R.P. Mondaini)," Springer 2019, ISBN: 9783030234324.

Viability Analysis of Labor Force in an Agroforestry System

I. M. Cholo Camargo, J. A. Amador Moncada, C. A. Peña Rincón, and G. Olivart Tost

1 Introduction

Societies in general incorporate their environment that includes supporting ecosystems as an essential part for economic growth that allows them to offer well-being to their population. For this purpose, strategies that frame the protection of natural resources have been developed, for example, through the common pool resource (CPR) theory [1]. However, the results of the implementation of these strategies are not fully achieved in practice[2]. Moreover, the dynamic complexity of the relationships between different economic, governmental, and natural systems proposes great challenges to the agro-ecological systems that are essential to understand food production as well as the challenges of environmental impacts and their consequences on the environment [3–5]. On the other hand, socio-ecological systems coupled nature and humans, which recognize people as part and not part

I. M. Cholo Camargo (✉)
Universidad Nacional de Colombia, Sede Manizales, Campus la Nubia, Manizales, Colombia
e-mail: imcholoc@unal.edu.co

J. A. Amador Moncada
Instituto de Investigación de Recursos Biológicos Alexander von Humboldt, Bogotá D.C., Colombia
e-mail: jamador@humboldt.org.co

C. A. Peña Rincón
Universidad Sergio Arboleda, Departamento de Matemáticas, Bogotá D.C., Colombia
e-mail: carlos.pena@usa.edu.co

G. Olivart Tost
Department of Natural Sciences and Technology, Universidad de Aysén, Coyhaique, Chile
e-mail: gerard.olivar@uaysen.cl

R. P. Mondaini (ed.), *Trends in Biomathematics: Chaos and Control in Epidemics, Ecosystems, and Cells*, https://doi.org/10.1007/978-3-030-73241-7_10

of nature [6], where the dynamics of the social system influence an ecological system and vice versa [7], encouraging to lead scenarios for natural resources to be overexploited [8, 9].

The most affected natural resources are found in forests on a global scale, and they are deforested mainly by the change in land use due to agriculture, timber production, and infrastructure investment [10]; most deforestation occurs in the tropics [11, 12]. Therefore, this problem has been addressed from the socio-ecological modeling by making models that consider several ecological dynamic configurations thus allowing to analyze different types of social pressure on resources [13]. Additionally, models that include technology to overcome the increase in the scarcity of renewable resources have been considered [14]; models that take into account economic growth fluctuations motivated by dynamic resources have also been studied [15, 16]. A very inclusive model was proposed by Brander and Taylor [15], often called BT-type models, characterized mainly by the following attributes: (1) population growth, (2) substitutability, (3) innovation, (4) capital accumulation, (5) property rights and conservation policies for renewable and non-renewable resources, and (6) modeling approach with the purpose of understanding the dynamics between society and natural resources by including renewable resources, agriculture, and a manufactured good [17].

In the 2D model proposed by DAlessandro [16], two important considerations are included: agriculture as an economic activity parallel to resource extraction and a critical level of resources in which its regeneration rate becomes negative and, therefore, total resource depletion becomes inevitable [18]. Results in that paper are basically phase portraits that show the change in the vector field of the system under parameter changes. Other works analyzed the model from the bifurcation theory in order to characterize all the possible steady-state scenarios in the parametric space [19–22], showing that adequate parameter sets can lead to sustainable trajectories where population and resource level are higher than zero in the long run.

In this chapter, we modify the model in [16] to perform the analytical study of its steady-state dynamics and approached it from the viability theory to evaluate the trajectory under some restrictions that guarantee a minimum value for the state variable at each instant of time t. This approach focuses on the transient state of the system to identify the set of thresholds associated with the system solution that ensures the coexistence of the social and ecological component rather than pointing to steady-state analysis, see [23, 24].

The chapter is organized as follows. In Sect. 2, we introduce some description of DAlessandro's model [16] and its purpose and, additionally, the modification and its advantages to the local dynamic analysis. In Sect. 3, we define some concepts regarding viability theory and their application to the modified model. In Sect. 4, an analysis was made of the numerical simulations performed, which reflect the theoretical results. We conclude in Sect. 5, by discussing the exposed results and by giving our contributions and some topics considered as challenges.

2 Mathematical Model

The mathematical model proposed in this chapter for the viability analysis is a modification to DAlessandro's system [16], which considers a population that obtains its livelihoods mainly from the exploitation of renewable resources, as well as from its agricultural activities within its territory. The following is an introduction to the generalities of the base model [16]. In addition, the modification made is shown to facilitate the application of analytical methods.

2.1 Base Model

The base model presents a system of ordinary differential equations (ODEs) representing the dynamic interaction between the population growth and the exploitation of available renewable resources in an isolated society. It is assumed that the dynamics of the population depends on the income acquired by the economic activities within its territory, being agriculture represented by a Cobb–Douglas production function and the exploitation of the natural resource that must satisfy the minimum basic needs required by the population. The model assumes that the forest grows logistically and decreases according to a Schaefer production function [25]. This model has been studied from the perspective of bifurcation analysis in order to understand the behavior of steady-state variables [21, 22, 26]. The coupled system of ODEs for the base model is

$$\begin{cases} \dot{L} = \gamma \left(\alpha_1 \left(1-\beta\right)^{\delta} L^{\delta-1} + \phi\alpha_2\beta S - \sigma \right) L, \\ \dot{S} = \left[\rho \left(\frac{S}{k_2} - 1 \right) \left(1 - \frac{S}{k_1} \right) - \alpha_2 \beta L \right] S, \end{cases} \tag{1}$$

where

- L is the level of population.
- S is the level of renewable resources available.
- β is the proportion of people dedicated to the exploitation of the resource. Thus, $1-\beta$ is the proportion of population dedicated to agriculture.
- ρ represents the natural growth rate of the forest.
- k_1 is the carrying capacity of the resource.
- k_2 is a threshold where the forest growth rate becomes negative, and therefore, the depletion of the resource is inevitable; this is called the strong Allee effect.
- ϕ and γ are the representative values of the resource and agricultural products in terms of calories, respectively.
- α_1 is a measure of the productivity of the land.

- α_2 is a measure of effectiveness in resource extraction.
- σ is the minimum value of per capita income in terms of calories necessary to survive.
- δ is the elasticity of the Cobb–Douglas function.

2.2 Modified Model

The base model (1) presents equilibrium points with a value of $L = 0$, where it was not feasible to determine its local behavior analytically by means of the linear approximation. Furthermore, an explicit expression of the internal equilibrium points was not determined in the positive quadrant of the system. To overcome these difficulties, we propose a quadratic approximation of Lagrange in the term L^{δ} assuming a maximum population level of 5000.

$$L^{\delta} \approx g(L) = aL^2 + bL, \tag{2}$$

where

$$a = -5000^{\delta-2}(1 - 2^{\delta-1}) < 0 \text{ y } b = 5000^{\delta-1}(2 - 2^{\delta-1}) > 0.$$

The modified model incorporating Eq. (2) is

$$\begin{cases} \dot{L} &= \gamma\left[\alpha_1(1-\beta)^{\delta} g(L) + \phi\alpha_2\beta LS - \sigma L\right]. \\ \dot{S} &= \rho S\left(\frac{S}{k_2} - 1\right)\left(1 - \frac{S}{k_1}\right) - \alpha_2\beta LS, \\ & L(t) \geq 0 \;\; S(t) \geq 0. \end{cases} \tag{3}$$

2.3 Equilibrium Points

The modified system presents five or six equilibrium points, of which up to two are in the positive quadrant and are characterized by $L > 0$ and $S > 0$, these being the points of interest for this chapter. By using the definition of equilibria of a system of ODEs and performing algebraic operations, a quadratic equation for S of the form $AS^2 + BS + C = 0$ is obtained, where

$$A = a\alpha_1(1-\beta)^{\delta}\rho,$$

$$B = -A(k_1 + k_2) - k_1k_2\phi\alpha_2^2\beta^2,$$

$$C = k_1k_2\alpha_2\beta\left(\sigma - b\alpha_1(1-\beta)^{\delta}\right) + a\alpha_1(1-\beta)^{\delta}\rho k_1k_2.$$

If it is defined that

$$\Delta = \alpha_2^2\beta^2\phi k_1 k_2 + a\alpha_1 k_1\rho(1-\beta)^{\delta} + a\alpha_1 k_2\rho(1-\beta)^{\delta},$$

the possible equilibrium points are

$$(L_1.S_1),\ \ (L_2.S_2),\ \text{y}\ (L_{00}, S_{00}),$$

where

$$S_1 = \frac{\Delta + \sqrt{B^2 - 4AC}}{2a(1-\beta)^{\delta}\alpha_1\rho}, \tag{4}$$

if is satisfied that

$$\alpha_2^2\beta^2\phi k_1 k_2 + \sqrt{B^2 - 4AC} < -a\alpha_1\rho(1-\beta)^{\delta}(k_1 + k_2),$$

and

$$S_2 = \frac{\Delta - \sqrt{B^2 - 4AC}}{2a(1-\beta)^{\delta}\alpha_1\rho}, \tag{5}$$

if it is satisfied that

$$\alpha_2^2\beta^2\phi k_1 k_2 < -a\alpha_1\rho(1-\beta)^{\delta}(k_1 + k_2) + \sqrt{B^2 - 4AC}.$$

By replacing the values of S obtained in (4) and (5) in (6), coordinates of $L > 0$ for the internal equilibrium points are obtained

$$L_{1,2} = \frac{\sigma - b\alpha_1(1-\beta)^{\delta} - \phi\alpha_2\beta S_{1,2}}{a\alpha_1(1-\beta)^{\delta}}, \tag{6}$$

as long as it is true that

$$\sigma < b\alpha_1(1-\beta)^{\delta} + \phi\alpha_2\beta S_{1,2}.$$

These two internal points exist when the discriminant $B^2 - 4AC > 0$. If the discriminant is zero, we obtain that

$$S_{00} = \frac{\Delta}{2a(1-\beta)^{\delta}\alpha_1\rho}$$

with the restriction

$$\alpha_2^2 \beta^2 \phi k_1 k_2 < -a\alpha_1 \rho (1-\beta)^{\delta} (k_1 + k_2) .$$

Finally, the value of L for S_{00} is obtained

$$L_{00} = \frac{\sigma - b\alpha_1 (1-\beta)^{\delta} - \phi\alpha_2 \beta S_{00}}{a\alpha_1 (1-\beta)^{\delta}}.$$

3 Viability

A qualitative analysis for the base model (3) shows the existence of stationary state scenarios in which the population can consume natural resources without completely depleting them, thus guaranteeing their own existence. This behavior is possible when the trajectory converges either to an internal equilibria or to a limit cycle, depending on the configuration of the system parameters and the initial conditions, see, for example, [22].

Now, if the purpose is to evaluate the trajectory under some restrictions that guarantee a minimum value for the state variables at each instant of time t, it is necessary to use the viability theory. From [27], viability is defined as the capacity for a system to maintain conditions of existence through time given certain constraints; the set of initial conditions for which a control exists in such a way that the system satisfies and complies with the restrictions is called the viability kernel. In practice, the initial conditions cannot easily be controlled, while the restrictions are more likely to be modified. Therefore, an equivalent definition of viability kernel is the set of thresholds values for which the dynamical system (7) becomes compliant with the constraints (8) during a period of time by applying an admissible control strategy given a certain initial condition [28]. This set of thresholds is called sustainable thresholds. We use this last definition for viability analysis in the work.

3.1 Preliminary

Consider the following system:

$$\begin{cases} \dot{x}(t) = f(x(t), \mu(t)) \\ x(0) = x_0 \\ \mu(t) \in [\mu_{min}, \mu_{max}], \end{cases} \tag{7}$$

where $x(t) \in \Re^n$ is the vector of state variables and $\mu(t) \in \Re$ is the control variable that represents a decision that would be applied to the system.

For the system (7) to have a solution and to be unique, it is assumed that $f(x(t), \mu(t))$ is locally Lipschitz.

Depending on the initial condition, additional conditions (8) may be required to be met, which shall be considered as system constraints of (7).

$$I_j(x(t), \mu(t)) \geq \theta_j \quad j = 1, \ldots p. \tag{8}$$

Therefore, we have the following definition.

Definition 3.1 The set of sustainable thresholds of the system (7) with control $\mu(t)$ is given by

$$U_{t^*}(x_0) = \left\{\theta | \exists (x(t), \mu(t)), \text{satisfies (7) and (8)} \; \forall t \in \left(0, t^*\right)\right\}. \tag{9}$$

Schaefer [25] expresses the dynamics of a renewable resource in terms of its natural growth $G(S)$ and its exploitation $h(S)$ as: $\dot{S} = G(S) - h(S)$. By varying a factor in such a dynamics that affects the harvesting of the resource, a different trajectory is obtained; for example, if the extraction workforce increases, renewable resources will disappear faster. Theorem 3.1 is motivated from the above, where each Cauchy problem refers to the resource dynamics with a different control.

Theorem 3.1 *Let $f : A \to \Re$ be a continuous function with $A \subseteq \Re \times \Re$ open. Let us suppose that there is a function $g : \Re \times \Re \to \Re$ that is continuous and locally Lipschitz in $x(t)$ such that $f(x, \mu) \leq g(x, \mu)$ for all $(x, \mu) \in A$, $\frac{\partial g}{\partial \mu} \leq 0$, where $\mu(t) \in \Re$ is the control variable. Moreover, let $(x_0, \mu_1(t_0))$, $(y_0, \mu_2(t_0)) \in A$ be two initial conditions, such that $x_0 \leq y_0$ and $\mu_1(t) \geq \mu_2(t) \, \forall t \geq t_0$. if $x(t)$ and $y(t)$ are the solutions of the following Cauchy problems:*

$$\dot{x}(t) = f(x(t), \mu_1(t), t) \qquad \dot{y}(t) = g(y(t), \mu_2(t), t)$$
$$x(t_0) = x_0 \qquad y(t_0) = y_0;$$

then

$$x(t) \leq y(t) \quad \forall t \in I.$$

I is the solution existence interval for $x(t)$ and $y(t)$.

Proof ***(Contradiction)*** Let us suppose that there exists $\bar{t} \geq t_0, \bar{t} \in I$, such that $x(\bar{t}) > y(\bar{t})$.

Then, we define t^* by

$$t^* = \sup\{t \in [t_0, \bar{t}] \mid x(t) \leq y(t)\},$$

by the continuity of the solutions $x(.)$ e $y(.)$, we have $x(t^*) = y(t^*)$. On the other hand, f is locally Lipschitz in $x(t^*)$, hence, the constants $\epsilon_1 > 0$ and $L_f \geq 0$ will exist, such that $|f(x, s) - f(y, s)| \leq L_f |x - y|$ for every $x, y \in (x(t^*) - \epsilon_1, x(t^*) + \epsilon_1)$ and for every $s \geq 0$. Moreover, as $t^* < t - a$ new constant $\epsilon_2 > 0$ appears, such that $t^* + \epsilon_2 < t-$. Finally, for every $s \in (t^*, t^* + \epsilon_2)$, $x(s), y(s) \in (x(t^*) -$

$\epsilon_1, x(t^*) + \epsilon_1)$. Thus, for every $s \in (t^*, t^* + \epsilon_2)$, it is satisfied that $|f(x(s), s) - f(y(s), s)| \leq L_f|x(s) - y(s)|$. Let us define a continuous function $w(t)$ as $w(t) = x(t) - y(t) > 0 \; \forall t \in (t^*, t^* + \epsilon_2]$; then,

$$
\begin{aligned}
0 < w(t) &= x(t) - y(t) \\
&= x_0 + \int_{t_0}^{t} f(x(s), \mu_1(s), s)ds - y_0 - \int_{t_0}^{t} g(y(s), \mu_2(s), s)ds \\
&= x_0 + \int_{t_0}^{t^*} f(x(s), \mu_1(s), s)ds + \int_{t^*}^{t} f(x(s), \mu_1(s), s)ds - y_0 \\
&\quad - \int_{t_0}^{t^*} g(y(s), \mu_2(s), s)ds - \int_{t^*}^{t} g(y(s), \mu_2(s), s)ds \\
&= x(t^*) + \int_{t^*}^{t} f(x(s), \mu_1(s), s)ds - y(t^*) - \int_{t^*}^{t} g(y(s), \mu_2(s), s)ds \\
&= \int_{t^*}^{t} f(x(s), \mu_1(s), s)ds - \int_{t^*}^{t} g(y(s), \mu_2(s), s)ds \\
&\leq \int_{t^*}^{t} g(x(s), \mu_1(s), s)ds - \int_{t^*}^{t} g(y(s), \mu_2(s), s)ds \qquad (f(x, \mu) \leq g(x, \mu)) \\
&\leq \int_{t^*}^{t} g(x(s), \mu_2(s), s)ds - \int_{t^*}^{t} g(y(s), \mu_2(s), s)ds \qquad \left(\frac{\partial g}{\partial \mu} \leq 0, \quad \mu_1 \geq \mu_2\right) \\
&= \int_{t^*}^{t} g(x(s), \mu_2(t), s) - g(y(s), \mu_2(s), s)ds \\
&\leq L_g \int_{t^*}^{t} |x(s) - y(s)|ds \\
&= L_g \int_{t^*}^{t} |w(s)|ds \\
&= L_g \int_{t^*}^{t} w(s)ds.
\end{aligned}
$$

From Gronwall's lemma, it is concluded that $w(t) = 0$, which contradicts the approach that $w(t) > 0$, thus $x(t) \leq y(t) \; \forall t \in I$. □

If two different controls are applied starting from the same initial point, the corresponding trajectories will be kept separated during a time interval I, because it may happen that there is a different crossing from the initial condition at a time t, as seen in Fig. 1. Proposition 3.1 demonstrates the existence of this interval I.

Proposition 3.1 *Let $f, g : A \to \Re$ be continuous functions with $A \subseteq \Re^2$ open. Consider the following system of ordinary differential equations:*

$$
\begin{aligned}
\dot{x}(t) &= f(x(t), t) \\
\dot{y}(t) &= g(y(t), t),
\end{aligned}
$$

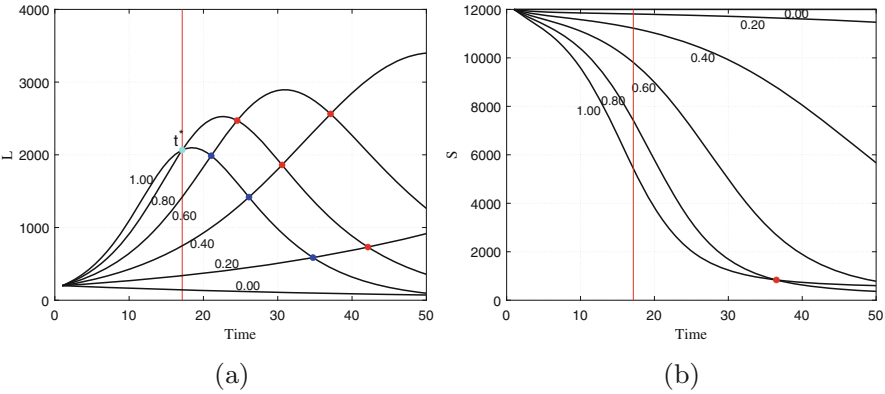

(a) (b)

Fig. 1 Monotonicity of the state variables in the interval $(0, t^*)$ and $(L_0, S_0) = (200, 12000)$

such that $x(0) = y(0) = \bar{x}$ *y* $f(\bar{x}, 0) < g(\bar{x}, 0)$. *Then, there is an interval* I *where*

$$x(t) < y(t) \quad \forall t \in I. \tag{10}$$

Proof Let be $z = x - y$; then,

$$\begin{aligned} z(0) &= x(0) - y(0) \\ &= \bar{x} - \bar{x} \\ &= 0. \end{aligned}$$

On the other hand, $\dot{z}(t) = f(x(t), t) - g(y(t), t)$, and thus

$$\begin{aligned} \dot{z}(0) &= f(x(0), 0) - g(y(0), 0)) \\ &= f(\bar{x}, 0) - g(\bar{x}, 0) < 0, \end{aligned}$$

but

$$\begin{aligned} \dot{z}(0) &= \lim_{t \to 0} \frac{z(t) - z(0)}{t} \\ &= \lim_{t \to 0} \frac{z(t)}{t} < 0, \end{aligned}$$

which implies that $z(t) < 0$, that is, $x(t) - y(t) < 0$, thus, by the sign conservation theorem, there is a $\epsilon > 0$ such that $x(t) < y(t)$ for every $t \in (0, \epsilon)$. □

If we look at the solution of the system (3) in Fig. 1, it can be seen that there is an interval I where there is a monotonicity of the trajectories for both L and S, taking different controls of $0 \leq \beta \leq 1$. The interval corresponding to the state variable L

is contained in the interval associated with the state variable S; in other words, the monotonicity of L implies the monotonicity of S, which leads to Theorem 3.2.

Theorem 3.2 *Let $f : A \to \Re$ be a continuous and locally Lipschitz function with $A \subseteq \Re$ open. Suppose that there are two controls $\mu_1(t)$ and $\mu_2(t)$ such that $\mu_1(t) \geq \mu_2(t)$ and $L_1(t) \geq L_2(t)$ for all $t \geq t_0$, where $L_i(t)$ is the fixed solution of $\dot{L}(t)$ with the respective control. Consider the solutions $x(t)$ and $y(t)$ of the following problems:*

$$\dot{x}(t) = f(x(t)) - \mu_1(t)L_1(t)x(t) \qquad \dot{y}(t) = f(y(t)) - \mu_2(t)L_2(t)y(t)$$
$$x(t_0) = x_0 \qquad y(t_0) = y_0$$

with $x_0 = y_0$.

Then, $x(t) \leq y(t)$ for all $t \in I$, where I is the solution existence interval.

Proof ***(Contradiction)*** Suppose there is a $\bar{t} > t_0, \bar{t} \in I$ such that $x(\bar{t}) > y(\bar{t})$.

Then, t is defined as

$$t^* = \sup\{t \in [t_0, \bar{t}) \mid x(t) \leq y(t)\}.$$

Now, $x(\cdot)$ and $y(\cdot)$ are continuous in t^*; then, $x(t^*) = y(t^*)$, f is locally Lipschitz in $x(t^*)$, and hence there is $\epsilon_1 > 0$, $L_f \geq 0$ such that $|f(x) - f(y)| \leq L_f|x - y|$ for every $x, y \in (x(t^*) - \epsilon_1, x(t^*) + \epsilon_1)$ and for every $s \geq 0$. In addition, by definition of t^*, $t^* < \bar{t}$, and thus there is $\epsilon_2 > 0$ such that $t^* + \epsilon_2 < \bar{t}$, and for every $s \in (t^*, t^* + \epsilon_2)$, we have $x(s), y(s) \in (x(t^*) - \epsilon_1, x(t^*) + \epsilon_1)$. Thus, for every $s \in (t^*, t^* + \epsilon_2)$, we have $|f(x(s)) - f(y(s))| \leq L_f|x(s) - y(s)|$. Let us define a continuous function $w(t)$ as $w(t) = x(t) - y(t) > 0 \; \forall t \in (t^*, t^* + \epsilon_2]$; then,

$$\begin{aligned}
0 < w(t) &= x(t) - y(t) \\
&= x_0 + \int_{t_0}^{t} f(x(s)) - \mu_1(s)L_1(s)x(s)ds - y_0 - \int_{t_0}^{t} f(y(s)) - \mu_2(s)L_2(s)y(s)ds \\
&= x_0 + \int_{t_0}^{t^*} f(x(s)) - \mu_1(s)L_1(s)x(s)ds + \int_{t^*}^{t} f(x(s)) - \mu_1(s)L_1(s)x(s)ds - y_0 \\
&\quad - \int_{t_0}^{t^*} f(y(s)) - \mu_2(s)L_2(s)y(s)ds - \int_{t^*}^{t} f(y(s)) - \mu_2(s)L_2(s)y(s)ds \\
&= x(t^*) + \int_{t^*}^{t} f(x(s)) - \mu_1(s)L_1(s)x(s)ds - y(t^*) - \int_{t^*}^{t} f(y(s)) - \mu_2(s)L_2(s)y(s)ds \\
&= \int_{t^*}^{t} f(x(s)) - \mu_1(s)L_1(s)x(s)ds - \int_{t^*}^{t} f(y(s)) - \mu_2(s)L_2(s)y(s)ds \\
&= \int_{t^*}^{t} f(x(s)) - \mu_1(s)L_1(s)x(s) - f(y(s)) + \mu_2(s)L_2(s)y(s)ds \\
&\leq \int_{t^*}^{t} f(x(s)) - \mu_1(s)L_1(s)x(s) - f(y(s)) + \mu_1(s)L_1(s)x(s)ds
\end{aligned}$$

$$= \int_{t^*}^{t} f(x(s)) - f(y(s))ds$$

$$\leq L_f \int_{t^*}^{t} |x(s) - y(s)|ds$$

$$= L_f \int_{t^*}^{t} |w(s)|ds$$

$$= L_f \int_{t^*}^{t} w(s)ds.$$

From Gronwall's lemma, it is concluded that $w(t) = 0$, which contradicts the approach that $w(t) > 0$. Thus, $x(t) \leq y(t) \ \ \forall t \in I$. □

Solow [29] studied the sustainability in an economic model of consumption–production of non-renewable resources, and he found an expression for maximal sustainable consumption without considering a restriction on the conservation of the resource, while Martinet in [30] considered the restriction and found a relationship between a guaranteed minimum consumption and the minimum reserve of the resource. There is something similar for the case under study. An important factor in the exploitation of a renewable resource is the labor force that allows to obtain enough from the natural environment, thus guaranteeing the livelihood of the population and a sustainable level of resources. With the above, there is the minimum level of resources that ensure livelihood with a minimum level of population given. This relationship can be generalized by using Proposition 3.2 where $p - 1$ constraints are set to find the sustainable threshold θ_p.

Proposition 3.2 *Consider a system of the form* (7) *and the constraints* (8)*. For a given initial condition, the set of sustainable thresholds* $\mathscr{U}_{t^*}(x_0)$ *that depends on* $p - 1$ *guaranteed constraints is given by*

$$\mathscr{U}_{t^*}(x_0) = \{(\theta_1, \ldots, \theta_p) \ | \ \theta_1, \theta_2, \ldots \theta_{p-1} \geq 0 \ \ \theta_p \leq \theta_p^+(\theta_1, \ldots \theta_{p-1})\},$$

where $\theta_p^+(\theta_1 \ldots \theta_{p-1}) := \max\{\theta \ | \ \exists \ \ \mu(t), x(t)$ *starting from* x_0*, such that satisfy* (7) *and* $I_j(x(t), \mu(t)) \geq \theta_j, \ \ j = 1, \ldots p \ \ \forall t \in (0, t^*)\}$

Proof $(\Rightarrow)$

Let be $A = \{(\theta_1, \ldots, \theta_p) | \theta_1, \theta_2, \ldots \theta_p - 1 \geq 0$ and $\theta_p \leq \theta_+ p(\theta_1, \ldots \theta_p - 1)\}$. Let us suppose that $\theta \leq \mathscr{U} t^*(x_0)$. Therefore, there exists one control $\mu(t)$ and one path $x(t)$ starting from x_0 satisfying both the dynamics (7) and the restriction $I_j(x(t), \mu(t)) \geq \theta_j$ for all $j = 1, \cdots, p$ at any $t \in (0, t^*)$. Now as, $\theta_j \geq 0 \forall_j = 1 \cdots p - 1$ and $\theta_p \leq \theta + p$, since, is the maximun of the θ_j that satisfy (7) and (8) then $\theta \in A$. By definition, $\theta_j \geq 0 \ \ \forall j = 1 \cdots p - 1$, and from the same definition of θ_p^+, $\theta_p \leq \theta_p^+$ since θ_p complies with the characteristics to be in the set of which θ_p^+ is the maximum.

$(\Leftarrow)$

Let us consider $\theta_j \geq 0$ with $j = 1 \cdots p - 1$ and $\theta_p \leq \theta_+ p(\theta_1, \ldots \theta_p - 1)$, and suppose that $\theta + p$ is one of the sustainable thresholds, which means that

there is one control $\mu(t)$ and one path $x(t)$ starting from x_0 and satisfying both the dynamics (7) and the constraint $Ip(x, \mu) \geq \theta + p \, \forall t \in (0, t^*)$. Now, as $\theta_p \leq \theta + p$ then $Ip(x, \mu) \geq \theta_p$, hence, $\theta \in \mathscr{U}t^*(x_0)$.

□

3.2 Sustainable Thresholds

3.2.1 One-Dimensional Case

Consider the following Cauchy problem:

$$\begin{cases} \dot{S}(t) = f(S(t), \beta) \\ S(0) = S_0 \\ \beta \in [0, 1] \end{cases} \tag{11}$$

with the condition

$$S(t) \geq \underline{S} > 0 \;\; \forall t \in (0, t^*), \tag{12}$$

and $f(S(t), \beta)$ is the expression given by the system (3) for S. By Definition 3.1, we have that given an initial condition S_0, the set of sustainable thresholds for the problem (11) with restriction (12) is

$$\begin{aligned} \mathscr{U}_{t^*}(S_0) &= \{\underline{S} \mid \exists (S(\cdot), \beta(\cdot)) \;\text{ such that }\; S(t) \geq \underline{S}\} \\ &= \{\underline{S} \mid \exists (S(\cdot), \beta(\cdot)) \;\text{ such that }\; \underline{S} \leq \hat{S}\}. \end{aligned}$$

Since S is decreasing with respect to the β control, the set of sustainable thresholds is given by Proposition 3.3.

Proposition 3.3 *Let S_0 be an initial condition; then,*

$$\mathscr{U}_T(S_0) = (-\infty, \hat{S}]$$

with

$$\hat{S} = \inf_{t \geq 0} S^*(t),$$

and $S^*(t)$ is the solution of the system with the maximum control β.

Proof ($\Leftarrow$)

Let $\underline{S} \in (-\infty, \hat{S}]$; then, $\underline{S} \leq \hat{S}$, a control that maintains this relationship needs to be found. As $0 \leq \beta \leq 1$, if $\beta = 0$ implies that

$$\dot{S}^* = \rho S^* \left(\frac{S^*}{k_2} - 1\right)\left(1 - \frac{S^*}{k_1}\right). \tag{13}$$

Thus, $\hat{S} \leq S^*(t)$ and by hypothesis $\underline{S} \leq \hat{S}$, hence $\underline{S} \leq S^*(t)$, thus $\underline{S} \in \mathscr{U}_{t^*}(S_0)$.

($\Rightarrow$)

Let be $\underline{S} \in \mathscr{U}_{t^*}(S_0)$; then, there is a β such that (11) is satisfied and $\underline{S} \leq S(t)\ \ \forall t \in (0, t^*)$. It is known that $0 \leq \beta \leq 1$, let be $\beta = 0$; then, we have (13), since f is decreasing with respect to the control $S^*(t) \geq S(t)\ \ \forall t \in (0, t^*)$ (Theorem 3.1), and by the assumption $\underline{S} \leq S(t)$, we then conclude $\underline{S} \leq S^*(t)$ consequently $\underline{S} \leq \hat{S}$.

□

3.2.2 Two-Dimensional Case

Consider the system (3) in the form (7)

$$\begin{cases} \dot{L} & = \gamma\left[\alpha_1(1-\beta)^\delta g(L) + \phi\alpha_2\beta LS - \sigma L\right] \\ \dot{S} & = \rho S\left(\frac{S}{k_2} - 1\right)\left(1 - \frac{S}{k_1}\right) - \alpha_2\beta LS \\ & \beta \in [0, 1] \end{cases} \tag{14}$$

with the restrictions

$$L(t) \geq \underline{L} \geq 0\ \ S(t) \geq \underline{S} \geq 0\ \ \forall t \in (0, t^*). \tag{15}$$

Using Proposition 3.2, sustainable thresholds $\mathscr{U}_{t^*}$ are defined. For this, two restrictions are established, one for the level of people and the other for the forestry resource reserve, that is, the restrictions (15).

After that, Definition 3.1 of the set of sustainable thresholds $\mathscr{U}_{t^*}(L_0, S_0)$ is applied for the reserve level of the resource $\underline{S}$ and of people $\underline{L}$ given an initial condition (L_0, S_0).

Definition 3.2 For a given initial condition (L_0, S_0) of the system (14) with constraints (15), we have

$$\mathscr{U}_{t^*}(L_0, S_0) = \{(\underline{L}, \underline{S}) \mid \exists\ \beta(\cdot)\ \text{satisfying dynamics (14) and constraints}$$
$$L(t) \geq \underline{L},\ \ S(t) \geq \underline{S}\ \ \forall t \in (0, t^*)\}.$$

To determine this set, we considered the maximum $\underline{S}$ that can be sustained given $\underline{L}$.

Definition 3.3 Given an initial condition (L_0, S_0) and a minimum reserve level of people $\underline{L}$, $S^+(L_0, S_0, \underline{L})$ is defined as

$$S^{+}(L_0, S_0, \underline{L}) := \max\{\underline{S} \geq 0 \mid \exists\ \beta(\cdot)\ \text{satisfying dynamics (14) and constraints}\ L(t) \geq \underline{L},\ \ S(t) \geq \underline{S}\ \ \forall t \in (0, t^*)\}.$$

Thus, this set is characterized by Proposition 3.4, which is obtained by applying Proposition 3.2 to the system (14).

Proposition 3.4 *Let* (L_0, S_0) *be an initial condition of the system* (14).

$$\mathscr{U}_{t^*}(L_0, S_0) = \{(\underline{L}, \underline{S}) \mid \underline{S} \leq S^{+}(L_0, S_0, \underline{L})\ \ \underline{L} \geq 0\ \ \forall t \in (0, t^*)\}.$$

Proof See the proof of Proposition 3.2. □

Note that a condition for $\underline{L}$ to be a sustainable threshold $\underline{L} \leq L_0$ must be met, since otherwise, from the beginning the sustainability restriction is violated. In addition, there is no control whose associated trajectory is above $\underline{L}$, which is why it is defined $L^{+}(L_0, S_0)$.

Definition 3.4 Let (L_0, S_0) be an initial condition; then,

$$L^{+}(L_0, S_0) = \max\{\underline{L} \geq 0 \mid \exists\ \beta(\cdot)\ \text{such that}\ L(t) \geq \underline{L}\ \ \forall t \in (0, t^*)\}.$$

Numerical simulations in Fig. 1 show that the trajectory $L(t)$ associated to the maximum control $\beta = 1$ is increasing, namely, $L + (L_0, S_0) = L_0$. Now, if trajectory $L(t)$ is increasing for any control $\beta \in [0, 1]$, $L+(L_0, S_0)$ is characterized by Proposition 3.5.

Proposition 3.5 *If an initial condition* (L_0, S_0) *is considered, then*

$$L^{+}(L_0, S_0) = \min_{t \in (0, t^*)} L_{\beta=1}(t).$$

Proof Let be $A = \{\underline{L} \geq 0 \mid \exists\ \beta(\cdot)\ \text{such that}\ L(t) \geq \underline{L}\ \ \forall t \in (0, t^*)\}$.

($\leq$)

Let us suppose that $\underline{L} \in A$. Then, there exists one control $0 \leq \beta \leq 1$ such that $L_\beta \geq \underline{L}$ at any time $t \in (0, t^*)$. Besides, by the monotonity of $L(t)$ we have that $L\beta = 1(t) \geq L\beta \geq \underline{L}$, which implies that the minimum value of the trajectory $L_{\beta=1}(t))$ is greater than or equal to $\underline{L}$, consequently $\min_{t \in (0, t^*)} L_{\beta=1}(t) \geq L^{+}(L_0, S_0)\ \ \forall t \in (0, t^*)$.

($\geq$)

Let be $\underline{L} = \min_{t \in (0, t^*)} L_{\beta=1}(t)$, then there is $\beta = 1$ such that $L_\beta \geq \underline{L}$ and hence by definition, $\underline{L} \in A$, then $\underline{L} \leq \max A$, thus $\underline{L} = \min_{t \in (0, t^*)} L_{\beta=1}(t) \leq L^{+}(L_0, S_0)$.

□

Now, if we consider the restriction for the level of people, by Theorem 3.2, we have that if the dynamics of the system are run with the maximum control, i.e.,

$\beta = 1$, then $L_1(t) \geq \underline{L}\ \ \forall t \in (0, t^*)$ with $0 \leq \underline{L} \leq L^+(L_0, S_0)$, which implies that in the same interval all trajectories $S(t)$ with any other control will be above of the minimum value of the trajectory of S; thus, the maximum level of resource reserve that can be sustained is defined as indicated in Proposition 3.6.

Proposition 3.6 *Let* (L_0, S_0) *be an initial condition, if* $0 \leq \underline{L} \leq L^+(L_0, S_0)$*, then*

$$S^+(L_0, S_0, \underline{L}) = \min_{t \in (0,t^*)} S_{\beta=1}(t).$$

Proof Let be $a = \min_{t \in (0,t^*)} S_{\beta=1}(t)$. Suppose that $L(t) \geq \underline{L}$ at any time $t \in (0, t^*)$ with $0 \leq \underline{L} \leq L^+(L_0, S_0)\}$. Let us see that $S^+(L_0, S_0, \underline{L}) = a$.

$(\leq)$

Suppose $S^+(L_0, S_0, \underline{L})$ is a sustainable threshold, so there is a control $0 \leq \beta \leq 1$ such that the associated trajectory (L_β, S_β) starting at (L_0, S_0) satisfies the system dynamics and the constraints $L_\beta \geq \underline{L}$ and $S_\beta \geq S^+(L_0, S_0, \underline{L})$ at any time $t \in (0, t^*)$. If $\beta = 1$, then $S_1(t) \geq S^+(L_0, S_0, \underline{L})$; particularly, the minimum observed value of the trajectory of $S_1(t)$ meets this restriction in the same interval, thus $S^+(L_0, S_0, \underline{L}) \leq a$.

$(\geq)$

If $0 \leq \beta \leq 1$, consider a control $\beta_1 = 1$ and a $\beta_2 < 1$, then by Proposition 3.1, there is an interval $(0, t^*)$ where two trajectories beginning from the same starting point remain separate and, by Theorem 3.1, the trajectory associated with the greatest control ($\beta = 1$) is less than any other, especially the smallest value of $S(t)$ associated with $\beta_1 = 1$, that is, $\min S_1(t) = a \leq S_{\beta_2}(t)$ in this interval, and hence, it can be said that a is a sustainable threshold, since there is a control, in this case β_2 such that the associated trajectory is above a, and thus, a is less than or equal to the maximum of the set of sustainable thresholds that is $S^+(L_0, S_0, \underline{L})$ (Definition 3.3), consequently $S^+(L_0, S_0, \underline{L}) \geq a$.

□

Proposition 3.7 *If* $\underline{L} > L^+(L_0, S_0)$*, then* $S^+(L_0, S_0, \underline{L}) = 0$.

Proof Let $\underline{L}$ be a value above $L^+(L_0, S_0)$, then $\underline{L}$ is not a sustainable threshold, since by definition, $L^+(L_0, S_0)$ (Definition 3.4) is the maximum of the sustainable thresholds, which implies that for whatever control, there is an instant $t \in (0, t^*)$ at which $L(t) \leq \underline{L}$, and thus there is no such a control that leads to satisfy the restriction for $L(t)$ and $S(t)$ at the time, but by definition, it is considered that always $S(t) \geq 0$ and then $S^+(L_0, S_0) = 0$. □

3.3 Viability: Equilibrium Points

The equilibrium points of a system are viable points [27]. In Sect. (2.3), maximum two equilibria were found where the human population and the natural resource for

the system (14) coexist, and these equilibria are viable as long as they satisfy the viability restrictions (15); thus, the following must be fulfilled:

$$L_i(t) \geq L^+(L_0, S_0) \text{ y } S_i(t) \geq S^+(L_0, S_0, \underline{L}). \tag{16}$$

4 Results

Simulations were performed for parameter values in Table 1; the values are taken from [16]. An initial condition was considered such that the dynamic of L is increasing with respect to the control β.

In Fig. 2, the brown area bounded by $L^+(L_0, S_0)$ and $S^+(L_0, S_0, \underline{L})$ represents the set of thresholds that are sustainable. That is, given an initial condition (L_0, S_0), there is a control β, which makes the trajectory that starts in this condition satisfy the dynamics of the system and the restrictions that these thresholds involve at any time $t \in (0, t^*)$. Specifically, Fig. 2a, b shows the sets of thresholds $\underline{L}$ and $\underline{S}$, considering as initial condition the carrying capacity $S_0 = 12000$ and the initial value of the population $L_0 = 500$ y $L_0 = 1500$, respectively. It is worth noting that, the initial condition for L corresponds to the maximum threshold $L^+(L_0, S_0)$; this is because the trajectory of L with the maximum control is increasing in the interval $(0, t^*)$.

The points that are outside U_{t^*} are thresholds that regardless of the control used, at some point, some of the restrictions given by these thresholds are not satisfied. That is, the trajectory of L is not above $\underline{L}$ and/or the trajectory of S is not above $\underline{S}$.

As a further result, the U_{t^*} was found considering $\alpha_2 = 0.0003$, which means evaluating how an increase in the speed of extraction affects the set of sustainable thresholds. The results are shown in Figs. 2c, d. When comparing these results with those shown in Figs. 2a, b, a decrease of 60.6% in the values of $S^+(L_0, S_0, \underline{L})$ is observed; this is because a higher extraction rate reduces the level of resources available more quickly.

The time t^* during which U_{t^*} is defined is relevant since from that moment the monotonicity of the trajectories of the state variables is not fulfilled. In Fig. 3, it can be seen that this time regardless of the initial conditions is shorter for $L(t)$, which means that the monotonicity of $L(t)$ implies the monotonicity of $S(t)$, which is the result of Theorem 3.2.

Table 1 Parameter values

Parameter	Value	Parameter	Value
		k_2	700
ϕ	3	ρ	0.025
α_1	12.95	γ	0.1
α_2	0.0001	δ	0.7
k_1	12000	σ	1.4

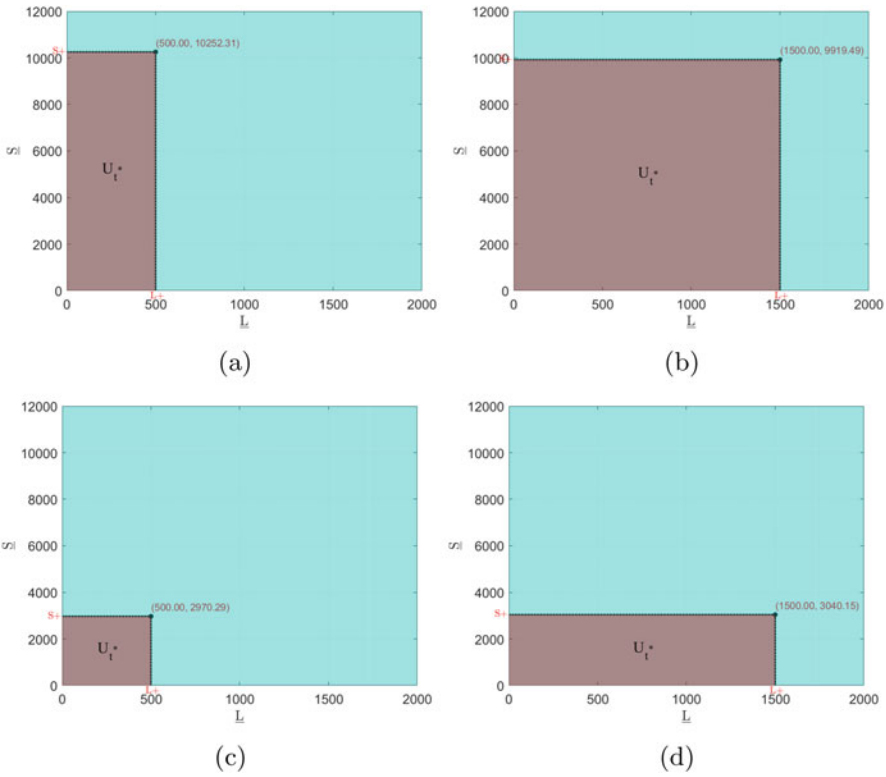

Fig. 2 Sustainable thresholds for different initial conditions in L and $\alpha_2 = 0.0003$

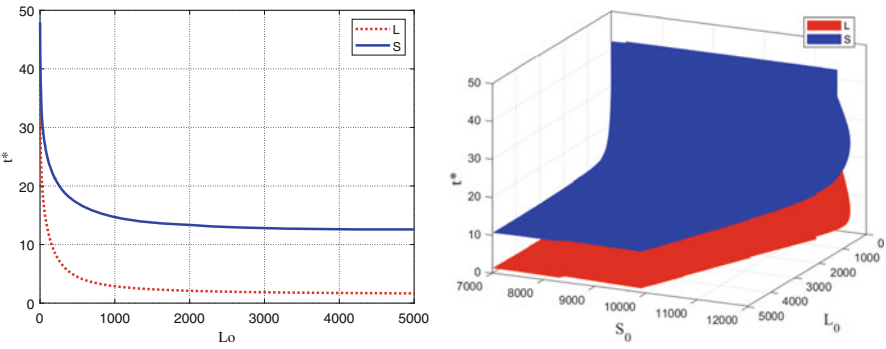

Fig. 3 Instant of time for the first crossing of the L and S trajectories with different initial conditions

With the previous results, we can say that U_{t^*} is sensitive to changes, not only in the values of the system parameters but also to changes in the initial conditions. In Fig. 4, the curve with coordinates $(L_i^+(L_0, S_0), S_i^+(L_0, S_0, \underline{L}))$ for $L_0 \in (0, 5000]$

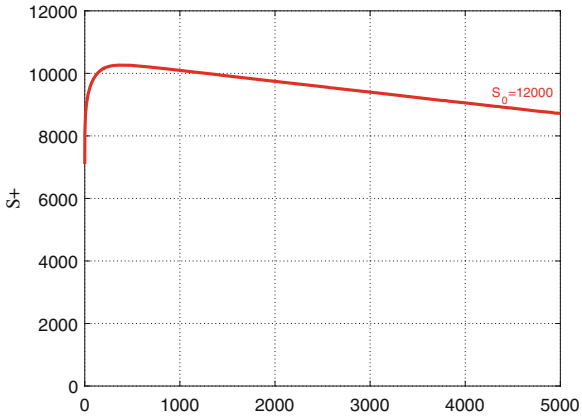

Fig. 4 Maximum sustainable thresholds for different initial conditions L_0

and $S_0 = 12000$ is shown. Taking into account that $L^+(L_0, S_0) = L_0$ because $L(t)$ is increasing with the maximum control, it is observed that the curve has a maximum, which implies that there is an L_0 for which a maximum value of $S^+(L_0, S_0\underline{L})$ is obtained.

5 Discussion: Key Challenges and Ways Forward

From model (3), the internal equilibrium points were found analytically. Additionally, the viability theory was applied to find the sustainable thresholds U_{t^*} that define the conditions of coexistence between humans and renewable resources within a time interval $(0, t^*)$ given an initial state. If the initial condition is an equilibrium point of the system and the trajectory originating there complies with the viability restrictions, it is said that this point is viable.

In literature in general [28, 30–34], the systems have monotonicity at every instant of time, that is, the trajectories do not cross and it is not necessary to calculate t^*. Furthermore, in these papers, it was possible to find a specific expression for sustainable thresholds. The proposal made in this chapter is focused on those models that have monotonic behavior only in the time interval $(0, t^*)$, since there is a crossing of trajectories for different controls. Specifically, we work with a model that represents the pressure that population makes on renewable resources, considering that they are extracted at a certain rate that depends on the labor force (β) involved in the activity. The extraction of these resources allows an increase in the level of population and a decrease in the level of the forestry resource, that is, the dynamics of the population is increasing and that of the resource is decreasing. Additionally, the intensity of the labor force (high β values) enables faster increases for the population and faster decreases for the resource. This means that with maximum control, the maximum trajectory for L and the minimum for S are obtained.

Analytically, the existence of the interval $(0, t^*)$ was demonstrated, in which the monotonicity of L implies the monotonicity of S; this means that the first crossing of trajectories associated with two different controls occurs in L, that is, it is guaranteed that for the same two controls, there is no crossing of the trajectories of S in the same interval.

Numerically, the value of t^* was found showing the existence of the interval and the monotonicity of the trajectories for different configurations in the initial conditions and values of α_2, which is a measure of the efficiency in which the resources are extracted. It was found that t^* is the time in which the trajectory with the maximum control intersects with another, determining the maximum sustainable thresholds $S^+(L_0, S_0, \underline{L})$ and $L^+(L_0, S_0)$ that comply with the restrictions of the system.

In this study, the value of t^* was not considered in the analysis, as it focused mainly on determining the value of sustainable thresholds. However, from practice, it is important to take into account the time during which compliance with the restrictions can be guaranteed, because large sustainable thresholds for a very short time may not be the best option for a decision-maker, but thresholds of moderate size for a long time may be. As a future paper, a viability analysis that integrates the sustainable thresholds U_{t^*} with the value of t^* is proposed.

For future papers, it is proposed to carry out a sensitivity analysis, varying not only the initial conditions but also the parameters of the system other than the β control, which allow to identify the different scenarios given a certain configuration.

It is also proposed to work on the problem for the case in which the dynamics of L is decreasing with respect to the control. This implies rethinking the problem and proposing the theory to define the corresponding sustainable thresholds.

Acknowledgments I. M. Cholo Camargo acknowledges Colciencias for its partial support, under Convocatoria Doctorados Nacionales No. 727 de 2015 Colciencias, and Universidad Nacional de Colombia-Sede Manizales under Convocatoria para el apoyo a la movilidad internacional de la facultad de Ingenieria y Arquitenctura de la Universidad Nacional de Colombia, Sede Manizales–Vigencia 2019.

References

1. Ostrom, E., Gardner R., Walker J., and Walker J. Rules, games, and common-pool resources. University of Michigan Press, (2014).
2. Saunders, F. P. The promise of common pool resource theory and the reality of commons projects. International Journal of the Commons, 8(2), 636656.(2014).
3. Pulver, S., Ulibarri, N., Sobocinski, K. L., Alexander, S. M., Johnson, M. L., McCord, P. F., & Dell'Angelo, J. Frontiers in socio-environmental research, *Ecology and Society*, 23(3).(2018).
4. Vatn, A., Bakken, L., Botterweg, P., & Romstad, E. ECECMOD: an interdisciplinary modelling system for analyzing nutrient and soil losses from agriculture. *Ecological Economics*, 30(2), 189–206.(1999).
5. Filatova, T., Polhill, J. G., & Van Ewijk, S. Regime shifts in coupled socio-environmental systems: review of modelling challenges and approaches. *Environmental Modelling & Software*, 75, 333–347.(2016).

6. Fikret, Berkes, Carl Folke, and Johan Colding. “Linking social and ecological systems: management practices and social mechanisms for building resilience.” (2000).
7. Innes, C., Anand, M. & Bauch, C. The impact of human-environment interactions on the stability of forest-grassland mosaic ecosystems. *Sci* Rep 3, 2689 (2013).
8. Ostrom, E. Challenges and growth: The development of the interdisciplinary field of institutional analysis. *Journal of Institutional Economics*, 3(3), 239–264.(2007).
9. Ostrom, E. A general framework for analyzing sustainability of social-ecological systems. *Science*, 325(5939), 419–422.(2009).
10. Busch J and Ferretti-Gallon K, What drives deforestation and what stops it? A meta-analysis. *Rev. Environ. Econ. Policy* 11 323. (2017)
11. Baccini, A., Walker, W., Carvalho, L., Farina, M., Sulla-Menashe, D., & Houghton, R. A. Tropical forests are a net carbon source based on aboveground measurements of gain and loss. *Science*, 358(6360), 230–234.(2017).
12. Song X P, Hansen M C, Stehman S V, Potapov P, V, Tyukavina A, Vermote E F and Townshend J R Global land change from 1982 to 2016*Nature* 560 63943, (2018).
13. Sigdel, R., Anand, M. and Bauch, C.T. Convergence of socio-ecological dynamics in disparate ecological systems under strong coupling to human social systems. *Theor Ecol* 12, 285296 (2019).
14. Solow, Robert M., “Neoclassical growth theory,” Handbook of Macroeconomics, in: J. B. Taylor & M. Woodford (ed.), Handbook of Macroeconomics, edition 1, volume 1, chapter 9, pages 637–667, Elsevier (1999).
15. James Brander and M. Scott Taylor, The Simple Economics of Easter Island: A Ricardo-Malthus Model of Renewable Resource Use, *American Economic Review*, 88, (1), 119–38, (1998)
16. S. D’Alessandro. Non-linear dynamics of population and natural resources: the emergence of different patterns of development. *Ecological Economics*, vol.62, pp. 473–481 (2007).
17. Nagase, Y. and Uehara, T. Evolution of population-resource dynamics models. *Ecological Economics*, 72, 9–17. (2011).
18. Taylor, M.S. Innis Lecture: Environmental crises: past, present, and future. *Canadian Journal of Economics/Revue canadienne d’conomique*, 42(4), pp.1240–1275.(2009.)
19. Angulo, Fabiola and Olivar, Gerard and Osorio, A and Velásquez, Luz S. Nonlinear dynamics and bifurcation analysis in two models of sustainable development. *Revista Internacional Sostenibilidad, Tecnologia y Humanismo*, (4), pp. 41–46 (2009).
20. Ming-Chun, Zhou and Zong-Yu, Liu. Hopf bifurcation in a Ricardo-Malthus model. *Applied Mathematics and Computation*, vol.217, pp. 2425–2432 (2010).
21. J. A. Amador, G. Olivar and F. Angulo. Smooth and Filippov models of sustainable development: Bifurcations and numerical computations. Differential Equations and Dynamical Systems, 21(1):173184 (2013).
22. J. A. Amador. Escenarios prospectivos de sostenibilidad en la coop-eracin entre comunidades rurales: an álisis de bifurcaciones y sistemas de Filippov. PhDthesis, Universidad Nacional de Colombia-Sede Manizales, (2019)
23. Cury, P. M., Mullon, C., Garcia, S. M., & Shannon, L. J. Viability theory for an ecosystem approach to fisheries. *ICES journal of marine science*, 62(3), 577–584.(2005).
24. Doyen, L., Armstrong, C., Baumgrtner, S., Bn, C., Blanchard, F., Ciss, A. A., . . . & Gourguet, S. From no whinge scenarios to viability tree. *Ecological Economics*, 163, 183–188.(2019).
25. M. B. Schaefer. Some aspects of the dynamics of populations important to the management of the commercial marine fisheries. *Bulletin of Mathematical Biology*, 53(1):253 279 (1991).
26. I.M. Cholo Camargo, G. Olivar Tost and I. Dikariev. Bifurcations in a Mathematical Model for Study of the Human Population and Natural Resource Exploitation. In: Mondaini R. (eds) Trends in Biomathematics: Mathematical Modeling for Health, Harvesting, and Population Dynamics. *Springer, Cham* (2019).
27. M. De Lara and L. Doyen. Sustainable Management of Natural Resources Mathematical Models and Methods. *Environmental Science and Engineering*, Allan, R., Forstner, U., Salomons, W., Ed. Berlin (2008).

28. E. Barrios, P. Gajardo and O. Vasilieva. Sustainable thresh-olds for cooperative epidemiological models. *Mathematical Biosciences*. 302:9–18 (2018).
29. R. M. Solow. Intergenerational equity and exhaustible resources.*The Review of Economic Studies*, 41:2945 (1974).
30. V. Martinet and L. Doyen. Sustainability of an economy with an exhaustible resource: A viable control approach. *Resource and Energy Economics*,29(1):17–39 (2007).
31. P. Gajardo, M. Olivares and C. H. Ramirez. Methods for the sustainable rebuilding of overexploited natural resources. *Environmental Modeling & Assessment*, 23(6):713727 (2018).
32. P. Gajardo and C. Hermosilla. Pareto fronts of the set of sustainable thresholds for constrained control systems. *Applied Mathematics & Optimization* (2019).
33. V. Martinet. A characterization of sustainability with indicators. *Journal of Environmental Economics and Management*, 61(2):183 - 197 (2011).
34. L. Doyen and Martinet, V. Maximin, Viability and sustainability. *Journal of Economic Dynamics and Control*, 36(9):1414 1430 (2012).

Modeling Covid-19 Considering Asymptomatic Cases and Avoided Contacts

Iulia Martina Bulai

1 Introduction

World Health Organization (WHO) defined coronaviruses (CoV) as a large family of viruses that cause illness ranging from the common cold to more severe diseases such as Middle East Respiratory Syndrome (MERS-CoV) and Severe Acute Respiratory Syndrome (SARS-CoV). The novel coronavirus (SARS-CoV-2) is a new strain that has not been previously identified in humans. Coronaviruses are zoonotic, meaning they are transmitted between animals and people, [1].

In this chapter we introduce a mathematical model, a modified version of an SIR (Susceptible-Infected-Recovered) model, which describes the dynamics in time of Covid-19. One of the novelties of this model is that it considers both symptomatic and asymptomatic cases. Several studies showed the importance of asymptomatic individuals in SARS-CoV-2 transmission, e.g., [2]–[5]. Other diseases such as malaria can be asymptomatic, in [6]–[8] can be seen some of the mathematical models that include also the asymptomatic cases. Here we model the dynamics of four different classes of individuals. First the healthy individuals that coincide with susceptible; we assume that at the beginning of the epidemics no immunity is present. Then the infected individuals are divided in two different groups, those that do not present any symptoms, asymptomatic individuals, and those with symptoms, symptomatic individuals. And finally the recovered individuals that get the immunity to the disease. The total population number, in this case of Italy, is

Member of the research group GNCS of INdAM.

I. M. Bulai (✉)
Department of Mathematics, Informatics and Economics, University of Basilicata, Potenza, Italy
e-mail: iulia.bulai@unibas.it

R. P. Mondaini (ed.), *Trends in Biomathematics: Chaos and Control in Epidemics, Ecosystems, and Cells*, https://doi.org/10.1007/978-3-030-73241-7_11

assumed constant since we consider the scenario at the beginning of the epidemics and for a short interval of time.

This is a predictive model, and we look at different scenarios; first of all assuming any prevention to avoid the diffusion of the virus is taken and secondly different scenarios where precautionary measures to avoid contact between individuals are taken, such as quarantine and social distancing. We consider a measure to contain the disease already studied for a predator–prey system with the disease in the prey population, [9], assuming that the infection rate can be decreased avoiding contacts between preys (people in our case). Notice that we do not consider the exposed class since the infected individuals can infect even before developing symptoms, while asymptomatic, (or presymptomatic as defined in [3]).

The overview of the chapter is as follows: In the next section we introduce the mathematical model, the assumptions that were made to build the model and the parameter values considered to study the model. In Sect. 3 we did a qualitative analysis of the model, studying the equilibrium points and their stability, and furthermore we analyzed the dependence of the basic reproduction number from the parameter values that define it. In Sect. 4 the results are reinforced by numerical simulations and biological interpretation of the obtained results. Last we conclude the chapter with discussing the obtained results.

2 Model Formulation

In this section we introduce the novel mathematical model that describes the interactions between healthy and SARS-CoV-2 infected individuals, and finally the parameters of the model.

2.1 The Mathematical Model

We build a fourth dimensional nonlinear mathematical model describing the interaction and evolution in time of healthy individuals (susceptible), denoted by H; SARS-CoV-2 virus infected individuals that present symptoms, denoted by S; SARS-CoV-2 virus infected individuals without any symptoms, denoted by A; and recovered individuals denoted by R. We assume that once the individuals recover they get the immunity for the disease. N is the total population that we assume constant since we consider the beginning of the epidemics and a short interval of time (several months).

We consider the mathematical model:

$$\frac{dH}{dt} = \Omega - \beta \frac{H(A+S)}{N} - \mu_N H, \tag{1}$$

$$\frac{dA}{dt} = \phi\beta\frac{H(A+S)}{N} - \gamma_A A - \mu_N A - \delta A,$$
$$\frac{dS}{dt} = (1-\phi)\beta\frac{H(A+S)}{N} - \gamma_S S - \mu_N S + \delta A - \mu_S S,$$
$$\frac{dR}{dt} = \gamma_A A + \gamma_S S - \mu_N R,$$

where the infection rate can be written as $\beta = \lambda(1-\psi)$, where the fraction $0 \leq \psi \leq 1$ of avoided contacts is introduced. This term is given from assuming a more realistic situation where the rate of contacts between infected and susceptible individuals gets reduced, in case prevention measures are taken by the individuals, to avoid contagion.

The first equation of (1) describes the evolution in time of healthy individuals (susceptible), Ω represent birth/immigration, and μ_N is the mortality rate due to other causes than Covid-19. The susceptible individuals can be infected at rate β; this newly infected individuals can become asymptomatic (probability ϕ) or symptomatic (probability $1-\phi$). We assume that asymptomatic and symptomatic can recover at rate γ_A and γ_S, respectively.

The second equation describes the asymptomatic population; they get infected as described earlier, recover at rate γ_A, and die at rate μ_N. We suppose that the asymptomatic individuals can also develop symptoms and become symptomatic; this happens at rate δ.

The third equation describes the symptomatic individuals; notice that differently from the asymptomatic individuals the symptomatic individuals have an extra mortality rate due to Covid-19 disease, μ_S.

The fourth and last equation describes the dynamics in time of the recovered population.

2.2 Parameter Values

In Table 1 are described the parameters of system (1) and the values that can be assumed.

3 Qualitative Analysis of the Model

In this section we compute the basic reproduction number for the introduced model (1), and analyze how we can change depending on the parameters that define it; in particular we focus our attention on all the parameters related with the disease, excluding the parameters related to demography, (N, Ω and μ_N). Notice that here we will not focus on the value of R_0 since it can depend on the population structure

Table 1 Parameters of the model for data considering Italy

Parameters	Name	Value	Unit
N	Total population	60.36×10^{6}[a]	human
Ω	Birth and immigration	633780[b]	human/day
λ	Infection rate	0.292[c]	day^{-1}
ψ	Fraction of avoided contacts	test	pure number
ϕ	Prob. of undergoing asympt. infection	0.5[d]	pure number
γ_A	Per capita recovery rate A	0.028	day^{-1}
γ_S	Per capita recovery rate S	0.028[e]	day^{-1}
μ_N	Mortality rate due to other causes	0.0105[a]	day^{-1}
δ	Transition from $A \to S$	0.067[d]	day^{-1}
μ_S	Mortality rate due Covid-19	0.0069[e]	day^{-1}

[a] [11] (ISTAT 2018)
[b] Ω was chosen such that $H(0) \simeq \Omega/\mu_N$
[c] [10]
[d] [4]
[e] Fitted using data from [12]

of the model, on the assumptions about demographic dynamics as well as on the critical model parameters, as described in [13]. Secondly we find the equilibrium points of the model, the coexistence equilibrium, and the disease free equilibrium (DFE), respectively, and we analyze their stability.

3.1 Basic Reproduction Number R_0

For the sake of simplicity, without the losing of generality, we consider a new version of model (1), with $a = \gamma_A + \mu_N + \delta > 0$ and $b = \gamma_S + \mu_S + \mu_N > 0$:

$$\begin{aligned}
\frac{dH}{dt} &= \Omega - \beta \frac{H(A+S)}{N} - \mu_N H, \\
\frac{dA}{dt} &= \phi\beta \frac{H(A+S)}{N} - aA, \\
\frac{dS}{dt} &= (1-\phi)\beta \frac{H(A+S)}{N} - bS + \delta A, \\
\frac{dR}{dt} &= \gamma_A A + \gamma_S S - \mu_N R.
\end{aligned} \tag{2}$$

The basic reproduction number, R_0, is "the expected number of secondary cases produced, in a completely susceptible population, by a typical infective individual," (e.g., [14]). The importance of R_0 in the spreading of a disease is related to its value. The ideal scenario is $R_0 < 1$; in this case the infection cannot grow. This means that

on average an infected individual produces less than one new infected individual over the course of its infectious period. Conversely if $R_0 > 1$, the disease spreads over the population; in fact each infected individual produces, on average, more than one new infection. We compute the basic reproduction number using the next generation matrix technique (for a detailed description of the method see [14, 15]), and we get

$$R_0 = \frac{\lambda(1-\psi)\Omega}{\mu_N N a b}\left(a(1-\phi) + \phi(b+\delta)\right), \tag{3}$$

where we used that $\beta = \lambda(1-\psi)$. R_0 can be explained in the following way: an infected person stays in the symptomatic (asymptomatic) class for an averaged time $1/(ab)$ $(1/a)$. During this time a symptomatic (asymptomatic) person infects $\lambda(1-\psi)$ persons per unit time.

To understand the importance of the parameters on the value of the basic reproduction number R_0 we can analyze the variation of it assuming that the parameter values change; this can be seen computing the quantities $\partial R_0/\partial p_i$, with $p_i = \lambda, \psi, \phi, \gamma_A, \gamma_S, \delta$ and μ_S:

$$\frac{\partial R_0}{\partial \lambda} = \frac{(\mu_N + (1-\phi)\gamma_A + (\gamma_S + \mu_S)\phi + \delta)(1-\psi)\Omega}{\mu_N N a b} > 0$$

$$\frac{\partial R_0}{\partial \psi} = -\frac{\lambda\Omega(\mu_N + (1-\phi)\gamma_A + (\gamma_S + \mu_S)\phi + \delta)}{\mu_N N a b} < 0$$

$$\frac{\partial R_0}{\partial \phi} = \frac{\lambda\Omega(1-\psi)(\mu_S - \gamma_A + \gamma_S)}{\mu_N N a b}$$

$$\frac{\partial R_0}{\partial \gamma_A} = -\frac{\lambda\Omega(1-\psi)\phi(b+\delta)}{\mu_N N a^2 b} < 0$$

$$\frac{\partial R_0}{\partial \gamma_S} = \frac{\partial R_0}{\partial \mu_S} = -\frac{\lambda\Omega(1-\psi)((1-\phi)\mu_N + (1-\phi)\gamma_A + \delta)}{\mu_N N a b^2} < 0$$

$$\frac{\partial R_0}{\partial \delta} = \frac{\lambda\Omega(1-\psi)(\gamma_A - \gamma_S - \mu_S)\phi}{\mu_N N a^2 b}.$$

Summing up, we get that R_0 increases increasing the infection rate, λ, increases increasing the probability of undergoing asymptomatic infection ϕ or the rate to show symptoms once infected, δ assuming $(\gamma_A - \gamma_S - \mu_S) > 0$ and vice versa decreases if this expression does not hold, while R_0 decreases increasing all the other parameters: fraction of avoided contacts, ψ, per capita recovery rate of asymptomatic individuals, γ_A, per capita recovery rate of symptomatic individuals, γ_S, or the mortality rate due to the disease, μ_S respectively.

3.2 Equilibrium Points and Their Stability

We find two equilibrium points of (2), the disease free equilibrium (DFE) $E_0 = (\Omega/\mu_N, 0, 0, 0)$ and the coexistence equilibrium $E^* = (H^*, A^*, S^*, R^*)$. The analytical expression of the coexistence equilibrium can be obtained following the next steps:

- From the first equation of (2) we get

$$H^* = \frac{\Omega N}{\mu_N N + \beta A + \beta S},$$

  that is always positive.
- We substitute H^* in the second and third equations of (2), and then we solve the second equation in S, and we get

$$S^* = \frac{-A\left[a\mu_N N + \beta(aA - \Omega\phi)\right]}{(aA - \Omega\phi)\beta}.$$

- We substitute S^* in the third equation of (2) and we get A

$$A^* = \frac{\phi\left[\Omega\beta(a(1-\phi) + \phi(b+\delta)) - \mu_N Nab\right]}{\beta a\left[a(1-\phi) + \phi(b+\delta)\right]},$$

  for the feasibility of A^*, $\Omega\beta\left[a(1-\phi) + \phi(b+\delta)\right] - \mu_N Nab > 0$ must hold. Notice that this is equivalent of asking $R_0 > 1$.
- Last we substitute A^* and S^* in the last equation and we get

$$R^* = \frac{A^*\gamma_A + S^*\gamma_S}{\mu_N},$$

  which is always feasible.

We get

$$H^* = \frac{Nab}{\beta[a(1-\phi) + \phi(b+\delta)]} > 0$$

and

$$S^* = \frac{[a(1-\phi) + \delta\phi]\left[\Omega\beta[a(1-\phi) + \phi(b+\delta)] - \mu_N Nab\right]}{\beta ab\left[a(1-\phi) + \phi(b+\delta)\right]}$$

is feasible if $R_0 > 1$. Under appropriate assumptions the DFE is stable if $R_0 < 1$ and unstable if $R_0 > 1$, see [15] for more details. This can be shown evaluating the Jacobian in E_0 and computing the characteristic polynomial. In fact we get

$$J = \begin{bmatrix} -\beta(A+S)/N - \mu_N & -\beta H/N & -\beta H/N & 0 \\ \phi\beta(A+S)/N & \phi\beta H/N - a & \phi\beta H/N & 0 \\ (1-\phi)\beta(A+S)/N & (1-\phi)\beta H/N + \delta & (1-\phi)\beta H/N - b & 0 \\ 0 & \gamma_A & \gamma_S & -\mu_N \end{bmatrix} \tag{4}$$

then the characteristic polynomial corresponding to the DFE is

$$p_0(\mu) = \left[\mu_N N\mu^2 + (\mu_N N(a+b) - \Omega\beta)\mu + \mu_N Nab - \Omega\beta(a(1-\phi) + \phi(b+\delta))\right] \\ (\mu_N + \mu)(\mu_N + \mu) \tag{5}$$

which has a negative root $\mu = -\mu_N$ with double multiplicity, while the other two roots are negative if $R_0 < 1$ and $\mu_N N(a+b) - \Omega\beta > 0$. In an analogous way we can compute the characteristic polynomial $p_*(\mu)$ given evaluating the Jacobian matrix (4) at the coexistence equilibrium. One eigenvalue is $\mu = -\mu_N$, while the other three can be found solving a three degree polynomial in μ, not reported here.

4 Numerical Simulations and Biological Interpretation of the Results

In this section we deepen the importance of the parameters values on the outcome of the model, in particular we plot the density of susceptible, asymptomatic, symptomatic, and recovered individuals. First we consider the transition phase of the model, choosing the integration time $t = 100$ days (Figs. 1, 3, 5) and secondly the coexistence or the disease free equilibrium reach the stability, for $t = 1000$ days (Figs. 2, 4, 6) respectively. These simulations are made varying two parameters at the same time in the grid [0, 1], the couple of parameters represented here are (λ, ψ), (λ, ϕ), and (λ, γ_A), respectively.

From Figs. 1 and 2 it is obvious the importance of the parameter ψ, fraction of avoided contacts, that in practice can be represented by social measures such as lockdown, social distancing, and wearing masks. For values of the infection rate close to zero ($\leq$0.044) the fraction of avoided contacts is not relevant since the DFE is stable while for values of the infection rate above this value the DFE stability can be reached only if the fraction of avoided contacts is different than zero (see Fig. 1). Another important observation is about the fact that both the infection rate and the

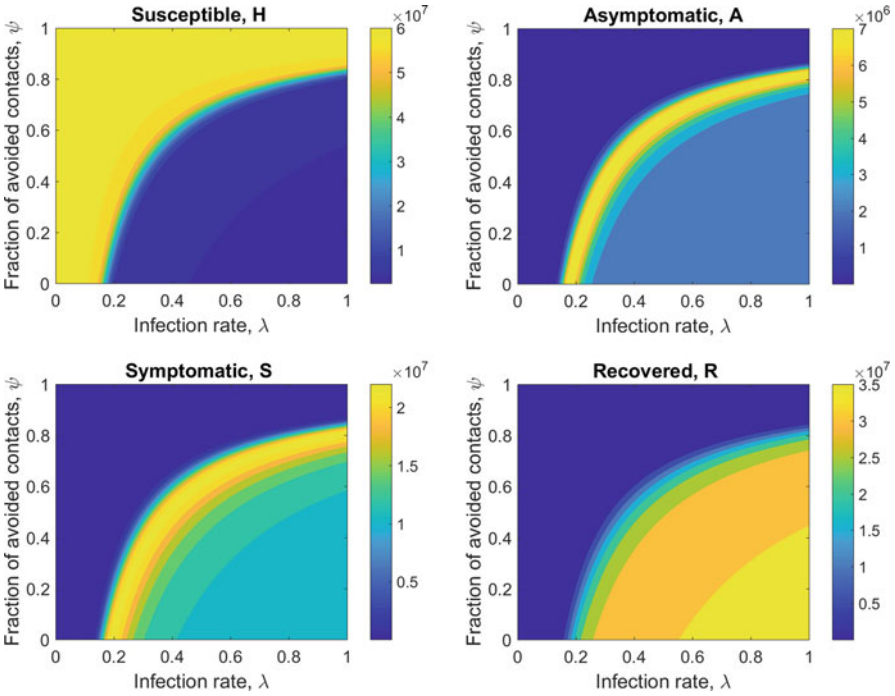

Fig. 1 Density of susceptible, asymptomatic, symptomatic, and recovered individuals, in the transition phase of the model, varying two parameters at the same time in the grid $[0, 1]$, (λ, ψ). The parameter values are as in the Table 1 while integration time $t = 100$ days. Initial conditions $H(0) = 60 \times 10^6$, $A(0) = 171$, $S(0) = 50$, $R(0) = 0$

fraction of avoided contacts have an important effect on the peak of the epidemics, in particular on the value of the maximum of the peak and on the time when is reached (see Fig. 1).

From Figs. 3 and 4 it can be seen that if the infection rate is small enough, the DFE is stable independently on the value of the probability of undergoing asymptomatic ϕ, while for values of $\lambda > 0.044$ increasing ϕ leads to an increase in the asymptomatic population and a decrease in the symptomatic, respectively (see Fig. 4). This is quite an intuitive result. However the density of susceptible and recovered individuals does not change significantly changing the value of the probability of undergoing asymptomatic. Furthermore another interesting result is that the value of ϕ affects the maximum value of the peak of symptomatic and asymptomatic individuals but not the time at which it is reached (here around sixtieth day), see Fig. 3.

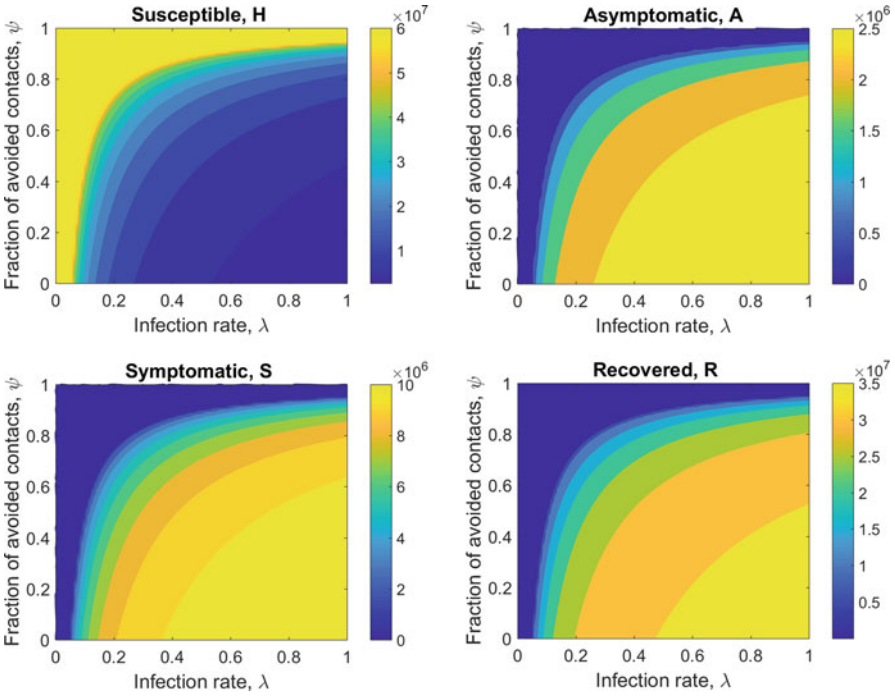

Fig. 2 Density of susceptible, asymptomatic, symptomatic, and recovered individuals, at the stability phase of the coexistence or disease free equilibrium, varying two parameters at the same time in the grid [0, 1], (λ, ψ). The parameter values are as in the Table 1 while integration time $t = 1000$ days. Initial conditions $H(0) = 60 \times 10^6$, $A(0) = 171$, $S(0) = 50$, $R(0) = 0$

Another important parameter in our analysis is the recovery rate of asymptomatic individuals, γ_A, for now little is known about it. Once more from Figs. 5 and 6 it can be seen that the DFE is stable for values of λ close to zero, independently of γ_A, while for values of λ close to 0.292 (the value from Table 1), increasing γ_A leads to an increase in the density of symptomatic population and a decrease in the density of asymptomatic population, while the density of susceptible and recovered individuals is not much affected by this parameter, see Fig. 6. Furthermore from Fig. 5 it can be seen that increasing the recovery rate of asymptomatic individuals impacts both peaks (of symptomatic and asymptomatic, respectively); in particular the maximum value of the peaks decreases and the time when it is reached is shifted to the right.

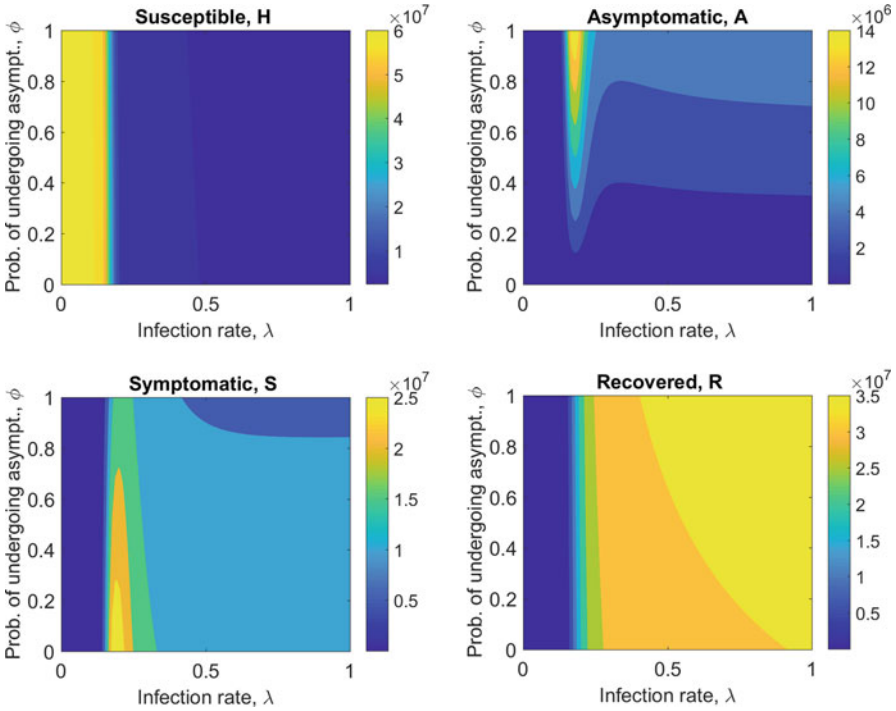

Fig. 3 Density of susceptible, asymptomatic, symptomatic, and recovered individuals, in the transition phase of the model, varying two parameters at the same time in the grid $[0, 1]$, (λ, ϕ). The parameter values are as in the Table 1 while integration time $t = 100$ days. Initial conditions $H(0) = 60 \times 10^6$, $A(0) = 171$, $S(0) = 50$, $R(0) = 0$

5 Discussion of the Results

In this chapter we have introduced a four dimensional ordinary differential system describing the interaction between individuals susceptible to SARS-CoV-2, infected with symptoms and without symptoms, respectively, and individuals recovered from the infection. We focused our attention on the basic reproduction number and how it depends on the parameter values of the model. Six of the parameter values can be found from literature, two of them are obtained by fitting real data, and the remaining ones are used as test parameter values and can give us a better understanding of the model. Little is known about the asymptomatic infections, for that reason we chose to use the fraction of avoided contacts and the recovery rate of asymptomatic individuals as tests (unknown). From the basic reproduction

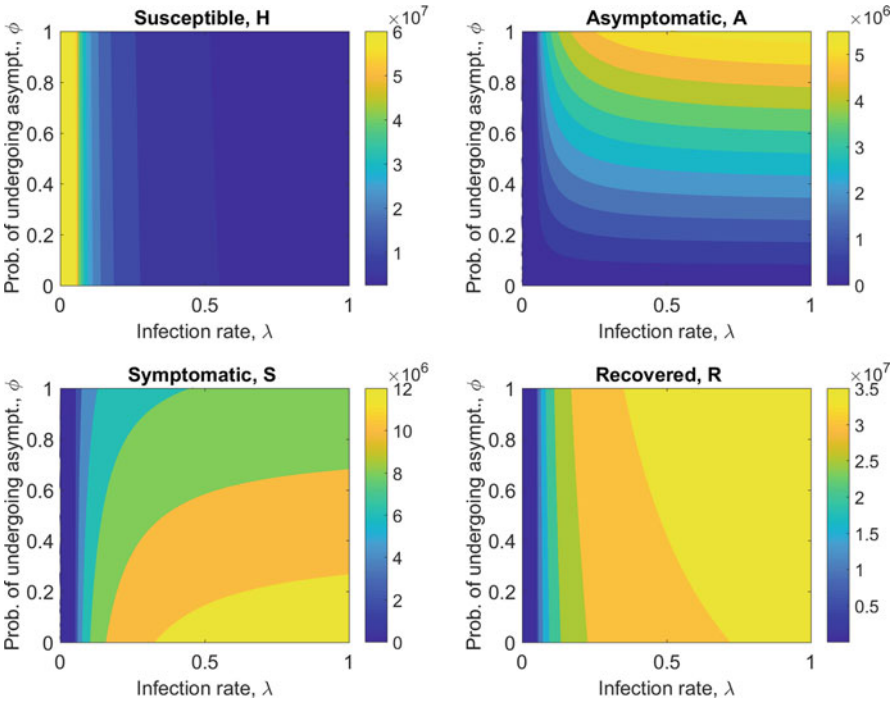

Fig. 4 Density of susceptible, asymptomatic, symptomatic, and recovered individuals, at the stability phase of the coexistence or disease free equilibrium, varying two parameters at the same time in the grid [0, 1], (λ, ϕ). The parameter values are as in the Table 1 while integration time $t = 1000$ days. Initial conditions $H(0) = 60 \times 10^6$, $A(0) = 171$, $S(0) = 50$, $R(0) = 0$

number analysis it can be seen that increases increasing the infection rate while decreases increasing the fraction of avoided contacts, or per capita recovery rate of asymptomatic individuals, or per capita recovery rate of symptomatic individuals, or the mortality rate due to the disease, respectively. More interestingly the probability of undergoing asymptomatic infection or the rate to show symptoms once infected can both increase or decrease the value of the basic reproduction number depending on the values that the mortality rate due to the infection, the recovery rate of symptomatic and asymptomatic individuals assume.

We can conclude that (i) avoiding contacts is important in the spreading of the disease (in practice it can be applied using social distancing and/or quarantine for the infected individuals, and/or using face masks), with concrete results on the maximum value of the peak and the time when occurs. (ii) The transition from the asymptomatic class to the symptomatic one has a positive impact on the disease

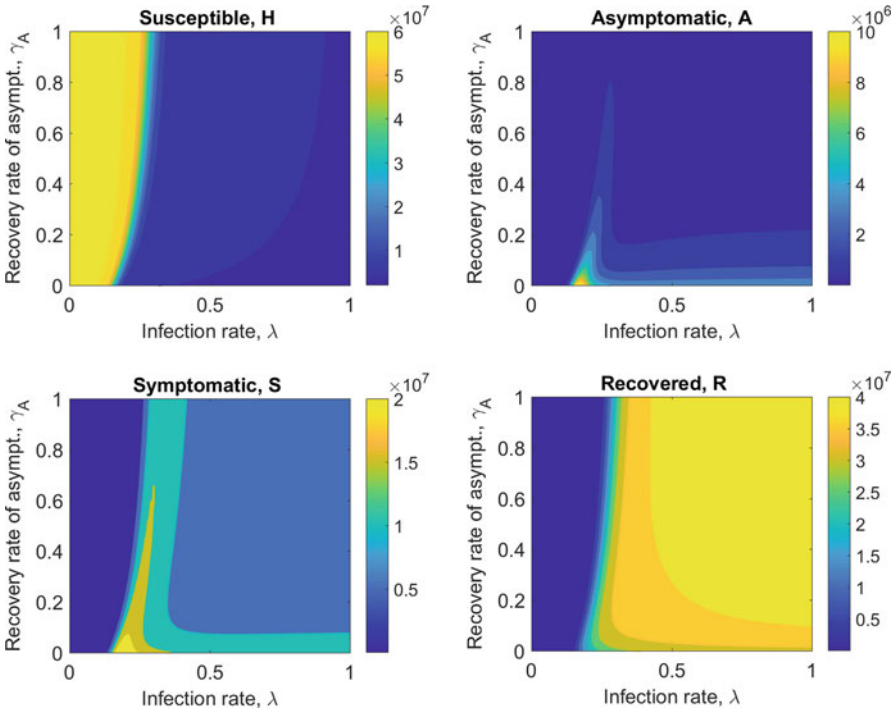

Fig. 5 Density of susceptible, asymptomatic, symptomatic, and recovered individuals, in the transition phase of the model, varying two parameters at the same time in the grid $[0, 1]$, (λ, γ_A). The parameter values are as in the Table 1 while integration time $t = 100$ days. Initial conditions $H(0) = 60 \times 10^6$, $A(0) = 171$, $S(0) = 50$, $R(0) = 0$

(meaning that leads to the disease free equilibrium case) only if the recovery rate of the asymptomatic individuals is smaller than the sum between the mortality rate due to the disease and the recovery rate of the symptomatic individuals. In practice, this means that if the asymptomatic individuals have a recovery rate smaller (need more days to recover) than the symptomatic ones, then it would be much easier to get the disease free equilibrium if more asymptomatic individuals show symptoms. (iii) The opposite reasoning as at the previous point holds for the probability of undergoing asymptomatic.

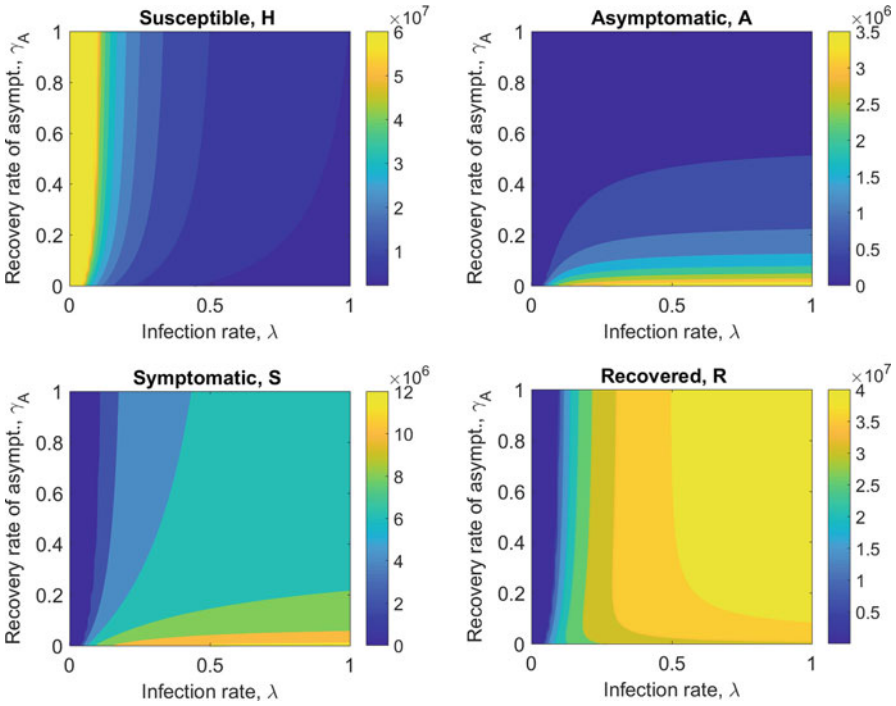

Fig. 6 Density of susceptible, asymptomatic, symptomatic, and recovered individuals, at the stability phase of the coexistence or disease free equilibrium, varying two parameters at the same time in the grid [0, 1], (λ, γ_A). The parameter values are as in the Table 1 while integration time $t = 1000$ days. Initial conditions $H(0) = 60 \times 10^6$, $A(0) = 171$, $S(0) = 50$, $R(0) = 0$

Acknowledgments This work was supported by MIUR through PON-AIM Linea 1 (AIM1852570-1) and by Research Grant "Finanziamento giovanni ricercatori" 2020/2021 GNCS to I.M.B.

References

1. https://www.who.int/health-topics/coronavirus.
2. Y. Bai, L. Yao, T. Wei, F. Tian, D.Y. Jin, L. Chen, et al, *Jama.* , 2020. https://doi.org/10.1001/jama.2020.2565.
3. X. He, E.H.Y Lau, P. Wu, X. Deng, J. Wang et al, *Nature Medicine* , 2020. https://doi.org/10.1038/s41591-020-0869-5.
4. National Institute of Infectious Diseases Japan. Field Briefing: Diamond Princess COVID- 19 Cases, 20 Feb Update. Last accessed March 12, 2020. Available from: https://www.niid.go.jp/niid/en/2019-ncov-e/9417-covid-dp-fe-02.html.
5. D. Cereda, et al, *arXiv*, **The early phase of the COVID-19 outbreak in Lombardy, Italy** 2020.
6. S. Mandal, R.R. Sarkar, S. Sinha *Malaria J*, 10(1) :202, 2011.

7. S.E. Kern et al. *Malaria J*, 10(1) :210, 2011.
8. I.M. Bulai, S. Depickre, V.H. Sanches *Journal of Biological Systems*, 28(01), 167–182, 2020.
9. I.M. Bulai, R. Cavoretto, B. Chialva, D. Duma, E. Venturino, *Nonlinear Dynamics* , 79, 1881–1900, 2015.
10. M.G. Pedersen, M. Meneghini, **Quantifying undetected COVID-19 cases and effects of containment measures in Italy**, [Preprint]. https://doi.org/10.13140/RG.2.2.11753.85600 (2020).
11. https://www.istat.it/storage/rapporto-annuale/2018/Rapportoannuale2018.pdf.
12. https://raw.githubusercontent.com/pcm-dpc/COVID-19/master/dati-json/dpc-covid19-ita-andamento-nazionale.json
13. P.L. Delamater, E.J. Street, T.F. Leslie, Y. Yang, K.H. Jacobsen, *Emerg Infect Dis*, 2019, 25(1):1–4.
14. O. Diekmann, J.A.P. Heesterbeek, J.A.J. Metz, *J. Math. Biol.*, 28 (1990) 365.
15. P. Van den Driessche, J. Watmough, *Math Biosci*, 180(1):29–48, 2002.

On the Stability of Periodic Solutions of an Impulsive System Arising in the Control of Agroecosystems

Youcef Belgaid, Mohamed Helal, Abdelkader Lakmeche, and Ezio Venturino

1 Introduction

Natural resources are being depleted nowadays at a fast rate. In agriculture, the use of synthetic fertilizers in the past several decades has brought two different types of problems. On one side, the poisoning of the environment, for which for instance DDT has been banned as a pest control since many years, but in any case after causing several problems in the environment. On the other hand, the insects in time tend to develop resistance to the pesticides used, by suitable mutations, which in turn generate the need of devising new poisons for their combat. An alternative to the widespread use of pesticides is to try to control pests via organic means, using for instance specific predators or parasitoids of the involved crop pests in the terrestrial ecosystems.

Wise et al. [20–22] proposed the spider as a model terrestrial predator and specified that some spider families differ so much in how they forage and utilize their surroundings . From a point of view, it can be assessed that the spiders frequently face a shortage of prey in nature. Confronted with prey shortages, the wandering spiders search for more productive microhabitats. Many wandering spiders, in fact, select microhabitat on the basis of prey abundance [6, 9, 16, 17].

Ezio Venturino is the member of the INdAM research group GNCS.

Y. Belgaid · M. Helal · A. Lakmeche
Laboratory of Biomathematics, Univ. Sidi Bel Abbès, Sidi Bel Abbès, Algeria
e-mail: y.belgaid@univ-chlef.dz; mohamed.helal@univ-sba.dz; abdelkader.lakmeche@univ-sba.dz

E. Venturino (✉)
Dipartimento di Matematica “Giuseppe Peano”, Università di Torino, Torino, Italy
e-mail: ezio.venturino@unito.it

R. P. Mondaini (ed.), *Trends in Biomathematics: Chaos and Control in Epidemics, Ecosystems, and Cells*, https://doi.org/10.1007/978-3-030-73241-7_12

Most agroecosystems provide no permanent habitats for many species. Hence, for the thriving of the latter, the presence of refuge areas, such as woods, is fundamental [7, 18].

A model for the biological control of agroecosystems has been proposed in [19], where the use of spiders is suggested, by preserving suitable habitats for these species around the fields where the crops grow.

The model has been analyzed, and finally coupled with the use of insecticides, because in particular environments the latter are heavily used anyway. Spraying insecticides from flying planes or helicopters on large fields will interfere also with the species that are helpful in controlling the pests and needs to be suitably taken into consideration. Spraying is usually administered at regular time intervals, a fact that in the corresponding dynamical system is modeled via impulsive functions.

The impulsive models arise, generally, in the description of phenomena subjected to abrupt external changes, where the time of the change can be neglected, and the change can be modeled as jump in the phenomena under study. A rich literature on the theory of impulsive differential equations can be found in [1, 2, 14]. This new branch of differential equations developed quickly over the past 50 years (see [15]). In particular, important contributions have been made by Bainov and Simeonov [1, 2], Lakshmikantham et al. [14], and their colleagues.

In [19] simulations have been carried out, but a theoretical analysis of the system behavior is lacking. The main objective is to study the stability of the periodic solutions that have been empirically found in [19].

For the ease of the reader we restate here the model introduced in [19], whose oscillating solutions are the aim of this chapter:

$$\frac{dx_1}{dt} = rx_1\left(1 - \frac{x_1}{W}\right) - cx_2x_1 \tag{1}$$

$$\frac{dx_2}{dt} = x_2\left(-a + \frac{kbx_3}{H + x_3} + kcx_1\right) \tag{2}$$

$$\frac{dx_3}{dt} = x_3\left(e - \frac{bx_2}{H + x_3}\right) \tag{3}$$

$$x_1(t_i^+) = x_1(t_i)\left(1 - \frac{h(1-q)}{\alpha}\right) \tag{4}$$

$$x_2(t_i^+) = x_2(t_i)\left(1 - \frac{hKq}{\alpha}\right) \tag{5}$$

$$x_3(t_i^+) = x_3(t_i)\left(1 - \frac{hq}{\alpha}\right), \tag{6}$$

Table 1 Model parameters and their meaning

r	Logistic growth
c	Spider's hunting rate on insects
W	Woods and green patches carrying capacity
e	Insect growth rate in open fields
b	Spider's hunting rate on field insects
a	Spider's mortality rate
H	Half saturation constant
$k < 1$	Conversion factor of prey into new spiders
q	Portion of insecticide sprayed on vineyards
$1 - q$	Portion of insecticide accidentally sprayed on the woods
h	Insecticide effectiveness against the parasites
$0 < K < 1$	Smaller insecticide effect on the spiders

where $t_{i+1} - t_i = \tau > 0, \forall i \in \mathbb{N}$. The meaning of the variables is as follows: x_1 represents the insects population living in the woods, x_2 represents the spiders populations, and x_3 represents the insects having the vineyards as habitat.

The positive parameters are defined in Table 1.

The rest of the chapter contains the theoretical analysis, organized in just one section. In it, the various subsections address in turn the basic definitions, the stability of the unique non-trivial, positive, well-defined, and stable periodic solution of the wood insects only. Then, the stability of the other solution is studied, namely the τ-periodic, pest-only solution and the τ-periodic, spider-free solution. The Appendices contain the most technical mathematical details.

2 Analysis of the Model

In the following, we proceed to analyze our model. To this purpose, we shall use a fixed point approach. Let $\Phi(t; X_0)$ be the solution of the system (1), (2), (3), (4), (5), and (6) for the initial condition X_0. We define the mappings $F_1, F_2, F_3 : \mathbb{R}^3 \longrightarrow \mathbb{R}$ by

$$F_1(x_1, x_2, x_3) = rx_1\left(1 - \frac{x_1}{W}\right) - cx_2x_1.$$

$$F_2(x_1, x_2, x_3) = x_2\left(-a + \frac{kbx_3}{H + x_3} + kcx_1\right).$$

$$F_3(x_1, x_2, x_3) = x_3\left(e - \frac{bx_2}{H + x_3}\right).$$

and $\Theta_1, \Theta_2, \Theta_3 : \mathbb{R}^3 \longrightarrow \mathbb{R}$ by

$$\Theta_1(x_1(t_i), x_2(t_t), x_3(t_i)) = x_1(t_i)\left(1 - \frac{h(1-q)}{\alpha}\right),$$

$$\Theta_2(x_1(t_i), x_2(t_t), x_3(t_i)) = x_2(t_i)\left(1 - \frac{hKq}{\alpha}\right),$$

$$\Theta_3(x_1(t_i), x_2(t_t), x_3(t_i)) = x_3(t_i)\left(1 - \frac{hq}{\alpha}\right).$$

2.1 Definitions and Assumptions

Definition 2.1 A solution $\zeta = (x_1; x_2; x_3)$ of the problem (1), (2), (3), (4), (5), and (6) is a function defined in $\mathbb{R}^+$, with nonnegative components, continuously differentiable in $\mathbb{R}^+ - \{t_i\}$ with $t_0 = 0$, and satisfying all relations (1) through (6).

Definition 2.2 ζ is called a wood insect-only solution of problem (1), (2), (3), (4), (5), and (6) if and only if its second and third components are zeros.

Definition 2.3 Also, ζ is called a τ-periodic wood insect-only solution if it is a wood insect-only solution satisfying $\zeta(n\tau) = \zeta((n+1)\tau)$, for all $n \geq 0$.

In our study, we further assume that $F = (F_1; F_2; F_3)$ and Θ are smooth enough, $\Theta = (\Theta_1; \Theta_2; \Theta_3)$ is positive, and $F_i(x_1, x_2, x_3) = 0$ for $x_i = 0$, $i = 1; 2; 3$.

Letting Φ be the flow associated with (1), (2), (3), (4), (5), and (6), we have

$$\zeta(t) = \Phi(t, X_0), 0 < t \leq \tau,$$

where $\zeta(0) = X_0$. We assume that the flow Φ applies up to time τ. So $\zeta(\tau) = \Phi(\tau, X_0)$ Then, within a very small time interval starting at time τ, we assume that the treatment is administered and instantaneously kills a fraction of the population. The term $\zeta(\tau^+)$ denotes the state of the population after the treatment, $\zeta(\tau^+)$ is determined in terms of $\zeta(\tau)$ according to equations (4), (5), and (6). We have $\zeta(\tau^+) = \Theta(\zeta(\tau)) = \Theta(\Phi(\tau, X_0))$. Let Ψ be the operator defined by

$$\begin{aligned} \Psi(\tau, .) : \mathbb{R}^3_+ &\longrightarrow \mathbb{R}^3_+ \\ X_0 &\longmapsto \Psi(\tau, X_0) = \Theta(\Phi(\tau, X_0)). \end{aligned}$$

and denote by $D_X\Psi$ the derivative of Ψ with respect to X.

Theorem 2.1 *The model* (1), (2), (3). (4), (5), *and* (6) *has a unique global positive solution for all positive initial conditions*

Proof Because F_i, $(i = 1, 2, 3)$ are smooth functions from the Cauchy–Lipschitz theorem we obtain the local existence and uniqueness of the solutions of (1), (2), and (3). Since the solutions are bounded then the solution is global in $[0, t_1]$.

The system (1), (2), and (3) is quasi-positive because for all $x_i \in \mathbb{R}^+$ we have $F_i(x_1, x_2, x_3) \geq 0$ for $x_i = 0$, $i = 1; 2; 3$. Thus a unique positive global solution exists in $[0, t_1]$.

By recurrence we can prove that $\forall k \in \mathbb{N}^*$, we have a unique positive global solution in the interval $[t_k; t_{k+1}]$. Hence, the existence of a unique positive global solution of (1), (2), (3), (4), (5), and (6) follows. □

We now recall the following result, [12].

Lemma 2.1 *$\zeta = \Phi(., X_0)$ is a τ -periodic solution of (1), (2), (3), (4), (5), and (6) if and only if $\Psi(\tau, X_0) = X_0$*

Remark 2.1 This lemma states that X_0 is a fixed point of $\Psi(\tau, .)$. A fixed point X_0 of $\Psi(\tau, .)$ is given by the initial ζ verifying $\zeta(0) = X_0$. Consequently, for each fixed point X_0 of $\Psi(\tau, .)$ there is an associated τ -periodic solution ζ.

Definition 2.4 ([8]) We say that a fixed point is trivial if it is associated with a trivial periodic solution.

Remark 2.2 The fixed point of $\Psi(\tau, .)$ can be determined using a fixed point method, [8].

Definition 2.5 ([8]) The solution ζ is exponentially stable if and only if the spectral radius $\rho(D_X\Psi(\tau, .))$ is strictly less than 1.

Remark 2.3 If $x_2 = x_3 = 0$ the problem (1), (4) has a τ_0-periodic solution denoted by $x_1(t) = x(t, \widehat{x}_1)$, where

$$x_1(t) = \frac{W\widehat{x}_1 e^{rt}}{W - \widehat{x}_1(1 - e^{rt})} \tag{7}$$

and $\widehat{x}_1$ is determined by

$$\widehat{x}_1 = \frac{W}{\alpha}\frac{\alpha(e^{r\tau_0} - 1) - h(1 - q)e^{r\tau_0}}{e^{r\tau_0} - 1} \tag{8}$$

which is positive if

$$h(1 - q) < \alpha, \quad \tau_0 > \frac{1}{r}\ln\frac{\alpha}{\alpha - h(1 - q)}, \tag{9}$$

conditions that ensure the following result.

Theorem 2.2 *If (9) is satisfied, then the problem (1), (4) has a τ_0-periodic solution $x_1(t) = x(t, \widehat{x}_1)$ determined by (7) where $\widehat{x}_1$ is given by (8).*

Remark 2.4 By extension it follows that the function $\zeta(t) = (x(t), 0, 0)$ is a τ_0-periodic solution of (1), (2), (3), (4), (5), and (6) in the three dimensional space.

2.2 Stability of ζ

In the case $x_2 = x_3 = 0$, then the system (1), (2), (3), (4), (5), and (6) reduces to the particular case (1), (2), (3), and (4). The latter has a unique non-trivial, positive, well-defined, and stable periodic solution x_s given by (7).

To determine the stability of the wood insect-only solution $\zeta = (x_s; 0; 0)$ in the three dimensional space, we must evaluate $D_X\Psi(\tau_0; X_0)$. Specifically, we find

$$D_X\Psi(\tau_0; X_0) = D_X\Theta(\Phi(\tau_0; X_0))\frac{\partial\Phi}{\partial X}(\tau_0; X_0) \tag{10}$$

$$= \begin{pmatrix} \frac{\partial\Theta_1}{\partial x_1} & \frac{\partial\Theta_1}{\partial x_2} & \frac{\partial\Theta_1}{\partial x_3} \\ \frac{\partial\Theta_2}{\partial x_1} & \frac{\partial\Theta_2}{\partial x_2} & \frac{\partial\Theta_2}{\partial x_3} \\ \frac{\partial\Theta_3}{\partial x_1} & \frac{\partial\Theta_3}{\partial x_2} & \frac{\partial\Theta_3}{\partial x_3} \end{pmatrix} \begin{pmatrix} \frac{\partial\Phi_1}{\partial x_1} & \frac{\partial\Phi_1}{\partial x_2} & \frac{\partial\Phi_1}{\partial x_3} \\ 0 & \frac{\partial\Phi_2}{\partial x_2} & 0 \\ 0 & 0 & \frac{\partial\Phi_3}{\partial x_3} \end{pmatrix} (\tau_0; X_0).$$

The solution ζ is exponentially stable if and only if the spectral radius is less than one, namely for $i = 1, 2, 3$,

$$\left| \frac{\partial\Theta_i}{\partial x_i}(\Phi(\tau_0; X_0))\frac{\partial\Phi_i}{\partial x_i}(\tau_0; X_0) \right| < 1.$$

Following [12] and [4], we now consider the variational equation associated with the system (1), (2), (3), (4), (5), and (6):

$$\frac{d}{dt}(D_X\Phi(t; X_0)) = D_X F(\Phi(t; X_0))(D_X\Phi(t; X_0)), \tag{11}$$

together with the initial condition $D_X\Phi(0; X_0) = Id_{\mathbb{R}^3}$. Following [12], integrating and deferring the details to the Appendix **A1**, we obtain

$$\frac{\partial\Phi_1(t; X_0)}{\partial x_1} = e^{\int_0^t \frac{\partial F_1(\zeta(r))}{\partial x_1} dr}, \quad \frac{\partial\Phi_2(t; X_0)}{\partial x_2} = e^{\int_0^t \frac{\partial F_2(\zeta(r))}{\partial x_2} dr}, \quad \frac{\partial\Phi_3(t; X_0)}{\partial x_3} = e^{\int_0^t \frac{\partial F_3(\zeta(r))}{\partial x_3} dr}. \tag{12}$$

We have the following stability result:

Theorem 2.3 *The trivial solution $\zeta = (x_s; 0; 0)$ is exponentially stable if and only if*

$$\frac{1}{r}\ln\frac{\alpha}{\alpha-h(1-q)} < \tau_0 \tag{13}$$
$$< \min\left\{\frac{1}{kcW-a}\ln\frac{\alpha^{\frac{kcW}{r}+1}}{(\alpha-hKq)(\alpha-h(1-q))^{\frac{kcW}{r}}};\quad \frac{1}{e}\ln\frac{\alpha}{\alpha-hq}\right\}.$$

Proof Observe that

$$\left|\frac{\partial\Theta_1}{\partial x_1}(\Phi(\tau_0;X_0))\frac{\partial\Phi_1}{\partial x_1}(\tau_0;X_0)\right| = \frac{\alpha e^{-r\tau_0}}{\alpha-h(1-q)},$$

$$\left|\frac{\partial\Theta_2}{\partial x_2}(\Phi(\tau_0;X_0))\frac{\partial\Phi_2}{\partial x_2}(\tau_0;X_0)\right| = \frac{(\alpha-hKq)(\alpha-h(1-q))^{\frac{kcW}{r}}e^{(kcW-a)\tau_0}}{\alpha^{\frac{kcW}{r}+1}}$$

and

$$\left|\frac{\partial\Theta_3}{\partial x_3}(\Phi(\tau_0;X_0))\frac{\partial\Phi_3}{\partial x_3}(\tau_0;X_0)\right| = \left(1-\frac{hq}{\alpha}\right)e^{e\tau_0}.$$

□

2.3 Stability of the Remaining τ-Periodic Solution

The system (1), (2), (3), (4), (5), and (6) has two more τ-periodic solution, namely the τ-periodic pest-only solution and τ-periodic spider-free solution:

$$\zeta(t) := \zeta_f = (0;0;x_3(t)), \quad \zeta(t) := \zeta_v = (x_1(t);0;x_3(t)),$$

The existence conditions of the τ-periodic solutions ζ_f and ζ_v are discussed in what follows.

Existence of the τ-Periodic Pest-Only Solution
If $x_1 = x_2 = 0$, the problem (3), (6) has a τ_0-periodic solution denoted by $x_3(t) = x(t,\widehat{x_3})$, where

$$x_3(t) = \widehat{x_3}e^{et}, \tag{14}$$

with $\widehat{x_3} \in \mathbb{R}^{*+}$. It is defined and positive if

$$hq < \alpha, \quad \tau_0 = \frac{1}{e}\ln\frac{\alpha}{\alpha-hq}, \tag{15}$$

conditions that ensure the following result.

Theorem 2.4 *If* (15) *is satisfied, then the problem* (3), (6) *has a stable* τ_0*-periodic solution* $x_3(t) = x(t, \widehat{x_3})$ *determined by* (14).

Remark 2.5 By extension it follows that the function $\zeta(t) = \zeta_f = (0, 0, x_3(t))$ is a τ_0-periodic solution of (1), (2), (3), (4), (5), and (6) in the three dimensional space with τ_0 given in (15).

Existence of the τ-Periodic Spider-Free Solution

If $x_2 = 0$, the problem (1), (3), (4), (6) has a τ_0-periodic solution denoted by $(x_1(t), x_3(t)) = (x_f(t, \widehat{x_1}), x_v(t, \widehat{x_3}))$, where

$$(x_1(t), x_3(t)) = \left(\frac{W\widehat{x_1}e^{rt}}{W - \widehat{x_1}(1 - e^{rt})}, \widehat{x_3}e^{et} \right). \tag{16}$$

With $\widehat{x_3} \in \mathbb{R}^{*+}$, $\widehat{x_1}$ is determined by

$$\widehat{x_1} = \frac{W}{\alpha} \frac{\alpha(e^{r\tau_0} - 1) - h(1 - q)e^{r\tau_0}}{e^{r\tau_0} - 1} \tag{17}$$

and it is defined and positive if

$$\frac{1}{e} \ln\left(1 - \frac{hq}{\alpha}\right) < \frac{1}{r} \ln\left(1 - \frac{h(1 - q)}{\alpha}\right), \quad \tau_0 = \frac{1}{e} \ln \frac{\alpha}{\alpha - hq}, \tag{18}$$

conditions that ensure the following result.

Theorem 2.5 *If* (18) *is satisfied, then the problem* (1), (3), (4), (6) *has a* τ_0*-periodic solution* $(x_1(t), x_3(t)) = (x_f(t, \widehat{x_1}), x_v(t, \widehat{x_3}))$ *determined by* (16)*, where* $\widehat{x_3} \in \mathbb{R}^{*+}$ *and* $\widehat{x_1}$ *is given by* (17).

Remark 2.6 By extension it follows that the function $\zeta(t) = \zeta_v = (x_1(t), 0, x_3(t))$ is a τ_0-periodic solution of (1), (2), (3), (4), (5), and (6) in the three dimensional space with

$$\tau_0 = \frac{1}{e} \ln \frac{\alpha}{\alpha - hq}, \quad \frac{1}{e} \ln\left(1 - \frac{hq}{\alpha}\right) < \frac{1}{r} \ln\left(1 - \frac{h(1 - q)}{\alpha}\right).$$

To study the stability of ζ_f ,ζ_v we use a fixed point approach.

Since solutions of (1), (2), and (3) exist globally in $\mathbb{R}^+$ and are nonnegative we have

$$X(t) = \Phi(t, X_0), \tag{19}$$

where $X(t) = (x_1, x_2, x_3)(t)$, $X(0) = X_0$ and Φ is the flow associated with (1), (2), (3), (4), (5), and (6).

The state of the population after the spraying is denoted by $X(\tau^+) = \Theta(X(\tau)) = \Theta(\Phi(\tau, X_0))$. To have a periodic solution we must have $X(\tau^+) = X_0$ that is $X_0 =$

$\Theta(\Phi(\tau, X_0))$. Now, for $X_0 = \zeta_j$, $j = f$ or $j = v$ and $\tau = \tau_0$ we have

$$D_X\Psi(\tau_0; X_0) = D_X\Theta(\Phi(\tau_0; X_0))\frac{\partial\Phi}{\partial X}(\tau_0; X_0)$$

$$= \begin{pmatrix} 1-\frac{h(1-q)}{\alpha} & 0 & 0 \\ 0 & 1-\frac{hKq}{\alpha} & 0 \\ 0 & 0 & 1-\frac{hq}{\alpha} \end{pmatrix} \begin{pmatrix} \frac{\partial\Phi_1}{\partial x_1} & \frac{\partial\Phi_1}{\partial x_2} & \frac{\partial\Phi_1}{\partial x_3} \\ \frac{\partial\Phi_2}{\partial x_1} & \frac{\partial\Phi_2}{\partial x_2} & \frac{\partial\Phi_2}{\partial x_3} \\ \frac{\partial\Phi_3}{\partial x_1} & \frac{\partial\Phi_3}{\partial x_2} & \frac{\partial\Phi_3}{\partial x_3} \end{pmatrix}(\tau_0; X_0)$$

$$= \begin{pmatrix} \left(1-\frac{h(1-q)}{\alpha}\right)\frac{\partial\Phi_1}{\partial x_1} & \left(1-\frac{h(1-q)}{\alpha}\right)\frac{\partial\Phi_1}{\partial x_2} & \left(1-\frac{h(1-q)}{\alpha}\right)\frac{\partial\Phi_1}{\partial x_3} \\ (1-\frac{hKq}{\alpha})\frac{\partial\Phi_2}{\partial x_1} & (1-\frac{hKq}{\alpha})\frac{\partial\Phi_2}{\partial x_2} & (1-\frac{hKq}{\alpha})\frac{\partial\Phi_2}{\partial x_3} \\ (1-\frac{hq}{\alpha})\frac{\partial\Phi_3}{\partial x_1} & (1-\frac{hq}{\alpha})\frac{\partial\Phi_3}{\partial x_2} & (1-\frac{hq}{\alpha})\frac{\partial\Phi_3}{\partial x_3} \end{pmatrix}(\tau_0; X_0).$$

Further,

$$D_X\Psi(\tau_0; \zeta_f) = \begin{pmatrix} \left(1-\frac{h(1-q)}{\alpha}\right)\frac{\partial\Phi_1}{\partial x_1} & 0 & 0 \\ 0 & (1-\frac{hKq}{\alpha})\frac{\partial\Phi_2}{\partial x_2} & 0 \\ 0 & (1-\frac{hq}{\alpha})\frac{\partial\Phi_3}{\partial x_2} & (1-\frac{hq}{\alpha})\frac{\partial\Phi_3}{\partial x_3} \end{pmatrix}(\tau_0; \zeta_f),$$

and

$$D_X\Psi(\tau_0; \zeta_v) = \begin{pmatrix} \left(1-\frac{h(1-q)}{\alpha}\right)\frac{\partial\Phi_1}{\partial x_1} & \left(1-\frac{h(1-q)}{\alpha}\right)\frac{\partial\Phi_1}{\partial x_2} & 0 \\ 0 & (1-\frac{hKq}{\alpha})\frac{\partial\Phi_2}{\partial x_2} & 0 \\ 0 & (1-\frac{hq}{\alpha})\frac{\partial\Phi_3}{\partial x_2} & (1-\frac{hq}{\alpha})\frac{\partial\Phi_3}{\partial x_3} \end{pmatrix}(\tau_0; \zeta_v).$$

To calculate $\dfrac{\partial\Phi_i}{\partial x_j}$ we used the variational equation (11) associated with the system (1), (2), (3), (4), (5), and (6), whose details are contained in **Appendix A1**.

For each τ-periodic solution, now we assess stability, recalling that exponential stability is equivalent to imposing that the spectral radius is less than one. We examine each solution separately in what follows.

2.3.1 Stability of ζ_f

For the solution ζ_f we need to solve $\det(D_X\Psi(\tau_0;\zeta_f)-\mu I)=0$, with

$$\det(D_X\Psi(\tau_0;\zeta_f)-\mu I)=\begin{vmatrix} D_{X,11}-\mu & 0 & 0 \\ 0 & D_{X,22}-\mu & 0 \\ 0 & D_{X,32} & D_{X,33}(\tau_0;\zeta_f)-\mu \end{vmatrix} \quad (20)$$

where

$$D_{X,11}=\left(1-\frac{h(1-q)}{\alpha}\right)\frac{\partial\Phi_1}{\partial x_1}(\tau_0;\zeta_f),$$
$$D_{X,22}=\left(1-\frac{hKq}{\alpha}\right)\frac{\partial\Phi_2}{\partial x_2}(\tau_0;\zeta_f),$$
$$D_{X,32}=\left(1-\frac{hq}{\alpha}\right)\frac{\partial\Phi_3}{\partial x_2}(\tau_0;\zeta_f),$$
$$D_{X,33}=\left(1-\frac{hq}{\alpha}\right)\frac{\partial\Phi_3}{\partial x_3}(\tau_0;\zeta_f).$$

From (20), it follows that the solution ζ_f is exponentially stable if and only if

$$\left|\left(1-\frac{h(1-q)}{\alpha}\right)\frac{\partial\Phi_1}{\partial x_1}(\tau_0;\zeta_f)\right|<1; \qquad \left|\left(1-\frac{hKq}{\alpha}\right)\frac{\partial\Phi_2}{\partial x_2}(\tau_0;\zeta_f)\right|<1;$$

and $\left|\left(1-\frac{hq}{\alpha}\right)\frac{\partial\Phi_3}{\partial x_3}(\tau_0;\zeta_f)\right|<1$. From the variational equation, for all $0<t\leq\tau_0$ we have

$$\begin{cases} \dfrac{\partial\Phi_1(t;X_0)}{x_1}=e^{rt} \\ \dfrac{\partial\Phi_2(t;X_0)}{\partial x_2}=e^{-at}\left[\dfrac{H+\widehat{x}_3e^{et}}{H+\widehat{x}_3}\right]^{\frac{kb}{e}} \\ \dfrac{\partial\Phi_3(t;X_0)}{\partial x_3}=e^{et} \end{cases}.$$

The details are contained in the Appendix **A2**. Therefore the following result holds:

Theorem 2.6 *The equilibrium ζ_f is unconditionally unstable.*

Proof From the conditions (15) of existence of the τ-periodic spider-free solution, we have $\tau_0=\frac{1}{e}\ln\frac{\alpha}{\alpha-hq}$. Using this value in the condition of stability we obtain

$$\left|\left(1-\frac{hq}{\alpha}\right)\frac{\partial\Phi_3}{\partial x_3}(\tau_0;\zeta_f)\right|<1$$

we obtain

$$\left|\left(1-\frac{hq}{\alpha}\right)e^{e\frac{1}{e}\ln\frac{\alpha}{\alpha-hq}}\right|$$

which is not strictly less than 1. □

2.3.2 Stability of ζ_v

For the solution ζ_v we need to solve $\det(D_X\Psi(\tau_0;\zeta_v)-\mu I)=0$ which amounts to the equation:

$$\left(\left(1-\frac{h(1-q)}{\alpha}\right)\frac{\partial\Phi_1(\tau_0;\zeta_v)}{\partial x_1}-\mu\right)\left((1-\frac{hKq}{\alpha})\frac{\partial\Phi_2(\tau_0;\zeta_v)}{\partial x_2}-\mu\right) \quad (21)$$
$$\times\left((1-\frac{hq}{\alpha})\frac{\partial\Phi_3(\tau_0;\zeta_v)}{\partial x_3}-\mu\right)=0.$$

From (21), the solution ζ_v is exponentially stable whenever

$$\left|\left(1-\frac{h(1-q)}{\alpha}\right)\frac{\partial\Phi_1}{\partial x_1}(\tau_0;\zeta_v)\right|<1; \qquad \left|(1-\frac{hKq}{\alpha})\frac{\partial\Phi_2}{\partial x_2}(\tau_0;\zeta_v)\right|<1;$$

$$\left|(1-\frac{hq}{\alpha})\frac{\partial\Phi_3}{\partial x_3}(\tau_0;\zeta_v)\right|<1.$$

From the variational equation, we have for all $0<t\le\tau_0$

$$\begin{cases}\dfrac{\partial\Phi_1(t;X_0)}{\partial x_1}=\dfrac{W^2e^{rt}}{[W-\widehat{x}_1(1-e^{rt})]^2},\\ \dfrac{\partial\Phi_2(t;X_0)}{\partial x_2}=e^{-at}\left[\dfrac{H+\widehat{x}_3e^{et}}{H+\widehat{x}_3}\right]^{\frac{kb}{e}}\left[\dfrac{W-\widehat{x}_1(1-e^{rt})}{W}\right]^{\frac{kcW}{r}},\\ \dfrac{\partial\Phi_3(t;X_0)}{x_3}=e^{et},\end{cases}$$

for which the details are contained in **Appendix A3**. From (18) we find

$$\left|\left(1-\frac{hq}{\alpha}\right)\frac{\partial\Phi_3}{\partial x_3}(\tau_0;\zeta_v)\right|=\left|\left(1-\frac{hq}{\alpha}\right)e^{e\frac{1}{e}\ln\frac{\alpha}{\alpha-hq}}\right|=1\not<1.$$

Then the following result follows:

Theorem 2.7 *The equilibrium ζ_v is unconditionally unstable.*

Appendix

We begin by giving some general computational results, in what follows, and then specialize them for each solution in the three following subsections.

For all $t \in (0, \tau]$ we have

$$\frac{d}{dt}(D_X\Phi(t; X_0)) = \frac{\partial F}{\partial X}(\Phi(t; X_0))\frac{\partial \Phi}{\partial X}(t; X_0)$$

with the initial condition $D_X\Phi(0; X_0) = Id_{\mathbb{R}^3}$. Here

$$\frac{d}{dt}D_X\Phi(t; X_0) = \frac{d}{dt}\begin{pmatrix} \frac{\partial \Phi_1}{\partial x_1} & \frac{\partial \Phi_1}{\partial x_2} & \frac{\partial \Phi_1}{\partial x_3} \\ \frac{\partial \Phi_2}{\partial x_1} & \frac{\partial \Phi_2}{\partial x_2} & \frac{\partial \Phi_2}{\partial x_3} \\ \frac{\partial \Phi_3}{\partial x_1} & \frac{\partial \Phi_3}{\partial x_2} & \frac{\partial \Phi_3}{\partial x_3} \end{pmatrix}(t; X_0),$$

and

$$\frac{\partial F}{\partial X}(\Phi(t; X_0)) = \begin{pmatrix} \frac{\partial F_1}{\partial x_1} & \frac{\partial F_1}{\partial x_2} & \frac{\partial F_1}{\partial x_3} \\ \frac{\partial F_2}{\partial x_1} & \frac{\partial F_2}{\partial x_2} & \frac{\partial F_2}{\partial x_3} \\ \frac{\partial F_3}{\partial x_1} & \frac{\partial F_3}{\partial x_2} & \frac{\partial F_3}{\partial x_3} \end{pmatrix}(t; X_0)$$

$$= \begin{pmatrix} r(1 - 2\frac{x_1}{W}) - cx_2 & -cx_1 & 0 \\ kcx_2 & \left(-a + \frac{kbx_3}{H + x_3} + kcx_1\right) & \frac{kbHx_2}{(H + x_3)^2} \\ 0 & \frac{bx_3}{H + x_3} & e - \frac{bHx_2}{(H + x_3)^2} \end{pmatrix}(t; X_0),$$

and

$$\frac{\partial \Phi}{\partial X}(\Phi(t; X_0)) = \begin{pmatrix} \frac{\partial \Phi_1}{\partial x_1} & \frac{\partial \Phi_1}{\partial x_2} & \frac{\partial \Phi_1}{\partial x_3} \\ \frac{\partial \Phi_2}{\partial x_1} & \frac{\partial \Phi_2}{\partial x_2} & \frac{\partial \Phi_2}{\partial x_3} \\ \frac{\partial \Phi_3}{\partial x_1} & \frac{\partial \Phi_3}{\partial x_2} & \frac{\partial \Phi_3}{\partial x_3} \end{pmatrix}(t; X_0).$$

Moreover, we have

$$\frac{d}{dt}\left(\frac{\partial\Phi_1(t;X_0)}{\partial x_1}\right)=\frac{\partial F_1(t;X_0)}{\partial x_1}\frac{\partial\Phi_1(t;X_0)}{\partial x_1}+\frac{\partial F_1(t;X_0)}{\partial x_2}\frac{\partial\Phi_2(t;X_0)}{\partial x_1}.$$

$$\frac{d}{dt}\left(\frac{\partial\Phi_1(t;X_0)}{\partial x_2}\right)=\frac{\partial F_1(t;X_0)}{\partial x_1}\frac{\partial\Phi_1(t;X_0)}{\partial x_2}+\frac{\partial F_1(t;X_0)}{\partial x_2}\frac{\partial\Phi_2(t;X_0)}{\partial x_2}.$$

$$\frac{d}{dt}\left(\frac{\partial\Phi_1(t;X_0)}{\partial x_3}\right)=\frac{\partial F_1(t;X_0)}{\partial x_2}\frac{\partial\Phi_2(t;X_0)}{\partial x_3}.$$

$$\frac{d}{dt}\left(\frac{\partial\Phi_2(t;X_0)}{\partial x_1}\right)=\frac{\partial F_2(t;X_0)}{\partial x_1}\frac{\partial\Phi_1(t;X_0)}{\partial x_1}+\frac{\partial F_2(t;X_0)}{\partial x_2}\frac{\partial\Phi_2(t;X_0)}{\partial x_1}.$$

$$\frac{d}{dt}\left(\frac{\partial\Phi_2(t;X_0)}{\partial x_2}\right)=\frac{\partial F_2(t;X_0)}{\partial x_1}\frac{\partial\Phi_1(t;X_0)}{\partial x_2}+\frac{\partial F_2(t;X_0)}{\partial x_2}\frac{\partial\Phi_2(t;X_0)}{\partial x_2}+\frac{\partial F_2(t;X_0)}{\partial x_3}\frac{\partial\Phi_3(t;X_0)}{\partial x_2}.$$

$$\frac{d}{dt}\left(\frac{\partial\Phi_2(t;X_0)}{\partial x_3}\right)=\frac{\partial F_2(t;X_0)}{\partial x_2}\frac{\partial\Phi_2(t;X_0)}{\partial x_3}+\frac{\partial F_2(t;X_0)}{\partial x_3}\frac{\partial\Phi_3(t;X_0)}{\partial x_3}.$$

$$\frac{d}{dt}\left(\frac{\partial\Phi_3(t;X_0)}{\partial x_1}\right)=\frac{\partial F_3(t;X_0)}{\partial x_2}\frac{\partial\Phi_2(t;X_0)}{\partial x_1}.$$

$$\frac{d}{dt}\left(\frac{\partial\Phi_3(t;X_0)}{\partial x_2}\right)=\frac{\partial F_3(t;X_0)}{\partial x_2}\frac{\partial\Phi_2(t;X_0)}{\partial x_2}+\frac{\partial F_3(t;X_0)}{\partial x_3}\frac{\partial\Phi_3(t;X_0)}{\partial x_2}.$$

$$\frac{d}{dt}\left(\frac{\partial\Phi_3(t;X_0)}{\partial x_3}\right)=\frac{\partial F_3(t;X_0)}{\partial x_2}\frac{\partial\Phi_2(t;X_0)}{\partial x_3}+\frac{\partial F_3(t;X_0)}{\partial x_3}\frac{\partial\Phi_3(t;X_0)}{\partial x_3}.$$

We next specialize these computations to each individual equilibrium.

Appendix A1

For the equilibrium $X_0=\zeta$ we have

$$\frac{\partial\Phi_1(t;X_0)}{\partial x_3}=\frac{\partial\Phi_2(t;X_0)}{\partial x_1}=\frac{\partial\Phi_2(t;X_0)}{\partial x_3}=\frac{\partial\Phi_3(t;X_0)}{\partial x_1}=\frac{\partial\Phi_3(t;X_0)}{\partial x_2}=0.$$

Further,

$$\frac{d}{dt}\left(\frac{\partial\Phi_1(t;X_0)}{\partial x_1}\right)=\frac{\partial F_1(t;X_0)}{\partial x_1}\frac{\partial\Phi_1(t;X_0)}{\partial x_1}\tag{12.22}$$

$$\frac{d}{dt}\left(\frac{\partial \Phi_1(t;X_0)}{\partial x_2}\right)=\frac{\partial F_1(t;X_0)}{\partial x_1}\frac{\partial \Phi_1(t;X_0)}{\partial x_2}+\frac{\partial F_1(t;X_0)}{\partial x_2}\frac{\partial \Phi_2(t;X_0)}{\partial x_2} \tag{12.23}$$

$$\frac{d}{dt}\left(\frac{\partial \Phi_2(t;X_0)}{\partial x_2}\right)=\frac{\partial F_2(t;X_0)}{\partial x_2}\frac{\partial \Phi_2(t;X_0)}{\partial x_2} \tag{12.24}$$

$$\frac{d}{dt}\left(\frac{\partial \Phi_3(t;X_0)}{\partial x_3}\right)=\frac{\partial F_3(t;X_0)}{\partial x_3}\frac{\partial \Phi_3(t;X_0)}{\partial x_3}. \tag{12.25}$$

From (12.22), (12.24), and (12.25) it follows

$$\frac{\partial \Phi_1(t;X_0)}{\partial x_1}=e^{\int_0^t\frac{\partial F_1(\zeta(r))}{\partial x_1}dr}=e^{\frac{r}{W}\int_0^t(W-2x_s(\rho))d\rho}=\frac{W^2e^{rt}}{[W-\widehat{x}_1(1-e^{rt})]^2}.$$

$$\frac{\partial \Phi_2(t;X_0)}{\partial x_2}=e^{\int_0^t\frac{\partial F_2(\zeta(r))}{\partial x_2}dr}=e^{\int_0^t(kcx_s(\rho)-a)d\rho}=\frac{[W-\widehat{x}_1(1-e^{rt})]^{\frac{kcW}{r}}}{W^{\frac{kcW}{r}}e^{at}}.$$

$$\frac{\partial \Phi_3(t;X_0)}{\partial x_3}=e^{\int_0^t\frac{\partial F_3(\zeta(r))}{\partial x_3}dr}=e^{et}.$$

Appendix A2

For the equilibrium $X_0=\zeta_f$ we have

$$\frac{\partial \Phi_1(t;X_0)}{\partial x_2}=\frac{\partial \Phi_1(t;X_0)}{\partial x_3}=\frac{\partial \Phi_2(t;X_0)}{\partial x_1}=\frac{\partial \Phi_2(t;X_0)}{\partial x_3}=\frac{\partial \Phi_3(t;X_0)}{\partial x_1}=0.$$

Further,

$$\frac{d}{dt}\left(\frac{\partial \Phi_1(t;X_0)}{\partial x_1}\right)=\frac{\partial F_1(t;X_0)}{\partial x_1}\frac{\partial \Phi_1(t;X_0)}{\partial x_1} \tag{12.26}$$

$$\frac{d}{dt}\left(\frac{\partial \Phi_2(t;X_0)}{\partial x_2}\right)=\frac{\partial F_2(t;X_0)}{\partial x_2}\frac{\partial \Phi_2(t;X_0)}{\partial x_2} \tag{12.27}$$

$$\frac{d}{dt}\left(\frac{\partial \Phi_3(t;X_0)}{\partial x_2}\right)=\frac{\partial F_3(t;X_0)}{\partial x_2}\frac{\partial \Phi_2(t;X_0)}{\partial x_2}+\frac{\partial F_3(t;X_0)}{\partial x_3}\frac{\partial \Phi_3(t;X_0)}{\partial x_2} \tag{12.28}$$

$$\frac{d}{dt}\left(\frac{\partial \Phi_3(t;X_0)}{\partial x_3}\right)=\frac{\partial F_3(t;X_0)}{x_3}\frac{\partial \Phi_3(t;X_0)}{\partial x_3}. \tag{12.29}$$

From (12.26) it follows

$$\frac{\partial \Phi_1(t; X_0)}{\partial x_1} = e^{\int_0^t \frac{\partial F_1(\zeta_f(r))}{\partial x_1} dr} = e^{rt}.$$

Moreover, from (12.27) and (12.29) we have instead

$$\frac{\partial \Phi_2(t; X_0)}{\partial x_2} = e^{\int_0^t \frac{\partial F_2(\zeta_f(r))}{\partial x_2} dr} = e^{\int_0^t (-a + \frac{kbx_3(r)}{H + x_3(r)}) dr} = e^{-at} \left[\frac{H + \widehat{x}_3 e^{et}}{H + \widehat{x}_3} \right]^{\frac{kb}{e}}.$$

and

$$\frac{\partial \Phi_3(t; X_0)}{\partial x_3} = e^{\int_0^t \frac{\partial F_3(\zeta_f(r))}{\partial x_3} dr} = e^{et}.$$

Appendix A3

For the point $X_0 = \zeta_v$ we have

$$\frac{\partial \Phi_1(t; X_0)}{\partial x_3} = \frac{\partial \Phi_2(t; X_0)}{\partial x_3} = \frac{\partial \Phi_3(t; X_0)}{\partial x_1} = \frac{\partial \Phi_2(t; X_0)}{\partial x_1} = 0$$

together with

$$\frac{d}{dt}\left(\frac{\partial \Phi_1(t; X_0)}{\partial x_1}\right) = \frac{\partial F_1(t; X_0)}{\partial x_1} \frac{\partial \Phi_1(t; X_0)}{\partial x_1} \tag{12.30}$$

$$\frac{d}{dt}\left(\frac{\partial \Phi_1(t; X_0)}{\partial x_2}\right) = \frac{\partial F_1(t; X_0)}{\partial x_1} \frac{\partial \Phi_1(t; X_0)}{\partial x_2} + \frac{\partial F_1(t; X_0)}{\partial x_2} \frac{\partial \Phi_2(t; X_0)}{\partial x_2} \tag{12.31}$$

$$\frac{d}{dt}\left(\frac{\partial \Phi_2(t; X_0)}{\partial x_2}\right) = \frac{\partial F_2(t; X_0)}{\partial x_2} \frac{\partial \Phi_2(t; X_0)}{\partial x_2} \tag{12.32}$$

$$\frac{d}{dt}\left(\frac{\partial \Phi_3(t; X_0)}{\partial x_2}\right) = \frac{\partial F_3(t; X_0)}{\partial x_2} \frac{\partial \Phi_2(t; X_0)}{\partial x_2} + \frac{\partial F_3(t; X_0)}{\partial x_3} \frac{\partial \Phi_3(t; X_0)}{\partial x_2} \tag{12.33}$$

$$\frac{d}{dt}\left(\frac{\partial \Phi_3(t; X_0)}{x_3}\right) = \frac{\partial F_3(t; X_0)}{x_3} \frac{\partial \Phi_3(t; X_0)}{x_3}. \tag{12.34}$$

From (12.34) it follows

$$\frac{\partial \Phi_3(t; X_0)}{x_3} = e^{\int_0^t \frac{\partial F_3(\zeta_v(r))}{\partial x_3} dr} = e^{et}.$$

From (12.30) it follows

$$\frac{\partial \Phi_1(t; X_0)}{\partial x_1} = e^{\int_0^t \frac{\partial F_1(\zeta_v(r))}{\partial x_1} dr} = e^{\frac{r}{W}\int_0^t (W - 2x_1(\rho))d\rho} = \frac{W^2 e^{rt}}{[W - \widehat{x}_1(1 - e^{rt})]^2}.$$

and finally, from (12.32) it follows

$$\frac{\partial \Phi_2(t; X_0)}{\partial x_2} = e^{\int_0^t \frac{\partial F_2(\zeta_v(r))}{\partial x_2} dr} = e^{\int_0^t \left(-a + \frac{kbx_3(r)}{H + x_3(r)} + kcx_1(r)\right) dr}$$

$$= e^{-at} \left[\frac{H + \widehat{x}_3 e^{et}}{H + \widehat{x}_3}\right]^{\frac{kb}{e}} \left[\frac{W - \widehat{x}_1(1 - e^{rt})}{W}\right]^{\frac{kcW}{r}}.$$

References

1. D. Bainov, P. Simeonov, Systems with Impulsive Effect: Stability, Theory and Applications, Ellis Horwood, Chichester, 1989.
2. D. Bainov, P. Simeonov, Theory of Impulsive Differential Equations: Periodic Solutions and Applications, Longman, Harlow, 1993.
3. A. Boudermine, M. Helal AND A. Lakmeche, Bifurcation of nontrivial periodic solutions for pulsed chemotherapy model, *Mathematical Sciences And Applications E-Notes*, vol. 2, no 2, 2014, pp. 22–44.
4. F.Charif, M. Helal and A.Lakmeche, Chemotherapy models. *Revue Africaine de la Recherche en Informatique et Mathematiques Appliquees, ARIMA Journal*, vol 23, 2016, pp. 115–124.
5. S. N. Chow and J. Hale, Bifurcation theory, Springer Verlag, 1984.
6. W.D.Edgar, Prey and predators of the wolf spider, Lycosa lugubris. *J. Zool*, 159, 1969,pp 405–411.
7. J.M.Halley, C.F.G.Thomas, P.C.Jepson, A model for the spatial dynamics of Linyphiid spiders in farmland. *J. Appl. Ecol*. 33 (3),1996, pp 471–492.
8. G. Iooss, Bifurcation of maps and applications, Study of mathematics, North Holland, 1979.
9. A.E.Kronk, S.E.Riechert, Parameters affecting the habitat choice of a desert wolf spider, Lycosa santrita Chamberlin and Ivie, *J. Arachnol*. 7,1979, pp 155–166.
10. A. Lakmeche, O. Arino, Bifurcation of non trivial periodic solutions of impulsive differential equations arising in chemotherapeutic treatment, *Dynamics Cont. Discr. Impl.Syst*, vol. 7, 2000, pp. 265–287.
11. A. Lakmeche, O. Arino, Nonlinear mathematical model of pulsed-therapy of heterogeneous tumors, *Nonlinear Anal. Real World Appl*, vol 2, 2001, pp. 455–465.
12. Ah. Lakmeche, M. Helal and Aek. Lakmeche, Pulsed chemotherapy model, *Electronic journal of mathematical analysis and applications*, vol 2(1), (2014), 127–148.
13. M. Marden, Geometry of polynomials, American mathematical society, Providence, Rhode Island, Second edition, 1966.

14. V. Lakshmikantham, D.D. Bainov, P.S. Simeonov, Theory of Impulsive Differential Equations, World ScientiHc, Singapore, 1989.
15. A.D. Mishkis, A.M. Samoilenko, Systems with impulses at prescribed moments of time, Math. Sb. 74 (2) 1967. 202–208.
16. D.H.Morse, R.S.Fritz, Experimental and observational studies of patch choice at different scales by the crab spider Misumena vatia. *Ecology*, 63,1982, pp 172–182.
17. S.E.Riechert, L.Bishop, Prey control by an assemblage of generalist predators: spiders in garden test systems. *Ecology* 71,1990, pp 1441–1450.
18. E.Venturino, M.Isaia, F.Bona, E.Issoglio, V. Triolo, G.Badino, Modelling the spiders ballooning effect on the vineyard ecology. *Math. Modell. Nat. Phenom.* 1, 2006,137–159.
19. E. Venturino, M. Isaia, F. Bona, S. Chatterjee, G. Badino, Biological controls of intensive agroecosystems: Wanderer spiders in the Langa Astigiana. *Ecological Complexity*, vol 5, 2008.
20. D.H.Wise, The role of competition in spider communities:insights from field experiments with a model organism. In:Simberloff, D.R.D., Abele, L.G., Thistle, A.B., Strong, (Eds.), Ecological Communities: Conceptual issues and evidences. Princeton University Press, Princeton, 1984, pp. 42–53.
21. D.H.Wise, Spiders in Ecological Webs. *Cambridge University Press*, Cambridge, UK.1993.
22. B.J.Wood, Development of integrated control programs for pests of tropical perennial crops in Malaysia. In: Huffaker, C.B. (Ed.), *Biological Control*. Plenum Press, New York,1971, pp. 423–457.

A Jaccard-Like Symbol and Its Usefulness in the Derivation of Amino Acid Distributions in Protein Domain Families

Rubem P. Mondaini and Simão C. de Albuquerque Neto

1 Introduction

The present work aims to put emphasis on a series of results associated with the Jaccard symbol [1, 2] in topics related to the application of Statistical Mechanics to model the evolution of protein domains and their origin as well as their association into families and clans [3–6]. We try to motivate the proposed approach by showing some characteristics of the direct process of saddle point approximation [7, 8] on the construction of probabilistic distributions. Some problems with the imposition of constraints are then circumvented by the proposal of adding to the Jaccard symbol a linear combination of elementary entropies. Actually, the Jaccard symbol is like a "harness" for dressing a chosen entropy measure in order to circumvent the problems introduced with necessary constraints. The efficiency of the proposed method should be tested intensively and the first steps in this sense are exposed here. An essential characteristic of the Jaccard symbol is its association to an entropy previously chosen. It is essentially a functional of the entropy measure which we choose to start with.

2 Saddle Points of the Constrained Lagrangian and Minima of the Euclidean Norm of Its Gradient

In this section we introduce the fundamental motivation of this work. We give simple examples to clarify the ideas to be exposed later. All the subsequent developments are based on the analysis of probabilistic distributions of amino acids on rectangular

R. P. Mondaini (✉) · S. C. de Albuquerque Neto
Centre of Technology, COPPE, Federal University of Rio de Janeiro, Rio de Janeiro, Brazil

R. P. Mondaini (ed.), *Trends in Biomathematics: Chaos and Control in Epidemics, Ecosystems, and Cells*, https://doi.org/10.1007/978-3-030-73241-7_13

arrays of m rows and n columns which are obtained by techniques of alignment of protein domains and have been presented in references [3, 6], as well as in references therein.

Let us consider the Lagrangian for calculating the extrema of a constrained generic entropy measure S_j of the probabilistic distribution of the jth column of amino acids on a Canonical ensemble.

$$\mathcal{L}_j = S_j + \lambda_j\Big(1 - \sum_a p_j(a)\Big) + \mu_j\Big(\langle E\rangle_j - \sum_a \hat{p}_j(a)E_j(a)\Big) \tag{1}$$

where $j = 1, \ldots, n$, a = A, C, D, E, ..., W, Y, for the 20 amino acids, $\hat{p}_j(a) = \big(p_j(a)\big)^s / \sum_b \big(p_j(b)\big)^s$ the escort probability [3, 6] associated with $p_j(a)$, $0 \leq s \leq 1$, and $E_j(a)$ is the energy of the a amino acid on the jth column with $\langle E\rangle_j$ standing for the energy mean.

We also consider the Euclidean Norm of its gradient, or,

$$N_{\mathcal{L}_j} = \left[\sum_a \left(\frac{\partial \mathcal{L}_j}{\partial p_j(a)}\right)^2 + \left(\frac{\partial \mathcal{L}_j}{\partial \lambda_j}\right)^2 + \left(\frac{\partial \mathcal{L}_j}{\partial \mu_j}\right)^2\right]^{1/2} \tag{2}$$

The point is that the surface $\mathcal{L}_j$ has a saddle point for each set of energies $E_j(a)$ and the surface $N_{\mathcal{L}_j}$ has a minimum on the same point for the same set of energies.

In order to show specific examples, we firstly choose the probabilistic distributions driven by the Gibbs–Shannon ($s \to 1$) entropy $(GS)_j = -\sum_a p_j(a)\log p_j(a)$ for two amino acids, $p_j(A) = p$, $p_j(C) = 1 - p$:

$$\mathcal{L}_j^{(GS)}(p, \mu) = -p\log p - (1-p)\log(1-p) + \mu(\xi - p\zeta) \tag{3}$$

$$N_{\mathcal{L}_j}^{(GS)}(p, \mu) = \left[\left(\log\left(\frac{1-p}{p}\right) - \mu\zeta\right)^2 + (\xi - p\zeta)^2\right]^{1/2} \tag{4}$$

where

$$\xi = \langle E\rangle - E_{1-p}\,; \quad \zeta = E_p - E_{1-p} \tag{5}$$

The coordinates of the saddle point of $\mathcal{L}_j^{(GS)}$ and the minimum of $N_{\mathcal{L}_j}^{(GS)}$ are

$$\tilde{p} = \frac{\xi}{\zeta}\,; \quad \tilde{\mu} = \frac{1}{\zeta}\log\left(\frac{\zeta - \xi}{\xi}\right), \quad \xi < \zeta \tag{6}$$

This can be seen from the calculation of the second derivatives and their Hessian matrix at the point given by Eq. (6):

$$\left.\frac{\partial^2\mathcal{L}_j}{\partial p^2}\right|_{\tilde{p},\tilde{\mu}} = -\frac{1}{\tilde{p}(\tilde{p}-1)} > 0\,; \quad \left.\frac{\partial^2\mathcal{L}_j}{\partial \mu^2}\right|_{\tilde{p},\tilde{\mu}} = 0\,; \quad \left.\frac{\partial^2\mathcal{L}_j}{\partial p\partial \mu}\right|_{\tilde{p},\tilde{\mu}} = -\zeta$$

$$\mathrm{Hess}(\tilde{p},\tilde{\mu}) = \det\begin{pmatrix} -\dfrac{1}{\tilde{p}(\tilde{p}-1)} & -\zeta \\ -\zeta & 0 \end{pmatrix} = -\zeta^2 < 0 \tag{7}$$

which is characteristic of a saddle point.

An analogous calculation is then performed for the distribution driven by a Havrda–Charvat Entropy: $(HC)_j = \frac{\alpha_j - 1}{1-s}$ where $\alpha_j = \sum_a \left(p_j(a)\right)^s$, $0 \le s < 1$, with $\lim_{s\to 1}(HC)_j = (GS)_j$

$$\mathcal{L}_j^{(HC)}(p,\mu) = \frac{p^s + (1-p)^s - 1}{1-s} + \mu\left(\xi - \frac{p^s}{p^s + (1-p)^s}\zeta\right) \tag{8}$$

$$N_{\mathcal{L}_j}^{(HC)}(p,\mu) = \left[s^2\left(\frac{p^{s-1} - (1-p)^{s-1}}{1-s} - \mu\zeta\,\frac{p^{s-1}(1-p)^{s-1}}{\left(p^s + (1-p)^s\right)^2}\right)^2 + \left(\xi - \frac{p^s}{p^s + (1-p)^s}\zeta\right)^2\right]^{1/2} \tag{9}$$

The saddle point of $\mathcal{L}^{(HC)}$ and the minimum of $N_{\mathcal{L}}^{(HC)}$ is then given by

$$\tilde{p} = \frac{1}{1 + \left(\frac{\zeta-\xi}{\xi}\right)^{1/s}}\,; \quad \tilde{\mu} = \frac{1}{\zeta}\left(\tilde{p}^s + (1-\tilde{p})^s\right)^2 \cdot \frac{(1-\tilde{p})^{1-s} - \tilde{p}^{1-s}}{1-s} \tag{10}$$

We have of course, $\lim_{s\to 1}\tilde{p} = \dfrac{\xi}{\zeta}$, $\lim_{s\to 1}\tilde{\mu} = \dfrac{1}{\zeta}\log\left(\dfrac{\zeta-\xi}{\xi}\right)$.

Sometimes the calculation of the minima of the Euclidean norm of the gradient involves discontinuities, and the existence of the minima should be proved alternatively since the test with second derivatives will fail. Unfortunately the $N_{\mathcal{L}}$ functions here do correspond to this case and we should then study the $N_{\mathcal{L}}$ function on the neighbourhood of the points given by Eqs. (6) or (10) above. We discard these elementary technicalities here by showing the Figs. 1a, b, 2a, b, below.

The second derivatives of the Lagrangian $\mathcal{L}^{(HC)}$ of Eq. (8) are given by

$$\left.\frac{\partial^2\mathcal{L}^{(HC)}}{\partial p^2}\right|_{\tilde{p},\tilde{\mu}} = -s\left(\tilde{p}^{s-2} + (1-\tilde{p})^{s-2}\right) - \tilde{\mu}\zeta s(s-1)\frac{\tilde{p}^{s-2}(1-\tilde{p})^{s-2}(1-2\tilde{p})}{\left(\tilde{p}^s + (1-\tilde{p})^s\right)^2}$$

$$+2\tilde{\mu}\,\zeta\, s^2\,\frac{\tilde{p}^{s-1}(1-\tilde{p})^{s-1}\left(\tilde{p}^{s-1} - (1-\tilde{p})^{s-1}\right)}{\left(\tilde{p}^s + (1-\tilde{p})^s\right)^3} \tag{11}$$

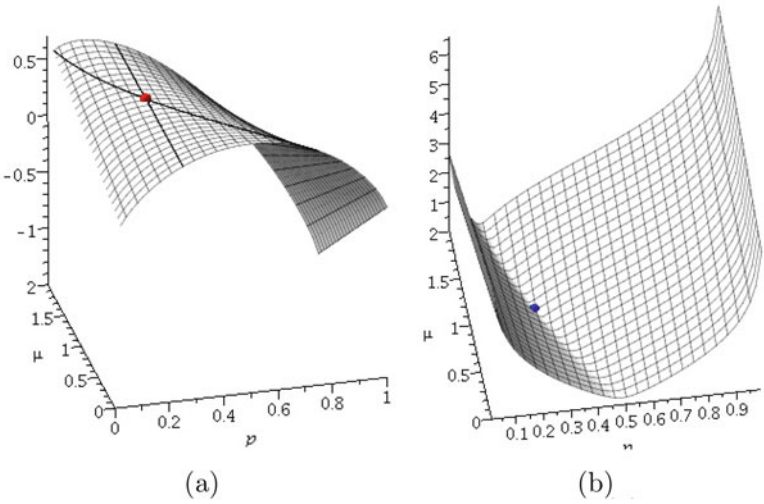

Fig. 1 (**a**) Constrained Lagrangian and the saddle point ($\tilde{p} = 0.25$, $\tilde{\mu} = \log(3)$, $\mathcal{L}_j(\tilde{p}, \tilde{\mu}) = 0.5623$) represented by a red dot for Gibbs–Shannon entropy measure, for $\xi = 0.25$, $\zeta = 1.00$. (**b**) Euclidean norm of the gradient and the minimum point ($\tilde{p} = 0.25$, $\tilde{\mu} = \log(3)$, $N_{\mathcal{L}_j}(\tilde{p}, \tilde{\mu}) = 0$) represented by a blue dot for Gibbs–Shannon entropy measure, for $\xi = 0.25$, $\zeta = 1.00$

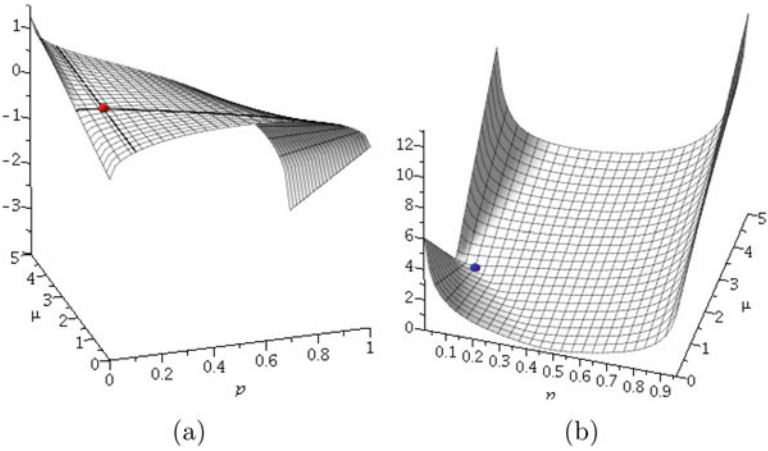

Fig. 2 (**a**) Constrained Lagrangian and the saddle point ($\tilde{p} = 0.1$, $\tilde{\mu} = 2.024$, $\mathcal{L}_j(\tilde{p}, \tilde{\mu}) = 0.5298$) represented by a red dot for Havrda–Charvat ($s = 0.5$) entropy measure, for $\xi = 0.25$, $\zeta = 1.00$. (**b**) Euclidean norm of the gradient and the minimum point ($\tilde{p} = 0.1$, $\tilde{\mu} = 2.024$, $N_{\mathcal{L}_j}(\tilde{p}, \tilde{\mu}) = 0$) represented by a blue dot for Havrda–Charvat ($s = 0.5$) entropy measure, for $\xi = 0.25$, $\zeta = 1.00$

$$\left.\frac{\partial^2 \mathcal{L}^{(HC)}}{\partial \mu^2}\right|_{\tilde{p},\tilde{\mu}} = 0 \tag{12}$$

$$\left.\frac{\partial^2 \mathcal{L}^{(HC)}}{\partial p \partial \mu}\right|_{\tilde{p},\tilde{\mu}} = -\zeta \, \frac{s\left(\tilde{p}^{s-1}(1-\tilde{p})^{s-1}\right)}{\left(\tilde{p}^s + (1-\tilde{p})^s\right)^2} \tag{13}$$

The Hessian is then written as

$$\mathrm{Hess}(\tilde{p},\tilde{\mu}) = -\zeta^2 \, \frac{s^2 \, \tilde{p}^{2s-2}(1-\tilde{p})^{2s-2}}{\left(\tilde{p}^s + (1-\tilde{p})^s\right)^4} < 0 \tag{14}$$

3 The Meaning of Constraints on the Variational Process for the Derivation of Probabilistic Distributions

In this section we study the problem of introduction of constraints on the variation of an entropy measure. The entropy is supposed to be able to clarify the rectangular arrays of amino acids as well as to allow for a statistical physics approach to the evolution of protein families and clans to be recognized on these arrays.

We start from a Lagrangian for the distribution of a pair of columns of amino acids by working with a generic entropy measure S_{jk}. The generalization to sets of t columns ($1 \leq t \leq n$) is straightforward and will be presented in Sect. 5. In the following section we specialize to the treatment to be made with the Jaccard functional symbol. We adopt all the terminology of Canonical Ensembles [9]

$$\begin{aligned}\mathcal{L}_{jk} = S_{jk} + \lambda_{jk}\left(1 - \sum_{a,b} p_{jk}(a,b)\right) + \lambda_j\left(1 - \sum_a p_j(a)\right) + \lambda_k\left(1 - \sum_b p_k(b)\right) \\ + \mu_{jk}\left(\langle E\rangle_{jk} - \sum_{a,b} \hat{p}_{jk}(a,b) E_{jk}(a,b)\right) + \mu_j\left(\langle E\rangle_j - \sum_a \hat{p}_j(a) E_j(a)\right) \\ + \mu_k\left(\langle E\rangle_k - \sum_b \hat{p}_k(b) E_k(b)\right)\end{aligned} \tag{15}$$

where $\hat{p}_{jk}(a,b)$, $\hat{p}_j(a)$, $\hat{p}_k(b)$ are the escort probabilities associated with the joint probability and the simple probabilities $p_{jk}(a,b)$, $p_j(a)$, $p_k(b)$, respectively,

$$\hat{p}_{jk}(a,b) = \frac{\left(p_{jk}(a,b)\right)^s}{\alpha_{jk}}, \quad \hat{p}_j(a) = \frac{\left(p_j(a)\right)^s}{\alpha_j}, \quad \hat{p}_k(b) = \frac{\left(p_k(b)\right)^s}{\alpha_k} \tag{16}$$

with

$$\alpha_{jk} = \sum_{a,b} \left(p_{jk}(a,b)\right)^s \,, \;\; \alpha_j = \sum_{a} \left(p_j(a)\right)^s \,, \;\; \alpha_k = \sum_{b} \left(p_k(b)\right)^s \,, \;\; 0 \leq s < 1 \tag{17}$$

We consider that S_{jk} is a function of α_{jk}, α_j, α_k standing for the partition functions of the probabilities distributions. Actually, in Eq. (15) we do not need to use constraints like

$$\sum_{a} p_j(a) = 1 \,, \quad \sum_{b} p_k(b) = 1 \tag{18}$$

together with $\sum_{a,b} p_{jk}(a,b) = 1$, since the expansion for the marginal probabilities

$$p_j(a) = \sum_{b} p_{jk}(a,b) \,, \quad p_k(b) = \sum_{a} p_{jk}(a,b) \,, \; \forall j \tag{19}$$

will then lead to Eqs. (18). However we work with the constrained Lagrangian given by Eq. (15) and we study all the possible special cases after deriving the extrema of the probabilistic distributions at the end of the variational process. We then undertake the independent variations of the Lagrangian of Eq. (15):

$$\delta_{p_{jk}(a,b)} \mathcal{L}_{jk} = \frac{\partial \mathcal{L}_{jk}}{\partial p_{jk}(a,b)} \, \delta p_{jk}(a,b) = 0 \tag{20}$$

$$\delta_{p_j(a)} \mathcal{L}_{jk} = \frac{\partial \mathcal{L}_{jk}}{\partial p_j(a)} \, \delta p_j(a) = 0 \tag{21}$$

$$\delta_{p_k(b)} \mathcal{L}_{jk} = \frac{\partial \mathcal{L}_{jk}}{\partial p_k(b)} \, \delta p_k(b) = 0 \tag{22}$$

The structure of the partial derivatives of the entropy function S_{jk} is given by

$$\left(\frac{\partial S_{jk}}{\partial p_{jk}(a,b)} \;\; \frac{\partial S_{jk}}{\partial p_j(a)} \;\; \frac{\partial S_{jk}}{\partial p_k(b)} \right) = \left(\frac{\partial S_{jk}}{\partial \alpha_{jk}} \;\; \frac{\partial S_{jk}}{\partial \alpha_j} \;\; \frac{\partial S_{jk}}{\partial \alpha_k} \right) \begin{pmatrix} \frac{\partial \alpha_{jk}}{\partial p_{jk}(a,b)} & \frac{\partial \alpha_{jk}}{\partial p_j(a)} & \frac{\partial \alpha_{jk}}{\partial p_k(b)} \\ \frac{\partial \alpha_j}{\partial p_{jk}(a,b)} & \frac{\partial \alpha_j}{\partial p_j(a)} & \frac{\partial \alpha_j}{\partial p_k(b)} \\ \frac{\partial \alpha_k}{\partial p_{jk}(a,b)} & \frac{\partial \alpha_k}{\partial p_j(a)} & \frac{\partial \alpha_k}{\partial p_k(b)} \end{pmatrix} \tag{23}$$

All the elements of the matrix above are easily calculated by formulae (17) and (19) and we then have

$$\begin{pmatrix} \frac{\partial \alpha_{jk}}{\partial p_{jk}(a,b)} = s\big(p_j(a,b)\big)^{s-1} & \frac{\partial \alpha_{jk}}{\partial p_j(a)} = \frac{s\sum\limits_b \big(p_{jk}(a,b)\big)^s}{p_j(a)} & \frac{\partial \alpha_{jk}}{\partial p_k(b)} = \frac{s\sum\limits_a \big(p_{jk}(a,b)\big)^s}{p_k(b)} \\ \frac{\partial \alpha_j}{\partial p_{jk}(a,b)} = s\big(p_j(a)\big)^s & \frac{\partial \alpha_j}{\partial p_j(a)} = s\big(p_j(a)\big)^s & \frac{\partial \alpha_j}{\partial p_k(b)} = 0 \\ \frac{\partial \alpha_k}{\partial p_{jk}(a,b)} = s\big(p_k(b)\big)^s & \frac{\partial \alpha_k}{\partial p_j(a)} = 0 & \frac{\partial \alpha_k}{\partial p_k(b)} = s\big(p_k(b)\big)^s \end{pmatrix} \tag{24}$$

where we have used the Bayes' law [10],

$$p_{jk}(a,b) = p_{jk}(a|b)p_k(b) = p_{kj}(b|a) = p_{kj}(b,a) \tag{25}$$

The variations of Eqs. (20), (21), (22) will lead to

$$T_{jk}(c,d)\, s\big(p_{jk}(c,d)\big)^{s-1} + T_j(c)\, s\big(p_j(c)\big)^{s-1} + T_k(d)\, s\big(p_k(d)\big)^{s-1} - \lambda_{jk} - \lambda_j - \lambda_k = 0 \tag{26}$$

$$T_j(c) s\big(p_j(c)\big)^{s-1} + s\big(p_j(c)\big)^{s-1}\Delta_{jk}(c) - \lambda_{jk} - \lambda_j = 0 \tag{27}$$

$$T_k(d) s\big(p_k(d)\big)^{s-1} + s\big(p_k(d)\big)^{s-1}\Delta_{jk}(d) - \lambda_{jk} - \lambda_k = 0 \tag{28}$$

where

$$T_{jk}(c,d) = \frac{\partial S_{jk}}{\partial \alpha_{jk}} + \frac{\mu_{jk}}{\alpha_{jk}}\big(\langle E\rangle_{jk} - E_{jk}(c,d)\big) \tag{29}$$

$$T_j(c) = \frac{\partial S_{jk}}{\partial \alpha_j} + \frac{\mu_j}{\alpha_j}\big(\langle E\rangle_j - E_j(c)\big) \tag{30}$$

$$T_k(d) = \frac{\partial S_{jk}}{\partial \alpha_k} + \frac{\mu_k}{\alpha_k}\big(\langle E\rangle_k - E_k(d)\big) \tag{31}$$

and

$$\Delta_{jk}(c) = \frac{1}{\big(p_j(c)\big)^s}\Bigg[\alpha_{jk}\frac{\partial S_{jk}}{\partial \alpha_{jk}}\sum_d \hat{p}_{jk}(c,d) + \mu\Big(\langle E\rangle_{jk}\sum_d \hat{p}_{jk}(c,d) - \sum_d \hat{p}_{jk}(c,d)E_{jk}(c,d)\Big)\Bigg] \tag{32}$$

$$\Delta_{jk}(d) = \frac{1}{\big(p_k(d)\big)^s}\Bigg[\alpha_{jk}\frac{\partial S_{jk}}{\partial \alpha_{jk}}\sum_c \hat{p}_{jk}(c,d) + \mu\Big(\langle E\rangle_{jk}\sum_c \hat{p}_{jk}(c,d) - \sum_c \hat{p}_{jk}(c,d)E_{jk}(c,d)\Big)\Bigg] \tag{33}$$

We have from Eqs. (32), (33):

$$\sum_c \big(p_j(c)\big)^s \Delta_{jk}(c) = \alpha_{jk} \frac{\partial S_{jk}}{\partial \alpha_{jk}} = \sum_d \big(p_k(d)\big)^s \Delta_{jk}(d) \tag{34}$$

After multiplying Eq. (26) by $p_{jk}(c,d)$ and summing up in c, d, we get

$$\sum_{c,d} T_{jk}(c,d)\, s\big(p_{jk}(c,d)\big)^s + \sum_{c,d} T_j(c)\, s\big(p_j(c)\big)^s p_{kj}(d|c)$$
$$+ \sum_{c,d} T_k(d)\, s\big(p_k(d)\big)^s p_{jk}(c|d) - (\lambda_{jk} + \lambda_j + \lambda_k) \sum_{c,d} p_{jk}(c,d) = 0 \tag{35}$$

The terms in Eq. (35) containing the symbols μ_{jk}, μ_j, μ_k will cancel due to the corresponding constraints on the Lagrangian Eq. (15), resulting in the following identities:

$$\sum_{c,d} T_{jk}(c,d)\, s\big(p_{jk}(c,d)\big)^s = \alpha_{jk} \frac{\partial S_{jk}}{\partial \alpha_{jk}} \tag{36}$$

$$\sum_{c,d} T_j(c)\, s\big(p_j(c)\big)^s p_{kj}(d|c) = \sum_c T_j(c)\, s\big(p_j(c)\big)^s = \alpha_j \frac{\partial S_{jk}}{\partial \alpha_j} \tag{37}$$

$$\sum_{c,d} T_k(d)\, s\big(p_k(d)\big)^s p_{jk}(c|d) = \sum_d T_k(d)\, s\big(p_k(d)\big)^s = \alpha_k \frac{\partial S_{jk}}{\partial \alpha_k} \tag{38}$$

where we have used,

$$\big(p_j(c)\big)^{s-1} p_{jk}(c,d) = \big(p_j(s)\big)^{s-1} p_{kj}(d|c) p_j(c) = \big(p_j(c)\big)^s p_{kj}(d|c)$$

and

$$\sum_{c,d} \big(p_j(c)\big)^{s-1} p_{jk}(c,d) = \sum_c \big(p_j(c)\big)^s \sum_d p_{kj}(d|c) = \sum_c \big(p_j(c)\big)^s = \alpha_j$$

Analogously, we also have

$$\sum_{c,d} \big(p_k(d)\big)^{s-1} p_{jk}(c,d) = \sum_d \big(p_k(d)\big)^s \sum_c p_{jk}(c|d) = \sum_d \big(p_k(d)\big)^s = \alpha_k$$

We can then write from Eqs. (35), (36), (37), and (38):

$$\lambda_{jk} + \lambda_j + \lambda_k = s \left[\alpha_{jk} \frac{\partial S_{jk}}{\partial \alpha_{jk}} + \alpha_j \frac{\partial S_{jk}}{\partial \alpha_j} + \alpha_k \frac{\partial S_k}{\partial \alpha_k} \right] \tag{39}$$

We now multiply Eq. (27) by $\left(p_j(c)\right)$ and we sum up in c:

$$\sum_c T_j(c)\, s\left(p_j(c)\right)^s + s\sum_c \left(p_j(c)\right)^s \Delta_{jk}(c) - (\lambda_{jk}+\lambda_j)\sum_c p_j(c) = 0 \tag{40}$$

We then have from Eqs. (32), (34) and (37):

$$\lambda_{jk}+\lambda_j = s\left[\alpha_j \frac{\partial S_{jk}}{\partial \alpha_j} + \alpha_{jk}\frac{\partial S_{jk}}{\partial \alpha_{jk}}\right] \tag{41}$$

Analogously, we multiply Eq. (28) by $p_k(d)$ and we sum up in d:

$$\lambda_{jk}+\lambda_k = s\left[\alpha_k \frac{\partial S_{jk}}{\partial \alpha_k} + \alpha_{jk}\frac{\partial S_{jk}}{\partial \alpha_{jk}}\right] \tag{42}$$

We have from Eqs. (39), (41), (42):

$$\lambda_j = s\,\alpha_j \frac{\partial S_{jk}}{\partial \alpha_j} \tag{43}$$

$$\lambda_k = s\,\alpha_k \frac{\partial S_{jk}}{\partial \alpha_k} \tag{44}$$

$$\lambda_{jk} = s\,\alpha_{jk} \frac{\partial S_{jk}}{\partial \alpha_{jk}} \tag{45}$$

We now substitute Eqs. (27), (28) into Eq. (26). We notice that after multiplying by $p_{jk}(c,d)$ and summing up into c,d we get an identity due to Eq. (45) and the results:

$$\begin{aligned}\sum_{c,d}\left(p_j(c)\right)^{s-1} p_{jk}(c,d)\Delta_{jk}(c) &= \sum_{c,d}\left(p_j(c)\right)^s p_{kj}(d|c)\Delta_{jk}(c)\\ &= \sum_c \left(p_j(c)\right)^s \Delta_{jk}(c) = \alpha_{jk}\frac{\partial S_{jk}}{\partial \alpha_{jk}}\end{aligned} \tag{46}$$

$$\begin{aligned}\sum_{c,d}\left(p_k(d)\right)^{s-1} p_{jk}(c,d)\Delta_{jk}(d) &= \sum_{c,d}\left(p_k(d)\right)^s p_{jk}(c|d)\Delta_{jk}(d)\\ &= \sum_d \left(p_k(d)\right)^s \Delta_{jk}(d) = \alpha_{jk}\frac{\partial S_{jk}}{\partial \alpha_{jk}}\end{aligned} \tag{47}$$

The substitution will then lead to

$$p_{jk}(c,d) = \frac{\left(T_{jk}(c,d)\right)^{\frac{1}{1-s}}}{\left(-\alpha_{jk}\frac{\partial S_{jk}}{\partial \alpha_{jk}} + \left(p_j(c)\right)^{s-1}\Delta_{jk}(c) + \left(p_k(d)\right)^{s-1}\Delta_{jk}(d)\right)^{\frac{1}{1-s}}} \tag{48}$$

and $\left(p_j(c)\right)^{s-1}$; $\left(p_k(d)\right)^{s-1}$ will be given by

$$\left(p_j(c)\right)^{s-1} = \frac{\alpha_{jk}\frac{\partial S_{jk}}{\partial \alpha_{jk}} + \alpha_j \frac{\partial S_{jk}}{\partial \alpha_j}}{T_j(c) + \Delta_{jk}(c)} \tag{49}$$

$$\left(p_k(d)\right)^{s-1} = \frac{\alpha_{jk}\frac{\partial S_{jk}}{\partial \alpha_{jk}} + \alpha_k \frac{\partial S_{jk}}{\partial \alpha_k}}{T_k(d) + \Delta_{jk}(d)} \tag{50}$$

Finally, we can write the probability distribution of amino acids for a pair of columns:

$$p_{jk}(c,d) = \frac{\left(T_{jk}(c,d)\right)^{\frac{1}{1-s}}}{\left[-\alpha_{jk}\frac{\partial S_{jk}}{\partial \alpha_{jk}} + \frac{\left(\alpha_{jk}\frac{\partial S_{jk}}{\partial \alpha_{jk}} + \alpha_j \frac{\partial S_{jk}}{\partial \alpha_j}\right)\Delta_{jk}(c)}{T_j(c) + \Delta_{jk}(c)} + \frac{\left(\alpha_{jk}\frac{\partial S_{jk}}{\partial \alpha_{jk}} + \alpha_k \frac{\partial S_{jk}}{\partial \alpha_k}\right)\Delta_{jk}(d)}{T_j(d) + \Delta_{jk}(d)}\right]^{\frac{1}{1-s}}} \tag{51}$$

From the right-hand sides of Eqs. (37) and (34) and depending on how greater is $\alpha_j\alpha_k$ compared to α_{jk} (the Khinchin–Shannon inequalities), it could be considered to satisfy

$$\alpha_{jk}\frac{\partial S_{jk}}{\partial \alpha_{jk}} \gg \alpha_j \frac{\partial S_{jk}}{\partial \alpha_j} \tag{52}$$

This will be shown to be the case for $S_{jk} = J_{jk}$, the Jaccard-like measure on the next section and we can have by assuming a convenient probabilistic distribution $p_j(c)$:

$$\Delta_{jk}(c) \gg T_j(c) \tag{53}$$

and analogously

$$\Delta_{jk}(d) \gg T_k(d) \tag{54}$$

This means that Eq. (51) could be approximated by

$$p_{jk}(c,d) \approx \frac{\left(\alpha_{jk}\frac{\partial S_{jk}}{\partial \alpha_{jk}} + \mu_{jk}\left(\langle E\rangle_{jk} - E_{jk}(c,d)\right)\right)^{\frac{1}{1-s}}}{(\alpha_{jk})^{\frac{1}{1-s}}\left(\alpha_{jk}\frac{\partial S_{jk}}{\partial \alpha_{jk}} + \alpha_j\frac{\partial S_{jk}}{\partial \alpha_j} + \alpha_k\frac{\partial S_{jk}}{\partial \alpha_k}\right)^{\frac{1}{1-s}}} \tag{55}$$

We will obtain the same result of Eq. (55) by discarding the constraints on the energy distributions of the columns by making $\mu_j = 0$, $\mu_k = 0$ in the original Lagrangian, Eq. (15).

4 The Jaccard-Like Functional Measure

In this section we introduce the Jaccard-like functional measure by following which have been presented in the 20th International BIOMAT Symposium on November 01–06, 2020. In that presentation we have summarized the ideas and results of a research period of 05 years.

First of all, we introduce the Sharma–Mittal set of entropy measures:

$$(SM)_{jk} = \frac{(\alpha_{jk})^{\frac{1-r}{1-s}} - 1}{1-r}, \quad \alpha_{jk} = \sum_{a,b}\left(p_{jk}(a,b)\right)^s \tag{56}$$

A concavity criterium is satisfied for $1 \geq r \geq s \geq 0$, or

$$\frac{\partial^2 (SM)_{jk}}{\partial p_{jk}^2(a,b)} = s(\alpha_{jk})^{\frac{1-r}{1-s}}\left(p_{jk}(a,b)\right)^{s-2}\left[\frac{s(s-r)}{(1-s)^2}\hat{p}_{jk}(a,b) - 1\right] < 0 \tag{57}$$

where $\hat{p}_{jk}(a,b) = \frac{\left(p_{jk}(a,b)\right)^s}{\alpha_{jk}}$ is the escort probability, Eq. (16). Many previous works of this series have emphasized the particular entropy measures associated with this set. These are given by

Havrda–Charvat's:

$$(HC)_{jk} = \lim_{r\to s}(SM)_{jk} = \frac{\alpha_{jk} - 1}{1-s} \tag{58}$$

Landsberg–Vedral's:

$$(LV)_{jk} = \lim_{r\to 2-s}(SM)_{jk} = \frac{\alpha_{jk} - 1}{(1-s)\alpha_{jk}} \equiv \frac{(HC)_{jk}}{\alpha_{jk}} \tag{59}$$

Renyi's:

$$R_{jk} = \lim_{r \to 1} (SM)_{jk} = \frac{\log \alpha_{jk}}{1 - s} \tag{60}$$

All these entropy measures will have the Gibbs–Shannon entropy measure as the limit $s \to 1$

$$\lim_{s \to 1} \left((HC)_{jk}\,,\ (LV)_{jk}\,,\ R_{jk} \right) = -\sum_{a,b} p_{jk}(a,b) \log p_{jk}(a,b) \tag{61}$$

A Jaccard-like measure is introduced as the "normalization" of the distance of information:

$$0 \leq J_{jk} = \frac{d_{jk}}{(SM)_{jk}} \leq 1$$

$$d_{jk} = (SM)_{jk} - M_{jk} \tag{62}$$

where M_{jk} is the "mutual information"

$$M_{jk} = \frac{1}{1 - r} \left(1 - \left(\frac{\alpha_{jk}}{\alpha_j \alpha_k} \right)^{\frac{1-r}{1-s}} \right) \tag{63}$$

we then see from Eqs. (17), (56) that $M_{jk} \equiv 0$ when the probabilistic distributions of single columns are independent.

We can then write for the Jaccard-like measure associated with the Sharma–Mittal set:

$$J_{jk}^{(SM)} = 1 + \frac{(\alpha_{jk})^{\frac{1-r}{1-s}} - (\alpha_j \alpha_k)^{\frac{1-r}{1-s}}}{(\alpha_j \alpha_k)^{\frac{1-r}{1-s}} \left((\alpha_{jk})^{\frac{1-r}{1-s}} - 1 \right)} \tag{64}$$

We remark that the inequality

$$\alpha_{jk} \leq \alpha_j \alpha_k \tag{65}$$

is the generalized Khinchin–Shannon inequality [5] for the columns of the rectangular array of amino acids built from the alignment of protein domains.

In order to look for an elementary 3-D representation of a Jaccard-like measure, we now proceed to a derivation of a convenient parametrization, by restricting ourselves to two amino acids only, a = A, C. Without loss of generality we now use Eq. (19) to write

$$\begin{aligned}
p_j(\mathrm{A}) &= q = p_{jk}(\mathrm{A},\mathrm{A}) + p_{jk}(\mathrm{A},\mathrm{C}) = qp + q(1-p)\\
p_j(\mathrm{C}) &= 1-q = p_{jk}(\mathrm{C},\mathrm{A}) + p_{jk}(\mathrm{C},\mathrm{C}) = (1-q)p + (1-q)(1-p)\\
p_k(\mathrm{A}) &= v = p_{jk}(\mathrm{A},\mathrm{A}) + p_{jk}(\mathrm{C},\mathrm{A}) = vu + v(1-u)\\
p_k(\mathrm{C}) &= 1-v = p_{jk}(\mathrm{A},\mathrm{C}) + p_{jk}(\mathrm{C},\mathrm{C}) = (1-v)u + (1-v)(1-u)
\end{aligned} \tag{66}$$

we can write from Eq. (17):

$$\alpha_j = \big(p_j(\mathrm{A})\big)^s + \big(p_j(\mathrm{C})\big)^s = q^s + (1-q)^s \tag{67}$$

$$\alpha_k = \big(p_k(\mathrm{A})\big)^s + \big(p_k(\mathrm{C})\big)^s = v^s + (1-v)^s \tag{68}$$

α_{jk} can be written twice. We have

$$\begin{aligned}
\alpha_{jk} &= (qp)^s + \big(q(1-p)\big)^s + \big((1-q)p\big)^s + \big((1-q)(1-p)\big)^s\\
&= \big(q^s + (1-q)^s\big)\big(p^s + (1-p)^s\big)
\end{aligned} \tag{69}$$

and

$$\begin{aligned}
\alpha_{jk} &= (vu)^s + \big(v(1-u)\big)^s + \big((1-v)u\big)^s + \big((1-v)(1-u)\big)^s\\
&= \big(v^s + (1-v)^s\big)\big(u^s + (1-u)^s\big)
\end{aligned} \tag{70}$$

From Eqs. (69), (70), we can have

(I) $q = u, v = p$

$$\Rightarrow \alpha_{jk} = \alpha_j\alpha_k = \big(u^s + (1-u)^s\big)\big(p^s + (1-p)^s\big), \tag{71}$$

which exhausts the Khinchin inequalities $\Rightarrow J_{jk} = 1$

(II) $q = v, p = u$

$$\Rightarrow \alpha_{jk} = \big(q^s + (1-q)^s\big)\big(p^s + (1-p)^s\big) \le \alpha_j\alpha_k = \big(q^s + (1-q)^s\big)^2 \tag{72}$$

We take the case II as our model for parametrization of J_{jk}.

We now choose to represent the Jaccard measure surface associated with the Havrda–Charvat entropy measure ($r = s$ in Eq. (64)) and we write

$$\begin{aligned}
J_{jk}^{(HC)} &= 1 + \frac{\alpha_{jk} - \alpha_j\alpha_k}{\alpha_j\alpha_k(\alpha_{jk} - 1)}\\
&= 1 + \frac{p^s + (1-p)^s - \big(q^s + (1-q)^s\big)}{\big(q^s + (1-q)^s\big)\Big(\big(q^s + (1-q)^s\big)\big(p^s + (1-p)^s\big) - 1\Big)}
\end{aligned} \tag{73}$$

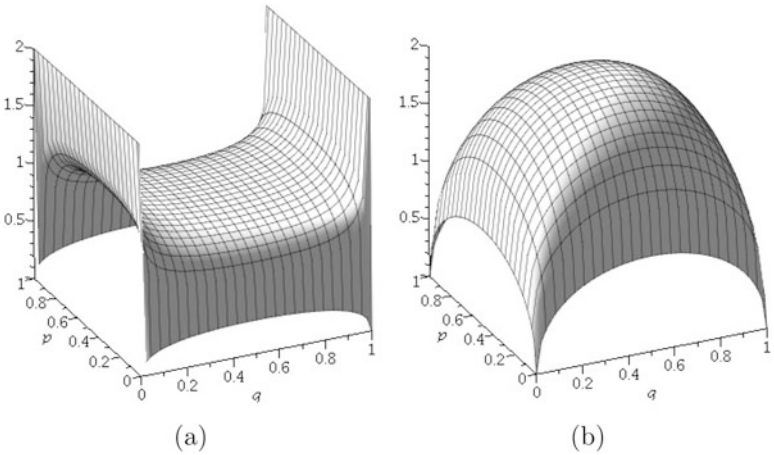

Fig. 3 (**a**) The Jaccard surface associated with Havrda–Charvat entropy measure for $s = 0.5$. (**b**) The Havrda–Charvat surface, $s = 0.5$

As a comparison, we also take the related Havrda–Charvat surface

$$(HC)_{jk} = \frac{\alpha_{jk} - 1}{1 - s} = \frac{\left(q^s + (1-q)^s\right)\left(p^s + (1-p)^s\right) - 1}{1 - s} \tag{74}$$

Their surfaces are represented on Fig. 3a, b below. The s-parameter has been chosen to be $s = 0.5$. The Jaccard surface has a saddle point at $(\tilde{p} = 0.5, \tilde{q} = 0.5)$ and the Havrda–Charvat one has a maximum at the same point, which could be confirmed by direct calculation of their derivatives:

$$\left.\frac{\partial J_{jk}}{\partial p}\right|_{\tilde{p},\tilde{q}} = \frac{(y^2-1)}{y(xy-1)^2}\frac{\mathrm{d}x}{\mathrm{d}p} = 0\,; \qquad \left.\frac{\partial J_{jk}}{\partial q}\right|_{\tilde{p},\tilde{q}} = \frac{x(y^2-2xy+1)}{y^2(xy-1)^2}\frac{\mathrm{d}y}{\mathrm{d}q} = 0 \tag{75}$$

with

$$x = p^s + (1-p)^s\,; \quad y = q^s + (1-q)^s \tag{76}$$

$$\left.\frac{\partial^2 J_{jk}}{\partial p^2}\right|_{\tilde{p},\tilde{q}} = \frac{(y^2-1)}{y(xy-1)^3}\left[(xy-1)\frac{\mathrm{d}^2x}{\mathrm{d}p^2} - 2y\left(\frac{\mathrm{d}x}{\mathrm{d}p}\right)^2\right] = \frac{4s(s-1)}{2^{2(1-s)}-1} < 0 \tag{77}$$

$$\left.\frac{\partial^2 J_{jk}}{\partial q^2}\right|_{\tilde{p},\tilde{q}} = \frac{x(y^2-2xy+1)}{y^2(xy-1)^2}\frac{\mathrm{d}^2 y}{\mathrm{d}q^2} - \frac{2x(xy^3-3x^2y+3xy-1)}{y^3(xy-1)^3}\left(\frac{\mathrm{d}y}{\mathrm{d}q}\right)^2$$

$$= \frac{4s(s-1)}{1-2^{2(1-s)}} > 0 \tag{78}$$

$$\left.\frac{\partial^2 J_{jk}}{\partial p \partial q}\right|_{\tilde{p},\tilde{q}} = -\frac{(xy^3-3xy+y^2+1)}{y^2(xy-1)^3}\frac{\mathrm{d}x}{\mathrm{d}p}\frac{\mathrm{d}y}{\mathrm{d}q} = 0 \tag{79}$$

$$\mathrm{Hess}(\tilde{p},\tilde{q}) = \left.\frac{\partial^2 J_{jk}}{\partial p^2}\right|_{\tilde{p},\tilde{q}} \cdot \left.\frac{\partial^2 J_{jk}}{\partial q^2}\right|_{\tilde{p},\tilde{q}} - \left(\left.\frac{\partial^2 J_{jk}}{\partial p \partial q}\right|_{\tilde{p},\tilde{q}}\right)^2 = \frac{-16s^2(s-1)^2}{(1-2^{2(1-s)})^2} < 0 \tag{80}$$

A model of bound on surfaces like that are feasible for the treatment with the direct methods of saddle point approximation of probability distributions of Statistical Mechanics [9]. This is seen as an advantage over the usual treatment based on the maximization of the entropy measures given by Eq. (74) and Fig. 3b.

Actually the surface of Fig. 3a should be presented by removing its parts above the plane $J_{jk} = 1$; we do that by specifying the domain of the coordinates, p, q, according to

$$p^s + (1-p)^s = q^s + (1-q)^s \tag{81}$$

and Fig. 4, below.

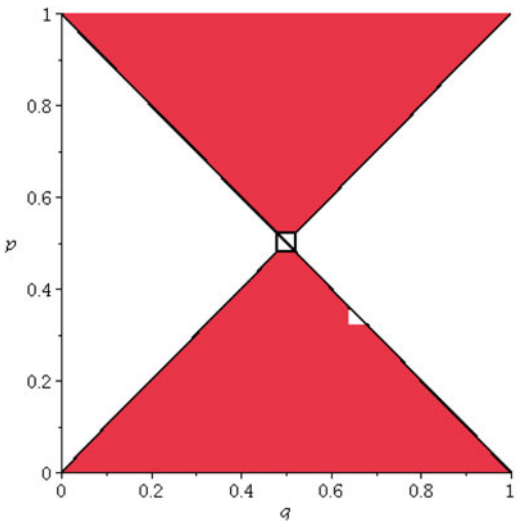

Fig. 4 The red regions correspond to the parametrization to be used for surface $J_{jk}(p,q)$, $s = 0.5$

The regions to be considered are then given by

$$\begin{aligned} &(0 \leq q \leq 0.5,\ 0 \leq p \leq q)\,; && (0 \leq q \leq 0.5,\ 1-q \leq p \leq 1) \\ &[1ex](0.5 \leq q \leq 1,\ 0 \leq p \leq 1-q)\,; && (0.5 \leq q \leq 1,\ q \leq p \leq 1) \end{aligned} \tag{82}$$

The surface $J_{jk}(p,q)$ will be then represented as in the Fig. 5, below.

Some elementary discussion for the case $t \geq 3$ is missing. The equation $J_{jk}(p,q)$ for t columns is easily derived by finite induction by assuming the same parametrization of Eq. (66):

$$J_{j_1 \ldots j_t}(p,q) = 1 + \frac{p^s + (1-p)^s - \left(q^s + (1-q)^s\right)^{t-1}}{\left(q^s + (1-q)^s\right)^{t-1}\left[\left(q^s + (1-q)^s\right)\left(p^s + (1-p)^s\right) - 1\right]} \tag{83}$$

The second derivatives at the critical point $(\tilde{p}, \tilde{q}) = (0.5, 0.5)$ are given by

$$\left.\frac{\partial^2 J_{j_1 \ldots j_t}}{\partial p^2}\right|_{\tilde{p},\tilde{q}} = \frac{4s(s-1)(t-1)}{2^{(1-s)(t-1)} - 1} < 0 \tag{84}$$

$$\left.\frac{\partial^2 J_{jk}}{\partial q^2}\right|_{\tilde{p},\tilde{q}} = s(s-1)(t-1)2^{3-s-(1-s)t}\frac{(2^{2(1-s)(t-1)} - 2^{1+(1-s)t} + 1)}{(2^{(1-s)t} - 1)^2} \tag{85}$$

$$\left.\frac{\partial^2 J_{jk}}{\partial p \partial q}\right|_{\tilde{p},\tilde{q}} = 0 \tag{86}$$

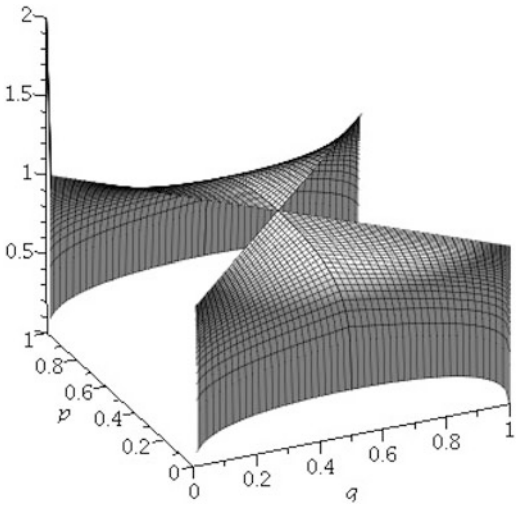

Fig. 5 The surface obtained with the restrictions on the regions of the parametrization in order to avoid $J_{jk} > 1$

For $1 > s \geq 0$, the second derivative will be positive or negative if $2^{(1-s)t}$ is inside or outside the interval $\left(\frac{1-\sqrt{1-2^{-2(1-s)}}}{2^{-2(1-s)}}, \frac{1+\sqrt{1-2^{-2(1-s)}}}{2^{-2(1-s)}} \right)$, respectively. However, the first case should be discarded, since $t(s)$ would be negative for $1 > s \geq 0$ according to Fig. 6 below and we have only negative values for Eq. (85) corresponding to the region above the blue curve of Fig. 6 and also negative values for the Hessian corresponding to a saddle point of the surface given by Eq. (83).

At this point we would like to stress that the requirement leading to Eqs. (53), (54) is trivially satisfied for the Jaccard-like measure. We take the example of Jaccard's associated with the Havrda–Charvat measure, Eq. (73):

$$\alpha_{jk} \frac{\partial J_{jk}}{\partial \alpha_{jk}} = \frac{\alpha_{jk}(\alpha_j \alpha_k - 1)}{\alpha_j \alpha_k (\alpha_{jk} - 1)^2}$$

$$\alpha_j \frac{\partial J_{jk}}{\partial \alpha_j} = \alpha_k \frac{\partial J_{jk}}{\partial \alpha_k} = -\frac{\alpha_{jk}}{\alpha_j \alpha_k (\alpha_{jk} - 1)}$$

the inequality

$$\alpha_{jk} \frac{\partial J_{jk}}{\partial \alpha_{jk}} \gg \alpha_j \frac{\partial J_{jk}}{\partial \alpha_j} = \alpha_k \frac{\partial J_{jk}}{\partial \alpha_k} \tag{87}$$

for $\alpha_{jk} \gg 1$, $\alpha_j \gg 1$, $\alpha_k \gg 1$ and still satisfying Khinchin–Shannon inequality. In addition, there is always a probability distribution $p_j(c)$ such that the inequalities of Eqs. (53), (54) are true.

The results of this section point to the possibility of deriving a probabilistic distribution for the Jaccard entropy measure associated with Havrda–Charvat entropy

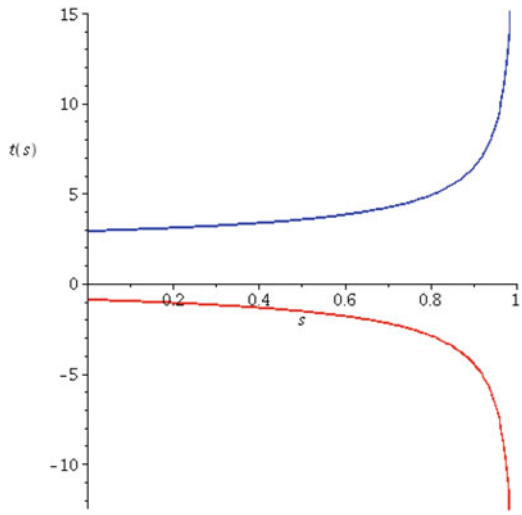

Fig. 6 The blue curve is the hypograph of the region corresponding to a negative Hessian at $(\tilde{p}, \tilde{q}) = (0.5, 0.5)$

measure by the alternative direct method of using the saddle point approximation, instead of maximizing Havrda–Charvat's. This process will be valid for the Jaccard measure associated with Landsberg–Vedral's and Renyi's as will be shown in a forthcoming chapter. This will favour the construction of an alternative Statistical Mechanics.

5 A Proposal for Information Measure and the Synergy of the Probabilistic Distributions

From the generalization of the equation (56) to distributions of sets of t columns, $t = 1, \ldots, n$ or

$$(SM)_{j_1 \ldots j_t} = \frac{(\alpha_{j_1 \ldots j_t})^{\frac{1-r}{1-s}} - 1}{1-r}, \quad \alpha_{j_1 \ldots j_t} = \sum_{a_1, \ldots, a_t} \left(p_{j_1 \ldots j_t}(a_1, \ldots, a_t)\right)^s \tag{88}$$

with $1 > r \geq s > 0$. We then define

$$I_{j_1 \ldots j_t} = -\frac{(SM)_{j_1 \ldots j_t}}{(\alpha_{j_1 \ldots j_t})^{\frac{1-r}{1-s}}} = \frac{-(SM)_{j_1 \ldots j_t}}{1 + (1-r)(SM)_{j_1 \ldots j_t}} \tag{89}$$

From Eq. (89), we write

$$(SM)_{j_1 \ldots j_t} = -\frac{I_{j_1 \ldots j_t}}{1 + (1-r) I_{j_1 \ldots j_t}} \tag{90}$$

From the generalization of the Khinchin–Shannon inequality [5]

$$\alpha_{j_1 \ldots j_t} \leq \prod_{l=1}^{t} \alpha_{j_l} \implies 1 + (1-r)(SM)_{j_1 \ldots j_t} \leq \prod_{l=1}^{t} \left(1 + (1-r)(SM)_{j_l}\right) \tag{91}$$

We then have from Eqs. (90), (91)

$$1 - (1-r)\frac{I_{j_1 \ldots j_t}}{1 + (1-r) I_{j_1 \ldots j_t}} \leq \prod_{l=1}^{t} \left(1 - (1-r)\frac{I_{j_l}}{1 + (1-r) I_{j_l}}\right) \tag{92}$$

or

$$1 + (1-r) I_{j_1 \ldots j_t} \geq \prod_{l=1}^{t} \left(1 + (1-r) I_{j_l}\right) \tag{93}$$

i.e. the information associated with a set of t columns is greater than the sum of information of each column. Hence, Eq. (93) corresponds to the expression of the synergy of the probabilistic distribution. For $t = 2$, $t = 3$, we have respectively from Eq. (93):

$$I_{j_1 j_2} \geq I_{j_1} + I_{j_2} + (1-r) I_{j_1} I_{j_2} \tag{94}$$

$$I_{j_1 j_2 j_3} \geq I_{j_1} + I_{j_2} + I_{j_3} + (1-r)(I_{j_1} I_{j_2} + I_{j_1} I_{j_3} + I_{j_2} I_{j_3}) + (1-r)^2 I_{j_1} I_{j_2} I_{j_3} \tag{95}$$

We can also define the "information gain". From Eq. (88), we have

$$\mathrm{d}I_{j_1 \ldots j_t} = -\frac{\mathrm{d}(SM)_{j_1 \ldots j_t}}{\left(1 + (1-r)(SM)_{j_1 \ldots j_t}\right)^2} \tag{96}$$

From the mean value theorem of Calculus, we write

$$\Delta I_{j_1 \ldots j_t} = -\frac{\Delta(SM)_{j_1 \ldots j_t}}{\left(1 + (1-r)\langle SM \rangle_{j_1 \ldots j_t}\right)^2} \tag{97}$$

where $\langle SM \rangle_{j_1 \ldots j_t}$ is a value of $(SM)_{j_1 \ldots j_t}$ inside of the interval $\Delta(SM)_{j_1 \ldots j_t}$. It follows the obvious interpretation of information gain with the decrease in entropy.

6 Some Useful Remarks and Planning for Future Work

There are many ways to continue the work on the research topics of this note. In particular:

(1) The problem of constructing a parametrization including 20 amino acids for the treatment of the constrained optimization problem of Sect. 3;
(2) To understand the real nature of the Jaccard-like functional entropy measure and the possible relation of the Gauss–Kuzmin probabilistic distribution associated with its continued fraction. Meanwhile we present here the continued fraction associated with the Jaccard-like measure introduced in this article which is given by the "cursed" example of continued fraction in the mathematical literature:

$$J_{jk} = 1 + \cfrac{1}{1 + \cfrac{1}{-1 + \cfrac{1}{1 + \cfrac{1}{-1 + \cfrac{1}{1 + \cfrac{1}{-1 + \ldots}}}}}}$$

$$= 1 + \frac{1}{1+}\frac{1}{(-1)+}\frac{1}{1+}\frac{1}{(-1)+}\frac{1}{1+}\frac{1}{(-1)+}\cdots$$
$$= (1; \overline{1, -1}) \tag{98}$$

(3) The use of the elementary algebra of partition functions $\alpha_{j_1 \ldots j_t}$, $t = 2, \ldots, n$, $\alpha_{j_l}, l = 1, \ldots, t$ to construct a probabilistic distribution $p_{j_1 \ldots j_t}(a_1, \ldots, a_t)$ free of the problems exposed in Sect. 3;
(4) The construction of a lattice model of Statistical Mechanics, like the Potts Model based on a Hamiltonian

$$\mathcal{H} = \sum_{j_1 < j_2 < \ldots < j_t} J_{j_1 \ldots j_t} \alpha_{j_1 \ldots j_t} + J \prod_{l=1}^{t} \alpha_{j_l} \tag{99}$$

where

$$J = \frac{t!(n-t)!}{n!} \sum_{j_1 < j_2 < \ldots < j_t} J_{j_1 \ldots j_t} \tag{100}$$

is the average of the Jaccard measure over all $\frac{n!}{t!(n-t)!}$ sets of t columns.

References

1. P. Jaccard – Étude comparative de la distribution florale dans une portion des Alpes et du Jura – *Bull. Soc. Vaud. Sci. Nat.*, **37** (142) (1901), 547–579.
2. P. Jaccard – The distribution of the Flora in the Alpine Zone – *New Phytol.*, **11** (2) (1912), 37–50.
3. R. P. Mondaini, S. C. de Albuquerque Neto – Stochastic assessment of protein databases by generalized entropy measures – *Trends in Biomathematics*, **1** (2018) 91–105, Springer Nature.
4. R. P. Mondaini, S. C. de Albuquerque Neto – Towards a Thermostatistics of the Evolution of protein domains through the formation of families and clans – *Trends in Biomathematics* **2** (2019) 139–152, Springer Nature.
5. R. P. Mondaini, S. C. de Albuquerque Neto – Khinchin-Shannon generalized inequalities for "Non-additive" entropy measures – *Trends in Biomathematics* **2** (2019) 177–190, Springer Nature.
6. R. P. Mondaini, S. C. de Albuquerque Neto – The statistical analysis of protein domain family distributions via Jaccard Entropy measures – *Trends in Biomathematics* **3** (2020) 169–207, Springer Nature.
7. G. Bricogne – Maximum Entropy and the Foundations of Direct Methods – *Acta Crystal.* **A40** (1984) 410–445.
8. H. E. Daniels Saddlepoint Approximations in Statistics – *Ann. Math. Stat.* **25** (1954) 631–650.
9. K. Huang – Statistical Mechanics, second edition. John Wiley & Sons, 1987.
10. R. P. Mondaini, S. C. de Albuquerque Neto – The Pattern Recognition of Probabilistic distributions of amino acids in protein families – in *Mathematical Biology and Biological Physics*, World Scientific (2017), pp. 29–50.

When Ideas Go Viral—Complex Bifurcations in a Two-Stage Transmission Model

J. Heidecke and M. V. Barbarossa

1 Introduction

Social contagion is the spread of behaviors or attitudes through (physical or virtual) groups of people [1]. From a mathematical point of view, modeling social contagion in large communities is very similar to modeling the transmission of an infectious disease in a population. Hence, it seems natural that methods from the field of mathematical epidemiology, such as compartmental models [2–8], are used to model social contagion phenomena. In certain cases social contagion and disease spread even have to be considered coupled to one another, as when a group in a social network criticizes vaccination [9]. Despite the analogies, social contagion differs from biological contagion in various aspects. For example, intellectual epidemics could be advantageous [3], ideas do not require interpersonal contact to spread [10], or people might be asked to choose between opposite opinions [7]. Thus, to mathematically describe social contagion processes, models from theoretical epidemiology might require adaptation to the specific context.

The classical SEIR (susceptible-exposed-infective-recovered) model in mathematical epidemiology describes the transmission of an infectious disease in a population [11]. When a susceptible individual comes in contact with an infective one, there is a certain probability that contagion occurs and the susceptible moves to the exposed compartment. After a latent period exposed individuals become infectious themselves and can infect others. Once the infectious period is over, the individual recovers, cannot anymore transmit the disease to others, and becomes immune. Waning of immunity, i.e., transitions from the recovered to the susceptible compartment, is possible for certain diseases [11, 12].

J. Heidecke (✉) · M. V. Barbarossa
Frankfurt Institute for Advanced Studies, Frankfurt, Germany
e-mail: heidecke@fias.uni-frankfurt.de; barbarossa@fias.uni-frankfurt.de

R. P. Mondaini (ed.), *Trends in Biomathematics: Chaos and Control in Epidemics, Ecosystems, and Cells*, https://doi.org/10.1007/978-3-030-73241-7_14

In the context of social contagion, the spreading of a specific behavior or opinion in a population could be described as the transition of individuals from the "naive" (susceptible) status to the "promoter" (infectious) one. This transition might require several steps and depend on repeated exposure to promoters [8, 13]. Therefore, we classify individuals as:

- **naive/susceptible** (S), those who have not yet been exposed to the considered behavior/opinion,
- **weakened** (W), those who came in contact with the considered behavior/opinion, but are not yet spreading to others,
- **promoters/infectious** (I), those who have embraced the considered behavior/opinion and are able to transmit it to others,
- **inactive/resistant** (R), those who have earlier been sharing the considered behavior/opinion but are now neither transmitting to others nor can be re-exposed.

In contrast to the classical SEIR approach, transition from the exposed/weakened stage to the promoter/infected stage depends on contacts with infectives/promoters. Promoters and susceptibles make contact sufficient to transmit the opinion/behavior at rate β. We assume that upon such a contact the susceptibles have a certain probability $\rho \in (0, 1)$ to enter the I-compartment directly, becoming a promoter themselves (*perfect contact*). With probability $1-\rho$ susceptible individuals enter the W-compartment (*imperfect contact*). When a W-individual comes in contact with promoters, the weakened enters the I-compartment at rate $\beta_2 \geq \beta$. In this sense, an individual in the W-compartment is more vulnerable to the opinion/behavior than an individual in the S-compartment. Over time promotors might reject the considered opinion/behavior. Thus, we assume that promotors leave the promoting class at rate α and become inactive/resistant. As we assume that the inactivity/resistance of a R-individual towards the considered opinion/behavior might wane over time, we allow transition from R back to S at rate η. Moreover, we assume that the infection can fade away in weakened individuals, whereby transitions from W to S are occuring at rate γ. We assume that $\gamma \geq \alpha$, suggesting that the average time an individual is able to promote a certain opinion is not shorter than his exposure time. A model sketch is given in Fig. 1 and the corresponding differential equations system is

$$\begin{aligned} S' &= -\beta I S + \gamma W + \eta R \\ W' &= (1-\rho)\beta I S - \beta_2 I W - \gamma W \\ I' &= \beta_2 I W + \rho \beta I S - \alpha I \\ R' &= \alpha I - \eta R. \end{aligned} \tag{1}$$

Limit cases of this system lead, on the one hand, to the standard SIRS model (cf. [11]) if $\rho = 1$ and the W-compartment is empty at the beginning of observations. On the other hand, if the transition from W to I would be a linear one and $\gamma = \rho = 0$, the model would be equivalent to the classical SEIRS model (cf. [11]).

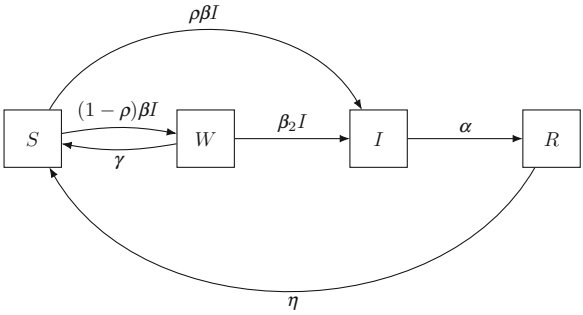

Fig. 1 Flowchart of the two-stage contagion model (1) with waning of immunity and fading of infection in weakened individuals

Observing that the total population $N = S + W + I + R$ does not vary over time, we set $N \equiv 1$. Clearly, system (1) has a unique non-negative global solution for every choice of non-negative initial values, and the set $\{(S, I, W, R) \in \mathbb{R}^4_{\geq 0} \mid S + W + I + R = 1\}$ is forward invariant. For analytical simplicity, we restrict to the case $\beta_2 = \beta$. Using the conservation relation $W = 1 - S - I - R$, we consider the reduced system

$$\begin{aligned} S' &= -\beta I S + \gamma(1 - S - I - R) + \eta R \\ I' &= \rho\beta I S - \alpha I + \beta I(1 - S - I - R) \\ R' &= \alpha I - \eta R. \end{aligned} \tag{2}$$

A similar compartmental model for two-stage contagion was previously proposed by Guy Katriel [8]. System (2) differs from Katriel's work in two aspects. First we include waning immunity and fading of infection, that is transitions from R, respectively W, to the susceptible compartment. Second, we do not consider population demography (births/deaths). Such differences lead to major analytical challenges with respect to Katriel's study [8]. In the rest of this chapter we study the qualitative properties of system (2) by means of analytical and numerical methods.

2 Existence and Local Stability of Equilibria

To understand the long-term behavior of the system we first investigate its equilibria. The criteria on the stability of the disease-free equilibrium, where the I compartment is empty, are commonly related to the so-called *basic reproduction number*, $\mathcal{R}_0$. We remark that the following results are derived assuming that $\gamma \geq \alpha$ holds.

Theorem 2.1

(a) System (2) has a unique disease-free (DFE) equilibrium $\mathcal{E}_0 := (1, 0, 0)$*, which exists for any choice of* $\beta,\ \gamma,\ \eta,\ \alpha > 0,\ \rho \in (0, 1)$.

(b) The DFE $\mathcal{E}_0$ is locally asymptotically stable (shortly, LAS) if $\mathcal{R}_0 := \frac{\rho\beta}{\alpha} < 1$, and unstable if $\mathcal{R}_0 > 1$.

Proof *(a)*: Equilibria of system (2) are determined setting the right-hand side of the system equal to zero,

$$\begin{aligned} 0 =& -\beta I^* S^* + \gamma(1 - S^* - I^* - R^*) + \eta R^* \\ 0 =& I^* \left(\rho\beta S^* - \alpha + \beta(1 - S^* - I^* - R^*)\right) \\ 0 =& \alpha I^* - \eta R^*. \end{aligned} \tag{3}$$

If $I^* = 0$ (DFE condition), then the third relation in (3) implies that $R^* = 0$ and the first relation in (3) implies that $S^* = 1$. Thus, $\mathcal{E}_0$ is the unique DFE of the system. *(b)*: For studying the local stability of the DFE we linearize about $\mathcal{E}_0$. The Jacobian matrix of (2) is

$$J = \begin{pmatrix} -\beta I - \gamma & -\beta S - \gamma & \eta - \gamma \\ (\rho - 1)\beta I & \beta((\rho - 1)S + 1 - 2I - R) - \alpha & -\beta I \\ 0 & \alpha & -\eta \end{pmatrix}. \tag{4}$$

Evaluation of J at $\mathcal{E}_0$ yields the eigenvalues $\lambda_1 = -\gamma < 0$, $\lambda_2 = \rho\beta - \alpha$, and $\lambda_3 = -\eta < 0$. The condition $\lambda_2 < 0 \iff \mathcal{R}_0 < 1$ guarantees local stability of the DFE. □

The above expression for $\mathcal{R}_0$ can be interpreted as the number of secondary infections that a single promoter introduced into a completely susceptible population produced through perfect contacts ($\rho\beta$) over the duration of its promoting period ($1/\alpha$). The secondary infections produced through imperfect contacts require two nonlinear transitions over the W-compartment, which is empty at $\mathcal{E}_0$, hence do not contribute to determining the local stability of the DFE.

Theorem 2.1 provides conditions for the local stability of the DFE. What exactly happens at the bifurcation value $\mathcal{R}_0 = 1$ can be determined with the help of Theorem A.1, first introduced by Castillo-Chavez and Song [14]. For convenience of notation we define $\kappa := (1 + \alpha/\eta)$.

Theorem 2.2 *Let $\rho^* := \frac{-\alpha + \sqrt{\alpha\gamma\kappa}}{\gamma\kappa - \alpha}$. If $\rho > \rho^*$, then a transcritical bifurcation of forward type occurs at $\mathcal{R}_0 = 1$. If $\rho < \rho^*$, then a transcritical bifurcation of backward type occurs at $\mathcal{R}_0 = 1$.*

Proof We use Theorem A.1 and take β as our bifurcation parameter, with $\beta^* := \frac{\alpha}{\rho}$ corresponding to $\mathcal{R}_0 = 1$. The Jacobian (4) of system (2) evaluated at $\mathcal{E}_0$ for $\beta = \beta^*$, $\mathcal{A} := J|_{\mathcal{E}_0, \beta^*}$, has a simple zero eigenvalue and two eigenvalues with negative real part. To compute a right eigenvector w of $\mathcal{A}$, solve $\mathcal{A}w = 0$, which is an underdetermined system. We fix $w_2 = 1$ and obtain $w_3 = \frac{\alpha}{\eta} w_2 = \frac{\alpha}{\eta}$ and $w_1 = -\frac{\alpha}{\rho\gamma} - 1 + \frac{\alpha}{\gamma} - \frac{\alpha}{\eta}$. Analogously, to find a left eigenvector of $\mathcal{A}$, we solve the system $v\mathcal{A} = 0$, obtaining $v = (0, 1, 0)$.

Next, we denote the vector field of system (2) by $f = (f_1, f_2, f_3)$ and we calculate second order partial derivatives to verify the conditions of Theorem A.1. As $v_1 = 0 = v_3$ the derivatives of f_1 and f_3 are not needed. All second order derivatives of f_2 are zero, except for

$$\frac{\partial^2 f_2}{\partial^2 I} = -2\beta^*, \qquad \frac{\partial^2 f_2}{\partial I \partial R} = -\beta^*,$$
$$\frac{\partial^2 f_2}{\partial S \partial I} = \rho\beta^* - \beta^*, \qquad \frac{\partial^2 f_2}{\partial I \partial \beta^*} = \rho.$$

Therefore, the quantities a and b in Theorem A.1 are given by

$$b = \sum_{i=1}^{3} v_2 w_i \frac{\partial^2 f_2}{\partial x_i \partial \beta}(0,0) = \rho v_2 w_2 = \rho > 0,$$

and

$$\begin{aligned} a &= \sum_{i,j=1}^{3} v_2 w_i w_j \frac{\partial^2 f_2}{\partial x_i \partial x_j}(0,0) \\ &= -2\frac{\alpha}{\rho} v_2 w_2^2 - 2\frac{\alpha}{\rho} v_2 w_2 w_3 + 2\left(\alpha - \frac{\alpha}{\rho}\right) v_2 w_1 w_2 \\ &= -2\frac{\alpha}{\rho} - 2\frac{\alpha^2}{\rho\eta} + 2\left(\alpha - \frac{\alpha}{\rho}\right)\left(-\frac{\alpha}{\rho\gamma} - 1 + \frac{\alpha}{\gamma} - \frac{\alpha}{\eta}\right), \end{aligned}$$

where $x = (x_1, x_2, x_3) = (S, I, R)$. The condition $a > 0$ is equivalent to

$$\psi(\rho) := \rho^2 (\gamma\kappa - \alpha) + 2\rho\alpha - \alpha < 0. \tag{5}$$

Because of the assumption $\gamma \geq \alpha$, we have $\gamma\kappa = \gamma(1 + \frac{\alpha}{\eta}) > \alpha$. The open up parabola $\psi(\rho)$ has negative intercept and vertex on the left half-plane. Thus, condition (5) is fulfilled only if $0 < \rho < \rho^*$, where

$$\rho^* = \frac{-\alpha + \sqrt{\alpha\gamma\kappa}}{\gamma\kappa - \alpha}$$

is the positive zero of $\psi(\rho)$. □

Endemic equilibria of (2) are determined by solving (3) for $I^* \neq 0$. From the third and the first in (3) we get

$$R^* = \frac{\alpha}{\eta} I^* \quad \text{and} \quad S^* = \frac{\gamma(1 - \kappa I^*) + \alpha I^*}{\beta I^* + \gamma}.$$

Note here that $1 - I^* - \frac{\alpha}{\eta} I^* = 1 - I^* - R^* \geq 0$, hence $S^* \geq 0$ if $I^* \geq 0$. The equilibria condition thus reduces to the quadratic equation

$$0 = aI^{*2} + bI^* + c =: \Phi(I^*), \tag{6}$$

with $a := \beta\kappa > 0$, $b := \alpha\,(2-\rho) + \rho\gamma\kappa - \beta$ and $c := \gamma\left(\frac{\alpha}{\beta} - \rho\right)$. Solutions to (6) are given by

$$I^*_{\pm} = \frac{1}{2\beta\kappa}\left[\beta - \rho\gamma\kappa - \alpha\,(2-\rho) \pm \sqrt{\Delta}\right],$$

where Δ is the discriminant of (6). Hence, system (2) has at most two endemic equilibria $\mathcal{E}_{\pm} := \left(S^*_{\pm}, I^*_{\pm}, R^*_{\pm}\right)$, whereby $I^*_{\pm}$ are the positive roots of the open up parabola $\Phi(I^*)$. We write the coefficients b and c of $\Phi(I^*)$ as functions of β,

$$b(\beta) := \alpha(2-\rho) + \rho\gamma\kappa - \beta$$
$$c(\beta) := \gamma\left(\frac{\alpha}{\beta} - \rho\right).$$

Note that $b(\beta)$ is a strictly decreasing linear function with zero at

$$\beta_b := \alpha(2-\rho) + \rho\gamma\kappa$$

and $c(\beta)$ is a strictly decreasing curve with zero at

$$\beta_c := \frac{\alpha}{\rho}.$$

Further

$$c(\beta)\begin{cases} > 0 \iff \mathcal{R}_0 < 1, \\ = 0 \iff \mathcal{R}_0 = 1, \\ < 0 \iff \mathcal{R}_0 > 1. \end{cases}$$

Theorem 2.2 suggest to consider the cases $\rho^* < \rho$ and $\rho^* > \rho$ separately.

Theorem 2.3 *If $\rho^* < \rho < 1$, then:*

- *For $\mathcal{R}_0 \leq 1$, there are no endemic equilibria.*
- *For $\mathcal{R}_0 > 1$, there is a unique endemic equilibrium $\mathcal{E}_+$.*

At $\mathcal{R}_0 = 1$ a transcritical bifurcation of forward type occurs, and a branch of stable endemic equilibria $\mathcal{E}_+$ emerges from $\mathcal{E}_0$.

Proof Observe that

$$\beta_b > \beta_c \iff 2\rho\alpha - \alpha\rho^2 + \rho^2\gamma\kappa > \alpha \iff \psi(\rho) > 0 \underbrace{\iff}_{\text{Thm. 2.2}} \rho^* < \rho. \tag{7}$$

Thus, if $\rho^* < \rho$ we have that the zero of $b(\beta)$ lies on the right of the zero of $c(\beta)$. In other words, if $c(\beta) \geq 0$ (that is $\mathcal{R}_0 \leq 1$), then necessarily $b(\beta) > 0$. This means that if the open up parabola $\Phi(I^*)$ has a positive y-intercept, then it also has vertex on the left half-plane, hence no positive root I^*. If $c(\beta) < 0$ (that is $\mathcal{R}_0 > 1$), $\Phi(I^*)$ has a negative y-intercept, thus only its larger root I^*_+ is positive. The rest follows from Theorem 2.2. □

Define

$$\mathcal{R}_C := \rho(2-\rho) - \rho^2\frac{\gamma\kappa}{\alpha} + 2\frac{\rho(1-\rho)}{\alpha}\sqrt{\alpha\gamma\kappa} \tag{8}$$

and consider the case $\rho^* > \rho$.

Theorem 2.4 *If $0 < \rho < \rho^*$, then the following results hold:*

(a) If $\mathcal{R}_0 < \mathcal{R}_C$, there are no endemic equilibria.
(b) If $\mathcal{R}_C \leq \mathcal{R}_0 < 1$, there are two endemic equilibria $\mathcal{E}_\pm$, which coincide if $\mathcal{R}_C = \mathcal{R}_0$.
(c) If $1 \leq \mathcal{R}_0$, there is a unique endemic equilibrium $\mathcal{E}_+$.

At $\mathcal{R}_0 = 1$ a transcritical bifurcation of backward type occurs, and a branch of unstable endemic equilibria $\mathcal{E}_-$ emerges from $\mathcal{E}_0$.

Proof From $\rho < \rho^*$ it follows from (7) that $\beta_b < \beta_c$. Hence if $c(\beta) \leq 0$ (that is $\mathcal{R}_0 \geq 1$), then necessarily $b(\beta) < 0$. This means that if the open up parabola $\Phi(I^*)$ has a non-positive y-intercept, it has vertex on the right half-plane as well, and hence a unique positive root I^*_+. This proofs statement c). For two positive roots $I^*_\pm$ the conditions $c(\beta) > 0$, $b(\beta) < 0$ and $\Delta(\beta) \geq 0$, where

$$\begin{aligned}\Delta(\beta) =& \beta^2 + \beta(2\rho\alpha + 2\rho\gamma\kappa - 4\alpha) \\ &+ \underbrace{4\alpha^2(1-\rho) + \rho^2\alpha^2 + \rho^2\gamma^2\kappa^2 + 4\rho\alpha\gamma\kappa - 2\rho^2\alpha\gamma\kappa - 4\alpha\gamma\kappa}_{:=c_\Delta},\end{aligned}$$

are necessary. For $\Delta(\beta) = 0$ the two roots coincide. The discriminant $\Delta(\beta)$ as a function of β is an open up parabola itself. Short computation shows that

$$c_\Delta < 0 \iff \rho < 2\rho^*,$$

hence c_Δ is always negative under the assumptions of the theorem. Thus $\Delta(\beta) \geq 0$ for β larger than the positive zero of the discriminant-parabola, that is

$$\beta \geq \alpha(2-\rho) - \rho\gamma\kappa + 2(1-\rho)\sqrt{\alpha\gamma\kappa} =: \beta_\Delta,$$

and $\Delta(\beta) = 0 \iff \beta = \beta_\Delta$. Observe that

$$\begin{aligned} \beta_b < \beta_\Delta &\iff \rho^2\gamma^2\kappa^2 < (1-\rho)^2\alpha\gamma\kappa \\ &\iff \rho^2(\gamma\kappa - \alpha) + \rho 2\alpha - \alpha < 0 \\ &\iff \rho < \rho^*. \end{aligned} \tag{9}$$

Further

$$\begin{aligned} \beta_\Delta < \beta_c &\iff \alpha(2-\rho) - \rho\gamma\kappa + 2(1-\rho)\sqrt{\alpha\gamma\kappa} < \frac{\alpha}{\rho} \\ &\iff \underbrace{\rho^2\left(-\alpha - \gamma\kappa - 2\sqrt{\alpha\gamma\kappa}\right) + \rho 2\left(\alpha + \sqrt{\alpha\gamma\kappa}\right) - \alpha}_{=:\chi(\rho)} < 0. \end{aligned}$$

Note that $\chi(\rho)$ is an open down parabola with vertex on the right half-plane, negative y-intercept, and zero discriminant. Therefore, $\chi(\rho)$ has a unique zero at

$$\rho = \frac{(\alpha + \gamma\kappa + 2\sqrt{\alpha\gamma\kappa})(-\alpha + \sqrt{\alpha\gamma\kappa})}{(\gamma\kappa - \alpha)(\alpha + \gamma\kappa + 2\sqrt{\alpha\gamma\kappa})} = \rho^*.$$

Hence,

$$\rho < \rho^* \implies \chi(\rho) < 0 \iff \beta_\Delta < \beta_c.$$

With (9) this means that for $\rho < \rho^*$ it holds that $\beta_b < \beta_\Delta < \beta_c$. As the positive root β_Δ of $\Delta(\beta)$ lies on the right of the zero of $b(\beta)$, then for $\beta \geq \beta_\Delta$ we have $\Delta(\beta) \geq 0$ and necessarily $b(\beta) < 0$. As $c(\beta) > 0$ (that is $\mathcal{R}_0 < 1$) for $\beta < \beta_c$, the condition on β to have positive roots $I_\pm^*$ of $\Phi(I^*)$ is $\beta_\Delta \leq \beta < \beta_c$. Dividing by β_c and using the definition (8) of $\mathcal{R}_C$, we obtain the condition on $\mathcal{R}_0$ as in statement *b)* of the theorem. The rest follows from Theorem 2.2. □

The results of Theorems 2.3 and 2.4 are summarized in Fig. 2. Local stability of the endemic equilibria can be determined evaluating the Jacobian matrix (4) of the system at $\mathcal{E}_\pm$,

$$J|_{\mathcal{E}_\pm} = \begin{pmatrix} -\beta I_\pm^* - \gamma & -\beta S_\pm^* - \gamma & \eta - \gamma \\ (\rho-1)\,\beta I_\pm^* & \beta\left((\rho-1)\,S_\pm^* + 1 - (1+\kappa)\,I_\pm^*\right) - \alpha & -\beta I_\pm^* \\ 0 & \alpha & -\eta \end{pmatrix}.$$

The characteristic polynomial of $J|_{\mathcal{E}_\pm}$ is given by

$$\Pi(\lambda) = \lambda^3 + \lambda^2 a_2 + \lambda a_1 + a_0, \tag{10}$$

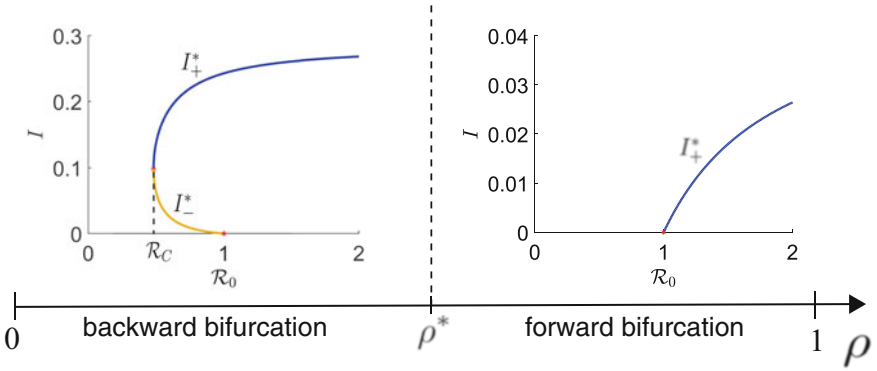

Fig. 2 Visualization of statements in Theorems 2.3 and 2.4: Endemic equilibria of system (2) in dependence on ρ

where

$$
\begin{aligned}
a_2 &= \beta I_\pm^* (2+\kappa) + \gamma + \alpha + 2\beta S_\pm^* (1-\rho) - \beta + \eta \\
&= (\frac{1}{\kappa} + \frac{1}{2}) \left[\beta - \rho\gamma\kappa - \alpha(2-\rho) \pm \sqrt{\Delta} \right] + \gamma + \alpha \\
&\quad + 2\beta S_\pm^* (1-\rho) - \beta + \eta \\
a_1 &= 2\beta^2 I_\pm^* S_\pm^* (1-\rho) + \beta^2 {I_\pm^*}^2 (1+\kappa) + \gamma\alpha + \gamma\beta S_\pm^* (1-\rho) \\
&\quad + \gamma\beta I_\pm^* (3-\rho) + \gamma\beta \frac{\alpha}{\eta} I_\pm^* + \eta\alpha + \eta\beta S^* (1-\rho) + 3\eta\beta I_\pm^* \\
&\quad + \alpha\beta I_\pm^* + \eta\gamma - \beta^2 I_\pm^* - \eta\beta - \gamma\beta \\
a_0 &= \eta\beta^2 I_\pm^* \left(2 \left(S_\pm^* (1-\rho) + I_\pm^* \right) - 1 \right) + \gamma\eta\beta (S_\pm^* (1-\rho) \\
&\quad + I_\pm^* (3-\rho) - 1) + (\eta - \gamma)\alpha\beta I_\pm^* (2-\rho) + \gamma\eta\alpha.
\end{aligned}
$$

With the Routh–Hurwitz criteria [15] it follows that:

Theorem 2.5 *Let $\mathcal{E}^*$ be an endemic equilibrium of system (2) and let $J|_{\mathcal{E}^*}$ the coefficient matrix of the linearization of the system (2) about $\mathcal{E}^*$. Then $\mathcal{E}^*$ is LAS if the coefficients of the characteristic polynomial (10) satisfy $a_2 > 0$, $a_0 > 0$, and $a_1 a_2 > a_0$.*

We enrich the analytical results obtained so far by means of numerical investigations.

3 Numerical Bifurcation Analysis

From the analysis in Sect. 2 it becomes clear that β and ρ are critical parameters affecting the qualitative behavior of the system. In this section we extensively investigate the (β, ρ)-parameter plane and numerically identify bifurcations of codimension 1 and 2. The remaining parameters are fixed $\eta = 0.02$, $\alpha = 0.2$, $\gamma = 0.3$, such that $\rho^* \approx 0.1976$. This choice is not motivated by a specific application or data, but highlights the rich dynamics the model can produce. All parametric portraits and simulations shown in what follows are produced using the numerical bifurcation software MATCONT [16]. Background on bifurcation theory can be found e.g. in the seminal books by Yuri Kuznetsov [17] or Stephen Wiggins [18].

At first we investigate regions of the (β, ρ)-plane where ρ is constant and look for bifurcations in β only. Figure 3 shows the (β, I)-plane, where curves of (the I-component of) endemic equilibria in dependence of β are plotted for six different values of ρ, ordered by ascending ρ. Branches in blue (respectively, yellow) represent locally asymptotically stable (respectively, unstable) equilibria. Red asterisks mark either a transcritical bifurcation point (BP), a fold bifurcation point (LP), a supercritical Hopf bifurcation point (H^{sup}), a subcritical Hopf bifurcation point (H^{sub}), or a neutral saddle equilibrium (NS, no bifurcation point). Figure 3 shows that as ρ increases there is a continuous change from a backward bifurcation (Fig. 3a–d) to a forward bifurcation (Fig. 3e–f), as the fold bifurcation point LP crosses the β-axis to the lower half-plane. This is in line with our analytical

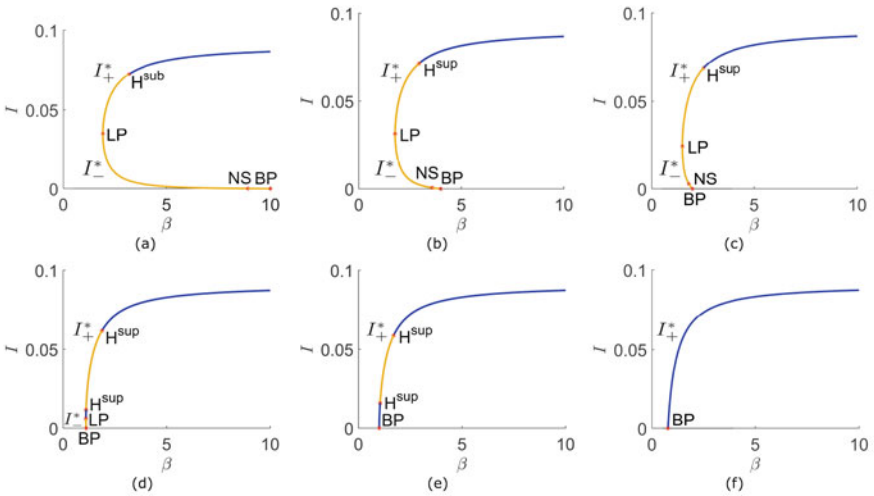

Fig. 3 Curves of (the I-component of) endemic equilibria in dependence of β are plotted for different values of ρ. Branches in blue (respectively, yellow) represent LAS (respectively, unstable) equilibria. (**a**) $\rho = 0.02$. (**b**) $\rho = 0.05$. (**c**) $\rho = 0.1$. (**d**) $\rho = 0.18$. (**e**) $\rho = 0.2$. (**f**) $\rho = 0.25$

results from the previous section (cf. Theorems 2.2–2.4). Further, Hopf bifurcations occur on the equilibria branch corresponding to $\mathcal{E}_+$. We observe a change from a subcritical Hopf bifurcation (Fig. 3a) to a supercritical Hopf bifurcation (Fig. 3b–e). The neutral saddle equilibrium (Fig. 3a–c) gets closer to the fold bifurcation point and finally collides with it and turns into a second supercritical Hopf bifurcation point on the branch of $\mathcal{E}_+$ (Fig. 3d–e). Increasing ρ, the two supercritical Hopf bifurcation points approach each other (Fig. 3d–e) and finally collapse into one point and eventually vanish (Fig. 3f).

MATCONT provides additional information on the eigenvalues of the linearization about the endemic equilibria. In case of a backward bifurcation with a single Hopf bifurcation point (Fig. 3a–c), both endemic equilibria are born unstable at the fold bifurcation. The unstable manifold of $\mathcal{E}_+$ is two dimensional and the one of $\mathcal{E}_-$ is one dimensional. The two eigenvalues of the linearization about $\mathcal{E}_+$ with positive real part cross the imaginary axis at the Hopf bifurcation point so that $\mathcal{E}_+$ becomes LAS. In the situation where we observe two (supercritical, Fig. 3d–e) Hopf bifurcation points on the branch of $\mathcal{E}_+$, this equilibrium was born LAS at the fold bifurcation. Two eigenvalues cross the imaginary axis to the right half-plane at the first Hopf bifurcation point and cross it again back to the left half-plane at the second Hopf bifurcation point.

The above observations help us to understand the parametric portrait in β and ρ, and the arising codimension 2 bifurcations. Continuation of fold and transcritical bifurcation points with respect to β and ρ leads to Fig. 4a. The curve of fold bifurcations (straight line) and the curve of transcritical bifurcations (curved line) meet at the point labeled CP. This point marks a cusp bifurcation where the normal form coefficient of the fold bifurcation vanishes. It divides the curve of transcritical bifurcations into the branch of forward bifurcations (upper part) and backward bifurcations (lower part). In addition, a Bogdanov–Takens (BT) bifurcation occurs on the curve of fold bifurcation points, where an additional eigenvalue approaches

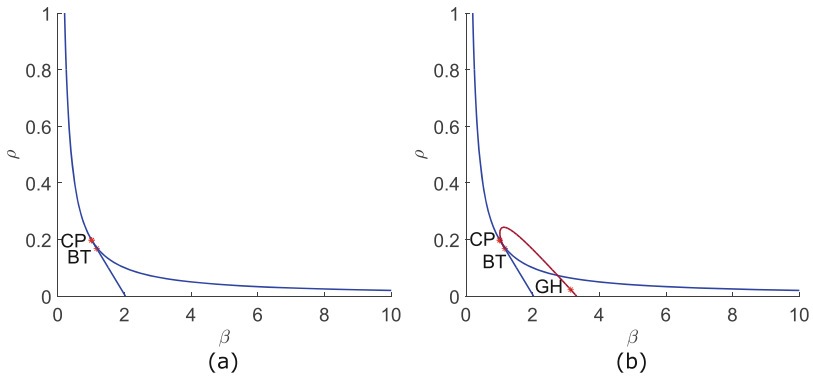

Fig. 4 (**a**) Continuation of fold and transcritical bifurcation points with respect to β and ρ; (**b**) Continuation of Hopf bifurcation points with respect to β and ρ starting from the Bogdanov–Takens point BT

the imaginary axis. At the BT point the curve of Hopf bifurcation points collides with the curve of fold bifurcations. Continuation of the Hopf bifurcation curve from BT leads to the red curve in Fig. 4b (neutral saddle equilibria are not shown here). The Bogdanov–Takens point BT marks the point where the neutral saddle equilibrium turns into a supercritical Hopf bifurcation point or vice versa. The semi-elliptic shape of the Hopf curve leads to the occurrence of two Hopf bifurcations for values of ρ above the Bogdanov–Takens point (cf. Fig. 3d–e). Another codimension 2 bifurcation arises on the curve of Hopf bifurcations. A generalized Hopf bifurcation, where the first Lyapunov coefficient is zero and changes its sign, labeled GH marks the point where the Hopf bifurcation changes from subcritical (lower part) to supercritical (upper part). In what follows, we study the branches of limit cycles emerging from these Hopf bifurcation points.

In Fig. 5a–b we see that, for sufficiently small values of ρ, as β increases the amplitudes of the unstable limit cycles born at the subcritical Hopf bifurcation

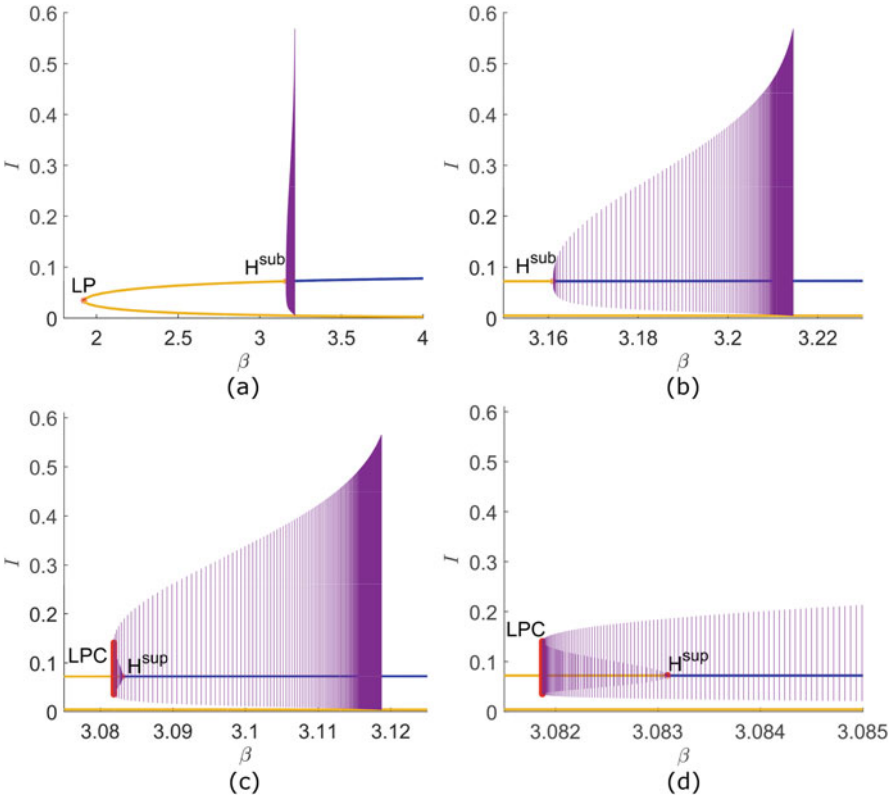

Fig. 5 (**a**) Continuation of limit cycles with respect to β starting from subcritical Hopf bifurcation point for $\rho = 0.02$; (**b**) Zoom of (**a**); (**c**) Continuation of limit cycles with respect to β starting from supercritical Hopf bifurcation point for $\rho = 0.03$. The branch of stable limit cycles reaches a limit point cycle, folds back, and becomes unstable; (**d**) Zoom of (**c**)

increase as well. The limit cycles get closer and closer to $\mathcal{E}_-$. This increases the period of the closed orbits, and a point moving on such orbits spends more and more time in the proximity of the equilibrium. The branch of limit cycles disappears by colliding with the one-dimensional unstable manifold of $\mathcal{E}_-$ leading to a saddle homoclinic bifurcation (more details are provided in the master thesis [19] of the first author).

Figure 5c–d shows the same plot for a slightly larger value of ρ such that the involved Hopf bifurcation is supercritical. The branch of stable limit cycles reaches a limit point cycle (LPC) then folds back and becomes unstable. Thus, there is a small interval of values of β in which a stable limit cycle and an unstable one coexist. The unstable branch of limit cycles vanishes through a saddle homoclinic bifurcation. Increasing ρ further, the interval of values of β where a stable limit cycle exists becomes larger, while the interval where an unstable limit cycle exists gets smaller and eventually vanishes (i.e. there is no LPC involved anymore). In this case it is the branch of stable limit cycles that vanishes through a saddle homoclinic bifurcation (not shown here, cf. [19]).

Increasing ρ further, two Hopf Bifurcation points, hence two branches of stable limit cycles exist, both vanishing through a saddle homoclinic bifurcation (not shown here, cf. [19]). For even larger values of ρ there exists a bubble of limit cycles, starting and ending at the Hopf Bifurcation points (cf. Fig. 6a). Increasing ρ the bubble becomes smaller (cf. Fig. 6b), until the two Hopf points collide and the limit cycles vanish (cf. Fig. 3f).

Continuation of the curve of saddle homoclinic bifurcations (light green) and fold bifurcations of limit cycles (magenta) yield the complete parametric portrait in Fig. 7. The different bifurcation curves subdivide the (β, ρ)-plane into regions where the system shows different qualitative behavior. We conclude this numerical study by a discussion of typical solution trajectories and orbits for each region.

Region I The disease-free equilibrium $\mathcal{E}_0$ is the only equilibrium and it is LAS (Fig. 8). Crossing the boundary to region IX leads to a transcritical bifurcation

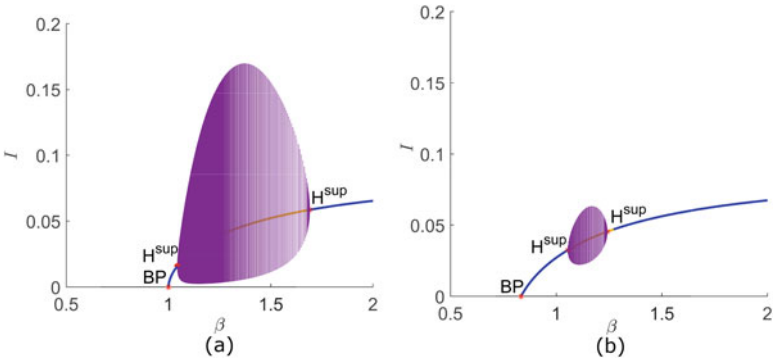

Fig. 6 Continuation of limit cycles with respect to β starting from two supercritical Hopf bifurcation points for (**a**) $\rho = 0.2$ and (**b**) $\rho = 0.24$. The two branches of stable limit cycles meet and form an endemic bubble

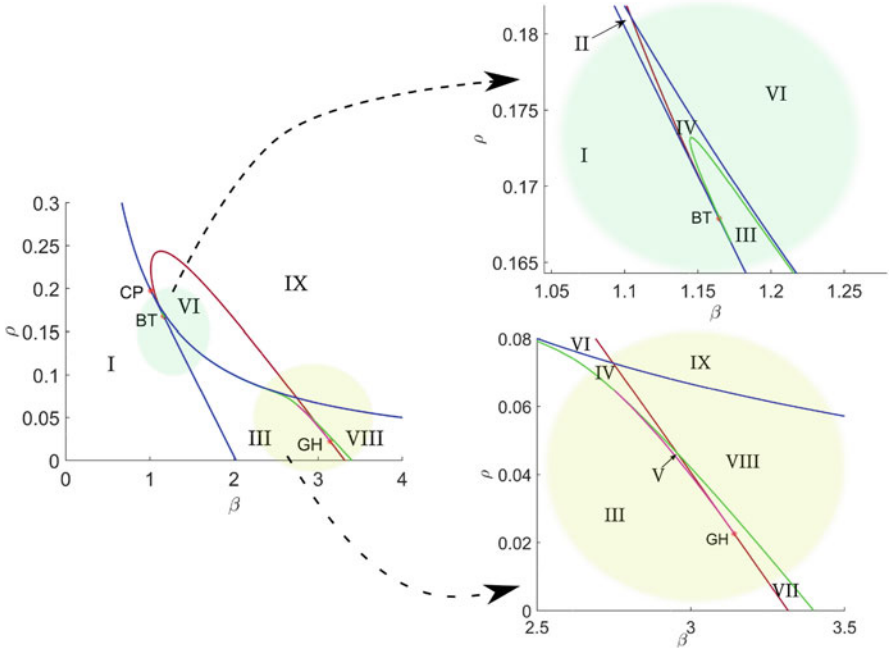

Fig. 7 Parametric portrait with respect to β and ρ. The different bifurcation curves subdivide the (β, ρ)-plane into regions. The green and yellow balloons show zoomed regions around the BT and GH point, respectively

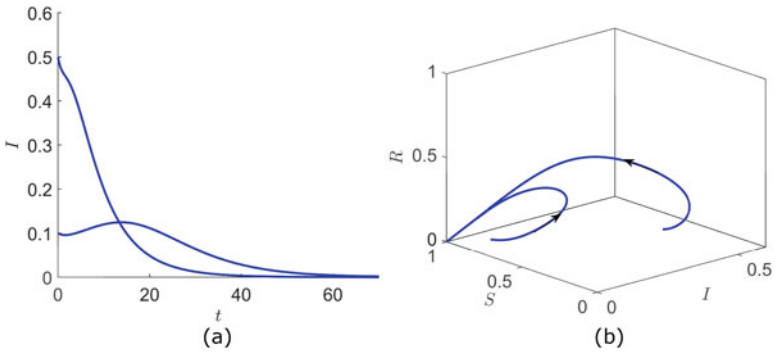

Fig. 8 Dynamics in region I: Convergence to $\mathcal{E}_0$ shown in (**a**) (t, I)-plane and (**b**) (S, I, R)-phase space. For these simulations we set parameter values: $\beta = 1$, $\rho = 0.15$, $\alpha = 0.2$, $\gamma = 0.3$, and $\eta = 0.02$; and initial conditions: $R_0 = 0$, $I_0 = 0.5$ and $I_0 = 0.1$, $S = 1 - I_0$

through which $\mathcal{E}_0$ loses stability and the LAS $\mathcal{E}_+$ arises. Crossing the boundary to region II results into a fold bifurcation, with the LAS equilibrium $\mathcal{E}_+$ and the unstable equilibrium $\mathcal{E}_-$ (with one-dimensional unstable manifold). Passing from region I to region III also leads to a fold bifurcation, through which both $\mathcal{E}_+$ (two-

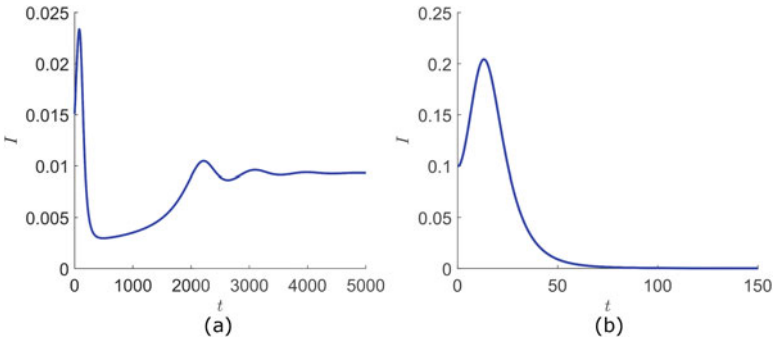

Fig. 9 Dynamics in region II: Bistability of $\mathcal{E}_0$ and $\mathcal{E}_+$. For these simulations we set parameter values: $\beta = 1.1$, $\rho = 0.181$, $\alpha = 0.2$, $\gamma = 0.3$, and $\eta = 0.02$, and initial conditions: (**a**) $R_0 = 0.1,\ S_0 = 0.85,\ I_0 = 0.015$; (**b**) $R_0 = 0,\ S_0 = 0.9,\ I_0 = 0.1$

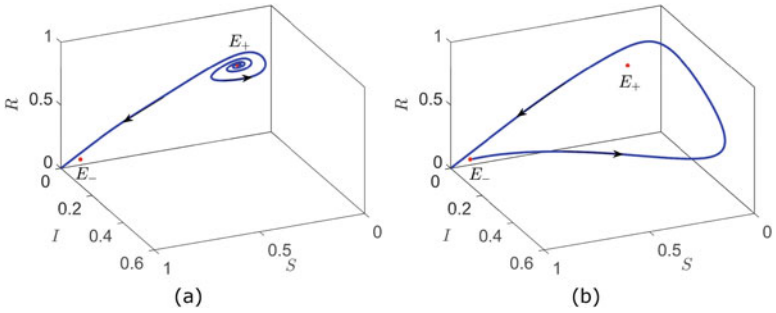

Fig. 10 Dynamics in region III: Convergence to the DFE $\mathcal{E}_0$. Both endemic equilibria $\mathcal{E}_\pm$ are unstable. For these simulations we set parameter values: $\beta = 2.5$, $\rho = 0.05$, $\alpha = 0.2$, $\gamma = 0.3$, and $\eta = 0.02$; and initial conditions: (**a**) $R_0 = 0.65,\ S_0 = 0.207,\ I_0 = 0.065$; (**b**) $R_0 = 0.05,\ S_0 = 0.9,\ I_0 = 0.006$

dimensional unstable manifold) and $\mathcal{E}_-$ (one-dimensional unstable manifold) arise unstable.

Region II The disease-free equilibrium $\mathcal{E}_0$ is LAS. Both endemic equilibria $\mathcal{E}_\pm$ exist, $\mathcal{E}_+$ being LAS and $\mathcal{E}_-$ being unstable with one-dimensional unstable manifold. Figure 9 shows the bistability of $\mathcal{E}_0$ and $\mathcal{E}_+$. Crossing the boundary to region IX leads to a transcritical bifurcation through which $\mathcal{E}_0$ loses stability and $\mathcal{E}_-$ moves out of the first quadrant. Passing from region II to region IV leads to a Hopf bifurcation through which $\mathcal{E}_+$ becomes unstable with two-dimensional unstable manifold, and a stable periodic orbit emerges. Crossing the boundary between region II and region VI (intersection of Hopf and transcritical bifurcation curve) the above bifurcations happen simultaneously.

Region III The system has three equilibria (cf. Fig. 10). The DFE $\mathcal{E}_0$ is LAS and both endemic equilibria $\mathcal{E}_\pm$ are unstable, the unstable manifold of $\mathcal{E}_+$ being

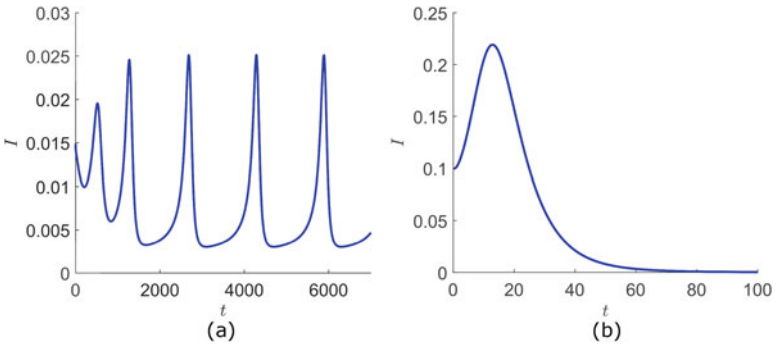

Fig. 11 Dynamics in region IV: Bistability of $\mathcal{E}_0$ and a limit cycle. For these simulations we set parameter values: $\beta = 1.14,\ \rho = 0.174,\ \alpha = 0.2,\ \gamma = 0.3$, and $\eta = 0.02$; and initial conditions: (**a**) $R_0 = 0.15,\ S_0 = 0.82,\ I_0 = 0.015$; (**b**) $R_0 = 0,\ S_0 = 0.9,\ I_0 = 0.1$

two dimensional, that of $\mathcal{E}_-$ one dimensional. We observe the phenomenon of excitability: Solutions starting close to $\mathcal{E}_-$ follow its unstable manifold, which leads to a large epidemic outbreak before converging to $\mathcal{E}_0$ (cf. Fig. 10b). Crossing the boundary to region IV results into a saddle homoclinic bifurcation, which produces a stable periodic orbit. Passing the boundary to region V, a fold bifurcation of limit cycles takes place and a stable and an unstable periodic orbit are born. Moving from region III to region VII leads to a subcritical Hopf bifurcation; $\mathcal{E}_+$ becomes LAS and an unstable limit cycle arises.

Region IV The disease-free equilibrium $\mathcal{E}_0$ is LAS and both endemic equilibria $\mathcal{E}_\pm$ are unstable, the unstable manifold of $\mathcal{E}_+$ being two dimensional, that of $\mathcal{E}_-$ one dimensional. Additionally, a stable limit cycle exists. This leads to a bistability of the disease-free equilibrium and a periodic solution (cf. Fig. 11). Crossing the boundary to region V results in a saddle homoclinic bifurcation, which produces a second (unstable) periodic orbit. Passing the boundary to region VI, a transcritical bifurcation occurs, through which $\mathcal{E}_0$ loses stability and $\mathcal{E}_-$ moves out of the first quadrant. Moving from region IV to region VIII leads to a Hopf bifurcation, $\mathcal{E}_+$ becomes LAS, and the stable periodic orbit vanishes. Crossing the boundary to region IX (intersection of Hopf and transcritical bifurcation curve) the last two bifurcations happen simultaneously.

Region V The dynamical behavior in this region is similar to that in Region IV (cf. Fig. 12). Additionally to the stable limit cycle, an unstable limit cycle exists, separating the basin of attraction of $\mathcal{E}_0$ and of the stable limit cycle. Like in Region III, we observe the phenomenon of excitability for orbits starting close to $\mathcal{E}_-$ (cf. Fig. 12a). Moving to region VII leads to a supercritical Hopf bifurcation. The stable limit cycle disappears and $\mathcal{E}_+$ becomes LAS. Crossing the boundary to region VIII (intersection of Hopf and saddle homoclinic bifurcation curve) the

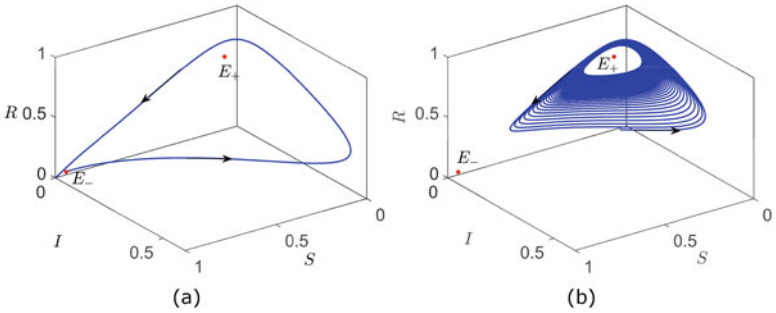

Fig. 12 Dynamics in region V: Bistability of $\mathcal{E}_0$ and a limit cycle. For these simulations we set parameter values: $\beta = 2.952,\ \rho = 0.046,\ \alpha = 0.2,\ \gamma = 0.3,\ \eta = 0.02$ and initial conditions: (**a**) $R_0 = 0.03,\ S_0 = 0.94,\ I_0 = 0.003$; (**b**) $R_0 = 0.3,\ S_0 = 0.3,\ I_0 = 0.2$

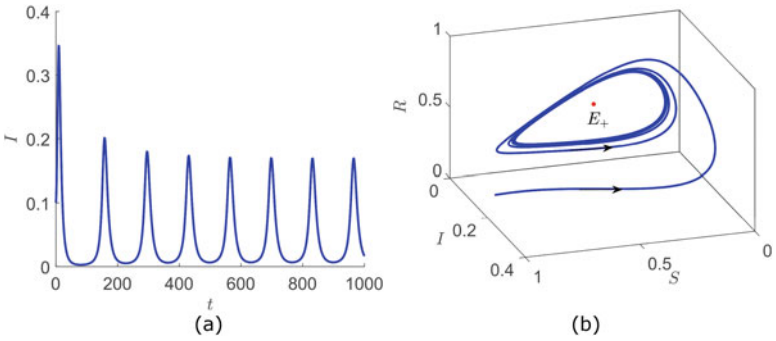

Fig. 13 Dynamics in region VI: Convergence to a stable limit cycle shown in (**a**) (t, I)-plane and (**b**) (S, I, R)-phase space. For these simulations we set parameter values: $\beta = 1.4,\ \rho = 0.2,\ \alpha = 0.2,\ \gamma = 0.3,\ \eta = 0.02$ and initial conditions: $R_0 = 0,\ S_0 = 0.9,\ I_0 = 0.1$

supercritical Hopf bifurcation happens simultaneously with a saddle homoclinic bifurcation through which also the unstable limit cycle vanishes.

Region VI The disease-free equilibrium $\mathcal{E}_0$ is unstable, and so is also the only endemic equilibrium $\mathcal{E}_+$. There exists a stable limit cycle to which solutions converge (cf. Fig. 13). Moving from region VI to region IX leads to a supercritical Hopf bifurcation, the stable limit cycle vanishes, and $\mathcal{E}_+$ becomes LAS.

Region VII The equilibria $\mathcal{E}_0$ and $\mathcal{E}_+$ are both LAS (cf. Fig. 14), whereas the third equilibrium $\mathcal{E}_-$ is unstable with one-dimensional unstable manifold. Furthermore, there exists an unstable periodic orbit that separates the basin of attraction of $\mathcal{E}_0$ and $\mathcal{E}_+$. Like in Region III, we observe the phenomenon of excitability for orbits starting close to $\mathcal{E}_-$ (cf. Fig. 14b). Crossing the boundary to region VIII leads to a saddle homoclinic bifurcation and the unstable periodic orbit vanishes.

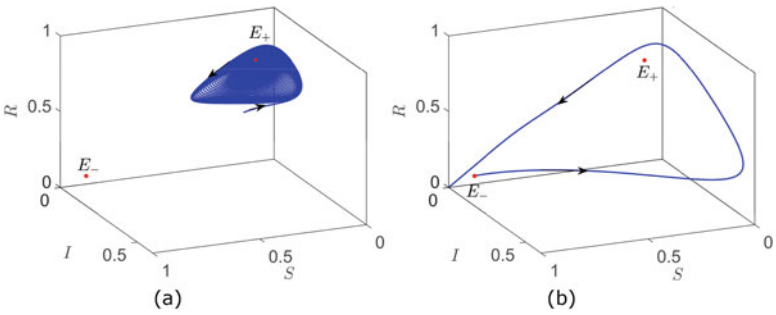

Fig. 14 Dynamics in region VII: Bistability of $\mathcal{E}_0$ and $\mathcal{E}_+$. For these simulations we set parameter values: $\beta = 3.27$, $\rho = 0.01$, $\alpha = 0.2$, $\gamma = 0.3$, $\eta = 0.02$ and initial conditions: (**a**) $R_0 = 0.5$, $S_0 = 0.3$, $I_0 = 0.2$; (**b**) $R_0 = 0.06$, $S_0 = 0.88$, $I_0 = 0.006$

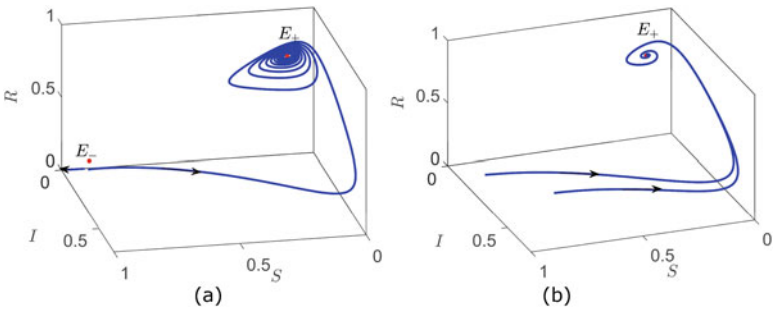

Fig. 15 (**a**) Dynamics in region VIII: Bistability of $\mathcal{E}_0$ and $\mathcal{E}_+$. For these simulations we set parameter values: $\beta = 3.4$, $\rho = 0.01$, $\alpha = 0.2$, $\gamma = 0.3$, $\eta = 0.02$ and initial values: $R_0 = 0$, $S_0 = 0.9$, $I_0 = 0.001$ and $I_0 = 0.01$. (**b**) Dynamics in region IX: Convergence to the unique endemic equilibrium $\mathcal{E}_+$. For these simulations we set parameter values: $\beta = 2.5$, $\rho = 0.25$, $\alpha = 0.2$, $\gamma = 0.3$, $\eta = 0.02$ and initial conditions: $R_0 = 0$, $I_0 = 0.1$ and $I_0 = 0.3$, $S_0 = 1 - I_0$

Region VIII In this region, we have bistability of $\mathcal{E}_0$ and $\mathcal{E}_+$ (cf. Fig. 15a). The second endemic equilibrium $\mathcal{E}_-$ is unstable with one-dimensional unstable manifold connecting to $\mathcal{E}_+$. Crossing the boundary to region IX, a transcritical bifurcation takes place, such that $\mathcal{E}_0$ loses stability and $\mathcal{E}_-$ leaves the positive quadrant.

Region IX The DFE $\mathcal{E}_0$ is unstable, and the unique endemic equilibrium $\mathcal{E}_+$ is LAS (cf. Fig. 15b).

So far we have investigated the (β, ρ)-parameter plane fixing the values of α, γ, η. One might ask how the qualitative behavior of system (2) is affected by the particular choice of these three parameters. For instance, we constructed the parametric portrait from Fig. 7 for different values of η (same was done for α and γ, though not shown here). The result is shown in Fig. 16. Reducing η (Fig. 16a) region VI gets significantly larger. Slowing down the transition from R to S makes the model closer to a SIRS system with delay (cf. [20, 21]) enhancing the occurrence of

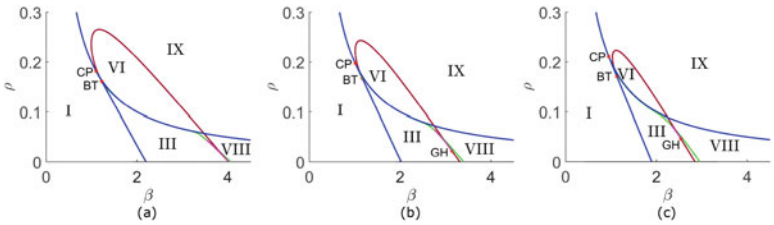

Fig. 16 Parametric portrait in β and ρ, for $\alpha = 0.2$, $\gamma = 0.3$, and (**a**) $\eta = 0.016$; (**b**) $\eta = 0.02$; (**c**) $\eta = 0.024$

oscillations. Moreover, the generalized Hopf point in Fig. 16b moves to the fourth quadrant. In contrast, increasing η (Fig. 16c) region VI gets significantly smaller, whereas the points GH, CP, BT move up along the bifurcation curves.

4 Discussion

In this chapter we have presented a mathematical model for transmission dynamics with two nonlinear stages of contagion, applying analytical and numerical methods to analyze its qualitative behavior. The two-stage contagion is combined with a renewal of the susceptible compartment, modeled by (i) the waning of immunity in inactive/resistant individuals and (ii) the fading of infection in those individuals who are weakened after the first contact with the promoting/infected community. This leads to rich dynamics, including bistability of equilibria or bistability of an equilibrium and a periodic solution, discontinuous regime shifts through hysteresis effects, and excitability. Thus, the multi-stage nature of social contagion processes might explain some of the complex phenomena observed in social dynamics (see e.g. the irregular [22] or periodic [23] outcomes in political elections, or the emergence of new trends in the usage of social media [24]). In a previous study by Guy Katriel [8] similar properties were determined for a two-stage contagion model with demographic turnover. This lets us conjecture that the rich dynamics observed in our work and in [8] is due to the coupling of a two-stage contagion process with any (demographic or "immunological") source of renewal of the susceptible population. Despite of the analogies with Katriel's work, the combination of waning of immunity and fading of infection in our model leads to additional analytical complexity. The analytical advantage of Katriel's model was possibly due to the choice of the birth rate in the S-compartment matching with the death rates of all compartments. Katriel's model shows also both backward and forward bifurcation, and in the latter case it behaves like a one-stage contagion model for any choice of β. In contrast, our model shows Hopf bifurcations, hence periodic solutions, also in case of a forward bifurcation (cf. Fig. 7e). Single phenomena which can be observed in our model have been previously found also for variations of the

classical one-stage contagion models. For example SIRS models with delayed loss of immunity [20] naturally show stable periodic solutions, whereas bistability of equilibria was found e. g. in models with exogenous reinfection [14] or imperfect vaccination [25].

In this work we have focused on the investigation of the qualitative properties of a simple two-stage contagion model. We have numerically investigated the parameter space, focusing in particular on the effects of the transmission rate (β) and the probability of a perfect contact (ρ). Of course the study could be repeated deriving the parametric portrait of the system (2) with respect to the other model parameters as well. Moreover, we see three possible generalizations of our model: (i) the assumption that $\beta = \beta_2$ could be relaxed, and e.g. W-individuals might be assumed to have a higher susceptibility than S-individuals; (ii) individuals in the W-compartment could also be contagious (cf. also [26]); (iii) the model could also include births and deaths, in addition to waning/fading processes. All these variations would make the analytical investigations more challenging; however, a similar numerical investigation as presented in this work could be performed. Thinking of applications and comparison with data, the major limitation of our work is due to the deterministic approach. Dividing a population into a few homogeneous compartments, without taking into account interpersonal variability, is indeed a major simplification of reality. Refining our approach, agent-based modeling [27] and complex networks [28] could be used. In certain cases, previous works based on these methods also included two-stage contagion [29, 30].

Appendix A

In the proof of Theorem 2.2 we referred to the following result by Castillo-Chavez and Song [14] proved using center-manifold theory.

Theorem A.1 *Let $f \in C^2(\mathbb{R}^n \times \mathbb{R}, \mathbb{R}^n)$. Consider the following general system of ODEs with a parameter β:*

$$\frac{dx}{dt} = f(x, \beta). \tag{A.1}$$

Without loss of generality assume that $x_0 = 0$ is an equilibrium point of the system, that is, $f(0, \beta) = 0$ for all $\beta \in \mathbb{R}$. Assume the following:

- *The linearization of the system (A.1) $\mathcal{A} := D_x f(0, 0) = \left(\frac{\partial f_i}{\partial x_j}(0, 0)\right)$ has zero as a simple eigenvalue and all other eigenvalues of $\mathcal{A}$ have negative real parts.*
- *The matrix $\mathcal{A}$ has a non-negative right eigenvector w and a left eigenvector v each corresponding to the zero eigenvalue.*

Let f_k be the k-th component of f and

$$a = \sum_{k,i,j=1}^{n} v_k w_i w_j \frac{\partial^2 f_k}{\partial x_i \partial x_j}(0,0)$$

$$b = \sum_{k,i=1}^{n} v_k w_i \frac{\partial^2 f_k}{\partial x_i \partial \beta}(0,0).$$

Then, the local dynamics of the system around 0 is completely determined by the signs of a and b:

1. *$a > 0$, $b > 0$. When $\beta < 0$ with $|\beta| \ll 1$, 0 is locally asymptotically stable and there exists a positive unstable equilibrium; when $0 < \beta \ll 1$, 0 is unstable and there exists a negative and locally asymptotically stable equilibrium.*
2. *$a < 0$, $b < 0$. When $\beta < 0$ with $|\beta| \ll 1$, 0 is unstable; when $0 < \beta \ll 1$, 0 is locally asymptotically stable and there exists a positive unstable equilibrium.*
3. *$a > 0$, $b < 0$. When $\beta < 0$ with $|\beta| \ll 1$, 0 is unstable and there exists a locally asymptotically stable negative equilibrium; when $0 < \beta \ll 1$, 0 is stable and a positive unstable equilibrium appears.*
4. *$a < 0$, $b > 0$. When β changes from negative to positive, 0 changes its stability from stable to unstable. Correspondingly, a negative unstable equilibrium becomes positive and locally asymptotically stable.*

In particular, if $a > 0$ and $b > 0$, a backward bifurcation occurs at $\beta = 0$, and if $a < 0$ and $b > 0$, a forward bifurcation occurs at $\beta = 0$.

Remark A.1 Remark 1 in [14] suggests that if the equilibrium of interest in Theorem A.1 is a non-negative equilibrium x_0, then the requirement that w is non-negative is not necessary. When some components in w are negative, one can still apply Theorem A.1 provided that the j-th component of w is positive whenever the j-th component of x_0 is zero. If the j-th component of x_0 is positive, then the j-th component of w need not be positive.

References

1. American Psychological Association, *Dictionary of Psychology*, https://dictionary.apa.org/social-contagion (last accessed 10 Sept, 2020).
2. J. Sooknanan, and D. M. Comissiong, *When behaviour turns contagious: the use of deterministic epidemiological models in modeling social contagion phenomena*, Int. J. Dyn. Control **5(4)**, 1046 (2017).
3. W. Goffman, and V. A. Newill, *Generalization of epidemic theory: An application to the transmission of ideas*, Nature **204(4955)**, 225 (1964).
4. L. M. Bettencourt, A. Cintrn-Arias, D. I. Kaiser and C. Castillo-Chvez, *The power of a good idea: Quantitative modeling of the spread of ideas from epidemiological models*, Physica A **364**, 513 (2006).

5. F. Jin, E. Dougherty, P. Saraf, Y. Cao and N. Ramakrishnan, *Epidemiological modeling of news and rumors on twitter*, In SNAKKD'13: Proceedings of The 7th Workshop on Social Network Mining and Analysis (2013).
6. J. Woo and H. Chen, *Epidemic model for information diffusion in web forums: experiments in marketing exchange and political dialog*, Springer (2016).
7. S. Wang, L. Rong and J. Wu, *Bistability and multistability in opinion dynamics models*, Appl. Math. Comput. **289**, 388 (2016).
8. G. Katriel, *The dynamics of two-stage contagion*, Chaos Solitons Fract. **2**, 100010 (2019).
9. C. T. Bauch and A. P. Galvani, *Social factors in epidemiology*, Science **342(6154)**, 47 (2013).
10. A. L. Hill, D. G. Rand, M. A. Nowak and N. A. Christakis, *Infectious disease modeling of social contagion in networks*, PLoS Comp. Biol. **6(11)**, e1000968 (2010).
11. M. Martcheva, *An introduction to mathematical epidemiology*, Springer (2015).
12. M.V. Barbarossa and G. Rst,*Immuno-epidemiology of a population structured by immune status: a mathematical study of waning immunity and immune system boosting*, J. Math. Biol. **71(6)**, 1737 (2015).
13. E. M. Rogers, *Diffusion of Innovations*, Free Press (2010).
14. C. Castillo-Chavez and B. Song, *Dynamical models of tuberculosis and their applications*, Math. Bioscie. Eng. **1(2)**, 361 (2004).
15. J. D. Murray, *Mathematical biology: I. An introduction*, Springer (2007).
16. A. Dhooge, W. Govaerts and Y. A. Kuznetsov *MATCONT: a MATLAB package for numerical bifurcation analysis of ODEs*, ACM Trans. Math. Software **29(2)**, 141 (2003).
17. Y. A. Kuznetsov, *Elements of applied bifurcation theory*, Springer (2013).
18. S. Wiggins, *Introduction to applied nonlinear dynamical systems and chaos*, Springer (2003).
19. J. Heidecke, *Mathematical modelling of transmission processes with two-stage contagion*, Master Thesis, Heidelberg University, Heidelberg (2020).
20. M. L. Taylor and T. W. Carr, *An SIR epidemic model with partial temporary immunity modeled with delay*, J. Math. Biol. **59(6)**, 841 (2009).
21. M. V. Barbarossa, M. Polner and G. Röst, *Stability switches induced by immune system boosting in an SIRS model with discrete and distributed delays*, SIAM J. Appl. Math. **77(3)**, 905 (2017).
22. Politico. *Italy – National parliament voting intention* https://www.politico.eu/europe-poll-of-polls/italy/ (last accessed Oct 14 2020)
23. Wikipedia. *United States presidential election* https://en.wikipedia.org/wiki/United_States_presidential_election (last accessed Oct 14 2020)
24. E. Ortiz-Ospina. *The rise of social media. Our world in data, Sept 28 2019* https://ourworldindata.org/rise-of-social-media (last accessed Oct 14 2020)
25. F. Brauer, *Backward bifurcations in simple vaccination models*, J. Math. Anal. Appl. **298(2)**, 418 (2004).
26. N. M. Crisosto, C. M. Kribs-Zaleta, C. Castillo-Chvez and S. Wirkus, *Community resilience in collaborative learning*, Discr. Cont. Dyn. Sys. B **14(1)**, 17 (2010).
27. G. Deffuant, D. Neau, F. Amblard and G. Weisbuch, *Mixing beliefs among interacting agents*, Adv. Complex Sys. **3(01n04)**, 87 (2000).
28. G. Albi, L. Pareschi and M. Zanella, *Opinion dynamics over complex networks: kinetic modeling and numerical methods*, Kin. Rel. Models **10(1)** (2017).
29. T. Hasegawa and K. Nemoto, *Discontinuous transition of a multistage independent cascade model on networks*, J. Stat. Mech. **2014(11)**, P11024 (2014).
30. S. Melnik, J. A. Ward, J. P. Gleeson and M. A. Porter *Multi-stage complex contagions*, Chaos **23(1)**, 013124 (2013).

Dynamic Analysis of SLIR Model Describing the Effectiveness of Quarantine Against the Spread of COVID-19

Omar Khyar and Karam Allali

1 Introduction

Mathematical models play an essential role to describe the dynamics of many infectious diseases. The first models usually use three main populations that are the susceptible $S(t)$, the infectious $I(t)$, and the removed individuals $R(t)$ at a specific time t. The basic SIR formulation is introduced in the pioneer work [1]; but, when an individual is incubated but still not yet infectious, another class should be added; this class is called latent compartment noted by $L(t)$. A mutation process was observed in many infections such as tuberculosis [2], human immunodeficiency virus [3], dengue fever [4], influenza [5], and other sexually transmitted diseases. This phenomenon can result in the observation on two or more strains of the studied pathogen. Hence, multi-strain model can better describe different type of diseases.

Recently, two-strain SLIR epidemic model has been tackled [6], the authors consider two incidence rates, the first is bilinear while the second is non-monotonic. More recently, the same problem with two strains is treated by choosing both the incidences as non-monotonic [7]. The generalization of a multi-strain SLIR epidemiological model with general incidence rates is studied in [8]; the authors compare the numerical simulations with COVID-19 clinical data. In this work, we continue the investigation of this last kind of problems by taking into consideration the effect of quarantine measures on SLIR model with two non-monotonic incidence rates. The two-strains SLIR epidemiological model that we consider is formulated as follows:

O. Khyar (✉) · K. Allali
Department of Mathematics, Faculty of Sciences and Technology, Mohammedia University Hassan II-Casablanca, Mohammedia, Morocco

R. P. Mondaini (ed.), *Trends in Biomathematics: Chaos and Control in Epidemics, Ecosystems, and Cells*, https://doi.org/10.1007/978-3-030-73241-7_15

$$\begin{cases} \dfrac{dS}{dt} = \Lambda - \dfrac{\alpha(1-u_1)SI_1}{1+mI_1^2} - \dfrac{\beta(1-u_2)SI_2}{1+kI_2^2} - \delta S\ , \\ \dfrac{dL_1}{dt} = \dfrac{\alpha(1-u_1)SI_1}{1+mI_1^2} - (\gamma_1+\delta)L_1\ , \\ \dfrac{dL_2}{dt} = \dfrac{\beta(1-u_2)SI_2}{1+kI_2^2} - (\gamma_2+\delta)L_2\ , \\ \dfrac{dI_1}{dt} = \gamma_1 L_1 - (\mu_1+\delta)I_1\ , \\ \dfrac{dI_2}{dt} = \gamma_2 L_2 - (\mu_2+\delta)I_2\ , \\ \dfrac{dR}{dt} = \mu_1 I_1 + \mu_2 I_2 - \delta R\ , \end{cases} \tag{1}$$

with

$$S(0) \geq 0,\ L_1(0) \geq 0,\ L_2(0) \geq 0,\ I_1(0) \geq 0,\ I_2(0) \geq 0,\ R(0) \geq 0.$$

This model contains six variables, that are, susceptible individuals (S), two categories of latent individuals: (L_1) and (L_2), two categories of infectious individuals: (I_1) and (I_2), and removed individuals (R). The parameters of the model (1) are described in Table 1 and the two-strain SLIR diagram is illustrated in Fig. 1; the

Table 1 Description of parameters of the model (1)

Parameters	Description
Λ	Recruitment rate
$1/\delta$	Average life expectancy of the population
α	Infection rate of the strain 1
β	Infection rate of the strain 2
$1/\mu_1$	Average infection period of strain 1
$1/\mu_2$	Average infection period of strain 2
$1/\gamma_1$	The average latency period of strain 1
$1/\gamma_2$	The average latency period of strain 2
m	Parameter that measures the psychological or inhibitory effect of strain 1
k	Parameter that measures the psychological or inhibitory effect of strain 2

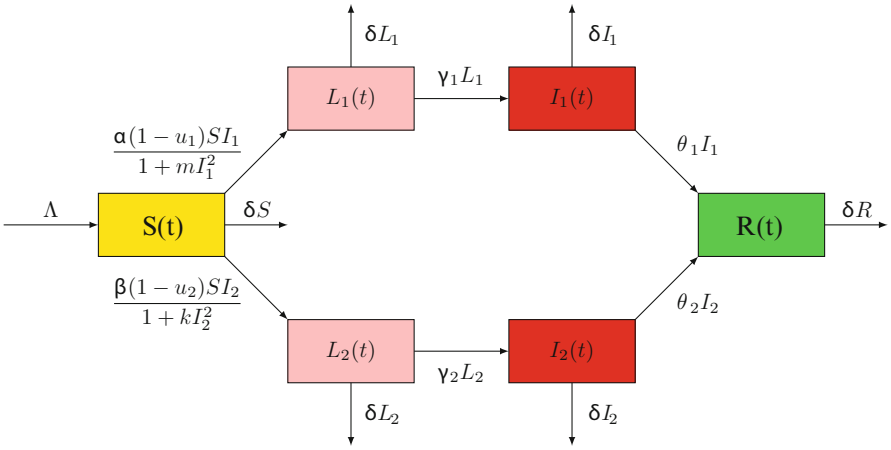

Fig. 1 The diagram of SLIR two-strain model

parameters are given in Table 1. The last two new parameters to the model u_1 and u_2 represent the efficiency of quarantine in reducing the first strain infection and the second strain infection, respectively.

The present work is organized as follows. In the next section, we will prove the positivity and the boundedness results. In Sect. 3, we fulfilled the global analysis of our model. In Sect. 4, we will give some results of the numerical simulations. Short conclusion is given in the last section.

2 Positivity and Boundedness of Solutions

Since our problem is related to the population dynamics, we will prove that all model variables are positive and bounded. First, we will assume that all the parameters in our model are positive.

Proposition 2.1 *For any positive initial conditions* $S(0)$, $L_1(0)$, $L_2(0)$, $I_1(0)$, $I_2(0)$, $R(0)$, *the variables of the model* (1) $S(t)$, $L_1(t)$, $L_2(t)$, $I_1(t)$, $I_2(t)$, *and* $R(t)$ *will remain positive for all* $t > 0$.

Proof First, let

$$T = sup\{\tau \geq 0 \mid \forall t, 0 \leq t \leq \tau \text{ such that } S(t) \geq 0,\ L_1(t) \geq 0,\ L_2(t) \geq 0,$$
$$I_1(t) \geq 0, I_2(t) \geq 0\ , R(t) \geq 0\}.$$

Let us now demonstrate that $T = +\infty$.

Assume that $0 < T < +\infty$; by continuity, we will have $S(T) = 0$ or $L_1(T) = 0$ or $L_2(T) = 0$ or $I_1(T) = 0$ or $I_2(T) = 0$ or $R(T) = 0$. If $S(T) = 0$ before the

other variables L_1, L_2, I_1, I_2, R, become zero. Therefore

$$\frac{dS(T)}{dt} = \lim_{t \to T^-} \frac{S(T) - S(t)}{T - t} = \lim_{t \to T^-} \frac{-S(t)}{T - t} \leq 0.$$

From the first equation of the system (1), we have

$$\frac{dS(T)}{dt} = \Lambda > 0.$$

If $L_1(T) = 0$ before S, L_2, I_1, I_2, and R. Then

$$\frac{dL_1(T)}{dt} = \lim_{t \to T^-} \frac{L_1(T) - L_1(t)}{T - t} = \lim_{t \to T^-} \frac{-L_1(t)}{T - t} \leq 0.$$

From the second equation of the system (1) with the fact $L_1(T) = 0$, which gives

$$\frac{dL_1(T)}{dt} = \frac{\alpha(1 - u_1)SI_1}{1 + mI_1^2}.$$

Since u_1 and u_2 reflect the effectiveness of quarantine, we have $u_i \in [0, 1]$, $i = 1, 2$. Therefore, $\alpha(1 - u_1)$ and m are positive, and we have

$$\frac{dL_1(T)}{dt} > 0.$$

Also, if $I_1 = 0$ before S, L_1, L_2, I_2, R become zero, then

$$\frac{dI_1(T)}{dt} = \lim_{t \to T^-} \frac{I_1(T) - I_1(t)}{T - t} = \lim_{t \to T^-} \frac{-I_1(t)}{T - t} \leq 0.$$

But from the fourth equation of the system (1) with $I_1(T) = 0$, we will have

$$\frac{dI_1(T)}{dt} = \gamma_1 L_1.$$

Since $\gamma_1 > 0$, we have

$$\frac{dI_1(T)}{dt} = \gamma_1 L_1 > 0.$$

Similar proofs for $L_2(t)$, $I_2(t)$, and $R(t)$.

We conclude that T could not be finite; this completes the proof.

Proposition 2.2 *The biologically feasible region is represented by*

$$\mathcal{H} = \{(S, L_1, L_2, I_1, I_2, R) \in \mathbb{R}^6_+ \text{ such that } S + L_1 + L_2 + I_1 + I_2 + R \leq \frac{\Lambda}{\delta}\}$$

is positively invariant.

Proof Let the total acting population

$$N(t) = S(t) + L_1(t) + L_2(t) + I_1(t) + I_2(t) + R(t).$$

By adding all equations in system (1), we will have

$$\frac{dN(t)}{dt} = \Lambda - \delta N(t),$$

therefore,

$$N(t) = \frac{\Lambda}{\delta} + Ce^{-\delta t}, \tag{2}$$

when $t = 0$, we will have

$$N(0) = \frac{\Lambda}{\delta} + C.$$

Therefore

$$N(t) = \frac{\Lambda}{\delta} + (N(0) - \frac{\Lambda}{\delta})e^{-\delta t},$$

hence,

$$\lim_{t \to +\infty} N(t) = \frac{\Lambda}{\delta}.$$

Consequently, we conclude that $\mathcal{H}$ is positively invariant which completes the proof.

3 Analysis of the Model

This section is devoted to the equilibria global stability by using some suitable Lyapunov functionals [9, 10]. Since the first five equations of the system (1) are not dependent of R and since the total population verifies Eq. (2), thus we can omit the sixth equation and the system (1) can be reduced to

$$\begin{cases} \dfrac{dS}{dt} = \Lambda - \dfrac{\alpha(1-u_1)SI_1}{1+mI_1^2} - \dfrac{\beta(1-u_2)SI_2}{1+kI_2^2} - \delta S \ , \\ \dfrac{dL_1}{dt} = \dfrac{\alpha(1-u_1)SI_1}{1+mI_1^2} - (\gamma_1+\delta)L_1 \ , \\ \dfrac{dL_2}{dt} = \dfrac{\beta(1-u_2)SI_2}{1+kI_2^2} - (\gamma_2+\delta)L_2 \ , \\ \dfrac{dI_1}{dt} = \gamma_1 L_1 - (\mu_1+\delta)I_1 \ , \\ \dfrac{dI_2}{dt} = \gamma_2 L_2 - (\mu_2+\delta)I_2 \ , \end{cases} \tag{3}$$

with

$$R = N - S - L_1 - L_2 - I_1 - I_2.$$

3.1 The Basic Reproduction Number

It is well known that the basic reproduction number can be defined as the average number of new cases of an infection caused by one infected individual, in a population consisting of susceptible individuals only. We use the next generation matrix FV^{-1} to calculate the basic reproduction number R_0. Indeed, the formula that gives us the basic reproduction number is $R_0 = \rho(FV^{-1})$, where ρ stands for the spectral radius, F is the nonnegative matrix of new infection cases, and V is the matrix of the transition infections associated with model (3).

$$F = \begin{pmatrix} 0 & 0 & \dfrac{\alpha(1-u_1)\Lambda}{\delta} & 0 \\ 0 & 0 & 0 & \dfrac{\beta(1-u_2)\Lambda}{\delta} \\ 0 & 0 & 0 & 0 \\ 0 & 0 & 0 & 0 \end{pmatrix}, \quad V = \begin{pmatrix} \gamma_1+\delta & 0 & 0 & 0 \\ 0 & \gamma_2+\delta & 0 & 0 \\ -\gamma_1 & 0 & \mu_1+\delta & 0 \\ 0 & -\gamma_2 & 0 & \mu_2+\delta \end{pmatrix}.$$

Then,

$$FV^{-1} = \begin{pmatrix} \frac{\alpha(1-u_1)\Lambda\gamma_1}{\delta(\gamma_1+\delta)(\mu_1+\delta)} & 0 & \frac{\alpha(1-u_1)\Lambda}{\delta(\mu_1+\delta)} & 0 \\ 0 & \frac{\beta(1-u_2)\Lambda\gamma_2}{\delta(\gamma_2+\delta)(\mu_2+\delta)} & 0 & \frac{\beta(1-u_2)\Lambda}{\delta(\mu_1+\delta)} \\ 0 & 0 & 0 & 0 \\ 0 & 0 & 0 & 0 \end{pmatrix}.$$

This implies that

$$R_0 = \max\{R_0^1, R_0^2\},$$

with

$$R_0^1 = \frac{\alpha(1-u_1)\Lambda\gamma_1}{\delta(\gamma_1+\delta)(\mu_1+\delta)}$$

and

$$R_0^2 = \frac{\beta(1-u_2)\Lambda\gamma_2}{\delta(\gamma_2+\delta)(\mu_2+\delta)}.$$

Denoting

$$a = \gamma_1 + \delta,\ b = \gamma_2 + \delta,\ c = \mu_1 + \delta,\ e = \mu_2 + \delta,$$

then,

$$R_0^1 = \frac{\alpha(1-u_1)\Lambda\gamma_1}{\delta ac}$$

and

$$R_0^2 = \frac{\beta(1-u_2)\Lambda\gamma_2}{\delta be}.$$

3.2 Steady States

The model (3) has four equilibrium points, one called disease-free equilibrium and the others called endemic equilibria given as follows:

- The disease-free equilibrium $\mathcal{E}_f = \left(\frac{\Lambda}{\delta}, 0, 0, 0, 0\right)$.
- The strain 1 endemic equilibrium $\mathcal{E}_{s_1} = \left(S_{s_1}^*, L_{1,s_1}^*, L_{2,s_1}^*, I_{1,s_1}^*, I_{2,s_1}^*\right)$, where

$$S^*_{s_1} = \frac{ac}{\alpha(1-u_1)\gamma_1}(R^1_0 - \frac{\alpha(1-u_1)}{\delta} I^*_{1,s_1}) \ , \ L^*_{1,s_1} = \frac{c}{\gamma_1} I^*_{1,s_1} \ ,$$

$$I^*_{1,s_1} = \frac{2\delta(R^1_0 - 1)}{\sqrt{\alpha(1-u_1)^2 + 4m\delta^2(R^1_0 - 1)} + \alpha(1-u_1)} \ ,$$

$$I^*_{2,s_1} = 0 \ , \ L^*_{2,s_1} = 0 \ .$$

- The strain 2 endemic equilibrium $\mathcal{E}_{s_2} = \left(S^*_{s_2}, L^*_{1,s_2}, L^*_{2,s_2}, I^*_{1,s_2}, I^*_{2,s_2}\right)$, where

$$S^*_{s_2} = \frac{be}{\beta(1-u_2)\gamma_2}(R^2_0 - \frac{\beta(1-u_2)}{\delta} I^*_{2,s_2}) \ , \ L^*_{2,s_2} = \frac{e}{\gamma_2} I^*_{2,s_2} \ ,$$

$$I^*_{2,s_2} = \frac{2\delta(R^2_0 - 1)}{\sqrt{\beta(1-u_2)^2 + 4k\delta^2(R^2_0 - 1)} + \beta(1-u_2)} \ ,$$

$$I^*_{1,s_2} = 0 \ , \ L^*_{1,s_2} = 0 \ .$$

- The endemic equilibrium $\mathcal{E}_t = \left(S^*_t, L^*_{1,t}, L^*_{2,t}, I^*_{1,t}, I^*_{2,t}\right)$, where

$$S^*_t = \frac{\Lambda}{\delta}(1 - \frac{\alpha(1-u_1)I^*_{1,t}}{\delta R^1_0} - \frac{\beta(1-u_2)I^*_{2,t}}{\delta R^2_0}) \ ,$$

$$L^*_{1,t} = \frac{c}{\gamma_1} I^*_{1,t} \ , \ L^*_{2,t} = \frac{e}{\gamma_2} I^*_{2,t} \ ,$$

$$I^*_{1,t} = \sqrt{\frac{1}{m}(R^1_0 \ S^*_t \frac{\delta}{\Lambda} - 1)} \ , \ I^*_{2,t} = \sqrt{\frac{1}{k}(R^2_0 \ S^*_t \frac{\delta}{\Lambda} - 1)} \ .$$

Remark 3.1

(1) From the components of the equilibrium point $\mathcal{E}_{s_1}$ (respectively, $\mathcal{E}_{s_2}$), we conclude that this strain 1 endemic equilibrium (respectively strain 2 endemic equilibrium) exists when $R^1_0 > 1$ (respectively, $R^2_0 > 1$).
(2) From the last equilibrium point $\mathcal{E}_t$ components, we can conclude that this endemic equilibrium exists when $R^1_0 > 1$ and $R^2_0 > 1$.

3.3 Global Stability

Theorem 1 *If $R^1_0 \leq 1$ and $R^2_0 \leq 1$. Then the disease-free equilibrium point $\mathcal{E}_f$ is globally asymptotically stable.*

Proof First, we consider the following Lyapunov function in $\mathbb{R}^5_+$:

$$\mathcal{L}_f(S, L_1, L_2, I_1, I_2) = S^*\left(\frac{S}{S^*} - \ln\left(\frac{S}{S^*}\right) - 1\right) + L_1 + L_2 + \frac{a}{\gamma_1}I_1 + \frac{b}{\gamma_2}I_2.$$

The time derivative is given by

$$\begin{aligned}
&\dot{\mathcal{L}}_f(S, L_1, L_2, I_1, I_2)\\
&\quad= \dot{S} - \frac{S}{S^*}\dot{S} + \dot{L_1} + \dot{L_2} + \frac{a}{\gamma_1}\dot{I_1} + \frac{b}{\gamma_2}\dot{I_2},\\
&\quad= \delta S_0^*\left(2 - \frac{S_0^*}{S} - \frac{S}{S_0^*}\right) + \frac{\alpha(1-u_1)S_0^*I_1}{1+mI_1^2} + \frac{\beta(1-u_2)S_0^*I_2}{1+kI_2^2} - \frac{ac}{\gamma_1}I_1 - \frac{be}{\gamma_2}I_2,\\
&\quad\leq \delta S^*\left(2 - \frac{S_0^*}{S} - \frac{S}{S_0^*}\right) + I_1\left(\alpha(1-u_1)S_0^* - \frac{ac}{\gamma_1}\right) + I_2\left(\beta(1-u_2)S_0^* - \frac{be}{\gamma_2}\right),\\
&\quad\leq \delta S^*\left(2 - \frac{S_0^*}{S} - \frac{S}{S_0^*}\right) + \frac{ac}{\gamma_1}I_1(R_0^1 - 1) + \frac{be}{\gamma_2}I_2(R_0^2 - 1),
\end{aligned}$$

since the arithmetic mean is greater than or equal to the geometric mean, it follows

$$2 - \frac{S_0^*}{S} - \frac{S}{S_0^*} \leq 0.$$

Therefore when $R_0^1 \leq 1$ and $R_0^2 \leq 1$, we will have $\dot{\mathcal{L}}_f \leq 0$, then the disease-free equilibrium point $\mathcal{E}_f$ is globally asymptotically stable. In order to establish the global stability of the endemic steady state $\mathcal{E}_{s_1}$, $\mathcal{E}_{s_2}$, and $\mathcal{E}_{s_t}$, we will need the following numbers:

$$R_m = \frac{\Lambda}{\delta}\sqrt{m}$$

$$R_k = \frac{\Lambda}{\delta}\sqrt{k}.$$

We call R_m (respectively R_k) the strain 1 inhibitory effect reproduction number (respectively the strain 2 inhibitory effect reproduction number).

Theorem 2 *If $R_0^2 \leq 1 < R_0^1$ and $R_m \leq 1$. Then the strain* 1 *endemic equilibrium point $\mathcal{E}_{s_1}$ is globally asymptotically stable.*

Proof First, we consider the Lyapunov function $\mathcal{L}_1$ defined by

$$\mathcal{L}_1(S, L_1, L_2, I_1, I_2) = S_{s_1}^*\left(\frac{S}{S_{s_1}^*} - \ln\left(\frac{S}{S_{s_1}^*}\right) - 1\right) + L_1^*\left(\frac{L_1}{L_{1,s_1}^*} - \ln\left(\frac{L_1}{L_{1,s_1}^*}\right) - 1\right)$$

$$+ L_2 + \frac{a}{\gamma_1} I^*_{1,s_1} \left(\frac{I_1}{I^*_{1,s_1}} - \ln\left(\frac{I_1}{I^*_{1,s_1}} \right) - 1 \right) + \frac{b}{\gamma_2} I_2.$$

The time derivative is given by

$$\begin{aligned}
&\dot{\mathcal{L}}_1(S, L_1, L_2, I_1, I_2) \\
&\quad = \left(1 - \frac{S^*_{s_1}}{S}\right) \left(\Lambda - \frac{\alpha(1-u_1)SI_1}{1+mI_1^2} - \frac{\beta(1-u_2)SI_2}{1+kI_2^2} - \delta S \right) \\
&\qquad + \left(1 - \frac{L^*_{1,s_1}}{L_1}\right) \left(\frac{\alpha(1-u_1)SI_1}{1+mI_1^2} - aL_1 \right) + \frac{\beta(1-u_2)SI_2}{1+kI_2^2} - bL_2 \\
&\qquad + \frac{a}{\gamma_1} (\gamma_1 L_1 - cI_1) \left(1 - \frac{I^*_{1,s_1}}{I_1}\right) + \frac{b}{\gamma_2} (\gamma_2 L_2 - eI_2).
\end{aligned}$$

We have

$$\begin{cases}
\Lambda = \delta S^*_{s_1} + \dfrac{\alpha(1-u_1) S^*_{s_1} I^*_{1,s_1}}{1+mI^{*2}_1}, \\
\dfrac{\alpha(1-u_1) S^*_{s_1} I^*_{1,s_1}}{1+mI^{*2}_{1,s_1}} = aL^*_{1,s_1}, \\
\dfrac{L^*_{1,s_1}}{I^*_{1,s_1}} = \dfrac{\gamma_1}{c}.
\end{cases}$$

Therefore

$$\begin{aligned}
&\dot{\mathcal{L}}_1(S, L_1, L_2, I_1, I_2) \\
&\quad = \delta S^*_{s_1} \left(2 - \frac{S^*_{s_1}}{S} - \frac{S}{S^*_{s_1}}\right) + 3aL^*_{1,s_1} + \frac{\alpha(1-u_1)S^*_{s_1} I_1}{1+mI_1^2} + \frac{\beta(1-u_2)S^*_{s_1} I_2}{1+kI_2^2} \\
&\qquad - \frac{\alpha(1-u_1)SI_1 L^*_{1,s_1}}{L_1(1+mI_1^2)} - \frac{\alpha(1-u_1)S^*_{s_1}}{1+mI^{*2}_{1,s_1}} \frac{S^*_{s_1} I^*_{1,s_1}}{S} - \frac{\alpha(1-u_1)S^*_{s_1} I_1}{1+mI^{*2}_{1,s_1}} \\
&\qquad - \frac{aL_1 I_1}{I_1} - \frac{be}{\gamma_2} I_2.
\end{aligned}$$

Then,

$$\dot{\mathcal{L}}_1(S, L_1, L_2, I_1, I_2)$$

$$= aL^*_{1,s_1}\left(4 - \frac{S^*_{s_1}}{S} - \frac{I^*_{1,s_1}}{I_1}\frac{L_1}{L^*_{1,s_1}} - \frac{S}{S^*_{s_1}}\frac{L^*_{1,s_1}}{L_1}\frac{I_1}{I^*_{1,s_1}}\frac{1+mI_1^{*^2}}{1+mI_1^2} - \frac{1+mI_1^2}{1+mI_1^{*^2}}\right)$$
$$+ \delta S^*_{s_1}\left(2 - \frac{S^*_{s_1}}{S} - \frac{S}{S^*_{s_1}}\right) + \beta(1-u_2)I_2\left(\frac{S^*_{s_1}}{1+kI_2^2} - \frac{be}{\beta(1-u_2)\gamma_2}\right)$$
$$+ \frac{\alpha(1-u_1)S^*_{s_1}I^*_{1,s_1}}{1+mI^{*^2}_{1,s_1}}\left(\frac{1+mI_1^2}{1+mI_1^{*^2}} + \frac{1+mI_1^{*^2}}{1+mI_1^2}\frac{I_1}{I^*_{1,s_1}} - \frac{I_1}{I^*_{1,s_1}} - 1\right).$$

Therefore,

$$\dot{\mathcal{L}}_1(S, L_1, L_2, I_1, I_2)$$
$$= aL^*_{1,s_1}\left(4 - \frac{S^*_{s_1}}{S} - \frac{I^*_{1,s_1}}{I_1}\frac{L_1}{L^*_{1,s_1}} - \frac{S}{S^*_{s_1}}\frac{L^*_{1,s_1}}{L_1}\frac{I_1}{I^*_{1,s_1}}\frac{1+mI_{1,s_1}^{*^2}}{1+mI_1^2} - \frac{1+mI_1^2}{1+mI_{1,s_1}^{*^2}}\right)$$
$$+ \delta S^*_{s_1}\left(2 - \frac{S^*_{s_1}}{S} - \frac{S}{S^*_{s_1}}\right) + \beta(1-u_2)I_2\left(\frac{S^*_{s_1}}{1+kI_2^2} - \frac{be}{\beta(1-u_2)\gamma_2}\right)$$
$$- \frac{amc}{\gamma_1}\left(1 - mI_1I^*_{1,s_1}\right)\frac{(I+I^*_{1,s_1})(I-I^*_{1,s_1})^2}{(1+mI^{*^2}_{1,s_1})(1+mI_1^2)}.$$

By the relation between arithmetic and geometric means we have

$$2 - \frac{S^*_{s_1}}{S} - \frac{S}{S^*_{s_1}} \leq 0$$

and

$$4 - \frac{S^*_{s_1}}{S} - \frac{I^*_{1,s_1}}{I_1}\frac{L_1}{L^*_{1,s_1}} - \frac{S}{S^*_{s_1}}\frac{L^*_{1,s_1}}{L_1}\frac{I_1}{I^*_{1,s_1}}\frac{1+mI_{1,s_1}^{*^2}}{1+mI_1^2} - \frac{1+mI_1^2}{1+mI_{1,s_1}^{*^2}} \leq 0.$$

If $R_0^2 \leq 1$. Then

$$\frac{S^*_{s_1}}{1+kI_2^2} \leq \frac{be}{\beta(1-u_2)\gamma_2}.$$

Since $R_m \leq 1$, we have that $m(\frac{\Lambda}{\delta})^2 \leq 1$
which implies, $1 - mI_1I^*_{1,s_1} \geq 0$
Consequently,

$$\dot{\mathcal{L}}_1 \leq 0.$$

We conclude that the point $\mathcal{E}_{s_1}$ is globally asymptotically stable when $R_0^2 \leq 1$, $1 < R_0^1$, and $R_m \leq 1$.

Theorem 3 *If $R_0^1 \leq 1 < R_0^2$ and $R_k \leq 1$. Then the strain 2 endemic equilibrium point $\mathcal{E}_{s_2}$ is globally asymptotically stable.*

Proof Let us consider the following Lyapunov function:

$$\begin{aligned}
&\mathcal{L}_2(S, L_1, L_2, I_1, I_2) \\
&\quad = S_{s_2}^* \left(\frac{S}{S_{s_2}^*} - \ln\left(\frac{S}{S_{s_2}^*} \right) - 1 \right) + L_1 + L_2^* \left(\frac{L_2}{L_2^*} - \ln\left(\frac{L_2}{L_2^*} \right) - 1 \right) \\
&\qquad + \frac{a}{\gamma_1} I_1 + \frac{b}{\gamma_2} I_{2,2}^* \left(\frac{I_2}{I_{2,2}^*} - \ln\left(\frac{I_2}{I_{2,s_2}^*} \right) - 1 \right).
\end{aligned}$$

It easy to verify that

$$\begin{aligned}
&\dot{\mathcal{L}}_2(S, L_1, L_2, I_1, I_2) \\
&\quad = \left(1 - \frac{S_{s_2}^*}{S} \right) \left(\Lambda - \frac{\alpha(1-u_1)SI_1}{1+mI_1^2} - \frac{\beta(1-u_2)SI_2}{1+kI_2^2} - \delta S \right) \\
&\qquad + \left(1 - \frac{L_2^*}{L_2} \right) \left(\frac{\beta(1-u_2)SI_2}{1+kI_2^2} - bL_2 \right) + \left(\frac{\alpha(1-u_1)SI_1}{1+mI_1^2} - aL_1 \right) \\
&\qquad + \frac{b}{\gamma_2} (\gamma_2 L_2 - eI_2) \left(1 - \frac{I_{2,s_2}^*}{I_2} \right) + \frac{a}{\gamma_a} (\gamma_1 L_1 - cI_1).
\end{aligned}$$

It is easy to see that

$$\begin{cases}
\Lambda = \delta S_{s_2}^* + \dfrac{\beta(1-u_2) S_{s_2}^* I_{2,s_2}^*}{1 + kI_{2,s_2}^{*2}} \\
\dfrac{\beta(1-u_2) S_{s_2}^* I_{2,s_2}^*}{1 + kI_{2,s_2}^{*2}} = bL_{2,s_2}^*, \\
\dfrac{L_{2,s_2}^*}{I_{2,s_2}^*} = \dfrac{\gamma_2}{e}.
\end{cases}$$

We have

$$\dot{\mathcal{L}}_2(S, L_1, L_2, I_1, I_2)$$

$$= \delta S^*_{s_2}(2 - \frac{S^*_{s_2}}{S} - \frac{S}{S^*_{s_2}}) + 3bL^*_{2,s_2} + \frac{\beta(1-u_2)S^*_{s_2}I_2}{1+kI_2^2}$$
$$+ \frac{\alpha(1-u_1)S^*_{s_2}I_2}{1+mI_1^2} - \frac{\beta(1-u_2)SI_2L^*_2}{L_2(1+kI_2^2)} - \frac{\beta(1-u_2)S^*_{s_2}}{1+kI_2^{*^2}} \cdot \frac{S^*_{s_2}I^*_{2,s_2}}{S}$$
$$- \frac{\beta(1-u_2)S^*_{s_2}I_2}{1+kI_2^{*^2}} - \frac{bL_2I_2}{I_2} - \frac{ac}{\gamma_1}I_1.$$

Then,

$$\dot{\mathcal{L}}_2(S, L_1, L_2, I_1, I_2) = \delta S^*_{s_2}\left(2 - \frac{S^*_{s_2}}{S} - \frac{S}{S^*_{s_2}}\right) + \frac{\alpha(1-u_1)S^*_{s_2}I_1}{1+mI_1^2} - \frac{ac}{\gamma_1}I_1$$
$$+ bL^*_{2,s_2}\left(3 - \frac{S^*_{s_2}}{S} - \frac{I^*_{2,s_2}}{I_2}\frac{L_2}{L^*_{2,s_2}} - \frac{S}{S^*_{s_2}}\frac{L^*_{2,s_2}}{L_2}\frac{I_2}{I^*_{2,s_2}}\right)$$
$$+ \frac{\beta(1-u_2)S^*_{s_2}I^*_{2,s_2}}{1+kI^{*^2}_{2,s_2}}\frac{S}{S^*_{s_2}}\frac{L^*_{2,s_2}}{L_2}\frac{I_2}{I^*_{2,s_2}} + \frac{\beta(1-u_2)S^*_{s_2}I_2}{1+kI_2^2}$$
$$- \frac{\beta(1-u_2)SI_2}{1+kI_2^2}\frac{L^*_{2,s_2}}{L_2} - \frac{be}{\gamma_2}I_2.$$

Therefore

$$\dot{\mathcal{L}}_2(S, L_1, L_2, I_1, I_2)$$
$$\leq \delta S^*_{s_2}\left(2 - \frac{S^*_{s_2}}{S} - \frac{S}{S^*_{s_2}}\right) + \left(\frac{\alpha(1-u_1)S^*_{s_2}}{1+mI_1^2} - \frac{ac}{\gamma_1}\right)I_1$$
$$+ \frac{be}{\gamma_2}I_2\left(\frac{S}{S^*_{s_2}}\frac{L^*_{2,s_2}}{L_2} - 1\right) + \frac{\beta(1-u_2)S^*_{s_2}I_2}{1+kI_2^2}\left(1 - \frac{S}{S^*_{s_2}}\frac{L^*_{2,s_2}}{L_2}\right)$$
$$+ bL^*_{2,s_2}\left(3 - \frac{S^*_{s_2}}{S} - \frac{I^*_{2,s_2}}{I_2}\frac{L_2}{L^*_{2,s_2}} - \frac{S}{S^*_{s_2}}\frac{L^*_{2,s_2}}{L_2}\frac{I_2}{I^*_{2,s_2}}\right).$$

The hypothesis (H_2) implies that

$$\frac{be}{\gamma_2}I_2\left(\frac{S}{S^*_{s_2}}\frac{L^*_{2,s_2}}{L_2} - 1\right) + \frac{\beta(1-u_2)S^*_{s_2}I_2}{1+kI_2^2}\left(1 - \frac{S}{S^*_{s_2}}\frac{L^*_{2,s_2}}{L_2}\right) \leq 0.$$

Then,

$$\dot{\mathcal{L}}_2(S, L_1, L_2, I_1, I_2) \leq \delta S^*_{s_2}\left(2 - \frac{S^*_{s_2}}{S} - \frac{S}{S^*_{s_2}}\right) + \left(\frac{\alpha(1-u_1)S^*_{s_2}}{1+mI_1^2} - \frac{ac}{\gamma_1}\right) I_1 + bL^*_{2,s_2}\left(3 - \frac{S^*_{s_2}}{S} - \frac{I^*_{2,s_2}}{I_2}\frac{L_2}{L^*_{2,s_2}} - \frac{S}{S^*_{s_2}}\frac{L^*_{2,s_2}}{L_2}\frac{I_2}{I^*_{2,s_2}}\right),$$

hence,

$$\dot{\mathcal{L}}_2(S, L_1, L_2, I_1, I_2) \leq \delta S^*_{s_2}\left(2 - \frac{S^*_{s_2}}{S} - \frac{S}{S^*_{s_2}}\right) + \left(\alpha(1-u_1)S^*_{s_2} - \frac{ac}{\gamma_1}\right) I_1 + bL^*_{2,s_2}\left(3 - \frac{S^*_{s_2}}{S} - \frac{I^*_{2,s_2}}{I_2}\frac{L_2}{L^*_{2,s_2}} - \frac{S}{S^*_{s_2}}\frac{L^*_{2,s_2}}{L_2}\frac{I_2}{I^*_{2,s_2}}\right).$$

If $R_0^1 \leq 1$. Then

$$\alpha(1-u_1)S^*_{s_2} \leq \frac{ac}{\gamma_1}.$$

By the relation between arithmetic and geometric means we have

$$2 - \frac{S^*_{s_2}}{S} - \frac{S}{S^*_{s_2}} \leq 0$$

and

$$3 - \frac{S^*_{s_2}}{S} - \frac{I^*_{2,s_2}}{I_2}\frac{L_2}{L^*_{2,s_2}} - \frac{S}{S^*_{s_2}}\frac{L^*_{2,s_2}}{L_2}\frac{I_2}{I^*_{2,s_2}} \leq 0.$$

Then

$$\dot{\mathcal{L}}_2 \leq 0.$$

We conclude that the point $\mathcal{E}_{s_2}$ is globally asymptotically stable when $R_0^1 \leq 1 < R_0^2$.

Theorem 4 *If $R_0^1 > 1$, $R_0^2 > 1$, $R_m \leq 1$, and $R_k \leq 1$. Then the endemic equilibrium point $\mathcal{E}_{s_t}$ is globally asymptotically stable.*

Proof For the proof of this last result it will be enough to consider the following Lyapunov function $\mathcal{L}_3$:

$$\begin{aligned}
&\mathcal{L}_3(S, L_1, L_2, I_1, I_2) \\
&= S_t^* \left(\frac{S}{S_t^*} - \ln\left(\frac{S}{S_t^*} \right) - 1 \right) + L_{1,t}^* \left(\frac{L_1}{L_{1,t}^*} - \ln\left(\frac{L_1}{L_{1,t}^*} \right) - 1 \right) \\
&\quad + L_{2,t}^* \left(\frac{L_2}{L_{2,t}^*} - \ln\left(\frac{L_2}{L_{2,t}^*} \right) - 1 \right) + \frac{a}{\gamma_a} I_{1,t}^* \left(\frac{I_1}{I_{1,t}^*} - \ln\left(\frac{I_1}{I_{1,t}^*} \right) - 1 \right) \\
&\quad + \frac{b}{\gamma_2} I_{2,t}^* \left(\frac{I_2}{I_{2,t}^*} - \ln\left(\frac{I_2}{I_{2,t}^*} \right) - 1 \right).
\end{aligned}$$

4 Numerical Simulations

In this section, we will perform some numerical simulations in order to check the impact of quarantine measures in reducing the spread of COVID-19. Indeed, Fig. 2 shows the evolution of infection for $\lambda = 1$, $\alpha = 0.9$, $\beta = 1.45$, $\gamma_1 = 0.5$, $\gamma_2 = 0.3$, $\mu_1 = 0.15$, $\mu_2 = 0.15$, $\delta = 0.2$, $m = 1.75$, $k = 2.85$ and different values of u_1 and u_2.

In the case when no quarantine strategy is undertaken, i.e. $u_1 = u_2 = 0$, we observe that the disease persists and the infected cases stay at very high level. When the effectiveness of the quarantine measures is increased, $u_1 = u_2 = 0.25$ or $u_1 = u_2 = 0.75$, a significant reduce of the infection cases is observed; we can also observe a considerable reduce of the latent individuals. Finally, when the quarantine measures are fully established, i.e. $u_1 = u_2 = 1$, an interesting result is observed. In this last case, the disease dies out, which is represented by the vanishing of all strains infected individuals and also the latent ones. The susceptible individuals will reach in this situation their maximal level. We conclude that the quarantine measures reduce significantly the spread of COVID-19.

5 Conclusion

Modeling epidemiological phenomena makes it possible to better understand several mechanisms that influence the spread of many diseases. In this work, we have studied the effectiveness of quarantine against the spread of COVID-19. Indeed, we have established the problem via six-compartment SLIR model, in which the dynamics of the COVID-19 epidemic is modeled by a system of six nonlinear differential equations, describing the interactions between susceptible, exposed, infected, and

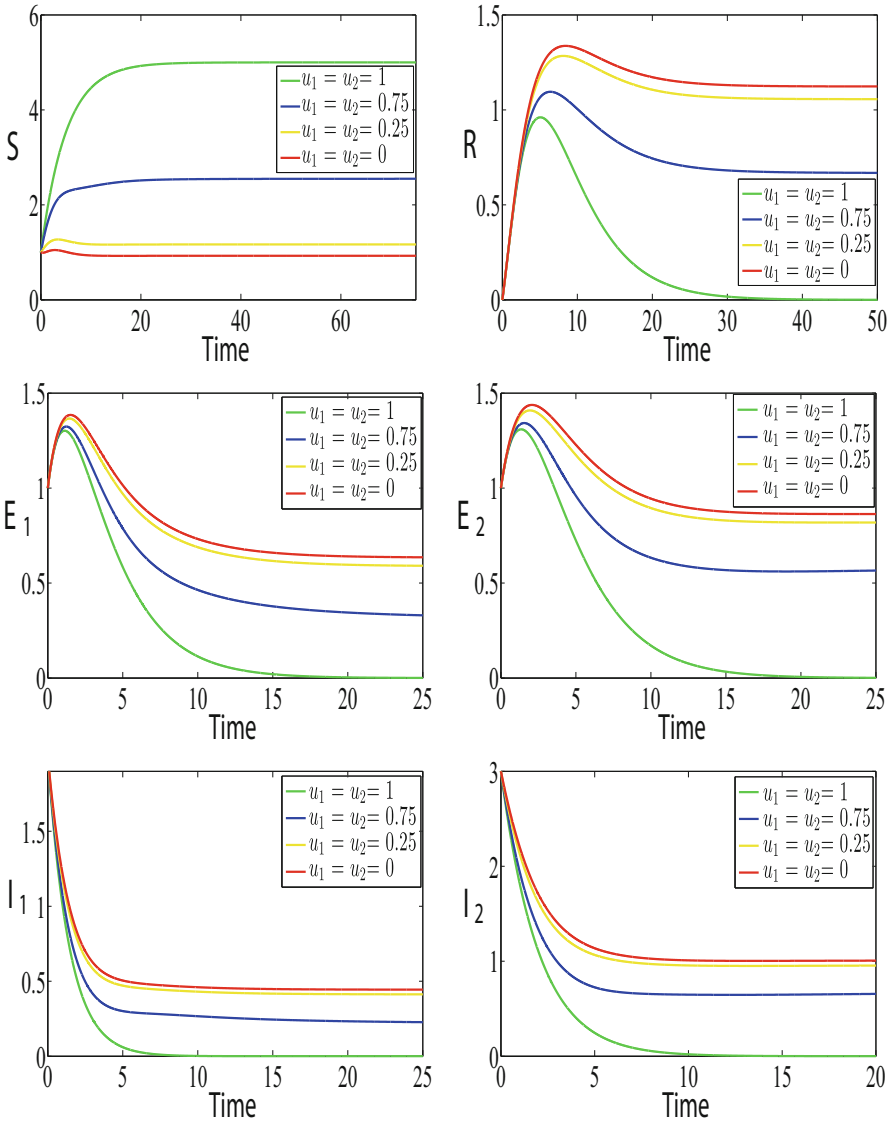

Fig. 2 The effect of quarantine strategy on the SLIR model dynamics

healed. First, we have calculated the basic reproduction number depending on the quarantine efficacy. Next, we have given the disease-free equilibrium and three other endemic equilibria, and then we have discussed, according to the value of the basic reproduction number, the global stability of each equilibrium. Numerical simulations are presented in order to discuss the effectiveness of quarantine measures in reducing the spread of COVID-19 pandemic.

References

1. Kermack WO, McKendrick AG. A contribution to the mathematical theory of epidemics. Proc R Soc London A 1927; 115(772):700–721.
2. Golub JE, Bur S, Cronin W, Gange S, Baruch N, Comstock G, Chaisson RE. Delayed tuberculosis diagnosis and tuberculosis transmission. Inter J Tuber 2006; 10(1):24–30.
3. Brenchley JM, Price DA, Schacker TW, Asher TE, Silvestri G, Rao S, Kazzaz Z, Bornstein E, Lambotte O, Altmann D, et al. Microbial translocation is a cause of systemic immune activation in chronic HIV infection. Nature Medicine 2006; 12(12):1365.
4. Gubler DJ. Dengue and dengue hemorrhagic fever. Clin Microb Reviews, 1998; 11(3):480–496.
5. Nuno M, Castillo-Chavez C, Feng Z, Martcheva M. Mathematical models of influenza: the role of cross-immunity, quarantine and age-structure. Math Epi Berlin: Springer; 2008.
6. Bentaleb D, Amine S. Lyapunov function and global stability for a two-strain SEIR model with bilinear and non-monotone. Inter J Biomath 2019; 12(02):1950021.
7. Meskaf, A., Khyar, O., Danane, J., Allali, K.: Global stability analysis of a two-strain epidemic model with non-monotone incidence rates. Chaos Sol. Frac. 133, 109647 (2020)
8. Khyar, O., Allali, K. Global dynamics of a multi-strain SEIR epidemic model with general incidence rates: application to COVID-19 pandemic. Nonlinear Dyn (2020). https://doi.org/10.1007/s11071-020-05929-4.
9. Korobeinikov A. Global properties of basic virus dynamics models. Bull Math Biol 2004; 66(4):879–883.
10. Souza MO, Zubelli JP. Global stability for a class of virus models with cytotoxic t lymphocyte immune response and antigenic variation. Bull Math Biol 2011; 73(3):609–625.

Non-FSI 3D Hemodynamic Simulations in Time-Dependent Domains

Y. V. Vassilevski, O. N. Bogdanov, X. V. Chesnokova, A. A. Danilov, T. K. Dobroserdova, D. D. Dobrovolsky, and A. V. Lozovskiy

1 Introduction

Computational analysis of functionality of the cardiovascular system is based on equations describing incompressible fluid flows. Blood flows interact inevitably with surrounding elastic tissues. The most general approach to hemodynamic simulations is the solution of fluid–structure interaction (FSI) problems [1–4]. The numerical solution of 3D FSI problems is computationally expensive, is time-consuming, and requires usage of parallel computers. In addition, FSI simulations are hard to personalize since elastic properties of vessels cannot be retrieved in vivo with appropriate accuracy. To overcome these difficulties, reduced hemodynamic models have been developed in the last few decades [5, 6]. The reduced models, however, cannot represent 3D flows and thus cannot provide important characteristics such as vorticity, wall shear stress, etc.

Several applications allow us to simulate 3D blood flows with less computational cost than the numerical solution of the 3D FSI problems. In this paper we address two such applications: blood flow in the left ventricle of a patient, and blood flow in the aortic bifurcation. In the first case the input data is dynamic ceCT medical images [7]; in the second case the input corresponds to a benchmark [8]. We consider mathematical formulations which can replace FSI formulations and still

Y. V. Vassilevski (✉) · A. A. Danilov
Marchuk Institute of Numerical Mathematics RAS, Moscow, Russia

Sechenov University, Moscow, Russia

O. N. Bogdanov · X. V. Chesnokova · D. D. Dobrovolsky
Sechenov University, Moscow, Russia

T. K. Dobroserdova · A. V. Lozovskiy
Marchuk Institute of Numerical Mathematics RAS, Moscow, Russia

R. P. Mondaini (ed.), *Trends in Biomathematics: Chaos and Control in Epidemics, Ecosystems, and Cells*, https://doi.org/10.1007/978-3-030-73241-7_16

provide feasible 3D solutions. For theoretical study and numerical details we refer to [1, 7, 9] for the first application and [8, 10] for the second application.

The paper is organized as follows. In Sect. 2 we pose the 3D FSI problem in a monolithic setting. In Sect. 3 we discuss the incompressible Navier–Stokes equations for flows in a time-dependent domain whose walls are moving (e.g. heart ventricles). In Sect. 4 we introduce a multiscale model for blood flows in the aortic bifurcation and compare it with the reference FSI solution.

2 Fluid–Structure Interaction

In the fluid–structure interaction setting, a time-dependent domain $\Omega(t) \subset \mathbb{R}^3$ is partitioned into fluid subdomain $\Omega^f(t)$ and structure subdomain $\Omega^s(t)$ with interface $\Gamma^{fs}(t) := \partial\Omega^f(t) \cap \partial\Omega^s(t)$ where the fluid–structure interaction occurs. The reference domains

$$\Omega_f = \Omega^f(0), \quad \Omega_s = \Omega^s(0)$$

are mapped by a deformation

$$\boldsymbol{\xi}^s : \Omega_s \times [0,t] \to \bigcup_{t\in[0,T]} \Omega^s(t), \quad \boldsymbol{\xi}^f : \Omega_f \times [0,t] \to \bigcup_{t\in[0,T]} \Omega^f(t).$$

For the structure, the deformation is naturally related to the displacement $\mathbf{u}^s$ via $\mathbf{u}^s(\mathbf{x},t) := \boldsymbol{\xi}^s(\mathbf{x},t) - \mathbf{x}$ and velocity $\mathbf{v}^s := \partial_t \mathbf{u}^s = \partial_t \boldsymbol{\xi}^s(\mathbf{x},t)$. For the fluid, the deformation is artificial and is defined by a continuous extension $\mathbf{u}^f := \mathrm{Ext}(\mathbf{u}^s)$ of the displacement field $\mathbf{u}^s$ to Ω_f:

$$\boldsymbol{\xi}^f(\mathbf{x},t) = \mathbf{u}^f + \mathbf{x} \quad \text{in } \Omega_f \times [0,t], \quad \boldsymbol{\xi}^f = \boldsymbol{\xi}^s \quad \text{on } \Gamma_{fs} \times [0,t],$$

where $\Gamma_{fs} := \Gamma^{fs}(0)$. There exist methods providing a mapping $\boldsymbol{\xi}^f$ [1]. Of course, $\boldsymbol{\xi}^f$ is not Lagrangian since it does not follow fluid particles trajectories.

In contrast to equations for the structure, equations for the fluid deal with the velocity vector field $\mathbf{v}^f$ and the pressure scalar field p^f given in the current domain $\Omega^f(t)$ for $t \in [0,T]$. We set $p^s = 0$ in Ω_s and define the global pressure variable $p = p^{f,s}$. For simplicity, we shall exploit the notations in the current configuration as $\mathbf{v}^f(\mathbf{x},t) := \mathbf{v}^f(\boldsymbol{\xi}^f(\mathbf{x},t),t)$, $p^f(\mathbf{x},t) := p^f(\boldsymbol{\xi}^f(\mathbf{x},t),t)$.

The monolithic approach [11] sets equations for displacements $\mathbf{u} = \mathbf{u}^{f,s}$ and velocities $\mathbf{v} = \mathbf{v}^{f,s}$ both in Ω^f and Ω^s. The globally defined deformation gradient $\mathbb{F} = \mathbb{I} + \nabla\mathbf{u}$ and its Jacobian $J := \det(\mathbb{F})$ contribute to each dynamic equation in the monolithic method:

$$\frac{\partial \mathbf{v}}{\partial t} = \begin{cases} \rho_s^{-1}\mathrm{div}\,(J(\boldsymbol{\sigma}_s \circ \boldsymbol{\xi}^s)\mathbb{F}^{-T}) & \text{in } \Omega_s, \\ (J\rho_f)^{-1}\mathrm{div}\,(J(\boldsymbol{\sigma}_f \circ \boldsymbol{\xi}^f)\mathbb{F}^{-T}) - (\nabla \mathbf{v})\left(\mathbb{F}^{-1}\left(\mathbf{v} - \dfrac{\partial \mathbf{u}}{\partial t}\right)\right) & \text{in } \Omega_f. \end{cases} \tag{1}$$

Here ρ_s and ρ_f are the solid and fluid densities, and $\boldsymbol{\sigma}_s$ and $\boldsymbol{\sigma}_f$ are the Cauchy stress tensors. Note that the dynamics of structure is given in the Lagrangian coordinates, whereas the dynamics of fluid is given in the Arbitrary Lagrangian–Eulerian framework. The kinematic equation in the structure

$$\frac{\partial \mathbf{u}}{\partial t} = \mathbf{v} \quad \text{in } \Omega_s \tag{2}$$

and incompressibility constraint in the fluid

$$\mathrm{div}\,(J\mathbb{F}^{-1}\mathbf{v}) = 0 \quad \text{in } \Omega_f \tag{3}$$

complete the system of the monolithic approach equations.

The above equations are complemented with initial conditions

$$\mathbf{u}(\mathbf{x}, 0) = \mathbf{0}, \quad \mathbf{v}(\mathbf{x}, 0) = \mathbf{v}_0(\mathbf{x}) \ \text{ in } \Omega(0) \tag{4}$$

and appropriate boundary conditions on the outer boundary. On the fluid–structure interface no-slip no-penetration of fluid and the balance of normal stresses are imposed

$$\mathbf{v}^s = \mathbf{v}^f \quad \text{and} \quad \boldsymbol{\sigma}_f \mathbb{F}^{-T}\mathbf{n} = \boldsymbol{\sigma}_s \mathbb{F}^{-T}\mathbf{n} \quad \text{on } \Gamma_{fs}, \tag{5}$$

where $\mathbf{n}$ is the unit normal vector on Γ_{fs}.

The solution of the FSI problem implies finding pressure p in fluid and continuous velocity and displacement fields $\mathbf{v}$, $\mathbf{u}$ in $\bar{\Omega}_f \cup \bar{\Omega}_s$ satisfying the set of Eqs. (1)–(5) and the boundary conditions. It is assumed that an extension rule $\mathbf{u}^f := \mathrm{Ext}(\mathbf{u}^s)$ is given.

It remains to define the Cauchy tensors for the fluid and the structure. They depend on chosen rheological model. For instance, for Newtonian fluid with viscosity μ_f

$$\boldsymbol{\sigma}_f = -p_f\mathbb{I} + \mu_f(\nabla \mathbf{v}\mathbb{F}^{-1} + \mathbb{F}^{-T}(\nabla \mathbf{v})^T) \tag{6}$$

and for Saint Venant–Kirchhoff material of the structure with Lame constants λ_s, μ_s

$$\boldsymbol{\sigma}_s = \frac{1}{J}\mathbb{F}(\lambda_s \mathrm{tr}(\mathbb{E})\mathbb{I} + 2\mu_s\mathbb{E})\mathbb{F}^T, \tag{7}$$

where $\mathbb{E} = \frac{1}{2}\left(\mathbb{F}^T\mathbb{F} - \mathbb{I}\right)$ is the Lagrange–Green strain tensor.

The common approach to the solution of the FSI problem in domains with complex geometry is the finite element method on unstructured tetrahedral meshes since these meshes can be generated in any domain, and may be locally refined. Fractional time stepping is computationally cheaper than implicit schemes, but imposes restrictions on the time step. Implicit and semi-implicit schemes may afford large time steps [1, 11–13]. In any case, the solution of a 3D FSI problem is computationally expensive: passing 3D benchmarks may require hundreds and thousands of core-hours. Moreover, patient-specific simulations require personalized elastic models of wall tissues which cannot be retrieved in clinical practice.

3 Navier–Stokes Equations in Time-Dependent Domain

Let the computational domain contain only fluid and the mapping $\Omega(t) = \boldsymbol{\xi}(\Omega_0 \times \{t\})$ be given, the deformation gradient $\mathbb{F} = \nabla_{\mathbf{x}}\boldsymbol{\xi}$ and its Jacobian $J = \det(\mathbb{F})$ satisfy

$$\inf_Q J \geq c_J > 0, \quad \sup_Q(\|\mathbb{F}\|_F + \|\mathbb{F}^{-1}\|_F) \leq C_F, \quad \text{with } \|\mathbb{F}\|_F := \mathrm{tr}(\mathbb{F}\mathbb{F}^T)^{\frac{1}{2}}, \tag{8}$$

where $Q := \Omega_0 \times [0, T]$ denotes the space-time cylinder and C_F, c_J denote positive constants.

The dynamics of incompressible Newtonian fluid is described by the fluid subset of Eqs. (1)–(5) for velocity $\mathbf{v}$ and pressure p defined in Q

$$\begin{cases} \dfrac{\partial \mathbf{v}}{\partial t} - (J\rho_f)^{-1}\mathrm{div}\,(J(\boldsymbol{\sigma}_f \circ \boldsymbol{\xi})\mathbb{F}^{-T}) + (\nabla \mathbf{v})\left(\mathbb{F}^{-1}\left(\mathbf{v} - \dfrac{\partial \boldsymbol{\xi}}{\partial t}\right)\right) = \mathbf{f} \\ \mathrm{div}\,(J\mathbb{F}^{-1}\mathbf{v}) = 0 \end{cases} \quad \text{in } Q, \tag{9}$$

with body forces $\mathbf{f}$ (e.g. gravity) and the initial condition $\mathbf{v}(\mathbf{x}, 0) = \mathbf{v}_0(\mathbf{x})$ in Ω_0. The fluid is assumed to be Newtonian (6) although a nonlinear rheological law is also applicable.

The boundary conditions depend on physical characteristics of boundary parts: on the wall part one imposes no-penetration no-slip or slip condition for velocity, on the inlet/outlet one may impose the free flow condition involving the Cauchy tensor; for details we refer to [1, 9].

An approximate solution of (9) may be obtained by the finite element method on a tetrahedral mesh in Ω_0. A popular choice is P2-P1 Taylor–Hood elements (piecewise quadratic continuous velocities and piecewise linear continuous pressures). According to the stability and convergence analysis [9], the Taylor–Hood elements and the backward Euler discretization in time (with linearized inertia term) provide the optimal error bound $O(\max\{h^2; \Delta t\})$ under feasible assumptions. The error norm is the same for the stability and the convergence estimates and is typical for the numerical analysis of the finite element solution of the Navier–Stokes equations.

The time step Δt is not limited by the CFL restriction. The second order in time approximation can be achieved by using the second order backward differences in time instead of the backward Euler time stepping. Numerical tests confirm the second order (in space) convergence of the Taylor–Hood solution to an analytical solution [9].

In practice, the mapping $\boldsymbol{\xi}$ may be defined by a sequence of topologically invariant meshes which differ only in nodes positions. The first mesh in the sequence is referred to as the reference mesh at time $t = 0$ with reference mesh nodes. Let $\boldsymbol{\xi}(\mathbf{x}, t_k)$ be the position of a reference mesh node with position $\mathbf{x}$ at time $t = t_k$. We define the mapping $\boldsymbol{\xi}^k$ as the continuous piecewise linear vector function with values $\boldsymbol{\xi}(\mathbf{x}, t)$ at mesh nodes for $t = t_k$, and define the function $\boldsymbol{\xi}(\mathbf{x}, t)$ as the linear interpolation between mappings $\boldsymbol{\xi}^{k-1}$ and $\boldsymbol{\xi}^k$ for $t_{k-1} < t < t_k$. Such continuous in space and time piecewise linear in mesh cells and time intervals mapping is an approximation of an unknown smooth mapping $\boldsymbol{\xi}$ contributing an additional modelling error. However, this error is small and does not pollute the solution essentially. The approach was successfully applied to simulation of 3D blood flow in the left ventricle of a patient [1, 7]. Figure 1 demonstrates the computational tetrahedral mesh and computed blood velocities at two instants of the systole.

If the mapping $\boldsymbol{\xi}$ is reconstructed from medical images, no-penetration no-slip condition requires both normal and tangential components of the wall velocity. The normal velocity may be recovered from any dynamic sequence of medical images by $v_\Gamma = \mathbf{n} \cdot (\boldsymbol{\xi}_t \circ \boldsymbol{\xi}^{-1})$, whereas the tangential velocity needs special treatment of the images, e.g. speckle tracking.

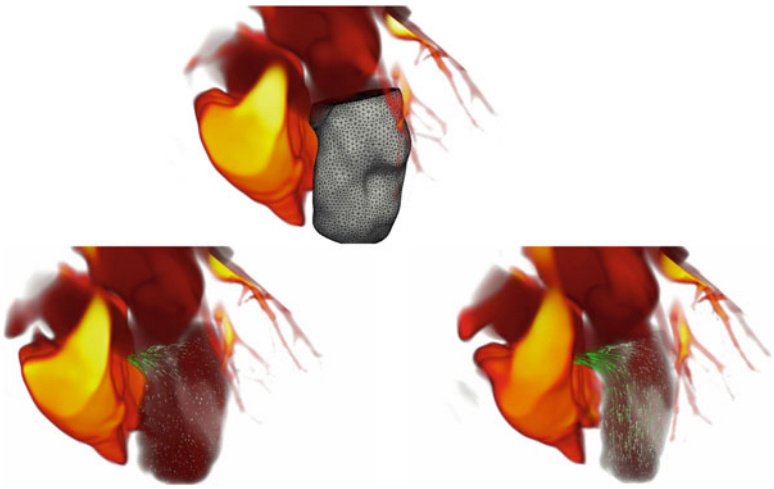

Fig. 1 Computational mesh for the left ventricle (top), blood velocities at two instants of the systole (bottom left, bottom right)

4 Multiscale Hemodynamic Model in Compliant Bifurcations

It is known [14] that pulsatile flows in vessels with rigid and compliant walls differs considerably. One cannot use the solution of the Navier–Stokes equations as an approximation to the solution of the FSI problem: flow rates and pressures are essentially different even for a straight tube. However, in case of compliant vessel bifurcation, one can use the Navier–Stokes equations in a domain with a rigid wall provided that the domain is a vicinity of the bifurcation and the 3D Navier–Stokes equations are coupled to 1D and 0D reduced hemodynamic models in a multiscale hemodynamic model [10].

The 3D Navier–Stokes equations in a short bifurcation domain Ω with rigid walls are reduced to

$$\begin{cases} \dfrac{\partial \mathbf{v}}{\partial t} - \rho_f^{-1} \operatorname{div} \boldsymbol{\sigma}_f + (\nabla \mathbf{v})\mathbf{v} = \mathbf{f} \\ \operatorname{div} \mathbf{v} = 0 \end{cases} \quad \text{in } \Omega, \tag{10}$$

with the initial condition $\mathbf{v}(\mathbf{x}, 0) = \mathbf{v}_0(\mathbf{x})$, no-slip boundary condition on the rigid wall, and interface boundary conditions on the inlet and two outlets. The latter conditions couple (10) with a 0D hydraulic model of an absorber which mimics an elastic sphere $\Omega_{0\mathrm{D}}$ filled with fluid. The parameters of the absorber model are volume $V(t)$ and variable $p_{0\mathrm{D}}(t)$ denoting the difference between fluid and external pressures. The kinematic equation for the elastic sphere filled with fluid is

$$I \frac{d^2 V}{dt^2} + R_0 \frac{dV}{dt} + \frac{V - V_0}{C} = p_{0\mathrm{D}}, \tag{11}$$

where V_0 is the volume at rest under $p_{0\mathrm{D}} = 0$; I, C, R_0 are inertia, expansibility, and resistance parameters of the sphere. The 0D absorber model mimics the compliance of the original compliant 3D bifurcation and interfaces the 3D Navier–Stokes equations in rigid walls from one side and 1D hemodynamic equations in the branches of the bifurcation, from the other side.

The 1D equations represent a reduced model for pulsatile flow in tubes with elastic walls. They are able to reproduce the pulse wave propagation under assumption of small ratio of tube diameter to its length. These equations stem from the mass and momentum conservation laws:

$$\partial A/\partial t + \partial (A\overline{v})/\partial x = 0, \tag{12}$$

$$\partial \overline{v}/\partial t + \partial \left(\overline{v}^2/2 + \overline{p}/\rho_b \right)/\partial x = f_{\overline{v}}, \tag{13}$$

where x is the coordinate along the tube, $A(t, x)$ is the cross-section area of the tube, $\overline{v}(t, x)$ and $\overline{p}$ are the averaged over the cross-section linear velocity and fluid pressure, ρ_b is the fluid density, $f_{\overline{v}} = -2(n+2)\mu_b \pi \overline{v} A^{-1} \rho_b^{-1}$ is the flow

deceleration friction term. The latter term is derived under assumption of the axisymmetric velocity profile [8]. The third equation of the 1D reduced model incorporates elastic properties of the tube wall via pressure to cross-section area relationship $p(A)$

$$\overline{p} = p_d + \beta A_d^{-1}(\sqrt{A} - \sqrt{A_d}), \qquad \beta = 4\sqrt{\pi}Eh/3, \tag{14}$$

where A_d is the diastolic cross-sectional area, $p_d = 9.5$ kPa is the diastolic pressure, E and h are the Young's modulus and thickness of the wall, respectively. For a review of different variants of (14) we refer to [6, 15].

The coupling equations at the 1D-0D and 3D-0D interfaces are

$$\begin{array}{ll} \frac{dV}{dt} = Q_{1\mathrm{D}} - Q_{3\mathrm{D}}, & \text{conservation of mass} \\ \overline{p} - p_{0\mathrm{D}} = R_{1\mathrm{DOD}} Q_{1\mathrm{D}}, & \text{Poiseuille law} \\ p_{0\mathrm{D}} - \overline{p} = R_{0\mathrm{D3D}} Q_{3\mathrm{D}}, & \text{Poiseuille law} \end{array} \tag{15}$$

where $Q_{1\mathrm{D}} = A\overline{v}$ is the 1D fluid flux, $Q_{3\mathrm{D}} = -\int_\Gamma \mathbf{v} \cdot \mathbf{n} ds$ is the 3D fluid flux through inlet/outlet from Ω_{0D} to Ω_{3D}, $R_{1\mathrm{D0D}}$ and $R_{0\mathrm{D3D}}$ are the resistance coefficients. Positive parameters R_0, $R_{1\mathrm{D0D}}$ and $R_{0\mathrm{D3D}}$ are shown to produce dissipation in the cumulative energy balance of the complete 1D–0D–3D system [16].

For numerical examination, we consider an idealized model of the aortic bifurcation [8]. The abdominal aorta is represented by the inlet cylinder Ω_a with length $L_a = 8.6$ cm, radius $r_a = 0.86$ cm, diastolic cross-sectional area $A_a = 1.8062\,\mathrm{cm}^2$, wall thickness $h_a = 1.032$ mm, Young's modulus $E_a = 500$ kPa, density $\rho_w = 1\,\mathrm{g/cm}^3$. The iliac arteries are represented by two equal outlet cylinders with length $L_i = 8.5$ cm, radius $r_i = 0.60$cm, diastolic cross-sectional area $A_i = 0.9479\,\mathrm{cm}^2$, wall thickness $h_i = 0.72$ mm, Young's modulus $E_i = 700$ kPa, and the same density $\rho_w = 1\,\mathrm{g/cm}^3$. The blood with viscosity $\mu_b = 4$ mPa s, density $\rho_b = 1060\,\mathrm{kg/m}^3$, mean flow rate $\bar{Q}_a = 0.4791$ l/min, and pulsatile velocity profile at the inlet $v(\xi, t) = \overline{v}(t)n^{-1}(n+2)[1 - (\xi r^{-1})^n]$, where r is the lumen radius, ξ is the radial coordinate, $n = 9$ is the polynomial order providing a good approximation of experimentally measured profile, $\overline{v}(t)$ is a given axial blood flow velocity averaged over the cross-section [8]. Each iliac cylinder is coupled with a three-element 0D Windkessel model [10].

The numerical solution of the 1D equation is based on the grid-characteristic method [1, 17, 18]. The numerical solution of the 3D Navier–Stokes equations is based on the P2-P1 Taylor–Hood finite elements and the backward Euler discretization in time (with linearized inertia term) on a tetrahedral mesh in bifurcation domain Ω. Coupling between the 1D,0D,3D models is achieved via iterations for (15) at the interfaces.

Table 1 presents the average relative error $avg\%$ and the maximum relative error $max\%$ for the flux and the pressure. The reference solution is provided by the 3D

Table 1 Error at the iliac arteries junction: flow rate and pressure computed by the numerical solutions of the Navier–Stokes equations in rigid walls and the multiscale method

	Flux		Pressure	
Error in method	avg%	max%	avg%	max%
NSE with rigid walls	9.15	30.02	1.41	8.31
Multiscale	1.15	4.49	2.02	3.48

FSI equations. The error produced by the Navier–Stokes equations in rigid walls is prohibitively large.

Acknowledgments The work has been supported by the Russian Science Foundation grant 19-71-10094.

References

1. Yu. Vassilevski et al. *Personalized Computational Hemodynamics: Models, Methods, and Applications for Vascular Surgery and Antitumor Therapy*, Academic Press (2020).
2. G. Kassab. *Coronary Circulation: Anatomy, Mechanical Properties, and Biomechanics*, Springer International Publishing (2019).
3. M. Labrosse, Ed. *Cardiovascular mechanics*, Taylor & Francis Group (2019).
4. A. Quarteroni et al. *Mathematical Modelling of the Human Cardiovascular System: Data, Numerical Approximation, Clinical Applications*, Cambridge University Press (2019).
5. Y. Shi, P. Lawford, R. Hose, Review of zero-D and 1D models of blood flow in the cardiovascular system. *Biomed. Eng. Online* **10**(33) (2011).
6. N. Bessonov et al., Methods of blood flow modelling. *Math. Model. Nat. Phenom.* **11** (1) (2016).
7. A. Danilov et al., A finite element method for the Navier-Stokes equations in moving domain with application to hemodynamics of the left ventricle. *Russian J. Numer. Anal. Math. Modelling* **32**(4) (2017).
8. N. Xiao, J. Alastruey-Arimon, C.A. Figueroa, A systematic comparison between 1D and 3D hemodynamics in compliant arterial models. *Int. J. Numer. Methods Biomed. Eng.* **30** (2) (2014).
9. A. Lozovskiy, M. Olshanskii, Y. Vassilevski, A quasi-Lagrangian finite element method for the Navier-Stokes equations in a time-dependent domain. *Comput. Methods Appl. Mech. Engrg.* **333** (2018).
10. T. Dobroserdova et al., Multiscale models of blood flow in the compliant aortic bifurcation. *Appl. Math. Lett.* **93**C (2019).
11. J. Hron and S. Turek. *A Monolithic FEM/multigrid Solver for an ALE Formulation of Fluid-Structure Interaction with Applications in Biomechanics*, Springer Berlin Heidelberg (2006).
12. A. Lozovskiy et al., An unconditionally stable semi-implicit FSI finite element method. *Comput.Methods Appl.Mech.Engrg.* **297** (2015).
13. A. Lozovskiy, M. Olshanskii, Y. Vassilevski, Analysis and assessment of a monolithic FSI finite element method. *Computers and Fluids*, **179** (2019).
14. C. Caro et al. *The Mechanics of the Circulation*, second ed. Cambridge University Press (2012).
15. Yu. Vassilevski, V. Salamatova and S. Simakov, On the elasticity of blood vessels in one-dimensional problems of hemodynamics. *J. Computational Mathematics and Mathematical Physics* **55**(9) (2015).

16. T. Dobroserdova, M. Olshanskii and S. Simakov, Multiscale coupling of compliant and rigid walls blood flow models. *Int. J. Numer. Methods In Fluids* **82** (12) (2016).
17. A. Kholodov, Some dynamical models of multi-dimensional problems of respiratory and circulatory systems including their interaction and matter transport. In: *Computer Models and Medicine Progress*, Nauka, Moskva (2001).
18. K. Magomedov and A. Kholodov, *Grid-Characteristics Numerical Methods*, second ed. Urait, Moscow (2018).

Co-existence of Chaos and Control in Generalized Lotka–Volterra Biological Model: A Comprehensive Analysis

Taqseer Khan and Harindri Chaudhary

1 Introduction

Over the years, chaos has been one of the most important characteristic of nonlinear phenomena mostly found in nature. Interestingly, it has been prescribed in numerous ways, some elaborate it as a disorder existing in the events so that they exhibit unpredictable behaviour. Chaotic behaviour exists vastly in biology, engineering, chemical, economics, physics, management, and many more scientific domains. In the beginning, chaos was not considered to be important in any area but it was only after the remarkable work of Pecora and Carroll [1] who initiated the idea of chaos synchronization among chaotic systems in 1990, started attracting researchers and scientists from many fields. Since then, various chaos synchronization techniques were introduced and presently several novel techniques are being introduced also. Some frequently introduced techniques are complete [2], hybrid [3], anti [4], function projective [5], hybrid projective [6, 7], combination synchronization [7], combination-combination [6], lag [8], triple compound [9], etc. Numerous control techniques are employed to achieve the aforementioned schemes, for instance, active [10], adaptive or parameter identification method [6], impulsive [11], sliding mode [12], feedback [13], and so on.

In this chapter, the combination difference anti-synchronization (DCAS) among identical chaotic generalized Lotka–Volterra (GLV) biological model [14, 15] using active control method has been achieved. The analytical results are justified graphically which clearly illustrate that the scheme used is effective and feasible for synchronizing the discussed GLV system. The remainder of the chapter is arranged as: In Sect. 2: problem formulation has been made. Section 3 describes the

T. Khan · H. Chaudhary (✉)
Department of Mathematics, Jamia Millia Islamia, New Delhi, India
e-mail: tkhan4@jmi.ac.in

R. P. Mondaini (ed.), *Trends in Biomathematics: Chaos and Control in Epidemics, Ecosystems, and Cells*, https://doi.org/10.1007/978-3-030-73241-7_17

synchronization methodology. Section 4 implements the DCAS scheme in chaotic GLV system. Section 5 comprises the discussions concerning numerical simulations and demonstrates the results performed in MATLAB. Section 6 concludes the chapter.

2 Problem Formulation

In this section, we outline combination synchronization [16] considering master–slave configuration in three chaotic/hyperchaotic systems which is essential in the following sections.

Suppose the first master system is given by

$$\dot{r}_{m1} = g_1(r_{m1}), \tag{1}$$

and the second master system is given by

$$\dot{r}_{m2} = g_2(r_{m2}). \tag{2}$$

Assume the slave system is given by

$$\dot{r}_{s1} = g_3(r_{s1}) + W(r_{m1}, r_{m2}, r_{s1}), \tag{3}$$

where $r_{m1} = (r_{m11}, r_{m12}, \ldots, r_{m1n})^T \in R^n$, $r_{m2} = (r_{m21}, r_{m22}, \ldots, r_{m2n})^T \in R^n$, $r_{s1} = (r_{s11}, r_{s12}, \ldots, r_{s1n})^T \in R^n$ are the state vectors of master and slave systems (1), (2), and (3), respectively, $g_1, g_2, g_3 : R^n \to R^n$ are three nonlinear continuous vector functions, $W = (W_1, W_2, \ldots, W_n)^T : R^n \times R^n \times R^n \to R^n$ are the controllers which are to be properly chosen.

We describe difference combination anti-synchronization (DCAS) error as

$$e = Cr_{s1} + (Br_{m2} - Ar_{m1}),$$

where $A = \text{diag}(a_1, a_2, \ldots, a_n)$, $B = \text{diag}(b_1, b_2, \ldots, b_n)$, $C = \text{diag}(c_1, c_2, \ldots, c_n)$ and $C \neq 0$.

Definition 2.1 The combination of two chaotic master systems (1)–(2) is said to achieve difference combination anti-synchronized (DCAS) state with slave system (3) if

$$\lim_{t\to\infty} \|e\| = \lim_{t\to\infty} \|Cr_{s1} + (Br_{m2} - Ar_{m1})\| = 0.$$

Remark 2.1 The matrices A, B, and C are called the scaling matrices. Moreover, A, B, and C can be extended as matrices of functions of state variables r_{m1}, r_{m2}, and r_{s1}.

Remark 2.2 The problem of combination synchronization would be converted into traditional chaos control issue for $A = B = 0$.

3 Synchronization Theory via Active Control Design

In this section, we study DCAS approach among chaotic systems (1)–(3) by defining the simplified active control laws.

Let us design the active controllers by

$$W_i = -\frac{\phi_i}{c_i} - (g_3)_i - \frac{M_i e_i}{c_i}, \tag{4}$$

where $\phi_i = (b_i(g_2)_i - a_i(g_1)_i)$, $i = 1, 2, \ldots, n$.

Theorem 3.1 *To achieve the DCAS technique via ACT in the chaotic systems* (1)–(3) *asymptotically, we choose the active controllers as designed in* (4).

Proof The synchronized errors are formulated as

$$e_i = c_i r_{s1i} + (b_i r_{m2i} - a_i r_{m1i}), \quad \text{for } i = 1, 2, \ldots, n.$$

The error dynamics turns into

$$\begin{aligned}
\dot{e_i} &= c_i \dot{r}_{s1i} + (b_i \dot{r}_{m2i} - a_i \dot{r}_{m1i}) \\
&= c_i((g_3)_i + W_i) + (b_i(g_2)_i - a_i(g_1)_i) \\
&= c_i((g_3)_i + \frac{\phi_i}{c_i} - (g_3)_i - \frac{M_i e_i}{c_i}) - \phi_i \\
&= \phi_i - M_i e_i - \phi_i \\
&= -M_i e_i.
\end{aligned} \tag{5}$$

The typical Lyapunov function, $V(e(t))$, is defined as

$$\begin{aligned}
V(e(t)) &= \frac{1}{2} e^T e \\
&= \frac{1}{2} \Sigma e_i^2.
\end{aligned} \tag{6}$$

On differentiating $V(e(t))$ as given in Eq. (6), we have

$$\begin{aligned}
\dot{V}(e(t)) &= \Sigma e_i \dot{e}_i \\
&= \Sigma e_i(-M_i e_i)
\end{aligned}$$

$$= -\Sigma M_i e_i^2, \quad \text{using Eq. (5).} \tag{7}$$

We now select $(M_1, M_1, \ldots, M_n)$ so that $\dot{V}(e(t))$ given by Eq. (7) becomes negative definite. Thus, by LST, we obtain

$$\lim_{t\to\infty} e_i(t) = 0 \quad \text{for } (i = 1, 2, 3).$$

Thus, the master systems (1)–(2) and slave system (3) have attained DCAS scheme.

4 A Simple Numerical Example

In this section, we firstly discuss in short the famously known chaotic Generalized Lotka–Volterra (GLV) three species biological system [17, 18], to be picked up for DCAS technique using ACT.

We now represent GLV model as the first master system:

$$\begin{cases} \dot{r}_{m11} = r_{m11} - r_{m11}r_{m12} + k_3 r_{m11}^2 - k_1 r_{m11}^2 r_{m13} \\ \dot{r}_{m12} = -r_{m12} + r_{m11}r_{m12} \\ \dot{r}_{m13} = k_2 r_{m13} + k_1 r_{m11}^2 r_{m13}, \end{cases} \tag{8}$$

where $(r_{m11}, r_{m12}, r_{m13})^T \in R^3$ are the state variables of given system and k_1, k_2, and k_3 are positive parameters. Further, in (8), r_{m11} represents the prey population and r_{m12}, r_{m13} denote the predator populations. For parameter values $k_1 = 2.9851$, $k_2 = 3$, $k_3 = 2$ and initial values $(27.5, 23.1, 11.4)$, the first master GLV system depicts chaotic behaviour as exhibited in Figs. 1a and 2a.

The second identical master GLV chaotic system prescribed, respectively, as

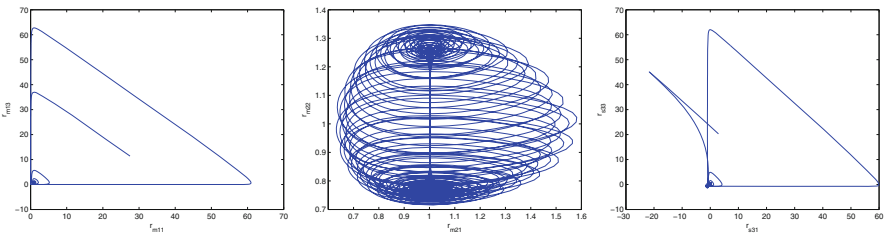

(a) (b) (c)

Fig. 1 Phase portraits of chaotic GLV biological system in (**a**) $r_{m11} - r_{m13}$ plane, (**b**) $r_{m21} - r_{m22}$ plane, (**c**) $r_{s31} - r_{s33}$ plane

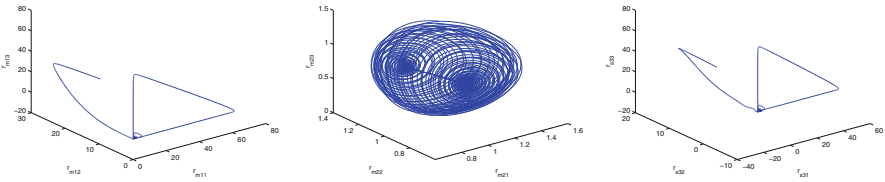

(a) (b) (c)

Fig. 2 Phase portraits of chaotic GLV biological system in (**a**) $r_{m11} - r_{m12} - r_{m13}$ space, (**b**) $r_{m21} - r_{m22} - r_{m23}$ space, (**c**) $r_{s31} - r_{s32} - r_{s33}$ space

$$\begin{cases} \dot{r}_{m21} = r_{m21} - r_{m21}r_{m22} + k_3 r_{m21}^2 - k_1 r_{m21}^2 r_{m23} \\ \dot{r}_{m22} = -r_{m22} + r_{m21}r_{m22} \\ \dot{r}_{m23} = k_2 r_{m23} + k_1 r_{m21}^2 r_{m23}, \end{cases} \tag{9}$$

where $(r_{m21}, r_{m22}, r_{m23})^T \in R^3$ are the state variables of the system and k_1, k_2, and k_3 are positive parameters. For parameter values $k_1 = 2.9851$, $k_2 = 3$, $k_3 = 2$, the second master GLV system shows chaotic behaviour for selected initial conditions (1.2, 1.2, 1.2) as exhibited in Figs. 1b and 2b.

The slave system, defined by the identical chaotic GLV system, is prescribed as

$$\begin{cases} \dot{r}_{s31} = r_{s31} - r_{s31}r_{s32} + k_3 r_{s31}^2 - k_1 r_{s31}^2 r_{s33} + W_1 \\ \dot{r}_{s32} = -r_{s32} + r_{s31}r_{s32} + W_2 \\ \dot{r}_{s33} = k_2 r_{s33} + k_1 r_{s31}^2 r_{s33} + W_3, \end{cases} \tag{10}$$

where $(r_{s11}, r_{s12}, r_{s13})^T \in R^3$ is the state vector of the system and k_1, k_2, and k_3 are positive parameters. For parameter values $k_1 = 2.9851$, $k_2 = 3$, $k_3 = 2$ and initial conditions (2.9, 12.8, 20.3), the slave GLV system displays chaotic behaviour as depicted in Figs. 1c and 2c. Further, W_1, W_2, and W_3 are active control functions to be determined so that DCAS among three identical GLV chaotic systems will be attained keeping Lyapunov stability theory (LST) in mind and hence required stability criterion has been derived.

Defining now the error functions (e_1, e_2, e_3) as

$$\begin{cases} e_1 = c_1 r_{s31} + (b_1 r_{m21} - a_1 r_{m11}) \\ e_2 = c_2 r_{s32} + (b_2 r_{m22} - a_2 r_{m12}) \\ e_3 = c_3 r_{s33} + (b_3 r_{m23} - a_3 r_{m13}). \end{cases} \tag{11}$$

The immediate goal in this work is to design controllers W_i, $(i = 1, 2, 3)$ ensuring that error functions defined in (11) satisfy

$$\lim_{t\to\infty} e_i(t) = 0 \quad \text{for } (i = 1, 2, 3).$$

The resulting error dynamics turns into

$$\begin{cases} \dot{e}_1 = c_1(r_{s31} - r_{s31}r_{s32} + k_3 r_{s31}^2 - k_1 r_{s31}^2 r_{s33} + W_1) \\ \qquad +b_1(r_{m21} - r_{m21}r_{m22} + k_3 r_{m21}^2 - k_1 r_{m21}^2 r_{m23}) \\ \qquad -a_1(r_{m11} - r_{m11}r_{m12} + k_3 r_{m11}^2 - k_1 r_{m11}^2 r_{m13}) \\ \dot{e}_2 = c_2(-r_{s32} + r_{s31}r_{s32} + W_2) + b_2(-r_{m22} + r_{m21}r_{m22}) \\ \qquad -a_2(-r_{m12} + r_{m11}r_{m12}) \\ \dot{e}_3 = c_3(k_2 r_{s33} + k_1 r_{s31}^2 r_{s33} + W_3) + b_3(k_2 r_{m23} + k_1 r_{m21}^2 r_{m23}) \\ \qquad -a_3(k_2 r_{m13} + k_1 r_{m11}^2 r_{m13}). \end{cases} \tag{12}$$

Let us now define the active controllers as

$$W_1 = -\frac{\phi_1}{c_1} - (g_3)_1 - \frac{M_1 e_1}{c_1}, \tag{13}$$

where $\phi_1 = (b_1(g_2)_1 - a_1(g_1)_1)$.

On putting the values of $a_1, b_1, \phi_1, (g_3)_1$ in (13) and simplifying, we get

$$\begin{aligned} W_1 = &-\frac{e_1}{c_1} + r_{s31}r_{s33} - k_3 r_{s31}^2 + k_1 r_{s31}^2 r_{s33} \\ &- \frac{b_1}{c_1}(-r_{m21}r_{m22} + k_3 r_{m21}^2 - k_1 r_{m21}^2 r_{m23}) \\ &+ \frac{a_1}{c_1}(r_{m11}r_{m12} - k_3 r_{m11}^2 + k_1 r_{m11}^2 r_{m13}) - \frac{M_1 e_1}{c_1}, \end{aligned} \tag{14}$$

$$W_2 = -\frac{\phi_2}{c_2} - (g_3)_2 - \frac{M_2 e_2}{c_2}, \tag{15}$$

where $\phi_2 = (b_2(g_2)_2 - a_2(g_1)_2)$.

By substituting the values of $a_2, b_2, \phi_2, (g_3)_2$ in (15) and solving, we find that

$$W_2 = \frac{e_2}{c_2} - r_{s31}r_{s32} - \frac{b_2}{c_2} r_{m21}r_{m22} + \frac{a_2}{c_2} r_{m11}r_{m12} - \frac{M_2 e_2}{c_2}, \tag{16}$$

$$W_3 = -\frac{\phi_3}{c_3} - (g_3)_3 - \frac{M_3 e_3}{c_3}, \tag{17}$$

where $\phi_3 = (b_3(g_2)_3 - a_3(g_1)_3)$.

By putting the values of $a_3, b_3, \phi_3, (g_3)_3$ in (17) and combining, we have

$$W_3 = \frac{k_2 e_3}{c_3} - k_1 r_{s31}^2 r_{s33} - \frac{b_3 k_1}{c_3} r_{m21}^2 r_{m23} + \frac{a_3 k_1}{c_3} r_{m11}^2 r_{m13} - \frac{M_3 e_3}{c_3}, \tag{18}$$

where $M_1 > 0$, $M_2 > 0$, and $M_3 > 0$ are gain constants.

On substituting the active controllers (14), (16), and (18) into error dynamics (12), we get

$$\begin{cases} \dot{e}_1 = -M_1 e_1 \\ \dot{e}_2 = -M_2 e_2 \\ \dot{e}_3 = -M_3 e_3. \end{cases} \tag{19}$$

The Lyapunov function is described as

$$V(e(t)) = \frac{1}{2}[e_1^2 + e_2^2 + e_3^2]. \tag{20}$$

It is obvious that Lyapunov function $V(e(t))$ is positive definite in R^3.

Then, the derivative of Lyapunov function $V(e(t))$ may be expressed as

$$\dot{V}(e(t)) = e_1\dot{e}_1 + e_2\dot{e}_2 + e_3\dot{e}_3. \tag{21}$$

Using Eq. (19) in (21), we obtain

$$\dot{V}(e(t)) = -M_1 e_1^2 - M_2 e_2^2 - M_3 e_3^2 < 0,$$

which displays that $\dot{V}(e(t))$ is negative definite.

Therefore, in view of LST, we find that the discussed DCAS error dynamics is asymptotically stable globally, i.e., the synchronization error $e(t) \to 0$ asymptotically with $t \to \infty$ for each initial value $e(0) \in R^3$.

5 Numerical Simulations and Discussions

In this section, we present few simulation experiments to show the effectiveness of the proposed DCAS scheme using ACT. Selected parameters for the given GLV model are $k_1 = 2.9851$, $k_2 = 3$, and $k_3 = 2$ which display that given GLV system behaves chaotically without the controllers. Initial conditions of master systems (8)–(9) and corresponding slave system (10) are (27.5, 23.1, 11.4), (1.2, 1.2, 1.2), and (2.9, 12.8, 20.3), respectively. We attain DCAS scheme between two master (8)–(9) and corresponding one slave systems (1)) by selecting scaling matrices A with $a_1 = 1$, $a_2 = 1$, $a_3 = 1$; B with $b_1 = 1$, $b_2 = 1$, $b_3 = 1$; C with $c_1 = 1$, $c_2 = 1$, $c_3 = 1$. Here, the control gains are taken as $M_i = 6$ for $i = 1, 2, 3$. Simulation results are depicted in Fig. 3(a–c) that display the state trajectories of master (8)–(9) and slave system (10). Synchronization errors $(e_1, e_2, e_3) = (-23.4, -9.1, 10.1)$ approach zero as t tending to infinity as shown in Fig. 4(a–d). Therefore, the discussed DCAS approach for master and slave systems is achieved computationally.

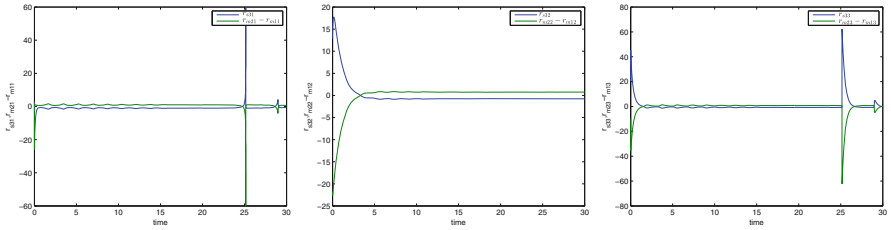

(a) (b) (c)

Fig. 3 Phase portraits of DCAS trajectories for GLV biological system (**a**) between $r_{s31}(t)$ and $r_{m21}(t) - r_{m11}(t)$, (**b**) between $r_{s32}(t)$ and $r_{m22}(t) - r_{m12}(t)$, (**c**) between $r_{s33}(t)$ and $r_{m23}(t) - r_{m13}(t)$

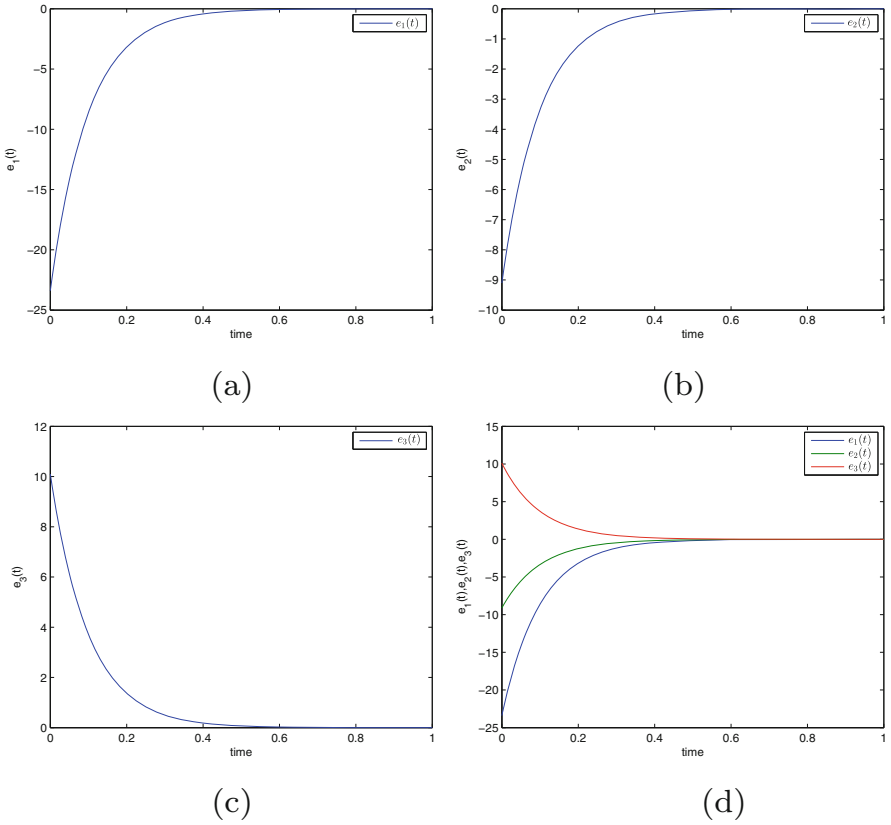

(a) (b) (c) (d)

Fig. 4 Phase portraits of time series in DCAS error for GLV biological system (**a**) (t, e_1), (**b**) (t, e_2), (**c**) (t, e_3), (**d**) (t, e_1, e_2, e_3)

6 Conclusion

In this chapter, the proposed DCAS scheme for chaotic GLV systems (identical) via active control design has been explored. Using suitably constructed nonlinear controllers which are based on classic LST, the considered DCAS strategy is attained. Additionally, MATLAB performed numerical simulations indicate that the designed controllers are efficient and accurate in controlling the chaotic regime of GLV systems to desired set points which depicts the effectiveness of our proposed DCAS technique. Specifically, the analytical theory as well as the numerical results both are in complete understanding. It is further intriguing and challenging to introduce new synchronization and control schemes to stabilize the chaos occurring in three species chaotic GLV biological system that generalize our discussed strategy.

References

1. L. M. Pecora and T. L. Carroll, *Physical Review Letters* **64**(8), 821 (1990).
2. A. K. Singh, V. K. Yadav and S. Das, *International Journal of Dynamics and Control* **5**(3), 756–770 (2017).
3. K. S. Sudheer and M. Sabir, *Pramana* **73**(4), 781 (2009).
4. G.-H. Li and S.-P. Zhou, Anti-synchronization in different chaotic systems. *Chaos, Solitons & Fractals* **32**(2), 516–520 (2007).
5. P. Zhou and W. Zhu, *Nonlinear Analysis: Real World Applications* **12**(2), 811–816 (2011).
6. A. Khan and H. Chaudhary, Hybrid projective combination-combination synchronization in non-identical hyperchaotic systems using adaptive control, *Arabian Journal of Mathematics* pp. 1–15 (2020).
7. A. Khan and H. Chaudhary, *BLOOMSBURY INDIA*, p. 174 (2019).
8. C. Li and X. Liao, *Chaos, Solitons & Fractals* **22**(4), 857–867 (2004).
9. V. K. Yadav, G. Prasad, M. Srivastava and S. Das, *Differential Equations and Dynamical Systems*, pp. 1–24 (2019).
10. H. Delavari and M. Mohadeszadeh, *Journal of Control Engineering and Applied Informatics* **20**(1), 67–74 (2018).
11. D. Li and X. Zhang, Impulsive synchronization of fractional order chaotic systems with time-delay, *Neurocomputing* **216**, 39–44 (2016).
12. S. Vaidyanathan and S. Sampath, Anti-synchronization of four-wing chaotic systems via sliding mode control, *International Journal of Automation and Computing* **9**(3), 274–279 (2012).
13. M. Chen and Z. Han, *Chaos, Solitons & Fractals* **17**(4), 709–716 (2003).
14. A. J. Lotka, *Science Progress in the Twentieth Century* (1919–1933), **21**(82), 341–343 (1926).
15. F. M. Scudo, *Theoretical Population Biology* **2**(1), 1–23 (1971).
16. L. Runzi, W. Yinglan and D. Shucheng, *Chaos: An Interdisciplinary Journal of Nonlinear Science* **21**(4), 043114 (2011).
17. A. Arneodo, P. Coullet and C. Tresser, *Physics Letters A* **79**(4), 259–263 (1980).
18. N. Samardzija and L. D. Greller, *Bulletin of Mathematical Biology* **50**(5), 465–491 (1988).

Global Dynamics of a Model for Anaerobic Wastewater Treatment Process

S. Barua and A. Dénes

1 Introduction

1.1 Anaerobic Wastewater Treatment Process

The anaerobic wastewater treatment process is a procedure where microorganisms degrade organic contaminants in an oxygen-free environment. This process has high capacity to break down biodegradable waste originating from agriculture (animal manures, energy crops, harvest remains, algal biomass), food industry (food/beverage processing, starch, dairy, sugar, pulp/paper, etc.), sewage sludge, etc. [1]. It requires little energy, produces very little sludge, and can even recover energy by burning methane in some cases [2]. Basically this process is a complex naturally occurring process called anaerobic digestion.

Nowadays, anaerobic digestion is one of the most successful waste management strategies worldwide, wherein microorganisms play a vital role in reducing organic pollutants and producing renewable energy [3].

In 1907, Karl Imhoff developed the first anaerobic digester for wastewater treatment. Later in the twentieth century several small-scale utilizations of anaerobic digestion for biogas production flourished in France and England [4]. By the year of 2014 more than 14,500 biogas plants were established in Europe with the total capacity of 7857 MWel [5].

Hydrolysis, acidogenesis, acetogenesis, and methanogenesis are the four successive stages of anaerobic digestion process which is dependent on the interactions between the diverse microorganisms that have ability to carry out the aforesaid stages [6]. In the process of hydrolysis, hydrolytic bacteria secrete extracellular

S. Barua (✉) · A. Dénes
Bolyai Institute, University of Szeged, Szeged, Hungary

R. P. Mondaini (ed.), *Trends in Biomathematics: Chaos and Control in Epidemics, Ecosystems, and Cells*, https://doi.org/10.1007/978-3-030-73241-7_18

enzymes that hydrolyzed lipids, proteins and carbohydrate polymers to long-chain fatty acids, amino acids, and sugars respectively.

It is notable that certain substrates like cellulose, hemicellulose, and lignin are difficult to degrade, as because of inaccessibility for microbes due to their complex structure. In this case enzymes are often added to accelerate the hydrolysis of these carbohydrates [6–8].

In the second stage of anaerobic digestion known as acidogenesis, acidogenic microorganisms convert the products of hydrolysis through their cell membranes and produce alcohol, carbon dioxide, hydrogen, volatile fatty acids (VFAs) such as propionic acid, butyric acid and acetic acid. In general, acidogenesis is believed to proceed at a faster rate than other three stages of anaerobic digestion where acidogenic bacteria having a generation time of less than 36 h. It is important to note that, as this stage is faster than others so the production of VFAs creates direct precursors for the fourth stage of methanogenesis, which is reported to be an aftermath for digester failure [4, 6, 9]. The product of acidogenesis, VFAs and alcohols are converted into acetic acid, hydrogen and carbon dioxide by acetogenic bacteria in the process of acetogenesis, third stage of anaerobic digestion.

Methanogenesis is marked as the fourth and final stage of anaerobic digestion where methanogens can produce methane using carbon dioxide, acetate, etc. In batch reactor when the biogas production stops then the end of the methanogenesis is determined, which can take about 40 days [6, 10].

1.2 Mathematical Models for Anaerobic Wastewater Treatment Process

Mathematical modeling of the anaerobic digestion process has drawn interest of the researchers during the past decades. Anaerobic digesters exhibit significant stability problems frequently that may be avoided only through suitable control strategies. In general, the development of appropriate mathematical models is needed, which adequately illustrate the key biological processes that take place in the reactor [11].

Hajji et al. [11] concentrated the reactionary part of the anaerobic digestion involving only acetogens and methanogens bacteria populations and study their syntrophic relationship. The volatile fatty acids and other products are degraded by acetogens, forming hydrogen, acetate and carbon dioxide which are the intermediate product, required by anaerobic methanogens in order to carry out anaerobic respiration. In the absence of H_2-producing acetogens bacteria, methanogens cannot grow. Applying the Poincaré–Bendixson theorem and the Dulac criterion they found that under general and natural assumptions of monotonicity on the functional responses, the stable asymptotic coexistence of acetogenic and methanogenic bacteria occurs.

Hess et al. [12] introduced a model considering acidogenesis and methanogenesis which provides the operator with a risk index associated with his main strategy, also can be used in parallel to a controller that only guarantees local convergence. They

proposed a criterion which can predict very early a future accumulation of acids, that is the main reason of instability of the reactor. The mass balanced model proposed by them is formulated as

$$\begin{aligned} X_1' &= \mu_1(S_1)X_1 - \alpha D X_1, \\ S_1' &= -k_1\mu_1(S_1)X_1 + D(S_{1in} - S_1), \\ X_2' &= \mu_2(S_2)X_2 - \alpha D X_2, \\ S_2' &= -k_3\mu_2(S_2)X_2 + k_2\mu_1(S_1)X_1 + D(S_{2in} - S_2), \end{aligned} \tag{1}$$

where S_1, S_2, X_1, X_2 represent organic substrate, VFAs, acidogenic bacteria, and methanogenic bacteria respectively. Also D, S_{1in}, S_{2in} are dilution rate, concentration of influent organic substrate and influent VFAs respectively. The k_is are pseudo-stoichiometric coefficients associated with the bioreaction and α appears here as the fraction of the biomass not retained in the digestor.

Weedermann et al. [4] studied the effects of inhibition on the microbes involved in the process. For that they assumed the temperature remains constant and consider continuously stirred tanks only. They did not consider hydrolysis in their model as it is a preliminary phase of the process. A bifurcation result for the preservation of global stability was provided by them which can be applied to an inhibition-free version of the model and it serves as a baseline for studying the consequences of inhibition. Assuming a continuous-flow constant-volume reactor and uniformly mixed substrate, and ignoring biomass decay rates they derive the system of differential equations

$$\begin{aligned} S' &= D(S^{(0)} - S) - \tilde{g}_S(S)X_S, \\ X_S' &= -DX_S + Y_{X_S}\tilde{g}_S(S)X_S, \\ V' &= -DV + Y_{sv}\tilde{g}_S(S)X_S - \tilde{g}_V(V,H)X_V, \\ X_V' &= -DX_V + Y_{X_V}\tilde{g}_V(V)X_V, \\ A' &= -DA + Y_{sa}\tilde{g}_S(S)X_S + Y_{va}\tilde{g}_V(V,H)X_V - \tilde{g}_A(A)X_A, \\ X_A' &= -DX_A + Y_{X_A}\tilde{g}_A(A)X_A, \\ H' &= -DH + Y_{sh}\tilde{g}_S(S)X_S + Y_{vh}\tilde{g}_V(V,H)X_V - \tilde{g}_H(H,A)X_H, \\ X_H' &= -DX_H + Y_{X_H}\tilde{g}_H(H,A)X_H, \end{aligned} \tag{2}$$

where simple substrates are denoted by S, VFAs by V, acetic acid by A, hydrogen by H. The notations $X_\alpha, \alpha = S, V, A, H$ represent bacteria for different nutrient groups. Again, $D, S^{(0)}, Y_i, g_\alpha(\cdot)$ stand for dilution rate, concentration of monomer inflow, yield coefficient, and bacterial growth rate, respectively.

Amster et al. [13] introduce a simple ω-periodic and delayed chemostat model and proved the existence of ω-periodic solutions. Their results partially generalize those obtained for the undelayed case and they have constructed Poincaré's transla-

tion operators tailored for a one-parameter family of integro-differential equations for the nutrient equation and a map related to the biomass equation defined over the fixed points of the above-mentioned Poincaré operators.

There exist general models with multiple microbial species. Hale et al. [14] considered a model where n species compete for a single essential periodically fluctuating nutrient in a chemostat. They assumed uptake rate functions are positive, increasing, and bounded above instead of the familiar Michaelis–Menten kinetics for nutrient uptake.

Wolkowicz and Zhao [15] studied an n-species competition model in a periodically operated chemostat and gave sufficient conditions for the uniform persistence of all species and for the existence of at least one positive, periodic solution.

2 Model Formulation

Inspired by the wastewater treatment process models given by Hess et al. [12] and Weederman et al. [4] and by the general, n-species chemostat models [14, 15], we establish a generalized model which describes n microbial species feeding on n types of substrates.

In the model, similarly as in (1) and (2), the n species and the corresponding substrates form a chain where the nutriments consumed by the ith microbial species are produced by the microbes denoted by a lower index. We will denote by $S_i(t)$ the amount of the ith substrate and by $X_i(t)$ the amount of the ith microbial species at time t. We use the notation $S_i^{(0)}$ for the concentrations of influent substrates. We will denote by D the dilution rate of the chemostat. The functions $g_i(S_i)$ represent the bacterial growth rates associated with the bioreactions during which the ith microorganism produces substrate for those with higher indices. The coefficients Y_i $(i = 1, \dots, n)$ and Y_{ki} $(k = 1, \dots, i-1)$ are pseudo-stoichiometric coefficients associated with the bioreactions. For technical reasons, in this work we will always assume that these functions only depend on the amount of substrates denoted with lower indices. Another important restriction on the functions $g_i(S_i)$ is that they are all assumed to be monotone increasing functions. For example, the functions g_i might be Monod type functions of the form $g_i(S_i) = \mu_i \frac{S_i}{S_i + k_i}$ with some positive constants μ_i and k_i.

Using the above notations and applying the assumptions described above, our model takes the form

$$\begin{aligned} S_1'(t) &= D(S_1^{(0)} - S_1(t)) - g_1(S_1(t))X_1(t), \\ X_1'(t) &= -DX_1(t) + Y_1 g_1(S_1(t))X_1(t), \end{aligned} \tag{3a}$$

$$\begin{aligned} S_i'(t) &= D(S_i^{(0)} - S_i(t)) + \sum_{k=1}^{i-1} Y_{ki} g_k(S_k(t)) X_k(t) - g_i(S_i(t)) X_i(t), \\ X_i'(t) &= -DX_i(t) + Y_i g_i(S_i(t)) X_i(t), \end{aligned} \tag{3b}$$

where $i = 2, 3, \ldots, n$.

3 Global Dynamics

In this subsection, we turn to the global analysis of system (3a). We will establish a procedure to completely describe the dynamics of our system. In each step of the procedure, as the right-hand sides of the equations do not depend on variables with higher indices, only on those with lower ones, we can always decouple two equations from the rest of equations and determine the dynamics of that planar system.

It is easy to check that, depending on the parameters, the system (3a) consisting of the first two equations of (3) may have two equilibria

$$E_0^1 = (S_1^{(0)}, 0) \quad \text{and} \quad E_+^1 = (g_1^{-1}(D/Y_1), Y_1[S_1^{(0)} - g_1^{-1}(D/Y_1)]).$$

Let us introduce the threshold parameter

$$\vartheta_1 := -D + Y_1 g_1(S_1^{(0)}).$$

We obtain that the equilibrium E_0^1 exists independently of the parameter values, while the positive equilibrium E_+^1 exists if and only for $\vartheta_1 > 0$.

The Jacobian of system (3a) can be calculated as

$$J = \begin{bmatrix} -D - \frac{\partial}{\partial S_1} g_1(S_1) X_1 & -g_1(S_1) \\ \frac{\partial}{\partial S_1} X_1 Y_1 g_1(S_1) & -D + Y_1 g_1(S_1) \end{bmatrix}.$$

At the trivial equilibrium E_0^1, the Jacobian takes the form

$$J_0 = \begin{bmatrix} -D & -g_1(S_1^{(0)}) \\ 0 & -D + Y_1 g_1(S_1^{(0)}) \end{bmatrix}$$

and has the eigenvalues $-D$ and $-D + Y_1 g_1(S_1^{(0)})$, hence, we can see that the equilibrium E_0^1 is locally asymptotically stable if $\vartheta_1 < 0$ and unstable if $\vartheta_1 > 0$. Now let us consider the Dulac function $\frac{1}{X_1}$. Then

$$\frac{\partial}{\partial S_1}\frac{D(S_1^{(0)}-S_1)-g_1(S_1)X_1}{X_1}+\frac{\partial}{\partial X_1}\frac{X_1Y_1g_1(S_1)-DX_1}{X_1}=-\frac{D}{X_1}-\frac{\partial}{\partial S_1}g_1(S_1)<0$$

for all parameter values, using the assumption that $g_1(S_1)$ is monotone increasing. Applying the Bendixson–Dulac theorem, we can observe that the system has no periodic solution. Hence, it follows from the Poincaré–Bendixson theorem that all solutions tend to one of the two equilibria. As we have seen above, if $\vartheta_1 < 0$, then only the trivial equilibrium E_0^1 exists, hence, all solutions will tend to E_0^1 as $t \to \infty$. We have also obtained above that E_0^1 is locally asymptotically stable if $\vartheta_1 < 0$, using this and the global attractivity, we obtain that the trivial equilibrium is globally asymptotically stable if $\vartheta_1 < 0$. Again, if $\vartheta_1 > 0$, then the trivial equilibrium E_0^1 becomes unstable and the positive equilibrium E_+^1 also exists. Because of the instability of E_0^1 all solutions tend to E_+^1, except the solutions started with $X_1 = 0$, thus, E_+^1 is globally attractive on the set

$$\mathbb{R}^2_+ \setminus \{(S_1, X_1) : X_1 = 0\}.$$

Let us now proceed to the second pair of equations of system (3), i.e., the two equations (3b) for $i = 2$, namely the equations

$$\begin{aligned} S_2'(t) &= D(S_2^{(0)} - S_2(t)) + Y_{12}g_1(S_1(t))X_1(t) - g_2(S_2(t))X_2(t),\\ X_2'(t) &= -DX_2(t) + Y_2g_2(S_2(t))X_2(t). \end{aligned} \tag{4}$$

Let (S_1^*, X_1^*) denote the global attractor of the system consisting of the first two equations (3a) and let us substitute these values into the first equation of (3b) to obtain

$$S_2' = D(S_2^{(0)} - S_2) + Y_{12}g_1(S_1^*)X_1^* - g_2(S_2)X_2$$

which, introducing the notation

$$C_2 := DS_2^{(0)} + Y_{12}g_1(S_1^*)X_1^*,$$

can be transformed into

$$\begin{aligned} S_2'(t) &= C_2 - DS_2(t) - g_2(S_2(t))X_2(t),\\ X_2'(t) &= -DX_2(t) + Y_2g_2(S_2(t))X_2(t). \end{aligned} \tag{5}$$

Observe that (5) is of the same structure as system (3a). Hence, a similar analysis can be performed for (5) as for (3a), yielding that the threshold parameter ϑ_2 defined as

$$\vartheta_2 = -D + Y_2g_2\left(\tfrac{C_2}{D}\right)$$

determines which of the two possible equilibria

$$E_0^2 = \left(\tfrac{C_2}{D}, 0\right) \quad \text{and} \quad E_+^2 = \left(g_2^{-1}\left(\tfrac{D}{Y_2}\right), Y_2\left(\tfrac{C_2}{D} - g_2^{-1}\left(\tfrac{D}{Y_2}\right)\right)\right)$$

is globally attractive. Performing similar steps as for the first pair of equations, we obtain the limit of the transformed equations (5) and we can proceed to the next pair of equations.

In the general step of the procedure, we study the dynamics of the ith pair of equations (3b), which are of the form

$$\begin{aligned} S_i'(t) &= D(S_i^{(0)} - S_i(t)) + \sum_{k=1}^{i-1} Y_{ki} g_k(S_k(t)) X_k(t) - g_i(S_i(t)) X_i(t), \\ X_i'(t) &= -DX_i(t) + Y_i g_i(S_i(t)) X_i(t). \end{aligned}$$

From the analysis performed before, we have already obtained the limit of all functions $S_k(t)$ and $X_k(t)$, $i = 1, 2, \ldots, i-1$, denote these again by S_k^* and X_k^*. Hence, we can substitute these values into the first equation of (3b) to get

$$\begin{aligned} S_i'(t) &= D(S_i^{(0)} - S_i(t)) + \sum_{k=1}^{i-1} Y_{ki} g_k(S_k^*) X_k^* - g_i(S_i(t)) X_i(t), \\ X_i'(t) &= -DX_i(t) + Y_i g_i(S_i(t)) X_i(t). \end{aligned}$$

By introducing the notation

$$C_i := DS_i^{(0)} + \sum_{k=1}^{i-1} Y_{ki} g_k(S_k^*) X_k^*,$$

we arrive at the system

$$\begin{aligned} S_i'(t) &= C_i - DS_i(t) - g_i(S_i(t)) X_i(t), \\ X_i'(t) &= -DX_i(t) + Y_i g_i(S_i(t)) X_i(t), \end{aligned} \tag{6}$$

which is again of the same structure as (3a).

Again, depending on the parameters, system (6) may have two equilibria,

$$E_0^i = \left(\tfrac{C_i}{D}, 0\right) \quad \text{and} \quad E_+^i = \left(g_i^{-1}\left(\tfrac{D}{Y_i}\right), Y_i\left(\tfrac{C_i}{D} - g_i^{-1}\left(\tfrac{D}{Y_i}\right)\right)\right).$$

Introducing the threshold parameter

$$\vartheta_i = -D + Y_i g_i\left(\tfrac{C_i}{D}\right),$$

we can see that E_0^i always exists, while the positive equilibrium E_+^i exists if and only if $\vartheta_i > 0$. The Jacobian of (6) has the form

$$J = \begin{bmatrix} -D - X_i \frac{\partial}{\partial S_i} g_i(S_i) & -g_i(S_i) \\ X_i Y_i \frac{\partial}{\partial S_i} g_i(S_i) & -D + Y_i g_i(S_i) \end{bmatrix}.$$

At the trivial equilibrium E_0^i, the Jacobian can be calculated as

$$J = \begin{bmatrix} -D & -g_i(\frac{C_i}{D}) \\ 0 & -D + Y_i g_i(\frac{C_i}{D}) \end{bmatrix}$$

and it has the two eigenvalues $-D$ and $-D + Y_i g_i\left(\frac{C_i}{D}\right)$. Hence, we obtain that E_0^i is a locally asymptotically stable equilibrium of system (6) if $\vartheta_i < 0$ and it is unstable $\vartheta_i > 0$. Now let us consider the Dulac function $\frac{1}{X_i}$. Then

$$\frac{\partial}{\partial S_i} \frac{C_i - DS_i - g_i(S_i)X_i}{X_i} + \frac{\partial}{\partial X_i} \frac{X_i Y_i g_i(S_i) - DX_i}{X_i} = -\frac{D}{X_i} - \frac{\partial}{\partial S_i} g_i(S_i) < 0,$$

so using the Bendixson–Dulac theorem we can say that the system has no periodic solution and it follows from the Poincaré–Bendixson theorem that all solutions tend to one of the two equilibria. If $\vartheta_i < 0$ the only trivial equilibrium E_0^i exists and it is locally asymptotically stable. Being a global attractor it is also globally asymptotically stable. On the other hand, if $\vartheta_i > 0$, then the trivial equilibrium E_0^i becomes unstable and the positive equilibrium E_+^i also exists. Because of the instability of E_0^i all solutions tend to E_+^i except the solutions started with $X_i = 0$. Hence, depending on the threshold parameter ϑ_i, we have determined the dynamics of (6) and we can again proceed to the next two equations.

Performing the above steps n times, we obtain a sequence of threshold parameters $\vartheta_1, \vartheta_2, \ldots, \vartheta_n$, which completely determine the global dynamics of the $2n$-dimensional system.

4 Numerical Simulations

In this section, we present some numerical simulations (Fig. 1) for the cases $n = 2$ to support and illustrate the theoretical results obtained in the previous section. In these simulations, we assume the functions $g_i(S_i)$ to be of Monod type and of the form

$$g_i(S_i) = \mu_i \frac{S_i}{S_i + k_i}.$$

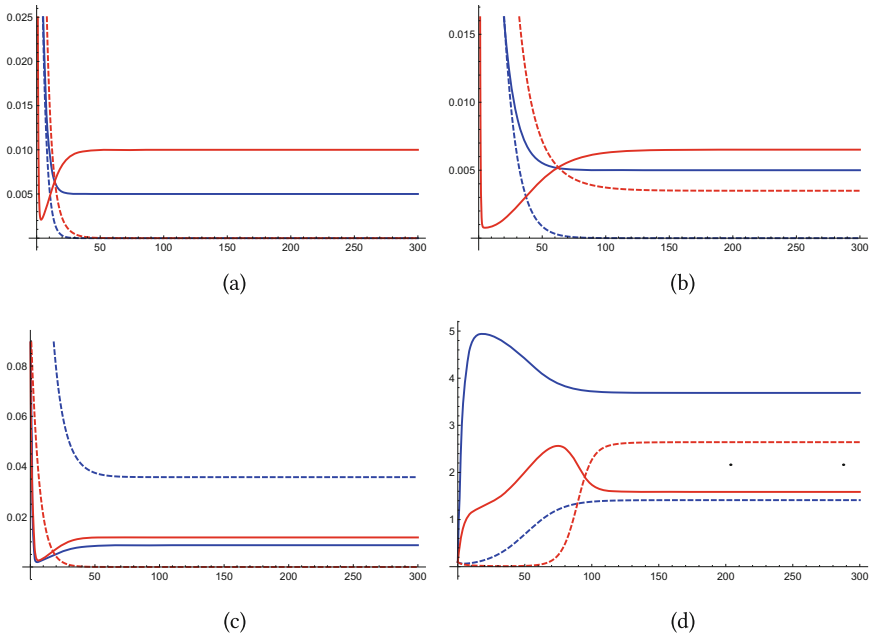

Fig. 1 Solutions of (3) in the case $n = 2$ for all possible combinations of the signs of the threshold parameters ϑ_1 and ϑ_2. Solid lines denote substrates, dashed lines denote bacteria. Blue lines stand for S_1 and X_1, red lines stand for S_2 and X_2. (**a**) The case $\vartheta_1, \vartheta_2 < 0$ when both bacteria go extinct. The parameter values are $d = 0.2932$, $S_1^{(0)} = 0.005$ $S_2^{(0)} = 0.01$, $Y_1 = 1.35$, $Y_2 = 1$; $Y_{12} = 1.168$, $\mu_1 = 1.086$, $k_1 = 7.17$, $\mu_2 = 1.626$, $k_2 = 0.1$, while the threshold parameters take the values $\vartheta_1 = -0.292$, $\vartheta_2 = -0.145$. (**b**) The case $\vartheta_1 < 0$, $\vartheta_2 > 0$ when the first bacterium goes extinct, the second one persists. The parameter values are $d = 0.0994$, $S_1^{(0)} = 0.005$ $S_2^{(0)} = 0.01$, $Y_1 = 1.35$, $Y_2 = 1$; $Y_{12} = 1.168$, $\mu_1 = 1.086$, $k_1 = 7.17$, $\mu_2 = 1.626$, $k_2 = 0.1$, while the threshold parameters take the values $\vartheta_1 = -0.098$, $\vartheta_2 = 0.048$. (**c**) The case $\vartheta_1 > 0$, $\vartheta_2 < 0$ when the first bacterium persists, the second one goes extinct. The parameter values are $d = 0.16062$, $S_1^{(0)} = 0.015$, $S_2^{(0)} = 0.0051$, $Y_1 = 5.65$; $Y_2 = 0.01$; $Y_{12} = 1.052$; $\mu_1 = 1.176$, $k_1 = 0.35$, $\mu_2 = 2.574$, $k_2 = 0.1$, while the threshold parameters take the values $\vartheta_1 = 0.112$, $\vartheta_2 = -0.144$. (**d**) The case $\vartheta_1, \vartheta_2 > 0$ when both types of bacteria persist. The parameter values are $d = 0.279$, $S_1^{(0)} = 5.1$, $S_2^{(0)} = 1.13$, $Y_1 = 1$, $Y_2 = 1.944$,$Y_{12} = 1.286$, $\mu_1 = \mu_2 = 1$, $k_1 = 9.53$, $k_2 = 9.47$, while the threshold parameters take the values $\vartheta_1 = 0.0696$, $\vartheta_2 = 0.116$

The solutions in the numerical examples show a behavior which is determined by the results of the previous section: the signs of the threshold parameters ϑ_1 and ϑ_2 determine which of the two bacterial species will die out or persist, demonstrating that all possible combinations are feasible, depending on the parameter values.

5 Discussion

In this paper we have studied a mathematical model for an anaerobic wastewater treatment process. Inspired by earlier models, we have established a generalized model of $2n$ equations for n types of bacteria and the corresponding nutriments consumed by those bacteria. In our model, the substrates and bacteria form a linear food chain in the sense that the ith bacterium produces nutriment for the $(i + 1)$th species. Under some conditions on the bacterial growth rates and the interactions among the different species and nutriments, we can establish a procedure to determine the global dynamics of the system where in each step we can decouple a pair of equations from the remaining ones and applying the Bendixson–Dulac and the Poincaré–Bendixson theorems, we can determine the globally attractive equilibrium of that given planar system. This way, we obtain a sequence of threshold parameters which completely determine the global dynamics of the system.

One of the limitations of the model is that for technical reasons, we have prescribed some properties for the bacterial growth rate functions. Also, in order to obtain a planar system in each step of the procedure, we neglected possible effects of bacteria and substrates denoted by higher indices on those with lower indices. Further improvements of the model might include the consideration of periodic coefficients. We leave these questions as a future work.

Acknowledgments This research was supported by grant TUDFO/47138-1/2019-ITM of the Ministry for Innovation and Technology, Hungary. S. Barua was supported by Stipendium Hungaricum scholarship and Ministry of Education, Government of Bangladesh. A. Dénes was supported by the projects No. 128363 and No. 129877, implemented with the support provided from the National Research, Development and Innovation Fund of Hungary, financed under the PD_18 and KKP_19 funding schemes, respectively.

References

1. D. P. Van, T. Fujiwara, B. L. Tho, P. P. Song Toan and G. H. Minh, *Environ. Eng. Res.* **25(1)**, 1 (2019).
2. O. Bernard, Z. Hadj-Sadok, D. Dochain, A. Genovesi and J.-P. Steyer, *Biotechnol. Bioeng.* **75(4)**, 424 (2001).
3. Q. Zhang, M. Wang, X. Ma, Q. Gao, T. Wang, X. Shi, J. Zhou, J. Zuo and Y. Yang, *Environ. Int.* **126**, 543 (2019).
4. M. Weedermann, G. Seo and G. Wolkowicz, *J. Biol. Dyn.* **7(1)**, 59 (2013).
5. D. Wu, L. Li, X. Zhao, Y. Peng, P. Yang and X. Peng, *Renew. Sust. Energ. Rev.*, **103**, 1 (2019).
6. J. Meegoda, B. Li, K. Patel, L. Wang *Int. J. Environ. Res. Public Health* **15(10)**, 2224 (2018).
7. Y. Li, S. Y. Park and J. Zhu, *Renew. Sust. Energ. Rev.* **15(1)**, 821 (2011).
8. L. Lin, R. Yan, Y. Liu and W. Jiang, *Bioresour. Technol.* **101(21)**, 8217 (2010).
9. M. Akuzawa, T. Hori, S. Haruta, Y. Ueno, M. Ishii and Y. Igarashi, *Microbial Ecology* **61(3)**, 595 (2011).
10. V. Patel, S. Pandit and K. Chandrasekhar, *Microbial applications Vol. 2* , 291 (2017).
11. M. El Hajji, F. Mazenc and J. Harmand, *Math. Biosci. Eng.* **7(3)**, 641 (2010).
12. J. Hess, O. Bernard, *J. Process Control* **18(1)**, 71 (2008).

13. P. Amster, G. Robledo and D. Sepúlveda, *Nonlinearity* **33(11)**, 5839 (2020).
14. J. K. Hale and A. S. Somolinos, *J. Math. Biol.* **18(3)**, 255 (1983).
15. G. S. K. Wolkowicz and X.-Q. Zhao, *Differential Integral Equations***11**, 465 (1998)

Spatiotemporal Dynamics of Fractional Hepatitis B Virus Infection Model with Humoral and Cellular Immunity

Moussa Bachraoui, Khalid Hattaf, and Noura Yousfi

1 Introduction

The liver is the largest abdominal organ and is part of the digestive tract secreting bile and performing more than 300 vital functions, including the following three: a cleansing function, a synthesis function, and a storage function. It is an amphicrine gland allowing the synthesis of bile (exocrine role) as well as that of several carbohydrates and lipids (endocrine role). It also plays an important role in haemostasis. It is a richly vascularized organ.

Hepatitis is an inflammation of the liver caused by toxic substances or viruses (majority of cases). To date, five viruses causing targeted infection and inflammation of the liver have been identified. These viruses, designated by the letters A, B, C, D, and E, differ in their mode of transmission (faecal-oral for viruses A and E, parenteral for viruses B and C) and their aggressiveness.

The WHO estimates that in 2016, hepatitis A would have caused approximately 7134 deaths (i.e. 0.5% of the mortality due to viral hepatitis), 257 million people were living with chronic hepatitis B (defined as positive for hepatitis B surface antigen) with 887,000 deaths, mainly due to cirrhosis or hepatocellular carcinoma (i.e. primary liver cancer), 71 million individuals are chronic carriers of hepatitis C and 399,000 deaths, most often from cirrhosis or hepatocellular carcinoma, and each year an estimated 20 million HEV infections occur worldwide, resulting in an

M. Bachraoui (✉) · N. Yousfi
Laboratory of Analysis, Modeling and Simulation (LAMS), Faculty of Science Ben M'sik, Hassan II University, Casablanca, Morocco

K. Hattaf
Laboratory of Analysis, Modeling and Simulation (LAMS), Faculty of Science Ben M'sik, Hassan II University, Casablanca, Morocco

Centre Régional des Métiers de l'Education et de la Formation (CRMEF), Casablanca, Morocco

R. P. Mondaini (ed.), *Trends in Biomathematics: Chaos and Control in Epidemics, Ecosystems, and Cells*, https://doi.org/10.1007/978-3-030-73241-7_19

estimated 3.3 million symptomatic cases of hepatitis E, and it has been responsible for approximately 44 000 deaths (3.3% of mortality due to viral hepatitis).

Faced with aggression by the hepatitis B virus, two types of immune reactions are set up successively. The first is called innate; it is immediate and is not specific to the pathogenic agent. In the second stage, a so-called adaptive immune reaction is directed specifically towards the virus. This response involves specialized cells called lymphocytes. There are two classes of lymphocytes: B lymphocytes, which are responsible for the production of antibodies. When they encounter an infectious agent, they produce specific antibodies directed against it. These antibodies are proteins capable of binding to foreign proteins and destroying the pathogen. They are also called immunoglobulins. T lymphocytes that can directly destroy foreign particles.

Recently, several mathematical models describing HBV dynamics including HBV DNA-containing capsids and adaptive immune response effects have appeared in literature. In [1], Manna investigated the role of the CTL immune response in a reaction-diffusion model of HBV with capsids. Their work was an extension of the work presented in [2]. In [3], Xu and Geng proposed and analysed a discrete-time model with CTL immune response and nonlinear incidence. Bachraoui et al. [4] proposed a fractional order model for HBV infection with capsids and CTL immune response that improved and generalized the mathematical models formulated by ordinary differential equations (ODEs) in [2, 5] and also the FDE models introduced in [6–8] by considering the Hattaf's incidence rate [9] that includes the common types such as the bilinear incidence rate, the saturated incidence rate, and the Beddington-De Angelis functional response [10, 11]. All these models take only into account the effect of the cellular response formed by the CTL cells and do not integrate the effects of the humoral response formed by the antibodies in the modeling approach. Therefore, Manna and Hattaf in [12] studied a new HBV infection model which contains two arms of immunity, three time delays, capsids, general incidence rate, and allows the movement of capsids and viruses by diffusion. The proposed model and the results obtained extended and improved the DDE and PDE models and the corresponding results are presented in [1, 13, 14].

The memory is an important characteristic of adaptive immunity, there are T and B lymphocytes known as memory lymphocytes. The latter retain the memory of a pathogen. If this agent re-infects the organism, the response will be much faster. The classical integer derivative does not reflect this characteristic because it is a local operator unlike the fractional derivative. In this chapter, we will develop a mathematical model governed by both FDEs and PDEs in order to describe the dynamics of HBV infection under the effects of diffusion and memory.

$$\begin{cases} \partial_t^\alpha U(x,t) & = \lambda - dU(x,t) - F(U(x,t), V(x,t))V(x,t), \\ \partial_t^\alpha I(x,t) & = F(U(x,t), V(x,t))V(x,t) - \gamma I(x,t) - pI(x,t)T(x,t), \\ \partial_t^\alpha C(x,t) & = d_C \Delta C + vI(x,t) - (\rho+\gamma)C(x,t), \\ \partial_t^\alpha V(x,t) & = d_V \Delta V + \rho C(x,t) - \mu V(x,t) - qV(x,t)W(x,t), \\ \partial_t^\alpha W(x,t) & = aV(x,t)W(x,t) - bW(x,t), \\ \partial_t^\alpha T(x,t) & = cI(x,t)T(x,t) - eT(x,t). \end{cases} \tag{1}$$

Here $U(x,t)$, $I(x,t)$, $C(x,t)$, $V(x,t)$, $W(x,t)$, and $T(x,t)$ are, respectively, the densities of uninfected cells, infected cells, capsids, free viral particles, antibodies, and CTL cells at location x and time t. Uninfected cells are produced at rate λ, die at rate dU, and become infected by virus at rate $F(U,V)V$. The death rate of infected cells and capsids is denoted by γ, while the death rates of free viral particles, antibodies, and CTL cells are, respectively, labeled by μ, b, and e. The capsids are produced from infected cells at rate vI and converted to virus at rate ρC. Free viral particles are neutralized by antibodies at rate qVW. Whereas, the infected cells are killed by CTL cells at rate pIT. Antibodies develop in response to free viral particles at rate aVW, while CTL cells expand in response to viral antigens derived from infected cells at rate cIT. The positive constants d_C and d_V denote, respectively, the diffusion coefficients of capsids and virus. $\Delta = \sum_{i=1}^{n} \frac{\partial^2}{\partial x_i^2}$ is the Laplacian operator. The incidence function of (1) is described by Hattaf-Yousfi functional response [9] of the form $F(U,V) = \frac{kU}{\epsilon_0+\epsilon_1 U+\epsilon_2 V+\epsilon_3 UV}$, where the nonnegative constants ϵ_i, $i = 0,1,2,3$, measure the saturation, inhibitory or psychological effects, and the positive constant k is the infection rate. D^α is the fractional derivative in the sense of Caputo with order $\alpha \in (0,1]$. Further, the proposed model (1) is subjected to the following initial conditions:

$$\begin{aligned} &U(x,0) = U_0(x) \geq 0\,,\ I(x,0) = I_0(x) \geq 0\,,\ C(x,0) = C_0(x) \geq 0, \\ &V(x,0) = V_0(x) \geq 0\,,\ W(x,0) = W_0(x) \geq 0\,,\ T(x,0) = T_0(x) \geq 0\,, \forall x \in \bar{\Omega}, \end{aligned} \tag{2}$$

and zero-flux boundary conditions

$$\frac{\partial C}{\partial \nu} = \frac{\partial V}{\partial \nu} = 0, \quad on\ \partial\Omega \times (0, +\infty),$$

where Ω is a bounded domain in $\mathbb{R}^n$ with smooth boundary $\partial\Omega$, and $\frac{\partial}{\partial \nu}$ denotes the outward normal derivative on $\partial\Omega$. From the biological point of view, these conditions mean that the capsids and free virus particles do not move across the boundary $\partial\Omega$.

Clearly, model (1) has one infection-free steady state $E_0(U^0, 0, 0, 0, 0, 0)$, where $U^0 = \frac{\lambda}{d}$. So, the basic reproduction number of (1) is given by

$$R_0 = \frac{v\rho F(U^0, 0)}{\mu\gamma(\rho + \gamma)}.$$

The remaining equilibria of system (1) satisfy the following algebraic equations:

$$\lambda - dU - F(U, V)V = 0, \tag{3}$$

$$F(U, V)V - \gamma I - pIT = 0, \tag{4}$$

$$vI - (\rho + \gamma)C = 0, \tag{5}$$

$$\rho C - \mu V - qVW = 0, \tag{6}$$

$$aVW - bW = 0, \tag{7}$$

$$cIT - eT = 0. \tag{8}$$

From Eq. (7), we get $T = 0$ or $I = \frac{e}{c}$ and by (8), we get $W = 0$ or $V = \frac{b}{a}$.

When $W = 0$ and $T = 0$, we find $I = \frac{\lambda - dU}{\gamma}$, $C = \frac{v(\lambda - dU)}{\gamma(\rho + \gamma)}$, $V = \frac{\rho v(\lambda - dU)}{\mu\gamma(\rho + \gamma)}$ and

$$F\left(U, \frac{\rho v(\lambda - dU)}{\mu\gamma(\rho + \gamma)}\right) = \frac{\mu\gamma\,(\rho + \gamma)}{\rho v}. \tag{9}$$

Since $I \geq 0$, we have $U \leq \frac{\lambda}{d}$. Define

$$g_1(U) = F\left(U, \frac{\rho v(\lambda - dU)}{\mu\gamma(\rho + \gamma)}\right) - \frac{\mu\gamma\,(\rho + \gamma)}{\rho v}.$$

We have $g_1(0) = -\frac{\mu\gamma(\rho + \gamma)}{\beta v} < 0$ and $g_1\left(\frac{\lambda}{d}\right) = \frac{\mu\gamma(\rho+\gamma)}{\rho v}(R_0 - 1)$ and

$$g_1'(U) = \frac{\partial F}{\partial U} - \frac{\rho d v}{\mu\gamma(\rho + \gamma)}\frac{\partial F}{\partial V} > 0.$$

When $R_0 > 1$, model (1) has a unique immune-free infection steady state $E_1(U_1, I_1, C_1, V_1, 0, 0)$ with $U_1 \in \left(0, \frac{\lambda}{\mu}\right)$, $I_1 = \frac{\lambda - dU_1}{\gamma}$, $C_1 = \frac{v(\lambda - dU_1)}{\gamma(\rho + \gamma)}$, and $V_1 = \frac{\rho v(\lambda - dU_1)}{\mu\gamma(\rho + \gamma)}$.

If $W \neq 0$ and $T = 0$, we have $I = \dfrac{\lambda - dU}{\gamma}$, $C = \dfrac{v(\lambda - dU)}{\gamma(\rho + \gamma)}$, $V = \dfrac{b}{a}$, $W = \dfrac{av\rho(\lambda - dU)}{qb\gamma(\rho + \gamma)} - \dfrac{\mu}{q}$, and

$$F\left(U, \frac{b}{a}\right) = \frac{a(\lambda - dU)}{b}.$$

Since $W \geq 0$, we have $U \leq \dfrac{\lambda}{d} - \dfrac{\mu b\gamma(\rho + \gamma)}{avd\rho}$. So, there is no equilibrium if $U > \dfrac{\lambda}{d} - \dfrac{e\gamma}{cd}$. Define the function g_2 on $[0, \dfrac{\lambda}{d} - \dfrac{\mu b\gamma(\rho + \gamma)}{avd\rho}]$ by

$$g_2(U) = F\left(U, \frac{b}{a}\right) - \frac{a(\lambda - dU)}{b}.$$

We have $g_2(0) = -\dfrac{a\lambda}{b} < 0$ and

$$g_2'(U) = \frac{\partial F}{\partial U} + \frac{ad}{b} > 0.$$

Define the reproduction number for humoral immunity as follows

$$R_1^W = \frac{aV_1}{b}, \tag{10}$$

which biologically represents the average number of the antibodies activated by virus when HBV infection is successful and CTL immune response has not been established [15].

When $R_1^W < 1$, $V_1 < \frac{b}{a}$, $U_1 > \dfrac{\lambda}{\mu} - \dfrac{\mu b\gamma(\rho + \gamma)}{avd\rho}$ and

$$\begin{aligned} g_2\left(\frac{\lambda}{d} - \frac{\mu b\gamma(\rho + \gamma)}{avd\rho}\right) &= F\left(\frac{\lambda}{d} - \frac{\mu b\gamma(\rho + \gamma)}{avd\rho}, \frac{b}{a}\right) - \frac{\mu\gamma\,(\rho + \gamma)}{\rho v} \\ &< F(U_1, V_1) - \frac{\gamma c\,(\rho + \gamma)}{\rho v} = 0. \end{aligned}$$

Thus, there is no steady state if $R_1^W < 1$.

When $R_1^W > 1$, we have $U_1 < \dfrac{\lambda}{d} - \dfrac{\mu h\gamma(\rho + \gamma)}{avd\rho}$ and $g_2\left(\dfrac{\lambda}{\mu} - \dfrac{\mu b\gamma(\rho + \gamma)}{avd\rho}\right) > 0$. Hence, (1) has another equilibrium $E_2(U_2, I_2, C_2, V_2, W_2, 0)$, where $U_2 \in \left(0, \dfrac{\lambda}{d} - \dfrac{\mu b\gamma(\rho + \gamma)}{av\rho}\right)$, $I_2 = \frac{\lambda - dU_2}{\delta}$, $C_2 = \dfrac{v(\lambda - dU_2)}{\gamma(\rho + \gamma)}$, $V_2 = \dfrac{b}{a}$ and $W_2 = \dfrac{av\rho(\lambda - dU_2)}{qb\gamma(\rho + \gamma)} - \dfrac{\mu}{q}$.

When $W = 0$ and $T \neq 0$, we get $I = \frac{e}{c}$, $C = \frac{ve}{c(\rho+\gamma)}$, $V = \frac{\rho ve}{\mu c(\rho+\gamma)}$, $T = \frac{c(\lambda - dU)}{pe} - \frac{\gamma}{p}$, and

$$F\left(U, \frac{\rho ve}{\mu c(\rho+\gamma)}\right) = \frac{\mu c(\rho+\gamma)(\lambda - dU)}{\rho ve}.$$

$T \geq 0$ leads to $U \leq \frac{\lambda}{\mu} - \frac{\gamma e}{cd}$. So, there is no steady state if $U > \frac{\lambda}{d} - \frac{\gamma e}{cd}$. Define the function g_3 on the interval $[0, \frac{\lambda}{d} - \frac{\gamma e}{cd}]$ by

$$g_3(U) = F\left(U, \frac{\rho ve}{\mu c(\rho+\gamma)}\right) - \frac{\mu c(\rho+\gamma)(\lambda - dU)}{\rho ve}.$$

In this case, $g_3(0) = -\frac{\mu cs(\rho+\gamma)}{\rho ve} < 0$ and

$$g_3'(U) = \frac{\partial F}{\partial U} + \frac{\mu cd(\rho+\gamma)}{\rho ve} > 0.$$

In addition to R_0 and R_1^W, We define the reproduction number for cellular immunity as follows

$$R_1^Z = \frac{cI_1}{e}, \tag{11}$$

which represents the average number of the CTL immune cells activated by infected hepatocytes when HBV infection is successful and humoral immune response has not been established [15].

If $R_1^Z < 1$, then $I_1 < \frac{e}{c}$, $U_1 > \frac{\lambda}{\mu} - \frac{\delta e}{c\mu}$ and

$$\begin{aligned} g_3\left(\frac{\lambda}{\mu} - \frac{\gamma e}{cd}\right) &= F\left(\frac{\lambda}{d} - \frac{\gamma e}{cd}, \frac{\rho ve}{\mu c(\rho+\gamma)}\right) - \frac{\mu c(\rho+\gamma)(\lambda - dU)}{v\rho e} \\ &< F(U_1, V_1) - \frac{\delta c\,(\rho+\gamma)}{\rho v} = 0. \end{aligned}$$

Hence, there is no steady state if $R_1^Z < 1$.

When $R_1^Z > 1$, $U_1 < \frac{\lambda}{d} - \frac{\gamma e}{cd}$ and $g_2\left(\frac{\lambda}{d} - \frac{\gamma e}{cd}\right) > 0$. Therefore, there exists an infection equilibrium $E_3(U_3, I_3, C_3, V_3, 0, T_3)$ with $U_3 \in \left(0, \frac{\lambda}{d} - \frac{\gamma e}{cd}\right)$, $I_3 = \frac{e}{c}$, $C_3 = \frac{ve}{c(\rho+\gamma)}$, $V_3 = \frac{\rho ve}{\mu c(\rho+\gamma)}$ and $T_3 = \frac{c(\lambda - dU_3)}{pe} - \frac{\gamma}{p}$.

When $W \neq 0$ and $T \neq 0$, $I = \frac{e}{c}$, $C = \frac{ae}{c(\rho+\gamma)}$, $V = \frac{b}{a}$, $T = \frac{c(\lambda - dU)}{pe} - \frac{\gamma}{p}$, $W = \frac{a\rho ve}{qc(\rho+\gamma)b} - \frac{\mu}{q}$ and

$$F\left(U, \frac{h}{a}\right) = \frac{a(\lambda - dU)}{b}.$$

As $T \geq 0$, we have $U \leq \frac{\lambda}{d} - \frac{\gamma e}{cd}$. Define the function g_4 on the interval $[0, \frac{\lambda}{d} - \frac{\gamma e}{cd}]$ by

$$g_4(U) = F\left(U, \frac{b}{a}\right) - \frac{a(\lambda - dU)}{b}.$$

We have $g_4(0) = -\frac{as}{b} < 0$ and

$$g_4'(U) = \frac{\partial F}{\partial U} + \frac{ad}{b} > 0.$$

We define the reproduction number for cellular immunity in competition as follows

$$R_2^Z = \frac{cI_2}{e}.$$

which represents the average number of the CTL immune cells activated by infected hepatocytes under the condition that humoral immunity has been established [15].

If $R_2^Z < 1$, then $I_2 < \frac{e}{c}$, $U_2 > \frac{\lambda}{d} - \frac{\gamma e}{cd}$ and

$$\begin{aligned} g_4\left(\frac{\lambda}{d} - \frac{\gamma e}{cd}\right) &= F\left(\frac{\lambda}{d} - \frac{\gamma e}{cd}, \frac{b}{a}\right) - \frac{ae\gamma}{cb} \\ &< F(U_2, V_2) - \frac{a(\lambda - dU_2)}{b} = 0. \end{aligned}$$

Therefore, there is no equilibrium when $R_2^Z < 1$.

If $R_2^Z > 1$, then $I_2 > \frac{b}{c}$, $U_2 < \frac{\lambda}{d} - \frac{\gamma b}{cd}$ and $g_4\left(\frac{\lambda}{d} - \frac{\gamma e}{cd}\right) > 0$. Thus, there exists a unique $U_4 \in \left(0, \frac{\lambda}{d} - \frac{\gamma e}{cd}\right)$ such that $g_4(U_4) = 0$.

From the fourth equation of system (1), we find that

$$W_4 = \frac{\mu}{q}\left(R_3^W - 1\right),$$

where R_3^W is the reproduction number for humoral immunity in competition defined by

$$R_3^W = \frac{aV_3}{b},$$

which denote the average number of the antibodies activated by virions under the condition that cellular immunity has been established [15]. So, if $R_2^z > 1$ and $R_3^W > 1$, then model (1) has an infection steady state $E_4(U_4, I_4, C_4, V_4, W_4, T_4)$, where $I_4 = \frac{e}{c}$, $C_4 = \frac{ve}{c(\rho+\gamma)}$, $V_4 = \frac{b}{a}$, $W_4 = \frac{\mu}{q}\left(\frac{a\rho ve}{cb\mu(\rho+\gamma)} - 1\right)$, and $T_4 = \frac{c(\lambda - dU_4)}{pe} - \frac{\gamma}{p}$.

The above discussions lead to the following result.

Theorem 1.1

(i) When $R_0 \leq 1$, model (1) always has one infection-free steady state $E_0(U^0, 0, 0, 0, 0, 0)$, where $U^0 = \frac{\lambda}{d}$.

(ii) When $R_0 > 1$, model (1) has an infection steady state without immunity $E_1(U_1, I_1, C_1, V_1, 0, 0)$, where $U_1 \in \left(0, \frac{\lambda}{d}\right)$, $I_1 = \frac{\lambda - dU_1}{\gamma}$, $C_1 = \frac{v(\lambda - dU_1)}{\gamma(\rho+\gamma)}$, and $V_1 = \frac{\rho v(\lambda - dU_1)}{\mu\gamma(\rho+\gamma)}$.

(iii) When $R_1^W > 1$, model (1) has an infection steady state with only humoral immunity $E_2(U_2, I_2, C_2, V_2, W_2, 0)$, where $U_2 \in \left(0, \frac{\lambda}{d} - \frac{\mu b\gamma(\rho+\gamma)}{avd\rho}\right)$, $I_2 = \frac{\lambda - dU_2}{\gamma}$, $C_2 = \frac{a(\lambda - dU_2)}{\gamma(\rho+\gamma)}$, $V_2 = \frac{b}{a}$, and $W_2 = \frac{av\rho(\lambda - dU_2)}{qb\gamma(\rho+\delta)} - \frac{\mu}{q}$.

(iv) When $R_1^Z > 1$, model (1) has an infection steady state with only cellular immunity $E_3(U_3, I_3, C_3, V_3, 0, T_3)$, where $U_3 \in \left(0, \frac{\lambda}{d} - \frac{\gamma e}{cd}\right)$, $I_3 = \frac{e}{c}$, $C_3 = \frac{ve}{c(\rho+\gamma)}$, $V_3 = \frac{\rho ve}{\mu c(\rho+\gamma)}$, and $T_3 = \frac{c(\lambda - dU_3)}{pe} - \frac{\gamma}{p}$.

(v) When $R_2^Z > 1$ and $R_3^W > 1$, model (1) has an infection steady state with both cellular and humoral immune responses $E_4(U_4, I_4, C_4, V_4, W_4, T_4)$, where $U_4 \in \left(0, \frac{\lambda}{d} - \frac{\delta e}{cd}\right)$, $I_4 = \frac{e}{c}$, $C_4 = \frac{ve}{c(\rho+\gamma)}$, $V_4 = \frac{b}{a}$, $W_4 = \frac{\mu}{q}\left(\frac{a\rho ve}{cb\mu(\rho+\gamma)} - 1\right)$, and $T_4 = \frac{c(\lambda - dU_4)}{pe} - \frac{\gamma}{p}$.

2 Global Stability

This section focuses on the global stability of the five steady states of (1).

Theorem 2.1 *The infection-free steady state E_0 is globally asymptotically stable if $R_0 \leq 1$.*

Proof Consider the following Lyapunov functional

$$L_0(t) = \int_\Omega \left[\frac{\epsilon_0}{\epsilon_0 + \epsilon_1 U^0} U^0 \Phi\left(\frac{U}{U^0}\right) + I(x,t) + \frac{\gamma}{v} C(x,t) + \frac{\gamma(\rho+\gamma)}{\rho v} V(x,t) \right.$$
$$\left. + \frac{q\gamma(\rho+\gamma)}{\rho v} W(x,t) + \frac{p}{q} T(x,t) \right] dx,$$

where $\Phi(x) = x - 1 - \ln(x)$ for $x > 0$. According to [16], we obtain

$$D^\alpha L_0(t) \leq \int_\Omega \left[\frac{\epsilon_0}{\epsilon_0 + \epsilon_1^0 U} \left(1 - \frac{U^0}{U}\right) \partial_t^\alpha U + D^\alpha I + \frac{\gamma}{v} \partial_t^\alpha C + \frac{\gamma(\rho+\gamma)}{\rho v} \partial_t^\alpha V \right.$$
$$\left. + \frac{q\gamma(\rho+\gamma)}{\rho v} \partial_t^\alpha W + \frac{p}{q} \partial_t^\alpha T \right] dx.$$

Using $\lambda = dU^0$, we get

$$\begin{aligned}
&D^\alpha L_0(t) \\
&\leq -\int_\Omega \left[\frac{d\epsilon_0 (U - U^0)^2}{\left(\epsilon_0 + \epsilon_1^0 U\right) U} - \frac{\gamma\mu(\rho+\gamma)}{\rho v} \left(\frac{F(U,V)}{F(U,0)} R_0 - 1 \right) V \right. \\
&\left. + \frac{q\gamma b(\rho+\gamma)}{a\rho v} W + \frac{pe}{q} T \right] dx \\
&\leq -\int_\Omega \left[\frac{d\epsilon_0 (U - U^0)^2}{\left(\epsilon_0 + \epsilon_1^0 U\right) U} - \frac{\gamma\mu(\rho+\gamma)}{\rho v} (R_0 - 1) V + \frac{q\gamma b(\rho+\gamma)}{a\rho v} W + \frac{pe}{q} T \right] dx.
\end{aligned}$$

hen $D^\alpha L_0(t) \leq 0$ when $R_0 \leq 1$. Furthermore, $D^\alpha L_0(t) = 0$ if and only if $U = U^0$, $I = 0$, $C = 0$, $W = 0$, $T = 0$ and $(R_0 - 1) V = 0$. Two cases arise:

- If $R_0 < 1$, then $V = 0$.
- If $R_0 = 1$. From the first equation of (1), we obtain $F(U_0, V)V = 0$. Then $V = 0$.

Therefore, E_0 is the largest invariant set in $\{(U, I, C, V, W, T) \mid D^\alpha L_0(t) = 0\}$. It follows from the LaSalle's invariance principle [17] that E_0 is globally asymptotically stable when $R_0 \leq 1$. □

Theorem 2.2 *Assume $R_0 > 1$.*

(i) The immune-free infection equilibrium E_1 is globally asymptotically stable if $R_1^W \leq 1$ and $R_1^Z \leq 1$.
(ii) The infection equilibrium with only humoral immunity E_2 is globally asymptotically stable if $R_1^W > 1$ and $R_2^Z \leq 1$.
(iii) The infection equilibrium with only cellular immunity E_3 is globally asymptotically stable if $R_1^Z > 1$ and $R_3^W \leq 1$.
(iv) The infection equilibrium with both cellular and humoral immune responses E_4 is globally asymptotically stable if $R_2^Z > 1$ and $R_3^W > 1$.

Proof For (**i**), we construct the Lyapunov functional as

$$L_1(t) = \int_\Omega \left[\frac{\epsilon_0 + \epsilon_2 V_1}{\epsilon_0 + \epsilon_{1U1} + \epsilon_2 V_1 + \epsilon_3 U_1 V_1} U_1 \Phi\left(\frac{U}{U_1}\right) + I_1 \Phi\left(\frac{I}{I_1}\right) + \frac{\gamma}{v} C_1 \Phi\left(\frac{C}{C_1}\right) \right.$$
$$\left. + \frac{q\gamma(\rho+\gamma)}{va\rho} W(x,t) + \frac{\gamma(\rho+\gamma)}{v\rho} V_1 \Phi\left(\frac{V}{V_1}\right) + \frac{p}{c} T(x,t) \right] dx.$$

Then

$$D^\alpha L_1(t) \leq \int_\Omega \left[\left(1 - \frac{F(U_1,V_1)}{F(U,V_1)}\right) \partial_t^\alpha U + \left(1 - \frac{I_1}{I}\right) \partial_t^\alpha I + \frac{\gamma}{v}\left(1 - \frac{C_1}{C}\right) \partial_t^\alpha C \right.$$
$$\left. + \frac{\gamma(\rho+\gamma)}{v\rho}\left(1 - \frac{V_1}{V}\right) \partial_t^\alpha V + \frac{q\gamma(\rho+\gamma)}{va\rho} \partial_t^\alpha W + \frac{p}{c} \partial_t^\alpha T \right] dx.$$

Since $\lambda = dU_1 + F(U_1, V_1)V_1$, we have

$$D^\alpha L_1(t) \leq -\int_\Omega \left[\frac{d\,(\epsilon_0 + \epsilon_2 V_1)\,(U - U_1)^2}{(\epsilon_0 + \epsilon_1 U_1 + \epsilon_2 V_1 + \epsilon_3 U_1 V_1)\,U} - \frac{pe}{c}\left(R_1^Z - 1\right) T \right.$$

$$- \frac{q\gamma b(\rho+\gamma)}{va\rho}\left(R_1^W - 1\right) W - F(U_1,V_1)V_1 \left(5 - \frac{F(U_1,V_1)}{F(U,V_1)}\right.$$

$$\left. - \frac{C_1 I}{C I_1} - \frac{F(U,V)}{F(U_1,V_1)} \frac{V I_1}{V_1 I} - \frac{C V_1}{C_1 V} - \frac{F(U,V_1)}{F(U,V)}\right)$$

$$\left. - \frac{F(U_1,V_1)V_1(\epsilon_0 + \epsilon_1 U)(\epsilon_2 + \epsilon_3 U)(V - V_1)^2}{(\epsilon_0 + \epsilon_1 U + \epsilon_2 V_1 + \epsilon_3 U V_1)(\epsilon_0 + \epsilon_1 U + \epsilon_2 V + \epsilon_3 U V) V_1} \right] dx$$

$$- \frac{d_C F(U_1,V_1) V_1}{v I_1} C_1 \int_\Omega \frac{\|\nabla C\|^2}{C^2} dx - \frac{d_V F(U_1,V_1) V_1}{\rho C_1} V_1 \int_\Omega \frac{\|\nabla V\|^2}{V^2} dx.$$

Since

$$5-\frac{F(U_i,V_i)}{F(U,V_i)}-\frac{C_iI}{CI_i}-\frac{F(U,V)}{F(U_i,V_i)}\frac{VI_i}{V_iI}-\frac{CV_i}{C_iV}-\frac{F(U,V_i)}{F(U,V)}\leq 0,\ \text{for } i\in\{1,2,3,4\} \tag{12}$$

we have, $D^\alpha L_1(t)\leq 0$ if $R_1^Z\leq 1$ and $R_1^W\leq 1$. Also, the largest compact invariant set in $\{(U,I,C,V,W,T)\mid D^\alpha L_1(t)=0\}$ is $\{E_1\}$. Therefore, it follows from LaSalle's invariance principle that E_1 is globally asymptotically stable when $R_1^Z\leq 1$ and $R_1^W\leq 1$.

For (**ii**), we consider the following Lyapunov functional

$$\begin{aligned}L_2(t)=\int_\Omega\Bigg[&\frac{\epsilon_0+\epsilon_2V_2}{\epsilon_0+\epsilon_1U_2+\epsilon_2V_2+\epsilon_3U_2V_2}U_2\Phi\left(\frac{U}{U_2}\right)+I_2\Phi\left(\frac{I}{I_2}\right)\\&+\frac{\gamma}{v}C_2\Phi\left(\frac{C}{C_2}\right)+\frac{\gamma(\rho+\gamma)}{v\rho}V_2\Phi\left(\frac{V}{V_2}\right)\\&+\frac{q\gamma(\rho+\gamma)}{va\rho}W_2\Phi\left(\frac{W}{W_2}\right)+\frac{p}{c}T\Bigg]dx.\end{aligned}$$

Then

$$\begin{aligned}D^\alpha L_2(t)\leq\int_\Omega\Bigg[&\left(1-\frac{F(U_2,V_2)}{F(U,V_2)}\right)\partial_t^\alpha U+\left(1-\frac{I_2}{I}\right)\partial_t^\alpha I+\frac{\gamma}{v}\left(1-\frac{C_2}{C}\right)\partial_t^\alpha C\\&+\frac{\gamma(\rho+\gamma)}{v\rho}\left(1-\frac{V_2}{V}\right)\partial_t^\alpha V+\frac{q\gamma(\rho+\gamma)}{va\rho}\left(1-\frac{W_2}{W}\right)\partial_t^\alpha W\\&+\frac{p}{c}\partial_t^\alpha T\Bigg]dx.\end{aligned}$$

By using $\lambda=dU_2+F(U_2,V_2)V_2$, we get

$$\begin{aligned}&D^\alpha L_2(t)\\\leq&-\int_\Omega\Bigg[\frac{d\,(\epsilon_0+\epsilon_2V_2)\,(U-U_2)^2}{(\epsilon_0+\epsilon_1H_2+\epsilon_2V_2+\epsilon_3H_2V_2)\,H_2}-\frac{pc}{e}\left(R_2^Z-1\right)\\&-F(U_2,V_2)V_2\left(5-\frac{F(U_2,V_2)}{F(U,V_2)}-\frac{C_2I}{CI_2}-\frac{F(U,V)}{F(U_2,V_2)}\frac{VI_2}{V_2I}-\frac{CV_2}{C_2V}-\frac{F(U,V_2)}{F(U,V)}\right)\\&+\frac{F(U_2,V_2)V_2(\epsilon_0+\epsilon_2U)(\epsilon_2+\epsilon_3U)(V-V_2)^2}{(\epsilon_0+\epsilon_1U+\epsilon_2V_2+\epsilon_3UV_2)(\epsilon_0+\epsilon_1U+\epsilon_2V+\epsilon_3UV)V_2}\Bigg]dx\\&-\frac{d_CF(U_2,V_2)V_2}{vI_2}C_2\int_\Omega\frac{\|\nabla C\|^2}{C^2}dx-\frac{d_VF(U_2,V_2)V_2}{\rho C_2}V_2\int_\Omega\frac{\|\nabla V\|^2}{V^2}dx.\end{aligned}$$

According to (12) and $R_2^Z \leq 1$, we deduce that $D^\alpha L_2(t) \leq 0$. Also that $D^\alpha L_2(t) = 0$ holds if and only if $U = U_2,\ I = I_2,\ C = C_2, V = V_2$, and $W = W_2$. So, the largest compact invariant set in $\{(U, I, C, V, W, T) \mid D^\alpha L_2(t) = 0\}$ is $\{E_2\}$. Hence, E_2 is globally asymptotically stable when $R_1^W > 1$ and $R_2^Z \leq 1$.

For (**iii**), we consider the following Lyapunov functional

$$\begin{aligned} L_3(t) = & \frac{\epsilon_0 + \epsilon_2 V_3}{\epsilon_0 + \epsilon_1 U_3 + \epsilon_2 V_3 + \epsilon_3 U_3 V_3} U_3 \Phi\left(\frac{U}{U_3}\right) + I_3 \Phi\left(\frac{I}{I_3}\right) \\ & + \frac{(\gamma + pT_3)}{v} C_3 \Phi\left(\frac{C}{C_3}\right) + \frac{(\gamma + pT_3)(\rho + \gamma)}{v\rho} V_3 \Phi\left(\frac{V}{V_3}\right) \\ & + \frac{q(\rho + \gamma)(\gamma + pT_3)}{va\rho} W + \frac{p}{c} T_3 \Phi\left(\frac{T}{T_3}\right). \end{aligned}$$

Then

$$\begin{aligned} D^\alpha L_3(t) \leq & \int_\Omega \left[\left(1 - \frac{F(U_3, V_3)}{F(U, V_3)}\right) \partial_t^\alpha U + \left(1 - \frac{I_3}{I}\right) \partial_t^\alpha I + \frac{(\gamma + pT_3)}{v} \left(1 - \frac{C_3}{C}\right) \partial_t^\alpha C \right. \\ & + \frac{(\gamma + pT_3)(\rho + \gamma)}{v\rho} \left(1 - \frac{V_3}{V}\right) \partial_t^\alpha V + \frac{q(\rho + \gamma)(\gamma + pT_3)}{va\rho} \partial_t^\alpha W \\ & \left. + \frac{p}{c} \left(1 - \frac{T_3}{T}\right) \partial_t^\alpha T \right] dx. \end{aligned}$$

By applying the equality $\lambda = dU_3 + F(U_3, V_3)V_3$, we obtain

$$\begin{aligned} D^\alpha L_3(t) \leq & -\int_\Omega \left[\frac{d(\epsilon_0 + \epsilon_2 V_2)(U - U_3)^2}{(\epsilon_0 + \epsilon_1 U_3 + \epsilon_2 V_3 + \epsilon_3 U_3 V_3) U_3} - \frac{q(\rho + \gamma)(\gamma + pT_3)}{va\rho} \left(R_3^W - 1\right) W \right. \\ & - F(U_3, V_3) V_3 \left(5 - \frac{F(U_3, V_3)}{F(U, V_3)} - \frac{C_3 I}{C I_3} - \frac{F(U, V)}{F(U_3, V_3)} \frac{V I_3}{V_3 I} - \frac{C V_3}{C_3 V} - \frac{F(U, V_3)}{F(U, V)}\right) \\ & \left. + \frac{F(U_3, V_3) V_3 (\epsilon_0 + \epsilon_2 U)(\epsilon_2 + \epsilon_3 U)(V - V_3)^2}{(\epsilon_0 + \epsilon_1 U_3 + \epsilon_2 V_3 + \epsilon_3 U_3 V_3)(\epsilon_0 + \epsilon_1 U + \epsilon_2 V + \epsilon_3 U V) V_3} \right] dx \\ & - \frac{d_C F(U_3, V_3) V_3}{v I_3} C_3 \int_\Omega \frac{\|\nabla C\|^2}{C^2} dx - \frac{d_V F(U_3, V_3) V_3}{\rho C_3} V_3 \int_\Omega \frac{\|\nabla V\|^2}{V^2} dx. \end{aligned}$$

Hence, $D^\alpha L_3(t) \leq 0$ with equality holds if and only if $U = U_3$, $I = I_3$, $C = C_3$, $V = V_3$, $W = W_3$, and $T = 0$. Therefore, E_3 is globally asymptotically stable if $R_1^Z > 1$ and $R_3^W \leq 1$.

Finally, we prove (**iv**) by considering the following Lyapunov functional

$$\begin{aligned} L_4(t) = & \int_\Omega \left[\frac{\epsilon_0 + \epsilon_2 V_4}{\epsilon_0 + \epsilon_1 U_4 + \epsilon_2 V_4 + \epsilon_3 U_4 V_4} U_4 \Phi\left(\frac{U}{U_4}\right) + I_4 \Phi\left(\frac{I}{I_4}\right) \right. \\ & \left. + \frac{(\gamma + pT_4)}{v} C_4 \Phi\left(\frac{C}{C_4}\right) + \frac{(\rho + \gamma)(\gamma + pZ_4)}{v\rho} V_4 \Phi\left(\frac{V}{V_4}\right) \right. \end{aligned}$$

$$+\frac{q(\rho+\gamma)(\gamma+pT_4)}{va\rho}W_4\Phi\left(\frac{W}{W_4}\right)+\frac{p}{c}T_4\Phi\left(\frac{T}{T_4}\right)\Bigg]dx.$$

Similarly to above, we get

$$\begin{aligned}D^\alpha L_4(t) \le &-\int_\Omega\Bigg[\frac{d(\epsilon_0+\epsilon_2V_4)(U-U_4)^2}{(\alpha\epsilon_0+\epsilon_1U_4+\epsilon_2V_4+\epsilon_3U_4V_4)U_4}\\ &-F(U_4,V_4)V_4\left(5-\frac{F(U_4,V_4)}{F(U,V_4)}-\frac{C_4I}{CI_4}-\frac{F(U,V)}{F(U_4,V_4)}\frac{VI_4}{V_4I}-\frac{CV_4}{C_4V}-\frac{F(U,V_4)}{F(U,V)}\right)\\ &+\frac{F(U_4,V_4)V_4(\epsilon_0+\epsilon_2U)(\epsilon_2+\epsilon_3U)(V-V_4)^2}{(\epsilon_0+\epsilon_1U+\epsilon_2V_4+\epsilon_3UV_4)(\epsilon_0+\epsilon_1U+\epsilon_2V+\epsilon_3UV)V_4}\Bigg]dx\\ &-\frac{d_CF(U_4,V_4)V_4}{vI_3}C_4\int_\Omega\frac{\|\nabla C\|^2}{C^2}dx-\frac{d_VF(U_4,V_4)V_4}{\rho C_4}V_4\int_\Omega\frac{\|\nabla V\|^2}{V^2}dx.\end{aligned}$$

Thus, $D^\alpha L_4(t) \le 0$ with equality holds if and only if $U = U_4$, $I = I_4$, $C = C_4$, $V = V_4$, $W = W_4$ and $T = T_4$. This implies that the largest compact invariant set in $\{(U, I, C, V, W, T) \mid D^\alpha L_2(t) = 0\}$ is $\{E_4\}$. Thus, E_4 is globally asymptotically stable. This completes the proof. □

3 Numerical Simulations

In this section, we carry out numerical simulations to confirm the above analytical results.

Let Δt be the time step size, $\Omega = [x_{\min}, x_{\max}]$ and $\Delta x = (x_{\max} - x_{\min})/N$ be the space step size with N is a positive integer. The grid points for the space are $x_i = x_{\min} + i\Delta x$ for $i \in \{0, \ldots, N\}$ and for time are $t_m = m\Delta t$ for $m \in \mathbb{N}$. Based on Grünwald-Letnikov method [18] which recently used in [19], the Caputo fractional derivative can be approximated by

$${}^C\partial_t^\alpha l(x_i, t_m) \approx \frac{1}{\Delta t^\alpha}\sum_{j=0}^{m}\beta_j^\alpha l\left(x_i, t_{m-j}\right) - \tilde{l}_m, \tag{13}$$

where $\tilde{l}_m = \frac{l(x_i,0)t_m^{-\alpha}}{\Gamma(1-\alpha)}$ and β_j^α are the fractional binomial coefficients $\binom{\alpha}{j}$ with the recursion formula

$$\beta_j^\alpha = \left(1-\frac{1+\alpha}{j}\right)\beta_{j-1}^\alpha, \quad \beta_0^\alpha = 1.$$

For simplicity, we denote the approximations of (U, I, C, V, W, T) solution of system (1) at the discretized point (x_i, t_m) by $(U_i^m, I_i^m, C_i^m, V_i^m, W_i^m, T_i^m)$. By applying (13), we find

$$\frac{1}{\Delta t^{\alpha}}\left(U_i^{m+1}+\sum_{j=1}^{m+1}\beta_j^{\alpha}U_i^{m+1-j}\right)-\tilde{U}_i^{m+1}=\lambda-dU_i^m-F(U_i^m,V_i^m)V_i^m,$$

$$\frac{1}{\Delta t^{\alpha}}\left(I_i^{m+1}+\sum_{j=1}^{m+1}\beta_j^{\alpha}I_i^{m+1-j}\right)-\tilde{I}_i^{m+1}=F(U_i^m,V_i^m)V_i^m-\gamma I_i^m-pI_i^mT_i^m,$$

$$\frac{1}{\Delta t^{\alpha}}\left(C_i^{m+1}+\sum_{j=1}^{m+1}\beta_j^{\alpha}C_i^{m+1-j}\right)-\tilde{C}_i^{m+1}=d_C\frac{C_{i+1}^m-2C_i^m+C_{i-1}^m}{\Delta x^2}+vI_i^m-(\rho+\gamma)C_i^m,$$

$$\frac{1}{\Delta t^{\alpha}}\left(V_i^{m+1}+\sum_{j=1}^{m+1}\beta_j^{\alpha}V_i^{m+1-j}\right)-\tilde{V}_i^{m+1}=d_V\frac{V_{i+1}^m-2V_i^m+V_{i-1}^m}{\Delta x^2}+\rho C_i^m-\mu V_i^m-qV_i^mW_i^m,$$

$$\frac{1}{\Delta t^{\alpha}}\left(W_i^{m+1}+\sum_{j=1}^{m+1}\beta_j^{\alpha}W_i^{m+1-j}\right)-\tilde{W}_i^{m+1}=aV_i^mW_i^m-bW_i^m,$$

$$\frac{1}{\Delta t^{\alpha}}\left(T_i^{m+1}+\sum_{j=1}^{m+1}\beta_j^{\alpha}T_i^{m+1-j}\right)-\tilde{T}_i^{m+1}=cI_i^mT_i^m-eT_i^m.$$

Thus,

$$U_i^{m+1}=-\beta_j^{\alpha}U_i^{m+1-j}+\Delta t^{\alpha}\left[\tilde{U}_i^{m+1}+\lambda-dU_i^m-F(U_i^m,V_i^m)V_i^m\right],$$

$$I_i^{m+1}=-\sum_{j=1}^{m+1}\beta_j^{\alpha}I_i^{m+1-j}+\Delta t^{\alpha}\left[\tilde{I}_i^{m+1}+F(U_i^m,V_i^m)V_i^m-\gamma I_i^m-pI_i^mT_i^m\right],$$

$$C_i^{m+1}=-\sum_{j=1}^{m+1}\beta_j^{\alpha}C_i^{m+1-j}+\Delta t^{\alpha}\left[\tilde{C}_i^{m+1}+d_C\frac{C_{i+1}^m-2C_i^m+C_{i-1}^m}{\Delta x^2}+vI_i^m-(\rho+\gamma)C_i^m\right],$$

$$V_i^{m+1}=-\sum_{j=1}^{m+1}\beta_j^{\alpha}V_i^{m+1-j}+\Delta t^{\alpha}\left[\tilde{V}_i^{m+1}+d_V\frac{V_{i+1}^m-2V_i^m+V_{i-1}^m}{\Delta x^2}+\rho C_i^m-\mu V_i^m-qV_i^mW_i^m\right],$$

$$T_i^{m+1}=-\sum_{j=1}^{m+1}\beta_j^{\alpha}T_i^{m+1-j}+\Delta t^{\alpha}\left[\tilde{T}_i^{m+1}+cI_i^mT_i^m-eT_i^m\right].$$

For numerical illustrations, we take in the whole section $\Omega=[0,4]$ and $d_C=d_V=0.1$. The initial conditions used are $H(x,0)=40{,}000$, $I(x,0)=500$, $C(x,0)=300$, $V(x,0)=50$, $W(x,0)=30$, and $T(x,0)=20$.

Firstly, we take $\lambda=5.04\times10^5$, $d=0.0039$, $k=10^{-6}$, $\gamma=0.0693$, $p=0.00064$, $v=150$, $\rho=0.2$, $\mu=0.67$, $q=10^{-5}$, $b=0.7$, $c=10^{-2}$, $a=10^{-5}$, $e=0.5$, $\alpha=0.8$, $\epsilon_0=0.1$, $\epsilon_1=1$, $\epsilon_2=0.1$, and $\epsilon_3=0.00001$. In this case, $R_0=0.0240<1$. According to Theorem 2.1, the infection-free equilibrium

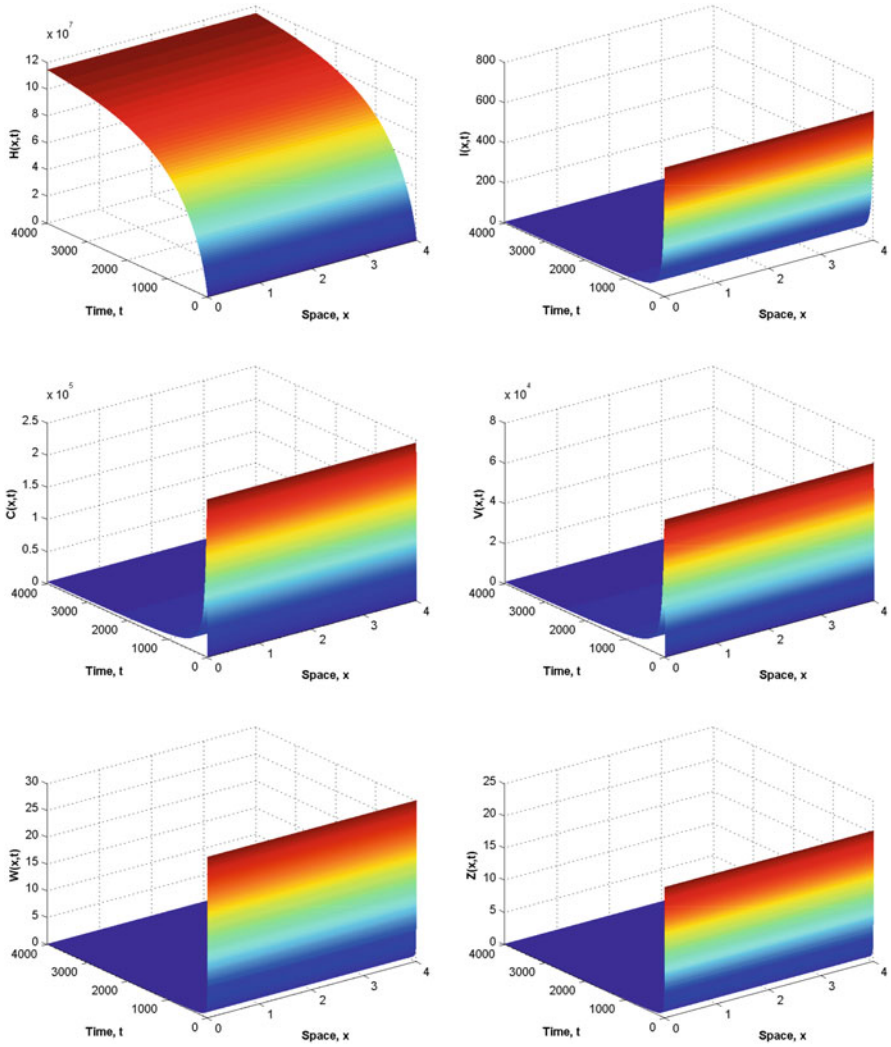

Fig. 1 Stability of the infection-free equilibrium E_0

$E_0(1.292 \times 10^8, 0, 0, 0, 0, 0)$ is globally asymptotically stable. Figure 1 confirms this result.

Next, we take $k = 10^{-3}$, $a = 10^{-7}$, $c = 10^{-5}$ and do not change the other values. By a simple computation, we have $R_0 = 2.3993 > 1$, $R_1^W = 0.1997$, and $R_1^z = 0.1682$. It follows that case (i) of Theorem 2.2 that $E_1(1.2908 \times 10^8, 8.4091 \times 10^3, 4.6839 \times 10^6, 1.3982 \times 10^6, 0, 0)$ is globally asymptotically stable. Figure 2 demonstrates this result.

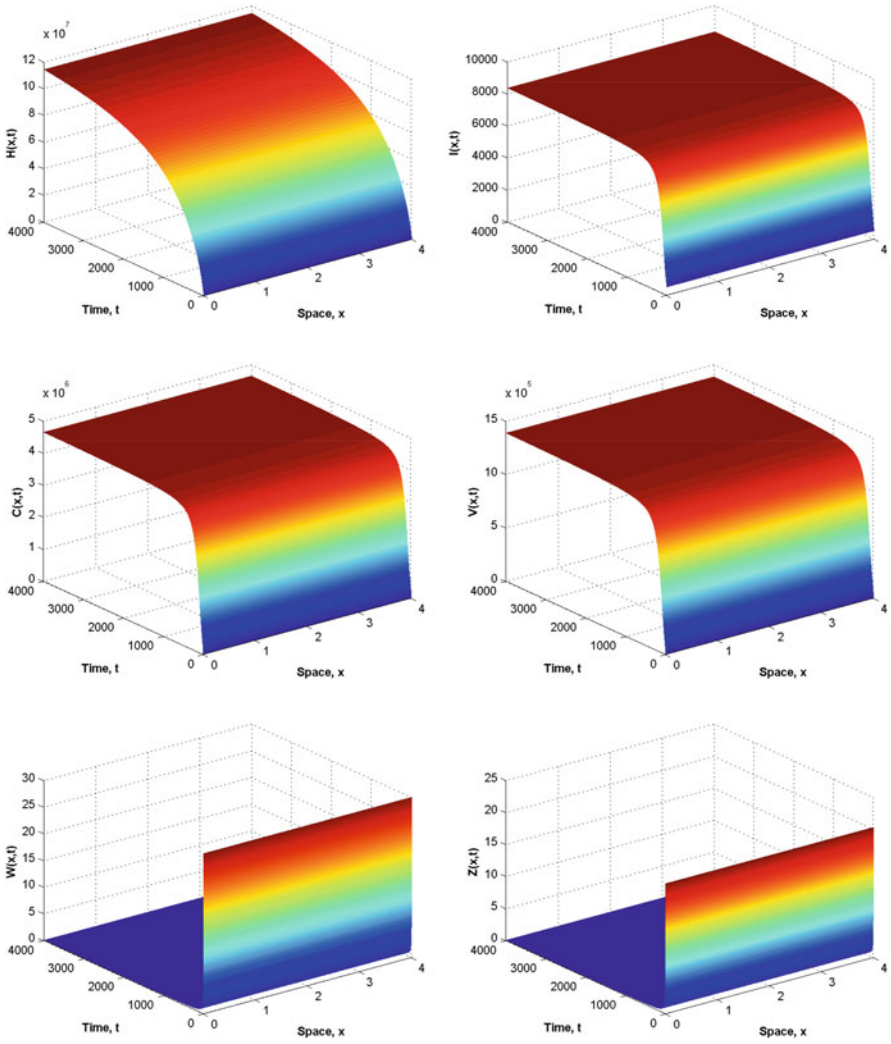

Fig. 2 Stability of the immune-free equilibrium E_1

For the case in which $k = 10^{-3}$, $a = 10^{-5}$, $c = 10^{-5}$, we obtain $R_0 = 2.3993 > 1$, $R_1^W = 1.9974$, and $R_2^z = 0.9178$. From (ii) of Theorem 2.2, $E_2(1.2908 \times 10^8, 4.5891 \times 10^4, 2.5562 \times 10^7, 7 \times 10^5, 6.6333 \times 10^5, 0)$ is globally asymptotically stable (see, Fig. 3).

For the case in which $k = 10^{-3}$, $a = 10^{-6}$, $c = 10^{-3}$, we obtain $R_0 = 2.3993 > 1$, $R_1^Z = 16.8183$, and $R_3^W = 0.1188$. By (iii) of Theorem 2.2, $E_3(1.2221 \times 10^8, 500, 2.7850 \times 10^5, 8313 \times 10^4, 0, 131.8464)$ is globally asymptotically stable (see, Fig. 4).

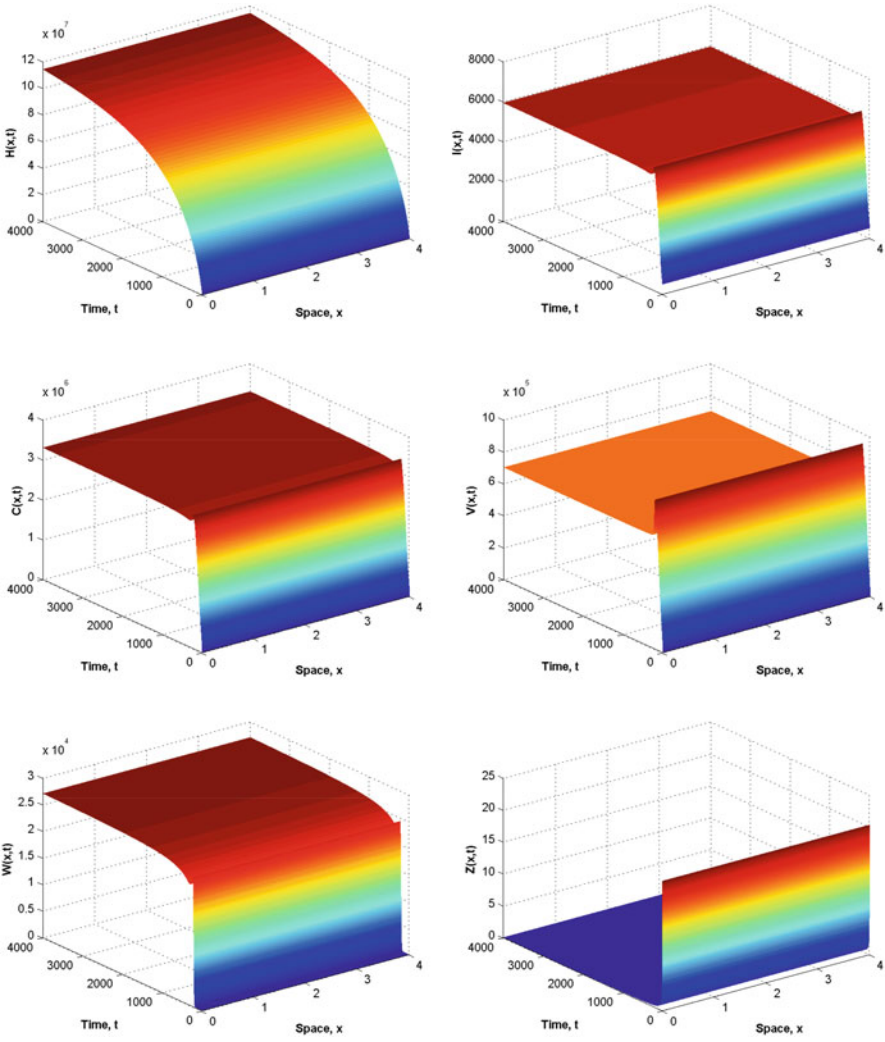

Fig. 3 Stability of the infection equilibrium with only humoral immunity E_2

For the case in which $k = 10^{-3}, a = 10^{-6}, c = 10^{-4}$, we obtain $R_0 = 2.3993 > 1$, $R_2^Z = 9.1783$, and $R_3^W = 1.1876$. By (iv) of Theorem 2.2, we deduce that $E_4(1.2913 \times 10^8, 5000, 2.785 \times 10^6, 7 \times 10^8, 1.2571 \times 10^4, 20.3542)$ is globally asymptotically stable (see, Fig. 5).

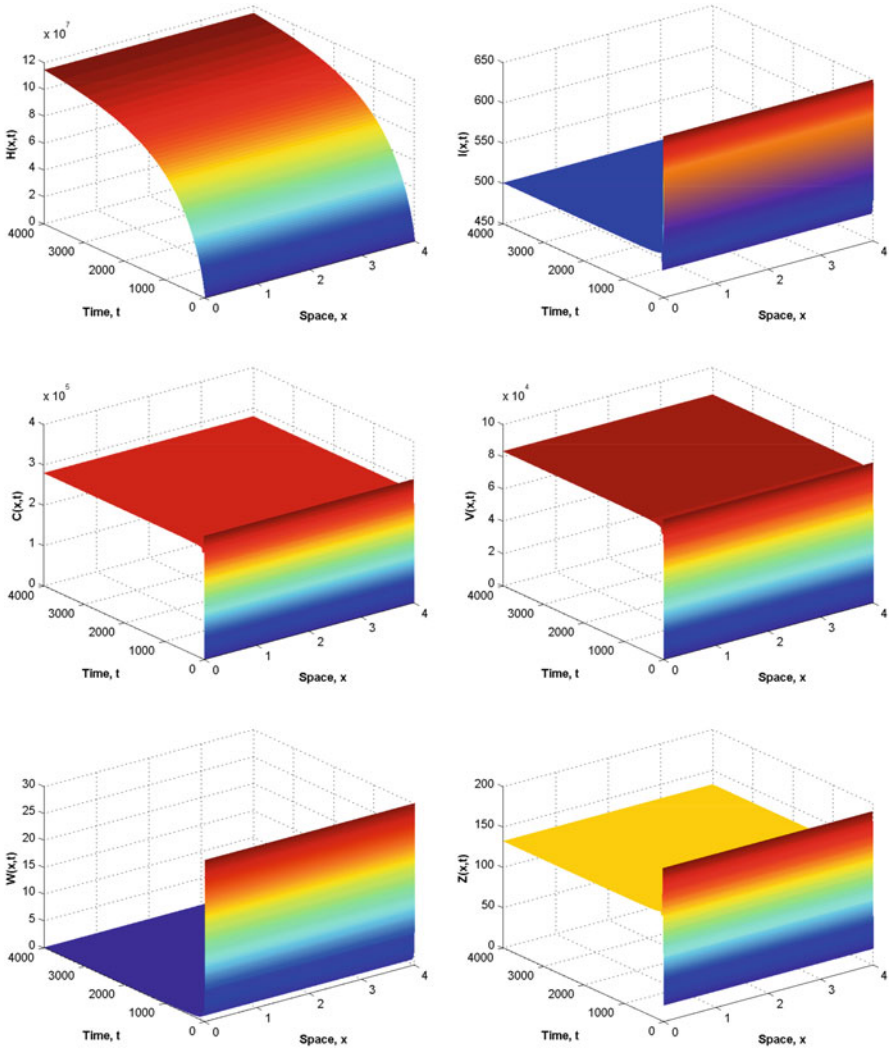

Fig. 4 Stability of the infection equilibrium with only cellular immunity E_3

4 Conclusions

In this work, we gave a rigorous mathematical analysis of a time-fractional diffusion model for HBV infection with capsids and two arms of adaptive immune responses that are the humoral and cellular immunity. We have shown that the model has five equilibrium points which are given by the infection-free equilibrium E_0, the infection equilibrium E_1, the infection equilibrium with only humoral immunity E_2, The infection equilibrium with only cellular immunity E_3, and the infection

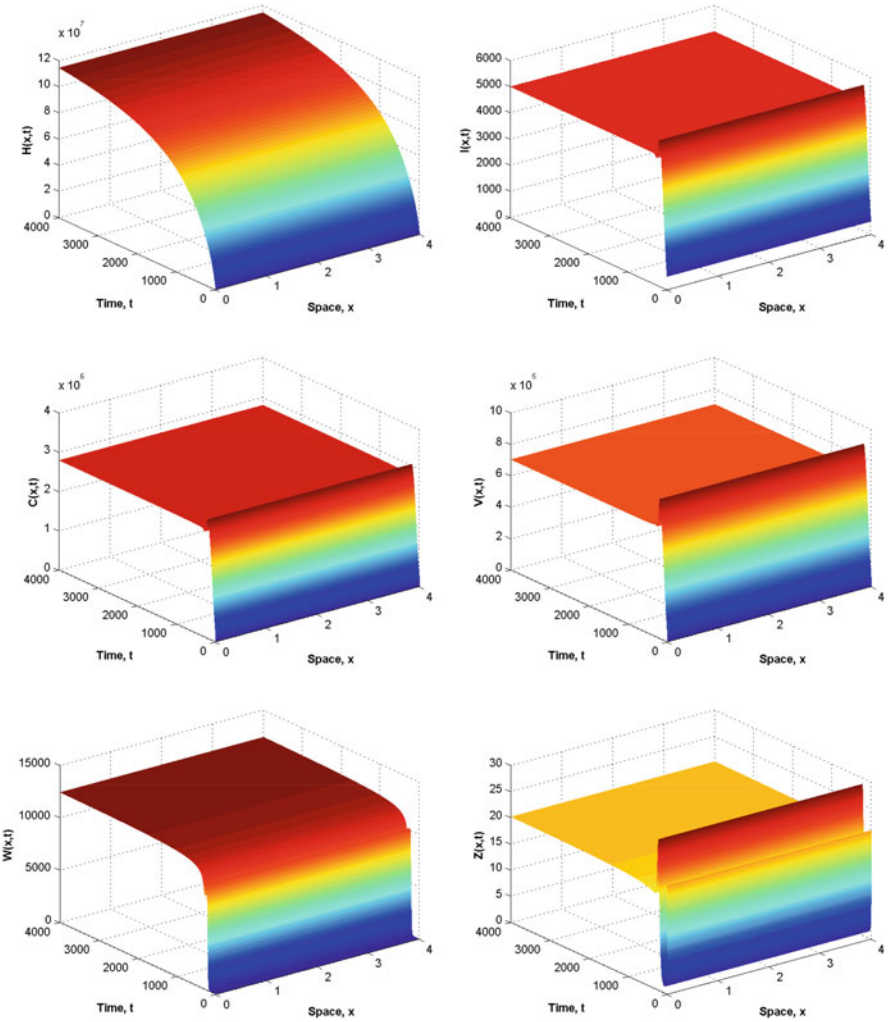

Fig. 5 Stability of the infection equilibrium with both cellular and humoral immune responses E_4

equilibrium with both cellular and humoral immune responses E_4. The global stability of the five infection equilibria is determined by five threshold parameters, which are the reproduction number R_0, the reproduction numbers for humoral immunity R_1^W, for cellular immunity R_1^Z, for cellular immunity in competition R_2^Z, and for humoral immunity in competition R_3^W. More concretely, the infection-free equilibrium E_0 is globally asymptotically stable if the basic infection reproduction number $R_0 \leq 1$, which biologically means that the HBV is cleared and the infection dies out. When $R_1^W \leq 1$ and $R_1^Z \leq 1$, the infection equilibrium E_1 is globally

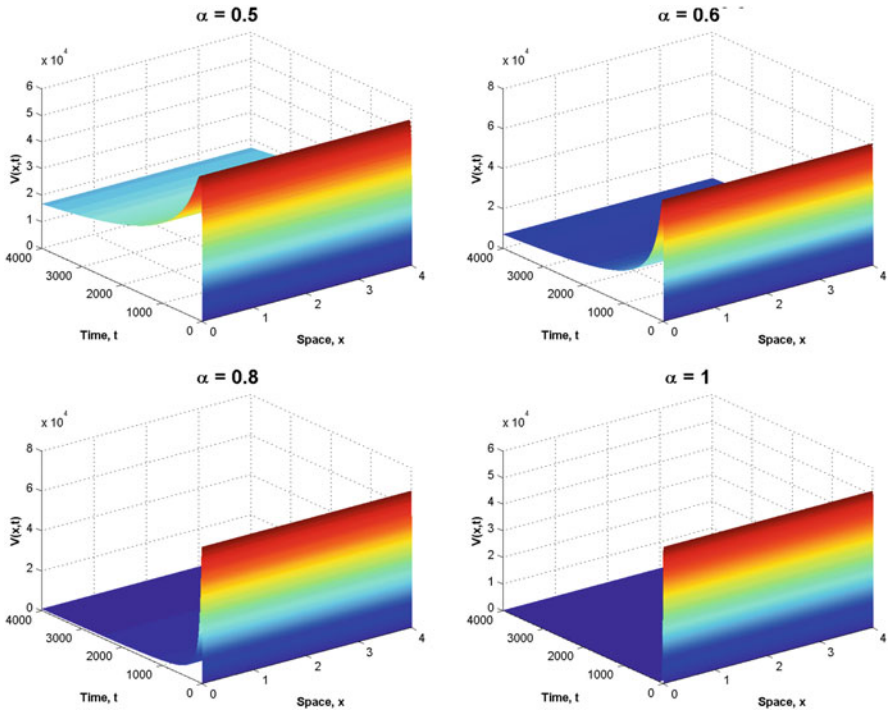

Fig. 6 The state variable $V(x,t)$ with different values of α

asymptotically stable. For $R_1^W > 1$ and $R_2^Z \leq 1$, the infection equilibrium with only humoral immunity E_2 is globally asymptotically stable. The infection equilibrium with only cellular immunity E_3 is globally asymptotically stable if $R_1^Z > 1$ and $R_3^W \leq 1$. Finally, when $R_2^Z > 1$ and $R_3^W > 1$, the infection equilibrium with both cellular and humoral immune responses E_4 is globally asymptotically stable. These findings demonstrate that HBV persists in the liver despite the activation of one or both arms of immunity.

From our analytical and numerical results, we conclude that the order α of the fractional derivative has no effect on the stability of the five equilibria, but it can affect the time for arriving to these equilibria and reduces the oscillations. For example, when α increases which describes the long memory, the solutions of the model converge rapidly to the steady states (Fig. 6). Additionally, the activation of one or both arms adaptive immunity is unable to eradicate the HBV from the liver. However, it plays a significant role in reducing viral load, increasing healthy hepatocytes and decreasing infected hepatocytes.

References

1. K. Manna, Dynamics of a delayed diffusive HBV infection model with capsids and CTL immune response, Int. J. Appl. Comput. Math 4 (5) (2018) 116.
2. K. Manna, Global properties of a HBV infection model with HBV DNA-containing capsids and CTL immune response, Int. J. Appl. Comput. Math. 3 (2017) 2323–2338.
3. J. Xu and Y. Geng, Dynamic consistent NSFD scheme for a delayed viral infection model with immune response and nonlinear incidence, Discrete Dyn. Nat. Soc. 2017 (2017) 1–12.
4. M. Bachraoui, K. Hattaf and N. Yousfi, Dynamics of a fractional order HBV infection model with capsids and CTL immune response, Communications in Mathematical Biology and Neuroscience 6 (2019) 1–15.
5. K. Manna and S. P. Chakrabarty, Chronic hepatitis B infection and HBV DNA-containing capsids: Modeling and analysis, Communications in Nonlinear Science and Numerical Simulation 22 (2015) 383–395.
6. X. Zhou and Q. Sun, Stability analysis of a fractional-order HBV infection model, Int. J. Adv. Appl. Math. and Mech. 2 (2014) 1–6.
7. S. M. Salman and A. M. Yousef, On a fractional-order model for HBV infection with cure of infected cells, Journal of the Egyptian Mathematical Society 25 (2017) 445–451.
8. L. C. Cardoso, F. L. P. Dos Santos and R. F. Camargo, Analysis of fractional-order models for hepatitis B, Computational and Applied Mathematics 37 (6) (2018) 4570–4586.
9. K. Hattaf and N. Yousfi, A class of delayed viral infection models with general incidence rate and adaptive immune response, Int. J. Dynam. Control 4 (2016) 254–265.
10. J. R. Beddington, Mutual interference between parasites or predators and its effect on searching efficiency, Journal of Animal Ecology 44 (1975) 331–340.
11. D. L. DeAngelis, A. H. Goldstein, and R.V. O'Neill, A model for trophic interaction, Ecology 56 (1975) 881–892.
12. K. Manna and K. Hattaf, Spatiotemporal dynamics of a generalized HBV infection model with capsids and adaptive immunity, Int J Appl Comput Math. (2019) 5:65. https://doi.org/10.1007/s40819-019-0651-x
13. T. Guo, H. Liu, C. Xu and F. Yan, Global stability of a diffusive and delayed HBV infection model with HBVDNA-containing capsids and general incidence rate, Discrete Contin. Dyn. Syst. B 23 (2018) 4223–4242.
14. Y. Geng, J. Xu and J. Hou, Discretization and dynamic consistency of a delayed and diffusive viral infection model, Appl. Math. Comput. 316 (2018) 282–295.
15. K. Hattaf, M. Khabouze and N. Yousfi, Dynamics of a generalized viral infection model with adaptive immune response, Int. J. Dynam. Control 3 (2015) 253–261.
16. C. V. De-Leon, Volterra-type Lyapunov functions for fractional-order epidemic systems, Communications in Nonlinear Science and Numerical Simulation 24 (2015) 75–85.
17. J. Huo, H. Zhao and L. Zhu, The effect of vaccines on backward bifurcation in a fractional order HIV model, Nonlinear Analysis: Real World Applications 26 (2015) 289–305.
18. I. Petrs, Fractional derivatives, fractional integrals, fractional differential equations in Matlab, In Engineering Education and Research Using MATLAB, InTech, 2011.
19. S. Samuel and V. Gill, Time-fractional diffusion model on dynamical effect of dendritic cells on HIV pathogenesis, Journal of Computational Methods in Sciences and Engineering 18 (1) (2018) 1–20.

A 3D Fractional Step Computational Modeling of Nerve Impulse Transmission Through an Axonal Membrane: Incorporating Calcium Buffer and Extrusion

H. Lefraich

1 Introduction and Motivation

Neurodegenerative disorders are diseases which are associated with the death of certain parts of the brain. They are some of the toughest illnesses to heal with excessive outcomes. Parkinson's and Huntington's diseases are among the most severe and the most widespread disorders. Despite the fact that a lot of information has been found about the reason why these diseases occur, neurodegenerative disorders are still complex and much remain to be revealed. The brain is an extremely complex organ which is made of billions of cells that ensure its proper functioning. Some of the most important cells in the brain are called neurons. Neurons communicate with each other to achieve every function of the brain including the muscles control. A very small miscommunication between neurons can cause a neurodegenerative illness.

A neuron is among the most important and interesting cells in the human body. The fundamental function of neurons consists in receiving, conducting, and transmitting chemical and electrical signals. Indeed, neurons can carry signals from the sensory organs inward to the central nervous system, which consists of the brain and spinal cord. In the central nervous system, these signals are analyzed and interpreted by a system of neurons, which then create a response. The response is sent, again by neurons, to muscle cells and glands. A typical neuron can be divided into four functionally distinct parts: cell body, or soma, which contains the nucleus and other organelles; branches of dendrites, which receive signals from other neurons; an axon, which is the long, slim nerve fiber that conducts signals away from the cell body and transmits them to other neurons; and many branches

H. Lefraich (✉)
Laboratory (MISI), Faculty of Sciences and Techniques, Department of Mathematics and Computer Science, University Hassan First, Settat, Morocco

R. P. Mondaini (ed.), *Trends in Biomathematics: Chaos and Control in Epidemics, Ecosystems, and Cells*, https://doi.org/10.1007/978-3-030-73241-7_20

at the far end of the axon, known as nerve terminals or presynaptic terminals. The junction between two neurons is called a synapse and consequently, if a neuron sends a signal across a synapse it is common to refer to the sending neuron as the presynaptic neuron and to the receiving neuron as the postsynaptic neuron. The axon is the essential signaling pathway from one neuron to another. This signaling is ensured by brief voltage pulses called action potentials (AP) which are initiated near the cell body and travel along the axon in order to reach the many presynaptic boutons. The axon makes use of the ionic concentration gradients across their membranes as a driving force for the ionic currents that generate the action potential.

Discerning the computational properties of single neurons is decisive for understanding their contribution to normal brain function and its breakdown during different pathologies. For anatomical reasons, the geometry of axons resembles that of an electric cable. Lord Kelvin[1–3], working on submarine cables, was the first to develop the theory of current flow in electric cables. This theory was first used in work related to neurons by Weber[4, 5], Cremer[6, 7], and Hermann[8–10]. Hermann suggested that current flow of the kind described by cable theory may be helpful to maintain nerve impulse propagation. After that, the theory has been often used in the study of nerve and muscle. The theory has had full success when applied to the mechanism of impulse transmission. In fact, the applications have grown rapidly in 1930s and 1940s (see Rashevsky[11]; Rushton[12, 13]; Monnier[14]; Cole and Curtis[15–17]; Rosenberg[18, 19]; Hodgkin[20]; Cole and Hodgkin[21]; Katz[22]; Offner, weinberg, and Young[23]; Weinberg[24]; Hodgkin and Rushton[25]; Lorente de No[26]). Although, the generation and propagation of signals have been extensively studied for the past century by physiologist; the most valuable work in these studies is that of Alan Hodgkin and Andrew Huxley. They established the first successful electrophysiological quantitative model of the propagation of an electrical signal along a squid giant axon and revealed the key properties of the ionic currents that underlie the nerve action potential. Their model describes the conduction of action potentials in axons by a nonlinear excitable cable (Hodgkin and Huxley[27]), moreover, the integration of postsynaptic signals in dendrites has been studied with analytical solutions to passive cables (Rall[28]).

Their work besides the experimental developments keeps inspiring other Hodgkin–Huxley type ionic models which have been created since then. In fact, many researchers have used the cable model to check the possibility of improving it to take account of more complex signal processing in dendrites with complex morphologies, multiple synaptic inputs, and passive or excitable membranes (Shepherd et al.[29]; Perkel and Perkel[30]; Wathey et al.[31]). These traditional mathematical models of electrical activity, which are based on the work of Hodgkin and Huxley, maybe collectively named cable models. The resting membrane potential is maintained by ionic concentration discrepancies across the membrane. Cable models are based upon a representation of the equilibrium potential of each ion by a battery whose electromotive force is given by the Nernst potential. Variations in the membrane permeability are modeled by variations of conductance in series with the batteries. The ionic concentrations are mostly not significantly affected by these conductance changes, so the equilibrium potentials are not affected

and consequently the potentials of the batteries can be considered fixed which may not always be a valid assumption. In fact, this is a good approximation when dealing with the squid giant axon and large neurons but may induce errors if the concentrations of some ions vary significantly, especially when the intracellular volume is relatively small, then ionic concentrations can change rapidly following a transient change in ionic conductance. This is more likely to arise in small processes and during synaptic triggering in small structures such as spines (Rall[32]; Koch and Poggio[33]). Besides, a sudden change in concentration at one area can create gradients of ionic concentration within a thin process, which transgresses another essential assumption of the cable model. That being said, it is necessary to consider the fundamental laws governing the movements of ions, as given by the Nernst–Planck equations for electro-diffusion (Jack et al.[34]).

Another motivation for meticulously treating the ionic concentrations and the diffusion of ions within neurons is the fact that many intracellular functions are regulated by concentrations of particular ions. For example, the concentration of Ca^{2+} inside presynaptic terminals has been proposed to play a pivotal role in a number of events, including neurotransmitter release [35–37]). Furthermore, the neuron's calcium concentration can change by an order of magnitude in milliseconds. Consequently, it is crucial to predict accurately the concentration changes of Ca^{2+} such as synaptic boutons and dendritic spines. Models based on the Nernst–Planck equation have been considered to model voltage-dependent concentration gradients. Previously, Qian and Sejnowski[38] applied the Nernst–Planck equation in one dimension for the modeling of excitatory postsynaptic potentials on dendritic spines, and showed in the case of large conductance changes, there are important differences between the cable and electro-diffusion models. In addition, Van Egeraat and Wikswo[39] applied a one-dimensional Nernst–Planck equation in order to study axonal propagation in injured axons over long time scales.

In this chapter we introduce an electro-diffusion model that is based on the Nernst–Planck equation. The electro-diffusion model provides a unified framework for the computation of both the membrane potentials and the intracellular ionic concentrations during synaptic activity. The Nernst-Planck equation is supplemented by a modified cable equation which rely membrane potential to ionic concentrations.

2 Materials and Methods

We model the detailed evolution of the concentrations of the most relevant ion species and the resulting electric field during the spread of an AP along an axonal membrane. To this end, the Nernst–Planck equation supplemented by a modified cable equation is solved numerically by application of the finite element method. In order to take full advantage of this framework, a numerical scheme capable of handling three-dimensional geometries and also preserving the positivity of concentrations, is required. That issue is tackled by using a fractional step method which, additionally, can take account of the multiscale aspect of the phenomenon.

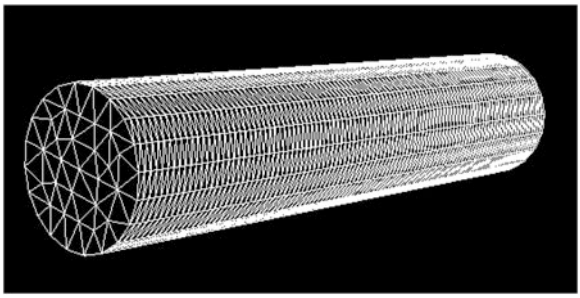

Fig. 1 Computational domain constructed. The cylinder represents an axon having a diameter of 0.05 μm. The domain is discretized with tetrahedrals

2.1 Representation of the Computational Domain

Our simulation model focuses on the axonal part of the neuron because it can capture the essential features of the latter and we can recover the functions of a neuron by representing the postsynaptic and presynaptic terminals. Let us consider a neuron which fills the bounded open set Ω of $\mathbb{R}^3$. Ω is assumed to be a cylinder with boundary $\partial\Omega$ (Fig. 1). The boundary of the domain consists of three parts $\partial\Omega = \Gamma_{post} \cup \Gamma_{lat} \cup \Gamma_{pre}$, where Γ_{post} refers to the left base of the cylinder and represents the postsynaptic terminal, Γ_{pre} refers to the right base, or end of the cylinder which represents the presynaptic terminal, and Γ_{lat} stands for the lateral boundary.

2.2 Modeling the Nernst–Planck Equation

We will derive here a system of time-dependent, coupled, nonlinear partial differential equations to describe ionic electro-diffusion in this domain. We consider a set of ion species K. Typically K will include sodium Na^+, potassium K^+, calcium Ca^{2+}, and chloride Cl^-. Calcium buffer and bound calcium will not be described explicitly in here, as it will be discussed in depth in another section. The movement of ions is supposed to be due to diffusion and also the effect of electrical field. The mass conservation equation for each ion specie $A_k \in K$ stipulate that

$$\frac{\partial C_k}{\partial t} + div(J_k) = F_k \tag{1}$$

where C_k is the concentration of species A_k, F_k denotes the production rate of A_k due to all the homogeneous reactions in which it is involved and J_k is its molar transport flux. Consequently, migration is included along with diffusion as possible modes of transport for each species. The molar flux J_k then becomes

$$J_k = -d_k \nabla C_k - m_k C_k \nabla V \tag{2}$$

where V is the electrical potential; d_k, m_k, and z_k are, respectively, the diffusion coefficient, the mobility, and the valence of the ionic specie A_k. There is a relationship between the mobility m_k and the diffusion constant d_k (see [40]), which is given by

$$m_k = \frac{d_k z_k F_a}{R T_e} \tag{3}$$

where $z_k F_a$ is the charge carried by a mole of species A_k, R is the universal gas constant, and T_e is the local temperature. The transport equation for each specie becomes

$$\frac{\partial C_k}{\partial t} - d_k \Delta C_k - m_k div(C_k \nabla V) = F_k(C_1, .., C_4) \tag{4}$$

We suppose that F_k depends continuously on the C_k 's, and obviously that d_k is a positive constant for each k.

2.3 Modeling the Modified Cable Equation

The neuron can be modeled as a capacitor related in parallel with variables resistances and batteries. The capacitance is due to the phospholipid bilayer that separates the ions on the inside and the outside of the axon. The resistances and batteries represent the different ionic currents. Consequently, in the one-dimensional cable model, the membrane potential, $V(x, t)$, at distance x and time t along an axon satisfies the equation [34]:

$$\frac{d}{4R_i}\frac{\partial^2 V}{\partial z^2} = C_m \frac{\partial V}{\partial t} + I_m + I_{stim} \tag{5}$$

where d is the diameter of the cable, R_i is the total intracellular cytoplasmic resistivity, C_m is the membrane capacitance per unit area, I_m represents the total non-capacitive membrane current density which is the summation of all non-capacitive membrane current densities for each ionic specie $I_{m,k}$ and I_{stim} is an applied external stimulation current. Assuming that the movement of ionic specie A_k across the membrane can be described by a membrane resistance of unit area $R_{m,k}$ in series with a battery whose electromotive force E_k is equal to the ionic equilibrium potential, then

$$I_{m,k} = \frac{(V - E_k)}{R_{m,k}}$$

and

$$I_m = \sum_k I_{m,k} = \frac{(V - V_{rest})}{R_m} \tag{6}$$

where the resting membrane potential, V_{rest}, and the total membrane resistance R_m, are given by

$$V_{rest} = R_m \sum_k (\frac{E_k}{R_{m,k}})$$

$$\frac{1}{R_m} = \sum_k (\frac{1}{R_{m,k}})$$

Now, if we assume that the potential change in a short segment of a process is equal to the change of the total charge in the segment divided by its membrane capacitance:

$$V(x,t) = V_{rest} + (\frac{Fd}{4C_m}) \sum_k (C_k(x,t) - C_{k,rest}) z_k \tag{7}$$

where V_{rest} is the initial potential and $C_{k,rest}$ is the initial ionic concentration of specie A_k. By substituting (6) into (5) and considering (7), we get

$$\frac{dR_m}{4R_i} \frac{\partial^2 V}{\partial z^2} = C_m R_m \frac{\partial V}{\partial t} + (\frac{Fd}{4C_m}) \sum_k (C_k(x,t) - C_{k,rest}) z_k + R_m I_{stim}$$

Analogously, the membrane potential in a 3D single neuron can be modeled as a continuous system with the following partial differential equation:

$$\lambda^2 \Delta V = \tau_m \frac{\partial V}{\partial t} + (\frac{Fd}{4C_m}) \sum_k (C_k(x,t) - C_{k,rest}) z_k + R_m I_{stim}(x,t), \tag{8}$$

where the space and time constants are defined as

$$\lambda = \sqrt{\frac{dR_m}{4R_i}}$$

$$\tau_m = R_m C_m$$

Let us mention that I_{stim} may only depend on time and space but may also depend on the electrical potential.

2.4 Calcium Buffer and Extrusion

Calcium ions play a pivotal role in the regulation of the functions of the neurons. The dynamics of the free intracellular calcium is controlled by diffusion and binding to host of different enzymes, which serves as calcium buffers and as calcium sensors. Certain proteins, such as calmodulin, change their structure when they bind to calcium and consequently activating or modulating enzymes and ionic channels. It is very important to understand the role of diffusion and chemical kinetics in controlling the cytosolic calcium. The Ca^{2+} binding can be modeled by the following chemical reaction:

$$Ca^{2+} + B \underset{K_-}{\overset{K_+}{\rightleftharpoons}} CaB$$

where B stands for a generic calcium buffer and CaB for bound calcium. K_+ and K_- are forward and backward binding rates, respectively (they are given in Table 1). The effect of buffering on the concentration of the different species is given by differential equations derived from the chemical reaction. Then, the differential equations for the buffer take the form:

$$\frac{\partial [Ca^{2+}]}{\partial t} = K_-[CaB] - K_+[Ca^{2+}][B],$$

$$\frac{\partial [B]}{\partial t} = K_-[CaB] - K_+[Ca^{2+}][B],$$

$$\frac{\partial [CaB]}{\partial t} = -K_-[CaB] + K_+[Ca^{2+}][B]$$

The total buffer concentration is given as $B_T = [B] + [CaB]$ and the rate of change of this quantity is null:

$$\frac{\partial B_T}{\partial t} = 0$$

Now we can rewrite

$$\frac{\partial [Ca^{2+}]}{\partial t} = K_-[CaB] - K_+(B_T - [CaB])[Ca^{2+}],$$

$$\frac{\partial [CaB]}{\partial t} = -K_-[CaB] + K_+(B_T - [CaB])[Ca^{2+}][B]$$

Furthermore, the basic equation of Nernst–Planck must be augmented to incorporate the physiological extrusion of calcium in the nerve cell. Consequently,

Table 1 Symbols, units, and default parameter values of the model

Symbol	Parameter	Value	Unit
F	Faraday constant	96,485	C/mol
R	Perfect Gaz constant	8.3144	J/(mol K)
T	Absolute temperature	310	K
K_+	Forward buffer rate	0.05	$\mu M^{-1}\,ms^{-1}$
K_-	backward buffer rate	0.5	ms^{-1}
P_m	Pump parameter	0.2	$\mu m\,ms^{-1}$
K_p	Dissociation constant	0.5	μM
τ_m	Electric time constant	20	ms
λ	Electric space constant	224	μm
R_m	Membrane resistivity	20	$K\Omega\,cm^2$
B_T	Total buffer concentration	100	μm

we include a simple calcium extrusion process $P(\left[Ca^{2+}\right])$ that saturates at high $\left[Ca^{2+}\right]$. That pump has the following form:

$$P(\left[Ca^{2+}\right]) = \frac{2P_m}{a}\frac{\left[Ca^{2+}\right]}{1+\frac{[Ca^{2+}]}{K_p}}$$

where K_p is the dissociation constant between the pump and calcium, $\frac{2}{a}$ is the surface area-to-volume ratio in a cylinder of radius a and P_m is the membrane pump parameter.

Incorporating the calcium buffering and its extrusion into the diffusion equation and accounting for the diffusibility of the buffer leads to

$$\begin{aligned}&\tfrac{\partial[Ca^{2+}]}{\partial t} - d_{Ca^{2+}}\Delta[Ca^{2+}] - m_{Ca^{2+}} div([Ca^{2+}]\nabla V)\\ &= -P(\left[Ca^{2+}\right]) + K_-[CaB] - K_+(B_T - [CaB])[Ca^{2+}],\end{aligned}$$

$$\begin{aligned}&\tfrac{\partial[CaB]}{\partial t} - d_{CaB}\Delta[CaB] - m_{CaB} div([CaB]\nabla V)\\ &= -K_-[CaB] + K_+(B_T - [CaB])[Ca^{2+}]\end{aligned}$$

2.5 Initial and Boundary Conditions

We assume that initial conditions are given for all ion concentrations,

$$C_k(x,0) = C_k^0(x) \quad \text{for all } x \in \Omega$$

In addition, we assume that an initial condition is given for the membrane potential:

$$V(x,0) = V_0(x) \quad \text{for all } x \in \Omega$$

Finally, we will close the system by a set of boundary conditions. At the open ends of the neuron Γ_{pre}, we impose Dirichlet conditions equal to the initial values of concentrations, which corresponds to the physical scenario of the system interacting with a large reservoir of ions.

$$C_k(x,t) = C_k^0(x) \quad \text{for all } x \in \Gamma_{pre}$$

Similarly, the voltage obeys

$$V(x,t) = 0 \quad \text{for all } x \in \Gamma_{pre}$$

The fixed concentrations and the grounded voltage on the outermost boundary provide an infinite source/sink of ions during the simulation. For the remaining part of the boundary, we opted for a sealed condition, thus there must be no flow of ions nor flux of the electric field into or out of the boundary $\Gamma_{lat} \cup \Gamma_{post}$,

$$\frac{\partial C_k}{\partial n} = 0 \quad \text{on } \Gamma_{lat} \cup \Gamma_{post},$$

$$\frac{\partial V}{\partial n} = 0 \quad \text{on } \Gamma_{lat} \cup \Gamma_{post}$$

2.6 Summary of Governing Equations

For our model we take the Calmodulin protein Ca-Cam as a calcium buffer. We denote the concentrations of the reactants by

$$C_1 = \left[Ca^{2+}\right], \quad C_2 = [Ca - Cam], \quad C_3 = \left[Na^{+}\right], \quad C_4 = \left[K^{+}\right], \; C_5 = [Cl^{-}]$$

The model is given by

$$
\begin{cases}
\dfrac{\partial C_1}{\partial t} - d_1\Delta C_1 - m_1 div(C_1\nabla V) = -P(C_1) + K_-C_2 - K_+(B_T - C_2)C_1 & \text{in }]0,T[\times\Omega \\
\dfrac{\partial C_2}{\partial t} - d_2\Delta C_2 - m_2 div(C_2\nabla V) = -K_-C_2 + K_+(B_T - C_2)C_1 & \text{in }]0,T[\times\Omega \\
\dfrac{\partial C_3}{\partial t} - d_3\Delta C_3 - m_3 div(C_3\nabla V) = 0 & \text{in }]0,T[\times\Omega \\
\dfrac{\partial C_4}{\partial t} - d_4\Delta C_4 - m_4 div(C_4\nabla V) = 0 & \text{in }]0,T[\times\Omega \\
\dfrac{\partial C_5}{\partial t} - d_5\Delta C_5 - m_5 div(C_5\nabla V) = 0 & \text{in }]0,T[\times\Omega \\
\tau_m \frac{\partial V}{\partial t} - \lambda^2\Delta V + (\frac{Fd}{4C_m})\sum_k (C_k(t,x) - C_{k,rest})z_k = -R_m I_{stim}(x,t) & \text{in }]0,T[\times\Omega \\
\dfrac{\partial C_k}{\partial n} = 0, & \text{in }]0,T[\times(\Gamma_{lat}\cup\Gamma_{post}), \quad \text{for } k = 1,2,..,5. \\
\dfrac{\partial V}{\partial n} = 0, & \text{in }]0,T[\times(\Gamma_{lat}\cup\Gamma_{post}), \quad \text{for } k = 1,2,..,5. \\
C_k(t,x) = C_k^0 & \text{in }]0,T[\times\Gamma_{pre} \\
V(t,x) = 0 & \text{in }]0,T[\times\Gamma_{pre} \\
C_k(0,x) = C_k^0 & \text{in } \Omega, \text{ for } k = 1,2,..,5. \\
V(0,x) = V_0(x) & \text{in } \Omega
\end{cases}
$$

where $T > 0$. We suppose that:

$$\text{for all } k = 1,\ldots,5 \quad C_k^0 \in L^2(\Omega) \text{ and satisfy } C_k^0 \geq 0\ .$$

2.7 Variational Formulation of the Problem

Let's consider the functional space W defined as follows:

$$W = \left\{\phi \in H^1(\Omega), \quad \phi = 0 \text{ on } \Gamma_{pre}\right\}$$

In order to show the numerical formulation of the problem, let $S = L^2(0,T;W)$ be the space of approximate solutions and obviously W is the space of tests functions. Let W^h be a finite element space of Lagrange $P1$ included in W and $S^h = L^2(0,T;W^h)$ be the finite dimensional subspace of S. The Faedo-Galerkin formulation for the problem is given by, finding $C_{k,h} - C_{k,h}^0 \in S_h$ for $i = 1,\ldots,5$ and $V_h \in S_h$:

$$\begin{cases} \bullet \text{ for every } w_h \in W_h \text{ a.e. t } \in]0, T[\text{ and for } 1 \leq k \leq 5, \\ \frac{d}{dt}\int_\Omega C_{k,h} w_h + d_k \int_\Omega \nabla C_{k,h} \nabla w_h + m_k \int_\Omega C_{k,h} \nabla V_h \nabla w_h = -\int_\Omega P_k(C_{k,h}) w_h \\ + \int_\Omega F_k(C_{1,h}, \ldots, C_{5,h}) w_h \\ C_{k,h}(0, x) = C^0_{k,h}(x) \text{ on } \Omega \\ \bullet \text{ for all } \phi_h \in W_h \text{ and a.e. t } \in]0, T[\\ \tau_m \frac{d}{dt}\int_\Omega V_h \phi_h + \lambda^2 \int_\Omega \nabla V_h \nabla \phi_h + (\frac{Fd}{4C_m}) \sum_k \int_\Omega z_k (C_{k,h}(t, x) - C^h_{k,rest}) \phi_h \\ = -\int_\Omega R_m I_{stim}(x, t) \phi_h \\ V_h(0, x) = V^h_0(x) \text{ on } \Omega \end{cases} \tag{9}$$

where in our case:

$$F_1(C_{1,h}, \ldots, C_{5,h}) = -F_2(C_{1,h}, \ldots, C_{5,h}) = K_- C_{2,h} - K_+(B_T - C_{2,h}) C_{1,h}$$
$$\text{and } F_3 = F_4 = F_5 = 0,$$

and

$$P_1 = P, \quad P_k = 0 \text{ for } k = 2, \ldots, 5$$

$C^0_{k,h}$ and V^h_0 are the projections of C^0_k and V_0 on W_h.

2.8 Numerical Scheme

The problem is hard to solve because of the strongly nonlinear terms and the important convective effects. Furthermore, a loose coupling exists between the different phenomena which evolve with different characteristic times. From the numerical view point, we propose a fractional step approach. This method consists in separating the operators of a partial differential equation, and dealing with each term successively. Let us recall the transport equation:

$$\frac{\partial C_{k,h}}{\partial t} - d_k \Delta C_{k,h} - m_k div(C_{k,h} \nabla V_h) = -P_k(C_{k,h}) + F_k(C_{1,h}, C_{2,h}, \ldots, C_{5,h})$$

This equation can be rewritten:

$$\frac{\partial C_{k,h}}{\partial t} - d_k \Delta C_{k,h} - m_k \nabla V_h \nabla C_{k,h} - m_k C_{k,h} \Delta V_h = -P_k(C_{k,h}) + F_k(C_{1,h}, C_{2,h}, \ldots, C_{5,h})$$

By denoting

$$u = -m_k \nabla V_h$$

The transport equation becomes

$$D_t C_{k,h} - d_k \Delta C_{k,h} - m_k C_{k,h} \Delta V_h = -P_k(C_{k,h}) + F_k(C_{1,h}, C_{2,h}, \ldots, C_{5,h})$$

where D_t denotes the particle derivative

$$D_t = \partial_t + u.\nabla$$

It is convenient to first solve

$$D_t C_{k,h} - d_k \Delta C_{k,h} = -P_k(C_{k,h}) + F_k(C_{1,h}, C_{2,h}, \ldots, C_{5,h})$$

which depends on V_h only by means of D_t, then solve the system

$$\frac{\partial C_{k,h}}{\partial t} - m_k C_{k,h} \Delta V_h = 0, \tag{10}$$

$$\tau_m \frac{\partial V_h}{\partial t} - \lambda^2 \Delta V_h + \left(\frac{Fd}{4C_m}\right) \sum_k (C_{k,h}(t,x) - C^h_{k,rest}) z_k = -R_m I_{stim}(x,t)$$

Let us remark that Eq. (10) can be rewritten in conservation form:

$$\partial_t \sigma_{k,h} - m_k \Delta V_h = 0$$

with $\sigma_k = \log(C_{k,h})$ and $\sigma_{k,h}$ is the projection of $\log(C_{k,h})$ on S_h.

2.8.1 Time Marching Scheme

Let us denote by $(C^{n+1}_{k,h}, V^{n+1}_h)$ and $(C^n_{k,h}, V^n_h)$ the approximate value at time $t = t^{n+1}$ and $t = t^n$, respectively, and by δt the time step size. Then by using (9) and the following algorithm, we determine the unknown fields.

Algorithm of Resolution
We used the following algorithm to calculate $C_{k,h}$ and V_h.

- Initialize for $k = 1, \ldots, 5$

$$C^0_{k,h} = C^0_{k,h}(x),$$

$$V^0_h = V^h_0(x)$$

- Loop over n
  At step n:

- Calculate $C^*_{k,h}$ solution of:

$$\int_\Omega \frac{C^*_{k,h} - C^n_{k,h} \circ X^n}{\delta t} w_h + \int_\Omega d_k \nabla C^*_{k,h} . \nabla w_h = -a_k \left(\frac{2P_m}{a}\right) \int_\Omega \frac{C^*_{k,h}}{1 + \frac{C^n_{k,h}}{K_p}} w_h + \int_\Omega F_k(C^n_{1,h}, ., C^*_{k,h}, ., C^n_{5,h}) w_h$$

where $a_1 = 1, a_2 = a_3 = a_4 = a_5 = 0$.

Once $C^*_{k,h}$ is computed then we compute

$$\sigma^*_{k,h} = P^{S_h}(\log(C^*_{k,h}))$$

as the projection on S_h of the field $\log(C^*_{k,h})$.

- Calculate $(\sigma^{n+1}_{k,h}, V^{n+1}_h)$ solutions of the system:

$$\int_\Omega \frac{\sigma^{n+1}_{k,h} - \sigma^*_{k,h}}{\delta t} \psi_h + \int_\Omega m_k \nabla V^{n+1}_h . \nabla \psi_h = 0, \quad \forall \psi_h \epsilon W_h$$

$$\tau_m \int_\Omega \frac{V^{n+1}_h - V^n_h}{\partial t} \phi_h + \lambda^2 \int_\Omega \nabla V^{n+1}_h \nabla \phi_h + \left(\frac{Fd}{4C_m}\right) \int_\Omega \sum z_k (C^*_{k,h}(x,t) - C^h_{k,rest}) \phi_h = -\int_\Omega R_m I_{stim}(x,t) \phi_h \ \forall \phi_h \epsilon W_h$$

Then, we compute

$$C^{n+1}_{k,h} = P^{S_h}(\exp(\sigma^{n+1}_{k,h}))$$

as the projection on S^h of the field $\exp(\sigma^{n+1}_{k,h})$.

3 Results and Discussion

In this section, aiming to understand how an action potential emerges from the mathematical structure that we have developed we study the dynamics of the model for different types of input. For all the results of this section, we considered the following parameters:

For the computations membrane capacitance per unit surface area is taken as $C_m = 1\,\mu\text{F/cm}^2$, following Zador et al.[41]. The radius of the neuron is $a = 0.05\,\mu\text{m}$, which is of the same magnitude used by Zador et al.[41]. The diffusion coefficients of the ions are $d_1 = 0.6\,\mu\text{m}^2\,\text{ms}^{-1}$, $d_2 = 0.13\,\mu\text{m}^2\,\text{ms}^{-1}$, $d_3 = 1.334\,\mu\text{m}^2\,\text{ms}^{-1}$, $d_4 = 1.96\,\mu\text{m}^2\,\text{ms}^{-1}$, and $d_5 = 2.03\,\mu\text{m}^2\,\text{ms}^{-1}$ following Cussler[42]. The charge number of the ions are $z_1 = 2$, $z_2 = 2$, $z_3 = 1$, $z_4 = 1$, and $z_5 = -1$.

The initial concentrations are set to $C_1^0 = 0.01\,\mu\text{M}$, $C_2^0 = 0.6\,\mu\text{M}$, $C_3^0 = 12\,\text{mM}$, $C_4^0 = 155\,\text{mM}$, $C_5^0 = 162\,\text{mM}$, and $\phi_0 = -80\,\text{mV}$. The data employed for initial concentrations were taken from Hille[43]. The time step of the simulation is $\delta t = 10^{-5}$ s, and $T = 0.003$ s.

3.1 Numerical Result 1: Electrophysiological Behavior of the Model in Absence of Stimulation

In order to experiment the scenario where the neuron is not receiving any stimulation from other neurons, we set $I_{stim} = 0$ and evaluate the electrical potential at the center of the longitudinal axis. Figure 2 illustrates the depolarization of the axon, which is a change during which the neuron undergoes a shift in electric charge distribution, resulting in less negative charge in the intracellular side. The computed electrical potential is in agreement with the physical experiments of Hodgkin and Huxley[20], which stipulates that the neuron's membrane potential moves to a more positive value (movement closer to zero from resting membrane potential). Moreover, the exponential increase of the electrical potential agrees with the curve of the analytical solution calculated for a linear cable by Jack et al. [34].

Figure 3 plots the temporal evolution of the Ca^{2+} concentration at the center of the longitudinal axis of the neuron. We can see that the concentration of calcium is increasing which is expected by biological experiments. In fact, when the membrane

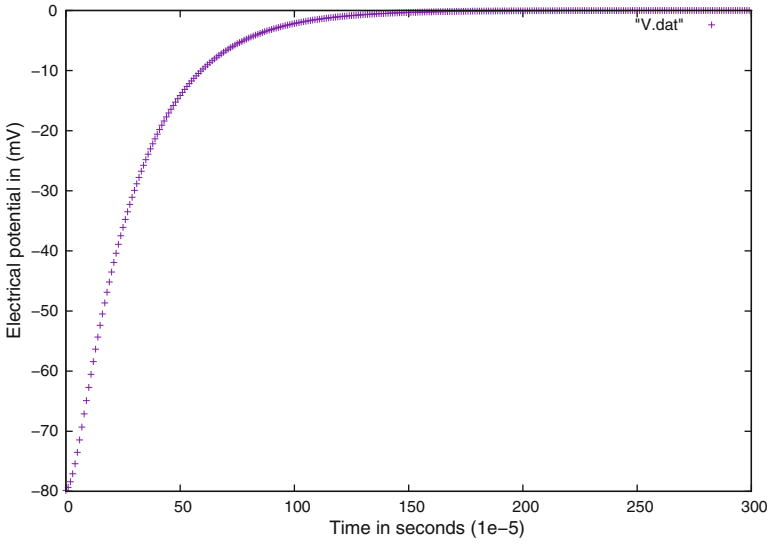

Fig. 2 Action potential in a neuron without stimulation showing depolarization

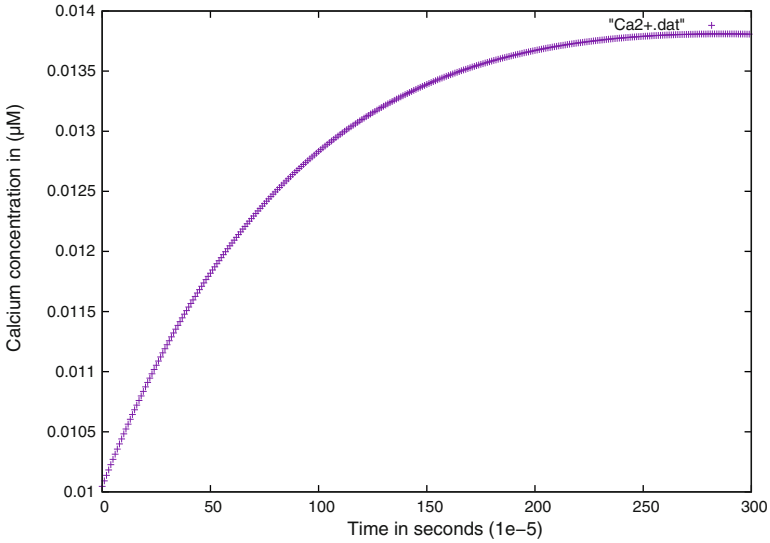

Fig. 3 Time course of Calcium concentration inside the neuron with $C_1^0 = 0.01\,\mu\text{M}$

potential becomes greater, it causes the opening of Ca^{2+} channels, then the Ca^{2+} rushes in inside the neuron.

Furthermore, we experimented the mechanism of calcium extrusion of our model. Let us notice that the calcium extrusion process $P([Ca^{2+}])$ can saturate at high $[Ca^{2+}]$. In fact, if the $[Ca^{2+}]$ is high relative to the pump dissociation constant (i.e., $[Ca^{2+}]/K_p >> 1$), then $P([Ca^{2+}])$ approaches a constant. At the other extreme, if the $[Ca^{2+}]$ is low relative to the pump dissociation constant (i.e., $[Ca^{2+}]/K_p << 1$), then the extrusion becomes a linear function of $[Ca^{2+}]$. Figure 4 corresponds to the case with high calcium concentrations compared to K_p, where we take $C_1^0 = 5\,\mu\text{M}$.

In Fig. 4, we see the calcium concentration decreasing which is justified by the fact that the pump behaves as a steady hyperpolarizing current flowing out across the membrane. Meanwhile, in Fig. 3 the pump behaves like the leak term in standard cable models.

3.2 Numerical Result 2: Electrophysiological Validation of the Model

To validate the model two criteria are considered (1) excitability (2) action potential morphology.

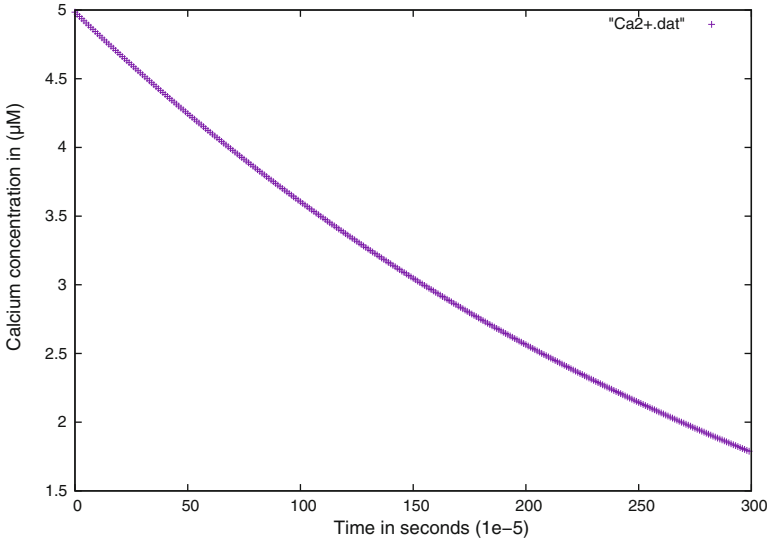

Fig. 4 Time course of Calcium concentration inside the neuron with $C_1^0 = 5\,\mu\text{M}$ (effect of pump saturating)

3.2.1 Excitability

This means that the neuron stays in its resting potential as long as no stimulation is applied to it. However, by using an efficient stimulus it produces AP. The stimulus current I_{stim} is the key to stimulate the system. In the neuron, the excitation is received from other neurons. Here we applied a single stimulus, which delivers a short current pulse of 0.5 ms and strength $-200\,\mu\text{A/cm}^2$, beginning at $t = 150 \times 10^{-5}$ s at the center of the longitudinal axis of the neuron. Figure 5 shows that before time $t = 150.10^{-5}$ s there was no stimulation and consequently there is no action potential but at time $t = 150.10^{-5}$ s an AP is generated. In Fig. 6 we display a 3D snapshot of the evolution of the response of the axon to the current stimulation.

3.2.2 Action Potential Morphology

This model reproduces the triangular AP morphology specific to excitable cells (see Fig. 5) with no sustained plateaus, which is similar to the AP shape obtained with more complex models Nygren et al. [44] and Cherry et al. [45].

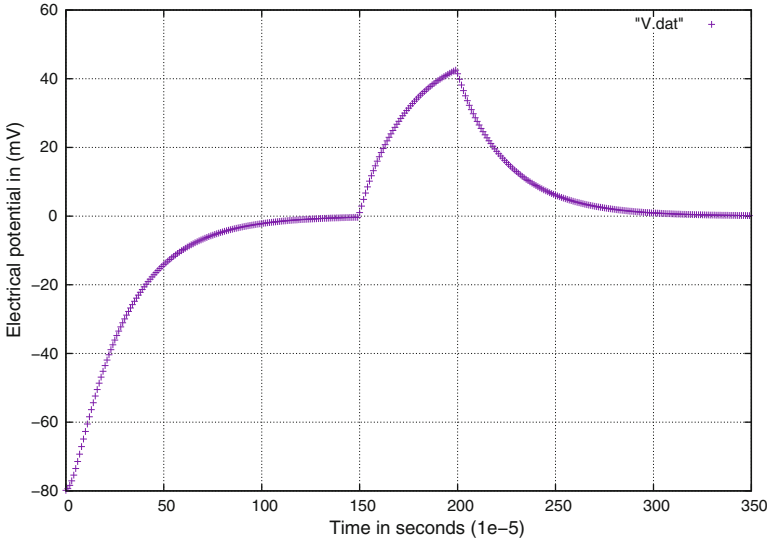

Fig. 5 Generated AP by stimulus current at time $t = 150 \times 10^{-5}$ s. Before time $t = 150 \times 10^{-5}$ s no stimulation is applied

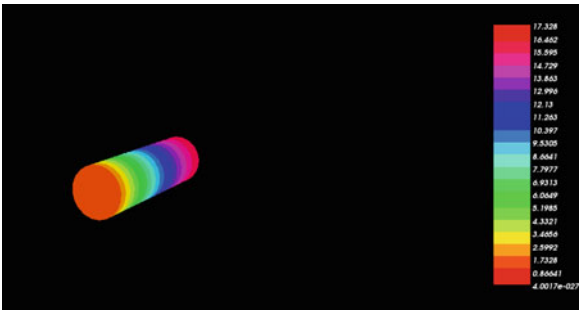

Fig. 6 A 3D snapshot of the propagation of the electrical potential along the cylindrical axon at the end of the stimulation

4 Conclusion

A computational model for the 3D dynamic of electric charges had been developed, with application to nerve impulse transmission. This model fills the gap in scale between the detailed molecular dynamic approach, which consider the role of ionic channels, and the semi-empirical approach of the cable equation and Hodgkin–Huxley equations. Our model has provided valuable insights and potential experimentally viable predictions which illustrates how the interdependence between electrical and chemical aspects of the phenomenon can help us to understand more perfectly the neuron signaling process. Numerical experiments qualitatively and quantitatively agree with the standard model. Other perspectives and developments of this model include: further investigations of the effect of the morphology of the neuron including the dendritic spine, modeling the synapses and gap junction and also modeling the extracellular space.

References

1. L. Kelvin, *Phil. Mag.* **11(4)**, 146–60 (1856).
2. L. Kelvin, *Macmillan*, p 26 (1872).
3. L. Kelvin, *Pro. R. Soc.* **7**, 382–99 (1855).
4. H. Weber, *Bochardt's J. Math.* **76**, 1 (1973).
5. H. Weber, *Pugers Arch. ges. Physiol.* **33**, 162 (1884).
6. M. Cremer, *Z. Biol.* **37**, 550 (1899).
7. X. Yan, *In Handbuch der Physiologie des Menschen* **4**, 793 (1909).
8. L. Hermann, *Handbuch der Physiologie*,(1879).
9. L. Hermann, *Pugers Arch. ges. Physiol.* **75**, 574 (1899).
10. L. Hermann, *Pugers Arch. ges. Physiol.* **109**, 95 (1905).
11. N. Rashevsky, *J. gen. Physiol* **14**, 517–28 (1931).
12. W. A. H. Rushton, *J. Physiol* **82**, 332–52 (1934).
13. W. A. H. Rushton, *Proc. R. Soc. B.* **124**, 210–43 (1937).
14. A. M. Monnier, *Hermon et Cie*, (1934).
15. K. S. Cole and H. J. Curtis, *C. S. H. Symp. Quant. Biol.* **4**, 73–89 (1936).
16. K. S. Cole and H. J. Curtis, *J. gen. Physiol.* **22**, 649–70 (1939).
17. K. S. Cole and H. J. Curtis, *J. gen. Physiol.* **24**, 551–63 (1941).
18. H. Rosenberg, *Proc. R. Soc.* **B124**, 308 (1937).
19. H. Rosenberg, *Trans. Faraday Soc.* **33**, 1028 (1937).
20. A. L. Hodgkin, *J. Physiol.* **90**, 183–210 and 211–32 (1937).
21. K. S. Cole and A. L. Hodgkin, *J. gen. Physiol.* **22**, 671–87 (1939).
22. B. Katz, *Oxford University Press*, (1939).
23. F. Offner, A. Weinberg and C. Young, *Bull. math. Biophys.* **2**, 89–103 (1940).
24. A. M. Weinberg, *Bull. math. Biophys.* **3**, 39 (1941).
25. A. L. Hodgkin and W. A. H. Rushton, *Proceedings of the Royal Society of London B* **133**, 444–479 (1946).
26. R. Lorente de No, *Rockefeller Institute* 3, 39 (1947).
27. A. Hodgkin and A. Huxley, *J. Physiol.* **117**, 500–540 (1952).
28. W. Rall, *American Physiological Society*, 39–97 (1977).
29. G. M. Shepherd, R. K. Brayton, J. P. Miller, I. Segev, J. Rinzel and W. Rall, *Proc. Natl. Acad.* **82**, 2192–2195 (1985).
30. D. H. Pekel and D. J. Perkel, *Brain. Res.* **325**, 331–335 (1985).
31. J. Wathey, W. Lytton, J. Jester and T. Sejnowski, *Soc. Neurosci.* **15**, (1989).
32. W. Rall, *Studies in Neurophysiology*, 203–209 (1978).
33. C. Koch, T. Poggio, *Proc. R. Soc. Lond. [Biol.]*, **218** 455–477 (1983).
34. J. J. B. Jack, D. Noble, R. W. Tsien *Oxford University Press*, **218** 455–477 (1975).
35. N. Stockbridge, J. W. Moore, *J. Neurosci*, **4** 803–811 (1984).
36. A. L. Fogelson, R. S. Zucker, *Biophys. J.*, **48** 1003–1017 (1985).
37. S. M. Simon, R. R. Llinas, *Biophys. J.*, **48** 485–498 (1985).
38. N. Qian, T. J. Sejnowski, *Biol. Cybern.*, **62** 1–15 (1989).
39. J. M. van Egeraat, J. P. Wikswo, *Biophys. J.*, **64** 1287–1289 (1993).
40. J. Keener, J. Sneyd, *New York Springer*, (1998).
41. A. Zador, C. Koch, *The journal of Neuroscience*, (1994).
42. E. L. Cussler, *Cambridge University Press*, **2** (1997).
43. B. Hille, *Sinauer Associates, Sunderland,MA*, **2** (1997).
44. A. Nygren, C. Fiset, L. Firek, J. W. Clark, D. S. Lindblad, R. B. Clark and W. R. Gilles, *Circ. Res.* **82**, 63–81 (1998).
45. E. M. Chery, h. m. Hastings and S. J. Evans, *Prog. Biophys. Mol. Biol.* **98**, 24–37 (2008).

Covid-19 Superspreading Events Network Analysis from Agent-Based Model with Mobility Restriction

L. L. Lima and A. P. F. Atman

1 Introduction

SARS-CoV-2 (severe acute respiratory syndrome coronavirus 2) has spread around the world, being an immediate major public health concern [1]. Governments and research centers around the world have joined efforts to help combat COVID-19, seeking alternative solutions to contain the pandemic while a vaccine had not been developed. Some countries, like China, have succeeded to control the first wave of the disease with some restrictions on travel and mobility, along with other action, as detecting and isolating cases [2, 3].

Epidemiological models can be of great help in understanding the spread of epidemics, becoming a tool used to assist decision making. Throughout the pandemic, the basic reproduction number (R_0) received much attention. It is defined as the mean number of infections generated by an infected individual in a susceptible population and has estimated values between 1.4 and 6.49 for COVID-19 [4].

If we analyze only R_0, we know that values less than 1 indicate that the infection will not be maintained and, on the other hand, when R_0 is greater than 1, the infection tends to spread in the population [5]. However, R_0 is an average value, and being below 1 may not be enough to indicate that the epidemic does not continue to spread, especially if we consider the occurrence of superspreading events (SSE): as a mean number, R_0 can distort individual infectiousness [6].

L. L. Lima (✉)
Pós-Graduação em Modelagem Matemática e Computacional, Centro Federal de Educação Tecnológica de Minas Gerais - CEFET-MG, Belo Horizonte, Brazil

A. P. F. Atman
Departamento de Física, Centro Federal de Educação Tecnológica de Minas Gerais - CEFET-MG and Instituto Nacional de Ciência e Tecnologia - Sistemas Complexos, Belo Horizonte, Brazil
e-mail: atman@cefetmg.br

R. P. Mondaini (ed.), *Trends in Biomathematics: Chaos and Control in Epidemics, Ecosystems, and Cells*, https://doi.org/10.1007/978-3-030-73241-7_21

SSE are defined as outbreaks where a large number of cases are caused by a small number of infected individuals, i.e., some individuals have high infection capacity [7]. A single case can be responsible for an explosive epidemic when a disease has a high individual variation [6]. Other factors, as transmission mode, contact frequency and duration, and public heath interventions, can also impact the occurrence of superspreading events [8].

The superspreading events had special attention in SARS outbreaks in Singapore and China in 2003, since they could assist in understanding transmission dynamics [9]. In Singapore, five people caused more than half of the 205 cases (and 163 cases caused zero secondary transmission) [10]. In 2015, in Korea, only 5 cases of MERS originated 154 secondary cases (166 cases caused zero secondary infections) [9, 11]. For COVID-19, one of the most famous cases of superspreading at the beginning of the pandemic is the "Patient 31," who is linked to a cluster with more than 5,000 cases in Daegu, South Korea [12].

Sometimes, looking at an average value (as R_0) for large regions may not be representative of the situation, especially if clusters are formed in isolated regions. It is necessary to consider the distribution of cases spatially and, if possible, trace the contacts. Thus, in this chapter, we aim to use an agent-based model to evaluate how reducing the human mobility during COVID-19 pandemic impacts the peak number of infected and the need for medical support (like ventilator) and how the individual number of transmissions change. For this, we evaluate the degree distribution, the betweenness and the closeness centrality in the COVID-19 transmission network.

2 Materials and Methods

2.1 Agent-Based Model

We developed an Agent-Based Model (ABM) using probabilistic cellular automata over a regular square lattice ($L \times L$ sites, with $9\,\mathrm{m}^2$ of area for each). The time step considered was 1 h, with synchronous updating, and the agents execute a random walk along the environment, using Moore's neighborhood and with periodic boundary conditions. Each agent can assume one of the following states: Susceptible, Incubated, Symptomatic Infected, Asymptomatic Infected, Infected in the Infirmary, Infected in ICU (Intensive Care Unit), Recovered, and Dead.

When two or more agents are on the same site and one of them is infected, the susceptible ones have a probability 80% of being infected, except if those individuals are in the infirmary or in the ICU, once they are isolated in these sites. Both symptomatic and asymptomatic can transmit the disease [13]. As it is a new disease with many characteristics still unknown, we do not consider the possibility of reinfection along the short period of the simulation run.

All the simulations started with only susceptible individuals and, then, we choose one to be infected to spread the disease. The permanence into a given state follows a Gaussian distribution around the time intervals shown in Table 1, which are reported in literature as typical for COVID-19 [14–17].

Table 1 Time (days) used as model parameters

State	Mean	Minimum	Maximum
Incubation	5.2	2	12
Infection (after incubation)	5.8	3	14
Infirmary (after infection, if hospitalized)	10.5	7	14
ICU (after Infirmary, if goes to ICU)	17.5	14	21

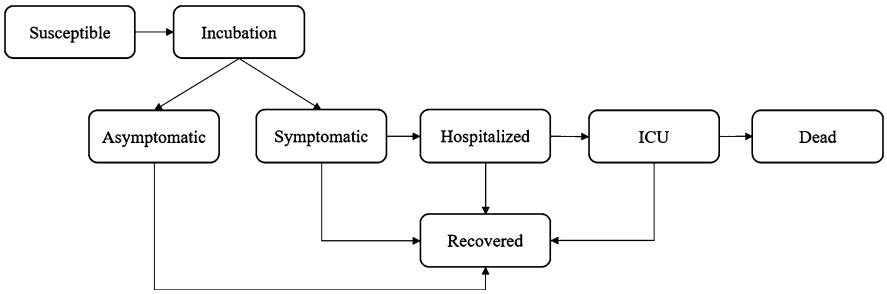

Fig. 1 Dynamics of the model: an infected individual can be symptomatic or asymptomatic. Symptomatic individuals can go to the infirmary and from there to the ICU

To analyze the effect of the mobility reduction (with people staying at home and less physical interaction), the model considers that the individual reduces the movement in a percentage (0% or no restriction, 10%, 20%, 30%, 40%, 50%, 60%, 70%, 80%, and 90% or lockdown). We apply the Monte Carlo method (64-bit Xorshift Method [18]) to implement the mobility restriction, that is, the agent moving less. This does not prevent the individual from meeting other humans, but since everyone is moving less, the chance of encounters is reduced. For this work, we used $L = 250$ and 10000 individuals. The population is distributed a priori with the following probabilities (considering the case of the individual be infected): 60% will become symptomatic [13]; 21% will need to go to a hospital [19]; 5% will need ICU [19]; and 2% of death rate, [19] as Fig. 1.

2.2 Network Analysis

By analyzing the results, it was possible to build a directed network from the original infected individual towards the subsequent infected ones to visualize the transmission of the disease. For this, we record the infection chain from individual to individual and build a graph. Agents not infected were not considered in the graph.

Each infected agent is considered as a vertex of the network and we considered the degree of a vertex v the number of links connected to v. We called this value as $deg(v)$. We calculate the out-degree, that is, how many people does an infected individual transmit the disease to. So, the degree distribution measured in this work only considers out-degree connections.

The betweenness centrality of a node v, $B(v)$, is given by

$$B(v) = \sum_{s \neq v \neq t} \frac{\sigma_{st}(v)}{\sigma_{st}} , \tag{1}$$

where σ_{st} is the total number of shortest paths from node s to t and $\sigma_{st}(v)$ is the number of those paths that pass through v. We also performed a normalization by dividing $B(v)$ by $(N-1)(N-2)$, since the graph is directed. N is the number of nodes (vertices) of the graph.

We also calculate the closeness centrality, which is given by $C(v)$.

$$C(v) = \frac{N-1}{\sum_u d(v,u)} \tag{2}$$

Note that the equation already considers a normalization when multiplies by the number of nodes minus 1. $d(v,u)$ is the distance (number of nodes) in the shortest path between vertices v and u.

3 Results and Discussion

In Fig. 2 we observed a remarkable difference between the infected curves in function of the mobility restriction. The results suggest that high mobility does not

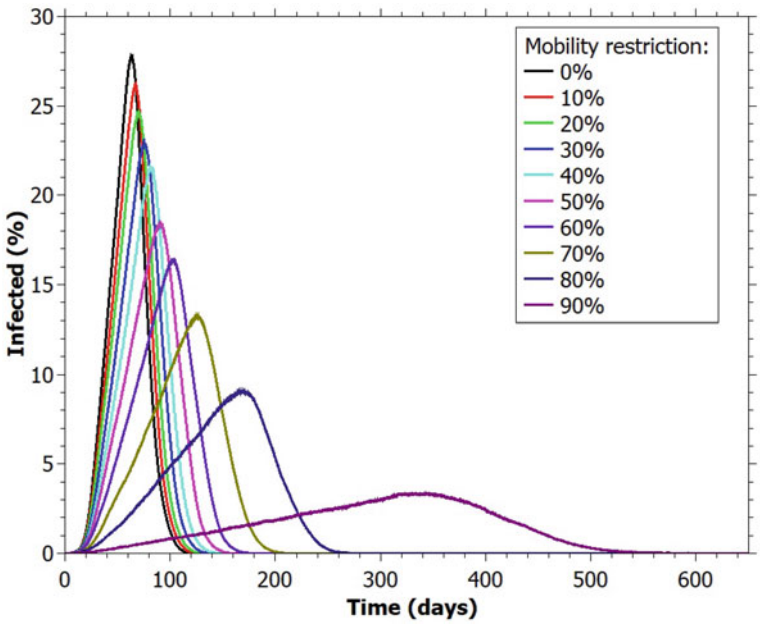

Fig. 2 Percentage of infected for different values of mobility restriction and for the scenario without restrictions (0%)

have a big impact in the infected individuals, as observed in the mobility reduction of 10%, 20%, 30%, and 40%. The most effective result for flattening the infected curve was to establish a restriction on the movement of people by 90%, similar to a lockdown situation, in which people leave the house only if strictly necessary. However, it is almost impossible to live a long time in lockdown, since we know how big is the impact not only socio-economic [20] but also in the physical and mental health of the populations [21, 22]. Reducing the mobility by 70% and 80% also showed a considerable flattening of the curve concerning to no mobility restriction (0%), as shown in Fig. 2. These curves correspond to the average over 30 runs for each value of mobility restriction.

In Table 2 it is possible to notice a difference of approximately 268 days at the peak of the pandemic and approximately 24% of infected individuals during the peak for a situation without mobility restriction (0%) compared with the case of 90% restriction. This is also reflected in the number of people hospitalized in ICUs, whose number jumps from 0.49% to 2.95% at the peak with a difference of 274 days. This implies a difference of about 246 ICU beds with a ventilator for every 10,000 inhabitants and shows how the mobility restrictions are important especially for the health system not collapse. In addition to having fewer individuals hospitalized simultaneously, there is time to prepare beds and purchase health supplies (such as ventilators and medications) when there are high levels of mobility restriction.

It is important to highlight that practically all individuals are infected in the model with up to 60% mobility restrictions. At 70%, the non-infected rate is about 0.4% and it reaches almost 16% for a restriction of 90% (Table 2).

Figure 3 shows the infection network of each simulation in function of the mobility restriction level. To analyze the differences between each one, we evaluated the distributions of the measures of degree, betweenness and closeness centrality. Figure 4 shows the degree distribution of the different simulations and the results indicate that there are a large number of people who do not transmit the disease to anyone, while a small number of individuals are responsible for a large number of infections, characterizing superspreading events. We can see a reduction in the maximum number of infected for each mobility restriction value, and superspreaders degree tend to decrease with a higher mobility restriction. In Fig. 4, the distribution exhibits heavy tails, as observed for SARS epidemic in Singapore in 2003 [10]. In this way, some researchers indicate that superspreading is a typical feature of disease spread [6] and that the data counting from infectious diseases tend to have a variance greater than the mean, that is, they tend to be over dispersed [10].

The slope of the heavy tails versus the order parameter is shown in Fig. 5. For low values of reduced mobility, the dependence is almost linear, which corroborates the observation made previously that there is no big difference in the spreading dynamics for small mobility restriction levels. A significant flattening of the curves is observed only for restriction mobility above 70%.

Figures 6 and 7 corroborate with the out-degree data that there is a change in the network due to the mobility restriction. In Fig. 6, the higher the restriction, the higher the maximum values found in the distribution of betweenness centrality.

Table 2 Maximum infected and maximum number of people in the ICU and their respective times due to mobility restrictions and number of ICU equipped with a ventilator every 10,000 individuals for each percentage of mobility restriction

Mobility restriction	Max. infected (%)	Time (days) max. inf	Max. in ICU(%)	Time (days) max. ICU	ICU requiring ventilator/ 10,000 individuals	Total of infected
0%	28.276±0.877	63.093±1.950	2.950±0.164	82.893±2.608	295±16	99.988±0.005
10%	26.643±0.865	66.758±2.303	2.760±0.225	85.753±2.825	276±22	99.989±0.003
20%	25.171±0.886	69.846±2.410	2.618±0.218	89.514±3.557	262±22	99.984±0.008
30%	23.523±0.805	75.813±2.474	2.412±0.207	94.588±3.553	241±21	99.983±0.008
40%	21.989±1.077	81.631±2.595	2.267±0.134	101.217±4.091	227±13	99.973±0.014
50%	18.870±0.574	90.258±3.805	1.989±0.133	109.418±4.877	199±13	99.947±0.023
60%	16.861±0.820	102.461±4.411	1.708±0.109	121.254±5.442	171±11	99.864±0.040
70%	13.918±0.730	125.349±7.230	1.461±0.092	144.367±9.268	146±9	99.576±0.061
80%	9.977±0.569	168.782±8.434	1.066±0.095	185.168±12.188	107±10	98.224±0.145
90%	4.109±0.432	331.665±38.086	0.490±0.059	357.263±47.063	49±6	84.410±0.954

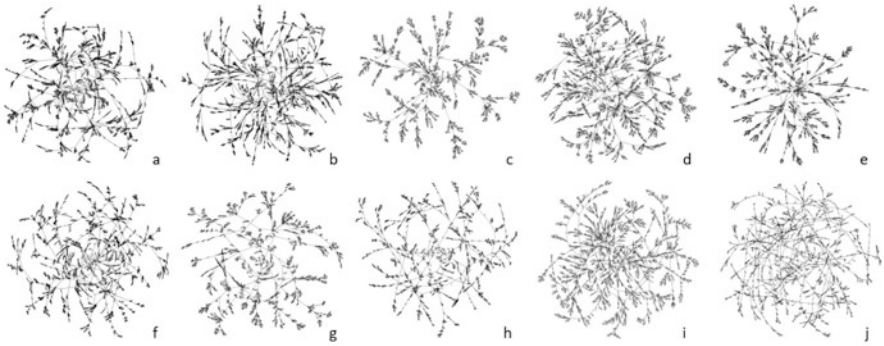

Fig. 3 Example of a transmission network generated at the end of a simulation for each mobility restriction: (**a**) 0%; (**b**) 10%; (**c**) 20%; (**d**) 30%; (**e**) 40%; (**f**) 50%; (**g**) 60%; (**h**) 70%; (**i**) 80%; (**j**) 90%

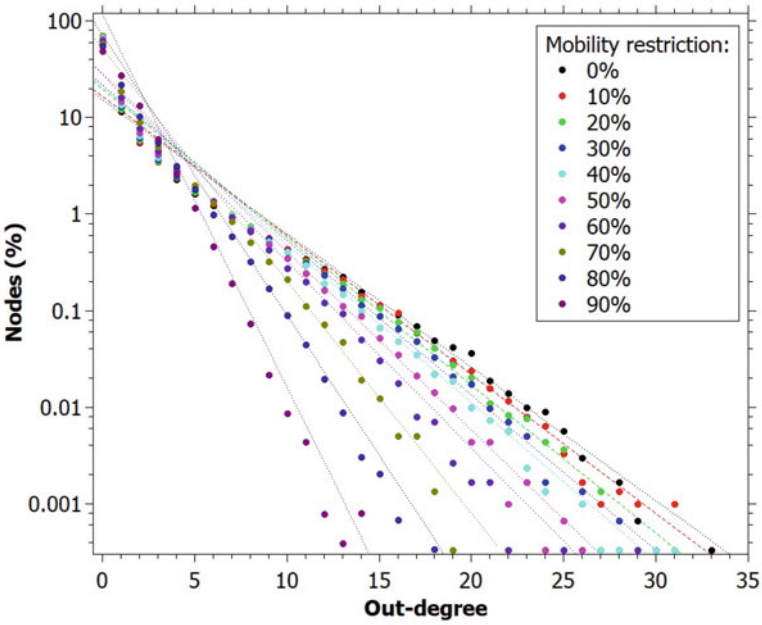

Fig. 4 Out-degree distribution of each mobility restriction value. Linear fit on a log scale on the y axis

Since betweenness is related to how many times a vertex appears in shorter paths, the higher values of this measure found for higher restriction values may be related to the fact that the infection spreads with a slower rate (having a flattened curve), causing a person to tend to be the point of connection with several others. However, there are many records of zero or close to zero betweenness, which shows that few individuals are responsible for the largest connections on the network, as

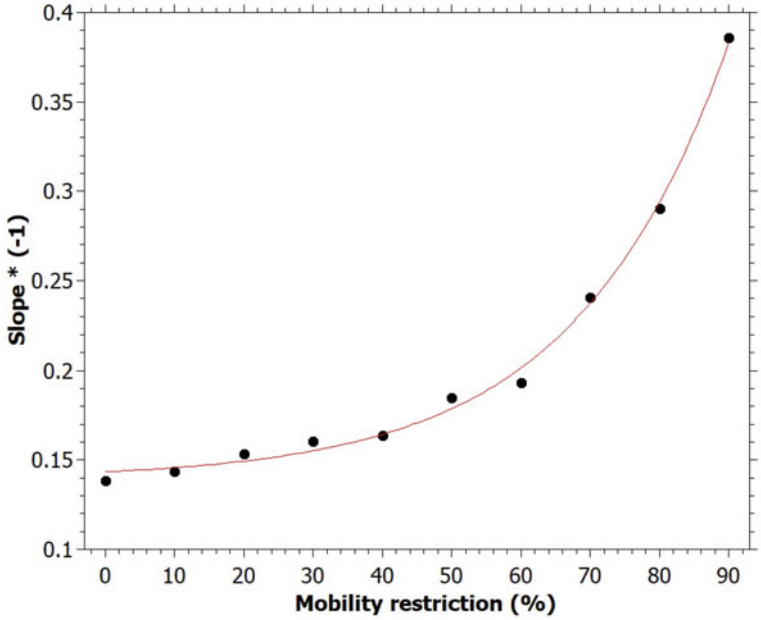

Fig. 5 Slope for the degree distribution of each mobility restriction value

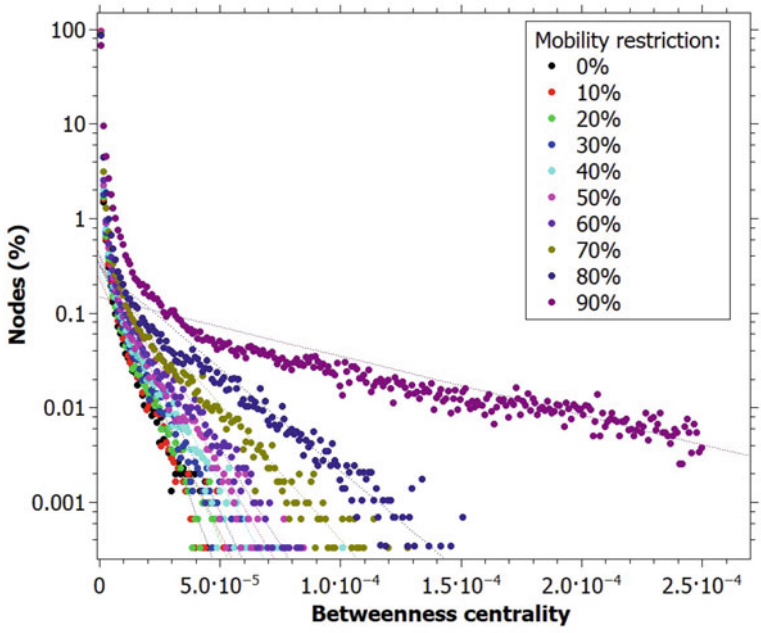

Fig. 6 Betweenness centrality distribution of each mobility restriction value

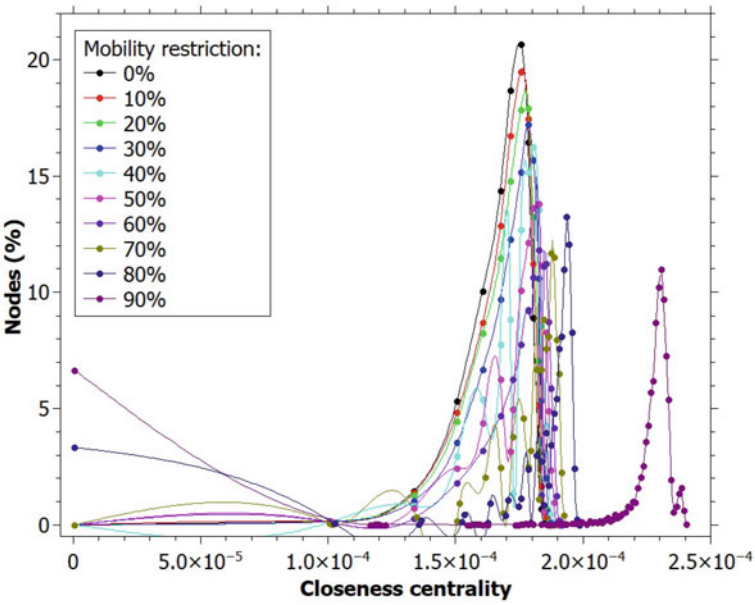

Fig. 7 Closeness centrality distribution of each mobility restriction value

shown by the measure of the degree (Fig. 4). On the other hand, when there are no restrictions, more people tend to be infected at the same time, transmitting to many others at first, but as time passes, people who have already been infected do not reinfect themselves, breaking the chain of transmission and having smaller betweenness value. This characteristic of superspreaders having a more important role in the spread of the infection as mobility decreases is not captured by the degree distribution but is evidenced by the betweenness measures.

A similar interpretation can be given for the measure of the closeness of the networks (Fig. 7). There is a small number of individuals with higher closeness in simulations with a higher mobility restriction, indicating that they transmit the disease more efficiently through the network. However, for networks built from smaller restrictions, there are a large number of individuals with intermediate closeness values. This agrees with the reasoning that there are more people infected transmitting the disease at the same time.

Even with the reduced mobility by 90%, there was still a record of individuals spreading it to many people. The high values of betweenness and closeness for higher mobility restriction highlights the importance of testing and trace infected people. By isolating these potential disseminators, it is possible to prevent the mass spread of the disease and allow more people in circulation in the cities. This consequently contributes to reducing the other impacts of the pandemic as economic and social.

4 Conclusions

In general, the simulation showed that reduced mobility is capable of flattening the curve. Regarding superspreading, the simulation analysis showed that there is a reduction in the degree of infected as the mobility restriction increases but the values of betweenness and closeness centrality reveal the most prominent role of the superspreaders. In addition to other preventive measures, as mobility restriction, testing and tracing contacts are necessary, allowing infected individuals to remain in isolation and not spread the disease to the susceptible.

Controlling a pandemic requires high-stakes decisions that involve different factors at different levels of government and public health organizations. It is necessary to use appropriate tools to support these decisions, which highlights the need for investment in science. Epidemics that came before COVID-19 showed the need to be prepared to face the adversities of a disease that can affect the entire world. Unfortunately, this was proven during the COVID-19 pandemic, showing how important it is to develop appropriate tools to study and support events as complex as this. In this way, understanding the role of some events as superspreading is extremely important for making prediction models and for establishing disease control strategies.

References

1. World Health Organization, *WHO Interim Guidance* **1** (2020).
2. M. Chinazzi1, J. T. Davis, M. Ajelli, C. Gioannini, M. Litvinova, S. Merler, A. P. Piontti, K. Mu, L. Rossi, K. Sun, C. Viboud, X. Xiong, H. Yu, M. E. Halloran, I. M. Longini Jr., A. Vespignani, *Science.* **368**, 395 (2013).
3. S. Lai, N. W. Ruktanonchai, L. Zhou, O. Prosper, W. Luo, J. R. Floyd, A. Wesolowski, M. Santillana, C. Zhang, X. Du, H. Yu and A. J. Tatem, *Nature.* (2020).
4. Y. Liu, A. A. Gayle, A. Wilder-Smith and J. Rocklov, *Journal of Travel Medicine.* **27.2** (2020).
5. C. T. Bauch, J. O. Lloyd-Smith, M. P. Coffee and A. P. Galvani, *Epidemiology.* 791 (2005).
6. J. O. Lloyd-Smith, S. J. Schreiber, P. E. Kopp and W. M. Getz, *Nature.* **438.7066**, 355 (2005).
7. R. A. Stein, *International Journal of Infectious Diseases.* **15.8**, 510 (2011).
8. W. Duan, X. Qiu, Z. Cao, X. Zheng and K. Cui, *IEEE Intelligent Systems.* **28.4**, 18 (2013).
9. B. C. Chun. *Infect. & Chemother.* **48.2**, 147 (2016).
10. P. Yang and G. Chowell. *Cham, Switzerland: Springer.* **70**, (2019).
11. Y. Kim, H. Ryu and S. Lee, *International Journal of Environmental Research and Public Health.* **15.11**, 2369 (2018).
12. S. Choi and M. Ki, *Epidemiology and health.* **42**, (2020).
13. D. P. Oran and E. J. Topol, *Annals of Internal Medicine.* (2020).
14. R. Y. Dodd and S. L. Stramer, *Transfusion Medicine Reviews.* **34**, 73 (2020).
15. S. A. Lauer, K. H. Grantz, Q. Bi, F. K. Jones, Q. Zheng, H. R. Meredith, A. S. Azman, N. G. Reich and J. Lesser, *Annals of Internal Medicine.* **172.9**, 577 (2020).
16. T. M. Chen, J. Rui, Q. P. Wang, Z. Y. Zhao, J. A. Cui and L. Yin, *Infectious diseases of poverty.* **9**, 1 (2020).
17. P. K. Bhatraju, B. J. Ghassemieh, M. Nichols, et al., *The New England Journal of Medicine.* **382;21** 2012 (2020).

18. W. H. Press, S. A. Teukolsky, W. T. Vetterling and B. P. Flannery, *Cambridge University Press.* **3**,(2007).
19. CDC and Team, *MMWR Morb Mortal Wkly Rep.* **69.12**, 343 (2020).
20. M. Nicola, Z. Alsafi, C. Sohrabi, A. Kerwan, A. Al-Jabir, C. Iosifidis, M. Agha and R. Aghaf, *International Journal of Surgery.* **78** (2020).
21. P. Hirematha, C. S. S. Kowshika, M. Manjunath and M. Shettar, *Asian Journal of Psychiatry.* **51**, 102088 (2020).
22. J.Qiu, B. Shen, M. Zhao, Z. Wang, B. Xie and Y. Xu, *General psychiatry.* **33.2** (2020).

Distinct Prognostic Values of *BCL2* Anti-apoptotic Members in Lung Cancer: An *In-Silico* Analysis

Pooja Mittal, Indrakant Kumar Singh, and Archana Singh

1 Introduction

Lung cancer (LC) is the most common cancer among men and women and accounts for a quarter of the cancer-associated deaths worldwide [1, 2]. It is constituted by two major histological types: small-cell lung carcinoma (SCLC), which comprises 15% of LC, and non-small-cell lung carcinoma (NSCLC), which comprises 80–85% of LC cases [2]. NSCLC includes the subcategories adenocarcinomas and squamous cell carcinomas [2, 3]. Recent advances have led to enhanced understanding of LC molecular pathology and molecular-targeted therapies, but despite these, the LC-associated mortality remains high due to late diagnosis and limited effectiveness of clinical interventions [2].

Evasion of the apoptotic signaling pathway is a major hallmark associated with cancer progression [4]. The apoptotic pathway is divided into extrinsic and intrinsic/mitochondrial pathways. The intrinsic apoptotic pathway comprises four subclasses of BCl2 proteins: anti-apoptotic, pro-apoptotic effectors, BH3-only direct activators, and BH3-only sensitizers.

cBioportal is an open platform to access and explore cancer genomic data [5, 6]. KM plotter (Kaplan-Meier plotter) database includes gene expression and patient survival datasets for various cancer types. KM plotter is a highly valuable platform for the preliminary biomarker analysis in cancer [7]. A number of potential prognostic biomarkers have been identified using KM plotter for various cancers, including lung cancer [8, 9]. MicroRNAs (miRNAs) are short and non-coding

P. Mittal, I. K. Singh (✉)
Molecular Biology Research Lab., Department of Zoology, Deshbandhu College, University of Delhi, New Delhi, India
e-mail: iksingh@db.du.ac.in

A. Singh
Department of Botany, Hansraj College, University of Delhi, New Delhi, India

R. P. Mondaini (ed.), *Trends in Biomathematics: Chaos and Control in Epidemics, Ecosystems, and Cells*, https://doi.org/10.1007/978-3-030-73241-7_22

RNAs that regulate gene expression through mRNA degradation and translational repression. MiRSystem is an online user-friendly tool that predicts miRNA targets as well as miRNAs with potential binding to target gene transcripts [10].

In the present study, we utilized three online platforms, cBioportal, KM plotter, and miRSystem to report the genomic alterations in target genes, effects of mRNA expression of selected *BCL-2* anti-apoptotic genes on overall survival (OS) and potential miRNA regulators of target genes, in context to lung cancer.

2 Materials and Methods

2.1 Gene Alteration Analysis Through cBioportal

The cBioportal (http://cbioportal.org) was accessed (on 2nd July 2020) and the gene alteration percentages were obtained for the four anti-apoptotic *BCL2* genes (*BCL2*, *MCL1*, *BCL2A1*, and *BCL2L1*) in two lung cancer datasets: Lung Adenocarcinoma (TCGA, PanCancer Atlas – 507 patients/samples) and Lung Squamous Cell Carcinoma (TCGA, PanCancer Atlas – 469 patients/samples) [5, 6]. The data was represented in the form of bubble plots (created through R) wherein the size of each is bubble is directly proportional to the percentage of samples with gene alterations (mutations + copy number variations).

2.2 Prognostic Analysis Through KMplotter

KM plotter was used to assess the prognostic relevance of four *BCL-2* anti-apoptotic genes (*BCL2*, *MCL1*, *BCL2A1*, and *BCL2L1*) mRNA expression in lung cancer. Also the correlation of mRNA expression, prognosis and clinicopathological features (tumor histology and patient smoking history) was assessed. The follow-up threshold was set at 5 years (60 months), and Kaplan-Meier survival curves were obtained (1st July 2020). HR, 95% CI, log-rank *P values*, and number-at-risk were also calculated and displayed along with survival curves. *P values* of less than 0.05 ($P < 0.05$) were considered as statistically significant.

2.3 miRNA Regulation Analysis Through miRSystem

The computational algorithm "miRSystem" was used to predict miRNAs that bind to the mRNA transcripts of our target genes (*BCL2*, *MCL1*, *BCL2A1*, and *BCL2L1*) at the 3′-Untranslated regions (UTRs) [10]. Then using Venny 2.1 tool we created

a Venn diagram and the three common miRNAs that potentially target all the four gene of interest in this study [11].

3 Results

3.1 Genomic Alterations in Target Genes in Lung Cancer

Based on our analysis, we showed the percentage of gene alterations in the four selected anti-apoptotic BCL2 members. In case of lung adenocarcinoma, *MCL1* possessed relatively higher genetic alterations in 11% of samples, followed by *BCL2* (2.8%), *BCL2L1* (2.6%), and *BCL2A1* (0.6%). In case of lung squamous cell carcinoma, *MCL1* possessed highest genetic alterations in 6% of samples, followed by *BCL2L1* (5%), *BCL2* (1.7%), and *BCL2A1* (1.1%). The results were represented as a bubble plot, wherein each bubble corresponds to the percentage of samples with corresponding gene alteration (Fig. 1) [12]. But gene expression or protein expression cannot be inferred from these percentages.

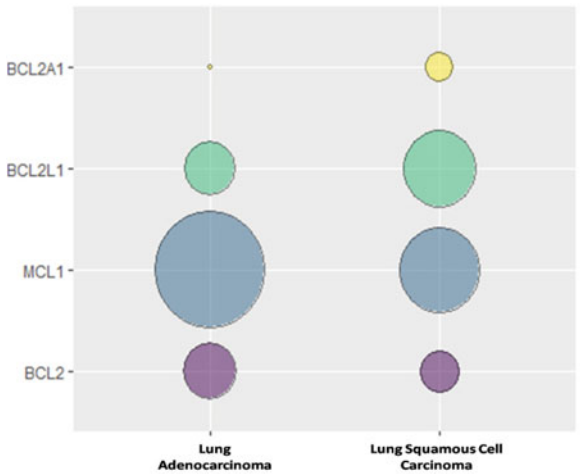

Fig. 1 Bubble plot illustrating the percent genomic alteration (mutation and copy number alteration) of BCL2 anti-apoptotic genes in lung adenocarcinoma and squamous cell carcinoma

3.2 Distinct Prognostic Values of the Selected BCl2 Anti-apoptotic Members

3.2.1 Prognostic Significance of Selected BCL2 Anti-apoptotic Members in All Lung Cancer Patients

The high mRNA expression of *BCL2L1* and *BCL2A1* correlated with poor overall survival (OS) while high mRNA expression of *MCL1* correlated with favorable OS outcome in all lung cancer patients. *BCL2* mRNA expression did not correlate with OS in all lung cancer patients (Table 1).

3.2.2 Prognostic Significance of Selected BCL2 Anti-apoptotic Members in All Lung Cancer Patients with Different Tumor Histology

The high mRNA levels of *BCL2L1* and *BCL2A1* significantly correlated with poor OS in lung adenocarcinoma patients while no correlation was found with lung squamous cell carcinoma. High *MCL1* mRNA expression was significantly correlated with favorable OS in both tumor histology types while *BCL2* mRNA expression did not correlate with any tumor histology type (Table 2).

3.2.3 Prognostic Significance of Selected BCL2 Anti-apoptotic Members in All Lung Cancer Patients with Different Smoking History

The high mRNA expression of *MCL1* significantly associated with better OS, while high *BCL2L1* mRNA expression significantly correlated with worse OS in both smoker and non-smoker lung cancer patients. *BCL2* and *BCL2A1* mRNA expression did not correlate with smoking history in lung cancer patients (Table 3).

Table 1 Prognostic values of *BCL-2* family anti-apoptotic members (*BCL2*, *MCL1*, *BCL2A1*, and *BCL2L1*) mRNA expression in all lung cancer patients (follow-up = 5 years)

BCL2 family genes (Affymetrix IDs)	OS		
	HR	95% CI	*P value*
BCL2 (207005_s_at)	1.07	0.93–1.23	**0.32**
MCL1 (200797_s_at)	0.67	0.58–0.76	**8e–09**
BCL2L1 (215037_s_at)	1.26	1.1–1.45	**0.00091**
BCL2A1 (205681_at)	1.2	1.04–1.38	**0.011**

P value < 0.05 were considered statistically significant. Bold values in the table indicate significant values

Table 2 Prognostic values of *BCL-2* family anti-apoptotic members (*BCL2*, *MCL1*, *BCL2A1*, and *BCL2L1*) mRNA expression in lung cancer patients with different tumor histology (follow-up = 5 years)

BCL2 family genes (affymetrix IDs)	Histology	OS		
		HR	95% CI	*P value*
BCL2 (207005_s_at)	Adenocarcinoma	1.06	0.83–1.37	0.64
	Squamous cell carcinoma	0.92	0.71–1.19	0.52
MCL1 (200797_s_at)	Adenocarcinoma	0.54	0.41–0.7	**1.6e–06**
	Squamous cell carcinoma	0.77	0.59–1	**0.046**
BCL2L1 (215037_s_at)	Adenocarcinoma	1.96	1.52–2.54	**1.7e–07**
	Squamous cell carcinoma	1	0.77–1.3	0.99
BCL2A1 (205681_at)	Adenocarcinoma	1.51	1.17–1.94	**0.0016**
	Squamous cell carcinoma	1	0.77–1.3	0.99

P value < 0.05 were considered statistically significant. Bold values in the table indicate significant values

Table 3 Prognostic values of *BCL-2* family anti-apoptotic members (*BCL2*, *MCL1*, *BCL2A1*, and *BCL2L1*) mRNA expression in lung cancer patients with different smoking history (follow-up = 5 years)

BCL2 family genes (affymetrix IDs)	Smoking history	OS		
		HR	95% CI	*P value*
BCL2	Smokers	1.1	0.88–1.38	0.39
(207005_s_at)	Non-smokers	1.15	0.62–2.14	0.65
MCL1	Smokers	0.68	0.54–0.85	**0.00067**
(200797_s_at)	Non-smokers	0.29	0.14–0.58	**0.00018**
BCL2L1	Smokers	1.28	1.02–1.61	**0.03**
(215037_s_at)	Non-smokers	2.52	1.3–4.89	**0.0046**
BCL2A1	Smokers	1.12	0.9–1.41	**0.31**
(205681_at)	Non-smokers	1.2	0.64–2.23	0.57

P value < 0.05 were considered statistically significant. Bold values in the table indicate significant values

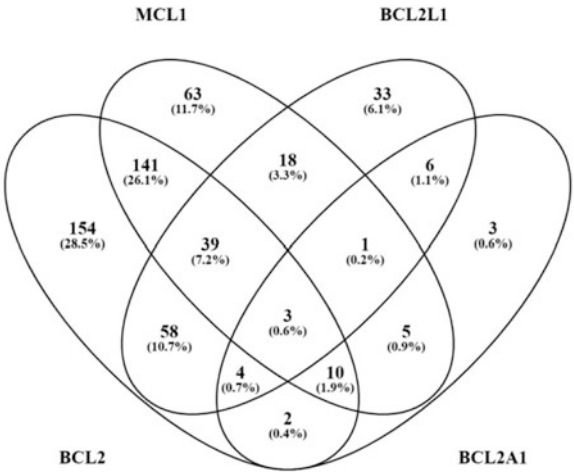

Fig. 2 Venn diagram showing the overlap of miRNAs predicted to bind to the target genes (*BCL2*, *MCL1*, *BCL2A1*, and *BCL2L1*) 3′-UTR by miRSystem algorithm

3.3 Potential miRNA Regulators of Selected Target Genes

MiR-182-5p, miR-587, and miR-513a-5p were predicted as the three common miRNAs for all four target genes (*BCL2*, *MCL1*, *BCL2A1*, and *BCL2L1*) were obtained for their potential binding to the 3′-UTR of the mRNA transcript (Fig. 2). The therapeutic efficacy of these miRNAs needs to be further validated.

4 Discussion

Apoptosis has major roles to play cancer growth and metastasis. Thus, the relevance of *BCL2* family members to patient survival in cancer becomes a major research question. The correlation of BCL2 family protein expression with prognosis is generally studied, while the role of mRNA expression of these genes in cancer prognosis remains largely elusive. Therefore, in this report we elucidated the prognostic values for four major anti-apoptotic genes (*BCL2*, *MCL1*, *BCL2A1*, and *BCL2L1*) in lung cancer.

BCL2 family gene amplification has been implicated in several human cancers. MCL1 was one of the genes to be found amplified in cytoband 1q21.2 in breast and lung cancers [13]. Both MCL1 and BCL2L1 have been found to be overexpressed in NSCLC cell lines [14].

BCL2 expression has been reported as a favorable prognostic marker in lung squamous cell carcinoma [15]. Tumor stage dependent analysis in NSCLC revealed that BCL2 protein expression did not significantly correlate with survival [16]. Another study demonstrated BCL as a prognostic indicator in localized NSCLC [17]. Our *in-silico* analysis did not show BCL2 as a prognostic indicator in LC, nor its correlation with tumor histology and smoking history. We

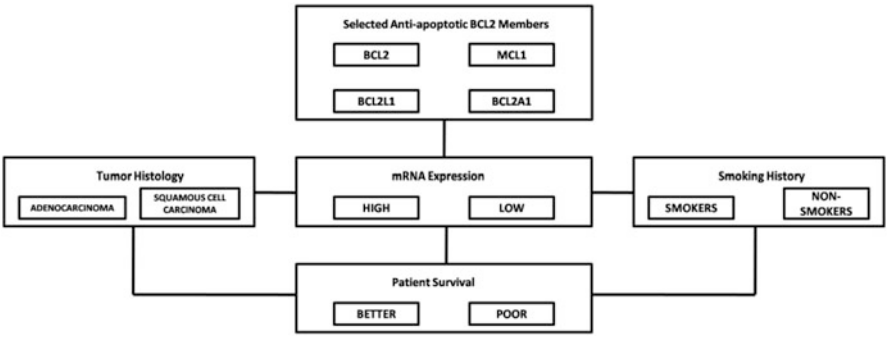

Fig. 3 Schematic representation of the model used for prognostic analysis of the target genes

found that the other members, *MCL1*, *BCL2L1*, and *BCL2A1*, hold great potential to be prognostic indicators in LC and need experimental validation. The schematic model representing our *in-silico* analysis using KM plotter is shown in Fig. 3.

MiR-182 expression dysregulation has been reported in cancer progression in a variety of human cancers. In mesothelioma, the downstream targets of miR-182 are FOXO1 and p27, and its upregulation are linked with cell invasion and proliferation [18]. Similar to this, miR-182-5p was found upregulated in NSCLC and one of its downstream targets was HOXA9. MiR-182-5p is upregulated in lung squamous cell carcinoma and serves as a biomarker [19]. BCL2 anti-apoptotic genes as targets for miR-182 in NSCLC need further validation [20]. MiR-587 antagonizes the colorectal cancer cells to 5-fluorouracil induced apoptosis by downregulation of PPP2R1B [21]. In lung adenocarcinoma, miR-513a-5p targets GSPT1 and sensitizes cancer cells to cisplatin therapy [22]. MiR-513a-5p also increases sensitivity to radiotherapy in osteosarcoma by targeting APE1 [23].

Acknowledgments The authors acknowledge Dr. Rajiv Aggarwal, Principal, Deshbandhu College for providing all the infrastructural support and research facility.

References

1. R. L. Siegel, K. D. Miller, A. Jemal, Cancer statistics, 2020, CA. Cancer J. Clin. 70 (2020) 7–30. https://doi.org/10.3322/caac.21590.
2. K. Inamura, Lung Cancer: Understanding Its Molecular Pathology and the 2015 WHO Classification, Front. Oncol. 7 (2017) 1–7. https://doi.org/10.3389/fonc.2017.00193.
3. C. M. Jones, A. Brunelli, M. E. Callister, K. N. Franks, Multimodality Treatment of Advanced Non-small Cell Lung Cancer: Where are we with the Evidence?, Curr. Surg. Reports. 6 (2018) 5. https://doi.org/10.1007/s40137-018-0202-0.
4. D. Hanahan, R. A. Weinberg, Hallmarks of cancer: the next generation., Cell. 144 (2011) 646–74. https://doi.org/10.1016/j.cell.2011.02.013.

5. J. Gao, B. A. Aksoy, U. Dogrusoz, G. Dresdner, B. Gross, S. O. Sumer, Y. Sun, A. Jacobsen, R. Sinha, E. Larsson, E. Cerami, C. Sander, N. Schultz, Integrative Analysis of Complex Cancer Genomics and Clinical Profiles Using the cBioPortal, Sci. Signal. 6 (2013) pl1pl1. https://doi.org/10.1126/scisignal.2004088.
6. E. Cerami, J. Gao, U. Dogrusoz, B.E. Gross, S.O. Sumer, B.A. Aksoy, A. Jacobsen, C.J. Byrne, M.L. Heuer, E. Larsson, Y. Antipin, B. Reva, A.P. Goldberg, C. Sander, N. Schultz, The cBio Cancer Genomics Portal: An Open Platform for Exploring Multidimensional Cancer Genomics Data: Figure 1., Cancer Discov. 2 (2012) 401–404. https://doi.org/10.1158/2159-8290.CD-12-0095.
7. B. Győrffy, A. Lanczky, A. C. Eklund, C. Denkert, J. Budczies, Q. Li, Z. Szallasi, An online survival analysis tool to rapidly assess the effect of 22,277 genes on breast cancer prognosis using microarray data of 1,809 patients, Breast Cancer Res. Treat. 123 (2010) 725–731. https://doi.org/10.1007/s10549-009-0674-9.
8. J. Xiong, X. Zhang, X. Chen, Y. Wei, D. Lu, Y. Han, J. Xu, D. Yu, Prognostic roles of mRNA expression of notch receptors in non-small cell lung cancer, Oncotarget. 8 (2017) 13157–13165. https://doi.org/10.18632/oncotarget.14483.
9. K. Liu, M. Jin, L. Xiao, H. Liu, S. Wei, Distinct prognostic values of mRNA expression of glutathione peroxidases in non-small cell lung cancer, Cancer Manag. Res. 10 (2018) 2997–3005. https://doi.org/10.2147/CMAR.S163432.
10. T. -P. Lu, C. -Y. Lee, M. -H. Tsai, Y. -C. Chiu, C. K. Hsiao, L. -C. Lai, E. Y. Chuang, miRSystem: An Integrated System for Characterizing Enriched Functions and Pathways of MicroRNA Targets, PLoS One. 7 (2012) e42390. https://doi.org/10.1371/journal.pone.0042390.
11. J. C. Oliveros, (2007–2015) Venny. An interactive tool for comparing lists with Venn's diagrams, (n.d.). https://bioinfogp.cnb.csic.es/tools/venny/index.html.
12. E. H. van Schie, R. van Amerongen, Aberrant WNT/CTNNB1 Signaling as a Therapeutic Target in Human Breast Cancer: Weighing the Evidence, Front. Cell Dev. Biol. 8 (2020) 1–14. https://doi.org/10.3389/fcell.2020.00025.
13. R. Beroukhim, C. H. Mermel, D. Porter, G. Wei, S. Raychaudhuri, J. Donovan, J. Barretina, J. S. Boehm, J. Dobson, M. Urashima, K. T. McHenry, R. M. Pinchback, A. H. Ligon, Y. -J. Cho, L. Haery, H. Greulich, M. Reich, W. Winckler, M. S. Lawrence, B. A. Weir, K. E. Tanaka, D. Y. Chiang, A. J. Bass, A. Loo, C. Hoffman, J. Prensner, T. Liefeld, Q. Gao, D. Yecies, S. Signoretti, E. Maher, F. J. Kaye, H. Sasaki, J. E. Tepper, J. A. Fletcher, J. Tabernero, J. Baselga, M. -S. Tsao, F. Demichelis, M. A. Rubin, P. A. Janne, M. J. Daly, C. Nucera, R. L. Levine, B. L. Ebert, S. Gabriel, A. K. Rustgi, C. R. Antonescu, M. Ladanyi, A. Letai, L. A. Garraway, M. Loda, D. G. Beer, L. D. True, A. Okamoto, S. L. Pomeroy, S. Singer, T. R. Golub, E. S. Lander, G. Getz, W. R. Sellers, M. Meyerson, The landscape of somatic copy-number alteration across human cancers, Nature. 463 (2010) 899–905. https://doi.org/10.1038/nature08822.
14. H. Zhang, S. Guttikonda, L. Roberts, T. Uziel, D. Semizarov, S. W. Elmore, J. D. Leverson, L. T. Lam, Mcl-1 is critical for survival in a subgroup of non-small-cell lung cancer cell lines, Oncogene. 30 (2011) 1963–1968. https://doi.org/10.1038/onc.2010.559.
15. C. Feng, J. Wu, F. Yang, M. Qiu, S. Hu, S. Guo, J. Wu, X. Ying, J. Wang, Expression of Bcl-2 is a favorable prognostic biomarker in lung squamous cell carcinoma, Oncol. Lett. 15 (2018) 6925–6930. https://doi.org/10.3892/ol.2018.8198.
16. H. Han, R. J. Landreneau, T. S. Santucci, M. Y. Tung, R. S. Macherey, S. E. Shackney, C. D. Sturgis, S. S. Raab, J. F. Silverman, Prognostic value of immunohistochemical expressions of p53, HER-2/neu, and bcl-2 in stage I non-small-cell lung cancer, Hum. Pathol. 33 (2002) 105–110. https://doi.org/10.1053/hupa.2002.30183.
17. L. H. Schmidt, D. Görlich, T. Spieker, C. Rohde, M. Schuler, M. Mohr, J. Humberg, T. Sauer, N. H. Thoenissen, A. Huge, R. Voss, A. Marra, A. Faldum, C. Müller-Tidow, W. E. Berdel, R. Wiewrodt, Prognostic Impact of Bcl-2 Depends on Tumor Histology and Expression of MALAT-1 lncRNA in NonSmall-Cell Lung Cancer, J. Thorac. Oncol. 9 (2014) 1294–1304. https://doi.org/10.1097/JTO.0000000000000243.

18. R. Suzuki, V. J. Amatya, K. Kushitani, Y. Kai, T. Kambara, Y. Takeshima, miR-182 and miR-183 Promote Cell Proliferation and Invasion by Targeting FOXO1 in Mesothelioma, Front. Oncol. 8 (2018) 1–9. https://doi.org/10.3389/fonc.2018.00446.
19. J. Luo, K. Shi, S. Yin, R. Tang, W. Chen, L. Huang, T. Gan, Z. Cai, G. Chen, Clinical value of miR-182-5p in lung squamous cell carcinoma: a study combining data from TCGA, GEO, and RT-qPCR validation, World J. Surg. Oncol. 16 (2018) 76. https://doi.org/10.1186/s12957-018-1378-6.
20. L. Gao, S. Yan, J. Yang, J. Kong, K. Shi, F. Ma, L. Huang, J. Luo, S. Yin, R. He, X. Hu, G. Chen, MiR-182-5p and its target HOXA9 in non-small cell lung cancer: a clinical and in-silico exploration with the combination of RT-qPCR, miRNA-seq and miRNA-chip, BMC Med. Genomics. 13 (2020) 3. https://doi.org/10.1186/s12920-019-0648-7.
21. Y. Zhang, G. Talmon, J. Wang, MicroRNA-587 antagonizes 5-FU-induced apoptosis and confers drug resistance by regulating PPP2R1B expression in colorectal cancer, Cell Death Dis. 6 (2015) e1845–e1845. https://doi.org/10.1038/cddis.2015.200.
22. X. Zhang, J. Zhu, R. Xing, Y. Tie, H. Fu, X. Zheng, B. Yu, miR-513a-3p sensitizes human lung adenocarcinoma cells to chemotherapy by targeting GSTP1, Lung Cancer. 77 (2012) 488–494. https://doi.org/10.1016/j.lungcan.2012.05.107.
23. N. Dai, Y. Qing, Y. Cun, Z. Zhong, C. Li, S. Zhang, J. Shan, X. Yang, X. Dai, Y. Cheng, H. Xiao, C. Xu, M. Li, D. Wang, miR-513a-5p regulates radiosensitivity of osteosarcoma by targeting human apurinic/apyrimidinic endonuclease, Oncotarget. 9 (2018) 25414–25426. https://doi.org/10.18632/oncotarget.11003.

Economic Development Process: A Compartmental Analysis of a Model with Two Delays

A. B. Ndione, A. Mendy, and C. A. Onana

1 Introduction

Economic development always remains an interesting topic for economists. Reasons for such interests are simply due to the fact that economic growth is variable among nations. Generally, economic growth is a result of greater quantity and better quality of naturalnature, human, capital resources, and also technological advances that boost productivity (Chen [6]). Recall that economic development is the process by which a nation enhances its standard of living (Chen [6]). However, economic development is not a random phenomenon, and it is greatly influenced by the policies and attitudes of the governments as well as by the international environment.

Several models of economic growth and development have been created to give some insights to economic development problems, but the question of development remains a major concern, especially for African countries that are involved in programs to achieve the emergence on a given horizon. These models are based on econometric concepts, mathematical optimization models, and so on (Kumar [16], Intriligator [13]).

Since development is a dynamical process, it can be modeled by dynamical systems, and compartment models are among the most popular tools used to analyze dynamical systems. Compartmental models have been traditionally used in physiology to describe the distribution of a substance among different tissues of an organism. It has been extensively used in chemistry (Nicolis et al. [25], Ladde [17]),

A. B. Ndione (✉) · C. A. Onana
University of Yaounde I, National Advanced School of Engineering, Department of Mathematics and Physics, Yaoundé, Cameroon

A. Mendy
Cheikh Anta Diop University, Faculty of Science and Technics, Department of Mathematics and Computer Science, Dakar, Senegal

R. P. Mondaini (ed.), *Trends in Biomathematics: Chaos and Control in Epidemics, Ecosystems, and Cells*, https://doi.org/10.1007/978-3-030-73241-7_23

medicine (Anderson [1], Jacquez [14]), epidemiology (Murray [23]), ecology (Matis et al. [20]), and pharmacokinetics (Anderson [1], Solimano et al. [30]). Many of the models and methods developed in these fields can be usefully applied, by analogy, in the description of economical and social systems. There are not, however, so many applications in the economic literature. Among these works, Tramontana [31] uses the compartmental approach applied to a macroeconomic model characterized by companies that can go bankrupt each time they are unable to repay their debts. Artzrouni and Tramontana [2] developed a model that relies on two compartments, Government and Company, with cash flows between the compartments and the outside world.

The objective of this chapter is to build a dynamical compartmental model describing the process of growth and economic development. We consider a total of N countries that are subdivided into three compartments according to their economic status: $D(t)$ denotes the compartment of developing countries at time t, $E(t)$ stands for the compartment of emerging countries at time t, while $A(t)$ represents advanced countries at time t. (In the sequel, our model is termed as the DEA model.) We also include two delays that describe the average time necessary for collaborations between countries to become efficient for their development process. In fact, the results of the economic measures are not immediate; thus, several economic models with delays have been developed in these recent years (Huang et al. [12], Bélair et al. [3], Matsumoto et al. [21], Matsumoto A. and Szidarovszky F. [22], etc). In the light of the above, we rely on the properties of dynamical systems for model analysis. Numerical simulations on real economic data further illustrate our analytical results.

This chapter is organized as follows: we start by introducing the economic model in Sect. 2 and proceed to Sect. 3 where we describe the basic properties of the model. In Sects. 4 and 5, we describe the mathematical analysis of the model. In Sect. 6, numerical simulations are carried out to illustrate the main results.

2 The DEA Model

Our model is composed of three compartments characterized by countries according to the stage of development of their economies. As mentioned in our previous work (Ndione and Awono [24]), we use the World Economic Forum (WEF) classification in the Global Competitiveness Report (Schwab et al. [28]) to represent the compartments. WEF classifies a total of 140 countries into 3 categories. Based on this classification, we consider a first compartment named developing countries D represented by countries whose Gross Domestic Product (GDP) per capita is less than 3000 $ and characterized by four pillars of competitiveness that are: Institutions, Infrastructure, Macroeconomic stability, and Health and primary education. These pillars are the basic requirements for developing countries.

In the second compartment, we have emerging countries E. These countries have a GDP per capita between 3000 and 17,000 $ and are characterized by six pillars of

competitiveness that are: Higher education and training, Goods market efficiency, Labor market efficiency, Financial market sophistication, Technological readiness, and Market size. These pillars represent the efficiency enhancers that characterize emerging countries.

The advanced countries A are in the third compartment with a GDP per capita of more than 17,000 $ and characterized by two pillars: Business sophistication and Innovation.

For a developing country to be able to emerge, it must significantly improve its growth rate by acting on the efficiency factors. Thus, it will be able to increase its GDP per capita and be in the class of emerging economies. From the WEF equation of competitiveness (Schwab et al. [29]), we consider the function σ_1 the growth rate obtained with performances on the efficiency factors also using an international collaboration with the emerging countries E. In fact, the data show that the more countries there are involved in the collaborations, the greater the benefits are (Vicente et al. [32]). These collaborations are in the form of international programs such as official development assistance or Foreign Direct Investment, which have a positive and significant effect on the growth (Camelia and Sanjay [5], Hansen and Tarp [10], Collier and Dollar [7], Burnside and Dollar [4]).

We assume that developing countries are involved in collaboration just with emerging countries and these are in collaboration with the advanced countries.

To reach the advanced countries compartment, emerging countries must increase their GDP per capita, by acting on the innovation and sophistication factors. Let σ_2 be the growth rate obtained with performances made in the innovation and sophistication factors. We further assume that emerging countries are in collaboration with the advanced countries A.

Two delays τ_1 and τ_2 are included to characterize the necessary time before these collaborations with the emerging and advanced countries, respectively, become productive.

Another fact that unfortunately affects economies is the economic crisis. Countries are fragile to economic and financial crises. Although the origin of the crises begins in the major financial centers of the developed countries, we can see how it also affects the developing and emerging countries (Bruno [9]). Thus, we consider β_1 and β_2 to be the probabilities of economic crisis that can weaken the emerging and advanced countries, respectively, and make them change their economic status. β_1 and β_2 may be viewed as underperformances; thus, the time scale of underperformances can be considered longer than the time scale of the growth rates.

The process of economic development is illustrated in Fig. 1. The model is given analytically by the following system of delayed differential equations:

$$\begin{cases} \dot{D}(t) = \beta_1 E(t) - \sigma_1 E(t) D(t-\tau_1), \\ \dot{E}(t) = \sigma_1 E(t) D(t-\tau_1) + \beta_2 A(t) - \beta_2 E(t) - \sigma_2 A(t) E(t-\tau_2), \\ \dot{A}(t) = \sigma_2 A(t) E(t-\tau_2) - \beta_2 A(t). \end{cases} \tag{1}$$

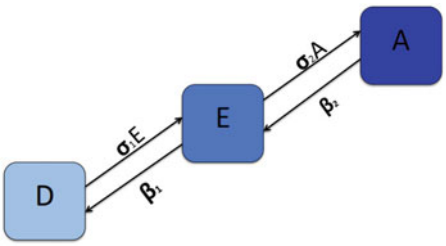

Fig. 1 The process of economic development

The positive initial conditions for the model are given by

$$D(\theta) = \psi_1(\theta), \quad E(\theta) = \psi_2(\theta),$$
$$A(\theta) = \psi_3(\theta), \quad \theta \in (-\tau, 0], \quad \psi_i \in \mathcal{C}\left((-\tau, 0], \mathbb{R}^+\right), i = 1, 2.$$

Now we present the analysis of model (1) by using theories of differential equations.

3 Basic Results

3.1 Positivity and Boundedness of Solutions

The first step is to show that solutions of the system remain nonnegative and are bounded, so that system is economically meaningful.

Lemma 3.1 *Solutions of system (1) are nonnegative and bounded.*

Proof Since $\dot{D}|_{D=0} > 0$, $\dot{E}|_{E=0} > 0$, and $\dot{A}|_{A=0} > 0$, solutions of system (1) remain nonnegative for $t \geq 0$. Furthermore, $\dot{D} + \dot{E} + \dot{A} = 0$, and thus $D(t) + E(t) + A(t) = D(0) + E(0) + A(0) = N$, where N is the total number of countries. Then, all the solutions of system are uniformly bounded. □

Since $\dot{D} + \dot{E} + \dot{A} = 0$ (the total number of countries is constant), the system (1) is conservative. We can study the system (1) using only the first two equations, and A can be computed by means of the following equation: $A(t) = N - D(t) - E(t)$.

Therefore, system (1) becomes

$$\begin{cases} \dot{D}(t) = \beta_1 E(t) - \sigma_1 E(t) D(t - \tau_1), \\ \dot{E}(t) = \sigma_1 E(t) D(t - \tau_1) + \sigma_2 D(t) E(t - \tau_2) + \sigma_2 E(t) E(t - \tau_2) \\ \qquad + \beta_2 N - \beta_2 D(t) - \sigma_2 N E(t - \tau_2) - (\beta_1 + \beta_2) E(t). \end{cases} \tag{2}$$

In the following, we will consider the system (2).

3.2 Equilibria

Equilibrium points of system (2) correspond to solutions of the algebraic system $\dot{D} = \dot{E} = 0$. Since any time delay does not change the equilibrium of the system, the following result holds.

Proposition 3.1 *The system (2) has three positive equilibria F_1, F_2, and F_3 defined by*

$$F_1 = (N, 0), \quad F_2 = \left(\frac{\beta_1}{\sigma_1}, N - \frac{\beta_1}{\sigma_1}\right), \quad \text{when } N - \frac{\beta_1}{\sigma_1} > 0. \quad \textit{and} \quad F_3 = \left(\frac{\beta_1}{\sigma_1}, \frac{\beta_2}{\sigma_2}\right).$$

Remark 3.1 These equilibria characterize the number of countries in each compartment. Thus, if we consider the system (1), with $A = N - D - E$, the equilibrium $F_1 = (N, 0, 0)$ means that all countries are underdeveloped, $F_2 = \left(\frac{\beta_1}{\sigma_1}, N - \frac{\beta_1}{\sigma_1}, 0\right)$ there are no advanced countries, and $F_3 = \left(\frac{\beta_1}{\sigma_1}, \frac{\beta_2}{\sigma_2}, N - \frac{\beta_1}{\sigma_1} - \frac{\beta_2}{\sigma_2}\right)$ is the equilibrium of coexistence which thatis the situation that corresponds to the current state of the economy. From the perspective of this model, considering the expression of equilibria, the economic class of each country may be described by the ratio of its underperformances on performances.

4 Stability Analysis of the System Without Delays ($\tau_1 = \tau_2 = 0$)

In this section, we deal with stability analysis of the aforementioned equilibria of system (2). We considered here that the system evolves without delays. This is motivated by the fact that if an equilibrium is unstable for system (2) without delays, it will remain unstable for system (2) with delays (Culshaw and Ruan [8], Martin and Ruan S [19]).

Let (D^*, E^*) be an equilibrium of system (2). The Jacobian matrix of system (2) at (D^*, E^*) reads as

$$\begin{pmatrix} -\sigma_1 E^* & \beta_1 - \sigma_1 D^* \\ (\sigma_1 + \sigma_2) E^* - \beta_2 & 2\sigma_2 E^* + (\sigma_1 + \sigma_2) D^* - (\beta_1 + \beta_2 + \sigma_2 N) \end{pmatrix}.$$

4.1 Local Stability Analysis for F_1

Theorem 1 *The equilibrium $F_1 = (N, 0)$ is a locally asymptotically stable node whenever $N - \frac{\beta_1}{\sigma_1} < 0$.*

Proof Considering $F_1 = (N, 0)$, the Jacobian matrix is

$$J(F_1) = \begin{pmatrix} 0 & \beta_1 - \sigma_1 N \\ -\beta_2 & \sigma_1 N - \beta_1 - \beta_2 \end{pmatrix}.$$

Let $trace(J(F_1)) = \sigma_1 N - \beta_1 - \beta_2$ and $det(J(F1)) = -\sigma_1 \beta_2 (N - \frac{\beta_1}{\sigma_1})$. Therefore, F_1 is locally asymptotically stable if $trace(J(F_1)) < 0$ and $det(J(F1)) > 0$, which leads to $N - \frac{\beta_1}{\sigma_1} - \frac{\beta_2}{\sigma_1} < 0$ and $N - \frac{\beta_1}{\sigma_1} < 0$.
In addition, since $\Delta = trace(J(F_1))^2 - 4det(J(F_1)) = (\sigma_1 N - (\beta_1 - \beta_2))^2 > 0$, eigenvalues of $J(F_1))$ are real. Therefore, F_1 is a locally asymptotically stable node if conditions of Theorem 1 hold. This ends the proof. □

4.2 Local Stability Analysis for F_2

Theorem 2 *The equilibrium $F_2 = \left(\frac{\beta_1}{\sigma_1}, N - \frac{\beta_1}{\sigma_1}\right)$ is a locally asymptotically stable node if $\frac{\beta_1}{\sigma_1} + \frac{\beta_2}{\sigma_2} > N$.*

Proof Considering the equilibrium F_2, the Jacobian matrix is $J(F_2) = \begin{pmatrix} \beta_1 - \sigma_1 N & 0 \\ (\sigma_1 + \sigma_2)(N - \frac{\beta_1}{\sigma_1}) - \beta_2 & \sigma_2 N - \frac{\beta_1 \sigma_2}{\sigma_1} - \beta_2 \end{pmatrix}$. The eigenvalues of the Jacobian matrix at F_2 are $\lambda_1 = \beta_1 - \sigma_1 N$ and $\lambda_2 = \sigma_2 N - \frac{\beta_1 \sigma_2}{\sigma_1} - \beta_2$. Therefore, F_2 is locally asymptotically stable if both eigenvalues are negatives. Since $\lambda_1 = -\sigma_1(N - \frac{\beta_1}{\sigma_1}) < 0$, then F_2 is stable if $\lambda_2 < 0$, which leads to $\frac{\beta_1}{\sigma_1} + \frac{\beta_2}{\sigma_2} > N$. □

4.3 Local Stability Analysis for F_3

Theorem 4.3 *The equilibrium $F_3 = \left(\frac{\beta_1}{\sigma_1}, \frac{\beta_2}{\sigma_2}\right)$ is locally asymptotically stable if $\frac{\beta_1}{\sigma_1} + \frac{\beta_2}{\sigma_2} < N$.*

Proof The Jacobian matrix at F_3 is $J(F_3) = \begin{pmatrix} -\frac{\beta_2 \sigma_1}{\sigma_2} & 0 \\ (\sigma_1+\sigma_2)\frac{\beta_2}{\sigma_2} - \beta_2 & \beta_2 + \frac{\beta_1 \sigma_2}{\sigma_1} - \sigma_2 N \end{pmatrix}$.

The eigenvalues of the Jacobian matrix at F_3 are $\lambda_1 = -\frac{\beta_2 \sigma_1}{\sigma_2}$ and $\lambda_2 = \beta_2 + \frac{\beta_1 \sigma_2}{\sigma_1} - \sigma_2 N$. Therefore, F_3 is locally asymptotically stable if $\lambda_2 < 0$, i.e., $\frac{\beta_1}{\sigma_1} + \frac{\beta_2}{\sigma_2} < N$. □

Remark 4.1 We notice that with the conditions of existence and stability, if F_2 is stable, then F_3 is unstable and the existence of F_2 implicates the unstability of F_1.

We summarize the statement of equilibria and condition for existence and stability in the following table:

Equilibrium	Expression	Condition for existence	Condition for stability
F_1	$(N, 0)$	No condition	$N - \frac{\beta_1}{\sigma_1} < 0$
F_2	$\left(\frac{\beta_1}{\sigma_1}, N - \frac{\beta_1}{\sigma_1}\right)$	$N - \frac{\beta_1}{\sigma_1} > 0$	$\frac{\beta_1}{\sigma_1} + \frac{\beta_2}{\sigma_2} > N$
F_3	$\left(\frac{\beta_1}{\sigma_1}, \frac{\beta_2}{\sigma_2}\right)$	No condition	$\frac{\beta_1}{\sigma_1} + \frac{\beta_2}{\sigma_2} < N$

Stability allows us to move from an initial condition (D_0, E_0) to a new equilibrium state (D_1, E_1). Then, it is possible to act on the parameters so that the number of developing countries decreases $(D_0 > D_1)$, while that of emerging countries increases $(E_0 < E_1)$ as long as the conditions of equilibrium stability is verified (Fig. 2).

The condition for stability of F_1 is equivalent to $N\sigma_1 < \beta_1$. This means that as long as the underperformance exceeds the performance of all countries, there will be no change in economic status and all countries will remain in phase one. Therefore, F_2 exists if and only if $N\sigma_1 > \beta_1$, with the condition for stablity $\beta_1\sigma_2 + \beta_2\sigma_1 > \sigma_1\sigma_2 N$. The condition for stability of the coexistence equilibrium F_3 is equivalent to $\beta_1\sigma_2 + \beta_2\sigma_1 < \sigma_1\sigma_2 N$, which means that the combined performance of all countries must be greater than the sum of the product of the performance of the developing countries and the underperformance of the emerging countries and the opposite product.

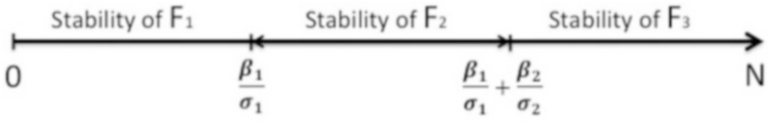

Fig. 2 Equilibria stability

We analyze in the next section the model when the delays τ_1 and τ_2 are positive.

5 Stability Analysis of the System with Time Delays

In this section, we study the stability of equilibria in the presence of discrete delays $\tau_1 > 0$ and $\tau_2 > 0$. It is well known that if an equilibrium is unstable for $\tau_1 = \tau_2 = 0$, it remains unstable for $\tau_1 > 0$, $\tau_2 > 0$ (Culshaw and Ruan [8], Martin and Ruan [19]). Therefore, throughout this section, we assume that stability conditions of F_1, F_2, and F_3 hold.

5.1 Linearization and Characteristic Equation

We first linearize the system (2) around an equilibrium $F = (D^*, E^*)$ and deduce the characteristic equation.

Setting $u(t) = D(t) - D^*$ and $v(t) = E(t) - E^*$, the linearized system (2) around $F = (D^*, E^*)$ is then given by

$$\begin{cases} \dot{u}(t) = (\beta_1 - \sigma_1 D^*)\, v(t) - \sigma_1 E^*\, u(t-\tau_1), \\ \\ \dot{v}(t) = (\sigma_1 D^* + \sigma_2 E^* - (\beta_1 + \beta_2))\, v(t) + (\sigma_2 E^* - \beta_2)\, u(t) \\ \qquad + \sigma_1 E^* u(t-\tau_1) + (\sigma_2 D^* + \sigma_2 E^* + \sigma_2 N)\, v(t-\tau_2). \end{cases} \tag{3}$$

Define

$$A_0 = \begin{pmatrix} 0 & \beta_1 - \sigma_1 D^* \\ \sigma_2 E^* - \beta_2 & \sigma_1 D^* + \sigma_2 E^* - (\beta_1 + \beta_2) \end{pmatrix};$$

$$A_1 = \begin{pmatrix} -\sigma_1 E^* & 0 \\ \sigma_1 E^* & 0 \end{pmatrix}; \text{ and } A_2 = \begin{pmatrix} 0 & 0 \\ 0 & \sigma_2 D^* + \sigma_2 E^* - \sigma_2 N \end{pmatrix}.$$

The characteristic equation associated with (3) is given by

$$\Delta(\lambda, \tau_1, \tau_2) = \lambda\, I_2 - A_0 - A_1\, e^{-\lambda \tau_1} - A_2\, e^{-\lambda \tau_2} = 0. \tag{4}$$

Let $a_1 = \beta_1 - \sigma_1 D^*$, $a_2 = \sigma_2 E^* - \beta_2$, $a_3 = \sigma_1 D^* + \sigma_2 E^* - (\beta_1 + \beta_2)$, $b_1 = -\sigma_1 E^*$, $b_2 = \sigma_1 E^*$, and $c = \sigma_2 D^* + \sigma_2 E^* - \sigma_2 N$.

After simplifications, Eq. 4 becomes

$$\Delta(\lambda, \tau_1, \tau_2) = P_0(\lambda) + P_1(\lambda) e^{-\lambda \tau_1} + P_2(\lambda) e^{-\lambda \tau_2} + P_3(\lambda) e^{-\lambda(\tau_1 + \tau_2)} = 0, \tag{5}$$

where $P_0(\lambda) = \lambda^2 - a_3\, \lambda - a_1\, a_2$, $P_1(\lambda) = -b_1\, \lambda + a_3\, b_1 - a_1\, b_2$, $P_2(\lambda) = -c\, \lambda$, and $P_3(\lambda) = b_1\, c$.

5.2 Stability Analysis When $\tau_1 > 0$ and $\tau_2 = 0$

5.2.1 Stability Analysis at Equilibrium F_1

When $\tau_1 > 0$ and $\tau_2 = 0$, the characteristic equation at $F_1 = (N, 0)$ is given by
$\Delta(\lambda, \tau_1) = \lambda^2 - (\sigma_1 N - \beta_1 - \beta_2)\lambda + \beta_2(\beta_1 - \sigma_1 N) = 0.$
The characteristic equation is independent of the delay τ_1, and then F_1 retains its stability when $\tau_1 > 0$ and $\tau_2 = 0$.

5.2.2 Stability Analysis at Equilibrium F_2

When $\tau_1 > 0$ and $\tau_2 = 0$, the characteristic equation at $F_2 = \left(\frac{\beta_1}{\sigma_1}, N - \frac{\beta_1}{\sigma_1}\right)$ is given by

$$\Delta(\lambda, \tau_1) = \lambda^2 + (\beta_2 - \sigma_2 E^*)\lambda + (\sigma_1 E^* \lambda + (\beta_2 - \sigma_2 E^*)\sigma_1 E^*)\, e^{-\lambda \tau_1} = 0.$$

For reader's convenience, let us set $p = \beta_2 - \sigma_2 E^*$, $q = (\beta_2 - \sigma_2 E^*)\sigma_1 E^*$, and $s = \sigma_1 E^*$, and then

$$\Delta(\lambda, \tau_1) = \lambda^2 + p\lambda + (s\lambda + q)\, e^{-\lambda \tau_1} = 0. \tag{6}$$

Stability analysis and Hopf bifurcation

It is known that the steady state is asymptotically stable if all roots of the characteristic equation (6) have negative real parts. In order to investigate the stability of the positive equilibrium F_2 of system (2), we need to study the distribution of roots of Eq. (6).

We want to determine if the real part of some root increases to reach zero and eventually becomes positive as τ_1 varies. If $i\omega(\omega > 0)$ is a root of Eq. (6), then

$$-\omega^2 + ip\omega + is\omega\cos(\omega\tau_1) + s\omega\sin(\omega\tau_1) + q\cos(\omega\tau_1) - iqp\sin(\omega\tau_1) = 0. \tag{7}$$

Separating the real and imaginary parts, we have

$$\begin{cases} -\omega^2 = -q\cos(\omega\tau_1) - s\omega\sin(\omega\tau_1). \\ p\omega = -s\omega\cos(\omega\tau_1) + q\sin(\omega\tau_1). \end{cases} \tag{8}$$

It follows that ω satisfies

$$\omega^4 + (p^2 - s^2)\omega^2 - q^2 = 0. \tag{9}$$

Let $\Delta = (p^2 - s^2)^2 + 4q^2$.

Since $\Delta > 0$ and $-q^2 < 0$, then Eq. (9) has a unique positive root ω_0^2. Therefore, the characteristic equation (6) has purely imaginary roots when τ_1 takes certain values. These critical values τ_{1j} of τ_1 can be determined from (8). They are given by

$$\tau_{1j} = \frac{1}{\omega_0} \arccos\left(\frac{q\omega_0^2 - ps\omega_0^2}{s^2\omega_0^2 + q^2}\right) + \frac{2\pi j}{\omega_0}, \; j = 0, 1, 2, .. \tag{10}$$

at which Eq. 6 has a pair of purely imaginary roots $\pm i\omega$.

Let $\lambda(\tau_1) = \alpha(\tau_1) + i\omega(\tau_1)$ be a root of Eq. (6) near $\tau_1 = \tau_{1j}$ with $\alpha(\tau_{1j}) = 0$, $\omega(\tau_{1j}) = \omega_0$. From functional differential equation theory, for every τ_{1j}, $j = 0, 1, 2, \cdots$, there exists $\epsilon > 0$ such that $\lambda(\tau_1)$ is continuously differentiable at τ_1 for $|\tau_1 - \tau_{1j}| < \epsilon$. Substituting $\lambda(\tau_1)$ into (6) and taking the derivative with respect to τ_1, we obtain

$$\left[\frac{d\lambda}{d\tau_1}\right]^{-1} = \frac{2\lambda + p}{\lambda(s\lambda + q)e^{-\lambda\tau_1}} + \frac{s}{(s\lambda + q)e^{-\lambda\tau_1}} - \frac{\tau_1}{\lambda}.$$

Since $2\lambda^2 + \lambda P = \lambda^2 - (s\lambda + q)e^{-\lambda\tau_1}$, we obtain

$$\begin{aligned}\left[\frac{d\lambda}{d\tau_1}\right]^{-1} &= \frac{1}{(s\lambda + q)e^{-\lambda\tau_1}} - \frac{1}{\lambda^2} + \frac{s\lambda}{\lambda^2(s\lambda + q)} - \frac{\tau_1}{\lambda}, \\ &= \frac{1}{-(\lambda^2 + q)} - \frac{q}{\lambda^2(s\lambda + q)} - \frac{\tau_1}{\lambda};\end{aligned}$$

thus,

$$\begin{aligned}sign\left\{\frac{d(Re\lambda(\tau_1))}{d\tau_1}\right\}\Big|_{\lambda = i\omega_0} &= sign\left\{Re\left(\frac{d\lambda}{d\tau_1}\right)^{-1}\right\}, \\ &= sign\left\{\frac{\omega_0^2}{\omega_0^4 + p^2\omega_0^2} + \frac{q^2}{\omega_0^2(s^2\omega_0^2 + q)}\right\}.\end{aligned}$$

Since $q > 0$, we have $\dfrac{d}{d\tau_1}(Re\lambda(\tau_1)) > 0$.

Thus, from the previous discussions, we can obtain the following results about the distribution of the characteristic roots of Eq. (8) (Ruan [26]).

Lemma 5.1 *Let τ_{1j} $(j = 0, 1, 2, \ldots)$ be defined by (10), and when $\tau_1 \in [0, \tau_{1j})$ all roots of Eq. (6) have negative real parts, when $\tau_1 = \tau_{1j}$ Eq. (6) has a pair of purely imaginary roots $\pm i\omega_0$, and when $\tau_1 > \tau_{1j}$ Eq. (6) has at least one root with positive real part.*

Applying the above lemma, we then obtain the following theorem:

Theorem 5.1 *Let* $\tau_1^0 = \min_{j=0,1,2,\ldots} \tau_{1j}$, *and then the positive equilibrium* F_2 *is asymptotically stable if* $\tau_1 \in [0, \tau_1^0)$, *and unstable for* $\tau_1 > \tau_1^0$. *Furthermore, system 2 undergoes a Hopf bifurcation at equilibrium* F_2 *when* $\tau_1 = \tau_1^0$.

Direction and stability of the Hopf bifurcation

In the previous section, we obtain the conditions under which the system (2) undergoes Hopf bifurcation from the positive steady state F_2 at the critical values of τ_1. Using the normal form theory and center manifold reduction by Hassard et al. [11], we are able to determine the Hopf bifurcation direction and investigate the properties of these bifurcating periodic solutions, for example, stability on the center manifold and period. Throughout this section, we always assume that the system (2) undergoes Hopf bifurcations at the critical value τ_1^0 of τ_1, and then $\pm\omega_0$ is the corresponding purely imaginary roots of the characteristic equation associated with the positive steady state F_2. Renaming $x_1(t) = D(t) - D^*$, and $x_2(t) = E(t) - E^*$, then the system (2) is equivalent to

$$\begin{cases} \dot{x_1}(t) = -\sigma_1 E^* x_1(t-\tau_1) + f_1(x_1(t-\tau_1), x_2(t)) \\ \\ \dot{x_2}(t) = (\sigma_1 D^* + \sigma_2 D^* - \beta_1 - \beta_2 - \sigma_2 N) x_2(t) \\ \qquad + (\sigma_2 E^* - \beta_2) x_1(t) + \sigma_1 E^* x_1(t-\tau_1) + f_2(x_1(t), x_2(t), x_1(t-\tau_1)) \end{cases}, \tag{11}$$

where $f_1(x_1(t-\tau_1), x_2(t) = -\sigma_1 x_2(t) x_1(t-\tau_1)$,
$f_2(x_1(t), x_2(t), x_1(t-\tau_1)) = \sigma_1 x_1(t) x_2(t-\tau_1) + \sigma_2 x_1(t) x_2(t) + \sigma_2 x_2^2(t)$.

Let $\tau_1 = \tau^* + \mu$, and then $\mu = 0$ is the Hopf bifurcation value of system (2) at the positive equilibrium F_2. Since the system (2) is equivalent to system (11) in what follows we consider the system (11).
Let $u_i(t) = x_i(\tau_1 t)$, and then the system (11) can be rewritten as follows:

$$\begin{cases} \dot{u_1}(t) = (\tau^* + \mu)\left[-\sigma_1 E^* u_1(t-\tau_1) + f_1(u_1(t-\tau_1), u_2(t)\right], \\ \\ \dot{u_2}(t) = (\tau^* + \mu)\big[((\sigma_1 + \sigma_2) D^* + 2\sigma_2 E^* - \beta_1 - \beta_2 - \sigma_2 N) u_2(t) \\ \qquad + (\sigma_2 E^* - \beta_2) u_1(t) + \sigma_1 E^* u_1(t-\tau_1) + f_2(u_1(t), u_2(t), u_1(t-\tau_1))\big]. \end{cases} \tag{12}$$

If we consider the equilibrium F_2, we have $D^* = \dfrac{\beta_1}{\sigma_1}$ and $E^* = N - \dfrac{\beta_1}{\sigma_1}$, then

$$(\sigma_1 + \sigma_2) D^* + 2\sigma_2 E^* - \beta_1 - \beta_2 - \sigma_2 N = \sigma_2 (N - \frac{\beta_1}{\sigma_1}) - \beta_2 = \sigma_2 E^* - \beta_2.$$

The system (12) is transformed into a functional differential equation (FDE) in $C = C([-1, 0], \mathbb{R}^2)$ as

$$\dot{u}(t) = L_\mu(u_t) + f(\mu, u_t), \tag{13}$$

where $u(t) = (u_1(t), u_2(t))^T \in \mathbb{R}^2$, $L_\mu : C \leftrightarrow \mathbb{R}$ is the linear operator and $f : \mathbb{R} \times C \leftrightarrow \mathbb{R}$ is given, respectively, by

$$L_\mu(\phi) = (\tau_1^0 + \mu)\begin{pmatrix} 0 & 0 \\ \sigma_2 E^* - \beta_2 & \sigma_2 E^* - \beta_2 \end{pmatrix}\begin{pmatrix} \phi_1(0) \\ \phi_2(0) \end{pmatrix} + (\tau_1^0 + \mu)\begin{pmatrix} -\sigma_1 E^* & 0 \\ \sigma_1 E^* & 0 \end{pmatrix}\begin{pmatrix} \phi_1(-1) \\ \phi_2(-1) \end{pmatrix} \tag{14}$$

and

$$f(\phi, \mu) = (\tau_1^0 + \mu)\begin{pmatrix} f_1(\phi(-1), \phi_2(0)) \\ f_2(\phi_1(0), \phi_2(0), \phi_1(-1)) \end{pmatrix}, \tag{15}$$

where $\phi = (\phi_1, \phi_2)^T$.

By the Riesz representation theorem, there exists a function $\eta(\theta, \mu)$ of bounded variation for $\theta \in [-1, 0]$, such that

$$L_\mu(\phi) = \int_{-1}^{0} d\eta(\theta, \mu)\phi(\theta), \text{for} \phi \in C. \tag{16}$$

In fact, we can choose

$$\eta(\theta, \mu) = (\tau_1^0+\mu)\begin{pmatrix} 0 & 0 \\ \sigma_2 E^* - \beta_2 & \sigma_2 E^* - \beta_2 \end{pmatrix}\delta(\theta) - (\tau_1^0+\mu)\begin{pmatrix} -\sigma_2 E^* & 0 \\ \sigma_2 E^* & 0 \end{pmatrix}\delta(\theta+1), \tag{17}$$

where δ is defined by

$$\delta(\theta) = \begin{cases} 0, \ \theta \neq 0, \\ 1, \ \theta = 0. \end{cases} \tag{18}$$

For $\phi \in C([-1, 0], \mathbb{R}^2)$, define

$$A(\mu)\phi = \begin{cases} \dfrac{d\phi(\theta)}{d\theta}, & \theta \in [-1, 0), \\ \int_{-1}^{0} d\eta(\mu, s)\phi(s)), & \theta = 0, \end{cases} \tag{19}$$

and

$$R(\mu)\phi = \begin{cases} 0, & \theta \in [-1, 0), \\ f(\mu, \phi), & \theta = 0. \end{cases} \tag{20}$$

Then, the system (13) is equivalent to

$$\dot{u}(t) = A(\mu)u_t + R(\mu)u_t, \tag{21}$$

where $u_t(\theta) = u(t+\theta)$ for $\theta \in [1, 0]$.
For $\psi \in C^1([0,1], \mathbb{R}^2)$, define

$$A^*\psi(s) = \begin{cases} \dfrac{d\psi(s)}{ds}, & s \in (0,1], \\ \int_{-1}^{0} d\eta^T(t,0)\psi(-t), & s = 0, \end{cases} \tag{22}$$

and a bilinear inner product

$$< \psi(s), \phi(\theta) >= \bar{\psi}(0)\phi(0) - \int_{-1}^{0}\int_{\xi=0}^{\theta} \bar{\psi}(\xi-\theta)d\eta(\theta)\phi(\xi)d\xi, \tag{23}$$

where $\eta(\theta) = \eta(\theta, 0)$. Then, $A(0)$ and A^* are the adjoint operators. We know that $\pm i w_0 \tau_1^*$ are eigenvalues of $A(0)$. Thus, they are also eigenvalues of A^*. Let $q(\theta)$ be the eigenvector corresponding to $+i w_0 \tau_1^*$ and $q^*(\theta)$ be the eigenvector of A^* corresponding to $-i w_0 \tau_1^*$.

Suppose that $q(\theta) = (1, \alpha)^\top e^{i\theta w_0 \tau_1^0}$ is the eigenvector of $A(0)$ corresponding to $+i w_0 \tau_1^0$. Then, $A(0)q(0) = i w_0 \tau_1^0 q(0)$.
It follows from the definition of $A(0)$ and (16 and (17) that

$$\begin{pmatrix} i\omega_0 + \sigma_1 E^* e^{-i w_0 \tau_1^0} & 0 \\ -\sigma_2 E^* + \beta_2 - \sigma_1 E^* e^{-i w_0 \tau_1^0} & i w_0 - \sigma_2 E^* + \beta_2 \end{pmatrix} q(0) = \begin{pmatrix} 0 \\ 0 \end{pmatrix}. \tag{24}$$

Thus, we can easily obtain

$$q(0) = (1, \alpha)^\top = \left(1, \frac{\sigma_2 E^* - \beta_2 + \sigma_1 E^* e^{-i w_0 \tau_1^0}}{i w_0 - \sigma_2 E^* + \beta_2}\right)^\top.$$

On the other hand, suppose that $q^*(s) = D(1, \alpha^*)^\top e^{is w_0 \tau_1^0}$ is the eigenvector of A^* corresponding to $-i w_0 \tau_1^0$. Then, $A^*(0)q^*(0) = i w_0 \tau_1^0 q^*(0)$. By the definition of A^* and (16) and (17), we have

$$\begin{pmatrix} -i w_0 + \sigma_1 E^* e^{-i w_0 \tau_1^0} & -\sigma_2 E^* + \beta_2 - \sigma_1 E^* e^{-i w_0 \tau_1^0} \\ 0 & -i w_0 - \sigma_2 E^* + \beta_2 \end{pmatrix} (q^*(0))^\top = \begin{pmatrix} 0 \\ 0, \end{pmatrix} \tag{25}$$

which means that

$$q^*(0) = D\left(1, \frac{-i w_0 + \sigma_1 E^* e^{-i w_0 \tau_1^0}}{\sigma_2 E^* - \beta_2 + \sigma_1 E^* e^{-i w_0 \tau_1^0}}\right)^\top.$$

In order to have $< q^*(s), q(\theta) >= 1$, we need to determine the value of D. From (23), we have

$$\begin{aligned} < q^*(s), q(\theta) > &= \bar{q^*}(0)q(0) - \int_{-1}^{0}\int_{\xi=0}^{\theta} \bar{q}(\xi-\theta)d\eta(\theta)\phi(\xi)d\xi \\ &= \bar{D}\left\{1 + \bar{\alpha^*}\alpha - \int_{-1}^{0}(1,\alpha^*)\theta e^{iw_0\theta\tau_1^0}d\eta(\theta)(1,\alpha)^\top\right\} \\ &= \bar{D}\left\{1 + \bar{\alpha^*}\alpha + \tau_1^0\sigma_1 E^*(\alpha^*-1)e^{-iw_0\tau_1^0}top\right\}. \end{aligned}$$

So we have

$$\bar{D} = \frac{1}{1 + \bar{\alpha^*}\alpha + \tau_1^0\sigma_1 E^*(\alpha^*-1)e^{-iw_0\tau_1^0}}, \tag{26}$$

$$D = \frac{1}{1 + \alpha^*\bar{\alpha} + \tau_1^0\sigma_1 E^*(\alpha^*-1)e^{iw_0\tau_1^0}}. \tag{27}$$

In the remainder of this section, we use the same notations as in Hassard et al. [11], and we first compute the coordinate to describe the center manifold C_0 at $\mu = 0$. Let u_t be the solution of Eq. (13) when $\mu = 0$. Define

$$z_0(t) = < q^*, \mu_t >, W(t,\theta) = \mu_t(\theta) - 2Re(z_0(t)q(\theta)) = \mu_t(\theta) - (z_0(t)q(\theta) + \bar{z_0}(t)\bar{q}(\theta)). \tag{28}$$

On the center manifold C_0, we have

$$W(t,\theta) = W(z_0, \bar{z_0}, \theta), \tag{29}$$

where

$$W(z_0, \bar{z_0}, \theta) = W_{20}(\theta)\frac{z_0^2}{2} + W_{11}(\theta)z_0\bar{z_0} + W_{02}(\theta)\frac{\bar{z_0}^2}{2} + \ldots, \tag{30}$$

z_0 and $\bar{z_0}$ are the local coordinates for center manifold on C_0 in the direction of q^* and $\bar{q^*}$. Note that W is real if u_t is real. We consider only real solutions. For the solution $u_t \in C_0$ of (13), since $\mu = 0$, we have

$$\dot{z_0}(t) = iw_0\tau_1^0 z_0 + \bar{q^*} f\,(0, w(z_0, \bar{z_0}, 0) + 2Re(z_0 q(\theta))) \stackrel{def}{=} iw_0\tau_1^0 z_0 + \bar{q^*}(0)\, f_0(z_0, \bar{z_0}). \tag{31}$$

We rewrite this equation as

$$z_0(t) = iw_0\tau_1^0 z_0 + p(z_0, \bar{z_0}), \tag{32}$$

with

$$p(z_0,\bar{z_0}) = \bar{q^*}(0)\, f_0(z_0,\bar{z_0}) = p_{20}(\theta)\frac{z_0^2}{2} + p_{11}(\theta) z_0\bar{z_0} + p_{02}(\theta)\frac{\bar{z_0}^2}{2} + p_{21}(\theta)\frac{z_0^2\bar{z_0}}{2} + \cdots . \tag{33}$$

Remark 5.1 In what follows, our objective is to compute coefficients p_{20}, p_{11}, p_{02}, and p_{21} of $p(z_0, \bar{z_0})$. These coefficients will be used to find the direction of the Hopf bifurcation.

We have $u_t(\theta) = (u_{1t}(\theta), u_{2t}(\theta))$ and $q(\theta) = (1,\alpha)^\top e^{iw_0\tau_1^0\theta}$. From (28) and (30), we have

$$\begin{aligned} u_t(\theta) &= w(t,\theta) + 2Re(z_0(t)q(\theta)), \\ &= w(t,\theta) + z_0(t)q(\theta) + \bar{z_0}(t)\bar{q}(\theta), \\ &= W_{20}(\theta)\frac{z_0^2}{2} + W_{11}(\theta) z_0\bar{z_0} + W_{02}(\theta)\frac{\bar{z_0}^2}{2} \\ &\quad + (1,\alpha)^\top e^{iw_0\tau_1^0\theta} + (1,\bar{\alpha})^\top e^{-iw_0\tau_1^0\theta} + \cdots , \end{aligned} \tag{34}$$

and then we have

$$\begin{aligned} u_{1t}(0) &= z_0 + \bar{z_0} + W_{20}^{(1)}(0)\tfrac{z_0^2}{2} + W_{11}^{(1)}(0) z_0\bar{z_0} + W_{02}^{(1)}(0)\tfrac{\bar{z_0}^2}{2} + \cdots , \\ u_{2t}(0) &= \alpha z_0 + \bar{\alpha}\bar{z_0} + W_{20}^{(2)}(0)\tfrac{z_0^2}{2} + W_{11}^{(2)}(0) z_0\bar{z_0} + W_{02}^{(2)}(0)\tfrac{\bar{z_0}^2}{2} + \cdots , \\ u_{1t}(-1) &= z_0 e^{-iw_0\tau_1^0} + \bar{z_0} e^{iw_0\tau_1^0} + W_{20}^{(1)}(-1)\tfrac{z_0^2}{2} + W_{11}^{(1)}(-1) z_0\bar{z_0} + W_{02}^{(1)}(-1)\tfrac{\bar{z_0}^2}{2} + \cdots , \\ u_{2t}(-1) &= z_0\alpha e^{-iw_0\tau_1^0} + \bar{z_0}\bar{\alpha} e^{iw_0\tau_1^0} + W_{20}^{(2)}(-1)\tfrac{z_0^2}{2} + W_{11}^{(2)}(-1) z_0\bar{z_0} + W_{02}^{(2)}(-1)\tfrac{\bar{z_0}^2}{2} + \cdots . \end{aligned} \tag{35}$$

It follows together with Eq. (15) that

$$\begin{aligned} p(z_0,\bar{z_0}) &= \bar{q^*}(0)\, f_0(z_0,\bar{z_0}) = \bar{q^*}(0)\, f(0,u_t), \\ &= \tau_1^0 \bar{D}(1,\bar{\alpha^*}) \begin{pmatrix} -\sigma_1 u_{2t}(0) u_{1t}(-1) \\ \sigma_1 u_{2t}(0) u_{1t}(-1) + \sigma_2 u_{1t}(0) u_{2t}(0) + \sigma_2 u_{2t}^2(0) \end{pmatrix}, \\ &= \tau_1^0 \bar{D}\left\{ -\sigma_1 u_{2t}(0) u_{1t}(-1) + \bar{\alpha^*}(\sigma_1 u_{2t}(0) u_{1t}(-1) + \sigma_2 u_{1t}(0) u_{2t}(0) + \sigma_2 u_{2t}^2(0) \right\}. \end{aligned} \tag{36}$$

Using the expressions in (35), we have

$$\begin{aligned} p(z_0,\bar{z_0}) &= \tau_1^0 \bar{D}\big\{ -\sigma_1(\alpha z_0 + \bar{\alpha}\bar{z_0} + W_{20}^{(2)}(0)\tfrac{z_0^2}{2} + W_{11}^{(2)}(0) z_0\bar{z_0} + W_{02}^{(2)}(0)\tfrac{\bar{z_0}^2}{2}) \\ &\quad \times (z_0 e^{-iw_0\tau_1^0} + \bar{z_0} e^{iw_0\tau_1^0} + W_{20}^{(1)}(-1)\tfrac{z_0^2}{2} + W_{11}^{(1)}(-1) z_0\bar{z_0} + W_{02}^{(1)}(-1)\tfrac{\bar{z_0}^2}{2}) \\ &\quad + \bar{\alpha^*}(\alpha z_0 + \bar{\alpha}\bar{z_0} + W_{20}^{(2)}(0)\tfrac{z_0^2}{2} + W_{11}^{(2)}(0) z_0\bar{z_0} + W_{02}^{(2)}(0)\tfrac{\bar{z_0}^2}{2}) \\ &\quad \times \big[\sigma_1(z_0 e^{-iw_0\tau_1^0} + \bar{z_0} e^{iw_0\tau_1^0} + W_{20}^{(1)}(-1)\tfrac{z_0^2}{2} + W_{11}^{(1)}(-1) z_0\bar{z_0} + W_{02}^{(1)}(-1)\tfrac{\bar{z_0}^2}{2}) \\ &\quad + \sigma_2(z_0 + \bar{z_0} + W_{20}^{(1)}(0)\tfrac{z_0^2}{2} + W_{11}^{(1)}(0) z_0\bar{z_0} + W_{02}^{(1)}(0)\tfrac{\bar{z_0}^2}{2}) \\ &\quad + \sigma_2(\alpha z_0 + \bar{\alpha}\bar{z_0} + W_{20}^{(2)}(0)\tfrac{z_0^2}{2} + W_{11}^{(2)}(0) z_0\bar{z_0} + W_{02}^{(2)}(0)\tfrac{\bar{z_0}^2}{2})\big]\big\}. \end{aligned} \tag{37}$$

After calculation, we have

$$
\begin{aligned}
p(z_0,\bar{z}_0) &= \tfrac{z_0^2}{2}\left\{2\tau_1^0\bar{D}\left[(\bar{\alpha}^*-\alpha)\sigma_1 e^{-iw_0\tau_1^0}+\sigma_2\alpha(\alpha+\bar{\alpha}^*)\right]\right\}\\
&+\tfrac{\bar{z}_0^2}{2}\left\{2\tau_1^0\bar{D}\left[(\bar{\alpha}^*-1)\sigma_1\bar{\alpha}e^{iw_0\tau_1^0}+\sigma_2\bar{\alpha}(\bar{\alpha}+\bar{\alpha}^*)\right]\right\}\\
&+z_0\bar{z}_0\left\{\tau_1^0\bar{D}[(\bar{\alpha}^*-\alpha)\sigma_1 e^{iw_0\tau_1^0}+(\bar{\alpha}^*-1)\sigma_1\bar{\alpha}e^{-iw_0\tau_1^0}\right.\\
&\left.+\sigma_2\bar{\alpha}^*(\alpha+\bar{\alpha}+2\alpha\bar{\alpha}]\right\}\\
&+\tfrac{z_0^2\bar{z}_0}{2}\left\{\tau_1^0\bar{D}[(\bar{\alpha}^*W_{20}^{(1)}(0)-W_{20}^{(2)}(0))\sigma_1 e^{iw_0\tau_1^0}+(\bar{\alpha}^*W_{11}^{(1)}(0)-W_{11}^{(2)}(0))2\sigma_1 e^{-iw_0\tau_1^0}\right.\\
&+\sigma_1(\bar{\alpha}^*-1)2\alpha W_{11}^{(1)}(-1)+\sigma_1(\bar{\alpha}^*-1)\bar{\alpha}W_{20}^{(1)}(-1)\\
&+2\sigma_2\alpha\bar{\alpha}^*(W_{11}^{(1)}(0)+W_{11}^{(2)}(0))+\sigma_2\bar{\alpha}\bar{\alpha}^*(W_{20}^{(1)}(0)+W_{20}^{(2)}(0))\\
&\left.+\sigma_2(1+\bar{\alpha})\bar{\alpha}^*W_{20}^{(1)}(0)+\sigma_2(1+\alpha)2\bar{\alpha}^*W_{11}^{(2)}(0)]\right\}.
\end{aligned}
\tag{38}
$$

Comparing the coefficients with (33), we obtain

$$
\begin{aligned}
p_{20} &= 2\tau_1^0\bar{D}\left[\alpha(\sigma_2\alpha-\sigma_1 e^{-iw_0\tau_1^0})+\bar{\alpha}^*(\sigma_2\alpha+\sigma_1 e^{-iw_0\tau_1^0})\right]\\
p_{02} &= 2\tau_1^0\bar{D}\left[\bar{\alpha}(\sigma_2\bar{\alpha}-\sigma_1 e^{iw_0\tau_1^0})+\bar{\alpha}^*(\sigma_2\bar{\alpha}+\sigma_1 e^{iw_0\tau_1^0})\right]\\
p_{11} &= \tau_1^0\bar{D}\left[-\sigma_1(\alpha e^{iw_0\tau_1^0}+\bar{\alpha}e^{-iw_0\tau_1^0})+\bar{\alpha}^*\left\{\sigma_1(\alpha e^{iw_0\tau_1^0}+\bar{\alpha}e^{-iw_0\tau_1^0})+\sigma_2(\alpha+\bar{\alpha}+2\alpha\bar{\alpha})\right\}\right]\\
p_{21} &= \tau_1^0\bar{D}\big[(\bar{\alpha}^*W_{20}^{(1)}(0)-W_{20}^{(2)}(0))\sigma_1 e^{iw_0\tau_1^0}+(\bar{\alpha}^*W_{11}^{(1)}(0)-W_{11}^{(2)}(0))2\sigma_1 e^{-iw_0\tau_1^0}\\
&+\sigma_1(\bar{\alpha}^*-1)2\alpha W_{11}^{(1)}(-1)+\sigma_1(\bar{\alpha}^*-1)\bar{\alpha}W_{20}^{(1)}(-1)\\
&+2\sigma_2\alpha\bar{\alpha}^*(W_{11}^{(1)}(0)+W_{11}^{(2)}(0))+\sigma_2\bar{\alpha}\bar{\alpha}^*(W_{20}^{(1)}(0)+W_{20}^{(2)}(0))\\
&+\sigma_2(1+\bar{\alpha})\bar{\alpha}^*W_{20}^{(1)}(0)+\sigma_2(1+\alpha)2\bar{\alpha}^*W_{11}^{(2)}(0)\big].
\end{aligned}
\tag{39}
$$

Since there are W_{20} and W_{11} in p_{21}, in the sequel we shall compute them.

From (21) and (28), we have

$$
\begin{aligned}
\dot{W} = \dot{u}_t - z_0 q - \dot{\bar{z}}_0\bar{q} &= \begin{cases} AW - 2Re\{\bar{q}^* f_0 q(\theta)\}, & \theta\in[-1,0),\\ AW - 2Re\{\bar{q}^* f_0 q(0)\} + f_0, & \theta = 0,\end{cases}\\
&\overset{def}{=} AW + H(z_0,\bar{z}_0,\theta),
\end{aligned}
\tag{40}
$$

where

$$
H(z_0,\bar{z}_0,\theta) = H_{20}(\theta)\frac{z_0^2}{2} + H_{11}(\theta)z_0\bar{z}_0 + H_{02}(\theta)\frac{\bar{z}_0^2}{2} + \cdots. \tag{41}
$$

Substituting the corresponding series into Eq. (40) and comparing the coefficients, we obtain

$$
\begin{aligned}
(A - 2iw_0\tau_1^0)W_{20}(\theta) &= -H_{20}(\theta),\\
AW_{11}(\theta) &= -H_{11}(\theta).
\end{aligned}
\tag{42}
$$

From Eq. (40), we know that for $\theta\in[-1,0)$,

$$
\begin{aligned}
H(z_0,\bar{z}_0,\theta) &= -\bar{q}^* f_0 q(\theta) - q^*\bar{f}_0\bar{q}(\theta)\\
&= -p(z_0,\bar{z}_0)q(\theta) - \bar{p}(z_0,\bar{z}_0)\bar{q}(\theta).
\end{aligned}
\tag{43}
$$

Comparing the coefficients with Eq. (41), we obtain

$$H_{20}(\theta) = -p_{20}q(\theta) - \bar{p}_{02}\bar{q}(\theta). \tag{44}$$

$$H_{11}(\theta) = -p_{11}q(\theta) - \bar{p}_{11}\bar{q}(\theta). \tag{45}$$

From Eqs. (41) and (44) and the definition of A, it follows that

$$\dot{W}_{20}(\theta) = 2iw_0\tau_1^0 W_{20} + p_{20}q(\theta) + \bar{p}_{02}\bar{q}(\theta). \tag{46}$$

Notice that $q(\theta) = (1, \alpha)^\top e^{iw_0\tau_1^0\theta}$. Hence,

$$W_{20}(\theta) = \frac{ip_{20}}{w_0\tau_1^0}q(0)e^{iw_0\tau_1^0\theta} + \frac{i\bar{p}_{02}}{3w_0\tau_1^0}q(0)e^{-iw_0\tau_1^0\theta} + E_1e^{2iw_0\tau_1^0\theta}, \tag{47}$$

where $E_1 = (E_1^{(1)}, E_1^{(2)}) \in \mathbb{R}^2$ is a two-dimensional constant vector.

Similarly, from Eqs. (41) and (45), we can obtain

$$W_{11}(\theta) = -\frac{ip_{11}}{w_0\tau_1^0}q(0)e^{iw_0\tau_1^0\theta} + \frac{i\bar{p}_{11}}{3w_0\tau_1^0}q(0)e^{-iw_0\tau_1^0\theta} + E_2, \tag{48}$$

where $E_1 = (E_2^{(1)}, E_2^{(2)}) \in \mathbb{R}^2$ is also a constant vector.

In what follows, we shall seek appropriate E_1 and E_2 in (47) and (48). From the definition of A and (42), we obtain

$$\int_{-1}^{0} d\eta(\theta)W_{20}(\theta) = 2iw_0\tau_1^0 W_{20}(0) - H_{20}(0) \tag{49}$$

and

$$\int_{-1}^{0} d\eta(\theta)W_{11}(\theta) = -H_{11}(0), \tag{50}$$

where $\eta(\theta) = \eta(0, \theta)$. From (40) and (41), we have

$$H_{20} = -p_{20}q(0) - \bar{p}_{02}\bar{q}(0) + 2\tau_1^0 \begin{pmatrix} \alpha(\sigma_2\alpha - \sigma_1 e^{-iw_0\tau_1^0}) \\ \sigma_2\alpha + \sigma_1 e^{-iw_0\tau_1^0} \end{pmatrix} \tag{51}$$

and

$$H_{11} = -p_{11}q(0) - \bar{p}_{11}\bar{q}(0) + 2\tau_1^0 \begin{pmatrix} -\sigma_1 Re(\alpha e^{iw_0\tau_1^0} + \bar{\alpha}e^{-iw_0\tau_1^0}) \\ \sigma_1 Re(\alpha e^{iw_0\tau_1^0} + \bar{\alpha}e^{-iw_0\tau_1^0}) + \sigma_2 Re(\alpha + \bar{\alpha} + 2\alpha\bar{\alpha}) \end{pmatrix}. \tag{52}$$

Substituting (47) and (51) into (49) and noticing that

$$\begin{aligned}\left(iw_0\tau_1^0 I - \int_{-1}^{0} e^{iw_0\tau_1^0\theta} d\eta(\theta)\right) q(0) &= 0,\\ \left(-iw_0\tau_1^0 I - \int_{-1}^{0} e^{-iw_0\tau_1^0\theta} d\eta(\theta)\right) \bar{q}(0) &= 0,\end{aligned}$$

we obtain

$$2iw_0\tau_1^0 I - \int_{-1}^{0} e^{2iw_0\tau_1^0\theta} d\eta(\theta) = 2\tau_1 \begin{pmatrix} \alpha(\sigma_2\alpha - \sigma_1 e^{-iw_0\tau_1^0}) \\ \sigma_2\alpha + \sigma_1 e^{-iw_0\tau_1^0} \end{pmatrix},$$

which leads to

$$\begin{pmatrix} 2iw_0 + \sigma_1 E^* e^{-2iw_0\tau_1^0} & 0 \\ -\sigma_2 E^* + \beta_2 - \sigma_1 E^* e^{-2iw_0\tau_1^0} & 2iw_0 - \sigma_2 E^* + \beta_2 \end{pmatrix} E_1 = 2 \begin{pmatrix} \alpha(\sigma_2\alpha - \sigma_1 e^{-iw_0\tau_1^0}) \\ \sigma_2\alpha + \sigma_1 e^{-iw_0\tau_1^0} \end{pmatrix}.$$

It follows that

$$\begin{aligned} E_1^{(1)} &= \frac{\Delta_{11}}{\Delta_1};\\ E_1^{(2)} &= \frac{\Delta_{12}}{\Delta_1},\end{aligned}$$

where

$$\Delta_1 = \det \begin{pmatrix} v_1 & v_2 \\ v_3 & v_4 \end{pmatrix}, \Delta_{11} = 2\det \begin{pmatrix} X_1 & v_2 \\ X_2 & v_4 \end{pmatrix}, \Delta_{12} = 2\det \begin{pmatrix} v_1 & X_1 \\ v_3 & X_2 \end{pmatrix},$$

with

$$\begin{aligned} v_1 &= 2iw_0 + \sigma_1 E^* e^{-2iw_0\tau_1^0}; \quad v_2 = 0; \quad v_3 = -\sigma_2 E^* + \beta_2 - \sigma_1 E^* e^{-2iw_0\tau_1^0};\\ v_4 &= 2iw_0 - \sigma_2 E^* + \beta_2;\\ X_1 &= \alpha(\sigma_2\alpha - \sigma_1 e^{-iw_0\tau_1^0}); \quad X_2 = \sigma_2\alpha + \sigma_1 e^{-iw_0\tau_1^0}.\end{aligned}$$

Similarly, substituting (48) and (52) into (50), we can obtain

$$\begin{pmatrix} \sigma_1 E^* & 0 \\ -\sigma_1 E^* & -\sigma_2 E^* + \beta_2 \end{pmatrix} E_2 = 2 \begin{pmatrix} -\sigma_1 Re(\alpha e^{iw_0\tau_1^0} + \bar{\alpha} e^{-iw_0\tau_1^0}) \\ \sigma_1 Re(\alpha e^{iw_0\tau_1^0} + \bar{\alpha} e^{-iw_0\tau_1^0}) + \sigma_2 Re(\alpha + \bar{\alpha} + 2\alpha\bar{\alpha}) \end{pmatrix}.$$

It follows that

$$E_2^{(1)} = \frac{\Delta_{21}}{\Delta_2},$$

$$E_2^{(2)} = \frac{\Delta_{22}}{\Delta_2},$$

where

$$\Delta_2 = \det \begin{pmatrix} m_1 & m_2 \\ m_3 & m_4 \end{pmatrix},$$
$$\Delta_{11} = 2 \det \begin{pmatrix} Y_1 & m_2 \\ Y_2 & m_4 \end{pmatrix},$$
$$\Delta_{12} = 2 \det \begin{pmatrix} m_1 & Y_1 \\ M_3 & Y_2 \end{pmatrix},$$

with

$$m_1 = \sigma_1 E^*; \quad m_2 = 0; \quad m_3 = -\sigma_1 E^*; \quad m_4 = -\sigma_2 E^* + \beta_2;$$
$$Y_1 = -\sigma_1 Re(\alpha e^{iw_0\tau_1^0} + \bar{\alpha} e^{-iw_0\tau_1^0}); \quad Y_2 = \sigma_1 Re(\alpha e^{iw_0\tau_1^0} + \bar{\alpha} e^{-iw_0\tau_1^0}) + \sigma_2 Re(\alpha + \bar{\alpha} + 2\alpha\bar{\alpha}).$$

Therefore, we can determine W_{20} and W_{11} from (47) and (48). Furthermore, we can determine p_{21}. Therefore, each p_{ij} in (33) is determined by the parameters and delays. Thus, we can compute the following values:

$$\begin{aligned} C_2(0) &= \frac{i}{2w_0\tau_1^0}\left(p_{20}p_{11} - 2|p_{11}|^2 - \frac{|p_{02}|^2}{3}\right) + \frac{p_{21}}{2}, \\ \mu_2 &= -\frac{Re\,(C_2(0))}{Re\left(\lambda'(\tau_1^0)\right)}, \\ \gamma_2 &= 2Re\,(C_2(0)), \\ T_2 &= -\frac{Im\,(C_2(0)) + \mu_2 Im\left(\lambda'(\tau_1^0)\right)}{w_0\tau_1^0}, \end{aligned} \tag{53}$$

which determine the quantities of bifurcating periodic solution in the center manifold at the critical value τ_1^0. We have the following result.

Theorem 5.2 (Hassard et al. [11]) *In Eq. (53), the sign of μ_2 determines the direction of the Hopf bifurcation. If $\mu_2 > 0$, then the Hopf bifurcation is supercritical and the bifurcating periodic solutions exist for $\tau_1 > \tau_1^0$. If $\mu_2 < 0$, then the bifurcation is subcritical and the bifurcating periodic solutions exist for $\tau_1 < \tau_1^0$. γ_2 determines the stability of the bifurcating periodic solutions: The bifurcating periodic solutions are stable if $\gamma_2 < 0$ and unstable if $\gamma_2 > 0$. T_2 determines the period of the bifurcating periodic solutions. The period increases if $T_2 > 0$ and decreases if $T_2 < 0$.*

5.2.3 Stability Analysis at Equilibrium F_3

When $\tau_1 > 0$ and $\tau_2 = 0$, the characteristic equation at $F_3 = \left(\frac{\beta_1}{\sigma_1}, \frac{\beta_2}{\sigma_2}\right)$ is given by

$$\Delta(\lambda, \tau_1) = \lambda^2 + p_1\lambda + (s_1\lambda + q_1)\, e^{-\lambda\tau_1} = 0, \tag{54}$$

where $p_1 = \sigma_2(N - D^* - E^*) > 0, s_1 = \sigma_1 E^*,$ and $q_1 = \sigma_1\sigma_2 E^*(N - D^* - E^*)) > 0$.

Hopf bifurcation

Using the same methodology as in the previous section, we have the following theorem:

Theorem 5.3 *The positive equilibrium F_3 is asymptotically stable if $\tau_1 \in [0, \tau_1^*)$ and unstable for $\tau_1 > \tau_1^*$. Furthermore, then system 2 undergoes a Hopf bifurcation at equilibrium F_3 when $\tau_1 = \tau_1^*$.*

Proof Since Eq. (54) has the same form as that of Eq. (6), by analogy we get the critical values τ_{1j} of τ_1 for the equilibrium F_3 defined by

$$\tau_{1j} = \frac{1}{w_0}\arccos\left(\frac{q_1 w_0^2 - p_1 s_1 w_0^2}{s_1^2 w_0^2 + q_1^2}\right) + \frac{2\pi j}{w_0},\ j = 0, 1, 2, .. \tag{55}$$

And we have

$$\begin{aligned} sign\left\{\frac{d(Re\lambda(\tau_1))}{d\tau_1}\right\}\Big|_{\lambda=iw_0} &= sign\left\{Re\left(\frac{d\lambda}{d\tau_1}\right)^{-1}\right\}, \\ &= sign\left\{\frac{w_0^2}{w_0^4 + p_1^2 w_0^2} + \frac{q_1^2}{w_0^2(s_1^2 w_0^2 + q_1)}\right\}. \end{aligned}$$

Since $q_1 > 0$, we have $\frac{d}{d\tau_1}(Re\lambda(\tau_1)) > 0$. □

Direction and stability of the Hopf bifurcation

For the direction and stability of the Hopf bifurcation, we use the same methodology as for the equilibrium F_2. We just replace E^* by $E_3^* = \frac{\beta_2}{\sigma_2}$. Following the same

process until the end, we get the coefficients of bifurcation. Then, we have the following theorem:

Theorem 5.4 *There exist three real numbers μ_3, γ_3, and T_3 such that: if $\mu_3 > 0$, the Hopf bifurcation is supercritical and the bifurcating periodic solutions exist for $\tau_1 > \tau_1^*$, if $\mu_3 < 0$, the bifurcation is subcritical and the bifurcating periodic solutions exist for $\tau_1 < \tau_1^*$. The bifurcating periodic solutions are stable if $\gamma_3 < 0$ and unstable if $\gamma_3 > 0$. The period increases if $T_3 > 0$ and decreases if $T_3 < 0$.*

In the next section, we explore the case when $\tau_1 = 0$ and $\tau_2 > 0$.

5.3 Stability Analysis When $\tau_1 = 0$ and $\tau_2 > 0$

When $\tau_1 > 0$ and $\tau_2 = 0$, the characteristic equations at $F_1 = (N, 0)$ and $F_2 = \left(N, N - \dfrac{\beta_1}{\sigma_1}\right)$ are, respectively, given by

$$\lambda^2 + (\sigma_1 N - \beta_1 - \beta_2)\lambda + \beta_2(\beta_1 - \sigma_1 N) = 0$$

$$\lambda^2 + \left(\beta_2 + (\sigma_1 - \beta_2)E^*\right)\lambda + \sigma_1 E^*((\beta_2 - \sigma_2 E^*) = 0.$$

The characteristic equations are independent of the delay τ_2, and then F_1 and F_2 retain their stability when $\tau_1 = 0$ and $\tau_2 > 0$.

The characteristic equation at $F_3 = \left(\dfrac{\beta_1}{\sigma_1}, \dfrac{\beta_2}{\sigma_2}\right)$ is given by

$$\Delta(\lambda, \tau_2) = \lambda^2 + p\lambda + (s\lambda + q)e^{-\lambda\tau_2} = 0, \tag{56}$$

where $p_2 = \sigma_1 E^* > 0$, $s_2 = \sigma_2(N - D^* - E^*) > 0$, and $q_2 = \sigma_1\sigma_2 E^*(N - D^* - E^*)$.

For $w > 0$, iw being a root of (56), it follows that

$$\begin{cases} w^2 = q_2\cos(w\tau_2) + s_2 w\sin(w\tau_2), \\ pw = -s_2 w\cos(w\tau_2) + q_2\sin(w\tau_2), \end{cases} \tag{57}$$

which lead to

$$w^4 - (s_2^2 - p_2^2)w^2 - q_2^2 = 0. \tag{58}$$

Let $\Delta = (s_2^2 - p_2^2)^2 + 4q_2^2$. Since $\Delta > 0$ and $-q_2^2 < 0$, then Eq. (58) has only one positive root $w_+ = \dfrac{\sqrt{2}}{2}\left[s_2^2 - p_2^2 + \sqrt{\Delta}\right]^{\frac{1}{2}}$.
From (57), we can obtain

$$\tau_{2j} = \frac{1}{w_+} \arccos\left(\frac{(q_2 - p_2 s_2) w_+^2}{s_2^2 w_+^2 + q_2^2}\right) + \frac{2\pi j}{w_+}, \; j = 0, 1, 2, \cdots . \tag{59}$$

Denote by $\lambda(\tau_2) = \alpha(\tau_2) + iw(\tau 2)$ the root of Eq. (56) such that $\alpha(\tau_{2j}) = 0$, $w(\tau_{2j}) = w_+$.

Substituting $\lambda(\tau_2)$ into the left-hand side of (56) and differentiating with respect to τ_2, we have

$$\left[\frac{d\lambda}{d\tau_2}\right]^{-1} = \frac{2\lambda + p_2}{\lambda(s_2\lambda + q_2)e^{-\lambda\tau_1}} + \frac{s_2}{(s_2\lambda + q_2)} - \frac{\tau_2}{\lambda}, \tag{60}$$

which leads to

$$\begin{aligned}\left\{\frac{d(Re\lambda(\tau_1))}{d\tau_2}\right\}\Big|_{\lambda = iw_+} &= \left\{Re\left(\frac{d\lambda}{d\tau_2}\right)^{-1}\right\}, \\ &= \frac{1}{w_+^2 + p_2^2} + \frac{q_2^2}{w_+^2(s_2^2 w_+^2 + q_2^2)} > 0.\end{aligned}$$

According to the above analysis and Ruan et al. [26], we have the following results.

Theorem 5.5 *The positive equilibrium F_3 is asymptotically stable if $\tau_2 \in [0, \tau_2^0)$, and unstable for $\tau_2 > \tau_2^0$. Furthermore, the system 2 undergoes a Hopf bifurcation at equilibrium F_3 when $\tau_2 = \tau_2^0$.*

Remark 5.2 We notice that the direction of the bifurcation is obtained by replacing τ_1 by τ_2 in the proof of the bifurcation direction of the equilibrium F_2.

5.4 Stability Analysis of Equilibrium F_3 When $\tau_1 > 0$ and $\tau_2 > 0$

From the above discussion, we see that F_1 is independent of the delays τ_1 and τ_2, and F_2 is dependent only on the delay τ_1. Therefore, when $\tau_1 > 0$ and $\tau_2 > 0$, we just consider the equilibrium F_3 that depends on both the delays τ_1 and τ_2.

When $\tau_1 > 0$ and $\tau_2 > 0$, at the equilibrium F_3, the characteristic equation is

$$\Delta(\lambda, \tau_1, \tau_2) = P_0(\lambda) + P_1(\lambda)e^{-\lambda\tau_1} + P_2(\lambda)e^{-\lambda\tau_2} + P_3(\lambda)e^{-\lambda(\tau_1+\tau_2)} = 0, \tag{61}$$

and the coefficients become $P_0(\lambda) = \lambda^2$, $P_1(\lambda) = \sigma_1 E^*\lambda = x_1\lambda$, $P_2(\lambda) = \sigma_2(N - D^* - E^*)\lambda = x_2\lambda$, and $P_3(\lambda) = \sigma_1 E^*\sigma_2(N - D^* - E^*) = x_1 x_2$.

In what follows, we will use the methodology developed by X. Lin and H. Wang [18] to analyze (61) in our special case when $P_0(\lambda)$ is quadratic, $P_1(\lambda)$ and $P_2(\lambda)$ are linear, and $P_3(\lambda)$ is constant.

5.4.1 Stability Switching Curves

We will study the change of the number of zeros of (61) on $\mathbb{C}_+$, as the delays (τ_1, τ_2) vary on $\mathbb{R}^2_+$. The following lemma guarantees the continuity of the zeros with respect to the delay parameters.

Lemma 5.2 *As the delays (τ_1, τ_2) continuously vary within $\mathbb{R}^2_+$, the number of zeros (counting multiplicity) of $\Delta(\lambda, \tau_1, \tau_2)$ on $\mathbb{C}_+$ can change only if a zero appears on or cross the imaginary axis.*

The proof of this lemma can be found in any book on functional differential equations, for example, in Kuang [15], Smith [27].

From the above lemma, to study stability switching, we wish to have purely imaginary characteristic roots.

We assume that $\lambda = iw (w > 0)$. Substituting this into (61), we get

$$\Delta(iw, \tau_1, \tau_2) = \left(P_0(iw) + P_1(iw)e^{-iw\tau_1}\right) + \left(P_2(iw) + P_3(iw)e^{-iw(\tau_1}\right)e^{-iw\tau_2}. \tag{62}$$

Since $\left|e^{-iw\tau_2}\right| = 1$, we have

$$\left|P_0 + P_1 e^{-iw\tau_1}\right| = \left|P_2 + P_3 e^{-iw\tau_1}\right|, \tag{63}$$

which is equivalent to

$$\left(P_0 + P_1 e^{-iw\tau_1}\right)\left(\bar{P}_0 + \bar{P}_1 e^{iw\tau_1}\right) = \left(P_2 + P_3 e^{-iw\tau_1}\right)\left(\bar{P}_2 + \bar{P}_3 e^{iw\tau_1}\right),$$

where $P_0 = -w^2$, $P_1 = ix_1 w$, $P_2 = ix_2 w$, and $P_3 = x_1 x_2$.

After simplification, we obtain

$$\begin{aligned} &|P_0|^2 + |P_1|^2 + 2Re\left(P_0\bar{P}_1\right)\cos(w\tau_1) - 2Im\left(P_0\bar{P}_1\right)\cos(w\tau_1) \\ &= |P_2|^2 + |P_3|^2 + 2Re\left(P_2\bar{P}_3\right)\cos(w\tau_1) - 2Im\left(P_2\bar{P}_3\right)\cos(w\tau_1). \end{aligned}$$

Thus,

$$|P_0|^2 + |P_1|^2 - |P_2|^2 - |P_3|^2 = 2A_1(w)\cos(w\tau_1) - 2B_1(w)\sin(w\tau_1), \tag{64}$$

where

$$\begin{aligned} A_1(w) &= Re\left(P_2\bar{P}_3\right) - Re\left(P_0\bar{P}_1\right), \\ B_1(w) &= Im\left(P_2\bar{P}_3\right) - Im\left(P_0\bar{P}_1\right), \end{aligned}$$

with $P_0\bar{P}_1 = ix_1 w^3$ and $P_2\bar{P}_3 = ix_1 x_2^2 w$. Then,

$$A_1(w) = 0,$$
$$B_1(w) = x_1 w \left(x_2^2 - w^2\right).$$

If $w = x_2$, then

$$A_1(w) = B_1(w) = 0 \Leftrightarrow P_0 \bar{P}_1 = P_2 \bar{P}_3. \tag{65}$$

The right-hand side of (64) is 0 with any τ_1, and

$$|P_0|^2 + |P_1|^2 = |P_2|^2 + |P_3|^2. \tag{66}$$

Therefore, if $w = x_2$, then (65) and (66) are satisfied, and then all $\tau_1 \in \mathbb{R}_+$ are solutions of (63).

If $w \neq x_2$, then Eq. (64) becomes

$$|P_0|^2 + |P_1|^2 - |P_2|^2 - |P_3|^2 = -2B_1(w)\sin(w\tau_1). \tag{67}$$

Obviously, a sufficient and necessary condition for the existence of $\tau_1 \in \mathbb{R}_+$, satisfying the above equation, is

$$\left||P_2|^2 + |P_3|^2 - |P_0|^2 - |P_1|^2\right| \leq 2|B_1|. \tag{68}$$

Denote

$$\Omega = \left\{w \in \mathbb{R}_+ : \left||P_2|^2 + |P_3|^2 - |P_0|^2 - |P_1|^2\right| \leq 2|B_1|\right\}.$$

Lemma 5.3 *The set Ω is not empty.*

Proof It suffices to prove there exists $\bar{w} \in \mathbb{R}_+$ such that

$$|P_2|^2 + |P_3|^2 - |P_0|^2 - |P_1|^2 = 0, \tag{69}$$

and this equation is equivalent to

$$\bar{w}^4 + \left(a_1^2 - a_2^2\right)\bar{w}^2 - a_1^2 a_2^2 = 0. \tag{70}$$

Since the coefficient of w^4 is positive and $(a_1 a_2)^2$ is negative, using Descarte's change of sign rule, the above equation has a positive root. This achieves the proof. □

Let

$$\sin(\psi_1) = \frac{|P_2|^2 + |P_3|^2 - |P_0|^2 - |P_1|^2}{2|B_1|}, \ \psi \in [0, \pi],$$

and we have $\psi_1 = \omega\tau_1 + 2n_1\pi$ or $\psi_1 = \pi - \omega\tau_1 + 2n_1\pi$, $n_1 \in \mathbb{Z}$. Then,

$$\begin{cases} \tau^{+}_{1,n_1}(\omega) = \dfrac{\psi_1 + 2n_1\pi}{\omega}, \\ \tau^{-}_{1,n_1}(\omega) = \dfrac{-\psi_1 + (2n_1+1)\pi}{\omega}. \end{cases} \tag{71}$$

All the formulas in these steps can be obtained explicitly.

Once we get $\tau_1(\omega)$ given by (71), substitute it into (62), and we get an explicit formula for $\tau_2(\omega)$ unconditionally with each $\omega \in \Omega$, i.e.,

$$\tau^{\pm}_{2,n_1}(\omega) = \frac{1}{\omega}\arg\left\{-\frac{P_2 + P_3 e^{-i\omega\tau_1^{\pm}}}{P_0 + P_1 e^{-i\omega\tau_1^{\pm}}}\right\} + n_2\pi, \quad n_2 \in \mathbb{Z}. \tag{72}$$

Thus, the stability crossing curves are

$$\mathcal{T} = \left\{\left(\tau^{\pm}_{1,n_1}(\omega), \tau^{\pm}_{2,n_2}(\omega)\right) \in \mathbb{R}^2_+ : \omega \in \Omega, \ \ n_1, n_2 \in \mathbb{Z}\right\}. \tag{73}$$

5.4.2 Crossing Direction

Let $\lambda = \alpha + i\omega$. Then by the implicit function theorem, τ_1, τ_2 can be expressed as functions of α and ω under some non-singular condition. For symbolic convenience, denote $\tau_3 = \tau_1 + \tau_2$.
Define

$$\begin{aligned} R_0 &= \left.\frac{\partial Re(\Delta(\lambda,\tau_1,\tau_2))}{\partial\alpha}\right|_{\lambda=i\omega} \\ &= Re\left\{P_0'(i\omega) + \sum_{k=1}^{3}\left(P_k'(i\omega) - \tau_k P_k(i\omega)\right)e^{-i\omega\tau_k}\right\} \\ &= a_1\cos(\tau_1\omega) - a_1\tau_1\omega\sin(\tau_1\omega) + a_2\cos(\tau_2\omega) - a_2\tau_2\omega\sin(\tau_2\omega) - a_1a_2\tau_3\cos(\tau - 3\omega), \end{aligned} \tag{74}$$

$$\begin{aligned} I_0 &= \left.\frac{\partial Im(\Delta(\lambda,\tau_1,\tau_2))}{\partial\alpha}\right|_{\lambda=i\omega} \\ &= Im\left\{P_0'(i\omega) + \sum_{k=1}^{3}\left(P_k'(i\omega) - \tau_k P_k(i\omega)\right)e^{-i\omega\tau_k}\right\}, \\ &= 2\omega - a_1\sin(\tau_1\omega) - a_1\tau_1\omega\cos(\tau_1\omega) - a_2\sin(\tau_2\omega) - a_2\tau_2\omega\cos(\tau_2\omega) + a_1a_2\tau_3\sin(\tau - 3\omega). \end{aligned} \tag{75}$$

Similarly, we have

$$\left.\frac{\partial Re(\Delta(\lambda,\tau_1,\tau_2))}{\partial\omega}\right|_{\lambda=i\omega} = -I_0, \tag{76}$$

$$\left.\frac{\partial Im(\Delta(\lambda,\tau_1,\tau_2))}{\partial\omega}\right|_{\lambda=i\omega} = R_0. \tag{77}$$

We also have

$$\begin{aligned} R_l &= \left.\frac{\partial Re(\Delta(\lambda,\tau_1,\tau_2))}{\partial \tau_l}\right|_{\lambda=i\omega} \\ &= Re\left\{-i\omega\left(P_l(i\omega)e^{-i\omega\tau_l} + P_3(i\omega)e^{-i\omega(\tau_1+\tau_2)}\right)\right\}, \end{aligned} \tag{78}$$

$$\begin{aligned} I_l &= \left.\frac{\partial Im(\Delta(\lambda,\tau_1,\tau_2))}{\partial \tau_l}\right|_{\lambda=i\omega} \\ &= Im\left\{-i\omega\left(P_l(i\omega)e^{-i\omega\tau_l} + P_3(i\omega)e^{-i\omega(\tau_1+\tau_2)}\right)\right\}, \end{aligned} \tag{79}$$

where $l = 1, 2$. From the derivation, $\mathcal{T}^{\pm k}_{n_1,n_2}$ are piecewise differentiable. By the implicit function theory, we have

$$\Delta(\omega) = \begin{pmatrix} \dfrac{\partial\tau_1}{\partial\alpha} & \dfrac{\partial\tau_1}{\partial\omega} \\ \dfrac{\partial\tau_2}{\partial\alpha} & \dfrac{\partial\tau_2}{\partial\omega} \end{pmatrix}_{\alpha=0,\ \omega\in\Omega} = \begin{pmatrix} R_1 & R_2 \\ I_1 & I_2 \end{pmatrix}^{-1} \begin{pmatrix} R_0 & -I_0 \\ I_0 & R_0 \end{pmatrix}. \tag{80}$$

The implicit function theorem applies as long as

$$\det\begin{pmatrix} R_1 & R_2 \\ I_1 & I_2 \end{pmatrix} = R_1 I_2 - R_2 I_1 \neq 0.$$

For any crossing curve $\mathcal{T}^{\pm k}_{n_1,n_2}$, we call the direction of the curve corresponding to increasing $\omega \in \Omega_k$ the positive direction, and the region on the left-hand (right-hand) side when we move in the positive direction of the curve the on the left (right). Since the tangent vector of $\mathcal{T}^{\pm k}_{n_1,n_2}$ along the positive direction is $\left(\dfrac{\partial\tau_1}{\partial\omega}, \dfrac{\partial\tau_2}{\partial\omega}\right)$, the normal vector of $\mathcal{T}^{\pm k}_{n_1,n_2}$ pointing to the right region is $\left(\dfrac{\partial\tau_2}{\partial\omega}, -\dfrac{\partial\tau_1}{\partial\omega}\right)$. As we know, a pair of complex characteristic roots across the imaginary axis to the right on thr complex plane as α increases from negative to positive through 0, thus (τ_1, τ_2) moves along the direction $\left(\dfrac{\partial\tau_1}{\partial\alpha}, \dfrac{\partial\tau_2}{\partial\alpha}\right)$. As a consequence, we can conclude that if

$$\begin{aligned} \delta(\omega) &= \left(\frac{\partial\tau_1}{\partial\alpha}, \frac{\partial\tau_2}{\partial\alpha}\right)\cdot\left(\frac{\partial\tau_2}{\partial\omega}, -\frac{\partial\tau_1}{\partial\omega}\right) \\ &= \frac{\partial\tau_1}{\partial\alpha}\frac{\partial\tau_2}{\partial\omega} - \frac{\partial\tau_2}{\partial\alpha}\frac{\partial\tau_1}{\partial\omega} \\ &= \det\Delta(\omega) > 0, \end{aligned} \tag{81}$$

the region on the right of $\mathcal{T}^{\pm k}_{n_1,n_2}$ has two more characteristic roots with positive real parts. On the other hand, if inequality (81) is reversed, then the region on the left has two more characteristic roots with positive real parts.
Since

$$\det\begin{pmatrix} R_0 & -I_0 \\ I_0 & R_0 \end{pmatrix} = R_0^2 + I_0^2 > 0,$$

we have

$$sign\ \delta(\omega) = sign\left\{R_1 I_2 - R_2 I_1\right\}. \tag{82}$$

Since $R_0 \neq 0$ and $I_0 \neq 0$, for any $(\tau_1^{\pm}, \tau_2^{\pm}) \in \mathcal{T}^{\pm k}_{n_1,n_2}$, we have

$$P_2(i\omega)e^{-iw(\tau_1^{\pm}-\tau_2^{\pm})} = -P_0(i\omega)e^{-iw\tau_1^{\pm}} - P_1(i\omega) - P_(i\omega)e^{-iw\tau_2^{\pm}}.$$

If $z_1 = R_1 + iI_1$, $z_2 = R_2 + iI_2$, we have $z_1 \times z_2 = (R_1R_2 - I_1I_2, R_1I_2 + R_2I_1)$. Then,

$$\begin{aligned}
R_1 I_2 - R_2 I_1 &= Im\Big\{\overline{-iw\left(P_1 e^{-iw(\tau_1^{\pm}} + P_3 e^{-iw(\tau_1^{\pm}+\tau_2^{\pm}}\right)} \\
&\quad \times -iw\left(P_2 e^{-iw(\tau_2^{\pm}} + P_3 e^{-iw(\tau_1^{\pm}+\tau_2^{\pm}}\right)\Big\} \\
&= \omega^2 Im\left\{\bar{P}_1 P_2 e^{-iw(\tau_1^{\pm}-\tau_2^{\pm})} + \bar{P}_1 P_3 e^{-iw\tau_2^{\pm}} + \bar{P}_3 P_2 e^{-iw\tau_1^{\pm}}\right\} \\
&= \omega^2 Im\left\{\left(P_2\bar{P}_3 - P_0\bar{P}_1\right)e^{iw\tau_1^{\pm}}\right\} \\
&= \omega^2 Im\left\{\left|P_2\bar{P}_3 - P_0\bar{P}_1\right| e^{i\frac{\pi}{2}} e^{iw\tau_1^{\pm}}\right\} \\
&= \omega^2 \left|P_2\bar{P}_3 - P_0\bar{P}_1\right| \sin(\tfrac{\pi}{2} + w\tau_1^{\pm}) \\
&= \omega^2 \left|P_2\bar{P}_3 - P_0\bar{P}_1\right| \cos(w\tau_1^{\pm}).
\end{aligned} \tag{83}$$

Hence, $\delta(\omega \in \Omega) = sign(\omega^2 \left|P_2\bar{P}_3 - P_0\bar{P}_1\right| \cos(w\tau_1^{\pm})$, and we have the following result.

Theorem 5.6 *For any $k = 1, 2, \cdots, N$.*

- *If $\cos(w\tau_1^{\pm}) < 0$, then the region on the right of $\mathcal{T}^{+k}_{n_1,n_2}$ ($\mathcal{T}^{-k}_{n_1,n_2}$) has two more (less) characteristic roots with positive real parts.*
- *If $\cos(w\tau_1^{\pm}) > 0$, then the region on the left of $\mathcal{T}^{+k}_{n_1,n_2}$ ($\mathcal{T}^{-k}_{n_1,n_2}$) has two more (less) characteristic roots with positive real parts.*

If we know the number of characteristic roots with positive real parts when $\tau_1 = \tau_2 = 0$, we can use criterion 81 to find the number of characteristic roots with positive real parts for any $(\tau_1, \tau_2) \in \mathbb{R}^2$. In this way, stability based on the characteristic equation is completely known.

In what follows, we present numerical simulations to illustrate the above results.

6 Numerical Simulations

In this section, we present some numerical results of the system (2) to illustrate the analytical predictions obtained in the previous section.

6.1 Numerical Examples When $\tau_1 = \tau_2 = 0$

We present the numerical results that illustrate analytical results obtained with $\tau_1 = \tau_2 = 0$. The system (2) is integrated using a nonstandard scheme method with the following set of parameter values: $N = 100$, $\beta_1 = 0.6$, $\beta_2 = 0.35$, $\sigma_1 = 0.01$, and $\sigma_2 = 0.07$. For these parameter values, the conditions for stability for F_2 are satisfied and the solutions converge to $(60, 40)$ for different initial conditions illustrated by Fig. 3a, b). On the other hand, Fig. 3c, d) shows that the solutions converge to the equilibrium F_3 with the set of parameter values: $N = 200$, $\beta_1 = 0.6$, $\beta_2 = 0.7$, $\sigma_1 = 0.01$, $\sigma_2 = 0.07$ that assume its conditions for stability.

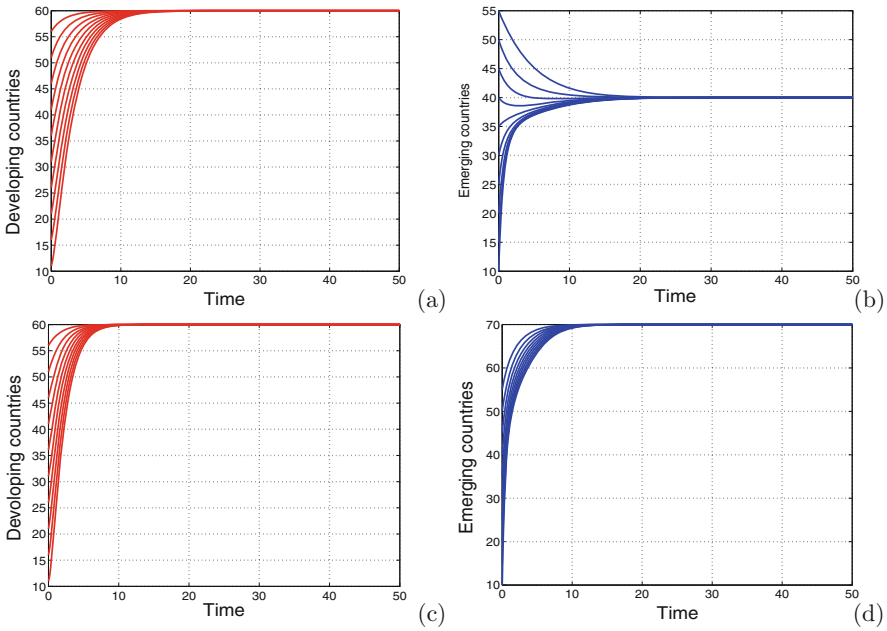

Fig. 3 Plot of trajectories of system 2. For different initial conditions, solutions converge to the stable equilibrium $F_2 = (60, 40)$ (**a**), (**b**) and to the stable equilibrium $F_3 = (60, 70)$ (**c**), (**d**)

6.2 *Numerical Examples When $\tau_1 > 0$, $\tau_2 > 0$*

From Sect. 5, we may determine the direction of a Hopf bifurcation and the stability of the bifurcation periodic solutions. We first consider the case when $\tau_1 > 0$ and $\tau_2 = 0$. From the set of parameter values $N = 100$, $\beta_1 = 0.6$, $\beta_1 = 0.7$, $\sigma_1 = 0.01$, and $\sigma_2 = 0.01$, we obtain that $\omega_0 = 0.4$, $\tau_1^0 \approx 3.927$, and τ_1^0 is the critical value for Hopf bifurcation. It follows from Theorem 5.1 that if $\tau_1 \in [0, 3.927)$, the equilibrium $F_2 = (60, 40)$ is asymptotically stable. System (2) undergoes a Hopf bifurcation at $\tau_1 \approx 3.927$. Furthermore, using Theorem 5.2, after simple computation, we have $C_2(0) = -0.0009 - 0.0023i$, $\mu_2 = 0.0268 > 0$, $\gamma_2 = -0.0019 < 0$, and $T_2 = 0.0013 > 0$. Therefore, the Hopf bifurcation of system (2) is supercritical, and the bifurcation periodic solutions are stable. These conclusions are verified by the numerical simulation in Figs. 4 and 5.

We consider the positive equilibrium $F_3 = (60, 70)$, obtained with the set of parameter values: $N = 200$, $\beta_1 = 0.6$, $\beta_1 = 0.7$, $\sigma_1 = 0.01$, and $\sigma_2 = 0.01$. We have $\omega_{01} = 0.1$ and $\tau_1^* = 2,244$. Thus, the positive equilibrium $F_3 = (60, 70)$ is stable when $\tau_1 < \tau_1^*$ as is illustrated by computer simulations (see Fig. 6). When τ_1 passes through the critical value $\tau_1^* = 2,244$, the positive equilibrium $F_3 = (60, 70)$ loses its stability and a Hopf bifurcation occurs, i.e., a family of periodic solutions bifurcate from the positive equilibrium $F_3 = (60, 70)$. Since $\mu_2 > 0$ and $\gamma_2 < 0$,

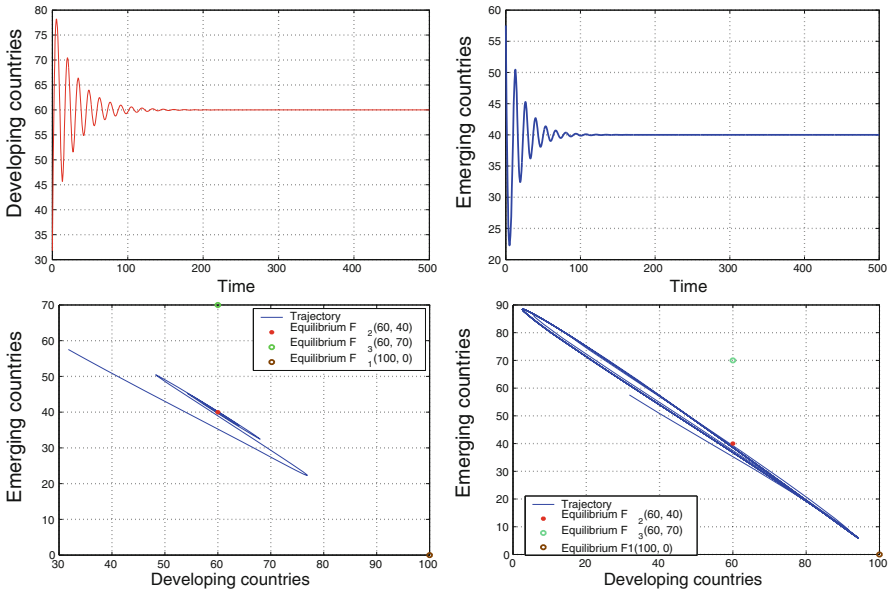

Fig. 4 Behavior and phase portrait of the system (2), with $\tau_2 = 0$, $\tau_1 = 3.20 < \tau_1^0 \approx 3.927$. The positive equilibrium $F_2 = (60, 40)$ is asymptotically stable. Hopf bifurcation occurs from the positive equilibrium F_2 when $\tau_1 = \tau_1^0$

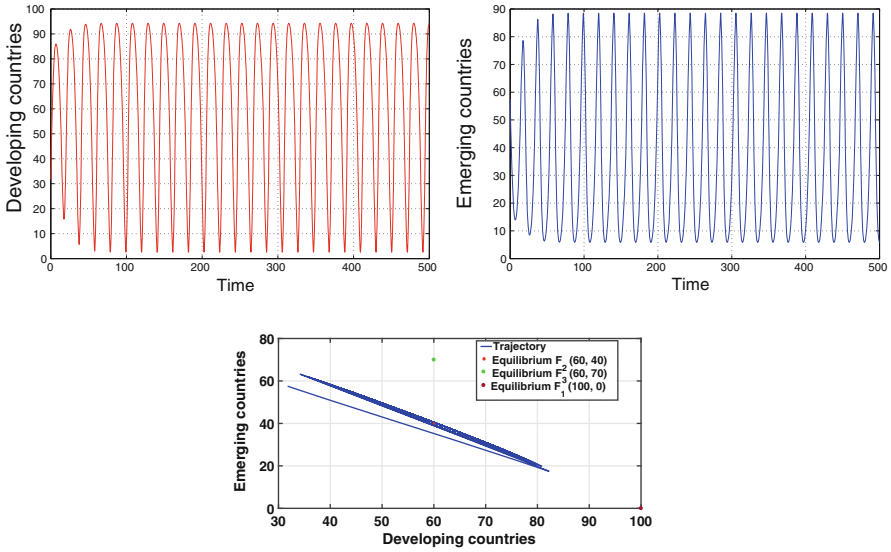

Fig. 5 Behavior and phase portrait of the system (2), with $\tau_2 = 0$, $\tau_1 = 4.9 > \tau_1^0 \approx 3.927$. The positive equilibrium $F_2 = (60, 40)$ is unstable

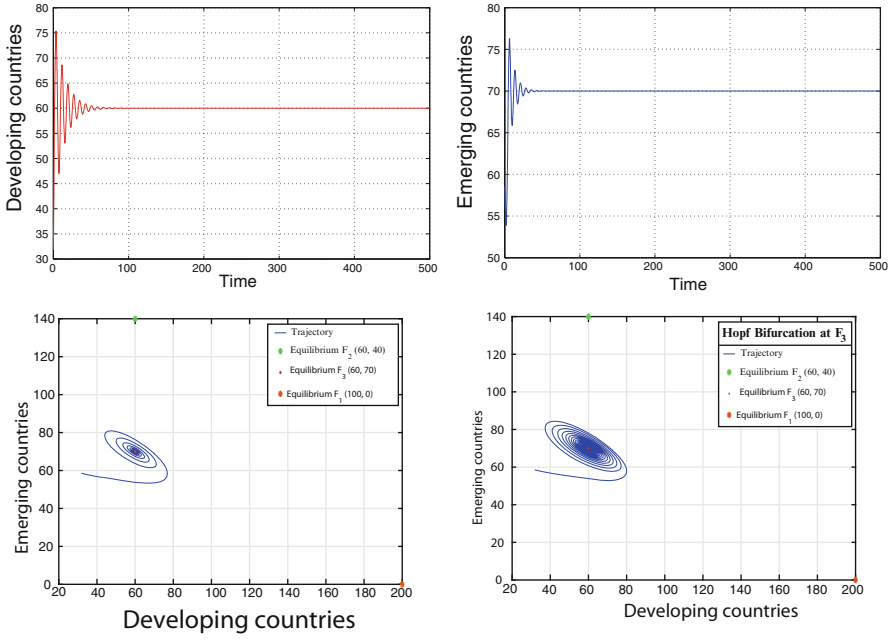

Fig. 6 Behavior and phase portrait of the system (2), with $\tau_2 = 0$, $\tau_1 = 1.7 < \tau_1^* \approx 2241$. The positive equilibrium $F_3 = (60, 70)$ is asymptotically stable. Hopf bifurcation occurs from the positive equilibrium F_3 when $\tau_1 = \tau_1^0$

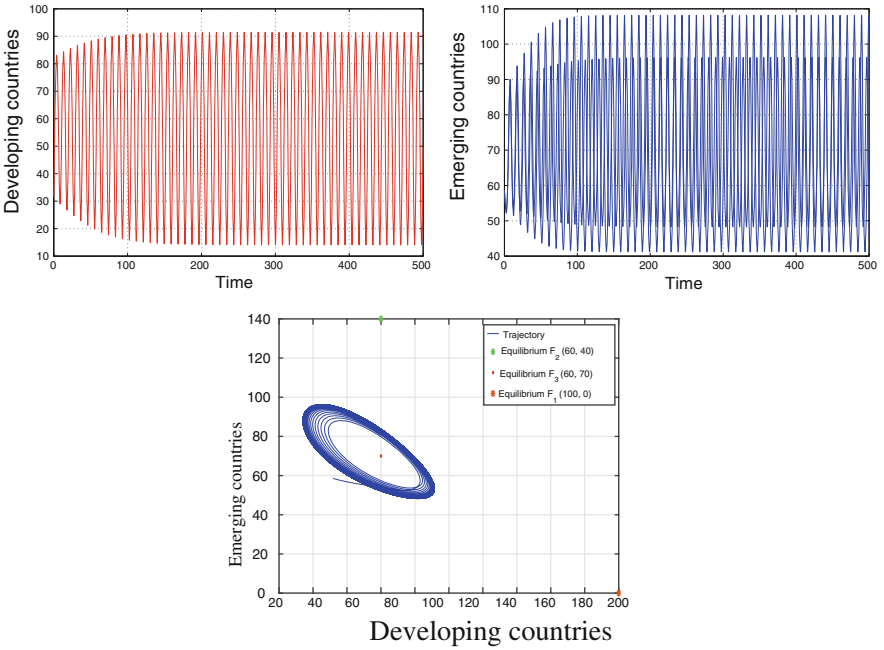

Fig. 7 Behavior and phase portrait of the system (2), with $\tau_2 = 0$, $\tau_1 = 2.4 > \tau_1^* \approx 2241$. The positive equilibrium $F_3 = (60, 70)$ is unstable

the direction of Hopf bifurcation is $\tau_1 > \tau_1^*$, and these bifurcating periodic solutions from $F_3 = (60, 70)$ at τ_1^* are stable, which is depicted in Fig. 7.

If $\tau_1 = 0$ and $\tau_2 > 0$, just the equilibrium F_3 depends on τ_2. From the set of parameter values $N = 200$, $\beta_1 = 0.6$, $\beta_1 = 0.7$, $\sigma_1 = 0.01$, and $\sigma_2 = 0.01$, we obtain $\omega_{02} = 0.7$ and $\tau_2^0 = 2,244$. Thus, the positive equilibrium $F_3 = (60, 70)$ is stable when $\tau_2 < \tau_2^0$ as is illustrated by computer simulations (see Fig. 8). System (2) undergoes a Hopf bifurcation at $\tau_2 \approx 2,244$, and F_3 becomes unstable when $\tau_2 > \tau_2^0$ (see Fig. 9).

And finally when $\tau_1 > 0$ and $\tau_2 > 0$, we choose the same parameter values as in Fig. 9. $F(\omega)$ has only one root $\omega = 0.7$ and $\Omega = \{\omega\}$ (see Fig. 10). When (τ_1, τ_2) varies within a region formed by two curves, the number of characteristic roots with positive real parts stays the same. It can change only when (τ_1, τ_2) crosses the curve $\tau_2(\tau_1)$. Hence from Fig. 11, the coexistence equilibrium F_3 is stable if and only if (τ_1, τ_2) is between the region delimited by τ_1 and τ_2 of the (τ_1, τ_2)-plane.

7 Conclusion and Discussion

In this chapter, we described a process of economic development using a compartmental approach. We have proposed a simple model of compartment characterized by countries based on their economic status. The model is an extension of our

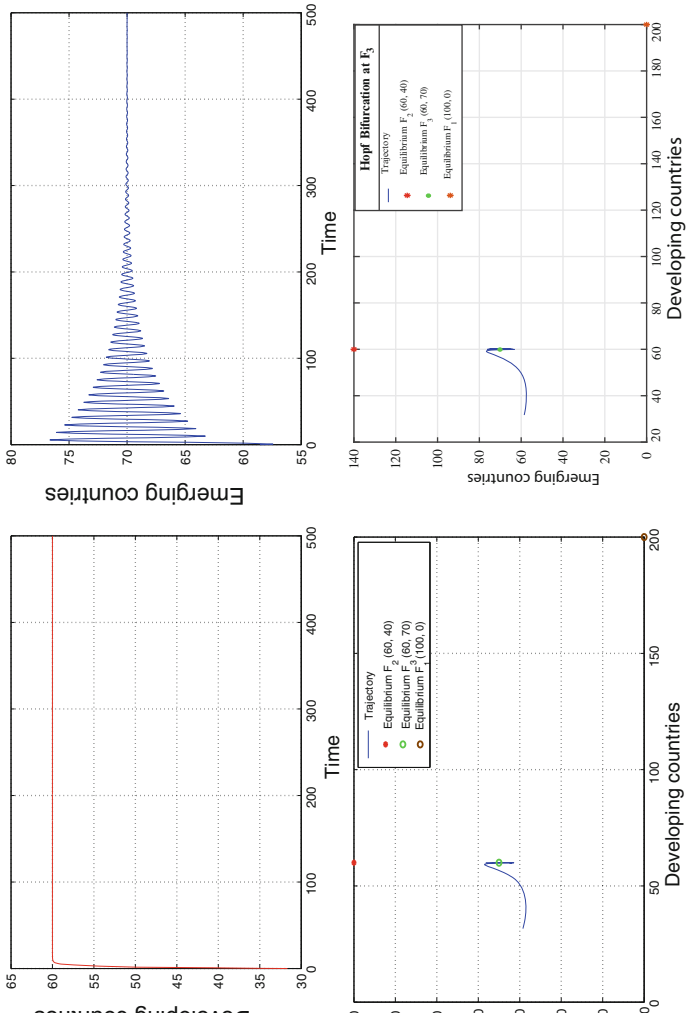

Fig. 8 Behavior and phase portrait of the system (2), with $\tau_1 = 0$, $\tau_2 = 2.20 < \tau_2^0 \approx 2244$. The positive equilibrium $F_3 = (60, 70)$ is asymptotically stable. Hopf bifurcation occurs from the positive equilibrium F_3 when $\tau_2 = \tau_2^0$

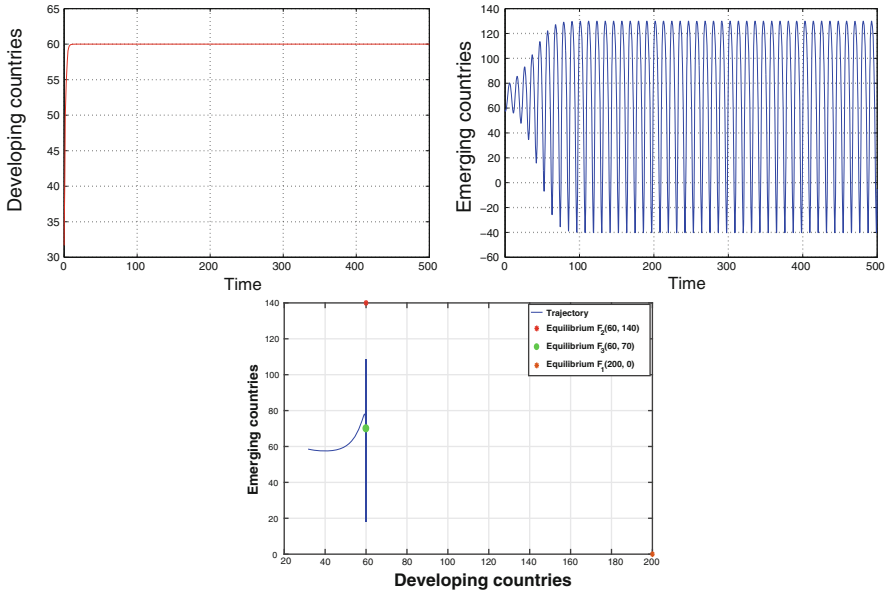

Fig. 9 Behavior and phase portrait of the system (2), with $\tau_1 = 0$, $\tau_2 = 2.7 > \tau_2^0 \approx 2244$. The positive equilibrium $F_3 = (60, 70)$ is unstable

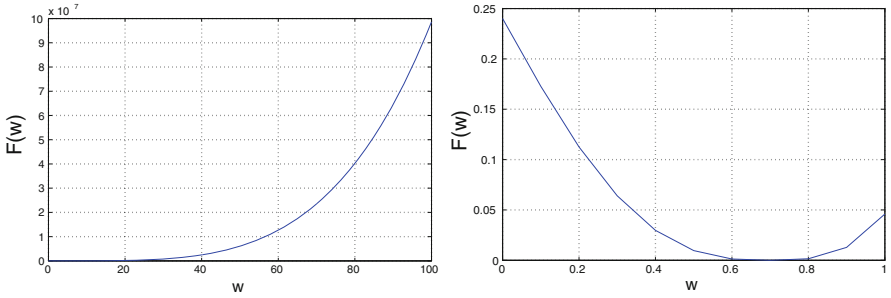

Fig. 10 Graph of F(w)

previous model, to which country collaboration and two delays have been added. The main result of this exercise consists in showing how the number of countries of each compartment changes from period to period. Thus, we have shown, under certain conditions, that it is possible to reduce the number of developing countries and thus increase the number of emerging and advanced countries.

The model reflects collaboration between developing and emerging countries on the one hand and between emerging and advanced countries on the other. The model also assumes that this collaboration is done without counterpart. Nevertheless, the implementation of the compartmental approach in a model that is as simple as possible can be useful to understand better the process of economic development and can be used by the fiscal policy authority to improve their development policy.

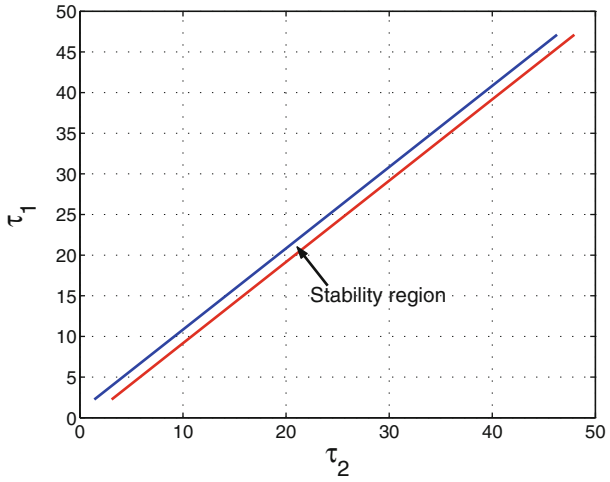

Fig. 11 Plot of switching curve

Our mathematic model describes complex macro-economic realities. Through the bifurcations, we were able to analyze the effect of collaboration on economic growth. We have seen that external inputs contribute to strengthening the growth of developing countries over a period of about 4 years and 2 years for emerging countries. These results confirm the positive short-term effect of openness on the economic system of developing and emerging countries. Thus in terms of economic implication, it is important for developing and emerging countries to put in place economic strategies that can make them independent of external inputs in the medium and long term to ensure the improvement of their GDP per capita and to progress to higher development phases.

In the future, we intend to build a more complex model by taking into account all kinds of collaboration and by including the limits of these collaborations.

Acknowledgments This research is supported by the European Union through the ERMIT project. We thank our colleagues from the University of Yaounde I who provided insights and expertise that greatly assisted the research. My thanks also go to Professor Gian Italo Bisch for his useful suggestions.

References

1. Anderson D.H. (1983). Compartmental modeling and tracer kinetics. Springer-Verlag.
2. Artzrouni M. and Tramontana F. (2013). The debt trap: a two-compartment train wreck. MPRA Paper No. 47578, posted 13.
3. Bélair J. and Mackey M. C. (1989). Consumer memory and price fluctuations in commodity markets: an integrodifferential model. Journal of Dynamics and Differential Equations, vol. 1, no. 3, pp. 299–325.

4. Burnside, C. and Dollar, D. (2000). Aid, policies and growth. American Economic Review Vol. 90(4), pp. 847–869.
5. Camelia M. and Sanjay G. (2009). Development Aid and Economic Growth: A Positive Long-Run Relation. International Monetary Fund, WP/09/118.
6. Chen P. (2006). An Investigation of Openness and Economic Growth Using Panel Estimation. University of Pretoria, Working Paper: 2006–22.
7. Collier, P. and Dollar D. (2002). Aid allocation and poverty reduction. European Economic Review, Vol. 46(8), pp. 1475–1500.
8. Culshaw R. V. and Ruan S. (2000). A delay differential equation model of HIV infection of CD4 T cells. Mathematical Biosciences. Elsevier, 165, pp 27–39.
9. Gurtner B. (2010). The financial and economic crisis and developing countries. United Nations New York and Geneva, p 201–207.
10. Hansen H. and Tarp F. (2001). Aid and growth regressions. Journal of Development Economics, Vol. 64(2), pp. 547–570.
11. Hassard B., Kazarino D. and Wan Y. (1981). Theory and Applications of Hopf Bifurcation. Cambridge University Press, Cambridge.
12. Huang C., Peng C., Chen X., and Wen F. (2013). Dynamics Analysis of a Class of Delayed Economic Model. Hindawi Publishing Corporation Abstract and Applied Analysis.
13. Intriligator M.D. (2002).Mathematical Optimization and Economic Theory. Society for Industrial and Applied Mathematics Philadelphia, PA, USA.
14. Jacquez J. A. (1972). Compartmental analysis in Biology biology and Medicinemedicine. Elsevier New York.
15. Kuang Y. (1993). Delay Differential Equations with Applications in Population Dynamics. Academic Press, Boston.
16. Kumar T.K. (1965). Models of optimization and control in the theory of economic policy. Retrospective Theses and Dissertations. 3305.
17. Ladde G. S. (1976). Cellular systems I. Stability of chemical systems. Math. Biosci. 29, 309–330.
18. Lin X. and Wang H. (2012). Stability analysis of delay differential equations with two discrete delays. Canadian Applied Mathematics Quarterly, Volume 20, Number 4.
19. Martin A. and Ruan S. (2001). Predator-prey models with delay and prey harvesting. J. Math. Biol. 43, pp.247–267.
20. Matis J. M., Patten B. C. and White G. C. (1979). Compartmental analysis of ecosystem models. International Cooperative Pub. House.
21. Matsumoto A. and Szidarovszky F. (2011). Delay differential neoclassical growth model. Journal of Economic behavior and Organization, vol. 78, no. 3, pp. 272–289.
22. Matsumoto A. and Szidarovszky F. (2012). Nonlinear delay monopoly with bounded rationality. Chaos, Solitons & Fractals, vol. 45, no.4, pp. 507–519.
23. Murray J. D. (1989). Mathematical biology. Springer - Verlag.
24. NDIONE, A. and ONANA, C. (2018). Economic Development development Processprocess: a compartmental analysis of a macroeconomic model. Journal of Progressive Research in Mathematics, 14(2), 2366–2372
25. Nicolis G. and Prigogine I. (1977). Self-organization in nonequilibrium systems. Wiley, New York.
26. Ruan S. and Wei J. (2003). On the zero of some transcendental functions with applications to stability of delay differential equations with two delays. Dynamics of Continuous, Discrete and Impulsive Systems Series A 10(1): 863–874.
27. Smith H. (2010). An Introduction to Delay Differential Equations with Applications to the Life Sciences. Springer, New York.
28. Schwab K., Xavier S. M. and Fiona P. (2016). The Global Competitiveness Report 2015–2016. World Economic Forum Geneva, Switzerland.
29. Schwab K., Xavier S. M. and Fiona P. (2007). The Global Competitiveness Report 2007–2008. World Economic Forum Geneva, Switzerland.

30. Solimano F., Bischi G.I., Bianchi M., Rossi L. and Magnani M. (1990). A nonlinear three-compartment model for the administration of 2',3'- dideoxycytidine by using red blood cells as bioreactors. Bulletin of Mathematical Biology, 52, 785–796.
31. Tramontana F., Gallegati M. (2010). Economics as a compartmental system: a simple macroeconomic example, Working Papers 1011, University of Urbino Carlo Bo, Department of Economics, Society & Politics – Scientific Committee – L. Stefanini & G. Travaglini, revised, 2010.
32. Vicente P., Carlos O. and Félix M. (2013). Quantifying the Benefits of International Scientific Collaboration. Journal of the American Society for Information Science and Technology, 64(2): 392–404.

Index

R. P. Mondaini (ed.), *Trends in Biomathematics: Chaos and Control in Epidemics, Ecosystems, and Cells*, https://doi.org/10.1007/978-3-030-73241-7